Modelling the Dynamics of Cellular Motility, from Adhesion Dynamics to Cellular Migration

Laurent MacKay

Doctor of Philosophy

Department of Physiology
McGill University
Montreal, Quebec, Canada

December 2020

A thesis submitted to McGill University in partial
fulfillment of the requirements of the degree of
Doctor of Philosophy

Abstract

Cellular migration is a complex phenomenon where cells displace themselves by integrating many intracellular processes that autonomously respond to motility cues in their environments. As it usually allows for the cells to carry out their biological functions in a specific location, it is considered essential to a number of physiological processes (e.g., embryonic development, wound healing, and immune responses). Defects in cellular migration are implicated in pathological conditions (e.g., immune disorders and cancer metastasis). Understanding the interdependencies of the various cellular processes and how they integrate external cues to produce motility is a challenging task, due to both the intrinsic complexity of the processes as well as the large variability in migration modes. Here we have focused on mathematical modeling of processes related to integrin-based adhesions, which are macromolecular complexes that serve as force-transmission points and signaling hubs during mesenchymal migration. We began by reviewing the literature of mathematical models of integrin-ligand bonds, and larger-scale models of adhesions that incorporate the molecular properties of integrins. We then developed a novel model of nascent adhesion formation that accounted for experimentally observed variations in integrin density, and predicted the mechanical conditions required for self-assembly of adhesions. Subsequently, we focused on cellular-scale models of motility and studied how the spatio-temporal dynamics of motility are influenced by two different adhesion-associated proteins, paxillin and VASP. First we studied how GTPase signaling can be used by a cell to produce a pattern formation system that defines its front and rear directions, and how adhesion-dependent signaling through paxillin influences this process. Pattern formation properties were studied using theoretical analysis and spatio-temporal simulations. The latter simulations were then coupled to a phenomenological model of cell motility, demonstrating that paxillin phosphorylation can directly increase motility of cells. Finally, in order to gain insight into a detailed spatio-temporal model of VASP-dependent actin-based protrusion dynamics, we derived a simplified model and characterized its full set of dynamics. Using this characterization, we then combined spatio-temporal simulations and a theoretical analysis of population-level statistics to identify how the model can be used to explain the poorly understood rough motility phenotype.

Abrégé

La migration cellulaire est un phénomène complexe par lequel les cellules se déplacent en intégrant de nombreux processus intracellulaires autonomes qui répondent aux signaux environnementaux de motilité. Comme elle permet généralement aux cellules de remplir une fonction biologique à un endroit spécifique, elle est considérée essentielle à plusieurs processus physiologiques dont le développement embryonnaire, la cicatrisation des plaies et les réponses immunitaires. Les défauts de migration cellulaire mènent à des états pathologiques dont les troubles immunitaires et les métastases cancéreuses. La compréhensions des processus cellulaires interdépendants et l'intégration des signaux externes menant à la motilité est une tâche ardue étant donné la complexité intrinsèque des processus et la grande variabilité des modes de migration. Ici, nous nous sommes concentrés sur la modélisation mathématique des processus liés aux adhérences à base d'intégrines, qui sont des complexes macromoléculaires servant de points de transmission de force et de centres de signalisation pendant la migration mésenchymateuse. L'étude a commencé par une revue de la littérature des modèles mathématiques de liaisons intégrine-ligand et les modèles d'adhérences à plus grande échelle qui intègrent les propriétés moléculaires des intégrines. Nous avons ensuite développé un nouveau modèle de formation d'adhérences naissantes qui incorpore des variations de densité d'intégrines observées expérimentalement, et prédit les conditions mécaniques requises pour l'auto-assemblage des adhérences. Nous avons ensuite etudié des modèles de motilité à l'échelle cellulaire et avons étudié la dynamique spatio-temporelle de la motilité et avons évalué l'influence de la paxilline et la VASP, deux protéines associées à l'adhésion. Nous avons d'abord étudié la signalisation par des GTPases comme mécanisme cellulaire permettant de produire un système de formation de motifs qui définit les directions avant et arrière de la cellule, et le rôle de la signalisation dépendante à la paxilline dans ce processus. Les propriétés de formation de motifs ont été étudiées à l'aide d'une analyse théorique et de simulations spatio-temporelles. Ces dernières simulations ont ensuite été couplées à un modèle phénoménologique de la motilité cellulaire, démontrant que la phosphorylation de la paxilline peut directement augmenter la motilité des cellules. Enfin, afin de mieux comprendre un modèle détaillé de la dynamique spatio-temporel de la protrusion cellulaire dépendante de la VASP, nous avons dérivé un modèle simplifié et caractérisé l'ensemble de dynamiques associées. En utilisant cette caractérisation, nous avons ensuite combiné des simulations spatio-temporelles et une analyse théorique des statistiques au niveau de la population ce qui a permis d'identifier comment le modèle permet d'expliquer le phénotype de « rough motility » qui étais mal compris jusqu'à présent.

Statement of Contributions

This thesis is comprised of four main chapters, each of which is based on an article that I co-authored. Chapters 1, 2, and 4 have been published in peer reviewed journals: [MK20], [MK19b], and [MLK20], respectively. Chapter 3 is currently in preparation to be submitted, and will likely constitute at least 2 publications. Chapter 1 is a literature review of mathematical models of integrin-based adhesions, and as such does not contain significant contributions to original knowledge. Below we have briefly summarized the contributions to original knowledge by chapter.

Chapter 2

- We developed a novel data analysis methodology, termed Conditional Expectation Analysis, that allows us to infer a constitutive relationship between two physical variables from histograms of their measurements. Such a relationship was then used to derive a model of nascent adhesion formation dynamics.
- This combination of modelling and data analysis contributed to the understanding of the molecular level organization of nascent adhesions, their macromolecular assembly dynamics in response to applied force, and provides a more physiologically-relevant description of their disassembly than previous models in the field.

Chapter 3

- We presented a deterministic macroscopic framework for understanding the spatio-temporal dynamics of chemical reactions, and use results from geometric singular perturbation analysis to show how one can systematically impose the conservation of matter when employing quasi-steady state assumptions.
  - This framework should be more approachable for non-mathematicians compared to what can be found in the literature, as it is based on the familiar concept of chemical reactions (rather than abstract mathematical formulation, formal definitions, proofs, and lemmas), it should be much more approachable for non-mathematicians.

- We extended the non-linear stability analysis termed local perturbation analysis (LPA) to better reconcile its results with observed pattern formation phenomenon.
- Using LPA, we demonstrated that a pattern-formation model published in [TBBK18] and fit to data from Chinese Hamster Ovary (CHO-K1) cell data lies inside a Turing unstable regime.
  - This allows simulated CHO-K1 cells to self-polarize (a finding that is consistent with experimental observations).
  - This regime is poorly studied in the field, but our findings suggest it could be highly relevant to the migration of some cell-types.

Chapter 4

- Using a model of cellular protrusion from [BAL+17], we were able to propose the dynamical origins underlying a poorly understood keratocyte motility phenotype, known as rough motility.
- We also demonstrated that the previously described waving regime is produced by canard explosion with orbits passing through a folded-saddle.
- We incorporated some mechanosensitive properties of nascent adhesions (discussed in Chapter 1) and identified novel parameter regimes that appear to be relevant for fibroblast-like cells.

I was responsible for writing all of the text in Chapters 1-4, and obtained significant feedback from my supervisor, Anmar Khadra. I was solely responsible for the development of the code in Chapters 2 and 4. Furthermore, the code in Chapter 3 can be found at `https://github.com/laurentmackay/CPM_RD_matlab`, and is the cumulative effort of Zhang Tan, Ashesh Momi, Ellie Zhang with myself contributing through guidance and extensive re-writes to speed up the computations. Etienne Lehman contributed significantly to the initial model analysis in Chapter 4.

Acknowledgments

I would like to state my overwhelming appreciation towards my PhD (and M. Sc.) supervisor, Professor Anmar Khadra, for continuing to work with me as his student. Professor Khadra immersed me in the fascinating world of dynamical systems, helped steer me back on track when I strayed into the never-ending rabbit holes of biological complexity, and has provided me with insightful feedback at every step of this PhD. For these reasons and more, I will forever be grateful.

I would like to extend my gratitude to my supervisory committee members, Professor Claire Brown, Professor Allen Erlicher, and Professor Michael Geuvara. They provided invaluable feedback on my work, that immensely helped Anmar and I check our mental blind-spots.

I would also like to thank my graduate program coordinator Rosie Vasile. The attention and care that she gives to all her students is unparalleled and deeply appreciated.

Finally, I would to thank my mysterious neighbour known only as the "Garden King" for his continued DJ-ing throughout the thesis writing process. His deafening tunes were unwanted and unrelenting, but inevitably he acted as the little drummer boy I never asked for.

Contents

List of Figures

List of Tables

List of Algorithms

0.1 General Introduction

Cellular migration is a process involved in many physiological contexts, including wound healing [JCX+14], embryonic development [FG09], and immune response [LAvA05]. In these scenarios, a population of cells need to migrate individually or collectively from one location to another in order to carry out a certain function. While nearly all cells exhibit some form of random undirected motility, migration specifically refers to the integration of motility cues by a cell to produce controlled motion. Defects in the regulation of migration have been implicated in neurodegenerative, (auto)immune , and cardiac disorders [WR12, BMW14, dADS17, KMT+12]; moreover, during cancer metastasis, tumor cells utilize their motility machinery to significantly increase the severity of the already pathological condition. One means by which cells achieve motility is by pulling/pushing on their environment through integrin-based adhesions [AE07]. The actin cytoskeleton, a network of filamentous structures that give the cell its rigidity, is mechanically linked to the external environment by these macromolecular complexes, allowing intracellular forces to be transmitted extracellular. In the context of integrin-based adhesions, the physical link between inside and out is provided by the integrin receptor [AON14]. Cells also form cadherin-based adhesions that behave in many ways quite similarly to integrin-based adhesions, but with cadherin receptors binding to proteins on the surface of other cells [PH10]. Thus cells can adhere to each other as well as to some of the structures found in connective tissue (e.g., β_1-integrins bind to collagen) and move throughout an organism to carry out (patho)physiological functions. Adhesions also serve as signaling hubs that, among other functions, promote cell survival and can guide cell differentiation through mechanotransduction pathways [HD09, HIKS+06, WFA05]. For these reasons, adhesion associated proteins have been considered as therapeutic targets in a wide-range of physiological contexts [LRNSS16, CCLSD10, KVM+20, WKFGL14].

The challenges that arise in understanding the function of the myriad of proteins involved in adhesion assembly and disassembly have helped to drive advances in spatio-temporal resolution of microscopy approaches [CLW+14, CCWS18, CKY+11, KSP+10, CW15], live-cell imaging conditions [EW14, KVM+20], and reporters/manipulators of biochemical activity and force [WHW+10, RCGRS09, GML+12, GHB+10]. Over the past three decades or so, this has lead to a wealth of knowledge on these topics, and a situation where one sometimes feels that they are “drowning in data, but starving for insights” [FB]. There is little doubt that this is partially due to the biochemical complexity of the system under study; there are approximately 150 proteins that make up the adhe-

some with a complex network of interactions responsible for the assembly and disassembly of adhesions [ZBIM+07]. To further complicate things, many of these proteins have overlapping functions with nuanced differences in activity (e.g., differences in rate of function or sensitivity to some stimulatory signal) [CLH+20, HBA+15]. This makes it difficult to clearly identify the role of any given protein, as removing it completely from a cell may only have a graded effect due to compensation by other proteins. Interestingly, different cell types exhibit strikingly different migration modes that can be modulated by external chemical and mechanical cues. Together, these facts make understanding integrin-based adhesion assembly and disassembly and associated cellular motility a significant challenge.

Complementary to the biochemical networks that govern adhesion assembly and disassembly, the movement of a cell also plays a critical role in determining adhesion dynamics [RSG+05, GSASW10, MKS+12]. This movement partially results from forces that are transmitted through adhesions [AE07], which also modulate the biochemical activities of the molecules that make up adhesions [NBS08, LKZ16]. Moreover, as the cell moves, its adhesions remain roughly immobile relative to the external environment, causing them to be transported from one morphological region to another [BWK08]. Accordingly, adhesions experience time-varying chemical and mechanical conditions, producing time- and space-dependent variations in adhesion characteristics (e.g., size and shape) that mirror changes in molecular states of their constituent proteins [BWK08, RBI+19].

Movement of the cell is driven biochemically by the members of the Rho-family of GTPases (RhoGTPases), that form a complex biochemical signalling network to produce concerted protrusion and contraction of the actin cytoskelton [DH15]. Here we focus on two such GTPases Rac1 (Rac) and RhoA (Rho), that are associated with protrusion and contraction, respectively. Interestingly, many of the signalling pathways that regulate the activity of these RhoGTPases use adhesions as dynamic signaling hubs [HD09]. For example, a Rac-dependent pathway is modulated by the same adhesion-associated proteins known to drive adhesion disassembly [RKS+00, TBBK18]. In other words, adhesion dynamics and cellular motility are intricately linked. Therefore, it is not possible to fully understand one without the other [MHB20, ORG19].

Aside from the myriad of experimental techniques that have been used to investigate adhesion dynamics and associated cellular motility, mathematical modeling has also been fruitfully used as a tool for gaining insights into the mechanisms that govern these phenomena [SS13, MR10]. This thesis

has focused on modeling both adhesion dynamics as well as cellular motility. Accordingly, it is divided into two parts. In Part I, we investigate models of mechanosensitive adhesion dynamics, i.e., how the mechanochemical properties of integrin receptors are integrated at the adhesion level to produce the behaviour of adhesions experiencing forces. In Part II, we turn our attention to mathematical models of cellular motility with an emphasis on how adhesions influence the spatio-temporal dynamics of motility to produce cell movement.

0.1.1 The Adhesion Life Cycle

Integrin-based adhesions are macromolecules that provide a mechanical link between the extracellular environment and the actin cytoskeleton. They are intrinsically dynamic structures that form as a result of and also heavily influence cellular motility. The adhesion lifecycle typically initiates in protrusive regions of the cell when small ($\sim$100 nm in diameter) radially symmetric clusters of integrin, called nascent adhesions (NAs), form, connecting the substrate-facing membrane to extracellular ligands [CXM+15,CVMZ+08]. Their formation is triggered by protrusion of the lamellipodium, a heavily branched network of actin filaments that extends 1-5 μm into the cell and terminates in a zone of actin depolymerization [CVMZ+08, PHS10, PMG+17]. Despite NAs being only loosely associated to this actin network [BHK+06], once protrusion causes the depolymerization zone to pass over them, the majority quickly disassemble [CVMZ+08]. Together these effects produce NAs with a typical lifetime of 60-120 s [CVMZ+08, TTB+13], but we note that, under certain conditions, they are stable for hundreds of seconds [CXM+15]. A small fraction of NAs do not disassemble, but are instead stabilized through increased association with actin filaments and become enlarged [TTB+13, SFW16]. These adhesions are termed focal complexes (FCs) and typically have an area of <1 μm^2 with a lifetime of 4-30 minutes [GYS02, SSA+15]. The transition from a NA to a FC requires both Rac-dependent increases in traction force and proper organization of the actin network adjacent to the aforementioned depolymerization zone [GYS02, CVMZ+08].

FCs, in turn, serve as precursors for focal adhesions (FAs), where the transition between the two classes of adhesions is mediated by association with Rho-dependent contractile stress fibres [OBSG12]. FAs are characterized by an elongated elliptic shape of 1-5 μm in length, with elongation rate being highly dependent on the rate of rearward flow exhibited by the lamellipodial actin network [TTB+13, OBSG12, SBDG13]. As the cell-body moves forward, FAs experience a relative rearward movement and undergo repeated gradual disassembly events [RSG+05]. In fibroblast cells, the majority of FAs

that form at the cell-front do not reach the cell-rear but are completely degraded by this effect, producing FAs with a typical lifetime of 20-90 minutes. Small laterally protrusive zones near the cell-rear instead, often termed uropods in the context of leukocytes, act as sources of FA precursors, allowing the cell-rear to have its own distinct population of FAs. These FAs allow the cell to maintain a spread shape and resist its forward movement [RSG+05]. In order for a cell to continue moving forward, these FAs either exhibit cycles of mechanically-driven forward treadmilling [BHIWH01, WH12, SMP+99] or are pulled apart molecularly by a combination of protease activity and high contractile forces found at the cell-rear [CAW+03, MOH+08, PDG99].

In this thesis, we have focused on three classes of adhesion: NAs, FCs, and FAs. We note, however, that the boundaries between such classes are not very well defined in the literature, and studies use them interchangeably. This may in part be due to the fact that quantitative classification of adhesions, based on fluorescence microscopy data, shows that most quantifiable properties (e.g., size, aspect-ratio, assembly rate, lifetime) of adhesions exist as a continuum [Lyd20]. Furthermore, as we have outlined above, some properties, such as lifetime, are emergent and dynamic properties that depend on the motility of the cell, which in turn depends on the properties of its adhesions. Therefore, there is a significant inter- and intracellular heterogeneity between these properties [SSA+15]. Thus the lack of a consensus definition of adhesion classes based on such observable properties is not surprising. Nonetheless, based on the typical lifecycle of adhesions, it is clear that as adhesions progress from NAs to FAs they become significantly larger and more stable structures that are increasingly associated with the actin cytoskeleton. It is worth mentioning here that an alternative terminology has been used by Peter Friedl [FW10, FG09, HSF18], where NAs and FAs are understood as two extreme cases of a continually changing adhesions. Accordingly, adhesions can be viewed as being more or less focalized, with NAs (FAs) being referred to as non-focalized (focalized) adhesions.

Part I of this thesis focuses on how the dynamics of all classes of integrin-based adhesions are modulated by mechanical forces. In Chapter 1, we review the literature of biophysically-based models describing adhesion dynamics. In this literature review, we pay particular attention to the molecular details that underlie integrin binding kinetics, and their mathematical/thermodynamic descriptions [MK20]. Using a common thermodynamic framework based on chemical potentials, we explore how mechanical unfolding of integrin receptors manifests itself at both the single-molecule and adhesion level to produce complex mechanically-driven dynamics. In Chapter 2, we present our previously developed and novel mathematical model of NA-dynamics. This model accounted for a trend that we

inferred from previously published data using a novel data analysis technique, termed Conditional Expectation Analysis, suggesting that the density of molecules within adhesions increases with increasing NA-area. Furthermore, due to some unique features of the model, the model was used to draw conclusions about the mechanical conditions required for NA-assembly.

0.1.2 Paxillin: A dual regulator of adhesion and motility dynamics

Paxillin is a 68-kDa adaptor protein that is found in the the adhesion plaque, a multi-molecular dynamic scaffold that links integrins to the actin cytoskeleton [DT08]. The paxillin C-terminal region contains four LIM domains, characterized by double-zinc finger motifs, that are essential for its recruitment to adhesions [DT08]. When it is found in adhesions, it carries out a number of functions that include organization of the adhesion plaque [CW15], modulation of adhesion disassembly dynamics [ZBMKG07, NWB$^+$06, EK09], and signaling to biochemical networks involved in cellular protrusion/contraction [DT08]. Interestingly, all of these functions are dependent on the phosphorylation of residues in one of the five leucine- and aspartate-rich LD domains (LD1-LD5) found close to the N-terminal region of paxillin [DT08]. Of particular interest are the tyrosine residues 31 and 118 which are phosphorylated by focal adhesion kinase (FAK) [SP95], and the serine residue 273 which is phosphorylated by p21-activated kinase (PAK) [NWB$^+$06]. Both tyrosine and serine phosphorylation appear to produce very similar distributions of adhesion classes, where phosphomimetic paxillin constructs favour small dynamic NAs and FCs while non-phosphorylatable constructs favour elongated and stable FAs [NWB$^+$06, ZBMKG07]. Cells expressing these constructs exhibit enhanced and diminished motility, respectively. This suggests that while adhesion can be used by cells to produce motility, excessive populations of FAs also tend to hinder their movement.

Due to its near omnipresence in all adhesion classes, paxillin is one of the most used fluorescence markers for visualizing integrin-based adhesions [GKTV18]. However, as outlined above, it is far from a passive marker. Understanding how it exerts its control on the cell is of therapeutic interest, as it is known to contribute to a number of pathological conditions by aberrant changes in cellular motility [LCLRBHL17, AXT20]. Due to the multiple functions downstream of paxillin phosphorylation, dissecting how its effects on adhesion dynamics and protrusion/contraction contribute to motility phenotypes is non-trivial. In order to begin doing so, our group has developed and experimentally validated a mathematical model of paxillin-dependent feedback on Rac and Rho [TBBK18]. Subsequent experimental motility assays showed that whole-cell inhibition of a Rho effector increased motility

and reduced the enrichment of paxillin inside adhesion as well as the mean size of adhesions, but did not significantly increase the directionality of cells [LTR+19]. Modeling these experimental manipulations suggested that, without directional cues, the biochemical signaling network does not enhance polarization, consistent with the experimental findings [LTR+19].

In Chapter 3, we review the mathematical model presented in [TBBK18] and [LTR+19]. In order to aid us in doing so, we present a systematic approach to modeling the spatio-temporal dynamics of reaction-diffusion (RD) system with quasi-steady state (QSS) assumptions, and detail how this is implemented into a computational tool that allows us to produce stochastic simulations of RD systems. This has helped to understand some of the differences in model outcomes observed in [TBBK18] and [LTR+19]. We also explored the effects of paxillin phosphorylation on the establishment of protrusive and contractile regions of the cell. Finally, we showed some preliminary results obtained by coupling stochastic spatio-temporal simulations of the model developed in [TBBK18] to the Cellular Potts Model (CPM), a phenomenological model of cellular motility. This has allowed us to demonstrate that signaling from paxillin onto the Rac-Rho network, combined with a dynamic cell-shape, can explain the experimentally observed increase in migration speed that results from increased paxillin phosphorylation.

0.1.3 Cell Polarization Driven By RhoGTPases

The proteins Rac and Rho drive two opposing aspects of the physical deformation of migrating cells, and, in order to produce net migration, must do so in a way that is tightly spatio-temporally regulated [Rid01]. This may be achieved, in a cell-autonomous way, through mutual inhibition between the two proteins [JMEK07, EK16]. This mutual inhibition results in biochemical systems where a high activity level of one protein prevents the other from having a high activity level in the same region. Interestingly, computational studies have shown that this type of system is competent in producing patterns containing spatially segregated zones of high activity of either protein, leading to long-lived regions that exhibit contractile and protrusive behaviour [MJD+06, JMEK07, EKHZD13]. The models used in these studies have further been analyzed mathematically to understand, with precise detail, the ingredients that allow for pattern formation and how to trigger such a process [MJEK08, MJEK11, HCEK12, MDEKH13]. Interestingly, these ingredients seem to be generic properties of many RhoGTPases, including Rac and Rho [MJEK08]. Thus the intrinsic properties of RhoGTPases make them prime candidates for biochemically-driven front-to-rear polarization of migrating

cells.

As mentioned above, paxillin phosphorylation is known to influence the mutual inhibition of Rac and Rho. Therefore, it is of interest to understand how how these effects manifest themselves at the whole-cell level. In Chapter 3, review the mathematical principles that underlie the pattern formation mechanism, known as wave-pinning, that has been hypothesized to cause both RhoGTPase-driven front-to-rear polarization and cellular migration. Furthermore, we also use a combination of spatio-temporal simulations and local perturbation analysis (LPA) to understand how signaling from paxillin onto RhoGTPases affects front-to-rear polarization. In doing so, we have found a number of discrepancies between the predictions of LPA and the results of spatio-temporal simulations, and hypothesized about the cause of these discrepancies. As a partial remedy to this issue, we have proposed an extension of LPA, termed pinned wave analysis (PWA), whose results can be better reconciled with those of our spatio-temporal simulations. Finally, by performing spatio-temporal simulations in time-varying domains produced by the CPM, we found that, when paxillin phosphorylation is increased moderately, cells exhibit faster motility but, at very high phosphorylation rates, multiple competing protrusive regions can actually arrest cell motility.

0.1.4 Migration Modes

Based on what we have already discussed, we can see that cellular motility and migration are complex processes that integrate multiple interrelated phenomena (e.g., adhesion dynamics, biochemical signaling, and cellular deformation) across many length and timescales. In multicellular organisms, variations in these phenomenon combined with complex interactions between a cell and its environment produce a diverse set of migration modes. For example, one may distinguish between single-cell and collective migration. During collective cell migration, a population of cells collectively exploit single-cell migration properties in order to enhance sensitivity to stimuli as well as produce emergent tissue- and organism-level migratory behaviour [EMB+16, HSF18, SM19]. The physiological contexts that use collective migration vary from wound healing and embryonic development to cancer metastasis, and thus the strategies used to achieve it are diverse; these strategies involve using a combination of cell-cell adhesions that provide both tensile [THA+11] and compressive [PKB+15] mechanical links between cells, direct transfer of biomolecules between cells through gap junctions [HCW+98, DNB+08], and multicellular leader-follower dynamics arising from intercellular signaling combined with contact inhibition of locomotion or cell-cell junctions [CZLR16, Rap16, YZZF19]. For the most part, collective

migration requires that individual cells be able to undergo single-cell migration. This type of migration also exhibits a great deal of cell-type and context-dependent diversity [HSF18]. Single-cell migration is broadly classified into two distinct forms: amoeboid and mesenchymal.

Amoeboid motility is characteristic of cells that exert low amounts of traction force on their surroundings [HSF18], and is often used to refer to cells that posses rapidly changing and irregular shapes (e.g., leukocytes) [FLLKM18]. This type of migration can further be dissected into a number of modes based on the relative balance between contractile, protrusive, and adhesive forces [LS09]. It has been suggested that this type of motility is poorly defined such that the term has been abused in the literature [FLLKM18], and that its use should be restricted to cells that migrate using contraction-driven blebs (a detachment of the plasma membrane from the actin cortex) [LS09]. On the other hand, when traction forces are high, cells exhibit mesenchymal motility, characterized by a spindle-like cell shape (e.g. fibroblasts). This shape results from actin stress fibres that are anchored to the substrate by FAs. The protrusive end of the spindle shape is typically broader than the contractile end; this is due to the presence of a lamellipodium and/or filopodia, where the latter denotes protrusive actin structures consisting of bundled parallel actin filaments [BPEP20, FLLKM18]. The lamellipodium, or similar protrusive structures (e.g., uropods), furthermore, act as sources of integrin-based adhesions. Thus, such adhesions are most prominent in cells exhibiting mesenchymal motility, but can also be found in cells that are typically associated with amoeboid motility.

This thesis has focused on single-cell mesenchymal motility, the most studied form of motility due to its relevance to cancer metastasis, wound healing, embryonic development, and tissue fibrosis [CD09, Nie11, KMT+12, HD18]. We have further restricted our focus to two cell-types that, when seeded on two-dimensional substrates, primarily use lamellipodia for protrusion: Chinese hamster ovary (CHO-K1) cells and fish keratocytes.

Beyond the observational description of mesenchymal motility given above, a relatively complete mechanistic picture of mesenchymal motility can be obtained from the famous Abercrombie model of crawling cellular motility [Abe80]. While the model was not mathematical and many of the molecules involved remained to be identified, it proposed a framework for motility that involves four major steps: protrusion of the cell front, formation of cell-substrate adhesions at the front, detachment of cell-substrate adhesions at the rear, and actomyosin contraction to pull the cell rear forward. The model further postulated that a set of autonomous processes govern each of these steps, and that interactions

between these processes lead to a cyclic repetition of the steps, resulting in persistent motility.

These four steps remain foundational to understanding nearly all mesenchymal motility, with experimental and computational studies continually giving increasingly nuanced insight into molecular and mechanical details driving these four steps. Both environmental factors and cell-autonomous factors feed into the relative dynamics with which a cell executes the various steps, leading to qualitatively and quantitatively distinct migration modes [FW10]. For example, fish keratocytes have been used extensively as a simple model of migrating cells due to their gliding mode of motility that does not produce significant changes in shape [MBK20], possibly suggesting that a common mechanism underlies the motility of these cells. However, upon closer inspection, this assumption turns out to an over-simplification, as even within the gliding mode of motility, there are different mechanisms that determine migration speed and cell shape in different environments [MBK20]. For example, when keratocytes migrate on a substrate with a low density of extracellular ligands, they adopt a relatively rounded shape with cell speed determined by the balance between actin polymerization and myosin-aided rearward flow of the actin network over mechanically weak adhesions [BLK+11]. On the other hand, when keratocytes are on a substrate with an intermediate ligand density, they spread out perpendicularly to the direction of motion and their elevated speed is solely determined by the polymerization rate of actin, as adhesions become strong enough to withstand slippage of the actin-myosin network [BLK+11]. Thus, due to the intrinsic connections between the four steps of Abercrombie model, altering any one step (e.g., adhesion or detachment) can have non-trivial consequences on the other steps (e.g., protrusion and contraction).

Interestingly, when keratocytes are plated on highly adhesive substrates, a significant sub-population exhibits traveling waves of protrusion that initiate at one end of the cell and spread laterally until they terminate at the other end of the cell [BAL+17]. These protrusive waves result from complex spatio-temporal interactions between actin polymerization and maturing adhesions [BAL+17]. On both intermediate and low adhesive substrates, another sub-population of cells exhibit a third mode of motility that is distinct from both gliding and waving, namely, rough motility [BLK+11, BAL+17]. This poorly understood mode of motility is characterized by transient protrusions that are aperiodic in nature and travel short distances along the membrane before terminating. Because all cells used to produce these observations were fish keratocytes, it seems likely that differences in observed migration modes are due to intercellular heterogeneity in some rates of the molecular processes driving the steps of the Abercrombie model. Understanding how this heterogeneity combines with variations in environment

to produce the observed sub-populations is both mechanistically insightful and a useful strategy for model validation.

In Chapter 4, we re-analyze a mathematical model that had successfully captured the smooth gliding and waving motility of keratocytes [BAL+17]. This has been done using slow-fast analysis understand its underlying dynamics, and bifurcation analysis to understand how heterogeneity produces sub-populations with different migration modes. Furthermore, combining both these strategies, we have identified the parameter regime that is most-likely responsible for producing rough motility in keratocytes. We also show how this model of protrusion can be extended by incorporating some of the mechanosensitive properties of nascent adhesions covered in Part I to predict novel motility phenotypes that may be relevant in other cell types.

In conclusion, due to the complexity of the processes involved in cellular motility, experimental observations can be made significantly more impactful by being complemented with appropriate mathematical modeling. Mathematical modeling gives much more control over the systems being studied and yields considerably higher spatio-temporal resolution than can be acheived experimentally. This thesis uses experimentally-driven mathematical modeling of motility-related phenomena across many lengthscales and timescales, providing important insights into how cellular motility arises from their interactions.

Part I

Mechanosensitive Adhesion Dynamics

Chapter 1

Literature Review: The bioenergetics of integrin-based adhesion, from single molecule dynamics to stability of macromolecular complexes.

Abstract

The forces actively generated by motile cells must be transmitted to their environment in a spatiotemporally regulated manner, in order to produce directional cellular motion. This task is accomplished through integrin-based adhesions, large macromolecular complexes that link the actin-cytoskeleton inside the cell to its external environment. Despite their relatively large size, adhesions exhibit rapid dynamics, switching between assembly and disassembly in response to chemical and mechanical cues exerted by cytoplasmic biochemical signals, and intracellular/extracellular forces, respectively. While in material science, force typically disrupts adhesive contact, in this biological system, force has a more nuanced effect, capable of causing assembly or disassembly. This initially puzzled experimentalists and theorists alike, but investigation into the mechanisms regulating adhesion dynamics have progressively elucidated the origin of these phenomena. This review provides an overview of recent studies focused on the theoretical understanding of adhesion assembly and disassembly as well as the experimental studies that motivated them. We first concentrate on the kinetics of integrin receptors, which exhibit a complex response to force, and then investigate how this response manifests itself in macromolecular adhesion complexes. We then turn our attention to studies of adhesion plaque dynamics that link integrins to the actin-cytoskeleton, and explain how force can influence the assembly/disassembly of these macromolecular structure. Subsequently, we analyze the effect of force on integrins populations across lengthscales larger than single adhesions. Finally, we cover some theoretical studies that have considered both integrins and the adhesion plaque and discuss some potential future avenues of research.

1.1 Introduction

The joint effect of the chemical and mechanical environment a cell experiences influences it behaviour across many timescales. For example, on short timescales (minutes to hours) a cell may exhibit motile behaviour in response to chemical and mechanical cues [1, 2], while on longer timescales (hours to days) these same cues affect cell survival and differentiation into distinct lineages [3–6]. Although associated with behaviour at comparatively short timescales, cellular motility plays a central role in a number of long-lasting physiological and pathophysiological processes [7–9]. The visualization of its associated displacements of molecules [10–16], cellular structures [17–20], and cells [21–24] have made it an alluring area of research across many fields. Fluorescence-based microscopy has not only allowed for the visualization of these displacements, but also the biochemical characterization of the

structures involved. In conjunction with biochemical and genetic manipulations, fluorescence-based microscopy data has resulted in an extensive literature detailing the processes involved in motility across many lengthscales: from the single molecule scale to the tissue-level scale. A significant challenge in the field has been to take these complex, and sometimes seemingly contradictory, experimental characterizations and arrive at a mechanistic understanding of what drives a specific cellular behaviour. While proper experimental design is crucial in this endeavour, theoretical models, both mathematical and computational, have proven to be useful in providing a level of control, spatiotemporal resolution, visualization, and quantification that may go well beyond what can be achieved experimentally.

The motile behaviour of cells highlights the importance of force-generation in cells, which is largely thought to arise from a combination of actin polymerization and myosin-driven contraction [25]. However, in order for directed cellular motion to occur, the internal forces of the cell must be transmitted to its environment. One means by which cells accomplish this force transmission are integrin-based adhesions, macromolecular structures that act as a mechanical linkage between the cell's environment and its actin-cytoskeleton [15,25]. Interestingly, integrin-based adhesions are mechanosensitive, assembling and adjusting their size and strength in response to force [17, 18, 26–31]. The highly dynamic nature of these relatively large structures poses a significant modeling challenge as it involves interactions across many length- and timescales. Indeed, adhesions are formed as the result of interactions between over 100 different proteins which often exhibit some form of redundancy [32], making it difficult to both isolate key players and determine how nuanced interactions may lead to divergent behaviours. Nonetheless, many models of adhesions and the molecules which comprise them have been successful in furthering our understanding of adhesion dynamics and the role that forces play in determining these dynamics.

In this review we will cover some of these models and the experimental findings which motivated their formulation. In particular, we will focus on the mathematical forms which give rise to specific model behaviours, and the relation these forms have to the underlying physics and biological structure of adhesions. The emphasis on mathematical forms is made to help clarify the critical determinants of cellular behaviour rather than the specific results of a simulation which may depend heavily on indeterminate parameter values. We will see how these mathematical forms are used to predict both steady-state and transient behaviours of this system at the single-molecule, adhesion, and membrane level.

This review is organized as follows. First, we briefly discuss the architecture of adhesions and how it relates to their function, and then highlight some aspects of the adhesion life cycle which will be relevant to modeling. The bulk of the review will then be allocated to covering various mathematical models which have yielded insight into the dynamics of adhesions. Broadly speaking, we will focus on models have that either analyzed integrins receptors and their bonds to ligands or studied the condensed phase of adaptor proteins which form a plaque that sits atop the integrins. First, we will show how a combination of experiments and modeling have enriched our understanding of single integrin dynamics, and then explore how the properties of the integrin-ligand bond can be incorporated into bond-cluster models that predict the mechanical response of a collection of integrin receptors. Subsequently, we will cover some theoretical treatments of the adaptor protein plaque and its response to anisotropic applied forces. This will be followed by briefly describing a model that helped bridge the two classes of models of adhesions, and reconcile some of the differences between the outcomes of the two classes of models. Finally, we will draw some conclusions and give an outlook on future challenges in the field. An appendix detailing the common thermodynamic formulation of the models presented here is also included at the end of the review.

1.2 Biological Background

1.2.1 Adhesion Architecture

Adhesions are comprised of a very large number of dynamically interacting proteins to produce a bio-mechanically regulated force transmission point between a cell's actin-cytoskeleton and its environment [32]. Central to this force transmission is the integrin receptor, a heterodimeric transmembrane protein which binds extracellularly to ligands typically found in connective tissue and whose cytoplasmic domain is linked to the actin-cytoskeleton through interactions with adaptor proteins (see Fig. 1.1, [15, 33]). Adaptor proteins are a class of cytosolic proteins which form a membrane-proximal plaque. This plaque aides in the spatial organization of integrins, into discrete adhesions [16, 34, 35], and serves as a mechanical linkage between integrins and the actin-cytoskeleton. The adhesion plaque is formed as a result of adaptor proteins binding to integrins as well as one another. Aggregation of adaptor proteins leads to the growth of the adhesion plaque through adsorption, while the reverse process of desorption may explain shrinkage of the plaque [19, 36–39]. The term net adsorption will be used to refer to the combined effect of both processes. Biochemical signaling events and mechanical

forces have both been implicated in modifying the propensities of these adsorption/desorption processes, providing the cell with means to dynamically alter the size and stability of adhesions.

The adhesion plaque is divided into functionally distinct layers (see Fig. 1.1, [15, 40]). The lowest layer is known as the integrin signaling layer (terminating cytosolically $10 - 20$ nm away from the membrane), where adpator proteins are closely associated with integrins, allowing paxillin- and FAK-dependent signals to relay information about the integrin-ECM linkage to various biochemical signaling pathways [41, 42]. Above the signaling layer lies a force transduction layer (terminating cytosolically $50 - 60$ nm away from the membrane) which links integrins to filamentous actin (F-actin), and is primarily comprised of talin (which both activates integrins and binds to F-actin [43]) and vinculin (which reinforces the talin-actin bond [44, 45]); this latter layer is responsible for the transmission of forces from the actin-cytoskeleton to integrins. One would expect the many proteins in the force transduction layer to be associated with actin filaments, which requires actin filaments to be brought into contact with the adhesion. Consequently, immediately above the transduction layer, is an actin regulatory layer which contains the proteins VASP, zyxin, and α-actinin [40]. The proteins in this uppermost regulatory layer promote filament growth and F-actin bundling into very stable and contractile stress fibres [46, 47]. This means that these three functional layers interact to self-assemble into the mechanical linkage between the actin-cytoskeleton and the external environment [15]. Within this framework, the signaling layer contains the mechanical link to the external environment (i.e., integrins), the transduction layer connects these integrins to the actin-cytoskeleton, and the regulatory layer helps to organize the actin-cytoskeleton around the adhesion into structures that produce the force transmitted through integrins to the external environment.

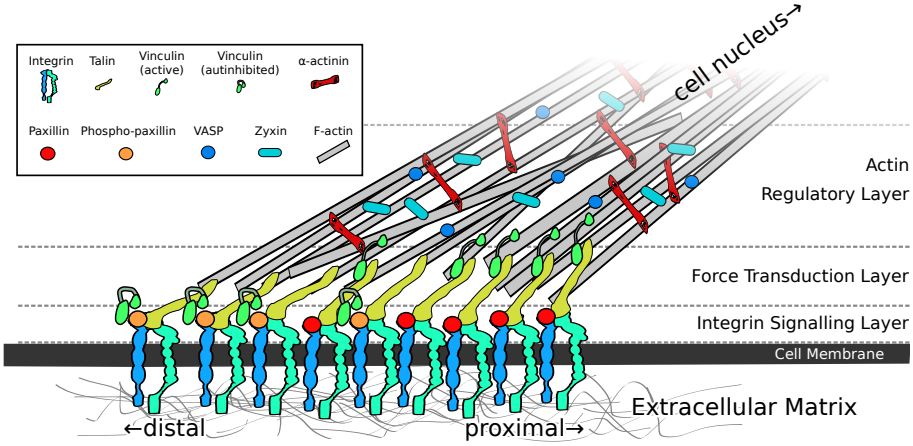

Figure 1.1: Structural diagram of the nanoscale architecture of integrin-based adhesions in a protrusive region of a motile cell. Integrin receptors span the cell membrane, binding to ligands in the extracellular matrix. Their cytoplasmic tails are complexed with adaptor proteins, forming an adhesion plaque that connects them to F-actin. The integrin signaling layer is the juxtamembrane region (10-20 nm in thickness) where adaptor proteins involved in signaling pathways are found (e.g., paxillin). Above this layer is the force transduction layer (terminating cytosolically 50-60 nm above the membrane) enriched with talin and active vinculin, proteins that form a linkage between the actin-cytoskeleton and integrin. Finally, the actin regulatory layer contains proteins that help organize actin into contractile stress fibres. A stress fibre typically points from the adhesion towards the cell nucleus; this directionality is used to define the adhesion's frame of reference in which distal (proximal) refers to the tip furthest away from (closest to) the nucleus. A gradient in paxillin phosphorylation leads to an asymmetry in the distribution of active vinculin [15, 48], while the elastic response of the adhesion plaque has been theorized to produce a gradient in the tilt of proteins in the transduction layer [39]. Figure adapted from [15] and [39].

1.2.2 Adhesion Life Cycle in Motile Cells

Focal adhesions form through a series of biochemically- and mechanically-driven steps. They initially start as highly dynamic nanoscale clusters of integrins, termed nascent adhesions (NAs), in the lamellipodium [49], a morphological compartment with a very dense quasi-two-dimensional polymerizing actin meshwork. This semi-rigid network of F-actin projects from the actin-cytoskeleton to form the leading edge of a polarized cell [50], while the polymerization of the filaments drives the leading edge forward by using NAs as anchor points [51, 52]. As the leading edge of a migrating cell moves forward, so does its lamellipodium; once a NA is no longer covered by the lamellipodium it disassembles

rapidly [19]. However, a small fraction of NAs stabilize and persist beyond the lamellipodium, growing centripetally inwards into mature focal complexes (FCs) and focal adhesions (FAs) [19, 53].

The decision for a NA to disassemble or initiate its maturation is regulated biochemically by changes in the molecular state of adaptor proteins (e.g., phosphorylation of FAK or paxillin) [48,54,55]. From a mechanical perspective, maturation is associated with an increase in traction stress [30, 56, 57]. Therefore, it is not surprising that the association of a FA with a contractile actin stress fibres results in its stabilization [29]. As the whole cell moves forward, its FAs either gradually disassemble as they steadily move towards the cell rear [58], or, in some cell types, they may become highly stable fibrillar adhesions which form as a result of cell-dependent reorganization of the ECM [59]. In fibroblasts, the former effect is fairly robust with only $\sim$10% of FAs at the trailing edge originating from the front of the cell, whereas trailing FAs primarily originate in small protrusions at the rear and lateral zones of the cell [58].

The spatiotemporal regulation of disassembly for non-fibrillar FAs remains incompletely understood. Yet, it has been found that (i) FAs undergo repeated periods of disassembly which are correlated with their proximity to the growing tips of microtubules [58], (ii) microtubule tips are targeted to FAs in a paxillin-dependent manner [60], and (iii) abrogating microtubule growth halts the disassembly of FAs [61, 62]. Interestingly, this microtubule-dependent disassembly seems to be mediated by clathrin-dependent endocytosis of integrins [63–65], while other internalization routes (e.g., caveolin-dependent endocytosis) may also contribute to adhesion disassembly [66]. Furthermore, in some cellular contexts, internalization may be further aided by the exocytosis of matrix metalloproteases that degrade the ECM [67, 68]. For more on the interplay between microtubules and adhesions or the internalization of integrins, we refer the reader to the reviews by Seetharaman and Etienne-Manneville [69], or De Franceschi et al. [66], respectively.

Within motile cells, FAs that form at the front of the cell are effectively immobile relative to the ECM. When these FAs reach the rear of the cell they must disassemble in order for the cell to continue migrating. FA-disassembly at the cell rear allows for the trailing membrane to roll forward which in turn permits further extension of the lamellipodium. While the presence of FAs in this region of the cell is necessary for proper cell spreading and resisting the tension generated in the lamellipodium, their timely disassembly is necessary for efficient cell migration. This disassembly occurs primarily by two means: integrin/adhesion release and adhesion sliding.

Integrins are "released" from the trailing edge of a migrating cell [70, 71]. On a highly adhesive ECM, this process is caused by intracellular breakage of the FA plaque-integrin linkage, leaving integrins stuck to the ECM after the trailing edge moves forward; on the other hand, on less adhesive substrates, release of integrins from the cell is infrequent with breakage occurring extracellularly at the integrin-ECM linkage [71], a process we term adhesion release. Regardless of the adhesiveness of the ECM, however, strong traction forces produced by RhoA-dependent myosin-driven contraction of the actin cytoskeleton drive the breakage of bonds that hold the FA together, leading to their disassembly. At least two biochemical mechanisms have been identified as modulators of adhesion release. First, the calpain family of intracellular Ca^{2+}-dependent proteases have been shown to cleave a number of FA proteins which can (directly or indirectly) mechanically decouple integrins from the actin cytoskeleton [71–74]. Second, in lymphocytes, it has been experimentally found that the protein SHARPIN associates with the integrin (LFA-1) preferentially at the cell rear and maintains it in a low-affinity inactive conformation that facilitates the mechanical breakage of the integrin-ligand bond [75, 76]. Notably, this low affinity state does not exhibit the normal mechanosensitive binding properties of the integrin bond [76, 77].

Alternatively, adhesion sliding may also occur in a subset of FAs at the cell rear [78], and unlike integrin release, it is not migration-dependent [79], but is a tension-dependent process [80]. During FA-maturation, the proximal tip of an elongated adhesion grows more rapidly than the distal tip shrinks, leading to further elongation [18, 19], in contrast to adhesion sliding where the distal tip typically shrinks more rapidly than the proximal tip grows. This striking phenomenon leads to an apparent sliding of FAs towards the center of the cell, and a gradual decrease in their size. Although these sliding adhesions visually appear to exhibit slippage, this phenomenon is more likely due to an asymmetry in matter exchange rates between the two tips of adhesions [12, 80, 81]. Biochemically, a number of proteases have been implicated in this process [81], but as we shall see in this review, a number of mechanical effects may also be implicated in adhesion sliding.

1.3 Integrin Activation and Mechanosensitivity

Integrin receptors exist as non-covalently bonded heterodimeric pairs of α and β subunits. There are 18 α and 8 β subunits in vertebrates, which allow different cell-types to exhibit diverse responses to extracellular signals through differential ECM ligand binding, cytoskeletal association, and biochemical

signaling [82]. Initial crystal structures of integrins showed that the heads of the extracellular domains of both α and β subunits are bent towards the membrane [83]. This conformation is now regarded as the inactive form of the integrin receptor, capable of binding to ligands with a low affinity. In order for the receptors to bind their ligands with high affinity, integrins must first become activated through global conformational changes that expose the binding head of the receptors [84]. This conformational change can be induced chemically by replacing extracellular Ca^{2+} with Mg^{2+} or Mn^{2+}, resulting in an equivalent change in the identity of the divalent cation contained in the metal-binding sites of the integrin receptor [85, 86]. Alternatively, the binding of the cytoplasmic protein talin to the intracellular tail of the β subunit has also been found to activate integrins through equivalent conformational changes [87, 88]. The latter form of activation is the more physiologically relevant pathway and is termed inside-out activation, which is associated with numerous downstream signaling effects [89,90].

During the conformation changes associated with activation, integrins become extended in such a way that their binding heads points towards extracellular ligands [84]. In this extended state, the binding head can be either in a closed or an open state [91]. It was previously shown that the opening of the headpiece is the step required for high affinity binding [92]. This was in line with molecular dynamics simulations suggesting that an intermediate affinity state could correspond to a force-stabilized intermediate step in the physical extension of the α subunit that is associated with the switch from the low affinity inactive state to the high affinity active state [93,94]. Such a view agrees with the experimental observation that activated integrins typically exhibit less ligand binding than that of the high affinity binding state induced by divalent cations, with the high affinity state being achieved transiently in some activated cells [95–98]. Based on this, we can conclude that the complete integrin activation process involves the extension of the receptor followed by the opening of the headpiece, and that the extended state with a closed headpiece may represent a force-induced partially activated state. The three major *active* and *inactive* conformations of integrin can thus be described as follows:

1. The *inactive* bent closed (BC) conformation that has its binding head bent towards the membrane, away from extracellular ligands, and binds ligand with a low affinity.
2. The *inactive* extended closed (EC) conformation that has its legs extended, with the binding head pointing away from the membrane (towards extracellular ligands), and exhibits a low binding affinity due to a partially occluded binding site.
3. The *active* extended open (EO) conformation that has its legs not only extended but also sepa-

rated, reflecting the opening of the headpiece, and as a result exhibits high binding affinity.

While the structural details of the activation process have been studied extensively, some questions still remain. In particular, what are the relative contributions of mechanical and chemical cues in the activation process? Can either effect explain activation alone? How do these aforementioned conformational changes manifest themselves in the ligand binding kinetics of integrin?

1.3.1 Mechanism of Activation

Differences in the structural and functional properties of the three conformations, mentioned above, have lead to the genesis of the so-called force-activation hypothesis [82]. Within this framework, it is assumed that naive receptors are overwhelmingly found in the BC conformation, but upon loading them with mechanical force, the extended conformations (EC & EO) of integrin are stabilized by the work needed to refold the protein under load [93,94,99]. This allows integrins to be primed for higher affinity ligand binding through the application of force [100,101]. Because integrins are the primary component of adhesions, their mechanosensitive affinity regulation has been posited as a possible mechanism for the initiation of cellular responses to force [20].

We now ask whether or not force activation is the unique mechanism of activation. As mentioned above, binding of talin (or kindlin, [102]) to integrins cytoplasmic tails is widely regarded as the biochemical step necessary for activation. However, it is unclear if talin binding is sufficient for activation. In other words, can a lack of mechanical activation be compensated for by a high enough talin concentration? A recent theoretical study by Li and Springer has investigated this question using a thermodynamic approach to model the conformational equilibria of $\alpha_5\beta_1$ integrin receptors [99]. To quantify the probability of activation as both the force and the concentration of relevant chemical species (e.g., talin and fibronectin) are varied, they considered the molar free energy of the bare receptors (i.e., their reference chemical potential μ^0 as determined by fluorescence polarization [99], see 1.13 for more on μ^0). They also included the contributions of relevant chemical reactions as well as the mechanical work needed to revert a receptor back to its inactive BC conformation. In particular, they assumed that integrins are only loaded with force when bound to both a cytoplasmic adaptor protein and an extracellular ligand, In this case, an integrin receptor has a chemical potential given by

$$\Delta\mu_i = \mu_i^0 - k_B T \ln\left(C_{\text{ada}}/K_{\text{ada}}^i\right) - k_B T \ln\left(C_{\text{lig}}/K_{\text{lig}}^i\right) - F\Delta x^i, \tag{1.1}$$

where $i \in \{\text{BC}, \text{EC}, \text{EO}\}$, C_{ada} (C_{lig}) is the concentration of adaptor proteins (extracellular ligands), K^i_{ada} (K^i_{lig}) is the experimentally determined dissociation constant for complexes formed between an integrin with conformation i and adaptor proteins (extracellular ligand), F magnitude of the applied force, and Δx^i is the characteristic displacement length of conformation i relative to the BC conformation (i.e., $\Delta x^{\text{BC}} = 0$). We note here that the original study used the symbol ΔG_i rather than $\Delta \mu_i$ to denote the molar Gibbs free energy, however since the systems under consideration are individual molecules these two quantities are equivalent (see 1.13.1). The probability of being in an active state in the absence of applied force was then computed using the Boltzmann distribution, where in the absence of applied force, $\sim 99.7\%$ of $\alpha_5\beta_1$ integrins were expected to be in the inactive BC conformation. In comparison, the conformational equilibria of $\alpha_4\beta_1$ integrins were found to have $\sim 98.4\%$ of integrins in the BC conformation (i.e., $\sim 1.0\%$ of $\alpha_4\beta_1$ are in the active EO conformation compared to $\sim 0.17\%$ for $\alpha_5\beta_1$), suggesting that the conformational energies of $\alpha_4\beta_1$ integrins may prime them for the rapid adhesion involved in rolling leukocyte extravasation [103, 104].

While Eq. (1.1) is only part of the complete thermodynamic model, it highlights the dependence of free energy on chemical and mechanical contributions. Changes in chemical concentration affect free energy in a logarithmic manner, while changes in mechanical force have a linear effect on the free energy. Thus under the physiological assumption that both ligand and adaptor proteins are present at non-zero concentrations, variations in their concentration will have little effect on the outcome of the activation process. On the other hand, mechanical force has a much more potent effect, with an intrinsic free energy difference between the BC and EO conformation ($\mu^0_{\text{EO}} - \mu^0_{\text{BC}}$) equivalent to only ~ 1 pN of applied force when $\Delta x = 14.5$ nm [99]. This suggests that integrin activation is ultra-sensitive to changes in applied force, with an activation probability that can jump from ~ 0 to ~ 1 over a range of only ~ 2 pN. We note here that this force range should be readily attained in networks of polymerizing F-actin (~ 1 pN per filament, [105, 106]). Chemical effects, on the other hand, produce a much more graded response, requiring chemical concentrations to vary over many orders of magnitude to produce significant changes in extension/activation of integrin receptors. Due to the rapid dynamics of integrin activation [107], the extension of integrins, and their subsequent activation, seems much more likely to be caused by mechanical forces than by chemical effects. It is important to point out here that, at very low adaptor protein concentrations, the second term in Eq. (1.1) will dominate over μ^0_i, indicating that almost no receptors will be bound to an adaptor protein due to the chemical potential of adaptor-bound conformations being exceedingly high. In such a scenario, the force-dependence of

activation will vanish, as almost no receptors will be loaded with force. This implies that, neither talin binding nor mechanical forces are sufficient for activation, rather both are necessary. Interestingly with a physiologically reasonable applied force of 1.5 pN [108], the energy differences intrinsic to $\alpha_4\beta_1$ also seems to give these integrins enhanced sensitivity to changes in adaptor protein concentration/affinity relative to $\alpha_5\beta_1$ [103]. Furthermore, the intrinsic conformational energies were also found to vary across cell-types [103]. These cell-specific differences were likely due to variations in physicochemical environments, which may be caused by differences in membrane composition and cytoplasmic proteins that interact with integrins such as adaptor proteins or inhibitors of activation [103]. This variability highlights that the interplay between chemical and mechanical effects is non-trivial as well as cell- and integrin subtype-specific, but that it may be explored using the thermodynamic framework developed by Li and Springer. For more on the mechanosensitive activation of integrins, we refer the reader to the reviews by Sun, Costell, and Fassler [109] as well as Kechagia, Ivaska, and Roca-Cusachs [110].

1.3.2 Unbinding Kinetics of Integrin

While we have seen how structural changes in integrin receptors can lead to their activation and how these changes are driven by a combination of mechanical and chemical effects, it remains unclear how such processes manifest themselves in the dynamics of adhesions. To answer this question, we will first explore how the conformational changes discussed above result in a very specific mechanical response for integrin receptors using a combination of theoretical and experimental perspectives. In order to appreciate the richness of the resulting behaviour, we begin by considering a generic theory for the unbinding of molecular bonds under mechanical load. In [111], a phenomenological expression for the rate of unbinding of a collection of molecular bonds all experiencing a mechanical load F was originally proposed by Bell; it was given by $k_{off} \propto \exp\left(F/F_0\right)$. Such an expression may be derived from Eq. (1.25) by accounting for the work done by the force $\vec{F}\left(\vec{\ell}\right)$ along the reaction path $\vec{\ell}$ starting from the bound state; that is

$$\begin{aligned} \mu\left(x\right) &= \mu^0\left(x\right) + \int_x^{x_0} \vec{F}\left(\vec{\ell}\right) \cdot d\vec{\ell}, \\ &= \mu^0\left(x\right) + \mu_F\left(x\right) \end{aligned} \tag{1.2}$$

where x is the position of bonded molecule, x_0 is the position of the bound state, $\mu^0(x)$ is its chemical potential in the absence of force, $d\vec{\ell}$ is the infinitesimal displacement of the molecule along the reaction path from the bound state, and $\mu_F(x)$ is the chemical potential due to the applied force. Using Eq. (1.25), we may arrive at $k_{off} \propto \exp\left(-\Delta\mu_0^\ddagger/k_BT\right) \exp\left(\int_{x^\ddagger}^{x_0} \vec{F}\left(\vec{\ell}\right) \cdot d\vec{\ell}/k_BT\right)$, where $x^\ddagger$ is the position of the transition state and $\Delta\mu_\ddagger^0 = \mu^0\left(x^\ddagger\right) - \mu^0(x_0)$ is the intrinsic chemical potential difference of the transition state in the absence of force. It is indeed possible to use spatial potentials to investigate the unbinding rate in a way that actually considers the reaction path, revealing a threshold in force ramping rate required to produce a force-dependent unbinding rate [112]. Moreover, such predictions have lead to an experimentally validated theory of dynamic force spectroscopy for weak non-covalent bonds [113]. However, it is more common to simply abstract the molecular movements and rewrite the integral as $\Delta\mu_\ddagger = \Delta\mu_\ddagger^0 - F\Delta_\parallel x^\ddagger$ where $\Delta_\parallel x^\ddagger$ is the displacement from the bound state to the transition state parallel to the direction of the force. Defining the bound state as having a chemical potential of zero, we may use Eq. (1.25) to compute the unbinding rate as

$$\begin{aligned} k_{off}(F) &= \gamma \exp\left(-\Delta\mu_\ddagger/k_BT\right) \\ &= \gamma \exp\left(-\Delta\mu_\ddagger^0/k_BT\right) \exp\left(F\Delta_\parallel x^\ddagger/k_BT\right) \\ &\propto \exp\left(F/F_0\right), \end{aligned} \tag{1.3}$$

where $\gamma > 0$ is a kinetic parameter and $F_0 = k_BT/\Delta_\parallel x^\ddagger$ is a force scale that characterizes the force-dependence of the transition. Here, we have assumed that the position of the transition state is independent of F, which may not be strictly true, but is a common assumption in the field that agrees well with experimental measurements [112, 114–117]. Such a formalism defines the behaviour of what is commonly referred to as a slip bond, where the unbinding rate increases monotonically with applied force [118, 119].

Alternatively, by imposing some theoretical assumptions on the potential energy landscape of bonds involved in peeling a membrane off a surface, Dembo et al. predicted a different type of bond, a catch bond, whose off-rate decreases rather than increases with applied force [118]. They also hypothesized that such a bond may be central to a number of biological adhesion phenomenon. Initial experiments using atomic force microscopy under force-ramp conditions suggested that integrin-ligand pairs behave as slip bonds [120–122]. However, under force-clamped conditions, Kong et al. 2009 demon-

strated that these pairs can exhibit a catch bond behaviour, with a short-lived lifetime of ~ 1 s in the absence of force and a long-lived lifetime of > 10 s for forces in the 20-30 pN range [123].

A number of physically realistic yet mathematically tractable models have been proposed to explain the catch bond behaviour in a way that is more realistic than its original conception, which predicted a vanishing unbinding rate for arbitrarily large forces. Firstly, Evans et al. developed a five-parameter "state" model with two bound states (see Fig. 1.2A) [115]. The interconversion between the two states in this model was assumed to equilibrate rapidly, i.e.,

$$\frac{P_1(t)}{P_2(t)} \approx \exp\left(\Delta\mu_{12}/k_BT\right) = \exp\left(\Delta\mu_{12}^0/k_BT\right)\exp\left(-F/F_{12}\right), \tag{1.4}$$

where $P_1(t)$ ($P_2(t)$) is the probability of being in the bound state 1 (2), $\Delta\mu_{12}^0$ is the intrinsic energy difference between the two bound states (in the absence of force), and F_{12} is a force-scale which characterizes the transition between states 1 and 2. Furthermore, they assumed that only bound state 2 exhibits a force-accelerated ubinding rate (i.e., $\Delta_\parallel x_{,1}^\ddagger = 0$ and $\Delta_\parallel x_{,2}^\ddagger > 0$) [115]. With $\Delta\mu_{12}^0 > 0$, unbinding from state 1, according to this model, dominates at low forces, while the interconversion to state 2 becomes more favourable as force is increased. Therefore, if the intrinsic unbinding rate for state 2 (k_2^0) is significantly lower than that for state 1 (k_1^0) the observed bond lifetime will increase within a force range that (i) favours the interconversion to state 2 and (ii) also satisfies the inequality $k_2^0\exp\left(F/F_2\right) < k_1^0$, producing the catch bond behaviour. Alternatively, in [117], Pereverzev et al. also developed a "pathway" model with two dissociation pathways from one bound state (see Fig. 1.2B). The transition states associated with each pathway are assumed to be in opposite directions when projected onto the force vector, i.e.,

$$\Delta_\parallel x_c^\ddagger < 0 < \Delta_\parallel x_s^\ddagger$$

where $\Delta_\parallel x_c^\ddagger$ ($\Delta_\parallel x_s^\ddagger$) is the displacement parallel to the force in the catch (slip) pathway. With this difference in sign, the force-dependent unbinding rate can be expressed as

$$k_{off} = k_s^0\exp\left(F/F_s\right) + k_c^0\exp\left(-F/F_c\right) \tag{1.5}$$

where $F_s, F_c > 0$, and an efficient catch bond can be produced when $k_c^0 \gg k_s^0$ [117]. The state model is more consistent with the experimental evidence for multiple conformations of integrin, but it is also

tempting to use the pathway model as it performs almost identically to the state model but has one less parameter to be determined from data [117]. Interestingly, the pathway model may be derived by applying the assumption defined by Eq. (1.4) to a more general model of unbinding in the presence of allostery which, unlike the state model, explicitly tracks the allosteric interconversion between bound states [124,125]. This may explain the relative popularity of the two-pathway model despite the lack of evidence for multiple dissociation pathways from a single bound state [126–130]. For more on models and experiments related to bond dynamics in the context of cellular adhesion, we refer the reader to a review by Rakshit and Sivasankar [131].

Thus far we have hinted at a relation between bound states of integrins and the conformations that are associated with its activation. Interestingly, it was found that by applying cyclic forces to integrin, rather than using a constant force-clamp, the long lived bound state could be attained at significantly lower force magnitudes, an effect termed cyclic mechanical reinforcement [100]. In order to capture the history-dependence of unbinding, it was crucial to use a kinetic model with three bound states (see Fig. 1.2C) that unbinds according to Eq. (1.3) (i.e., three slip bonds) and and assume that the interconversion between states is force-dependent but not instantaneous [101]. The biophysical properties of these three bound states and the sign of the force-dependence of their interconversion unambiguously allowed for ascribing an equivalence between the bound states and the three main integrin conformations: BC, EC, and EO. This suggests that the integrin activation process is reflected in the kinetics of integrin unbinding, with each conformation behaving as a slip bond with different properties, while mechanical forces govern the interconversion between the conformations (e.g., extension is favoured in the presence of appropriately directed force) in order to produce the observed catch bond behaviour.

It is worth noting that thermodynamic model of Section 1.3.1 (see Eq. (1.1)) predicts that integrin activation can be induced by as little as ~ 2 pN of force, whereas experimental evidence suggests that the catch bond behaviour of integrins is triggered at a threshold of $\sim 10 - 20$ pN for constant forces [92,123,132,133], and ~ 5 pN for repetitive forces [100,101]. This discrepancy remains incompletely understood, but may be due to assumption that K^i_{lig} is independent of force. As we have seen in this section, integrin unbinding rates vary with force, and thus we may expect the binding affinity $(1/K^i_{\text{lig}})$ to vary as well. In the following section, we will show how a combination of simulations and theoretical work has been used to investigate the dependence of binding affinity on applied force in the context of generic receptor-ligand binding.

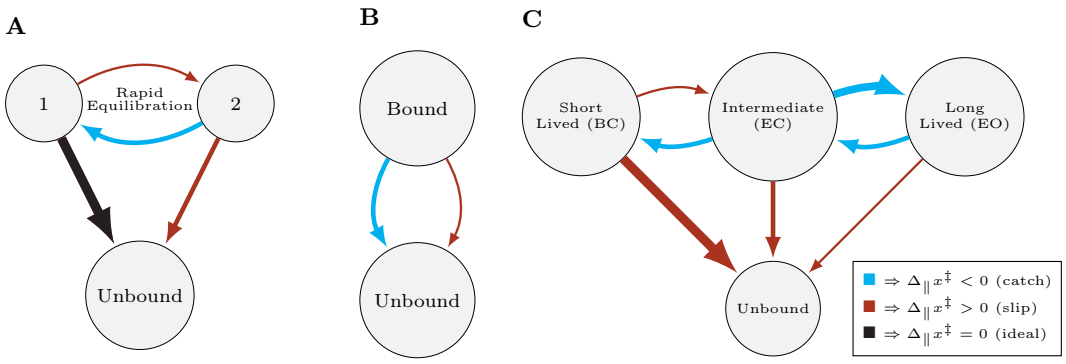

Figure 1.2: Models of integrin unbinding kinetics. (A & B) Two generic models of catch bonds: the two bound state model [115] (A), and the two-pathway model [117] (B). (C) Kinetic model of the mechanosensitive integrin-ligand bond that explains cyclic mechanical reinforcement [101]. Arrow thickness reflects the transition rate between the different states in the absence of force: the thicker the arrow, the the faster rate in the absence of force. In all three models, as force is varied, the transition rates of the transitions depicted by red (blue) arrows increase (decrease), resulting in the observed catch bond behaviour. The black arrow in A signifies an ideal bond whose unbinding rate does not vary with force.

1.4 Normal Forces and the Binding Affinity of Transmembrane Receptors

As discussed above, how applied force affects the unbinding process is now relatively well understood from a microscopic point of view. As can be seen in Eq. (1.2), the interaction potential $\mu^0(x)$ between the receptor and ligand pair interacts with the work done by the applied force $\Delta\mu_F(x)$. Of particular interest is the work done at the transition state $\Delta\mu_F\left(x^{\ddagger}\right)$, which either aids ($\Delta\mu_F\left(x^{\ddagger}\right) > 0$) or hinders ($\Delta\mu_F\left(x^{\ddagger}\right) < 0$) the stochastic evolution of the system from the bound state to the transition state. On the other hand, during the binding process, the interaction potential is quite shallow, implying that the unbound molecules will be relatively unconstrained. This makes it unclear as to how to define x_0 in Eq. (1.2) for the binding process. Furthermore, prior to binding, it is somewhat ambiguous how force will modify the energy of the system given that the force applied to the receptor cannot be transmitted to the ligand and vice versa. One can intuit that the molecules under force will be displaced, such that the four factors: (i) the geometry of the molecules (i.e., not simple point particles), (ii) the location of their binding sites (e.g., near the tip of the binding head of integrin receptors), (iii) the geometric

constraints on the molecules (e.g., a trans-membrane receptor being anchored to the membrane), and (iv) the direction of the applied force, will all play important roles in determining the binding rates. Due to these displacements, it seems therefore likely that a single molecule description will not be sufficient to study the problem accurately.

To tackle this problem, recent studies [134, 135] [135] have modeled the force-dependent binding affinity of generic receptor-ligand pairs as simple rods anchored to one of two apposing membranes, where the rods have binding sites at their tips. Using Monte Carlo simulations, they produced molecular dynamics (MD) data for the receptor and ligand rods diffusing along thermally fluctuating membranes as well as rotating about their respective anchor points on the membrane. This MD data was used to obtain estimates of binding affinity which were subsequently compared to results obtained from a statistical thermodynamics model (derived in these studies to describe the MD simulations) showing that they were in close agreement. While the statistical thermodynamic model used a more general framework than the one presented in 1.13, it nevertheless did employ very similar energetic considerations. In order to understand this model, we begin first by considering the change in Gibbs free energy due to the binding of receptor-ligand pairs in free solution, given by

$$\Delta G_{3D} \approx U_0 - \underbrace{k_B T \ln\left(V_b/V\right)}_{\Delta G_{\text{trans}}} - \underbrace{k_B T \ln\left(\Omega_b/4\pi\right)}_{\Delta G_{\text{rot}}},$$

where V_b and Ω_b are the translational and rotational phase-space volumes of the bound receptor-ligand pair, V is the volume of the simulations, and U_0 is minimum binding energy [134, 135]. The phase space volumes in this model were primarily determined using MD data. More specifically, it was assumed that $V_b = (2\pi)^{3/2}\xi_x\xi_y\xi_z$ where ξ_x, ξ_y, and ξ_z are the standard deviations of the distributions for the x, y, and z coordinates of the binding vector that connects the two binding sites, respectively. The binding affinity was then computed using $K_{3D} = V \exp\left(-\Delta G_{3D}/k_B T\right)$, where V is the volume of the simulation. For membrane bound receptors, the separation between the two membranes, l, is critical in determining the binding affinity of the receptor-ligand pairs [135]. Accordingly, Xu et al. have derived the separation-dependent change in Gibbs free energy using the expression

$$\Delta G_{2D}\left(l\right) \approx U_0 - k_B T \ln\left(A_b/A\right) - k_B T \ln\left(\Omega_b \Omega_{RL}/\Omega_R \Omega_L\right) \tag{1.6}$$

where A_b is the translational phase space area of the receptor-ligand complex, A is the area of the

membrane, Ω_R (Ω_L) is the rotational phase space volume of the unbound receptors (ligands), and Ω_{RL} is the rotational phase space volume of the receptor-ligand complex. This latter term Ω_{RL} is given by

$$\Omega_{RL}(l) \backsimeq 2\pi \int_0^{\pi/2} \exp\left(-H_{\text{RL}}(\theta; l)/k_B T\right) \sin(\theta)\, d\theta, \tag{1.7}$$

where $H_{\text{RL}}(\theta; l) \approx k_a \theta^2 + k_{RL}\left(l\sec(\theta) - L_0\right)^2$ is the contribution to the Hamiltonian due to anchoring and binding interactions of receptor-ligand complexes, θ is the angle between the membrane normal and the receptor (ligand) rod, k_a is the anchoring strength, k_{RL} is the spring-constant of the receptor-ligand complex, and L_0 is its preferred length (these last two parameters are determined from a combination of theory and MD data). The rotational phase space volume of the unbound receptors (ligands) Ω_R (Ω_L) is determined by an approach similar to Eq. (1.7), but is independent of the membrane separation ℓ. Similarly to the free-solution case, the separation-dependent binding affinity is given by

$$K_{2D}(l) = A \exp\left(-\Delta G_{2D}(l)/k_B T\right),$$

where, for thermally fluctuating membranes, the binding affinity can be determined by integrating against the probability distribution of membrane separations, as described by the equation

$$K_{2D} = \int K_{2D}(l)\, P(l)\, dl.$$

From MD data, Xu et al. found that the membrane separation is normally distributed, with $P(l) \propto \exp\left((l-\bar{l})^2/2\epsilon_\perp\right)$ where $\bar{l}$ is the mean membrane separation and $\epsilon_\perp$ is its standard deviation.

According to Eqs. (1.6) and (1.7), the binding affinity $K_{2D}(l)$ is maximal at some $l_0 \leqslant L_0$, an inequality that follows from the geometric constraint implicit in the $\ell/\cos(\theta)$ term as well as fact that $\sin(\theta)$ is monotonically increasing for $\theta \in \left[0, \pi/2\right]$. In order to directly investigate the effect of force on binding affinity, Xu et al. [136] leveraged this fact and used a harmonic approximation for the binding affinity, given by,

$$K_{2D}(l) = K_{\text{max}} \exp\left[-\frac{k_{RL}(l-l_0)^2}{2k_B T}\right], \tag{1.8}$$

where K_{max} is the maximal binding affinity. Given that their model deals with variations in membrane

separation, it was appropriate to use it to investigate the effects of compressive and tensile forces on binding affinity (in contrast to the Bell formalism which can be used to model the effect of force applied in any direction). For compressive/tensile forces, the membranes will be at equilibrium when the force applied to the membrane is equal to the force exerted by the receptor-ligand pairs. This was be expressed as a force-balance condition, given by

$$\sigma A = N_{RL} k_{RL} \left(l - l_0 \right),$$

where σ is the force per unit area (stress) applied to the membrane and N_{RL} is the number of receptor-ligand complexes on the membrane. When combined with Eq. (1.20), it is possible to compute the force-dependent binding affinity $K_{2D}(\sigma)$ implicitly by evaluating $\sigma = \pm g\left(K_{2D}\right)$, where g is a function. Numerical evaluation of this relation revealed that binding affinity is maximal for $\sigma = 0$ and decreases as the magnitude of σ increases. Moreover, this also revealed that there exists a critical stress threshold σ_c (where $\partial\sigma/\partial K_{2D} = 0$ and $\partial^2\sigma/\partial^2 K_{2D} < 0$) beyond which there is no solution for binding affinity. Beyond this critical stress, we cannot expect receptor-ligand pairs to form, and thus the membranes will either peel apart or collapse onto one another (i.e., $K_{2D} = 0$). The validity of these predictions was further investigated using simulations, where very good agreement between theory and simulations was confirmed for most cases. In particular, it was found that the effective critical stress observed in simulations is well-predicted for tensile forces (i.e., $\sigma_c^{\text{tensile}} \approx \sigma_c$) while it is always lower than the theoretical value for compressive force (i.e., $\sigma_c^{\text{compress}} < \sigma_c^{\text{tensile}}$). Through careful analysis of the critical stress for compressive forces, it was found that the deviations from theory could be well-explained by an Euler buckling instability.

Aside from pushing the boundaries of theoretical understanding of binding kinetics of transmembrane receptors, this theory gave some insights into the biophysical constraints that lead to adhesion release. At the rear of the cell, RhoA-dependent contractile stresses increase during the retraction of the trailing edge [137, 138]. According to the theory covered here, this will lead to a decrease in the binding affinity of integrins (likely leading to a decrease in the size of FAs). If stress eventually surpasses the critical stress threshold, σ_c, all integrins in the FA will unbind leading to release of the adhesion.

In this section, we have seen how a force-balance condition for the membrane leads to the existence of a critical stress value, beyond which the transmembrane receptors cannot support the applied force. Due to the intrinsic geometric aspects of the problem, it was treated as a fundamentally macroscopic

problem with the theory developed only applicable to compressive and tensile forces. In Section 1.6, we will use a microscopic approach based on the Bell formalism developed in Section 1.3.2 that also predicts the existence of a critical force value and can be used to model the effects of sheer force as well.

1.5 Mechanically-Driven Clustering of Integrins

The computational approach developed by Xu et al. (see Section 1.4, [135]) was also used to investigate the effect of the glycocalyx on integrin binding affinity as well as the spatial clustering it induces. The glycocalyx is a thin layer of anionic material that coats the cell and is made up of a network of glycoproteins and proteoglycans [139]. The glycocalyx has long been associated with the regulation of cell adhesion [140]. Moreover, Paszek et al. [141] recently found that metastatic tumors cells express an excess of large glycoproteins on their cell surface, and that the resulting thicker glycocalyx promotes clustering of integrins and adhesion formation. This finding had been predicted by a computational model previously developed by Paszek and collaborators [142]. Paszek's computational model explored numerical simulations of stochastically binding integrins with an extensive lattice spring model to account for membrane and ECM mechanics. They found that integrin clustering was due to an interplay between integrin binding affinity and glycocalyx repulsion [142]. Effectively, they proposed that a thick glycocalyx prevents integrin binding due to a large separation between the membrane and the ECM, while bound integrins will exclude thick glycoproteins from their vicinity, producing a kinetic trap where more integrins are likely to bind [141].

Due to membrane separation being a key factor in producing glycocalyx-driven integrin clustering, it seemed likely that the theory developed by Xu and collaborators (see Section 1.4) may be useful to understand this phenomenon. Indeed, in [136] Xu et al. modeled this integrin clustering phenomenon using their familiar system of rod-like receptors and ligands anchored to two apposing membranes, while simultaneously incorporating the effect of the glycocalyx by modeling it as a spring with a rest length of l_g and a stiffness per unit area of k_g . Using statistical mechanics methods, they then found that the separation between the two membranes is normally distributed, with a mean separation given by

$$\bar{l} = \frac{k_g A l_g + n k_b l_0 + \sigma A}{k_g A + n k_b}$$

and a standard deviation given by

$$\epsilon_{\perp} = \sqrt{k_B T / \left(k_g A + n k_b\right)}.$$

As can be seen in Eq. (1.8), the mean binding $K_{2D}\left(\bar{l}\right)$ affinity is a monotonically decreasing function of l_g (or k_g). In view of the fact that a thicker glycocalyx will inevitably have a lower binding affinity than one for which $l_g \approx l_0$ (a prediction experimentally validated in [141]), it seems paradoxical that a thicker glycocalyx can enhance clustering. However, since clustering produces a different organization at local scales compared to global scales, the global binding affinity may not be adequate or even an appropriate tool to study this phenomenon. As an illustrative simplification of the problem at hand, let us consider the scenario in which the first successful bond has just been formed between a receptor-ligand pair. Near this receptor ligand pair, the membranes will be separated by a distance $l \approx l_0$ and thus, locally, the binding affinity can be approximated as

$$K_{2D}\left(l \approx l_0\right) \quad \approx \quad K_{max},$$

while far-away from this receptor-ligand pair $l \approx l_g > l_0$ and the relevant binding affinity is

$$K_{2D}\left(l \approx l_g\right) \ll K_{max}.$$

Therefore, we will not only see more bonds form near an already-existing bond (as there is also a similar local enhancement of the binding rate k_{on} [136, 143]) but also see these bonds more likely to remain formed compared to lone ones forming far away. Statistically, this leads to integrin clustering that is driven purely by mechanical considerations, that does not require the active generation of forces in the actin cytoskeleton. While a qualitative mechanistic understanding of this phenomenon can be obtained from the original computational model [142], the study by Xu et al. found excellent agreement between their own MD data and a theoretical framework based on Eq. (1.8) [136]. This demonstrated that their theoretical framework is generic enough to study diverse problems through analytic means as an alternative to numerical simulations which are non-trivial to implement.

1.6 Mechanical Response of Integrin Clusters

We have thus far elucidated how the unbinding rates of single integrins vary with the applied force and how this relates to the conformational changes involved in activation, as well as how force affects the binding affinity of a spatially distributed population of transmembrane receptors on a membrane. As we explained in the previous section, the mechanical effect of the glycocalyx helps to organize integrins into clusters by making local binding-dependent kinetic traps. Furthermore, adaptor proteins in the adhesion plaque locally slow the diffusion of integrins [35]; this as a result enhances the kinetic trapping of integrin underneath the plaque to produce a feed-forward system that leads to organization of integrins (and adaptor proteins) into discrete adhesions [34, 130].

Therefore, it seems relevant to ask how these discrete adhesions, which consist of tens of integrin molecules that stochastically bind and unbind [16, 35, 144], are affected by the active forces generated in the actin cytoskeleton. This question was first investigated by Bell who modeled an adhesion as a collection of bonds sharing a fixed load while dynamically unbinding and rebinding [111]. For a cluster of slip bonds containing N_t integrins under a fixed load F, the mean number of closed bonds ($\langle N \rangle$) to obeys the rate equation given by

$$\frac{d}{dt}\langle N\rangle = -\langle N\rangle k_{off}^{0} \exp\left(F/\left(\langle N\rangle F_0\right)\right) + k_{on}\left(N_t - \langle N\rangle\right) \tag{1.9}$$

where $k_{off}^{0} > 0$ is the unbinding rate in the absence of force, $k_{on} > 0$ is the binding rate of a single integrin, and F_0 is as defined in Eq. (1.3). To characterize the long-term behaviour of such a model, one may seek steady states whose unbinding rate (first term in Eq. (1.9)) is equal to the binding rate (second term). Due to the fact that these rates are exponential and linear functions of $\langle N \rangle$, respectively, it is possible to obtain as many as two such states for $\langle N \rangle > 0$ [145]. In the scenario with two steady states, the elevated one has its load distributed over comparatively more bonds. This helps to explain why this elevated steady state is consistently found to be stable (see solid line in Fig. 1.3A), while the lower steady state is an unstable steady state (see black dashed line in Fig. 1.3A). When a bond is broken in the elevated steady state, denoted N_s, the increase in the unbinding rate (due to an increase in $F/\langle N \rangle$) is compensated by an increase in the binding rate (due to the increase in $N_t - \langle N \rangle$). When a bond is broken at the lower steady state, denoted N_u, however, the increase in the unbinding rate is larger than the corresponding increase in the binding rate and thus once a single bond breaks the cluster

as whole catastrophically unbinds. As the force F is increased, the two steady states come closer to one another, until they annihilate at a critical force F_c determined by a saddle-node bifurcation (see grey dotted line in Fig. 1.3A) located at

$$F_c = F_0 N_t W\left[k_{on}/\left(k_{off}^0 e\right)\right], \tag{1.10}$$

where W is the Lambert W function (i.e., the product-log function). For $F > F_c$, no steady state exists with $\langle N \rangle > 0$; this means that, a cluster with a fixed number of bonds can only support up to a finite load that can be predicted using Eq. (1.10). This also highlights the importance of rebinding for the cluster to be able to resist applied forces, as in the absence of rebinding, we have $F_C \propto W(0) = 0$.

The deterministic treatment of the model suggests that once the system reaches a stable steady state, it will remain there indefinitely. However, one may wonder if stochastic effects, particularly when adhesions only have a few closed bonds, may alter this outcome. In order to answer such a question, in [146], Erdmann and Schwarz reformulated Eq. (1.9) in a discrete setting as a one-step master equation given by

$$\frac{d}{dt}p_i = r_{i+1}p_{i+1} + g_{i-1}p_{i-1} - (r_i + g_i)\,p_i, \tag{1.11}$$

where p_i is the probability of having i closed bonds, and r_i and g_i are bond rupture and gain rate functions, respectively, defined by

$$r_i = ik_{off}^0 \exp\left(F/(iF_0)\right) \text{ and } g_i = k_{on}(N_t - i).$$

Within this setting, we may define the lifetime of a cluster to be the expected time it takes for a stochastic processes described by Eq. (1.11) starting with N_t closed bonds to reach a state with zero closed bonds. Using standard results from the theory of Markov Chains [147,148], such a quantity may readily be computed

$$T = \sum_{i=1}^{N_t} \frac{1}{r_i} + \sum_{i=1}^{N_t-1} \sum_{j=i+1}^{N_t} \frac{\prod_{k=j-i}^{j-1} g_k}{\prod_{k=j-i}^{j} r_k}. \tag{1.12}$$

By evaluating this expression for $N_t \geqslant 2$, one obtains an expression that increases polynomially with respect to the binding rate, but decreases exponentially with respect to force. This is reminiscent of

the difference we saw in the thermodynamic model of integrin activation, where the force-independent reaction had a much more limited effect compared to the force-dependent reaction. While the deterministic picture suggests that for $F < F_c$ the system will reach N_s provided that $N(t=0) > N_u$ and remain there indefinitely, a stochastic treatment of the problem shows that even for $N(t=0) = N_t > N_s > N_u$, the system will reach $N(t) = 0$ in finite time given by Eq. (1.12). Moreover, from the qualitative stability analysis described above, we may posit that for $F > 0$, the unstable steady state N_u acts as a threshold separating stochastic trajectories. If at any point in time an adhesion has (i) $N(t) < N_u$, it will almost surely undergo catastrophic unbinding where all bonds unbind very quickly or (ii) $N(t) > N_u$ it will grow towards N_s until stochastic fluctuations cause the system to be in scenario (i) and disassemble. This perspective has indeed been confirmed using stochastic simulations (see Fig. 1.3C and D, and [127]).

As suggested before, integrin bonds exhibit a catch bond behaviour, but the models of bond-clusters investigated thus far have all assumed a slip bond for the integrin-ligand pair. In order to account for this, in [127], Novikova and Storm used Eq. (1.11) with an expression for r_i derived from the two-pathway model for catch bonds, given by Eq. (1.5) with $F_s = F_c$, and kept $g_i = k_{on}(N_t - i)$ as before to describe the system. Using mean field analysis, they were able to implicitly solve for the steady states of $\langle N \rangle$ from an expression for the total force applied to the adhesion, given by

$$F = F_s \langle N \rangle \phi_{max} \pm F_s \langle N \rangle \cosh^{-1}\left(\frac{k_{on}}{k_{off}^0} \frac{\alpha \left(N_t - \langle N \rangle \right)}{2 \langle N \rangle} \right), \tag{1.13}$$

where $\phi_{max} > 0$ (a unitless parameter) determines the maximum bond lifetime as $F_s \phi_{max}$, and $\alpha > 0$ (also a unitless parameter) specifies the relative rates of the two pathways (according to the two-pathway interpretation of Eq. (1.5)). By plotting $\langle N \rangle$ versus F for both branches of Eq. (1.13), they obtained an elliptic-shaped curve with two (stable and unstable) branches that meet at a saddle-node bifurcation, leading to adhesion disassembly at large forces similar to the Bell model (see grey dotted line in Fig. 1.3B for various values of k_{on}). However, due to the increasing phase of the catch bond lifetime, the stable branch N_s increases significantly with applied force until it reaches a maximum value (highlighted by the grey solid line in Fig. 1.3B). This behaviour is strikingly different from what was seen for slip bonds where the stable branch N_s monotonically decreased with force (compare the solid black lines in Fig. 1.3A and B). This feature of the Novikova model thus gives a simple theoretical explanation for adhesion reinforcement, the observation that adhesions grow in response

to applied force [18, 30]. Interestingly, this latter model has very few closed bonds in the absence of force, implying that stable adhesions cannot form in the absence of significant force, which is at odds with experimental observations [149]. This discrepancy can be resolved by an appropriate change in parameters that abrogates the adhesion reinforcement phenomenon [127]. By considering the adhesion as a mixture of integrin heterodimers that contain either β_1 or β_3 subunits that behave as either catch or slip bonds, respectively [150, 151], the bond-cluster model can be made to be mechanically resilient at low forces while maintaining its ability to reinforce at high forces [152].

1.7 Adhesion Plaque Formation

As discussed in Section 1.2.1, the adhesion plaque forms due to adsorption of adaptor proteins, resulting in the net growth of the adhesion. The plaque is an intrinsically dynamic structure, which continually exchanges matter with the cytosol [12, 13, 153, 154]. At the molecular level, the dynamics of plaque assembly/disassembly appear to be related to the degree of aggregation of adaptor proteins, with the binding/unbinding of paxillin monomers to/from the plaque being associated with assembly while the unbinding of larger aggregates is associated with disassembly [12]. Interestingly, the size of adaptor protein aggregates observed in adhesions has been shown to be a biochemically regulated property that the cell can adjust through signaling pathways (e.g., phosphorylation events [154, 155]). This paints a picture of a plaque made of adaptor proteins which not only bind to integrins, but also to one another, forming pleiomorphic ensembles with dynamic composition, size, and rapid turnover [156]. Regardless of what is known about adaptor protein dynamics at the molecular level, it is typical to characterize adhesion dynamics by a net assembly or disassembly rate, depending on which phase of the adhesion life cycle is under consideration [19, 67, 157–159]. This provides a simplistic conceptual model with which we may understand plaque dynamics; a model that assumes that when the on-rate of adaptor proteins is larger than the off-rate adhesions will assemble, but when the reverse is true they disassemble. The experimental recordings of the different phases of the adhesion life cycle suggest that the net on- and off-rates of adaptor proteins varies in both space and time, and that adhesions do not seem to simply switch between assembly and disassembly, but also exhibit a plateau phase where adhesion size is roughly constant for some period of time [19, 67].

From Eq. (1.21), we can see that the net adsorption process will reach equilibrium when μ_{agg}, the chemical potential of adaptor proteins in their aggregated state inside the adhesion, is equal to

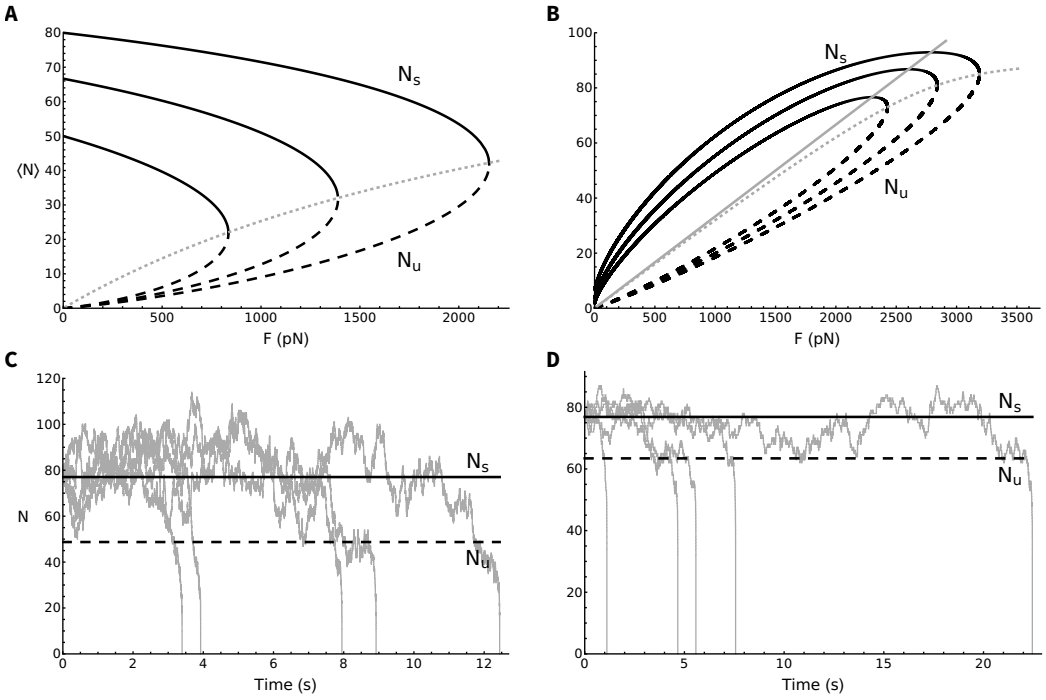

Figure 1.3: Bifurcation analysis of the deterministic bond-cluster models reveals saddle-node bifurcations, explaining disassembly dynamics observed in stochastic realizations of these models. Bifurcation diagrams of the mean number of closed integrin-ligand bonds $\langle N \rangle$ with respect to the mechanical load applied to a cluster of bonds that share the load equally. Branches of stable (black solid lines labeled N_s) and unstable (black dashed lines labeled N_u) steady states meet at saddle-node bifurcation points. This feature is present in (A) the Bell model of adhesion using slip bonds, and (B) the Novikova model of adhesion using catch bonds. Gray dotted lines in A and B represent the set of all saddle-node bifurcation points obtained as the value of k_{on} is varied, while the grey solid line in B represents the set of all maximum points on N_s as the value of k_{on} is varied. In stochastic realizations of the models, if the system crosses the threshold determined by N_u all bonds will catastrophically unbind and the adhesion will disassemble. Parameters used to compute the black curves are $N_t = 100$, $k_{off}^0 = 1\,\mathrm{s}^{-1}$, $F_0 = \phi_{max} F_s = 30\,\mathrm{pN}$, and $k_{on} = 1, 2, 4\,\mathrm{s}^{-1}$ from bottom to top. Representative stochastic realizations of (C) the Bell model with $N_t = 290$, $k_{on} = k_{off}^0 = 1\,\mathrm{s}^{-1}$, and $F \approx 2422\,\mathrm{pN}$, as well as (D) the Novikova model with $N_t = 100$, $k_{on} = k_{off}^0 = 1\,\mathrm{s}^{-1}$ and $F \approx 2306\,\mathrm{pN}$, depicted as gray lines exhibiting catastrophic unbinding when $N \approx N_u$ (N_t was chosen in C such that the values of N_s are comparable in C and D). The black solid and dashed lines in C and D are the values of the N_s and N_u, respectively, highlighted in panels A and B.

μ_{bulk}, their chemical potential in the cytosolic bulk. However, if one assumes that the adhesion plaque is a condensed phase of adaptor proteins with a fixed density and that the cytosol acts as a large bath of adaptor proteins (μ_{bulk} = constant), it is unclear how the system may reach equilibrium. By considering the geometric constraints of the adsorption process, Gov proposed a set of mathematical models which can explain the existence of the plateau phase observed during adhesion assembly as the system reaching equilibrium [160]. In contrast to the more common scenarios involving adsorption, where the binding sites for molecules are a preexisting feature of the liquid-solid interface, the binding sites for adaptor proteins are part of the adhesion itself. It is therefore necessary to consider the size and shape of the adhesion when quantifying its rate of growth. In order to do so, one must specify the region(s) where adsorption and desorption occur. Gov considered two possible regions; (i) the bulk of the adhesion, or (ii) the periphery of the adhesion [160].

By assuming that adsorption and desoprtion may not be symmetric, Gov derived four possible modes of growth for plaque dynamics: "Bulk-on/Bulk-off", "Bulk-on/End-off", "End-on/End-off", and "End-on/Bulk-off". For example, with a circular adhesion geometry, the "Bulk-on/Bulk-off" and "End-on/Bulk-off" models were given by $\frac{\partial A}{\partial t} = (k_{\text{on}} - k_{\text{off}})\, A$, and $\frac{\partial A}{\partial t} = k_{\text{on}}\sqrt{A/\pi} - k_{\text{off}} A$, respectively. The "Bulk-on/Bulk-off" model has no non-zero steady state, and the sign of $k_{\text{on}} - k_{\text{off}}$ determines whether the adhesion grows or shrinks exponentially in time. However, if a given adhesion grows arbitrarily large, the assumption of fixed μ_{bulk} will no longer be valid, and a steady state will be reached [130]. The "End-on/Bulk-off" model, on the other hand, has a steady state given by $\bar{A} = \pi(k_{\text{on}}/k_{\text{off}})^2$. This means that by either imposing the conservation of matter on a symmetric net adsorption process ("Bulk-on/Bulk-off") or by simply having an asymmetric net adsorption process ("End-on/Bulk-off"), the plaque reaches a steady state size. Although these models were applied to circular domains to describe adhesions, the results obtained for rectangular geometries were qualitatively the same [160]. Indeed, Gov showed that the rectangular geometry for FA produces the most compatible results with FA-size data provided that the "End-on/Bulk-off" ("End-on/End-off") model is considered when the FAs are small (large) [160]. The size-dependent switch in dynamics was interpreted as being reflective of the association of stable stress fibres to larger FAs which prevents loss of adaptor proteins through the bulk of the adhesions (i.e., the "Bulk-off" switches to "End-off" upon stress fibre association) [160].

While Gov's approach can explain the existence of the plateau phase during assembly, it does not explain the origin of disassembly. Within Gov's framework, the only way for disassembly to occur,

after an adhesion reaches its plateau phase, is through an imposed change in adaptor protein adsorption kinetics (via the parameters k_{on} and k_{off}). Nascent adhesions disassemble quickly once they are no longer underneath the dense actin meshwork of the lamellipodium [19, 53]. Therefore, it is possible that their disassembly directly reflects either an increased adaptor protein off-rate due to a decreased association with actin filaments [161], or a decrease in the availability of certain adaptor proteins that are delivered to NAs via diffusion along actin filaments (e.g., VASP [162]). Alternatively, in fibroblasts, an increased density of microtubule tips near the nucleus has been found to produce a gradual decrease in the size of mature FAs as they move rearward relative to the motion of the cell. This process is likely mediated by the endocytosis of integrins [58, 62], where it is unclear to what extent adaptor proteins are also internalized. Interestingly, a modification of Gov's formalism accounting for the interaction between integrins and adaptor proteins could explain the decrease in FA-area through an integrin-dependent increase in k_{off} [130]. For mature FAs, however, it has also been shown that disassembly can be initiated by a decrease in applied mechanical force [158]. In the following section, we will explore a model that incorporates the mechanics of the adhesion plaque into kinetics of adsorption while accounting for mechanosensitive integrin activation, and see how forces can be used to regulate adhesion assembly and disassembly.

1.8 Mechanical Response of the Adhesion Plaque

As the mechanical linkage between integrins and the actin-cytoskeleton, the adhesion plaque is subject to a number of mechanical forces which have been hypothesized to lead to biochemically-relevant deformation of adaptor proteins. In particular, it has been hypothesized that these deformations may underlie the phenomenon of adhesion sliding. The mathematical theory describing the mechanosensitivity of the adhesion plaque was pioneered by Nicolas, Safran, and collaborators in a number of studies [36–39, 163, 164]. Fundamentally, these studies focused on the mechanical response (i.e., deformation) of the adhesion plaque by treating it as an elastic thin film grafted onto the cytosol-membrane interface and subjecting it to shear forces [163]. The grafting boundary condition results in a force-balance equation, defined in one dimension by the following equation

$$k_0 a^2 \frac{d^2 u}{dx^2} - k_b u + F(x) = 0,$$

where u is the displacement of material due to the applied force, k_0 is the stiffness of the springs assumed to connect adjacent units in the plaque, a is a length-scale which characterizes the units, $k_b u$ is a restoring force caused by the connection between the fixed substrate and the adhesion (such that k_b is proportional to the stiffness of the composite integrin-adaptor-actin linkage), and $F(x)$ is an applied force. By considering a gate-like force applied just inside the adhesion's boundary, it was predicted that adhesion plaque material is compressed at the proximal tip of the adhesion while being expanded at its distal tip [163]. This prediction was then used to formulate a physically plausible mechanism for the anisotropic growth of adhesions in response to unidirectional force, whereby an unspecified "mechanosensitive unit" that constitutes the adhesion plaque responds to deformation through changes in its adsorption/desorption kinetics [36]. These kinetic changes are primarily understood through energetic considerations. For instance, in order for a mechanosensitive unit to be incorporated into a plaque under fixed stress it must bear some non-zero force, which will result in its deformation. By using Hooke's law, one can estimate the energetic cost of deformation using the equation $\Delta\mu_{el} \approx f^2 a^2/2k$, where f is the force per mechanosensitive unit, and k is a spring constant. While the cell is likely to have enough energy to deform these mechanosensitive units, in order to do so, they must be inside the plaque (i.e, adsorbed). The adsorption process (and subsequent deformation) will thus occur spontaneously only if the elastic deformation energy is offset by a larger decrease in free energy due to the adsorption process. This means that, adsorption only occurs if

$$\Delta\mu_{\text{agg}}(f) = \Delta\mu_{\text{el}} - \Delta\mu_{\text{chem}} \approx \frac{f^2 a^2}{2k} - \Delta\mu_{\text{chem}}(f) < 0, \tag{1.14}$$

where $\Delta\mu_{chem}$ is the intrinsic free energy change due to the adsorption of a single mechanosensitive unit. Nicolas and Safran assumed this change in free energy to be linearly proportional to the change in plaque density [36], and based on this deduced that at the proximal (compressed) tip, it is given by

$$\Delta\mu_{\text{chem}}(f) \approx e\frac{f}{\sqrt{kk_0}},$$

where e is the free energy of adsorption of a single unit ($e > 0$ for spontaneously forming adhesions). Implicit in this formulation is the assumption that the adhesion in question has reached its thermodynamic equilibrium prior to being loaded with force, since $\Delta\mu_{\text{agg}} = 0$ in the absence of the applied mechanical force. With these expressions, it is possible to investigate adhesion plaque dynamics once the applied force f is turned on. Since for $f \approx 0$, we have $\Delta\mu_{\text{agg}} < 0$ and that when $f \to \infty$ we have

$\Delta\mu_{\text{ads}} \to \infty$, it follows that there exists a critical f^* satisfying

$$f^* = \frac{2e}{a^2\sqrt{k_0/k}}$$

where $\Delta\mu_{\text{agg}}\left(f = f^*\right) = 0$ beyond which growth of the proximal tip becomes an unfavourable process. In order to refine the conditions for adhesion growth beyond the exothermic constraint defined by Eq. (1.14) Nicolas and Safran used Eq. (1.25) to determine ν_+ and ν_-, the rates of adsorption and desorption at the proximal and distal tips, respectively [36]. Subsequent analysis of the net adhesion growth rate (i.e., $\nu_+ - \nu_-$) revealed that, despite growth of the distal tip being energetically favourable for $f \approx 0$, the adhesion as a whole does not grow unless $0 \leqslant f_{\text{min}} < f < f_{\text{max}} < f^*$, while desorption at the distal tip dominates the growth process outside of this range. When, $f < f_{\text{min}}$, an adhesion will undergo resorption where it continually shrinks in size. For $f = f_{\text{min}}, f_{\text{max}}$, the desorption rate at the distal tip equals the adsorption rate at the proximal tip, representing a treadmilling regime for the plaque model where the adhesion is translocated towards the cell center while maintaining a constant size and remaining fixed to the substrate.

These results were expanded upon by Besser and Safran in a subsequent study, by considering the more biophysically-relevant scenario in which the plaque may be divided into two functionally distinct layers: the signaling layer and the force transduction layer [38]. The model in this study accounted for both the force-transmission through adaptor proteins in the transduction layer, as well as the force-induced activation of the mechanosensitive units in the signaling layer that could be due to (i) the expansion and compression of the plaque material (as was assumed by Nicolas and Safran [36]), or (ii) direct mechanical stretching of proteins (as had subsequently been predicted by Bruinsma [165]). In their model, adsorption kinetics were also incorporated in a congruent manner through the use of the equation

$$\partial\phi/\partial t \propto \left(\mu_{\text{bulk}} - \mu_{\text{agg}}\right)$$

that describes the dynamics of the fractional adaptor protein concentration $0 < \phi(x,t) < 1$ in the condensed plaque phase [166]. Through the application of traveling wave solutions ($\phi\left(x,t\right) = \phi\left(x - vt\right)$), net adsorption rates of the distal and proximal tips of the adhesion were successfully computed and the existence of new modes of growth not previously found in the original model were discovered. One of these modes is the sliding resorption mode for $f < f^0_{\text{min}} < f_{\text{min}}$ where adhesions shrink while being translocated in the direction of force. This approach, however, did not account for the energetic cost

of deforming the plaque ($\Delta\mu_{\text{el}}$), leading to the prediction that adhesions will always grow at arbitrarily high forces.

This last point was resolved in a a follow up study [39] that considered not only the intrinsic energy of plaque deformation $\Delta\mu_{\text{el}}$, but also the total energy of substrate deformation $H_{\text{el}}^{\text{substrate}}$. By using Eq. (1.30), it was shown that this latter consideration reduces the chemical potential μ_{agg} by a term that is proportional to the length of the adhesion and inversely proportional to the stiffness of the substrate (i.e., it vanishes for an infinitely rigid substrate). This allowed adhesions to have an equilibrium size, a feature that was lacking in previous iterations of the model. It also led to the very interesting prediction that both the equilibrium size and the adhesion's equilibration kinetics (i.e., the rate at which it reaches equilibrium) scale linearly with elastic modulus of the substrate (i.e., its stiffness). In other words, the model predicted that adhesion size grows linearly with the stiffness of the substrate, an outcome that was later been validated experimentally [167]. It is important, however, to note that this can only be true within a finite stiffness range as the finite size of the cell should prevent adhesions from growing indefinitely [168, 169].

The modes of growth reported in the studies highlighted here (summarized in Table 1.1) were echoed in others [170, 171], albeit with some differences in model formulation (see [147] and [171] for an in-depth discussion). Of particular interest, are the sliding resorption and sliding growth modes. The sliding resorption modes are likely to be relevant to the adhesion sliding phenomenon discussed in Section 1.2.2, while the sliding growth mode is likely to be relevant to adhesion maturation. The model presented in [39] predicted that the cell may switch between the two modes through an increase in the traction stress applied to adhesion. Traction forces are consistently higher at the retracting rear of migrating cells [137, 138, 172, 173], where sliding FAs are primarily found [78, 174, 175], compared to their mid-bodies, where FAs are typically stationary relative to the ECM. Moreover, this model predicted that, the sliding growth mode is likely to have a significantly smaller sliding velocity compared to the high-force sliding resorption mode. This mode of growth may explain the slow treadmilling behaviour that can be observed near the protrusive regions of motile cells where FAs typically mature [19, 176, 177].

Finally, while we have focused on force as the variable that can lead to adhesion sliding, it is important to note that the force thresholds that determine the growth mode of the cell and its sliding velocity can all be modified biochemically. For instance, by increasing the free energy change of adap-

Plaque Behaviour	Distal Tip	Proximal Tip	Sliding Velocity	Mechanical Condition
Resorption	$\longrightarrow$	$\leftarrow$	Negligible	$f < f^0_{\text{min}}$
Sliding Resorption	$\longrightarrow$	$\rightarrow$	Negligible	$f^0_{\text{min}} < f < f_{\text{min}}$
Treadmilling	$\rightarrow$	$\rightarrow$	Negligible	$f = f_{\text{min}}$
Sliding Growth	$\rightarrow$	$\rightarrow$	Negligible-Moderate	$f_{\text{min}} < f < f_{\text{max}}$
Treadmilling	$\rightarrow$	$\rightarrow$	Near Maximal	$f = f_{\text{max}}$
Sliding Resorption 2	$\longrightarrow$	$\rightarrow$	Maximal-Moderate	$f_{\text{max}} < f < f^0_{\text{max}}$
Resorption	$\longrightarrow$	$\leftarrow$	Moderate	$f^0_{\text{max}} < f$

Table 1.1: Summary of the different sliding modes predicted in Fig. 4A of [152].

tor protein adsorption, ϵ_B, we can expect the force threshold for the sliding resorption growth modes to increase; similar effects can be expected when increasing λ_{xz}, the rigidity of the integrin-adaptor-actin linkage (equivalent to k discussed previously in relation to [36]). The effect of the force-insensitive inactivation of LFA-1 (i.e., loss of affinity regulation by force) at the rear of neutrophils as seen in [76] may be understood as the limit when $\tau \rightarrow 0$, where τ is the force-sensitivity of the integrin activation energy barrier. By decreasing τ, the sliding velocity can be made arbitrarily small, suggesting that modulation of integrin force-sensitivity (either through biochemical modifications or through switching integrin subunits) may induce adhesion release by not only weakening the integrin-ECM bond but also by halting the movement of sliding adhesions. Furthermore, decreasing ϵ_B causes a decrease in both the sliding and growth velocities of the adhesion. Such a change in ϵ_B could be due to cleavage of bonds by proteases (e.g., calpain), suggesting that protease activity may have similar effect to the loss of affinity regulation on adhesion release. This body of work thus provided important insights into how the relative energetic contributions of biochemical reactions and mechanical deformation manifest themselves in the kinetics of adsorption/desorption and produce physiologically-relevant adhesion dynamics.

1.9 Mechanical Response of the Membrane

Building upon the success of the adhesion plaque models developed by Nicolas and collaborators, the long-range mechanical response of a membrane containing integrins was investigated by Xu and collaborators [178]. Their work did not explicitly consider the presence of FAs on the membrane, but focused on the activation, subsequent ligand-binding, and internalization of integrins on the membrane

and how these processes are modulated by ECM stiffness. Similar to previous work [39, 99, 165], they used a force-dependent energy difference between inactive and active conformations of integrin, given by

$$\Delta\mu_{\text{act}} = \mu^0 - F\Delta x,$$

where μ^0 is the intrinsic energy difference between the active and inactive conformations in the absence of force, F is the magnitude of the sheer force applied to the integrin, and Δx is the length difference that characterizes the conformational change. The force per integrin was determined by modeling the membrane as ribbon lying on an elastic ECM; under such assumptions the force varies is space [179], and is given by

$$F(x) \propto f_t \exp\left(-x/\lambda_T\right),$$

where f_T is the membrane tension at the leading edge and λ_T is a space-constant determined by the relative material stiffness of the ribbon (i.e., the composite system of membrane, integrins, and adaptors) and ECM as well as their heights [178]. The probability of integrin activation was computed using a Boltzmann factor, given by

$$p_{\text{act}} = \left(1 + \exp\left[\Delta\mu_{\text{act}}/k_BT\right]\right)^{-1}$$

or

$$p_{\text{act}}(x) = \left(1 + \exp\left[\left(\mu^0 - F(x)\,\Delta x\right)/k_BT\right]\right)^{-1}.$$

This effectively predicts activation probability is close to unity near the leading edge and remains roughly constant until it drops off to zero at some finite distance inside the cell. Due to the dependence of λ_T on ECM stiffness, Xu et al. found that the finite length at which activation drops off decreases with increasing ECM stiffness, indicating that more integrins can be activated on a softer ECM. Assuming that integrins must be activated to bind, they modeled the binding probability by considering two opposing effects (i) the release of energy ($U < 0$) due to receptor-ligand binding and (ii) the stretching of integrins by the force f_c that caveolin exerts on the membrane [180]. Accounting for both of these effects, the probability of an integrin being bound was found to be

$$p_{\text{bound}} = p_{\text{act}}(1 + \exp\left[(U + f_c^2/2k_{\text{eff}})/k_BT\right])^{-1},$$

where k_{eff} is the effective stiffness of the composite integrin-ECM system and is given by $k_{\text{eff}}^{-1} = k_I^{-1} + k_M^{-1}$ with $k_I(k_M)$ being the stiffness of integrin receptors (ECM). The term $f_c^2/2k_{\text{eff}}$ quantifies the

deformation energy induced by caveolin, which becomes arbitrarily large as $k_M, k_I \to 0$. On ECMs of all stiffness, $p_{\text{bound}} \propto p_{act}$; however, the constant of proportionality decreases on softer ECMs, suggesting that soft ECMs counter-intuitively favor both activation and unbinding. The force of caveolin on the membrane will only induce internalization if it is energetically favourable to do so. Xu et al. used a theory of invagination, developed by Sens and Turner in [180], to derive an exothermic condition for the internalization of the membrane (and any integrin present). By accounting for the energy of the integrins on the pre-internalized membrane, they were able to express this energetic condition as a function of p_{bound} , subsequently concluding that internalization occurs if $p_{\text{bound}} < p_c$, with $p_c \approx 0.25$ in the physiological parameter regime. These and previous results thus show that p_{bound} is consistently lower on a softer ECM, implying that a softer ECM will always exhibit more internalization. This dual effect of ECM stiffness on integrins may explain why bone marrow mesenchymal stem cells exhibit both increased integrin activation and internalization on soft matrices [181].

1.10 Comparison of Model Outcomes

Thus far, we have touched on two broad classes of adhesion models, bond-cluster models (see Section 1.6 [127, 145, 146, 152, 182]) and adhesion-plaque models (see Section 1.8 [36, 37, 39, 163]). Although these two classes of models differ in their construction, they both predict that adhesions can grow in size in response to force, and that beyond a critical force value, the adhesion will begin to disassemble. They also produce predictions that are inconsistent with each other. More specifically:

1. Bond-cluster models always predict an adhesion with finite size at zero force, while the mechanosensitive plaque models presented above suggest that there may exist a threshold in force required to produce adhesions. This is a consequence of the fact that bond-cluster models do not consider the dynamics of adaptor proteins, whereas the mechanosensitive plaque models suggest that adsorption becomes kinetically favourable only once force crosses a threshold.
2. In the adhesion-plaque models, disassembly is caused by a switch in net adsorption kinetics to favour desorption, but they consider that their adaptor protein-integrin complexes may become arbitrarily stretched (which is unlikely to be valid for large forces). On the other hand, in the bond-cluster models, disassembly is due to mechanical breakage of integrin bonds.

In order to remedy this, bond-cluster models should account for the kinetics of adsorption while the

plaque models should account for the force-dependent unbinding of integrin-ligand bonds. The former can be accomplished by explicitly tracking the growth of the plaque, and making the binding of integrins somehow dependent on the plaque size, while the latter may be implemented by assuming that, as integrin bonds become broken, the desorption of nearby adpator proteins will become overwhelmingly favoured.

1.11 A Hybrid Model

The bond-cluster models and adhesion-plaque models assume the presence of either adaptor proteins or integrins, respectively, and investigate the dynamics of the other class of proteins. As noted in Section 1.2, these two classes of proteins cooperate to form the adhesion and its associated cytoskeletal structures (F-actin and stress fibres). Based on this, in order to analyze adhesion dynamics, it seems imperative to model the cooperation between these two major types of proteins that make up the adhesion. Previous models that have taken into account both protein classes to study adhesions have either implicitly or explicitly assumed that adpator proteins and integrins form complexes with a 1:1 ratio, implying that the fluxes of the two proteins into or out of the adhesion are identical [171, 183]. This assumption is difficult to reconcile with the observation that integrin density within different FAs can vary by 3-fold in the same cell, whereas adaptor protein densities vary less and they have a characteristic pair-wise distance that is conserved across adhesion classes [80, 184, 185]. One exception to this modeling choice was the mechanosensitive model developed by Besser and Safran [38] (and subsequently augmented with energetic terms from Nicolas and Safran [39]), in which the force transmitted to integrins was hypothesized to be proportional to the local density of adaptor proteins (see above). In contrast to experimental observations, however, this model assumed that integrins are already organized as a template for the adhesion plaque to grow on [19, 34]. A model of nascent adhesions developed by MacKay and Khadra [130] resolved this issue, by explicitly specifying the spatial and binding dynamics of integrins and the adsorption kinetics of adaptor proteins, and generated a model that allowed for a variable density of integrins inside the adhesion.

The variable integrin-density model [130] has made a number of important contributions to the theoretical understanding of NAs. Firstly, as suggested by Fig. 1.3 A and B, there is always an unstable steady state N_u between the elevated stable steady state N_s and the single molecule initial condition $N = 1$ (for $F > 0$). This makes it unclear as to how adhesions can assemble in the presence of force

given that their trajectory through state space to N_s will always be impeded by N_u. Novikova and Storm took note of this issue and posited that in order to observe assembly in their model, it is necessary to consider the time-dependent force that results from assembly/contraction of stress fibres [127]. Indeed, the inclusion of a time-dependent forces did allow Walcott et al. to produce assembly starting from a single molecular complex when stochastically simulating the model [183]. Markedly, this latter model was too complex to allow for mean field analysis of the full system. To resolve this issue, Walcott et al. performed this analysis on a one-variable reduced system and found that it possesses a configuration of steady states equivalent to the bond-cluster models discussed above (i.e., $0 < N_u < N_s$). It remained, however, unclear how their model overcomes the aforementioned issue with the unstable steady state (or the saddle fixed point in the high dimensional state space Walcott et al. used in producing the stochastic simulations). MacKay and Khadra [130], on the other hand, performed their mean field analysis on their full three-variable model, ensuring that the saddle fixed point (N_u) remains relevant to the dynamics of the model while allowing the system more degrees of freedom to bypass it. Consistent with previous studies, they found that under fixed load, adhesions do not assemble for $F > 0$ when $N_u > 0$, as they are kinetically trapped by the stable manifold of the saddle. Unlike previous studies on bond–cluster models in which it was only possible to specify adhesion load [127, 146, 152, 182], the explicit modeling of the adhesion plaque in MacKay and Khadra [130] allowed them to define not only the load on the adhesion but also the stress. Indeed, with a fixed value of stress, they demonstrated that one can obtain adhesion-assembly from an initial condition consisting of a single integrin-adaptor protein complex, suggesting that stress is the permissive mechanical parameter which allows for assembly when $F, N_u > 0$. Thus, while the formation and contraction of a stress fibre is a physiologically-relevant origin for the force exerted on adhesions [164, 183], any dynamic model which results in a force that grows linearly with adhesion area should be able to produce assembly from a single molecule initial condition.

It should be mentioned here that MacKay and Khadra [130] have identified a parameter regime (labeled region 2) in which N_u is negative, making the stable manifold of the saddle no longer an obstacle for adhesion assembly (see Fig. 1.4). Within this region, it was possible to reach $N_s > 0$ regardless of the mechanical conditions imposed on the adhesion (Fig. 1.4). There are no equivalent parameter regimes in previously published models of bond-clusters [127, 145, 146, 152, 182] that could produce this type of behaviour. Interestingly, within this region one may find that adhesions will not form unless force (either load or stress) crosses a threshold (see Fig. (1.4)B). This finding reconciles the

differences in model outcomes between the bond-cluster and mechanosensitive adhesion-plaque models. Moreover, due to the explicit modeling of the adhesion plaque by MacKay and Khadra [130], the disassembled state ($\langle N \rangle = 0$) is a well-defined equilibrium in their mean field analysis (compare Figs. 3 and 4), whereas in previous models of bond-clusters, it was not and the behaviour of the system close to or beyond the saddle-node bifurcation had to be verified through stochastic simulations. It should be mentioned here that the model by MacKay and Khadra further assumed a relation between the net adsorption rate of adpator proteins and the density of integrins under the plaque [130]. This means that, upon collective integrin bond failure (at high forces), integrins will diffuse away, and the adhesion plaque will dissolve as a consequence. This is in contrast to the mechanosensitive adhesion-plaque models where adaptor proteins may be arbitrarily stretched at high forces. Thus, by jointly considering the dynamics of integrins and adaptor proteins, this newly developed model is a hybrid one that shares characteristics with both classes of models: the bond-cluster model and the mechanosensitive adhesion-plaque model.

1.12 Conclusions and Outlook

Focal adhesions are intrinsically dynamic structures which, for a long time, have fascinated biologists and physicists alike. The explosion of data related to focal adhesions in the past two decades has greatly assisted in delineating of the structural makeup of adhesions as well as the dynamics and interactions governing adhesions. At the single molecule level, the biochemical and mechanical steps involved in integrin activation are reflected in the mechanosensitive properties of the integrin-ligand bond [101, 103]. These mechanical properties have been used to build theoretical models of adhesions as cluster of bonds that fail beyond a critical load [111, 127, 145, 182]. Alternatively, the deformation of the adhesion plaque in response to applied mechanical force can be used to understand the complex sliding behaviour that adhesions exhibit [17, 18, 36, 39]. While these models have some fundamental differences in their predictions, recent work has helped to bridge this gap and explain how adhesions can form in the presence of mechanical forces [130].

While the combination of experimental data and theoretical modeling has been quite fruitful in explaining the mechanisms underlying some experimental observations, a number of unexplored phenomena remain. Nascent adhesions have not received as much attention as other more mature classes of adhesions, including FAs, either from an experimental or theoretical point of view. In fact, some

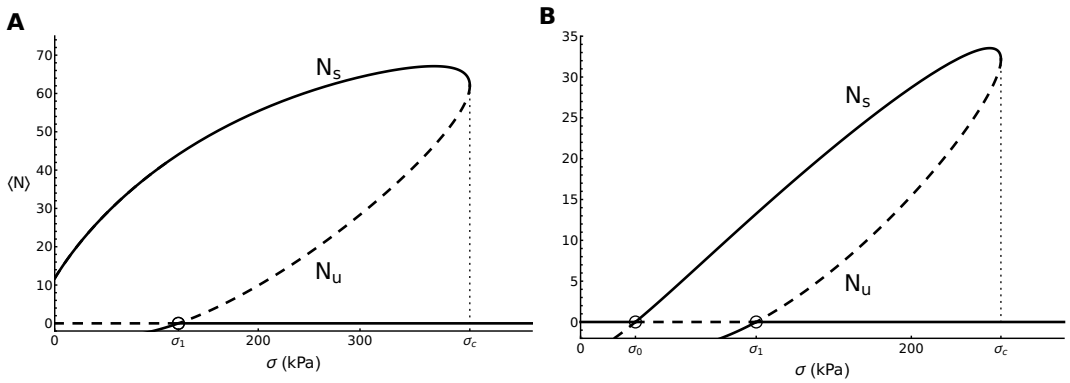

Figure 1.4: Bifurcation analysis of the deterministic hybrid model by MacKay and Khadra [130] in "region 2" of parameter space. Bifurcation diagrams of the number of closed integrin-ligand bonds $\langle N \rangle$ with respect to mechanical stress applied on NAs when the integrin-ligand binding rate is A) 5.9 s^{-1}, and B) 0.18 s^{-1}. Solid lines represent branches of stable steady states, whereas dashed lines represent branches of saddle fixed points. The two elevated branches of stable steady states and saddle fixed points labeled N_s and N_u, respectively, merge at saddle-node bifurcation points at a given critical stress σ_c in both A and B. These two branches also intersect the lower branch of trivial steady states $(A, \langle N \rangle, \langle M \rangle) = (0, 0, 0)$, where A ($\langle M \rangle$) is the area of the adhesion (the mean number of mobile integrins inside the adhesion), at transcritical bifurcation points (open circles) only once in A at $\sigma = \sigma_1$ and twice in B at $\sigma = \sigma_0 > 0$ and $\sigma = \sigma_1 > \sigma_0$. As a result, NAs exhibit finite adhesion size at zero force in A while NAs do not form in the absence of force in B (i.e., no clustered solution). Notice that for $\sigma \in [0, \sigma_1]$ in A and for $\sigma \in [\sigma_0, \sigma_1]$ in B, adhesions starting at $\langle N \rangle \approx 0$ can freely reach the stable steady state N_s (compare to Fig. 1.3 where no such region exists), and that force must cross a threshold σ_0 in B in order for NAs to assemble (as in the model by Nicolas and Safran [36]).

theorists have suggested that they exist only transiently as their formation is intrinsically thermodynamically unfavourable [36, 169]. Recent experimental findings have cast doubt on this notion, where NAs have been found to be stable for hundreds of seconds on supported lipid bilayers [149]. Moreover, membrane tension and buckling instabilities in the actin meshwork of the lamellipodium have recently emerged as the driving force which triggers NA formation [186, 187]. Although a theoretical framework to understand this has been outlined [52], it seems that it has not directly led to the formulation of a mathematical framework to describe it. This represents a challenging problem to tackle in a mathematically tractable manner as one must consider the temporal buildup of force, movement of the leading edge relative to the adhesions, as well as the assembly of the adhesion.

Although the mechanical properties of the integrin-ligand bond has been incorporated into a number of models, it is worth noting that it is not the only mechanosensitive bond present in the adhesion. Indeed, talin has been found to exhibit a weak slip bond while vinculin produces a stronger catch bond when bound to actin [188, 189]. Thus far, adhesion-plaque models have treated adaptor proteins rather generically [36, 39, 130, 160, 169, 171, 183, 190], despite extensive characterization of their biochemical and biophysical properties [12, 15, 40, 48, 154, 155, 159, 191, 192]. For instance, it is known that the binding dynamics of the adaptor protein paxillin is asymmetric along an adhesion and that these binding dynamics are likely related to phosphorylation events that are associated with highly dynamic adhesions (i.e., sliding adhesions) [48, 159, 191]. In addition, the bio-mechanically regulated vertical movement of adaptor proteins within the adhesion, such as the translocation of vinculin from the signaling layer to the transduction layer in response to changes in paxillin phosphorylation [15], has generally been neglected. Together, these effects, combined with vinculin's ability to reinforce the talin-actin bond, may provide a molecularly explicit mechanism for the plaque's mechanical response (a feature missing in the mechanosensitive plaque models developed thus far). With the large number of possible interactions, it may be challenging to keep such a model mathematically tractable while capturing the experimental observations. The force of the glycocalyx is likely to also induce conformational changes (e.g., activation) in integrin receptors [141]. While integrin activation and inactivation were indeed considered in the original computational model of glycocalyx-driven clustering by Paszek et al., these processes were modeled as being force-independent. Not surprisingly, activation was not found to influence clustering. However, it has been shown that not only activation is force-dependent (see Section 1.8), but also that the repulsive forces coming from the glycocalyx can indeed activate integrins [141]. Given that integrin binding affinity strongly influences this clustering [142], the rela-

tive contribution of the mechanosensitive integrin-ligand bond in glycocalyx-driven clustering remains unclear.

While most integrins exhibit the catch bond behaviour when presented with an appropriate ligand [92, 123, 133, 193], there are some differences in the force-lifetime relationship of these bonds. Moreover, it seems to have been previously thought that integrin heterodimers containing β_1 subunits behaved as catch bonds whereas those with β_3 subunits behave as slip bonds [194]. The idea that the mechanosensitive properties of the integrin bond are determined by the β subunit is logical, as it is the β subunit which associates with the actin cytoskeleton [82]. However, it was recently shown that $\alpha_V\beta_3$ integrins behave as a catch bond when presented with fibronectin under the right chemical conditions [132, 193], and as a slip bond when presented with for its a physiologically relevant ligand Thy-1 [195]. This highlights the complex interplay between chemical environment and ligand-specificity that determine the mechanosensitive properties of the integrin bond. Further theoretical investigation of the determinants of mechanosensitive properties of these bonds should be undertaken in order to understand how the integrin-ligand bond varies its catch bond properties and may be switched from a catch bond to a slip bond. An approach that uses thermodynamic considerations similar to [99] with a kinetic model similar to [101] may indeed be fruitful in this endeavour. Furthermore, the consequences of having a membrane populated by multiple integrin heterodimers remains relatively unexplored, with the exception of [152].

Another very interesting avenue for research is the bi-directional relation between biochemical signaling pathways regulating motility and adhesions. Rho GTPases such as Cdc42, Rac, and Rho are the drivers of cell migration, and the biochemical pathways that exert their control over the cell are subject to modulation by adhesion-dependent signaling [196–198]. Numerous models have been developed to account for the Rac-Rho signaling pathway responsible for establishing the cell polarity necessary for directed motility [23, 24, 199, 200]. While this polarization mechanism can be influenced by adhesion-dependent signaling pathways [23, 164], its influence on the mechanical state of the actin cytoskeleton [164] as well as adhesion-regulatory biochemical pathways [23] suggest that adhesion dynamics are also influenced by Rac-Rho signaling. Due to the bi-directional positive feedback between the two systems, it remains unclear to what extent these effects on adhesion dynamics are mechanical or biochemical in nature. Mathematical modeling may help to answer these questions as, in principle, it allows one to decouple the two effects from each other.

Cell migration is also regulated by a polarized gradient in calcium (Ca^{2+}) concentration and/or activity [201], exhibiting an increasing gradient from the front of a motile cell to the rear. These spatiotemporal activities are regulated by Ca^{2+} fluxes across the membrane, such as through stretch-activated channels (e.g., TRPV4 and TRPM7 channels) and numerous other pumps/receptors (for more details, see the review by Wei et al. [202]). Moreover, it has been observed that external mechanical stimulation results in mechanosensitive channel activation primarily in the vicinity of FAs, suggesting that these tension-sensing proteins are activated by membrane tension that builds up around FAs. Noting that both membrane tension and mechanosensitive channel activity are elevated at the leading edge of motile cells [52, 202, 203], this suggests that there is a link between adhesions and Ca^{2+} dynamics in the context of motility. It has been suggested that the calpain family of intracellular Ca^{2+}-dependent proteases plays a key role in regulating cell migration [71, 204–206], through their ability in modulating adhesion dynamics [207]. A number of adaptor proteins have been identified as targets for this protease, including talin, focal adhesion kinase (FAK) and paxillin [41]. Thus, the adhesion-dependent influx of Ca^{2+} through mechanosensitive channels is likely to have direct effect on adhesion dynamics. It remains unclear, however, how various Ca^{2+}-dependent signaling pathways interact at the cellular level to control adhesion assembly/disassembly through adaptor protein dynamics while maintaining the gradient in migrating cells. Although there is a wealth of studies analyzing Ca^{2+} handling in many cell-lines, this area continues to be largely unexplored mathematically in motile cells, which would provide insights into the role of Ca^{2+} in regulating cellular polarity and motility. Such studies will be crucial in elucidating the molecular coordination and propagation of Ca^{2+} signaling, particularly at the leading edge of the cell, the link between Ca^{2+} signaling, adhesions and membrane tension during migration and the role Ca^{2+} signaling in regulating collective migration.

1.13 Thermodynamics and Reaction Rates

The set of models of adhesion dynamics covered in this article may seem to employ quite different mathematical approaches to study their dynamics. However, the vast majority of these models can understood through a common framework that is based on thermodynamics. This framework uses the notion of a potential, where a system tends to evolve from a high potential state to a low potential state. The notion of a potential has been generalized to chemical systems through the intrinsic thermodynamic quantity: “chemical potential”. In this appendix we will derive an expression for the chemical potential in dilute solutions, show how it relates to chemical kinetic reaction rates, and extend the

definition beyond dilute solutions to include the effects of mechanical deformation.

1.13.1 Derivation of Chemical Potentials for Dilute Solutions

The thermodynamic quantity crucial for understanding biochemical dynamics is the free energy of a system; it represents the work that can be extracted from a system by accounting for energy loss through entropic heat production. In particular, biochemical systems are typically isothermal and isobaric and thus they are well described by the Gibbs free energy $G|_{P,T} = U + PV - TS$, where U is the internal energy of the system, P is its pressure, V is its volume, T is its temperature, and S is its entropy [208]. The differential form of the Gibbs free energy is given by

$$\begin{aligned} dG &= dU + d(PV) - d(TS) \\ &= VdP - SdT + \sum_i \mu_i dN_i \end{aligned} \tag{1.15}$$

where μ_i is the chemical potential of the i^{th} species in the system defined as $\mu_i = \partial G/\partial N_i\big|_{P,T}$, and N_i is the number of particles of the i^{th} species in the system [208].

From Eq. (1.15), we can compute the change in free energy from a reference state with pressure P_0 to another state with pressure P_1, keeping the number of particles and temperature remain fixed

$$\Delta G|_{T,N} = \int_{P_0}^{P_1} V dP.$$

Using the ideal gas law, $PV = NRT$ (where $N \equiv N_i$ is the number of molecules of the i^{th} species and P is the partial pressure of that species), we can rewrite this as

$$\Delta G|_{T,N} = NRT \int_{P_0}^{P_1} \frac{dP}{P} = NRT \ln\left(P_1/P_0\right). \tag{1.16}$$

This means that the chemical potential can be computed by taking the partial derivative of Eq. (1.16) with respect to N while keeping the pressure ($P = P_1$) and temperature (T) fixed. Together with the

ideal gas law, these conditions imply that the concentration is a conserved quantity in the system, i.e.,

$$\left.\begin{array}{l} \frac{\partial P}{\partial N} = 0 \\ \\ \frac{\partial T}{\partial N} = 0 \\ \\ P_1 V_1 = N k_B T \end{array}\right\} \Rightarrow \frac{\partial}{\partial N}\left(\frac{N}{V_1}\right) = 0 \Longleftrightarrow \frac{N}{V_1} = C = \text{constant},$$

which is equivalent to saying that

$$\Delta G|_{P,T} \equiv \Delta G|_{C,T} = NRT \ln\left(C/C_0\right), \tag{1.17}$$

where C_0 is the concentration at the reference state. Using Eq. (1.17), we can then compute an expression for chemical potential from its definition, as follows

$$\begin{aligned} \mu_i = \left.\frac{\partial G}{\partial N_i}\right|_{P,T} &= \frac{\partial\, \Delta G|_{C,T}}{\partial N_i} \\ &= RT \ln\left(C\right) \underbrace{-RT \ln\left(C_0\right)}_{\mu^0} \\ \Rightarrow \mu\left(C\right) &= \mu^0 + RT \ln\left(C\right), \end{aligned} \tag{1.18}$$

where μ^0 is referred to as the standard chemical potential. Eq. (1.18) provides a relationship between chemical potential and concentration by approximating the a dilute solution as an ideal gas (i.e., using the equation of state $PV = NRT$). For systems with a different equation of state one can obtain other formulations for the chemical potential. For example, the Van der Waals equation may be used to derive an alternative equation for $\mu\left(C\right)$ for non-ideal gases [209].

In our derivations, we have made reference to some arbitrary reference states. In the next subsection, we will show that in dilute solutions undergoing chemical reactions, these reference states are not entirely arbitrary but reflect the intrinsic kinetics of the reactions taking place.

1.13.2 Standard Chemical Potentials and the Law of Mass Action

Let us first consider a dilute solution undergoing a set of elementary chemical reactions (to be distinguished from composite reactions [210]) whose j^{th} reaction is expressed as

$$\sum_i \alpha_{i,j} X_i \underset{k_j^-}{\overset{k_j^+}{\rightleftharpoons}} \sum_i \beta_{i,j} X_i, \tag{1.19}$$

where X_i is the i^{th} chemical species in the system, $\alpha_{i,j}$ ($\beta_{i,j}$) is the stochiometric coefficient of X_i as a reactant (product) in the j^{th} reaction, and k_j^+ (k_j^-) is the forward (reverse) rate constant of the j^{th} reaction. According to the law of mass action [148, 211], at equilibrium this reaction is characterized by a relationship, given by

$$\frac{\prod_i \bar{C}_i^{\alpha_{i,j}}}{\prod_i \bar{C}_i^{\beta_{i,j}}} = \frac{k_j^-}{k_j^+},$$

or equivalently

$$\prod_i \bar{C}_i^{\nu_{i,i}} = K_j, \tag{1.20}$$

where $\left\{\bar{C}_i\right\}$ are the equilibrium concentrations, $\nu_{i,j} = \alpha_{i,j} - \beta_{i,j}$ is the net stochiometric coefficient of the i^{th} species in the j^{th} reaction, and $K_j = k_j^-/k_j^+$ is the equilibrium constant for the j^{th} reaction. By considering a closed isothermal and isobaric system at thermodynamic equilibrium (i.e. $dG = dP = dT = 0$), we may obtain from Eq. (1.15)

$$\sum_i \mu_i dN_i = 0.$$

For a closed system, fluctuations in N_i can only be due to the elementary reactions and thus

$$dN_i = \sum_j \nu_{i,j} d\chi_j$$

where χ_j is the extent of reaction for the j^{th} reaction [210]. This implies that

$$\sum_i \mu_i \sum_j \nu_{i,j} d\chi_j = \sum_j d\chi_j \sum_i \mu_i \nu_{i,j} = 0$$

which can only hold for arbitrary $d\chi_j$ if

$$\sum_i \mu_i \nu_{i,j} = 0, \qquad \forall j. \tag{1.21}$$

We note that this is the equilibrium condition relating the chemical potentials of chemical species undergoing elementary reaction. Using Eq. (1.18), we can rewrite this last expression as

$$\begin{aligned} -\sum_i \mu_i^0 \nu_{i,j} &= \sum_i RT \ln\left(\bar{C}_i\right) \nu_{i,j}, \\ &= RT \ln\left(\prod_i \bar{C}_i^{\nu_{i,j}}\right), \end{aligned}$$

where we can identify the product inside the logarithm as the left hand side of Eq. (1.20). Based on this we may finally write the relationship between standard chemical potentials and the equilibrium constant as

$$\sum_i \mu_i^0 \nu_{i,j} = -RT \ln\left(K_j\right), \qquad \forall j \tag{1.22}$$

which provides one constraint on the set $\left\{\mu_i^0\right\}$ for each reaction considered.

1.13.2.1 Application to an Isomerization Reaction

Consider the isomerization reaction

$$A \underset{k^-}{\overset{k^+}{\rightleftharpoons}} B,$$

where a molecules of A react to create one molecule of B. According to the definition of the standard chemical potential, $\mu_i^0 = -k_B T \ln\left(C_i^0\right)$ where C_i^0 is the concentration of the i^{th} species at an arbitrary reference state (see Eq. (1.18)). From Eq. (1.22), we have a condition which relates this reference state to the equilibrium constant of a reaction. In particular, for the isomerization reaction, we have

$$-RT \ln\left(C_A^0\right) + RT \ln\left(C_B^0\right) = -RT \ln\left(K\right),$$

where $K = k^{-}/k^{+}$. By arbitrarily choosing $C_B^0 = 1$, we find that $C_A^0 = K$ and that the chemical potentials for A and B are given by

$$\mu_A\left(C_A\right) = RT \ln\left(C_A/K\right), \tag{1.23}$$

and

$$\mu_B\left(C_B\right) = RT \ln\left(C_B\right), \tag{1.24}$$

respectively.

1.13.3 Kinetic Rates

The calculation of reaction rates is a fundamental problem encountered in many fields of science; for molecular systems, these reactions are typically understood as the thermally-assisted escape from metastable states (e.g., the molecular state A in the isomerization reaction) [212]. The basic formalism can be derived from the empirical Van't Hoff-Arrhenius law [213, 214], given by

$$r = k \exp\left(-\Delta E^{\ddagger}/RT\right),$$

where r is the rate of escape, k is a pre-exponential factor, and $\Delta E^{\ddagger} = E_{\ddagger} - E_1$ is the activation energy which characterizes the energy difference between the metastable state (denoted by 1) and the transition state (denoted by ‡). The computation of the pre-exponential factor k from first principles has been the subject of much research, with different formalisms producing nuanced predictions that are challenging to verify in biochemical reactions [212]. Nonetheless, it has been found that a consistent thermodynamic formulation may be obtained by taking

$$r = k^0 \exp\left(-\left(\mu_{\ddagger}^0 - \mu_1\right)/RT\right), \tag{1.25}$$

where $\mu_{\ddagger}^0$ is the concentration-independent intrinsic molar free energy of the transition state, and $k^0 > 0$ is a kinetic prefactor [215, 216]. For single molecules, we simply have $\mu_1 = \mu_1^0$, whereas for dilute solutions undergoing reactions, the chemical potential of the reactant and product state of the j^{th} reaction are given by $\mu_{1,j} = \sum_i \alpha_{i,j}\mu_i$ and $\mu_{2,j} = \sum_i \beta_{i,j}\mu_i$, respectively, where μ_i is given by Eq. (1.18) with μ_i^0 determined according to Eq. (1.22). According to this view of chemical kinetics, the forward and

backward rates are given by

$$r_j^+ = k_{j,+}^0 \exp\left[-\left(\mu_{\ddagger,j}^0 - \mu_{1,j}\right)/RT\right],$$

and

$$r_j^- = k_{j,-}^0 \exp\left[-\left(\mu_{\ddagger,j}^0 - \mu_{2,j}\right)/RT\right],$$

respectively, where $k_{j,-}^0$ and $k_{j,+}^0$ are positive parameters and $\mu_{\ddagger,j}^0$ is the intrinsic free energy of the transition state for the j^{th} reaction. By noting that Eq. (1.21) (the condition for thermal equilibrium) can be rewritten as

$$\mu_{1,j} = \mu_{2,j}$$

and that, at thermodynamic equilibrium, we must have $r_j = r_j^+ - r_j^- = 0$, we may conclude that $k_{j,-}^0 = k_{j,+}^0$. In the case of the isomerization reaction described above, the choice $k_+^0 = k_-^0 = k_- \exp\left(\mu_0^\ddagger/RT\right)$ yields the net rate

$$r = k^+ C_A - k^- C_B, \tag{1.26}$$

which is consistent with the law of mass action [211]. This suggests that free energy of the transition state has already been implicitly included in the chemical potential of the reactive dilute solution through Eq. (1.22). Nonetheless, it is important to consider Eq. (1.25) for a system whose the equilibrium constant for a given reaction (K_j) may be tuned by a free parameter θ (e.g. applied force), as the equations $\mu_{1,j}^0(\theta) = \sum_i \alpha_{i,j}\mu_i^0(\theta)$, $\mu_{2,j}^0(\theta) = \sum_i \beta_{i,j}\mu_i^0(\theta)$ and $\mu_{\ddagger,j}^0(\theta)$ will determine how each reaction rate varies with θ. Thus, Eq. (1.25) provides us with a single formalism describes the non-equilibrium rates of reaction at both micro- and macroscopic scales.

1.13.4 Applications to Mechanochemistry

Within the context of mechanochemistry, various scenarios can arise requiring the knowledge of how μ varies with pressure (or applied force). This can be done by fixing the temperature and pressure and computing the change in Gibbs free energy during an increase in the number of particles in the system from N_0 to N, given by

$$\Delta G|_{T,P} = \int_{N_0}^{N} \mu\left(N'\right) dN'.$$

As we saw in 1.13.1, the condition of fixed pressure and temperature is equivalent to fixing the concentration, with $\mu(N) = \mu$, implying that

$$\Delta G|_{T,P} = \mu(N - N_0).$$

The latter can be used to compute the total differential of the Gibbs free energy

$$dG|_{T,P} = d\mu N + \mu dN. \tag{1.27}$$

Equating Eqs. (1.15) and (1.27), we arrive at the Gibbs-Duhem equation

$$Nd\mu = VdP - SdT. \tag{1.28}$$

Systems are typically assumed to be under isothermal conditions ($dT = 0$), allowing us to compute the force-dependent chemical potential, given by

$$\mu(P) = \int \frac{V(P)}{N(P)} dP. \tag{1.29}$$

This approach was used by Hill to derive a force-dependent chemical potential for the subunits that make up microtubules, modeling microtubules as one dimensional elastic polymers [217]. In this one dimensional polymer setting, we may use the negative applied force $-F$ (rather than P) and the length per monomer l (rather than V/N) [217]. Using Hooke's law, the force on a subunit of length l is given by

$$F = k(l - l_0),$$

where k is a spring constant and l_0 is the rest length of of the subunit. Substituting $l = l_0 + F/k$ into Eq. (1.29), we obtain

$$\begin{aligned} \mu(F) &= \mu_0 - \int \left(l_0 + F/k\right) dF \\ &= \mu_0 - l_0 F - F^2/2k. \\ &\backsimeq \mu_0 - l_0 F \end{aligned}$$

This example not only illustrates how force affects the chemical potential (and thus influences reaction rates), but also provides an expression that can be used to model the effect of applied force on adhesion plaque molecules in linear focal adhesions [170, 218].

On the other hand, if mass is not homogeneous but is characterized by a particle density $N(x)$, the Gibbs free energy can be written as a functional, given by

$$G = \int_V g\left(x, N(x), \nabla N(x)\right) dV,$$

and the chemical potential can be computed pointwise by taking the functional derivative

$$\mu(x) = \frac{\delta G}{\delta N} = \frac{\partial g}{\partial N} - \nabla \cdot \frac{\partial g}{\partial \nabla N}. \tag{1.30}$$

This approach thus allows us to consider situations beyond those that can be dealt with using the Gibbs-Duhem equation. Indeed, Safran and collaborators have used it to quantify the non-trivial relationship between a material science description of plaque deformation and the kinetics of adsorption which produce the plaque [37–39].

Acknowledgments

This work was supported by the Fonds Nature et technologies-Government du Quebec (http://www.frqnt.gouv.qc.ca/en/accueil) team grant to AK, and the Natural Sciences and Engineering Council of Canada (http://www.nserc-crsng.gc.ca/index_eng.asp) discovery grant to AK. L.M. was supported by the NSERC-CREATE in Complex Dynamics Graduate Scholarship. The funders had no role in decision to publish, or preparation of the review.

Bibliography

[1] C M Lo, H B Wang, M Dembo, and Y L Wang. Cell movement is guided by the rigidity of the substrate. *Biophysical journal*, 79:144–152, 2000. 1.1, 2.1

[2] Peter Devreotes and Chris Janetopoulos. Eukaryotic chemotaxis: distinctions between directional sensing and polarization. *The Journal of biological chemistry*, 278:20445–20448, 2003. 1.1, 2.1

[3] Adam J Engler, Shamik Sen, H Lee Sweeney, and Dennis E Discher. Matrix elasticity directs stem cell lineage specification. *Cell*, 126:677–689, 8 2006. 1.1

[4] C Huselstein, N De Isla, M N Kolopp-Sarda, H Kerdjoudj, S Muller, and J F Stoltz. Influence of mechanical stress on cell viability. volume 43, pages 371–375, 2006. 0.1, 1.1

[5] Jianping Fu, Yang Kao Wang, Michael T Yang, Ravi A Desai, Xiang Yu, Zhijun Liu, and Christopher S Chen. Mechanical regulation of cell function with geometrically modulated elastomeric substrates. *Nature Methods*, 7:733–736, 2010. 1.1

[6] Catarina Brás-Pereira and Eduardo Moreno. Mechanical cell competition. *Current Opinion in Cell Biology*, 51:15–21, 4 2018. 1.1

[7] Peter Friedl and Darren Gilmour. Collective cell migration in morphogenesis, regeneration and cancer. *Nature Reviews Molecular Cell Biology*, 10:445–457, 7 2009. 0.1, 0.1.1, 1.1, 2.1

[8] Andrew D Luster, Ronen Alon, and Ulrich H von Andrian. Immune cell migration in inflammation: present and future therapeutic targets. *Nature Immunology*, 6:1182–1190, 12 2005. 0.1, 1.1, 2.1

[9] Li Li, Yong He, Min Zhao, and Jianxin Jiang. Collective cell migration: Implications for wound healing and cancer invasion. *Burns & Trauma*, 1(1):21–26, 2013. 1.1, 2.1

[10] Dennis F Kucik, Michael L Dustin, Jim M Miller, and Eric J Brown. Adhesion-activating phorbol ester increases the mobility of leukocyte integrin lfa-1 in cultured lymphocytes. *Journal of Clinical Investigation*, 97:2139–2144, 5 1996. 1.1, 2.1

[11] Claire M Brown, Benedict Hebert, David L Kolin, Jessica Zareno, Leanna Whitmore, Alan Rick Horwitz, and Paul W Wiseman. Probing the integrin-actin linkage using high-resolution protein velocity mapping. *Journal of cell science*, 119:5204–5214, 12 2006. 0.1.1, 1.1, M2

[12] Michelle A Digman, Claire M Brown, Alan R Horwitz, William W Mantulin, and Enrico Gratton. Paxillin dynamics measured during adhesion assembly and disassembly by correlation spectroscopy. *Biophysical journal*, 94:2819–2831, 4 2008. 1.1, 1.2.2, 1.7, 1.12, O2, 2.4, 2.5.1

[13] Haguy Wolfenson, Ariel Lubelski, Tamar Regev, Joseph Klafter, Yoav I Henis, and Benjamin Geiger. A role for the juxtamembrane cytoplasm in the molecular dynamics of focal adhesions. *PLoS ONE*, 4:e4304, 2009. 1.1, 1.7, O2, 2.2.3, 2.4, 2.5.1, 2.5.1.8, 2.3

[14] Masatoshi Morimatsu, Armen H Mekhdjian, Arjun S Adhikari, and Alexander R Dunn. Molecular tension sensors report forces generated by single integrin molecules in living cells. *Nano Letters*, 13:3985–3989, 2013. 1.1

[15] Lindsay B Case and Clare M Waterman. Integration of actin dynamics and cell adhesion by a three-dimensional, mechanosensitive molecular clutch. *Nature Cell Biology*, 17:955–963, 6 2015. 0.1, 0.1.2, 1.1, 1.2.1, 1.1, 1.12

[16] Taka A Tsunoyama, Yusuke Watanabe, Junri Goto, Kazuma Naito, Rinshi S Kasai, Kenichi G N Suzuki, Takahiro K Fujiwara, and Akihiro Kusumi. Super-long single-molecule tracking reveals dynamic-anchorage-induced integrin function. *Nature Chemical Biology*, 14:497–506, 5 2018. 1.1, 1.2.1, 1.6, O4, 2.2.3, 2.4, 2.5.1, 2.5.1.2, 2.3, 5, 5

[17] N Q Balaban, U S Schwarz, D Riveline, P Goichberg, G Tzur, I Sabanay, D Mahalu, S Safran, A Bershadsky, L Addadi, and B Geiger. Force and focal adhesion assembly: a close relationship studied using elastic micropatterned substrates. *Nature cell biology*, 3:466–472, 5 2001. 1.1, 1.12, 5

[18] D Riveline, E Zamir, N Q Balaban, U S Schwarz, T Ishizaki, S Narumiya, Z Kam, B Geiger, and A D Bershadsky. Focal contacts as mechanosensors: externally applied local mechanical force induces growth of focal contacts by an mdia1-dependent and rock-independent mechanism. *The Journal of cell biology*, 153:1175–1186, 6 2001. 1.1, 1.2.2, 1.6, 1.12, 5

[19] Colin K Choi, Miguel Vicente-Manzanares, Jessica Zareno, Leanna A Whitmore, Alex Mogilner, and Alan Rick Horwitz. Actin and alpha-actinin orchestrate the assembly and maturation of nascent adhesions in a myosin ii motor-independent manner. *Nature cell biology*, 10:1039–1050, 9 2008. 0.1.1, 1.1, 1.2.1, 1.2.2, 1.7, 1.8, 1.11, O1, M2, 2.2.3, 2.3.5.2, 2.4, 2.5.1.2, 2.5.1.8, 3.1, 4.6.1, 4.6.4, 5

[20] Alexander Bershadsky, Michael Kozlov, and Benjamin Geiger. Adhesion-mediated mechanosensitivity: a time to experiment, and a time to theorize. *Current Opinion in Cell Biology*, 18:472–481, 10 2006. 1.1, 1.3.1

[21] Bi-Chang Chen, Wesley R. Legant, Kai Wang, Lin Shao, Daniel E. Milkie, Michael W. Davidson, Chris Janetopoulos, Xufeng S. Wu, John A. Hammer, Zhe Liu, Brian P. English, Yuko Mimori-Kiyosue, Daniel P. Romero, Alex T. Ritter, Jennifer Lippincott-Schwartz, Lillian Fritz-Laylin, R. Dyche Mullins, Diana M. Mitchell, Joshua N. Bembenek, Anne-Cecile Reymann, Ralph Bohme, Stephan W. Grill, Jennifer T. Wang, Geraldine Seydoux, U. Serdar Tulu, Daniel P. Kiehart, and Eric Betzig. Lattice light-sheet microscopy: Imaging molecules to embryos at high spatiotemporal resolution. *Science*, 346(6208):1257998, 10 2014. 0.1, 1.1

[22] James E N Jonkman, Judith A Cathcart, Feng Xu, Miria E Bartolini, Jennifer E Amon, Katarzyna M Stevens, and Pina Colarusso. An introduction to the wound healing assay using live-cell microscopy. *Cell adhesion & migration*, 8(5):440–451, sep 2014. 0.1, 1.1

[23] Kaixi Tang, Colton G. Boudreau, Claire M. Brown, and Anmar Khadra. Paxillin phosphorylation at serine 273 and its effects on rac, rho and adhesion dynamics. *PLOS Computational Biology*, 14(7):e1006303, jul 2018. (document), 0.1, 0.1.2, 1.1, 1.12, 2.2.3, 2.3.5.1, 2.4, 2.5.1.8, 2.1, 2.3, 3.1, 3.3.1, 3.3.1, 3.3.2, 3.3.2, 3.4, 3.4.1, 3.6.0.2, 3.7, 3.10, 5, 5, 5, 5, 5

[24] Jessica K Lyda, Jack Z Tan, Abira Rajah, Asheesh Momi, Laurent MacKay, Claire M Brown, and Anmar Khadra. Rac activation is key to cell motility and directionality: An experimental and

modelling investigation. *Computational and Structural Biotechnology Journal*, 17:1436–1452, 2019. 0.1.2, 1.1, 1.12, 3.2.2, 3.2.2.2, 3.7

[25] Revathi Ananthakrishnan and Allen Ehrlicher. The forces behind cell movement. *International journal of biological sciences*, 3:303–317, 6 2007. 0.1, 1.1, 4.1

[26] Benjamin Geiger and Kenneth M Yamada. Molecular architecture and function of matrix adhesions. *Cold Spring Harbor perspectives in biology*, 3, 2011. 1.1

[27] Benjamin Geiger and Alexander Bershadsky. Exploring the neighborhood: adhesion-coupled cell mechanosensors. *Cell*, 110:139–142, 2002. 1.1

[28] Grégory Giannone, Benjamin J. Dubin-Thaler, Olivier Rossier, Yunfei Cai, Oleg Chaga, Guoying Jiang, William Beaver, Hans-Günther Döbereiner, Yoav Freund, Gary Borisy, and Michael P. Sheetz. Lamellipodial actin mechanically links myosin activity with adhesion-site formation. *Cell*, 128(3):561–575, 2 2007. 1.1

[29] Patrick W Oakes, Yvonne Beckham, Jonathan Stricker, and Margaret L Gardel. Tension is required but not sufficient for focal adhesion maturation without a stress fiber template. *The Journal of Cell Biology*, 196:363–374, 2 2012. 0.1.1, 1.1, 1.2.2

[30] P. Roca-Cusachs, A. del Rio, E. Puklin-Faucher, N. C. Gauthier, N. Biais, and M. P. Sheetz. Integrin-dependent force transmission to the extracellular matrix by α-actinin triggers adhesion maturation. *Proceedings of the National Academy of Sciences*, 110(15):E1361–E1370, mar 2013. 1.1, 1.2.2, 1.6, 2.3.5.2

[31] Margaret L Gardel, Benedikt Sabass, Lin Ji, Gaudenz Danuser, Ulrich S Schwarz, and Clare M Waterman. Traction stress in focal adhesions correlates biphasically with actin retrograde flow speed. *The Journal of cell biology*, 183:999–1005, 2008. 1.1

[32] Ronen Zaidel-Bar, Shalev Itzkovitz, Avi Ma'ayan, Ravi Iyengar, and Benjamin Geiger. Functional atlas of the integrin adhesome. *Nature cell biology*, 9:858–867, 8 2007. 0.1, 1.1, 1.2.1, 2.1, 3.1

[33] Timothy A Springer and Michael L Dustin. Integrin inside-out signaling and the immunological synapse. *Current opinion in cell biology*, 24:107–115, 2 2012. 1.2.1

[34] Paul W Wiseman, Claire M Brown, Donna J Webb, Benedict Hebert, Natalie L Johnson, Jeff A Squier, Mark H Ellisman, and A F Horwitz. Spatial mapping of integrin interactions and dynamics during cell migration by image correlation microscopy. *Journal of Cell Science*, 117, 2004. 1.2.1, 1.6, 1.11, 2.3.1, 3.1

[35] Olivier Rossier, Vivien Octeau, Jean-Baptiste Sibarita, Cécile Leduc, Béatrice Tessier, Deepak Nair, Volker Gatterdam, Olivier Destaing, Corinne Albigès-Rizo, Robert Tampé, Laurent Cognet, Daniel Choquet, Brahim Lounis, and Grégory Giannone. Integrins $\beta 1$ and $\beta 3$ exhibit distinct dynamic nanoscale organizations inside focal adhesions. *Nature Cell Biology*, 14(10):1057–1067, sep 2012. 1.2.1, 1.6, 2.1, O3, 2.2.3, 2.4, 2.5.1, 2.5.1, 2.5.1.2, 2.5.1.8, 2.1, 2.3, 5, 5

[36] A. Nicolas, B. Geiger, and S. A. Safran. Cell mechanosensitivity controls the anisotropy of focal adhesions. *Proceedings of the National Academy of Sciences*, 101(34):12520–12525, aug 2004. 1.2.1, 1.8, 1.8, 1.10, 1.12, 1.4, 2.1, O1, 2.3.5.2, 2.4, 2.5.1.2

[37] Alice Nicolas and Samuel A Safran. Limitation of cell adhesion by the elasticity of the extracellular matrix. *Biophysical Journal*, 91:61–73, 2006. 1.2.1, 1.8, 1.10, 1.13.4, 2.1, 2.3.1, 2.3.5, 2.4, 2.5.1, 5

[38] Achim Besser and Samuel A Safran. Force-induced adsorption and anisotropic growth of focal adhesions. *Biophysical Journal*, 90:3469–3484, 2006. 1.2.1, 1.8, 1.8, 1.11, 1.13.4, 2.1, 2.3.1, 2.4, 5

[39] Alice Nicolas, Achim Besser, and Samuel A Safran. Dynamics of cellular focal adhesions on deformable substrates: Consequences for cell force microscopy. *Biophysical Journal*, 95:527, 2008. 0.1, 1.2.1, 1.1, 1.8, 1.8, 1.9, 1.10, 1.11, 1.12, 1.13.4, 5

[40] Pakorn Kanchanawong, Gleb Shtengel, Ana M Pasapera, Ericka B Ramko, Michael W Davidson, Harald F Hess, and Clare M Waterman. Nanoscale architecture of integrin-based cell adhesions. *Nature*, 468:580–584, 2010. 0.1, 1.2.1, 1.12

[41] Micheal Brown and Christopher E Turner. Paxillin: Adapting to change. *Physiological Reviews*, 84:1315–1339, 2004. 1.2.1, 1.12, 3.1

[42] Satyajit K Mitra, Daniel A Hanson, and David D Schlaepfer. Focal adhesion kinase: in command and control of cell motility. *Nature Reviews Molecular Cell Biology*, 6:56–68, 1 2005. 1.2.1

[43] David R Critchley. Biochemical and structural properties of the integrin-associated cytoskeletal protein talin. *Annual review of biophysics*, 38:235–254, 2009. 1.2.1

[44] David W Dumbauld, Ted T Lee, Ankur Singh, Jan Scrimgeour, Charles A Gersbach, Evan A Zamir, Jianping Fu, Christopher S Chen, Jennifer E Curtis, Susan W Craig, and Andrés J García. How vinculin regulates force transmission. *Proceedings of the National Academy of Sciences of the United States of America*, 110:9788–9793, 2013. 1.2.1

[45] Paul Atherton, Ben Stutchbury, De-Yao Wang, Devina Jethwa, Ricky Tsang, Eugenia Meiler-Rodriguez, Pengbo Wang, Neil Bate, Roy Zent, Igor L Barsukov, Benjamin T Goult, David R Critchley, and Christoph Ballestrem. Vinculin controls talin engagement with the actomyosin machinery. *Nature Communications*, 6:10038, 2015. 1.2.1

[46] H Hirata, H Tatsumi, and M Sokabe. Mechanical forces facilitate actin polymerization at focal adhesions in a zyxin-dependent manner. *Journal of Cell Science*, 121:2795–2804, 9 2008. 1.2.1

[47] Mark A Smith, Elizabeth Blankman, Margaret L Gardel, Laura Luettjohann, Clare M Waterman, and Mary C Beckerle. A zyxin-mediated mechanism for actin stress fiber maintenance and repair. *Developmental Cell*, 19:365–376, 2010. 1.2.1

[48] R Zaidel-Bar, R Milo, Z Kam, and B Geiger. A paxillin tyrosine phosphorylation switch regulates the assembly and form of cell-matrix adhesions. *Journal of Cell Science*, 120:137–148, 12 2007. 0.1.2, 1.1, 1.2.2, 1.12, 3.1, 3.3.2, 5

[49] Zhiqi Sun, Armin Lambacher, and Reinhard Fassler. Nascent adhesions: From fluctuations to a hierarchical organization. *Current Biology*, 24(17):R801–R803, sep 2014. 1.2.2

[50] J.Victor Small, Theresia Stradal, Emmanuel Vignal, and Klemens Rottner. The lamellipodium: where motility begins. *Trends in Cell Biology*, 12:112–120, 3 2002. 1.2.2

[51] A Mogilner and G Oster. Cell motility driven by actin polymerization. *Biophysical journal*, 71:3030–3045, 1996. 1.2.2, 3.1, 4.6

[52] Kinneret Keren and Tom Shemesh. Buckle up: Membrane tension drives lamellipodial network compression and adhesion deposition. *The Journal of cell biology*, 216:2619–2621, 2017. 1.2.2, 1.12, 4.6

[53] Ingo Thievessen, Peter M Thompson, Sylvain Berlemont, Karen M Plevock, Sergey V Plotnikov, Alice Zemljic-Harpf, Robert S Ross, Michael W Davidson, Gaudenz Danuser, Sharon L Campbell, and Clare M Waterman. Vinculin-actin interaction couples actin retrograde flow to focal adhesions, but is dispensable for focal adhesion growth. *The Journal of cell biology*, 202:163–177, 7 2013. 0.1.1, 1.2.2, 1.7, 4.6

[54] Markus Schober, Srikala Raghavan, Maria Nikolova, Lisa Polak, H Amalia Pasolli, Hilary E Beggs, Louis F Reichardt, and Elaine Fuchs. Focal adhesion kinase modulates tension signaling to control actin and focal adhesion dynamics. *The Journal of cell biology*, 176:667–680, 2 2007. 1.2.2

[55] C Ballestrem, Noam Erez, Joachim Kirchner, Zvi Kam, Alexander Bershadsky, and Benjamin Geiger. Molecular mapping of tyrosine-phosphorylated proteins in focal adhesions using fluorescence resonance energy transfer. *Journal of Cell Science*, 119:866–875, 3 2006. 1.2.2

[56] Götz von Wichert, Beatrice Haimovich, Gen-Sheng Feng, and Michael P Sheetz. Force-dependent integrin-cytoskeleton linkage formation requires downregulation of focal complex dynamics by shp2. *The EMBO journal*, 22:5023–5035, 10 2003. 1.2.2

[57] Miguel Vicente-Manzanares, Jessica Zareno, Leanna Whitmore, Colin K Choi, and Alan F Horwitz. Regulation of protrusion, adhesion dynamics, and polarity by myosins iia and iib in migrating cells. *The Journal of Cell Biology*, 176:573–580, 2 2007. 1.2.2

[58] Raphaela Rid, Natalia Schiefermeier, Ilya Grigoriev, J Victor Small, and Irina Kaverina. The last but not the least: The origin and significance of trailing adhesions in fibroblastic cells. *Cell Motility and the Cytoskeleton*, 61:161–171, 7 2005. 0.1, 0.1.1, 1.2.2, 1.7, 3.1

[59] Dusko Ilic, Branka Kovacic, Kohei Johkura, David D Schlaepfer, Nenad Tomasevic, Qin Han, Jae-Beom Kim, Kyle Howerton, Clark Baumbusch, Naoko Ogiwara, Daniel N Streblow, Jay A Nelson, Paul Dazin, Yuji Shino, Katsunori Sasaki, and Caroline H Damsky. FAK promotes

organization of fibronectin matrix and fibrillar adhesions. *Journal of Cell Science*, 117(2):177–187, jan 2004. 1.2.2

[60] Andrey Efimov, Natalia Schiefermeier, Ilya Grigoriev, Ryoma Ohi, Michael C Brown, Christopher E Turner, J Victor Small, and Irina Kaverina. Paxillin-dependent stimulation of microtubule catastrophes at focal adhesion sites. *Journal of cell science*, 121:196–204, 1 2008. 1.2.2

[61] Alexander Bershadsky, Alexander Chausovsky, Eitan Becker, Anna Lyubimova, and Benjamin Geiger. Involvement of microtubules in the control of adhesion-dependent signal transduction. *Current Biology*, 6:1279–1289, 10 1996. 1.2.2

[62] Irina Kaverina, Olga Krylyshkina, and J Victor Small. Microtubule targeting of substrate contacts promotes their relaxation and dissociation. *The Journal of Cell Biology*, 146:1033–1044, 1999. 1.2.2, 1.7

[63] Ellen J Ezratty, Michael A Partridge, and Gregg G Gundersen. Microtubule-induced focal adhesion disassembly is mediated by dynamin and focal adhesion kinase. *Nature Cell Biology*, 7:581–590, 6 2005. 1.2.2

[64] Wei-Ting Chao and Jeannette Kunz. Focal adhesion disassembly requires clathrin-dependent endocytosis of integrins. *FEBS Letters*, 583:1337–1343, 4 2009. 1.2.2

[65] Ellen J Ezratty, Claire Bertaux, Eugene E Marcantonio, and Gregg G Gundersen. Clathrin mediates integrin endocytosis for focal adhesion disassembly in migrating cells. *The Journal of Cell Biology*, 187:733–747, 11 2009. 1.2.2

[66] N De Franceschi, H Hamidi, J Alanko, P Sahgal, and J Ivaska. Integrin traffic - the update. *Journal of Cell Science*, 128:839–852, 2015. 1.2.2

[67] Samantha J Stehbens, Matthew Paszek, Hayley Pemble, Andreas Ettinger, Sarah Gierke, and Torsten Wittmann. Clasps link focal-adhesion-associated microtubule capture to localized exocytosis and adhesion site turnover. *Nature Cell Biology*, 16:558–570, 6 2014. 1.2.2, 1.7

[68] Tim Eiseler, Heike Döppler, Irene K Yan, Steve Goodison, and Peter Storz. Protein kinase d1 regulates matrix metalloproteinase expression and inhibits breast cancer cell invasion. *Breast Cancer Research*, 11:R13, 2009. 1.2.2

[69] Shailaja Seetharaman and Sandrine Etienne-Manneville. Microtubules at focal adhesions - a double-edged sword. *Journal of cell science*, 132, 2019. 1.2.2, 3.1

[70] C M Regen and A F Horwitz. Dynamics of beta 1 integrin-mediated adhesive contacts in motile fibroblasts. *The Journal of Cell Biology*, 119:1347–1359, 1992. 1.2.2

[71] S P Palecek, A Huttenlocher, A F Horwitz, and D A Lauffenburger. Physical and biochemical regulation of integrin release during rear detachment of migrating cells. *Journal of cell science*, 111 (Pt 7:929–940, 4 1998. 1.2.2, 1.12

[72] M Pfaff, X Du, and M H Ginsberg. Calpain cleavage of integrin beta cytoplasmic domains. *FEBS letters*, 460:17–22, 10 1999. 0.1.1, 1.2.2

[73] Bruce D Cuevas, Amy N Abell, James A Witowsky, Toshiaki Yujiri, Nancy Lassignal Johnson, Kamala Kesavan, Marti Ware, Peter L Jones, Scott A Weed, Roberta L DeBiasi, Yoshitomo Oka, Kenneth L Tyler, and Gary L Johnson. Mekk1 regulates calpain-dependent proteolysis of focal adhesion proteins for rear-end detachment of migrating fibroblasts. *The EMBO journal*, 22:3346–3355, 7 2003. 0.1.1, 1.2.2

[74] Keefe T Chan, David A Bennin, and Anna Huttenlocher. Regulation of adhesion dynamics by calpain-mediated proteolysis of focal adhesion kinase (fak). *The Journal of biological chemistry*, 285:11418–11426, 2010. 1.2.2

[75] Monika Semmrich, Andrew Smith, Carolin Feterowski, Sandra Beer, Britta Engelhardt, Dirk H Busch, Bernadett Bartsch, Melanie Laschinger, Nancy Hogg, Klaus Pfeffer, and Bernhard Holzmann. Importance of integrin lfa-1 deactivation for the generation of immune responses. *The Journal of experimental medicine*, 201:1987–1998, 2005. 1.2.2

[76] Nicole A Morin, Patrick W Oakes, Young-Min Hyun, Dooyoung Lee, Y Eugene Chin, Eugene Y Chin, Michael R King, Timothy A Springer, Motomu Shimaoka, Jay X Tang, Jonathan S Reichner, and Minsoo Kim. Nonmuscle myosin heavy chain iia mediates integrin lfa-1 de-adhesion during t lymphocyte migration. *The Journal of experimental medicine*, 205(1):195–205, 1 2008. 0.1.1, 1.2.2, 1.8

[77] J. Pouwels, J. Nevo, T. Pellinen, J. Ylanne, and J. Ivaska. Negative regulators of integrin activity. *Journal of Cell Science*, 125(14):3271–3280, 7 2012. 1.2.2

[78] Joshua A Broussard, Donna J Webb, and Irina Kaverina. Asymmetric focal adhesion disassembly in motile cells. *Current Opinion in Cell Biology*, 20:85–90, 2 2008. 0.1, 1.2.2, 1.8, 3.1

[79] L B Smilenov, A Mikhailov, R J Pelham, E E Marcantonio, and G G Gundersen. Focal adhesion motility revealed in stationary fibroblasts. *Science*, 286:1172–1174, 11 1999. 0.1.1, 1.2.2

[80] C Ballestrem, B Hinz, B A Imhof, and B Wehrle-Haller. Marching at the front and dragging behind: differential alphavbeta3-integrin turnover regulates focal adhesion behavior. *The Journal of cell biology*, 155:1319–1332, 2001. 0.1.1, 1.2.2, 1.11, 2.4, 2.5.1.8, 2.1, 5

[81] Bernhard Wehrle-Haller. Structure and function of focal adhesions. *Current Opinion in Cell Biology*, 24:116–124, 2012. 0.1.1, 1.2.2

[82] Bing-Hao Luo, Christopher V Carman, and Timothy A Springer. Structural basis of integrin regulation and signaling. *Annual review of immunology*, 25:619–647, 2007. 1.3, 1.3.1, 1.12, 2.1

[83] J P Xiong, T Stehle, B Diefenbach, R Zhang, R Dunker, D L Scott, A Joachimiak, S L Goodman, and M A Arnaout. Crystal structure of the extracellular segment of integrin alpha vbeta3. *Science (New York, N.Y.)*, 294:339–345, 10 2001. 1.3

[84] Junichi Takagi, Benjamin M Petre, Thomas Walz, and Timothy A Springer. Global conformational rearrangements in integrin extracellular domains in outside-in and inside-out signaling. *Cell*, 110:511–599, 9 2002. 1.3

[85] A Paul Mould, Stephanie J Barton, Janet A Askari, Susan E Craig, and Martin J Humphries. Role of admidas cation-binding site in ligand recognition by integrin α_5 β_1. *Journal of Biological Chemistry*, 278:51622–51629, 2003. 1.3

[86] JianFeng Chen, Azucena Salas, and Timothy A Springer. Bistable regulation of integrin adhesiveness by a bipolar metal ion cluster. *Nature Structural Biology*, 10:995–1001, 12 2003. 1.3

[87] Seiji Tadokoro, Sanford J Shattil, Koji Eto, Vera Tai, Robert C Liddington, Jose M de Pereda, Mark H Ginsberg, and David A Calderwood. Talin binding to integrin beta tails: a final common step in integrin activation. 302, 2003. 1.3

[88] Sanford J Shattil, Chungho Kim, and Mark H Ginsberg. The final steps of integrin activation: the end game. *Nature Reviews Molecular Cell Biology*, 11:288–300, 2010. 1.3

[89] David S Harburger and David A Calderwood. Integrin signalling at a glance. *Journal of cell science*, 122:159–163, 1 2009. 1.3

[90] Jun Qin, Olga Vinogradova, and Edward F Plow. Integrin bidirectional signaling: A molecular view. *PLoS Biology*, 2:e169, 2004. 1.3

[91] Noritaka Nishida, Can Xie, Motomu Shimaoka, Yifan Cheng, Thomas Walz, and Timothy A. Springer. Activation of leukocyte $\beta 2$ integrins by conversion from bent to extended conformations. *Immunity*, 25(4):583–594, 10 2006. 1.3, 2.1

[92] Xing Chen, Can Xie, Noritaka Nishida, Zongli Li, Thomas Walz, and Timothy A Springer. Requirement of open headpiece conformation for activation of leukocyte integrin alphaxbeta2. *Proceedings of the National Academy of Sciences of the United States of America*, 107:14727–14732, 8 2010. 1.3, 1.3.2, 1.12

[93] Moonsoo Jin, Ioan Andricioaei, and Timothy A Springer. Conversion between three conformational states of integrin i domains with a c-terminal pull spring studied with molecular dynamics. *Structure*, 12:2137–2147, 12 2004. 1.3, 1.3.1

[94] Eileen Puklin-Faucher, Mu Gao, Klaus Schulten, and Viola Vogel. How the headpiece hinge angle is opened: New insights into the dynamics of integrin activation. *The Journal of cell biology*, 175:349–360, 10 2006. 1.3, 1.3.1

[95] B A Lollo, K W Chan, E M Hanson, V T Moy, and A A Brian. Direct evidence for two affinity states for lymphocyte function-associated antigen 1 on activated t cells. *The Journal of biological chemistry*, 268:21693–21700, 10 1993. 1.3

[96] M Shimaoka, C Lu, R T Palframan, U H von Andrian, A McCormack, J Takagi, and T A Springer. Reversibly locking a protein fold in an active conformation with a disulfide bond: integrin alphal i domains with high affinity and antagonist activity in vivo. *Proceedings of the National Academy of Sciences of the United States of America*, 98:6009–6014, 5 2001. 1.3

[97] G Constantin, M Majeed, C Giagulli, L Piccio, J Y Kim, E C Butcher, and C Laudanna. Chemokines trigger immediate beta2 integrin affinity and mobility changes: differential regulation and roles in lymphocyte arrest under flow. *Immunity*, 13:759–769, 12 2000. 1.3

[98] Jason R Chan, Sharon J Hyduk, and Myron I Cybulsky. Detecting rapid and transient upregulation of leukocyte integrin affinity induced by chemokines and chemoattractants. *Journal of immunological methods*, 273:43–52, 2 2003. 1.3

[99] Jing Li and Timothy A. Springer. Integrin extension enables ultrasensitive regulation by cytoskeletal force. *Proceedings of the National Academy of Sciences*, 114(18):4685–4690, apr 2017. 1.3.1, 1.3.1, 1.9, 1.12, 2.1, 2.5.1.6, 4.6

[100] Fang Kong, Zhenhai Li, William M. Parks, David W. Dumbauld, Andrés J. García, A. Paul Mould, Martin J. Humphries, and Cheng Zhu. Cyclic mechanical reinforcement of integrin–ligand interactions. *Molecular Cell*, 49(6):1060–1068, mar 2013. 1.3.1, 1.3.2, 2.4, 2.1, 2.5.1.8

[101] Zhenhai Li, Fang Kong, and Cheng Zhu. A model for cyclic mechanical reinforcement. *Scientific Reports*, 6:35954, 12 2016. 0.1, 1.3.1, 1.3.2, 1.2, 1.12, 2.1, 2.4, 2.5.1.6, 5

[102] Feng Ye, Brian G Petrich, Praju Anekal, Craig T Lefort, Ana Kasirer-Friede, Sanford J Shattil, Raphael Ruppert, Markus Moser, Reinhard Fassler, and Mark H Ginsberg. The mechanism of kindlin-mediated activation of integrin αiibβ3. *Current Biology*, 23:2288–2295, 11 2013. 1.3.1

[103] Jing Li and Timothy A Springer. Energy landscape differences among integrins establish the framework for understanding activation. *The Journal of cell biology*, 217:397–412, 2018. 1.3.1, 1.12

[104] R Alon, P D Kassner, M W Carr, E B Finger, M E Hemler, and T A Springer. The integrin vla-4 supports tethering and rolling in flow on vcam-1. *The Journal of cell biology*, 128:1243–1253, 3 1995. 1.3.1

[105] Matthew J Footer, Jacob W J Kerssemakers, Julie A Theriot, and Marileen Dogterom. Direct measurement of force generation by actin filament polymerization using an optical trap. *Proceedings of the National Academy of Sciences of the United States of America*, 104:2181–2186, 2007. 1.3.1

[106] David R Kovar and Thomas D Pollard. Insertional assembly of actin filament barbed ends in association with formins produces piconewton forces. *Proceedings of the National Academy of Sciences of the United States of America*, 101:14725–14730, 10 2004. 1.3.1

[107] Carlo Laudanna, Ji Yun Kim, Gabriela Constantin, and Eugene C Butcher. Rapid leukocyte integrin activation by chemokines. *Immunological Reviews*, 186:37–46, 8 2002. 1.3.1

[108] Alice C Chang, Armen H Mekhdjian, Masatoshi Morimatsu, Aleksandra Kirillovna Denisin, Beth L Pruitt, and Alexander R Dunn. Single molecule force measurements in living cells reveal a minimally tensioned integrin state. *ACS Nano*, 10:10745–10752, 12 2016. 1.3.1, 2.4, 2.5.1.2

[109] Zhiqi Sun, Mercedes Costell, and Reinhard Fässler. Integrin activation by talin, kindlin and mechanical forces. *Nature Cell Biology*, 21:25–31, 2019. 1.3.1

[110] Jenny Z Kechagia, Johanna Ivaska, and Pere Roca-Cusachs. Integrins as biomechanical sensors of the microenvironment, 8 2019. 1.3.1

[111] George I Bell. Models for the specific adhesion of cells to cells, 5 1978. 1.3.2, 1.6, 1.12, 2.1

[112] E Evans and K Ritchie. Dynamic strength of molecular adhesion bonds. *Biophysical journal*, 72:1541–1555, 4 1997. 1.3.2, 1.3.2

[113] Evan A Evans and David A Calderwood. Forces and bond dynamics in cell adhesion. *Science*, 316, 2007. 1.3.2

[114] E Evans, A Leung, D Hammer, and S Simon. Chemically distinct transition states govern rapid dissociation of single l-selectin bonds under force. *Proceedings of the National Academy of Sciences of the United States of America*, 98:3784–3789, 3 2001. 1.3.2

[115] Evan Evans, Andrew Leung, Volkmar Heinrich, and Cheng Zhu. Mechanical switching and coupling between two dissociation pathways in a p-selectin adhesion bond. *Proceedings of the National Academy of Sciences of the United States of America*, 101:11281–11286, 8 2004. 1.3.2, 1.3.2, 1.2

[116] Chunbo Yuan, Aileen Chen, Pamela Kolb, and Vincent T Moy. Energy landscape of streptavidin-biotin complexes measured by atomic force microscopy. *Biochemistry*, 39:10219–10223, 2000. 1.3.2

[117] Yuriy V Pereverzev, Oleg V Prezhdo, Manu Forero, Evgeni V Sokurenko, and Wendy E Thomas. The two-pathway model for the catch-slip transition in biological adhesion. *Biophysical Journal*, 89:1446–1454, 2005. 1.3.2, 1.3.2, 1.3.2, 1.2

[118] M Dembo, D C Torney, K Saxman, and D Hammer. The reaction-limited kinetics of membrane-to-surface adhesion and detachment. *Proceedings of the Royal Society B: Biological Sciences*, 234:55–83, 6 1988. 1.3.2

[119] Sabyasachi Rakshit, Yunxiang Zhang, Kristine Manibog, Omer Shafraz, and Sanjeevi Sivasankar. Ideal, catch, and slip bonds in cadherin adhesion. *Proceedings of the National Academy of Sciences of the United States of America*, 109:18815–18820, 11 2012. 1.3.2

[120] Feiya Li, Sambra D Redick, Harold P Erickson, and Vincent T Moy. Force measurements of the alpha5beta1 integrin-fibronectin interaction. *Biophysical journal*, 84:1252–1262, 2 2003. 1.3.2

[121] Xiaohui Zhang, Ewa Wojcikiewicz, and Vincent T Moy. Force spectroscopy of the leukocyte function-associated antigen-1/intercellular adhesion molecule-1 interaction. *Biophysical journal*, 83:2270–2279, 2002. 1.3.2

[122] Xiaohui Zhang, Susan E Craig, Hishani Kirby, Martin J Humphries, and Vincent T Moy. Molecular basis for the dynamic strength of the integrin $\alpha 4\beta 1$/vcam-1 interaction. *Biophysical Journal*, 87:3470–3478, 11 2004. 1.3.2

[123] Fang Kong, Andrés J. García, A. Paul Mould, Martin J. Humphries, and Cheng Zhu. Demonstration of catch bonds between an integrin and its ligand. *The Journal of cell biology*, 185(7):1275–1284, 6 2009. 1.3.2, 1.3.2, 1.12, 2.1, O5, 2.2.3, 2.4, 2.8, 2.1, 2.5.1.8

[124] Yuriy V Pereverzev, Oleg V Prezhdo, and Evgeni V Sokurenko. Allosteric role of the large-scale domain opening in biological catch-binding. *Physical Review E*, 79:51913, 5 2009. 1.3.2, 2.1

[125] Yuriy V Pereverzev, Eugenia Prezhdo, and Evgeni V Sokurenko. The two-pathway model of the biological catch-bond as a limit of the allosteric model. *Biophysical journal*, 101:2026–2036, 2011. 1.3.2, 2.4, 2.5.1.6

[126] Ying Li, Prabhakar Bhimalapuram, and Aaron R Dinner. Model for how retrograde actin flow regulates adhesion traction stresses. *Journal of Physics Condensed Matter*, 22:194113, 5 2010. 1.3.2

[127] Elizaveta A Novikova and Cornelis Storm. Contractile fibers and catch-bond clusters: A biological force sensor? *Biophysical Journal*, 105:1336–1345, 9 2013. 1.3.2, 1.6, 1.6, 1.10, 1.11, 1.12, 2.1, 2.3.5, 2.3.5.1, 2.3.5.1, 2.3.5.2, 2.3.6, 2.3.6, 2.4, 5, 5

[128] Benjamin L Bangasser, Steven S Rosenfeld, and David J Odde. Determinants of maximal force transmission in a motor-clutch model of cell traction in a compliant microenvironment. *Biophysical Journal*, 105:581–592, 2013. 1.3.2

[129] Patrick W Oakes, Tamara C Bidone, Yvonne Beckham, Austin V Skeeters, Guillermina R Ramirez-San Juan, Stephen P Winter, Gregory A Voth, and Margaret L Gardel. Lamellipodium is a myosin-independent mechanosensor. *Proceedings of the National Academy of Sciences*, 115:201715869, 2 2018. 1.3.2

[130] Laurent MacKay and Anmar Khadra. Dynamics of mechanosensitive nascent adhesion formation. *Biophysical Journal*, 117(6):1057–1073, sep 2019. (document), 1.3.2, 1.6, 1.7, 1.11, 1.12, 1.4

[131] Sabyasachi Rakshit and Sanjeevi Sivasankar. Biomechanics of cell adhesion: how force regulates the lifetime of adhesive bonds at the single molecule level. *Physical Chemistry Chemical Physics*, 16:2211, 1 2014. 1.3.2

[132] Yunfeng Chen, Hyunjung Lee, Haibin Tong, Martin Schwartz, and Cheng Zhu. Force regulated conformational change of integrin αvβ3. *Matrix biology : journal of the International Society for Matrix Biology*, 60-61:70–85, 2017. 1.3.2, 1.12

[133] Florencia Rosetti, Yunfeng Chen, Mehmet Sen, Elizabeth Thayer, Veronica Azcutia, Jan M Herter, F William Luscinskas, Xavier Cullere, Cheng Zhu, and Tanya N Mayadas. A lupus-

associated mac-1 variant has defects in integrin allostery and interaction with ligands under force. *Cell Reports*, 10:1655–1664, 3 2015. 1.3.2, 1.12

[134] Jinglei Hu, Reinhard Lipowsky, and Thomas R Weikl. Binding constants of membrane-anchored receptors and ligands depend strongly on the nanoscale roughness of membranes. *Proceedings of the National Academy of Sciences of the United States of America*, 110:15283–15288, 9 2013. 1.4

[135] Guang-Kui Xu, Jinglei Hu, Reinhard Lipowsky, and Thomas R Weikl. Binding constants of membrane-anchored receptors and ligands: A general theory corroborated by monte carlo simulations. *The Journal of Chemical Physics*, 143:243136, 2015. 1.4, 1.5

[136] Guang-Kui Xu, Jin Qian, and Jinglei Hu. The glycocalyx promotes cooperative binding and clustering of adhesion receptors. *Soft Matter*, 12:4572–4583, 5 2016. 1.4, 1.5

[137] Andrew Doyle, William Marganski, Juliet Lee, Z Goeckeler, G Côté, and R Wysolmerski. Calcium transients induce spatially coordinated increases in traction force during the movement of fish keratocytes. *Journal of cell science*, 117:2203–2214, 2004. 1.4, 1.8, 3.1

[138] Risat A Jannat, Micah Dembo, and Daniel A Hammer. Traction forces of neutrophils migrating on compliant substrates. *Biophysical Journal*, 101:575–584, 2011. 1.4, 1.8

[139] Bruce Alberts, Alexander Johnson, Julian Lewis, Martin Raff, Keith Roberts, and Peter Walter. *Molecular biology of the cell*. Garland Science, 2002. 1.5

[140] Michael R King. *Principles of cellular engineering : understanding the biomolecular interface*. Elsevier Academic Press, 2006. 1.5

[141] Matthew J. Paszek, Christopher C. DuFort, Olivier Rossier, Russell Bainer, Janna K. Mouw, Kamil Godula, Jason E. Hudak, Jonathon N. Lakins, Amanda C. Wijekoon, Luke Cassereau, Matthew G. Rubashkin, Mark J. Magbanua, Kurt S. Thorn, Michael W. Davidson, Hope S. Rugo, John W. Park, Daniel A. Hammer, Grégory Giannone, Carolyn R. Bertozzi, and Valerie M. Weaver. The cancer glycocalyx mechanically primes integrin-mediated growth and survival. *Nature*, 511(7509):319–325, 7 2014. 1.5, 1.12

[142] Matthew J Paszek, David Boettiger, Valerie M Weaver, and Daniel A Hammer. Integrin clustering is driven by mechanical resistance from the glycocalyx and the substrate. *PLoS Computational Biology*, 5:e1000604, 12 2009. 1.5, 1.12, 3.1

[143] Ying-Li Hu, Shaoying Lu, Kai W Szeto, Jie Sun, Yingxiao Wang, Juan C Lasheras, and Shu Chien. Fak and paxillin dynamics at focal adhesions in the protrusions of migrating cells. *Scientific Reports*, 4:6024, 5 2015. 1.5

[144] Rishita Changede, Haogang Cai, Shalom Wind, and Michael P Sheetz. Ligand geometry controls adhesion formation via integrin clustering. *bioRxiv*, page 435826, 2018. 0.1, 1.6, 2.1, 2.3.1

[145] Ulrich S Schwarz, Thorsten Erdmann, and Ilka B Bischofs. Focal adhesions as mechanosensors: The two-spring model. *BioSystems*, 83:225–232, 2 2006. 1.6, 1.10, 1.11, 1.12, 2.1, 2.3.5.1, 2.3.5.1, 2.3.6, 2.4

[146] T Erdmann and U S Schwarz. Stability of adhesion clusters under constant force. *Physical Review Letters*, 92:108102, 3 2004. 1.6, 1.10, 1.11

[147] Ulrich S Schwarz and Samuel A Safran. Physics of adherent cells. *Reviews of Modern Physics*, 85:1327–1381, 8 2013. 0.1, 1.6, 1.8

[148] N G van Kampen. *Stochastic processes in physics and chemistry*. North Holland, 3rd edition, 2007. 1.6, 1.13.2, 3.2.1

[149] Rishita Changede, Xiaochun Xu, Felix Margadant, Michael P Sheetz, D R Critchley, A Ravasio, Z Chen, Y H Wang, K Kawauchi, and Et Al. Nascent integrin adhesions form on all matrix rigidities after integrin activation. *Developmental Cell*, 35:614–621, 2015. 0.1.1, 1.6, 1.12, 2.1, 2.2.3, 2.3.1, 2.2, 2.3.1, 2.3.3, 2.3.5.2, 2.4, 2.5.1, 2.5.1.2, 2.5.1.8, 2.1, 2.5.1.8

[150] Pere Roca-Cusachs, Nils C Gauthier, Armando Del Rio, and Michael P Sheetz. Clustering of alpha(5)beta(1) integrins determines adhesion strength whereas alpha(v)beta(3) and talin enable mechanotransduction. *Proceedings of the National Academy of Sciences of the United States of America*, 106:16245–16250, 9 2009. 0.1, 1.6

[151] Hayri E Balcioglu, Hedde van Hoorn, Dominique M Donato, Thomas Schmidt, and Erik H J Danen. The integrin expression profile modulates orientation and dynamics of force transmission at cell-matrix adhesions. *Journal of Cell Science*, 128:1316–1326, 4 2015. 1.6

[152] Elizaveta A Novikova and Cornelis Storm. Evolving roles and dynamics for catch and slip bonds during adhesion cluster maturation. 8 2019. (document), 1.6, 1.1, 1.10, 1.11, 1.12

[153] Chi Li Chiu, Jose S Aguilar, Connie Y Tsai, Gui Kai Wu, Enrico Gratton, and Michelle A Digman. Nanoimaging of focal adhesion dynamics in 3d. *PLoS ONE*, 9:e99896, 2014. 1.7, O2, 2.4, 2.5.1

[154] Jan-Erik Hoffmann, Yessica Fermin, Ruth L O Stricker, Katja Ickstadt, and Eli Zamir. Symmetric exchange of multi-protein building blocks between stationary focal adhesions and the cytosol. *eLife*, 3, 6 2014. 1.7, 1.12

[155] Colin K Choi, Jessica Zareno, Michelle A Digman, Enrico Gratton, and Alan Rick Horwitz. Cross-correlated fluctuation analysis reveals phosphorylation-regulated paxillin-fak complexes in nascent adhesions. *Biophysical Journal*, 100:583–592, 2 2011. 1.7, 1.12, 3.3.2

[156] Cibele V Falkenberg, Michael L Blinov, and Leslie M Loew. Pleomorphic ensembles: Formation of large clusters composed of weakly interacting multivalent molecules. *Biophysical Journal*, 105:2451–2460, 12 2013. 1.7

[157] Donna J Webb, Karen Donais, Leanna A Whitmore, Sheila M Thomas, Christopher E Turner, J Thomas Parsons, and Alan F Horwitz. Fak-src signalling through paxillin, erk and mlck regulates adhesion disassembly. *Nature cell biology*, 6:154–161, 2 2004. 1.7, 3.1

[158] Haguy Wolfenson, Alexander Bershadsky, Yoav I Henis, and Benjamin Geiger. Actomyosin-generated tension controls the molecular kinetics of focal adhesions. *Journal of cell science*, 124:1425–1432, 5 2011. 1.7

[159] Abira Rajah, Colton G Boudreau, Alina Ilie, Tse-Luen Wee, Kaixi Tang, Aleksandar Z Borisov, John Orlowski, and Claire M Brown. Paxillin s273 phosphorylation regulates adhesion dynamics and cell migration through a common protein complex with pak1 and βpix. *Scientific Reports*, 9:11430, 2019. 0.1, 1.7, 1.12, 3.1, 3.3.2

[160] Nir S Gov. Modeling the size distribution of focal adhesions. *Biophysical journal*, 91:2844–2847, 2006. 1.7, 1.12, 2.1, M2, 2.3.3, 2.4, 2.5.1.3

[161] V Swaminathan, R S Fischer, and C M Waterman. The fak-arp2/3 interaction promotes leading edge advance and haptosensing by coupling nascent adhesions to lamellipodia actin. *Molecular Biology of the Cell*, 27:1085–1100, 2016. 0.1.1, 1.7

[162] Scott D Hansen and R Dyche Mullins. Vasp is a processive actin polymerase that requires monomeric actin for barbed end association. *The Journal of cell biology*, 191:571–584, 2010. 1.7

[163] A Nicolas and S A Safran. Elastic deformations of grafted layers with surface stress. *Physical Review E*, 69:51902, 5 2004. 1.8, 1.10

[164] Achim Besser and Ulrich S Schwarz. Coupling biochemistry and mechanics in cell adhesion: a model for inhomogeneous stress fiber contraction. *New Journal of Physics*, 9:425, 11 2007. 1.8, 1.11, 1.12

[165] Robijn Bruinsma. Theory of force regulation by nascent adhesion sites. *Biophysical Journal*, 89:87, 7 2005. 1.8, 1.9

[166] Haim Diamant and David Andelman. Kinetics of surfactant adsorption at fluid-fluid interfaces. *Journal of Physical Chemistry*, 100:13732–13742, 1996. 1.8

[167] Sangyoon J Han, Kevin S Bielawski, Lucas H Ting, Marita L Rodriguez, and Nathan J Sniadecki. Decoupling substrate stiffness, spread area, and micropost density: a close spatial relationship between traction forces and focal adhesions. *Biophysical journal*, 103:640–648, 2012. 1.8

[168] Shelly R Peyton and Andrew J Putnam. Extracellular matrix rigidity governs smooth muscle cell motility in a biphasic fashion. *Journal of Cellular Physiology*, 204:198–209, 7 2005. 1.8

[169] Xuan Cao, Ehsan Ban, Brendon M Baker, Yuan Lin, Jason A Burdick, Christopher S Chen, and Vivek B Shenoy. Multiscale model predicts increasing focal adhesion size with decreasing stiffness in fibrous matrices. *Proceedings of the National Academy of Sciences of the United States of America*, 114:E4549——E4555, 2017. 1.8, 1.12, 2.1, 2.4, 2.5.1.2

[170] Tom Shemesh, Benjamin Geiger, Alexander D Bershadsky, and Michael M Kozlov. Focal adhesions as mechanosensors: A physical mechanism. *Proceedings of the National Academy of Sciences*, 102:12383–12388, 2005. 1.8, 1.13.4

[171] Joseph E Olberding, Michael D Thouless, Ellen M Arruda, and Krishna Garikipati. The non-equilibrium thermodynamics and kinetics of focal adhesion dynamics. *PLoS ONE*, 5:e12043, 2010. 1.8, 1.11, 1.12, 2.1, 2.3.1, 2.3.5, 2.3.5.2, 2.4, 2.5.1.2, 5

[172] Maria L Lombardi, David A Knecht, Micah Dembo, and Juliet Lee. Traction force microscopy in dictyostelium reveals distinct roles for myosin ii motor and actin-crosslinking activity in polarized cell movement. *Journal of cell science*, 120:1624–1634, 2007. 1.8

[173] Clément Roux, Alain Duperray, Valérie M. Laurent, Richard Michel, Valentina Peschetola, Claude Verdier, and Jocelyn Étienne. Prediction of traction forces of motile cells. *Interface Focus*, 6(5):20160042, oct 2016. 1.8

[174] Kurt I Anderson and Rob Cross. Contact dynamics during keratocyte motility. *Current Biology*, 10:253–260, 3 2000. 1.8

[175] Zeno Messi, Alicia Bornert, Franck Raynaud, and Alexander Verkhovsky. Traction forces control cell-edge dynamics and mediate distance-sensitivity during cell polarization. *bioRxiv*, page 745687, 8 2019. 1.8

[176] Shiqiong Hu, Yee-Han Tee, Alexandre Kabla, Ronen Zaidel-Bar, Alexander Bershadsky, and Pascal Hersen. Structured illumination microscopy reveals focal adhesions are composed of linear subunits. *Cytoskeleton*, 72:235–245, 5 2015. 1.8

[177] Ben Stutchbury, Paul Atherton, Ricky Tsang, De-Yao Wang, and Christoph Ballestrem. Distinct focal adhesion protein modules control different aspects of mechanotransduction. *Journal of cell science*, 130:1612–1624, 2017. 1.8, 3.1

[178] Guang-Kui Xu, Chun Yang, Jing Du, and Xi-Qiao Feng. Integrin activation and internalization mediated by extracellular matrix elasticity: A biomechanical model. *Journal of Biomechanics*, 47:1479–1484, 4 2014. 1.9

[179] D H Kaelble. Theory and analysis of peel adhesion: Bond stresses and distributions. *Transactions of the Society of Rheology*, 4:45–73, 3 1960. 1.9

[180] Pierre Sens and Matthew S Turner. Theoretical model for the formation of caveolae and similar membrane invaginations. *Biophysical journal*, 86:2049–2057, 2004. 1.9

[181] Jing Du, Xiaofei Chen, Xudong Liang, Guangyao Zhang, Jia Xu, Linrong He, Qingyuan Zhan, Xi Qiao Feng, Shu Chien, and Chun Yang. Integrin activation and internalization on soft ecm as a mechanism of induction of stem cell differentiation by ecm elasticity. *Proceedings of the National Academy of Sciences of the United States of America*, 108:9466–9471, 2011. 1.9

[182] Thorsten Erdmann and Ulrich S Schwarz. Stochastic dynamics of adhesion clusters under shared constant force and with rebinding. *Journal of Chemical Physics*, 121:8997–9017, 11 2004. 1.10, 1.11, 1.12, 2.1, 2.3.5.1, 2.3.5.1, 2.3.6, 2.4, 5

[183] Sam Walcott, Dong-Hwee Kim, Denis Wirtz, and Sean X Sun. Nucleation and decay initiation are the stiffness-sensitive phases of focal adhesion maturation. *Biophysical journal*, 101:2919–2928, 12 2011. 1.11, 1.12, 2.1, 2.3.5.1, 2.3.6, 2.3.6, 2.4

[184] Rahuman S. Malik-Sheriff, Sarah Imtiaz, Hernán E. Grecco, and Eli Zamir. Diverse patterns of molecular changes in the mechano-responsiveness of focal adhesions. *Scientific Reports*, 8(1):2187, feb 2018. 1.11

[185] Fan-Ching Chien, Chiung Wen Kuo, Zong-Han Yang, Di-Yen Chueh, and Peilin Chen. Exploring the formation of focal adhesions on patterned surfaces using super-resolution imaging. *Small*, 7:2906–2913, 10 2011. 0.1, 1.11

[186] Bruno Pontes, Pascale Monzo, Laurent Gole, Anabel Lise Le Roux, Anita Joanna Kosmalska, Zhi Yang Tam, Weiwei Luo, Sophie Kan, Virgile Viasnoff, Pere Roca-Cusachs, Lisa Tucker-Kellogg, and Nils C Gauthier. Membrane tension controls adhesion positioning at the leading edge of cells. *Journal of Cell Biology*, 216:2959–2977, 9 2017. 0.1.1, 1.12, 3.1, 4.6

[187] Carsten Schulte, Gian Maria Sarra Ferraris, Amanda Oldani, Massimiliano Galluzzi, Alessandro Podestà, Luca Puricelli, Valentina de Lorenzi, Cristina Lenardi, Paolo Milani, and Nicolai Sidenius. Lamellipodial tension, not integrin/ligand binding, is the crucial factor to realise integrin activation and cell migration. *European Journal of Cell Biology*, 95(1):1–14, 1 2016. 1.12

[188] Guoying Jiang, Grégory Giannone, David R. Critchley, Emiko Fukumoto, and Michael P. Sheetz. Two-piconewton slip bond between fibronectin and the cytoskeleton depends on talin. *Nature*, 424(6946):334–337, jul 2003. 1.12

[189] Derek L Huang, Nicolas A Bax, Craig D Buckley, William I Weis, and Alexander R Dunn. Vinculin forms a directionally asymmetric catch bond with f-actin. *Science*, 357:703–706, 8 2017. 1.12

[190] Zhanghan Wu, Sergey V Plotnikov, Abdiwahab Y Moalim, Clare M Waterman, and Jian Liu. Two distinct actin networks mediate traction oscillations to confer focal adhesion mechanosensing. *Biophysical Journal*, 112:780–794, 2 2017. 1.12, 2.1, 2.4

[191] Anjana Nayal, Donna J Webb, Claire M Brown, Erik M Schaefer, Miguel Vicente-Manzanares, and Alan Rick Horwitz. Paxillin phosphorylation at ser273 localizes a git1-pix-pak complex and regulates adhesion and protrusion dynamics. *Journal of Cell Biology*, 173:587–589, 5 2006. 0.1.2, 1.12, 3.1, 3.3.2, 5

[192] Benjamin T Goult, Jie Yan, and Martin A Schwartz. Talin as a mechanosensitive signaling hub. *The Journal of cell biology*, 217:3776–3784, 11 2018. 1.12

[193] Alberto Elosegui-Artola, Roger Oria, Yunfeng Chen, Anita Kosmalska, Carlos Pérez-González, Natalia Castro, Cheng Zhu, Xavier Trepat, and Pere Roca-Cusachs. Mechanical regulation of a molecular clutch defines force transmission and transduction in response to matrix rigidity. *Nature Cell Biology*, 18:540–548, 2016. 1.12

[194] Pere Roca-Cusachs, Thomas Iskratsch, and Michael P. Sheetz. Finding the weakest link – exploring integrin-mediated mechanical molecular pathways. *Journal of Cell Science*, 125(13):3025–3038, 7 2012. 1.12

[195] Francesca Burgos-Bravo, Nataniel L Figueroa, Nathalie Casanova-Morales, Andrew F G Quest, Christian A M Wilson, and Lisette Leyton. Single-molecule measurements of the effect of force on thy-1/αvβ3-integrin interaction using nonpurified proteins. *Molecular Biology of the Cell*, 29(3):326–338, 2 2018. 1.12

[196] Samer Hanna and Mirvat El-Sibai. Signaling networks of rho gtpases in cell motility. *Cellular Signalling*, 25:1955–1961, 10 2013. 1.12, 3.1

[197] Harry Warner, Beverley J Wilson, and Patrick T Caswell. Control of adhesion and protrusion in cell migration by rho gtpases. *Current Opinion in Cell Biology*, 56:64–70, 2019. 1.12, 3.1, 3.3.1

[198] Campbell D Lawson and Keith Burridge. The on-off relationship of rho and rac during integrin-mediated adhesion and cell migration. *Small GTPases*, 5:e27958, 1 2014. 1.12, 3.1

[199] Yoichiro Mori, Alexandra Jilkine, and Leah Edelstein-Keshet. Wave-pinning and cell polarity from a bistable reaction-diffusion system. *Biophysical Journal*, 94:3684–3697, 5 2008. 0.1.3, 1.12, 2.1, 3.1, 3.3, 3.5.2, 3.6.0.1, 4.1

[200] Adriana T Dawes and Leah Edelstein-Keshet. Phosphoinositides and rho proteins spatially regulate actin polymerization to initiate and maintain directed movement in a one-dimensional model of a motile cell. *Biophysical Journal*, 92:744–768, 2 2007. 1.12, 3.1, 3.3

[201] Matthias Machacek, Louis Hodgson, Christopher Welch, Hunter Elliott, Olivier Pertz, Perihan Nalbant, Amy Abell, Gary L Johnson, Klaus M Hahn, and Gaudenz Danuser. Coordination of rho gtpase activities during cell protrusion. *Nature*, 461:99–103, 9 2009. 1.12

[202] Chaoliang Wei, Xianhua Wang, Min Chen, Kunfu Ouyang, Long-Sheng Song, and Heping Cheng. Calcium flickers steer cell migration. *Nature*, 457:901–905, 2009. 1.12

[203] Arnon D Lieber, Shlomit Yehudai-Resheff, Erin L Barnhart, Julie A Theriot, and Kinneret Keren. Membrane tension in rapidly moving cells is determined by cytoskeletal forces. *Current Biology*, 23:1409–1417, 2013. 1.12

[204] A Huttenlocher, S P Palecek, Q Lu, W Zhang, R L Mellgren, D A Lauffenburger, M H Ginsberg, and A F Horwitz. Regulation of cell migration by the calcium-dependent protease calpain. *The Journal of biological chemistry*, 272:32719–32722, 1997. 1.12

[205] Angela Glading, Douglas A Lauffenburger, and Alan Wells. Cutting to the chase: calpain proteases in cell motility. *Trends in cell biology*, 12:46–54, 1 2002. 1.12

[206] Santos J Franco and Anna Huttenlocher. Regulating cell migration: calpains make the cut. *Journal of cell science*, 118:3829–3838, 2005. 1.12

[207] Amit Bhatt, Irina Kaverina, Carol Otey, and Anna Huttenlocher. Regulation of focal complex composition and disassembly by the calcium-dependent protease calpain. *Journal of cell science*, 115:3415–3425, 9 2002. 1.12

[208] Robert A. Alberty. *Thermodynamics of Biochemical Reactions*. John Wiley & Sons, Inc., 2 2003. 1.13.1, 1.13.1

[209] F J Sevilla and L Olivares-Quiroz. Chemical potential for the interacting classical gas and the ideal quantum gas obeying a generalized exclusion principle. *EUROPEAN JOURNAL OF PHYSICS Eur. J. Phys*, 33:709–722, 2012. 1.13.1

[210] A D McNaught and A Wilkinson. Iupac. compendium of chemical terminology (the "gold book"). *IUPAC Compendium of Chemical Terminology*, 2014. 1.13.2, 1.13.2

[211] Eberhard O Voit, Harald A Martens, and Stig W Omholt. 150 years of the mass action law. *PLoS Computational Biology*, 11:e1004012, 2015. 1.13.2, 1.13.3

[212] Peter Hanggi, Peter Talkner, and Michal Borkovec. Reaction-rate theory: fifty years after kramers. *Reviews of Modern Physics*, 62(2):251–341, apr 1990. 1.13.3

[213] Svante Arrhenius. Über die reaktionsgeschwindigkeit bei der inversion von rohrzucker durch säuren. *Zeitschrift für Physikalische Chemie*, 4U, 1 1889. 1.13.3

[214] J H van't Hoff. *Etudes de dynamique chimique*. Frederik Muller, 1884. 1.13.3

[215] M Z Bazant. 10.626. fall 2011. electrochemical energy systems massachusetts institute of technology: Mit opencouseware. 1.13.3

[216] Martin Z Bazant. Theory of chemical kinetics and charge transfer based on nonequilibrium thermodynamics. *Accounts of Chemical Research*, 46:1144–1160, 5 2013. 1.13.3

[217] Terrell L Hill and Marc W Kirschner. Bioenergetics and kinetics of microtubule and actin filament assembly-disassembly. *International Review of Cytology*, 78:1–125, 1982. 1.13.4

[218] Dong Kong, Baohua Ji, and Lanhong Dai. Stabilizing to disruptive transition of focal adhesion response to mechanical forces. *Journal of Biomechanics*, 43:2524–2529, 2010. 1.13.4

Chapter 2

Dynamics of mechanosensitive nascent adhesion formation

Abstract

Cellular migration is a tightly regulated process that involves actin cytoskeleton, adaptor proteins, and integrin receptors. Forces are transmitted extracellularly through protein complexes of these molecules called adhesions. Adhesions anchor the cell to its substrate, allowing it to migrate. In Chinese hamster ovary cells, three classes of adhesion can be identified: nascent adhesions (NAs), focal complexes and focal adhesions, ranked here ascendingly based on size and stability. To understand the dynamics and mechanosensitive properties of NAs, a biophysical model of these NAs as co-localized clusters of integrins and adaptor proteins is developed. The model is then analyzed to characterize the dependence of NA area on biophysical parameters that regulate the number of integrins and adaptor proteins within NAs through a mechanosensitive co-aggregation mechanism. Our results reveal that NA formation is triggered beyond a threshold of adaptor protein, integrin, or extracellular ligand densities, where these three factors have been listed in descending order of their relative influence on NA-area. Further analysis of the model also reveals that an increase in co-aggregation, or reductions in integrin mobility inside the adhesion, potentiate NA formation. By extending the model to consider the mechanosensitivity of the integrin bond, we identify mechanical stress, rather than mechanical load, as a permissive mechanical parameter which allows for noise-dependent and independent NA-assembly, despite both parameters producing a bistable-switch possessing a hysteresis. Stochastic simulations of the model confirm these results computationally. This study thus provides insight into the mechanical conditions defining NA dynamics.

Statement of Significance

This manuscript makes valuable contributions in deciphering the dynamics of nascent adhesions (NAs). It presents a novel mathematical model that determines how mechanical stress applied to these adhesions governs their assembly and disassembly. The model is biophysically-relevant; it provides a framework that links NA-area to the number of mobile/immobile integrins along with adaptor proteins, and considers a multitude of experimental observations defining their mechanosensitive properties. The model is then examined to uncover how four components of this systems interact: NA-area, integrin/adaptor protein co-aggregation, number of integrins and adaptor proteins within NA, and force/stress exerted on NA. It is the first study that uniquely identifies adhesion stress, rather than its

total load, as the mechanical parameter conserved during NA-formation.

2.1 Introduction

Cellular migration plays a fundamental role in many physiological and pathophysiological systems, including embryonic morphogenesis and continual tissue regeneration [1], immune responses [2], tissue repair [3], and the metastatic properties of cancers [4]. Typically, cellular migration occurs in response to an extracellular signal in the form of a chemical or mechanical gradient [5, 6], leading to cellular polarization through nonlinear processes governing biochemical pathways that internally amplify the extracellular gradients to establish a front and rear of the cell [7, 8]. Cells attach themselves to their external environment by forming integrin-based adhesion complexes that anchor to the substrate and act as an extension of the cytoskeleton. This results in an active remodeling of the cytoskeleton, and causes a net displacement of the cell along the substrate [9, 10].

Adhesions serve as a point of force transmission to the external environment for motile cells. This force transmission is primarily mediated through integrin receptors, which span the cellular membrane and bind to their extracellular ligands (e.g. collagen and fibronectin). They form partially immobilized traction points that a cell can use to move itself, or deform the external environment. The cytoplasmic domains of integrins are linked to the actin cytoskeleton through a variety of adaptor proteins that interact through biochemical signaling pathways [11–13], creating a biologically regulated mechanical coupling system that links the actin cytoskeleton with the extracellular matrix (ECM). The interactions between these proteins, along with mechanical forces arising from active processes in the cytoskeleton, establish complex spatiotemporal patterns of activity [7, 8]. These patterns regulate the dynamics of adhesion assembly/disassembly [14, 15] and cytoskeletal organization [9, 14, 16], producing cellular migration in response to extracellular cues [10].

Adhesions are formed in a step-wise manner, starting as nascent adhesions (NA), a class of dynamic nanoscale clusters of integrin receptors (referred to hereafter as integrins) that contain on average 20-50 integrins [17, 18]. Many mechanisms, such as increases in the long-range lateral mobility of integrins (e.g., reduced corralling by actin cytoskeleton), local changes in their free-diffusivity, and modulation of their binding affinity through interactions with the adaptor protein talin, have been found to be relevant in the formation/regulation of integrin clusters [19–25]. Experimentally dissecting the effect of

each mechanism on adhesion formation has often been obscured by the fact that all these effects are simultaneously present in physiological conditions [20, 23, 26]. Theoretical models of adhesions allow for independent modulation of these mechanisms to study their effects. Existing models of adhesions either have idealized their physical model of an adhesion [10, 27–30] or have focused on certain phenomenological aspects of the system [29, 31–33] which are not applicable during the formation of NAs. Others are more biologically realistic with many variables, making it difficult to understand the underlying dynamics [34–40].

Integrins are intrinsically mechanosensitive, capable of exhibiting a catch-bond behaviour [41]. In contrast to the more common slip-bonds [42], catch-bonds exhibit a non-monotonic profile in their lifetime when plotted as a function of the applied force. This profile suggests that there exists a non-zero optimal applied force that maximizes the bond lifetime, where the increase in bond lifetime is associated with a conformational change to a long-lived bound state [43, 44]. It has been proposed that this phenomenon may reflect the activation of integrins (i.e., the induction of a high-affinity bound state) by mechanical forces [44, 45]. Due to their position in the mechanical linkage between the cell and its environment, the mechanosensitivity of integrins is likely to be implicated in adhesion dynamics. This has been investigated thoroughly from a theoretical perspective by considering a finite number of bonds which may rupture due to force and rebinding [27, 28, 33, 46]. These studies have reported disassembly of clusters of bonds, but have not yet examined how assembly is manifested in the presence of applied force. Thus determining the effect(s) of force on NA dynamics during assembly and disassembly remains incomplete.

The process of adhesion assembly into a cluster containing tens of molecules starting from a single molecular-complex initial condition (e.g., a single integrin-adaptor protein complex) was previously demonstrated through stochastic simulations of a molecular model which considered many possible state transitions [40]. However, mean-field analysis of this molecular model was performed using a simplified one-variable ordinary differential equation (ODE) model, predicting an unstable steady state that blocks the assembly of very small adhesions [40]. In theory, it should be possible to jump over this unstable state due to stochastic effects even in one-dimension. However, the conditions necessary to produce such a jump remain unexplored. Moreover, other studies which produce similar configurations of steady states also predict a net loss in both the number of bound integrins and adaptor proteins when adhesions are very small [38, 39, 46]. On the one hand, this is congruent with the proposition that NAs are thermodynamically unfavourable structures, and thus are the product of stochastic fluctuations

[29,39,47]. On the other hand, NAs have been shown to be stable for hundreds of second in appropriate mechanical conditions, suggesting that they are in fact thermodynamically favourable structures [17, 48]. To further investigate this, we develop here a mathematical model that possesses an elevated equilibrium representing NAs which can either (i) allow for NA-assembly independently of stochastic effects, or (ii) be used to understand in more detail the conditions required for noise-induced NA formation.

Due to the limited understanding of NA-assembly dynamics, we present in this study this biophysically-based mathematical model of NA formation and stabilization that considers a multitude of experimental observations and provides precise characterization of their underlying behaviour in various conditions. We then use the model, which not only considers the integrin bonds, but also the adhesion plaque formed by adaptor proteins, to demonstrate how assembly and disassembly are affected by force and their dynamics are manifested under various physiologically-relevant contexts.

2.2 Methods

2.2.1 Mathematical model of NA formation

We propose a biophysical model of NA formation based on a mechanism we term co-aggregation, where the interaction of integrins in the membrane with adaptor proteins in the cytoplasm leads to the co-localized aggregation of both into discrete structures (see Supporting Material for a detailed derivation of the model). This model is constructed to incorporate a number of experimental observations:

O1 NAs have a circular geometry and they grow isotropically [49]. This is in contrast to the growth of larger and typically elongated focal adhesions which is highly anisotropic [47, 49].

O2 Adaptor proteins exhibit a wide range of mobilities that vary in a location-dependent manner.

1. Adaptor proteins diffuse rapidly in the cytosol, while they diffuse more slowly inside adhesions [50].
2. Their mobility within adhesions is highly heterogeneous, suggesting that they exist in more than one state in the adhesion plaque [51, 52].

3. Some adaptor proteins have a longer residency time in adhesions containing a higher density of integrins, suggesting that a reduction in adaptor mobility is due to interactions (binding/tethering) with integrin [53].

O3 Integrins diffuse laterally along the membrane. Their free-diffusion is slower within the adhesion, and this effect is likely due to interactions with adaptor proteins on the cytoplasmic side of the membrane [24].

O4 Integrins become immobilized for extended periods of time upon binding to ligand, and this process is favoured inside adhesions [54].

O5 The integrin-ligand bond lifetime varies with force [41], exhibiting a biphasic profile with a maximal value at non-zero applied force ($\sim$37 pN).

Furthermore, in the derivation of model equations, we have also made a number of assumptions that are primarily based on experimental observations:

M1 As suggested in O1, the model defines a NA as a 2-dimensional region of space on the membrane demarcated by the boundary of a membrane-proximal circular adhesion plaque with area A (see Fig. 2.1).

M2 The adhesion plaque is a condensed phase of interacting adaptor proteins tethered to the membrane by integrins. Adaptor proteins are assumed to be incorporated with a fixed density through adsorption. The density, ρ, is determined by the mean volume of all adaptor proteins in the plaque, and the length of the bonds between them.

1. According to O2, we assume that the cytoplasmic pool of adaptor proteins is well-mixed (see Eq. (S6) in Supporting Material), while adaptor proteins in the adhesion plaque exhibit reduced mobility due to interactions with other adaptor proteins in the plaque and integrins in the membrane.
2. The adhesion plaque dynamics are derived based on the assumption that it can grow/shrink due to the adsorption/loss of adaptor proteins to/from any point in its interior, respectively; this assumption corresponds to the "Bulk-on/Bulk-off" formalism considered previously [29]. The choice of this formalism is motivated by the notion that NAs are not

strongly associated with the actin cytoskeleton during their assembly [55,56], allowing for the adsorption/loss of adaptor proteins through the dorsal face of the adhesion. This assumption would not be appropriate for models dealing with the maturation of NAs, as that process seems to be intrinsically tied to an increased association with organized actin filaments [49,55,57] that protect the adhesion from degradation by loss of matter through its dorsal face [29].

3. From OO2 and OO2 , the multiple mobility states of adaptor proteins in the adhesion are interpreted as being due to their tethering to the membrane by integrin receptors (i.e., in a state with lower mobility if the adaptor protein is tethered to the membrane while in a state with higher mobility if it is only associated with other adaptor proteins). This implies that a nonlinear relation between the adhesion's disassembly rate and its integrin content exists (see Eq. (S7) in Supporting Material).

M3 Underneath the adhesion plaque, there are a total of N_{in} integrins. L_{in} of these integrins are liganded and immobilized while M_{in} are mobile and diffuse freely (i.e., $N_{in} = L_{in} + M_{in}$; see Fig. 2.1).

1. Per O3, we use a position-dependent diffusion coefficient to abruptly change the diffusivity of integrins from D_{out} to D_{in} when they pass from the outside to the inside of the adhesion ($D_{out} > D_{in}$; see Eq. (S2) in Supporting Material).
2. Per O4, integrins inside the adhesion bind to their ligands with a rate k_{bind} (k_{unbind}). Furthermore, we assume that bound integrins are completely immobile. In order to account for the density of extracellular ligand, we take the binding rate to be proportional to ligand density (i.e., $k_{bind} = \overline{k}_{bind}\,[\text{Ligand}]$).
3. Per O5, bound integrins inside the adhesion unbind from their ligands with a rate $k_{unbind}\,(f)$, where f is the force applied to a single integrin (see Eq. (S14) in Supporting Material for details on the form of $k_{unbind}\,(f)$ and M4 for the determination of f). Bound integrins outside the adhesion unbind with a rate $k_{unbind}\,(0)$, with this situation only occurring when the adhesion plaque is shrinking.

M4 The total load applied to the adhesion is distributed evenly among all bound integrins. Therefore when an integrin unbinds, the load is distributed over the (fewer) remaining bound integrins such that each receptor feels an increase in applied force.

1. The force, f, applied to each integrin is computed by assuming that the NA is under fixed stress, $\sigma = \frac{fL_{in}}{A}$, and that each bound integrin bears an equal load (see Eq. (S18) in Supporting Material).

M5 For simplicity, we consider a periodic square lattice of adhesions with an inter-adhesion spacing of h (see Fig. 2.1). The flux of matter between the square latices is at equilibrium and thus assumed to be constant/conserved in each one of them. Model parameters are chosen in such a way that to prevent the adhesion from extending beyond the dimension of a single lattice cell (see Geometric Constraints in Supporting Information).

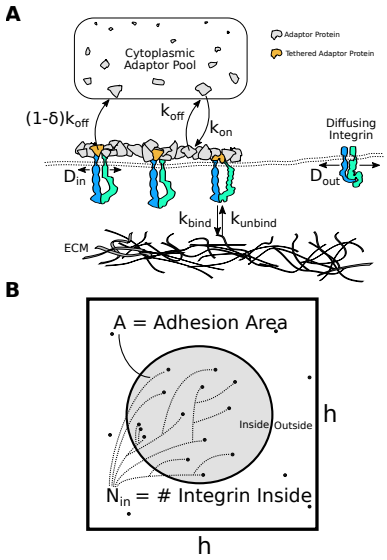

Figure 2.1: Schematic of the model describing adhesion formation. (A) Integrins and adaptor proteins co-aggregate to form a membrane-proximal adhesion plaque under which sits a cluster of integrins that exhibit a decreased diffusion coefficient ($D_{in} \leqslant D_{out}$) and become immobilized upon binding to ligand. Adaptor proteins that are in the proximity of integrins are assumed to be reversibly tethered to the membrane. Untethered adaptor proteins (grey) leave the plaque with a rate k_{off} while tethered ones (yellow) leave at a rate $(1-\delta)\, k_{off}$. (B) Geometry of the $h \times h$-square lattice containing the adhesion domain Ω. NAs possess a circular geometry confined to grow in this square lattice cell. The area of the adhesion plaque ($A\,(t)$) and the number of integrins it contains ($N_{in}\,(t)$) are dynamic variables which vary due to adsorption and diffusion, respectively.

Mathematically, the co-aggregation mechanism discussed above is implemented through the interaction of the integrin-dependent tethering mechanism (MM2) and the reduced integrin mobility inside

the adhesions (MM3 and MM3).

The behaviour of the model is investigated through two complementary approaches: (i) by investigating its full spatiotemporal dynamics using stochastic simulations, and (ii) by characterizing the outcomes of the stochastic simulations using a simplified differential equation model of NAs describing the dynamics near equilibrium. The simplified model is given by the following set of ODEs

$$\dot{A} = A\left[\underbrace{\left(k_{on}^{0}\left(\frac{C_P}{\rho}-\frac{A}{h^2}\right)\right)}_{\text{Plaque growth}} - \underbrace{k_{off}\left((1-\delta)+\delta\frac{b^n}{b^n+\left(\frac{M_{in}+L_{in}}{A}\right)^n}\right)}_{\text{Plaque shrinking}}\right] \tag{2.1a}$$

$$\dot{M}_{in} = \underbrace{2\sqrt{\pi A}\left(\frac{D_{out}(C_I h^2 - M_{in} - L_{in})}{h^2 - A} - \frac{D_{in} M_{in}}{A}\right)}_{\text{Mobile integrin net diffusion}} - \underbrace{\left(k_{bind} M_{in} - k_{unbind}\left(f\right) L_{in}\right)}_{\text{Integrin-ligand binding kinetics}} \tag{2.1b}$$

$$\dot{L}_{in} = k_{bind} M_{in} - k_{unbind}\left(f\right) L_{in}, \tag{2.1c}$$

where k_{on}^{0} is a kinetic parameter related to the rate of adsorption of adaptor proteins into the adhesion (see Parameter Estimation in Supporting Material for more details), k_{off} is the off-rate of adaptor proteins from the adhesion in the absence of integrins, δ is the fractional reduction in the off-rate of adaptor proteins when tethered to the membrane by integrins, b is the concentration of integrin inside the adhesion which results in the tethering of 50% of adaptor proteins in the adhesion plaque, n is the degree of cooperativity between integrins for the tethering of adaptor proteins, and C_I (C_P) is the mean density of integrins (adaptor proteins) taken by averaging over the $h \times h$ lattice cell. For detailed description and derivation of the model, see Supplementary Information.

2.2.2 Conditional Expectation Analysis

We have developed a computational method to infer the conditional mean of one physical variable given the value of another dependent physical variable. This technique is used to assess the relation between NA-area, A, and the number of integrins it contains, N_{in}, by using only the two terms P_A and $P_{N_{in}}$ representing the marginal distributions of these quantities, respectively. Briefly, we assume

$A = f\left(\bar{N}_{in}\right) = \mathbb{E}\left(A\,|N_{in}\right)$, where $\mathbb{E}\left(x\,|y\right)$ denotes the conditional expectation of the variable x given the value of another variable y, and then use Bayesian methods to quantitatively estimate $f\left(\cdot\right)$ using the change-of-variable formula given by $P_A = P_{N_{in}}/f'\left(N_{in}\right)$. See Supporting Material for further details.

2.2.3 Model parameters

We have used a complex systems approach to parameter determination, applying different estimation techniques to guarantee that our model produces predictions which are consistent with experimental findings while also exhibiting the emergent behaviour of the system under consideration (i.e., NAs). This is accomplished by deriving analytical expressions (e.g., steady states of the model) that can be equated to experimental measurements [17, 24, 41, 50], and then solving the resulting set of nonlinear equations to quantify model parameters. This approach is used to determine the parameters b, h, C_I, $K_{in} = D_{out}/D_{in}$, $K_{on} = k^0_{on}/k_{off}$, and $K_{bind} = k_{bind}/k_{unbind}$. Furthermore, the previously published data describing the distributions of protein cluster sizes and number of integrins within these protein clusters [17] is digitized and utilized to derive a relation between A and N_{in}, using Conditional Expectation Analysis (described above). The non-zero A-nullcline obtained by setting Eq. (2.1a) to zero while assuming no cooperativity (i.e., by letting $n = 1$), is then fit to this relation using a nonlinear least squares fitting procedure that yields estimates for the two identifiable parameters

$$A_0 = h^2\left(\frac{C_P}{\rho} - \frac{1}{K_{on}}\right)$$

and

$$A^\infty = h^2\left(\frac{C_P}{\rho} - \frac{1-\delta}{K_{on}}\right).$$

Estimating these identifiable parameters is necessary to determine the values of b and K_{on} (see Supporting Material). The parameters δ, D_{out}, k_{unbind}, and C_P are estimated directly from experimental data [24, 41, 54, 58]. Finally, the remaining two parameters k_{off} (or k^0_{on}) and ρ are manually tuned in order to obtain stochastic simulations that are comparable to experimental recordings of adhesion assembly/disassembly [49]. Parameter values are used to explain how the analytical results of our model manifest themselves numerically, when constrained by experimental data. The qualitative behaviour of the model does not depend critically on parameter choices made; this is to be expected as almost all results presented here have been obtained analytically. For more details about parameter estimation,

see Supplementary Information.

2.2.4 Software

Stability analysis for fixed protein density and binding affinity is performed symbolically using Mathematica Version 11.3 (Wolfram Research Inc., Champaign, IL). On the other hand, for fixed adhesion stress, stability analysis is conducted numerically using the continuation software AUTO-07p to obtain the location of bifurcation points [59], The stability of branches obtained are then cross-validated using Mathematica and MATLAB (MathWorks, Natick, MA). Stochastic simulations and nonlinear least squares fitting are performed using MATLAB. Parameter estimation is also done using Mathematica. The code used for ODE analysis, numerical continuation, and stochastic simulations can be obtained online [60]

2.3 Results

2.3.1 The relation between NA area and its integrin content

In order to understand NA dynamics, we first aim to establish how their area and integrin content are related. If this relation is linear, then the density of integrins inside the adhesion is constant and the area of the adhesion can be explained by N_{in} alone. Such a relation could be used to estimate the effective membrane area of a single integrin, and motivates the theoretical assumption of a fixed ratio of integrin to adaptor proteins [31–33, 35]. If this relation is nonlinear, on the other hand, then the area of the adhesion cannot be explained solely by the number of integrins and their physical dimensions. In such a case, it would be inaccurate to use models that assume a fixed ratio of integrin to adaptor proteins.

To investigate this, we have digitized previously published distributions of NA-diameter and their integrin content [17]. The distribution of NA-diameter is first converted to a distribution of NA-area A, by assuming a circular geometry, followed by applying Conditional Expectation Analysis (see Methods Section) to quantify the relation between the two random variable A and N_{in}. This analysis is motivated by the significant differences in skewness between the distributions, suggesting the possibility of a nonlinear relation. Indeed, our results (see Fig. 2.2A) reveal that this relation appears to have a saturating "sigmoidal" phase for NAs containing up to ~ 190 integrins, followed by a linear phase for larger adhesions. This indicates that the integrin density inside the adhesion, N_{in}/A, is not fixed in

small NAs (see dotted line in Fig. 2.2B), and therefore the size of these NAs cannot be explained by the number of integrins it contains. This sigmoid relation thus must be taken into consideration when formulating the model for NAs.

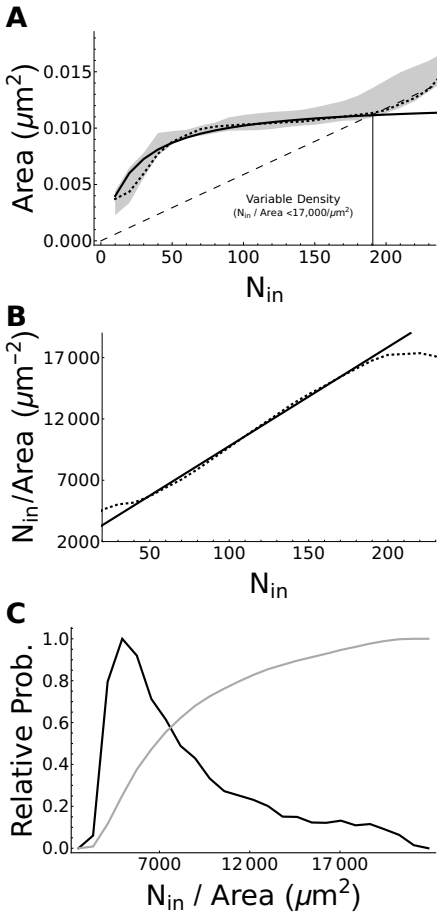

Figure 2.2: (A) Inferred relation between NA-area A and its integrin content N_{in} as determined by Conditional Expectation Analysis. Bayesian inference is used to determine an empirical relation between A and N_{in}, under the assumption that NAs are circular. After digitizing the distributions of NA-diameters and their integrin contents published in [17], a relation between them is quantified. A 99.95% confidence interval is plotted in grey demonstrating that the data generally exhibits a nonlinear relation between the two variables. The *maximum a posteriori* (MAP) estimate of this relation is also plotted as a dotted line, suggesting that NA-area depends sigmoidally on N_{in} for small adhesions, while this dependence is linear for large adhesions (compare to dashed line). The non-trivial A-nullcline of the model, describing the relation between the two variables near equilibrium as defined by Eq. (2.2) (solid line) is fit to the MAP estimate in the nonlinear phase, and found to be in agreement.(B) The computed integrin density inside the adhesion, $N_{in}/A\left(N_{in}\right)$. Estimates are computed from the data-derived MAP estimate of $A\left(N_{in}\right)$ (dotted line) and from the model prediction for $A\left(N_{in}\right)$ given by Eq. (2.2) (solid line). Both curves exhibit a linear increase in integrin density with respect to N_{in} for $N_{in} \in \left[50, 190\right]$. (C) Probability distribution of integrin densities. Black line: probability density function $P\left(N_{in}/A\right) = P\left(N_{in}\right)\left[d(N_{in}/A(N_{in}))/dN_{in}\right]^{-1}$, where $A(N_{in})$ is given by Eq. (2.2); grey line: cumulative density function.

To account for this, we have incorporated assumption MM2, into the model. By setting the left hand side of Eq. (2.1a) to zero we solve for the non-zero A-nullcline. This is equivalent to assuming that the observed differences in NA-area are due to local variations in integrin availability (i.e., differences in C_I). For simplicity, we consider the absence of cooperativity between integrins in the tethering of adaptor proteins ($n = 1$). The resulting expression for the A-nullcline is given by

$$A\left(N_{in}\right) = \frac{\left(4A^{\infty}bN_{in} + \left(N_{in} - A_0 b\right)\right)^{1/2} - \left(N_{in} - A_0 b\right)}{2b}, \tag{2.2}$$

where $A_0 = h^2\left[\left(C_P/\rho\right) - \left(1/K_{on}\right)\right]$ is the (possibly negative) area of the adhesion plaque in the absence of co-aggregation (i.e., when $\delta \to 0$) with $K_{on} = k_{on}^0/k_{off}$, and $A^{\infty} = h^2\left[\left(C_P/\rho\right) - \left(1-\delta\right)/K_{on}\right]$ is the maximum area of the adhesion plaque (attained when the mean integrin density in the membrane is arbitrarily high, see Geometric Constraints section in Supporting Material). The shape of the curve described by Eq. (2.2) is in agreement with the profile of the relation inferred by Conditional Expectation Analysis (solid line in Fig. 2.2A), supporting the hypothesis that the aforementioned variation in integrin density (inside NAs) may be explained by the tethering mechanism used to formulate Eq. (2.1a).

We note that the model suggests that integrin density may grow unboundedly (see solid line in Fig. 2.2B), which is due to the treatment of integrins as infinitesimally small point particles. In reality, the physical size of the integrins will eventually have non-negligible effects on their flux as the adhesion becomes increasingly crowded with integrins. Our data analysis demonstrates that adhesions containing integrin densities up to $\sim 17,000\ \mu\text{m}^{-2}$ are not strongly influenced by these molecular crowding effects, as can be seen from the saturating relation between A and N_{in} for $N_{in} < 190$. Conversely, above this threshold in density, we have $A \propto N_{in}$, suggesting that the crowding of integrins plays a significant role in determining the size of larger adhesions.

The maximal integrin density we have computed is significantly higher than the mean densities of $\sim 1,000\ \mu\text{m}^{-2}$ previously reported in Wiseman et al. [61], or the $\sim 6,600\ \mu\text{m}^{-2}$ computed by Changede et al. [17]. Firstly, we would like to note that the most likely integrin density according to our analysis is $\sim 4940\ \mu\text{m}^{-2}$ (see black line in Fig. 2.2C), which is comparable to the value reported by Changede et al. Secondly, it has been previously suggested that Wiseman et al. [61] estimated the mean density of integrins on the membrane, as their diffraction-limited imaging would not allow for

proper resolution of NA boundaries [17]. As such, we note that the value we have used for the mean density of integrins, $C_I = 1844\ \mu\text{m}^{-2}$, is comparable to what was reported by Wiseman et al. [61] (see Parameter Estimation in Supporting Material for more details).

Furthermore, our approach quantifies the variability of integrin density inside adhesion. Therefore, while our analysis suggests that this density may go as high as $\sim 17,000\ \mu\text{m}^{-2}$, it also predicts that 80% of adhesions have an integrin density that is less than $12,000\ \mu\text{m}^{-2}$ (see grey line in Fig. 2.2C). Changede et al. [17] previously computed a maximal theoretical density of $\sim 25,000\ \mu\text{m}^{-2}$ based on an estimated integrin footprint of $40\ \text{nm}^2$. Using a hypothetical model [62] built from multiple partial crystal structures of integrin [63–66], we estimate a rectangular bounding box footprint of 7.6 nm $\times$ 4.5 nm $\approx$ 34 nm^2 and 12 nm $\times$ 5 nm $\approx$ 60 nm^2 for the closed and open conformations of integrin, respectively. This provides us with corresponding bounds on the maximum possible density of integrins, given by $29,400\ \mu\text{m}^{-2}$ and 16,667 μm^{-2}, respectively. Interestingly, our estimate of 17,000 only marginally surpasses the lower bound on the theoretical maximum density (i.e., when all integrins are in the open conformation) and remains well below the upper bound. This suggests that the majority of the integrins within these high-density NAs are in a closed conformation.

In this study, we focus our analysis on the nonlinear regime identified for $N_{in} < 190$, as NAs typically have $N_{in} \in [20, 50]$ [18]. In what follows, we examine the chemical and mechanical regulation of this sigmoidal relation between NA-areas and their integrin content through the biophysical parameters which control both N_{in} and Eq. (2.2).

2.3.2 Stabilization of the adhesion plaque by integrin

One of the equilibria of Eqs. (2.1a)-(2.1c) is the unclustered steady state $(A, M_{in}, L_{in}) = (0, 0, 0)$. The stability of this steady state depends on the values of model parameters. In order to reduce the complexity of our analysis, we will first consider the model in the absence of force ($f = 0$). In subsequent sections, we will extend our steady state analysis to include force and then investigate the time-course of the model under applied force.

By analyzing the stability conditions of this steady state, we find that it becomes unstable once model parameters cross a threshold (see Supporting Material); we demonstrate later that this corresponds to the induction of adhesion formation. Given that the existence of the unclustered steady state $(0, 0, 0)$ is independent of the degree of cooperativity n, we first restrict our analysis to the case when

$n = 1$ for simplicity. This will allow us to build intuition about the behaviour of the system, and determine what happens for $n > 1$. Under these conditions, the unclustered steady state loses stability through a transcritical bifurcation occurring whenever $C_I > C_I^{\ddagger}$, $C_P > C_P^{\ddagger}$, or [Ligand] > [Ligand]‡ (see Eqs. (S11)-(S13) in Supporting Material). That is, once there are enough integrins, adaptor proteins, or ligands at the interface between the cell and its environment, the unclustered steady state becomes unstable and stable adhesion plaques form (see Fig. 2.3). This transition occurs when the system undergoes a transcritical bifurcation (see Fig. 2.3A, B and C), forming a stable non-trivial steady-state, given by

$$A^* = \frac{h^2\left(\Gamma\left(\hat{C}_I\right) - \hat{C}_I + b\beta\left(\phi K_{on} - \delta\right)\right)}{2b\beta K_{on}}, \tag{2.3}$$

$$M_{in}^* = \frac{h^2\left((2\beta\phi + 1)\hat{C}_I - \Gamma\left(\hat{C}_I\right) + b\left(\omega - \beta\delta\right)\right)}{2\beta\left(K_{bind} + 1\right)\omega}, \tag{2.4}$$

where $\hat{C}_I = \left(1 + K_{bind}\right) K_{in} K_{on} C_I$, $K_{bind} = k_{bind}/k_{unbind}$, $K_{in} = D_{out}/D_{in} \geqslant 1$,

$$\Gamma\left(\hat{C}_I\right) = \left(b^2\left(\omega - \beta\delta\right)^2 + 2b\hat{C}_I\left(\beta\delta + \omega\right) + \hat{C}_I^2\right)^{1/2},$$

$\omega = \left(\beta\phi + 1\right) K_{on}$ and L_{in}^* is defined by Eq. (S8) (see Supporting Material). These expressions thus determine analytically how different parameters of the model affect the existence of the non-trivial steady state and the threshold (the transcritical bifurcation).

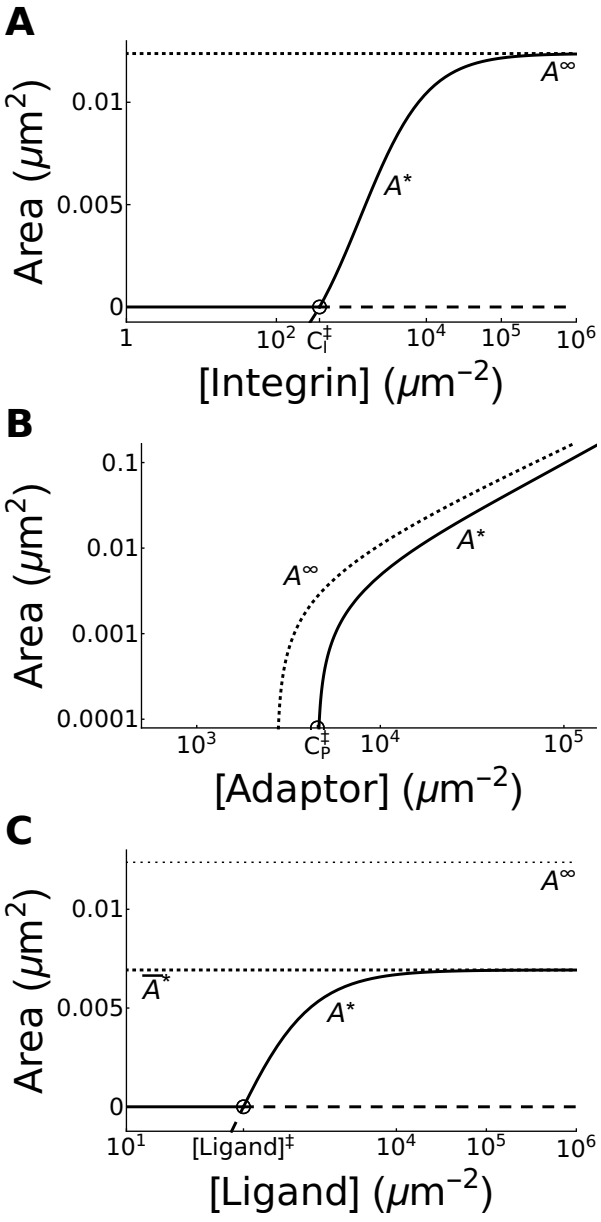

Figure 2.3: Effects of co-aggregation on NA-area. Bifurcation diagrams of equilibrium adhesion area A^* with respect to (A) C_I, (B) C_P, and (C) [Ligand], showing branches of stable (solid lines) and unstable (dashed lines) steady states separated by thresholds defined by transcritical bifurcation points (open circles). The bifurcation points occur when $C_I = C_I^\ddagger$ in A, $C_P = C_P^\ddagger$ in B and [Ligand] = [Ligand]‡ in C. The stable branches represent the (un)clustered steady states (before) after the threshold. Notice that increasing C_I leads to a saturating response, eventually plateauing at A^∞ (dotted line in A) defined by Eq. (S10) , whereas increasing C_P leads to an unbounded growth in adhesion area (panel B). Increasing [Ligand] also produces a saturating response, plateauing at $\bar{A}^* < A^\infty$ (panel C).

As discussed in the previous section, increasing the number of integrins inside the NA causes an increase in their area. According to the model, this may be accomplished directly through two approaches: (i) increasing the total number of integrins on the membrane through the parameter C_I, or (ii) increasing the likelihood that an integrin is inside the adhesion through the ligand concentration [Ligand] (see how K_{bind} is defined in MM3) or the reduction in diffusivity K_{in}. In the limit $C_I \to \infty$, the first approach yields adhesions with a finite size $A^\infty < h^2$ (see Eq. (S10) in Supporting Material, and Fig. 2.3A). On the other hand, the limiting case for the second approach is equivalent to all integrins being inside the adhesion, where (according to Eq. (2.2)) the area of the clustered steady state is given by

$$\bar{A}^* = A^* \left(C_I h^2\right) = \frac{h^2 \left(\bar{\Gamma}\left(\bar{C}_I\right) - \bar{C}_I + b\left(\phi K_{on} - \delta\right)\right)}{2bK_{on}}, \tag{2.5}$$

with $\bar{C}_I = K_{on} C_I$ and

$$\bar{\Gamma}\left(\bar{C}_I\right) = \left(b^2\left(\delta - \phi K_{on}\right)^2 + 2b\bar{C}_I\left(\delta + \phi K_{on}\right) + \bar{C}_I^2\right)^{1/2}.$$

We note that $\bar{A}^* \leqslant A^\infty$ (see Fig. 2.3C) and $\lim_{C_I \to \infty} \bar{A}^* = A^\infty$, which implies that ligand-dependent regulation of adhesion area cannot overcome integrin-dependent regulation. This means that a stable adhesion plaque may also grow if more plaque material is introduced into the system. Within the model, this is controlled by the parameter C_P, which is linearly proportional to A^∞. Therefore, increasing C_P leads to unbounded growth of the adhesion area (see Fig. 2.3B). Thus the maximum area of NAs is regulated intracellularly, through the parameters C_I and C_P, while the formation of adhesions and modulation of their area may be regulated intracellularly through these same parameters or extracellularly through [Ligand]. This, as a result, establishes a hierarchy in the determination of NA-area by these three physiologically regulated densities, ranked according to their relative importance as follows: $C_P > C_I >$ [Ligand].

2.3.3 Effects of the magnitude and degree of co-aggregation

To further understand the dynamics of the model, we will analyze the model under appropriate limits. Thus, we first consider the integrin-independent adhesion plaque formation when $\delta \to 0$. In this case, the model reduces to a fully deterministic version of the "Bulk-on/Bulk-off" adsorption model [29] with one added component for the conservation of matter. In this limit, we have $A^* \to A_0$, which im-

plies that adhesion area should grow linearly with adaptor concentration (see Fig. 2.3B). This demonstrates the basic chemical kinetic control system of the model. Regardless of integrin density, adhesion plaques may form if a large enough pool of adaptor proteins is present (i.e., $A_0 > 0$). In the absence of co-aggregation, the cell must control both the formation and area of adhesions through the concentration of adaptor proteins. Interestingly, reductions in adaptor protein concentration have been found to decrease adhesion size [67–71]. On the other hand, if there is co-aggregation between integrins and adaptor proteins, the cell can set the maximum area of adhesions, A^{∞}, by varying adaptor protein concentration while controlling their formation with the density of integrins. This is in line with the recent findings that NA size saturates as integrin density (or activation) is increased (see Fig. 2.2 and [17]); suggesting that the co-aggregation of the two proteins is a critical component of the model needed to capture experimental observations.

By tracking the location of the threshold (the transcritical bifurcation in Fig. 2.3) as the the values of both C_I and C_P are varied in a two-parameter bifurcation, we obtain two regimes of behavior separated by a monotonically decreasing boundary at a given value of δ (see Fig. 2.4A). This boundary divides the first quadrant into the two regimes of unclustered (below) and clustered (above) steady states, with the former expanding at the expense of the latter as the magnitude of co-aggregation δ is decreased. These results suggest that the adaptor protein concentration needed to induce clustering is always lower in the presence of co-aggregation (see Fig. 2.4A). The amount of reduction in adaptor protein density generated by the inclusion of co-aggregation is given by

$$\begin{aligned} \Delta C_P^{\ddagger} &:= C_P^{\ddagger}\Big|_{\delta=0} - C_P^{\ddagger}\Big|_{\delta}, \\ &= \frac{\delta\rho}{K_{on}} \frac{\left(1+K_{bind}\right) K_{in} C_I}{\left(b+\left(1+K_{bind}\right) K_{in} C_I\right)} > 0. \end{aligned}$$

Interestingly, in the limit of infinite integrin density, we have

$$\lim_{C_I \to \infty} \phi^{\ddagger} = 0.$$

This suggests that, even when integrin density is arbitrarily high, the cell can still turn off clustering by reducing C_P (or δ) to make ϕ negative.

To study the effects of altering the degree of cooperativity n on the steady state dynamics of adhe-

sion area, we plot in Fig. 2.4B the stable branch of clustered steady states (i.e., the stable branch to the right of the threshold in Fig. 2.3A) at various values of n. Our results reveal that increasing n increases the slope of A^* with respect to C_I, and that in the limit as $n \to \infty$, we obtain a step-like switching response in which protein clusters form beyond a threshold in integrin density occurring right at the transcritical bifurcation point (see Fig. 2.4B). The area of adhesions formed in this case remain roughly the same regardless of integrin density. Finally, we have used the MAP estimate of $A\left(N_{in}\right)$ (see Fig. 2.2) as means of estimating n numerically. This is done by solving for the non-zero A-nullcline with $n = 2, 3, 4$, where visual comparison with the data for $A\left(N_{in}\right)$ suggests $n = 2 - 3$ (data not shown).

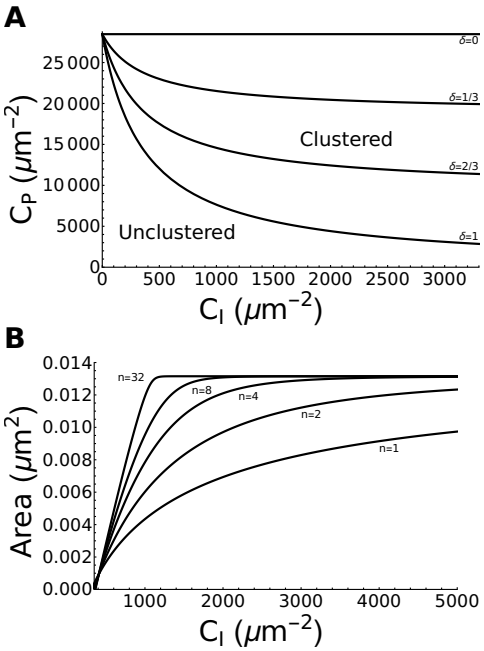

Figure 2.4: The effects of co-aggregation and cooperativity on steady state dynamics of protein clustering. (A) Two parameter bifurcation of adhesion area A with respect to C_I and C_P showing the boundary between the regimes of unclustered (below) and clustered (above) steady states for various values of co-aggregation δ. The boundary is defined by the transcritical bifurcation points in Fig. 2.3 when C_I and C_P are both varied.. Increasing δ reduces the adaptor protein density needed to induce aggregation. In the limit $\delta \to 0$, integrin density C_I has no effect on the aggregation of adaptor proteins. (B) Stable branches of clustered steady states shown in Fig. 2.3A for various degrees of cooperativity n. By increasing n, the density thresholds for clustering decreases and the steepness of the stable branch of clustered steady states increases.

2.3.4 The effects of reduced integrin lateral mobility

The model assumes that integrin mobility is significantly reduced inside the NA (see OO3 and OO4), and that, at equilibrium, this area is in turn dependent on the number of integrins it contains. This makes understanding the dependence of NA dynamics on changes in integrin lateral mobility non-trivial. We can quantitatively understand this by first noting that the area specified by Eq. 2.2 is a monotonically increasing function of the number of integrins inside the NA, N_{in}^*. Therefore, we may simply study the effects of the two parameters, which control changes in integrin lateral mobility (namely, K_{in} and K_{bind}), on the variable N_{in}^*. From Eqs. (S8) and (2.4), we have

$$N_{in}^* = (1 + K_{bind})\, M_{in}^* = \frac{h^2 \left((2\beta\phi + 1)\hat{C}_I - \Gamma\left(\hat{C}_I\right) + b\,(\omega - \beta\delta) \right)}{2\beta\omega}.$$

We can thus conclude that N_{in}^* depends on integrin mobility only through the term $K_{in}(1 + K_{bind})$ that appears implicitly in $\hat{C}_I$, ω, and β . This means that we cannot distinguish between the effects induced by the two parameters purely based on adhesion area or integrin content. On the other hand, the fraction of bound integrins, given by

$$\frac{L_{in}^*}{L_{in}^* + M_{in}^*} = \frac{K_{bind}}{1 + K_{bind}}$$

depends explicitly on the binding affinity. This means that while both reduced diffusivity (K_{in}) and ligand binding (K_{bind}) will result in an increase in the area and integrin content of adhesions, only ligand binding can increase the fraction of bound integrins.

Due to the similarity of the effects of ligand binding and reduced diffusivity, we focus our attention on analyzing more closely the effects of ligand binding, noting that the same analysis can be performed to study the effects of reduced diffusivity. In the absence of binding, we obtain the following unbound steady state

$$\tilde{\mathbf{S}}^* = \lim_{K_{bind}\to 0} (A^*, M_{in}^*, L_{in}^*) = \left(\tilde{A}^*, \tilde{M}_{in}^*, 0\right),$$

which has the associated critical protein thresholds

$$\tilde{C}_I^\ddagger = \lim_{K_{bind}\to 0} C_I^\ddagger, \quad \text{and} \quad \tilde{C}_P^\ddagger = \lim_{K_{bind}\to 0} C_P^\ddagger. \tag{2.6}$$

Based on Eq. (S11), we can conclude that $\tilde{C}_I^\ddagger$ is larger than $C_I^\ddagger$ by a factor of $1 + K_{bind}$. Similarly, from Eq. (S12), it can be shown that $\tilde{C}_P^\ddagger \geqslant C_P^\ddagger$. Thus another effect of binding (and reduced diffusivity) is that it increases the potency of integrins and adaptor proteins in the formation of adhesions, by decreasing the threshold for clustering (i.e., shifting the transcritical bifurcation to the left) and expanding the range of stability of the clustered steady state (see Fig. 2.5A).

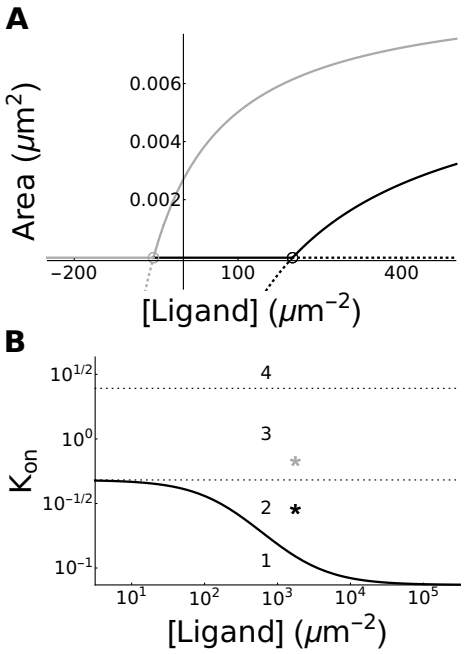

Figure 2.5: Distinct regions in parameter space are distinguished by their dependence on ligand binding. (A) Bifurcation diagram of adhesion area A with respect to [Ligand], showing branches of stable (solid lines) and unstable (dashed lines) steady states separated by thresholds of transcritical bifurcation points (open circles). Decreasing K_{on} from 0.7 (black lines) to 0.3 (grey lines) shifts the transcritical bifurcation point to the left, allowing for the unclustered stable steady state to be attained at $[\text{Ligand}] = 0$. (B) Two parameter bifurcation of adhesion area A with respect to [Ligand] and K_{on}, showing the boundary (black line) between the regions of unclustered (region 1) and clustered steady states lying below and above the boundary, respectively. The region of clustered steady states is further divided into three regions: region 2, defined by $[\text{Ligand}]^\ddagger > 0$, requiring the presence of both ligand and integrin to induce clustering; region 3, defined by $[\text{Ligand}]^\ddagger < 0$ with $A_0 < 0$, requiring the presence of integrin, but not necessarily ligand, to form stable adhesion plaques; and the unphysiological region 4, defined by $A_0 > 0$, which exhibits clustering irrespective of integrin or ligand densities.

For the more general scenario when $K_{bind} > 0$, we note that the state $\tilde{\mathbf{S}}^*$ is a biophysically relevant

metastable steady state only if all its coordinates are non-negative. This is equivalent to the experimentally verifiable criterion $[\text{Ligand}]^{\ddagger} > 0$, which can be used to further divide parameter space into ligand-dependent and -independent clustering regions (see Fig. 2.5). These regions are differentiated by their behaviour in the limit as $[\text{Ligand}] \to 0^{+}$, where in the former region the stable unclustered steady state is attained (black lines in Fig. 2.5A, with $K_{on} = 0.7$), while in the latter, the stable clustered steady state is attained (grey lines in Fig. 2.5A, with $K_{on} = 0.3$). This implies that if the interactions between adaptor proteins are strong enough (e.g., if K_{on} is large enough; see Fig. 2.5B), then adhesion plaques will form even in the absence of ligand binding. As discussed in the previous section, it is even possible for these interactions to be strong enough to induce the formation of an adhesion plaque in complete absence of integrins (as suggested by region 4 where $A_0 > 0$). Together, these consideration allow us to identify 4 regions in parameter space:

1. *No Clustering (region 1 in Fig. 2.5B):* This occurs when $[\text{Ligand}] < [\text{Ligand}]^{\ddagger}$, and the model predicts there is no clustering of adaptor proteins.
2. *Ligand-Dependent Clustering (region 2 in Fig. 2.5B):* This region is bounded by $[\text{Ligand}]^{\ddagger} \leqslant [\text{Ligand}]$ with $[\text{Ligand}]^{\ddagger} > 0$. Within this region, the model predicts clustering occurs only when $[\text{Ligand}]$ is high enough.
3. *Ligand-Independent Clustering (region 3 in Fig. 2.5B):* This region is defined by $[\text{Ligand}]^{\ddagger} \leqslant [\text{Ligand}]$ with $[\text{Ligand}]^{\ddagger} < 0$ and $A_0 < 0$. Within this region, the model predicts clustering to occur regardless of the value of $[\text{Ligand}]$.
4. *Integrin-Independent Clustering (region 4 in Fig. 2.5B):* This region is defined by $A_0 > 0$. Within this region, the model predicts clustering regardless of the value of $[\text{Ligand}]$ and C_I. This appears to be unphysiological.

Since clustering is absent in region 1 and unphysiological in region 4, one may conclude that cells have likely tuned the interaction of adaptor proteins and integrins to that in regions 2 or 3, which differ by whether or not adhesions form in the absence of ligand. Whereas some have hypothesized that activation of integrins by adaptor proteins may be sufficient to induce clustering of integrins [72], an observation consistent with the model in region 3, others have shown that a ligand spacing greater than $\sim 60\,\text{nm}$ drastically reduces the spreading of cells [73–75], an observation more consistent with crossing the transcritical bifurcation point in region 2. These two mutually exclusive hypotheses are considered in order to determine the two distinct sets of parameter values used to generate the curves

in Figure 2.5A (see Parameter Estimation in Supporting Material). .

2.3.5 Mechanosensitive ligand binding dynamics

Thus far we have not explicitly considered the effects of force on NA formation, although it is known that adhesions transmit force to the ECM. Mechanical forces can accelerate the dissociation of the integrin-ligand bond (see OO5 and MM3 in Methods). Moreover, a collection of catch bonds under fixed load will catastrophically fail once the number of bound integrins drops below a threshold [46]. Therefore, in order to effectively transmit force to its environment, a NA must contain a sufficient number of bound integrins. This raises the question of how the dynamics of force generation in NAs are manifested, or more specifically whether adhesion load (the total force) or stress (force per unit area) is the fixed mechanical parameter that allows for NA-assembly from a single integrin-adaptor protein complex [31, 35, 76].

If adhesion load is held constant, then adhesions needs to build up a sufficient integrin content to be able to bear the load. As shown earlier, a large equilibrium integrin content at steady state can be achieved by either increasing K_{in} or K_{bind}. However, previous work has found that clusters of catch bonds will disassemble when there are a small number of bound integrins [46]. Therefore, it is unclear how adhesions reach their stable equilibrium under fixed load. Alternatively, if stress is held constant, then the fraction of bound integrins must be large enough to bear the variable load that increases as the adhesion grows. The latter requires that K_{bind} be large enough (as discussed before). The mechanosensitivity of the integrin-ligand bond and the complex spatial dynamics of integrins make resolving this question non-trivial.

2.3.5.1 Bistable switch in regions 2 and 3 with respect to stress

To explore the effect of mechanical force on dynamics, we expand our equilibrium mean-field model described by Eqs. (2.1a)-(2.1c) to include the mechanosensitive binding affinity of integrin, as described by Eqs. (S17) and (S18) (for further details see Supporting Material). Our initial analysis, as well as previous studies [27, 28, 46], suggest that there is a maximum stress, σ_c, which NAs can sustain. To further expand on this result, we plot in Fig. 2.6 the dependence of the steady state adhesion area A^* (and $\tilde{A}^*$ in region 3) with respect to stress σ and label the different branches of the curve based on the stability properties of the steady states belonging to each branch (using the subscripts "s" and

"u" to label the stable and unstable ones, respectively). The resulting bifurcation diagram shows that the dynamics are governed by a bistable-switch possessing a hysteresis, similar to those previously observed in systems of Rho family of GTPases [8, 58]. The switch has a plateaued branch of elevated steady states (black line), labeled A_s^*, merging with another branch of unstable saddle points beneath it (dashed black line), labeled A_u^*, at a saddle-node bifurcation when $\sigma_c \approx 470$ kPa. In region 3, bistability is produced by another lower branch of metastable states formed by $\tilde{A}^*$ (grey line in Fig. 2.6B), while the branch $A = 0$ is unstable. In region 2, the unstable branch A_u^* intersects $A = 0$ at some value of stress σ_t ($0 \leqslant \sigma_t \leqslant \sigma_c$), leading to the formation of a transcritical bifurcation that produces a region of monostability for $\sigma < \sigma_t$ (horizontal dashed line in Fig. 2.6A) and bistability for $\sigma > \sigma_t$ (horizontal solid line in Fig. 2.6A).

The folded elevated stable and unstable branches seen in Fig. 2.6 have been previously reported in studies that considered only the number of liganded bonds [27, 28, 46] or adaptor proteins in the adhesion [40]; these studies have either reported a monotonically decreasing elevated stable branch [27, 28], or one which increases significantly with applied force or ECM stiffness [40, 46]. In either case, a lower stable/metastable branch ($\mathbf{Z} = (0, 0, 0)$ in region 2 with $\sigma > \sigma_t$ and the previously defined $\tilde{\mathbf{S}}^* = (\tilde{A}^*, \tilde{M}_{in}^*, 0)$ in region 3 with $\sigma < \sigma_c$) has not been previously reported for a model that considered only liganded bonds. Our results thus show that the system possesses bistability between clustered and the unbound or unclustered steady states, indicating that this bistability arises from the consideration of plaque dynamics. We denote the elevated stable and middle unstable branches by $\mathbf{S}^* = (A_s^*, M_s^*, L_s^*)$ and $\mathbf{U}^* = (A_u^*, M_u^*, L_u^*)$, respectively. These two steady states correspond to large clusters of integrins bearing a small load and small clusters bearing large loads, respectively. This correspondence may also be used to intuitively understand their stability, as the small (unstable) clusters will unbind catastrophically once a single integrin-ligand bond ruptures while the large (stable) clusters contain enough integrins for rebinding effects to outpace unbinding.

2.3.5.2 NA dynamics as determined by the bistable switch

Near the saddle node of Fig. 2.6A and B (i.e., near $\sigma \approx \sigma_c$) the basin of attraction of the clustered steady states shrinks significantly until it eventually disappears along with the steady state when $\sigma > \sigma_c$. This means that, the number of bound integrins at the steady state $\mathbf{S}^*$ are incapable of supporting the imposed stress, causing integrins within the NA to catastrophically unbind and the NA-area to revert to the unbound steady state $\tilde{A}^*$ in region 3 (Fig. 2.6A) and to $A = 0$ in region 2 (Fig. 2.6A).

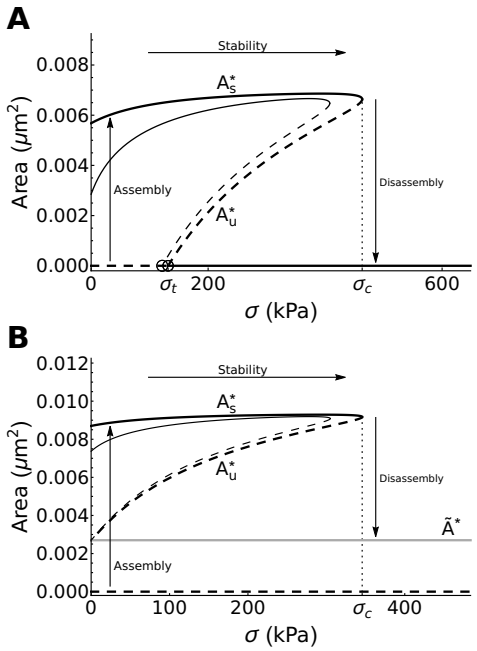

Figure 2.6: The effects of integrin mechanosensitivity on NA-area and integrin content. Bifurcation diagram of adhesion area with respect to stress as determined by (A) region 2, and (B) region 3, showing a bistable-switch with two semi-plateaued stable branches of steady states (solid lines), one of which is elevated representing A_s^* (black), while the other is lower representing $\tilde{A}^*$ (grey), separated by an unstable branch of saddle points A_u^* (short-dashed black line). A_s^* and A_u^* merge at a threshold determined by a saddle-node bifurcation point at $\sigma = \sigma_c$. Beyond this critical stress σ_c, all integrins rapidly unbind and adhesions disassemble to (A) the unclustered steady state or (B) the unbound steady state $\tilde{A}^*$. In region 2 (panel A), the unstable branch undergoes a transcritical bifurcation at $\sigma = \sigma_t$ (open circles), producing a region of monostability where adhesions may directly assemble to the stable branch. Thick lines: $[\text{Ligand}] = 8050\,\mu\text{m}^{-2}$; thin lines: $[\text{Ligand}] = 2012.5\,\mu\text{m}^{-2}$.

This type of behavior corresponds to NA-disassembly. On the other hand, in region 3 with $\sigma < \sigma_c$, stochastic fluctuations in the number of integrins inside the adhesion plaque can cause the system to jump from the unbound steady states $\tilde{A}^*$ to the clustered steady states A_s^*. In contrast to the previous jump, this type of behavior corresponds to NA-assembly. Alternatively, in the monostable regime of region 2 (see dashed horizontal line in Fig. 2.6A), there is no barrier to cross for assembly and NAs may form in a noise-independent manner. Interestingly, in both regions, the model predicts that the stable NA-area A_s^* does not vary significantly for a whole range of stress between $[0, \sigma_c]$, due to the plateau nature of the upper stable branch. This suggests that NAs may go through a cycle of adhesion

assembly/stability/disassembly based on the magnitude of stress exerted on them as previously seen experimentally [17, 49].

We have also investigated the effects of reduced ligand concentration on the mechanosensitivity of adhesions, by reducing the value of [Ligand] 4-fold (see thin lines in Fig. 2.6). Here we observe two notable differences in the model outcomes. Firstly, when ligand concentration is reduced the area of NAs under zero force (e.g. $\sigma = 0$) is reduced while the maximal value it attains remains roughly the same. This suggests that NAs, in these conditions, can exhibit significant reinforcement due to force, increasing in size upon application of force. This reinforcement is similar to what has been previously observed experimentally [77] and in other theoretical models of focal adhesions [35, 47] as well as clusters of catch bonds [46]. Secondly, we also find that the critical stress σ_c decreases when ligand concentration is reduced. This implies that the primary effect of reducing ligand concentration on NAs is to make them more susceptible to forces by (i) making their area more force-dependent and (ii) making them more likely to catastrophically disassemble due to force.

2.3.6 Stochastic simulation of the model

It has been previously shown through stochastic simulations that the upper branches of Fig. 2.6 are metastable equilibria for clusters of catch-bonds with a fixed load, and that upon crossing the lower branch, the cluster undergoes disassembly where all bonds rapidly unbind [46].

By running stochastic simulations with $\sigma \approx \sigma_c$ (see Supporting Material for more details on the implementation), the model also produces NA-disassembly under fixed stress regardless of the region (see Fig. 2.7A for simulations associated with region 3) and for fixed load (results not shown). The stochastic simulation of the model also exhibits NA-assembly from a single integrin-adaptor protein complex (see Fig. 2.7A). In region 2 with $\sigma < \sigma_t$, NA-assembly reaches $\mathbf{S}^*$ unimpeded by $\mathbf{U}^*$, due to lack of bistability for $0 \leqslant \sigma < \sigma_t$, whereas in region 3 (see Figs. 2.6B and 2.7B) the system must cross the stable manifold of $\mathbf{U}^*$. This manifold forms a threshold (highlighted by the dashed line in Fig. 7) that determines if the system jumps from (i) the single integrin-adaptor complex to the clustered steady state $\mathbf{S}^*$ (black solid line in 2.7B) during assembly, passing through the unbound metastable state $\tilde{\mathbf{S}}^*$ (grey line), and from (ii) the clustered steady $\mathbf{S}^*$ (black solid line in Panel B) to the unbound metastable state $\tilde{\mathbf{S}}^*$ (grey line) during disassembly. The mechanical conditions which allow for a stochastic jump to cross the barrier created by the unstable state were not previously determined [40, 46]. In this study, we

have explored (i) under what conditions noise-driven NA-assembly occurs and (ii) what role bistability plays in this process.

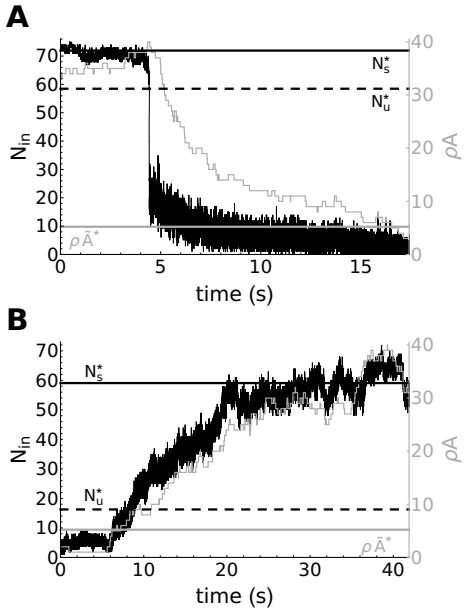

Figure 2.7: The assembly and disassembly of NAs is a force-dependent process. (A,B) Stochastic simulations of the number of bound integrins (thin black lines) and adaptor proteins (thin grey lines) during assembly and disassembly. (A) Under high stress ($\sigma = 0.92\sigma_c$) and starting from the equilibrium $\mathbf{S}^*$ (thick black horizontal line), integrins within NAs undergo catastrophic unbinding upon crossing the stable manifold of the saddle $\mathbf{U}^*$ (dotted black horizontal line), leading to disassembly as they diffuse away from the adhesion area. (B) A long-lived NA state is formed starting from a single integrin-adaptor protein complex when the applied stress is low ($\sigma = 0.25\sigma_c$). This process is driven primarily by plaque growth towards the metastable state with $A = \tilde{A}^*$ (thick grey horizontal line) which, in conjunction with ligand binding, increases N_{in}, the number of integrins inside the NA until it crosses the stable manifold of the saddle point $\mathbf{U}^*$). Beyond the stable manifold of $\mathbf{U}^*$, the trajectory flows to the stable steady state $\mathbf{S}^*$. Black horizontal lines are identical to those in A.

In order to verify if the model under fixed adhesion load produces results consistent with those previously seen [27, 28, 33, 46], we also performed stochastic simulations starting from a single integrin-adaptor protein complex, where adhesion load is held fixed. In this scenario, assembly is only observed for very small fixed loads (less than $\sim$1% of the critical load), as the force per integrin of small adhesions with a fixed load overwhelmingly favors the unbinding of integrin (data not shown). This is in agreement with the previous finding that fixed loads can only lead to adhesion disassembly [40, 46].

Interestingly, with the model presented here, we do observe assembly for fixed stresses arbitrarily close to the critical stress σ_c, albeit exceedingly rare. This highlights the unique nature of the model, identifying fixed stress as a mechanical condition allowing for NA-assembly, and predicting that cells can occasionally assemble NAs even at very high stresses.

The bistability characterizing this model also plays an important role in reaching the elevated steady state $\mathbf{S}^*$. Near the initial condition of a single integrin-adaptor protein complex, diffusion stochastically adds and removes integrins from underneath the adhesion plaque. However, as can be seen in Fig. 2.7A, these stochastic fluctuations do not bring the system close enough to the saddle point $\mathbf{U}^*$ (dotted line) to cross its stable manifold. The metastable state $\tilde{\mathbf{S}}^*$, on the other hand, acts as an attractor for the system, initiating the first phase of a robust growth in the adhesion plaque. In conjunction with ligand binding, this eventually pushes the system past the stable manifold of the saddle $\mathbf{U}^*$, allowing it to reliably reach the elevated stable steady state $\mathbf{S}^*$. As highlighted before, because fixed stress (but not fixed load) is permissive to ligand binding during the growth phase, we may conclude that the mechanical constraint on the system and the bistability with the metastable attractor $\tilde{\mathbf{S}}^*$ allows for the system to overcome the kinetic barrier created by the unstable steady state $\mathbf{U}^*$ such that adhesions may form from a single integrin-adaptor protein complex.

2.4 Discussion

In this study, we presented a biophysical model of NA formation as a condensed phase of adaptor proteins and integrins that forms along at the interface of the cytoplasm and the cell membrane due to a mechanism we term co-aggregation. From this biophysical model, we constructed a 3-dimensional minimal mathematical model of adhesion dynamics near-equilibrium, and a computational framework for realizing discrete simulations of adhesion formation. The nonlinearities included in the mathematical model were adapted from the biophysical framework used to describe NAs. The near-equilibrium dynamics used to analyze the stability of the equilibria showed that adhesions form, with an area and integrin content specified by $\mathbf{S}^*$, once either integrins, adaptor proteins, or extracellular ligands cross a well-defined density threshold. These thresholds are defined by transcritical bifurcation points where a stable branch of clustered steady states emerges in each case. We analytically determined the dependence of these thresholds on model parameters as specified by Eqs. (S11)-(S13). Our analysis of these results revealed that the stable branch plateaus at high integrin or ligand density, but monotonically

increases with respect to adaptor protein density, suggesting that adaptor proteins play a key role in regulating the size of NAs. It also showed that there is a hierarchy in the relative importance of the three protein densities regulating NA-area, given by adaptor proteins>integrins>extracellular ligands. The dependence of $\mathbf{S}^*$ on biophysical parameters was then analyzed to demonstrate that the immobilization of integrins upon binding to ligands inside the adhesion area (controlled by K_{bind}) lowers the density thresholds for adhesion formation.

In contrast to previous models of adhesions [31–33,35], we did not assume that the average density of integrins inside the adhesion plaque is a fixed quantity. This assumption is necessary for the model to be consistent with the observation that the integrin density measured in adhesions varies significantly within the same cell [78], and is motivated by the nonlinear relation between NA-area and its integrin content (see Fig. 2.2). Our model accounted for the variable density of integrins, by considering their interactions with adaptor proteins forming the adhesion plaque which spatially delimits the adhesion area. Similar interactions have also been considered in a more biophysically detailed model of adhesion dynamics [37], but the simplicity of the model presented here compared to this previous study allowed for further theoretical analysis of this system. Interestingly, it was previously estimated that the upper limit of N_{in}/A is $\sim 25,000\ \mu\text{m}^{-2}$ using structural considerations [17], but the results of our Conditional Expectation Analysis suggests that the effective limit of integrin density in the adhesion may be as low as $\sim 17,000\ \mu\text{m}^{-2}$. Below this threshold, NA-area may be a result of the tethering mechanism described by Eq. (S7), whereas above this threshold, adhesion area was the result of integrin crowding, which may be indicative of NAs transitioning to more mature classes of adhesions such as focal complexes. To the best of the authors' knowledge, the tethering mechanism proposed here represents a novel understanding of adhesion stabilization by integrins.

Due to the apparent isotropic growth of NAs [49], we have not considered anisotropic effects of compression/stretching on adaptor protein adsorption as has been done in other models [31, 32]. This can be justified by the fact that the dynamic nature of adaptor-cytoskeletal interactions leads to slippage under force [79], producing a viscoelastic mechanical response, where the effects of elasticity is lost on long timescales (e.g., at equilibrium). Furthermore, it was previously argued that the interactions between adaptor proteins are unlikely to be strong enough for the energy of deformation of the adhesion plaque to have a significant effect on the outcome of the adhesion formation process [35]. This assumption allowed us to use a simpler model of adaptor protein adsorption [29] and incorporate the effects of force in a manner that can be directly linked to experimental single-molecule observations [41].

2.4 Discussion

The mechanosensitive properties of integrin unbinding were included in the model as a force-dependent bond lifetime (see Eq. (S14)). Using this to determine integrin binding affinity, we managed to compute the equilibrium area of the adhesion as a function of applied force, revealing a saddle-node bifurcation at a critical value of stress (see Fig. 2.6D). Beyond this value of stress, all the integrins in the adhesion rapidly become unbound from their ligands and tension is no longer transmitted to the extracellular environment. Similar phenomena had been previously observed in other studies for fixed values of adhesion load [27, 28, 46]. By considering the effects of integrin content on the area of the adhesion plaque, we were able to use adhesion stress rather than load as a bifurcation parameter and study how its steady state effects may give rise to a mechanically-regulated NA life-cycle. We demonstrated that such a life-cycle is governed by a bistable switch with a saddle-node bifurcation when NA-area is plotted against fixed stress. The saddle node acts as a threshold for adhesion disassembly, the last phase of the life-cycle. Increasing the ligand concentration made the upper branch of the bistable switch more plateaued, such that increasing/decreasing the stress within a given range has little to no effect on NA-area.

Consistent with previous studies, stochastic realizations of our model with high values of stress (or load; results not shown) produced NA-disassembly close to the threshold determined by the saddle-node bifurcation, causing the trajectory to jump from the upper to the lower stable branch of the bistable switch. The jump is either due to crossing the threshold or to stochastic effects pushing trajectories beyond the stable manifold of the saddle points in the middle branch, leading to the rapid unbinding of all integrins in the adhesion, followed by slow adhesion plaque disassembly.

The process of adhesion plaque assembly, initiated from a single integrin-adaptor complex, was found to have a more diverse set of dynamics than disassembly. First, we discovered that, unlike during disassembly, the accumulation of bound integrins inside the adhesion area and the growth of the adhesion plaque occurs on a similar timescale during assembly. Second we identified a region in parameter space (region 2 in Fig. 2.5B and Fig. 2.6A with $\sigma < \sigma_t$) where assembly occurs independently of stochastic effects. This finding is noteworthy as previous models had reported, in their mean-field analysis, the presence of an unstable steady state which blocks the assembly of very small adhesions [40, 46]. The mean-field analyses were performed using a one-variable setting where the only way to reach the state corresponding to stable adhesions is through stochastic jump effects that were not very well understood. The mean-field analysis performed here was done in a three-variable setting where it was possible to shift the position of the unstable state to a non-physical regime, and

thus minimizing its interference with the flow of trajectories towards the upper stable steady state.

The difference in outcomes between this study and previous ones can also be attributed to the mechanical condition we considered in this study (fixed stress). This may be understood intuitively by the fact that, when stress is fixed, a small adhesion will have a correspondingly small load. However, when load is fixed [27, 28, 33, 46], the integrin bonds break too quickly for the equilibrium with area A^* to be readily attained. In previous models of clustered bonds, there was no explicit adhesion area, and therefore adhesion stress could not be defined in these models [27, 28, 33, 46]. In this study, we resolved this by considering the adsorption dynamics of the adaptor proteins which form the adhesion plaque [29]. Experimentally, NA formation and area were found to be independent of traction force, while they disassemble in a force-dependent manner [17]. These findings are consistent with our model predictions under fixed stress (but not fixed load), showing that NAs assemble to a roughly constant area for a wide range of stresses and disassemble at high stresses.

Similar to previous studies, the model also showed that there is a regime in parameter space within which the stable manifold of the saddle points acts as a barrier that can be crossed with stochastic effects (see region 3 in Fig. 2.5B and Fig. 2.6B). Within this regime, we demonstrated that fixing adhesion stress (but not load) allows for the assembly of adhesions, and that bistability between the elevated steady state $\mathbf{S}^*$ and the metastable state $\tilde{\mathbf{S}}^*$ plays a significant role in determining the dynamics of assembly in this region of parameter space. When we fixed the value of load (rather than stress), we found that assembly is exceedingly rare for non-zero values of load ($> 1\%$ the critical load; results not shown).

As suggested above, the mechanical control of the NA life-cycle, including assembly, stability and disassembly may be explained by a bistable-switch (possessing a hysteresis) with respect to adhesion stress and that this stress, rather than the total adhesion load, is the mechanical parameter conserved during noise-driven NA-assembly. As stress increases, NA-area may increase (causing adhesion reinforcement) when extracellular ligand density is low or remain relatively constant when it is high. Once stress becomes large enough, NA-disassembly can be initiated either by stochastic effects driving the system beyond a threshold corresponding to the stable manifold of saddle points in the middle branch of the bistable switch or an excess build-up of force pushing the system beyond the saddle-node of this switch.

Increasing the complexity of the model presented here by considering different types of adaptor

proteins forming the adhesion plaque to examine their effects on dynamics represents an interesting direction to pursue. This could be also combined with studying the effect of actin branching and bundling on NA dynamics. The latter, although very technically challenging, can provide further insights onto how they may exert force on the adhesion plaque.

Acknowledgments

This work was supported by the Fonds Nature et technologies—Gouvernement du Quebec (http://www.frqnt.gouv.qc.ca/en/accueil) team grant to A.K. L.M. was supported by the NSERC-CREATE in Complex Dynamics Graduate Scholarship. Discussion with Prof. Claire Brown, Department of Physiology—McGill University, greatly benefited the development of this paper.

Author Contributions

L.M. conceived the biophysical model, analyzed it, wrote the code for simulations, and drafted the manuscript. A.K. substantially revised the manuscript, and provided supervision throughout the project.

Competing Interests

The authors declare that they have no competing financial interests.

Corresponding Author

Correspondence and requests for materials should be addressed to AK (email: anmar.khadra@mail.mcgill.ca)

Supporting Citations

References [17, 24, 29, 31, 35, 39, 41, 44, 47, 49–54, 58, 72, 75, 78, 80–102] appear in the Supporting Material.

2.5 Supporting Material

2.5.1 Model Framework

The primary process which results in the formation of a nascent adhesion (NA) is the clustering of integrins [72]. It has been suggested that very small non-specific clusters of integrin spontaneously form even in the absence of ligand binding; however, their size and spatial distributions were inconsistent with that of NAs formed in the presence of ligand binding [17]. Generally speaking, in the presence of ligand, NAs were about twice as large (compared to those generated in the absence of ligand), exhibited high variability in their integrin content, and yet had a relatively restricted distribution in their size [17]. This suggests that (i) there is an intrinsic clustering mechanism for integrins, (ii) ligand binding enhances this clustering mechanism to form NAs, and (iii) the area of the cluster is not directly proportional to its integrin content (i.e., there is a nonlinear relation between NA-area and the number of integrins forming it). Interestingly, it has been observed that integrins exhibit reduced diffusivity within adhesions (defined experimentally by the area underneath an adaptor protein plaque), by at least a factor of three [24]. This decrease was found to be dependent on interactions with adaptor proteins through the cytoplasmic domain of integrins, suggesting that membrane-proximal adaptor proteins may exert a drag force on integrins [24]. Integrins also undergo extended periods of immobilization which further decreases their lateral mobility. The frequency of long-lived immobilization is enhanced inside adhesions and has been found to be dependent on integrin's interaction with both extracellular ligands and adaptor proteins [24,54]. Thus we propose that the NA-area, as defined by the adaptor protein plaque, provides an environment within which integrin lateral mobility is decreased due to both a reduced diffusion coefficient and increased likelihood of binding to extracellular ligand.

Reduced integrin lateral mobility, due to their interactions with the adaptor protein and extracellular ligands plaque, may explain aggregation of integrins into micron-scale clusters. This, however, does not explain the presence of the adhesion plaque. Firstly, its was previously argued, from a theoretical perspective, that adhesion plaques must be self-assembling structures in order to explain the stress-induced growth of adhesions [31]. Meanwhile, the adaptor protein talin and its interaction with integrins have been repeatedly found to be required for the formation of NAs [17,80,81]. These results suggest, that the self-assembly of adhesion plaques requires both integrin and adaptor proteins to be capable of forming complexes with one another. Furthermore, increased extracellular ligand density

(and thus integrin density inside the adhesion) has been shown to increase the residence time of the adaptor protein FAK inside the adhesion plaque [53]. Additionally, the diffusivity of the adaptor protein paxillin shows significant heterogeneity in its value inside a single adhesion plaque, suggesting that paxillin may exist in more than one association state within the adhesion [50–52]. We propose that adaptor proteins form membrane-proximal aggregates around a seed of a small number of integrins, and that subsequent retention of integrins inside the adhesion area (as discussed above) allows for growth of the adhesion plaque due to the decreased mobility of adaptor proteins. This decreased mobility manifests itself in the model as a decrease in the off-rate of adaptor proteins in the presence of integrins. The precise nature of the mechanism which reduces the off-rate will depend on the specific adaptor protein in question. In the model developed herein, we generically describe it as a reversible tethering to the membrane by integrin.

Together, these effects constitute a mechanism for the self-aggregation of cytoplasmic adaptor proteins and integrins, a phenomenon we refer to hereafter as co-aggregation. More specifically, we propose that (i) integrin lateral mobility is modulated locally by the presence of membrane-proximal adaptor proteins, and (ii) adaptor proteins are effectively tethered to the membrane by integrins. In this manner, the presence of a protein of one type increases the probability that a protein of the other type will be present in close proximity. This positive feedback between the two types of proteins would allow them to serve as templates for one another in the formation of membrane-proximal aggregates of adaptor protein (i.e., an adhesion plaque). We incorporate this mechanism into a mathematical model that satisfies the following assumptions (see Fig. 2.1A):

1. Adaptor proteins are modeled as either being in a well-mixed cytosolic bulk phase or in a spatially confined region $\Omega(t) \in \mathbb{R}^2$ which delimits the adhesion. Their density ρ inside NAs (i.e., the domain Ω) is assumed to be uniform. Furthermore, we impose the conservation of matter by assuming that the adaptor protein content of a NA is drawn from a finite reservoir of N_P adaptor proteins, and therefore the number of cytosolic adaptor proteins N_{cyto} is given by

$$N_{cyto} = N_P - \rho A, \tag{S1}$$

where $A := \|\Omega\|$ is the surface area of the adhesion plaque. This means that, as NAs grow very large, they will deplete the cytoplasmic pool of adaptor proteins until an equilibrium between their growth and shrinkage rates is reached. When adaptor proteins are in the adhesion plaque,

they can either be associated with the rest of the adaptor protein scaffold or they may be bound to an integrin receptor where they become reversibly tethered to the membrane. We assume that individual adaptor proteins leave the adhesion at a rate k_{off} and $(1-\delta)\,k_{off}$, where $\delta \in (0,1)$, when they are untethered and tethered to integrin, respectively. This difference in off-rate in the presence of integrins is what leads to the aggregation of adaptor proteins around integrins.

2. We model integrins as 2-dimensional (2D) Brownian particles that diffuse freely outside the adhesion, and exhibit reduced mobility within the adhesion domain Ω. This reduced mobility is implemented through two biophysical mechanisms. In the first, we assume that the diffusion coefficient of integrins is lower when they are underneath the adhesion plaque, i.e.,

$$D\left(x\right) = \begin{cases} D_{in} & x \in \Omega \\ D_{out} & \text{otherwise} \end{cases}, \tag{S2}$$

where $D_{in} \leqslant D_{out}$ are the diffusion coefficients inside and outside the adhesion domain Ω, respectively [24]. In the second, we make the simplifying assumption that only the adhesion environment provides the necessary ingredients for the long-lived immobilization of integrin, which we attribute to ligand binding [24]. Therefore, we assume that integrins inside Ω may bind to an extracellular ligand and become reversibly immobilized with a binding affinity K_{bind}.

2.5.1.1 Spatial Assumptions

We consider a periodic array of adhesions on a square lattice with an inter-adhesion spacing h. This simplifying assumption of periodicity allows us to study the problem on a small $h \times h$ square patch of membrane that is assumed to receive no net flux of matter from adjacent patches (see Fig. 2.1B) because they are all in equilibrium. We further consider that the $h \times h$ square patch contains N_I integrins and sits under the adhesion plaque consisting of N_P adaptor proteins. Integrins are assumed to diffuse in a 2-dimensional plane (i.e., the membrane), and a circular aggregation of adaptor proteins centered at the origin with an area A that delimits the region defining the adhesion plaque (i.e., $\Omega = \left\{(x,y) : \pi\left(x^2+y^2\right) \leqslant A\right\}$).

2.5.1.2 Integrin Reaction-Diffusion Model

In order for the force transmission through an adhesion to the ECM to be effective, its integrins must bind to their extracellular ligands. When bound to their ligand, integrins exhibit a diverse range of mobilities [24, 82, 83]. Generally, we can expect the integrins to have a reduced mobility upon binding to ligand. We consider the extreme case of complete immobilization in order to understand what can be expected at most from the ligand binding process. Within an adhesion, only a certain proportion of integrins are bound to ligand [24, 54, 84]. We denote the total number of integrins inside the adhesion area by N_{in}, while L_{in} and M_{in} denote the number of liganded and mobile integrins, respectively (i.e., $N_{in} = L_{in} + M_{in}$). If we assume that ligand-binding induced immobilization happens only within the adhesion, then the dynamics of M_{in} is given by

$$\dot{L}_{in}(t) = k_{unbind}\left(K_{bind} M_{in} - L_{in}\right) := R_{bind},$$

where k_{unbind} is the unbinding rate of an integrin, and K_{bind} is its binding affinity, given by

$$K_{bind} = \frac{k_{bind}}{k_{unbind}},$$

with k_{bind} denoting the first order binding rate of a single integrin (assuming fixed extracellular ligand density). In order to account for variations in the density of extracellular ligand, denoted [Ligand], we use the expression

$$k_{bind} = \overline{k}_{bind}\,[\text{Ligand}]\,, \tag{S3}$$

where $\overline{k}_{bind}$ is a the second order binding rate.

An unbound integrin is assumed to diffuse freely in the cellular membrane. We use the Fokker-Planck (FP) diffusion equation to describe the spatiotemporal evolution of the unbound integrin density $I(x)$. Such a model has a local flux $j(x)$, given by

$$j(x) = \nabla\left(D(x)\, I(x)\right), \tag{S4}$$

where ∇ is the gradient operator and $D(x)$ is the diffusion coefficient. In situations with inhomogeneous diffusion coefficient, such as Eq. S2, this FP flux equation is more applicable than the more widely used Fick's law [85]. We are interested in the time-invariant (equilibrium) behaviour of the ad-

hesion; we therefore assume zero-flux boundary conditions on the outer edge of the membrane patch. This corresponds to finding a solution where the flux is zero everywhere. For a piecewise constant diffusion coefficient, such a solution is expected to be piecewise constant at equilibrium, given by

$$I(x) = \begin{cases} I_{in} & x \in \Omega \\ I_{out} & \text{otherwise,} \end{cases}$$

where I_{in} (I_{out}) is the density of unbound integrins inside (outside) the adhesion [86]. However, the discontinuity in Eq. S2 leads to to a singular flux at the interface between the adhesion plaque boundary and the rest of the membrane, given by

$$j_0 = (D_{out} I_{out} - D_{in} I_{in})\, \hat{r},$$

where $\hat{r}$ is the radial unit vector [87]. As time tends towards infinity, diffusion smooths out all concentration gradients such that the non-singular portion of the flux in Eq. S4 becomes zero irrespective of the integrin densities in and out of the adhesion. Therefore, near equilibrium, we take the total flux of free integrins into the adhesion due to diffusion to be the integral along the interface of the singular component of the flux

$$J_{in} = \int_0^{2\pi} j_0 \cdot \hat{r} r d\theta = (D_{out} I_{out} - D_{in} I_{in})\, 2\pi r,$$

where r is the radius of the adhesion. We note that $I_{in} = M_{in}/A$ and thus, by imposing conservation of matter, we eliminate the variable I_{out} to obtain the relation $I_{out} = (N_I - N_{in})/(h^2 - A)$. Finally, the rate of change of unbound integrins inside the adhesion is given by the difference between the integrated diffusive flux and the binding reaction rate, i.e.,

$$\dot{M}_{in} = J_{in} - R_{bind}. \tag{S5}$$

We have assumed in the derivation of Eq. (S5) that diffusion reaches its equilibrium within NAs. Although it is often assumed that NAs are far from equilibrium due to their short stability period [35, 39, 47, 49], recent evidence suggests that conditions preventing NA-disassembly produces integrin clusters with very similar properties (in terms of number and size) to those that do disassemble [17].

This indicates that NAs come very close to their equilibrium before disassembling, and motivates the treatment of integrin dynamics near the equilibrium of the diffusion process in this study.

2.5.1.3 Adhesion Plaque Adsorption Model

To capture the kinetics of adaptor protein aggregation into a membrane-proximal plaque, we adapt the "Bulk-on/Bulk-off" model of adsorption [29], where adhesions are assumed to be able to grow (shrink) from any point in its interior by addition (subtraction) of adaptor proteins that are incorporated into the adhesion with a uniform density ρ. Adaptor proteins are assumed to be added to an adhesion at a rate

$$\gamma\left(A\right) = Ak_{on}^{0}P_{out}, \tag{S6}$$

where $P_{out} = \frac{N_{cyto}}{h^2}$ is the density (per unit area) of free adaptor proteins. Furthermore, we consider that integrins inside the adhesion stabilize the adhesion plaque leading to less adaptor proteins leaving the adhesion per unit time. In the model, this is implemented by assuming that adaptor proteins can exist in two states within the adhesion, one which is reversibly tethered to the membrane by integrins and the other loosely associated with adjacent adaptor proteins. Adaptor proteins can leave the adhesion plaque with a rate k_{off} and $\left(1-\delta\right)k_{off}$ for the untethered and tethered states, respectively. Assuming that fast kinetics govern the association of integrins and adaptor proteins within the adhesion, we prescribe a phenomenological Hill-function expression for the off-rate of an adaptor protein, given by

$$\kappa\left(N_{in}/A\right) = k_{off}\left(\left(1-\delta\right) + \delta\frac{b^n}{b^n + \left(N_{in}/A\right)^n}\right), \tag{S7}$$

where N_{in}/A is the total integrin density in the adhesion, k_{off} is the maximal observed degradation rate of the adhesion, δ is the magnitude of the co-aggregation between integrins and adaptor proteins (a value of 0 indicating no co-aggregation while a value of 1 indicating full co-aggregation), n is the degree of cooperativity between integrins for the tethering of adaptor proteins ($n = 1$ indicates no cooperativity while $n > 1$ indicates positive cooperativity), and b is the integrin density needed to tether 50% of adaptor proteins. Based on this, we obtain the following dynamic equation for adhesion area

$$\frac{dA}{dt} = \frac{1}{\rho}\left(\gamma\left(A\right) - A\rho\kappa\left(I_{in}\right)\right) = A\left[\frac{k_{on}^{0}P_{out}}{\rho} - \kappa\left(N_{in}/A\right)\right].$$

2.5.1.4 Geometric Constraints

The complete set of equations governing NA dynamics are given by Eqs. 2.1a-2.1c (see main text). The equilibria of the system lie at the intersection of its nullsurfaces. The plane $A = 0$ is one of the A-nullsurfaces, while

$$L_{in}^{*} = K_{bind} M_{in}^{*} \tag{S8}$$

is the L_{in}-nullsurface, and

$$M_{in}^{*} = \frac{A^{*} C_I K_{in} h^2}{A^{*}\beta + h^2} \tag{S9}$$

is the M_{in}-nullsurface, where $K_{in} = D_{out}/D_{in}$ and $\beta = \big(K_{in}\,(1 + K_{bind}) - 1\big)$. At the intersection of these nullsurfaces, we have the steady state $\mathbf{Z} = (A, M_{in}, L_{in}) = (0, 0, 0)$, representing the unclustered configuration of adhesion proteins (with both adaptor proteins and integrin receptors uniformly distributed in space). The second A-nullsurface (see Eq. 2.2) forms with the other nullsurfaces a steady state where adhesion proteins are co-aggregated into a dense cluster. The conditions which cause the system to switch between the unclustered and the clustered steady states are analyzed in the main text. Nonetheless, from Eq. S9, we can see that $N_{in} \to \infty$ as $C_I \to \infty$ provided that $A \neq 0$. In this limit, integrins have their maximum effect on the aggregation of adaptor proteins, and thus the clustered steady state will reach some maximum area A^{∞}. According to the second term in Eq. 2.1a, this maximum area is given by

$$A^{\infty} := h^2 \left(\frac{C_P}{\rho} - \frac{1 - \delta}{K_{on}} \right), \tag{S10}$$

where $K_{on} = k_{on}^{0}/k_{off}$. The first term in Eq. (S10) is the maximal fractional area the adhesion plaque can attain if all adaptor proteins become stuck to the membrane, while the second term is a correction factor that accounts for the finite binding affinity of adaptor proteins being absorbed into the plaque. This indicates that A^{∞} depends linearly on the adaptor protein density, and remains finite regardless of the integrin density. It is important to consider the geometric assumptions of our model, in order to ensure that its predictions are physically meaningful. By letting $\phi = [(C_P/\rho) - ((1 - \delta)/K_{on})]$, we obtain $A^{\infty} = h^2\phi$. For a circular adhesion lying strictly within a square lattice cell, we must have $\phi \in \big[0, \pi/4\big)$ in order for the results of our model to remain biophysically relevant.

Generally, if we were to formulate this model for some other lattice with a unit cell area A_{max} (e.g., $A_{max} = h^2$ for the square lattice), we can adapt all our results by replacing h^2 with the particular

value of A_{max}. In such a case, the upper bound on ϕ will depend on the geometry of the lattice and the adhesion; however, in general, we will always have $\phi < 1$ as a maximum upper bound. For $\phi \geqslant 1$, our circular adhesions will take up more area than is available for the given lattice, and thus the membrane will be saturated with adhesion plaque on the length scale h. Because ϕ is independent of the lattice geometry, we interpret this upper bound as being set by the biophysical and chemical properties of the proteins involved rather than an artifact of the periodic lattice assumption.

2.5.1.5 Transcritical Bifurcation

The switch between the unclustered $\mathbf{Z} = (0, 0, 0)$ and clustered $\mathbf{S}^* = (A^*, M_{in}^*, L_{in}^*)$ steady states occurs at a transcritical bifurcation point. In what follows, we analyze the stability properties of this steady state. As discussed in the main text, for simplicity we focus on the case $n = 1$. Under these conditions, the Jacobian matrix of the system evaluated at the unclustered steady state has three eigenvalues, two of which are strictly negative and one that can change its sign, given by

$$\lambda_1 = k_{on}^0 \left(\phi - \frac{b\delta}{bK_{on} + \hat{C}_I} \right).$$

Hence, the unclustered steady state is unstable if $\lambda_1 > 0$. A switch in the sign of λ_1 can occur when certain parameters of the model cross a threshold. For the intracellular densities C_I and C_P, these thresholds are given by

$$C_I > C_I^\ddagger := \frac{b\left(\delta - \phi K_{on}\right)}{\phi K_{on} K_{in}\left(1 + K_{bind}\right)} \tag{S11}$$

and

$$C_P > C_P^\ddagger := \frac{\rho\left(b + K_{in}\left(1 + K_{bind}\right) C_I\left(1 - \delta\right)\right)}{K_{on}\left(b + K_{in}\left(1 + K_{bind}\right) C_I\right)} \geqslant 0, \tag{S12}$$

respectively. Moreover, the threshold for the binding affinity K_{bind} is given by

$$K_{bind} > K_{bind}^\ddagger := \frac{b\delta - \phi K_{on}\left(b + C_I K_{in}\right)}{\phi C_I K_{in} K_{on}}$$

which, according to Eq. S3, can produce the following threshold for ligand concentration

$$[\text{Ligand}] > [\text{Ligand}]^\ddagger := \frac{k_{unbind}}{\overline{k}_{bind}} \frac{b\delta - \phi K_{on}\left(b + C_I K_{in}\right)}{\phi C_I K_{in} K_{on}}. \tag{S13}$$

Once the system passes through the transcritical bifurcation, the model gives birth to the clustered steady state $\mathbf{S}^*$ representing a stable adhesion plaque with area A^* that contains $N_{in}^* = M_{in}^* + L_{in}^*$ integrins.

2.5.1.6 Integrin Mechanosensitivity

Integrin mechanosensitivity is thought to arise from mechanically-induced conformational changes. It has been suggested that the mechanical extension and separation of the extracellular legs of integrin receptors results in a long-lived bound state [44, 45]. We incorporate these ideas into our model as a force-dependent ensemble average lifetime $\left\langle \tau\left(f\right)\right\rangle$, where f is the force applied on the integrin. This is modeled using the two-pathway model of bond-dissociation [88], given by

$$\left\langle \tau\left(f\right)\right\rangle = \tau_0 \left(de^{\hat{f}(c+d)} + c\right) \frac{1}{ce^{fd} + de^{\hat{f}(c+d)}e^{-cf}}, \tag{S14}$$

where τ_0 is the bond lifetime with zero applied force, $\hat{f}$ is the force which optimizes the bond lifetime, and $c, d > 0$ are coefficients. These coefficients are determined numerically by first setting

$$d = \frac{c\hat{\tau}}{\tau_0 e^{c\hat{f}} - \hat{\tau}} + \frac{1}{\hat{f}} \times W\left(-\frac{c\hat{f}\tau_0 e^{-\frac{c\hat{f}\hat{\tau}}{\tau_0 e^{c\hat{f}} - \hat{\tau}}}}{\tau_0 e^{c\hat{f}} - \hat{\tau}}\right),$$

where $\hat{\tau} = \left\langle \tau\left(\hat{f}\right)\right\rangle$ is the optimal bond lifetime and $W\left(\cdot\right)$ is the W-Lambert function, followed by varying c in such a way that $\left\langle \tau\left(60\,\text{pN}\right)\right\rangle \approx 0.1\,\text{s}$ (see Fig. 2.8 for profile and Parameter Estimation for numerical values). Finally, this give the numerical expression

$$\left\langle \tau\left(f\right)\right\rangle = \frac{1}{0.666667exp(-0.0876215F) + 6.60165 \times 10^{-8}\exp(0.313789f)} \tag{S15}$$

In order to incorporate the mechanosensitive properties of integrins into our binding model, we set the integrin unbinding rate k_{unbind} to be the reciprocal of $\left\langle \tau\left(f\right)\right\rangle$, the ensemble bond lifetime. This means that

$$K_{bind} = k_{bind}\left\langle \tau\left(f\right)\right\rangle, \tag{S16}$$

(i.e., all bound integrins are assumed to bear an equal load). The numerical value of f is determined by assuming that the NA experiences a fixed stress (force per unit area), given by

$$\sigma = \frac{f L_{in}}{A}. \tag{S17}$$

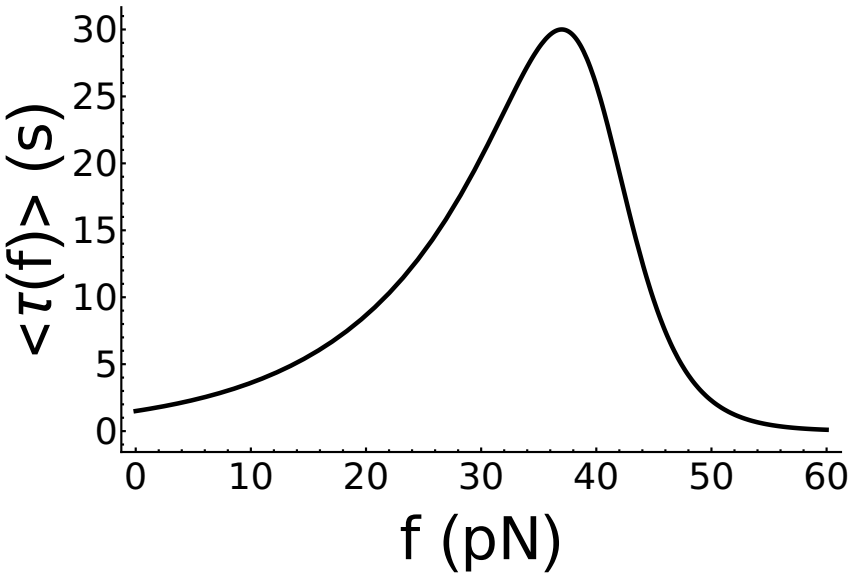

Figure 2.8: Integrin-ligand bond lifetime, $\langle \tau(f) \rangle$, as a function of f, the applied force per integrin. The biphasic profile resembles that obtained for catch bonds between integrin and fibronectin [41].

2.5.1.7 Stochastic Simulations

We note that the integrin flux described by Eq. S5 is only valid for small perturbations around the steady state as it neglects the effects of concentration gradients. In order to more accurately capture the full integrin dynamics specified in Eq. S4 far from equilibrium, we re-formulate our model as a discrete system, where we use a master equation approach to describe the aggregation of adaptor proteins at the adhesion plaque and the reversible binding of integrins within the adhesion region. Furthermore, to account for the diffusion of integrins along the membrane, we use a Brownian dynamics approach where each integrin is given a position $\vec{x}(t)$ that evolves in time according to a Brownian motion with local diffusivity given by Eq. S2, and use the Euler-Maruyama update scheme to obtain the time-dependent positions of integrins [89]. By denoting the number of adaptor proteins in the adhesion

plaque by i, we obtain the following total number of integrins $\nu(t)$ inside a NA of area $A = i/\rho$

$$\nu\left(t\right) = \sum_{k=1}^{N_I} \begin{cases} 1 & \text{if } \pi\vec{x}_k\left(t\right) \cdot \vec{x}_k\left(t\right) \leqslant i/\rho \\ 0 & \text{otherwise,} \end{cases}$$

where $\vec{x}_j\left(t\right)$ is the position of the j^{th} integrin at time t. Setting p_i to be the probability of having a NA with i adaptor proteins, we conclude that the aggregation of adaptor proteins at the adhesion plaque obeys a master equation, given by

$$\rho\dot{p}_i\left(t\right) = \left(g_{i-1}p_{i-1} + s_{i+1}(\nu\left(t\right))p_{i+1}\right) - \left(g_i + s_i(\nu\left(t\right))\right)p_i, \tag{S18}$$

where g_i (s_i) is the growth (shrinkage) reaction-rate, defined by $g_i = \gamma\left(i/\rho\right)$ and $s_i\left(\nu\right) = i\kappa\left(\rho\nu/i\right)$, respectively. Letting ℓ_j be the probability of having j bound integrins inside the adhesion, we obtain the following master equation for binding kinetics of integrin

$$\dot{\ell}_j\left(t\right) = k_{bind}\left(\nu\left(t\right) - (j-1)\right)\ell_{j-1} + (j+1)k_{unbind}\ell_{j+1} - \left(k_{bind}\left(\nu\left(t\right) - j\right) + jk_{unbind}\right)\ell_j. \tag{S19}$$

When integrins become bound, we reversibly set their diffusion coefficient to zero, and set their unbinding rate to $k_{unbind} = \left\langle \tau\left(i\sigma/\rho j\right)\right\rangle^{-1}$. The time-course of the chemical reactions is realized through a temporal Gillespie algorithm, that allows for efficient stochastic simulations of reactions with time-dependent propensities [90]. This is necessary to account for the fact that both reactions have propensities which depend on $\nu\left(t\right)$, and that integrins may diffuse into or out of the adhesion independently of the reactions governed by Eqs. S18 or S19.

2.5.1.8 Parameter Estimation

Model parameter values are inferred, when possible, using algebraic expressions from the model equated to values obtained from experimental measurements. In the main text, we have identified two regions of interest in parameters space, which we have denoted regions 2 & 3. The assumptions inherent in each region leads to slightly different algebraic expressions for model parameters. We begin by discussing the expressions that the two regions have in common, followed by explaining the distinct approaches used in each region.

Firstly, we introduce the relative enrichment of integrins inside the adhesion E, which has been

observed to be in the range of $E \in [2, 12]$ in various physiological conditions [24, 78]. Using the conservation of matter for integrins, we obtain the following expression for their density

$$C_I = \frac{I_{in}\left(A_1 + \left(h^2 - A_1\right)/E\right)}{h^2}, \tag{S20}$$

where I_{in} is the density of integrins inside the adhesion, A_1 is the mean area of NA (to be estimated from experimental measurements), and h is the mean inter-adhesion spacing. The parameter h is determined using

$$\bar{N}^*_{in} \coloneqq \lim_{K_{bind}\to\infty} M^*_{in} + L^*_{in} = C_I h^2$$

which can be combined with Eq. (S20) to yield

$$h = \left(A_1\left(1 - E\right) + E\frac{N_2}{I_{in}}\right)^{1/2}, \tag{S21}$$

where N_2 is the number of integrins in a NA when integrin binding is very strong (also to be determined from experimental measurements). Secondly, an expression for the parameter b can be obtained by solving $I_{in} = N^*_{in}/A^*$, with $N^*_{in} = L^*_{in} + M^*_{in}$, to obtain

$$b = \frac{I_{in}K_{on}\left(-(\beta+1)C_I + \beta\phi I_{in} + I_{in}\right)}{(\beta+1)C_I K_{on} - I_{in}\left(-\beta\delta + \beta\phi K_{on} + K_{on}\right)}, \tag{S22}$$

where the estimation of the parameters K_{on} and K_{in} (implicit in β) must be dealt with differently in the two regions. We may also use the model steady states to derive the expression

$$E = \frac{N^*_{in}/A^*}{\left(N_I - N^*_{in}\right)/\left(h^2 - A^*\right)} = \left(1 + K_{bind}\right)K_{in}$$

which may be rewritten as an expression for the binding affinity, given by

$$K_{bind} = \frac{E}{K_{in}} - 1. \tag{S23}$$

The parameter δ is estimated by considering the ratio of FRAP recovery times of the intermediate and slow fractions of the adaptor protein paxillin and vinculin within focal adhesions [50]. This ratio is

in the range of 20-80, corresponding to a value of $\delta \in [0.95, 0.99]$. We also estimate the value of the mean density of adaptor proteins prior to adhesion formation, C_P, using the literature value of paxillin concentration [paxillin] $\approx 2.3\,\mu$M multiplied by an estimate of cell volume $V_{cell} \approx 1000\,\mu\text{m}^3$ to get the total number of paxillin molecules in the cell $N_{pax} \approx 1.38 \times 10^6$ [58]. We then use the simple approximation $C_P \approx N_{pax}/A_{cell} = 8050\mu\text{m}^{-2}$, where $A_{cell} \approx 172\,\mu\text{m}^2$ is the estimated cell area determined from analysis of imaging data [17], to obtain $C_P \approx 8050\,\mu\text{m}^{-2}$. Finally, the parameters k_{off} and ρ are chosen in such a way that stochastic simulations of adhesion disassembly/assembly have a timescale and stochasticity comparable to that observed experimentally [49], respectively.

Table 2.1: Auxiliary parameter values used in the determination of model parameters (see Table 2.3 for model parameter values).

Symbol	Definition	Estimated Value	Reference(s)
E	Fold-enrichment of integrins within the adhesion	12	[24, 78]
I_{in}	Mean density of integrins within the adhesion	6600 μm^2	[17]
A_1	Mean NA-area	8.7×10^{-3} μm^2	[17]
N_2	Number of integrins inside NAs when Mn^{2+} is added to extracellular medium	75	[17]
[paxillin]	Physiological paxillin concentration	2.3 μM	[58]
V_{cell}	Volume of a mouse embryonic fibroblast (MEF) cell	1000 μm^3	-
A_{cell}	Area of a MEF cell	172 μm^2	[17]
N_3	Number of integrins inside NAs in the absence of extracellular ligands	6	[17]
A_3	Mean NA-area in the absence of extracellular ligands	2.7×10^{-3} μm^2	[17]
$\langle\tau\,(0\,\text{pN})\rangle$	Ensemble average of integrin-ligand bond lifetime in the absence of force	1.5 s	[41]
$\langle\tau(\hat{f})\rangle$	Ensemble average of the optimal integrin-ligand bond lifetime	30 s	[91]
$\hat{f}$	The force that optimizes bond lifetime	37 pN	[41]
$\langle\tau\,(60\,\text{pN})\rangle$	Ensemble average of the integrin-ligand bond at very large forces	0.1 s	[41]

Region 3 From a super-resolution quantification of adhesion size and integrin content [17], we can obtain the following estimates $I_{in} \approx 6600$ μm^{-2} and $A_1 \in [7, 9] \times 10^{-3}\,\mu m^2$. The integrin clusters produced by the same study [17], upon exposing cells to Mn^{+2} (which switches integrins into a high-affinity state), can be used to obtain the estimate $N_2 \approx 75$. Using Eq. (S21), with $E \approx 12$ (i.e., by assuming that NAs are among the most enriched in integrins) and $A_1 \approx 8.7 \times 10^{-3}\,\mu m^2$, we obtain $h \approx 0.2\,\mu m$. This estimate is further verified visually by analyzing the spacing between NAs in images [17]. Furthermore, region 3 is differentiated from region 2 by the fact that it produces adhesions

even in the absence of ligand binding. Experimentally, in the absence of ligand, it was found that small clusters of integrin containing $N_3 \in [4, 19]$ integrins form with an area $A_3 \in [1, 4.4] \times 10^{-3} \mu m^2$ [17]. We use these quantifications to aid us in our parameter estimation by setting them equal to appropriate model steady states, i.e., by letting

$$N_3 = \tilde{M}_{in}^* + \tilde{L}_{in}^* \tag{S24}$$

and

$$A_3 = \tilde{A}^*. \tag{S25}$$

These two expressions are then used in conjunction with Eqs. (S20), (S22), and (S23) to yield

$$K_{in} = \frac{N_3 \left(\left(A_1(E-1) + A_3 \right) I_{in} - EN_2 \right)}{A_3 \left(N_3 - N_2 \right) I_{in}} \approx 1.2, \tag{S26}$$

$$K_{on} = \frac{\delta \left(\frac{EN_2}{I_{in}} - A_1(E-1) \right) \left(A_3 \left(A_1 - A^\infty \right) I_{in} + N_3 \left(A^\infty - A_3 \right) \right)}{\left(A^\infty - A_1 \right) \left(A^\infty - A_3 \right) \left(N_3 - A_3 I_{in} \right)} \approx 0.70, \tag{S27}$$

$$K_{bind} = \frac{\left(A_1 - A_3 \right) (E-1) N_3 I_{in} + EN_2 \left(A_3 I_{in} - N_3 \right)}{N_3 \left(EN_2 - \left(A_1(E-1) + A_3 \right) I_{in} \right)} \approx 8.8, \tag{S28}$$

and

$$b = \frac{A_3 I_{in} \left(A^\infty - A_1 \right) + N_3 \left(A_3 - A^\infty \right)}{\left(A_1 - A_3 \right) A_3}, \tag{S29}$$

where we have used $\delta \approx 0.97$, $A_2 \approx 2.7 \times 10^{-3}$ μm^2, and $N_3 \approx 6$ (b remains to be determined). The parameter A^∞ is determined from data. More specifically, using the *maximum a posteriori* (MAP) estimate of the relation between adhesion area and its integrin content (see dotted line in Fig. 2.2). This data is fit to the A-nullcline given by Eq. (2.2) using a nonlinear least squares approach and taking Eq. (S29) into consideration . The values of the fit parameters and their 95% confidence bounds are provided in Table 2.2. The confidence interval on the quantities b and A_0 are relatively large, indicating that they are not well constrained by the data at hand. Nonetheless, these confidence intervals do not contain zero and only cover one order of magnitude, so we deem them to be acceptable. This completes model parameter estimation in Region 3 necessary to generate quantitative understanding of the model developed in this study.

Table 2.2: Least-squares estimates of model parameters and confidence intervals obtained from a nonlinear least squares fitting of the A-nullcline to data.

Symbol	Least-Squares Estimate	95% Confidence Interval
A^∞	$0.0124\,\mu\text{m}^2$	$[0.0118, 0.0129]\ \mu\text{m}^2$
b	$463\,\mu\text{m}^{-2}$	$[68.8, 806]\ \mu\text{m}^{-2}$
A_0	-0.038	$[-.0204, -0.239]\ \mu\text{m}^2$

Region 2 Region 2 ($[\text{Ligand}]^\ddagger > 0$) can be distinguished from region 3 ($[\text{Ligand}]^\ddagger < 0$) by the fact that NAs will not form in the absence of ligand. As discussed in the main text, the transition from region 2 to region 3 may be achieved by decreasing K_{on}. We therefore keep the numerical values of all other parameters determined in region 3 as is, and use a different formalism for determining K_{on}. More precisely, we use Eqs. (S13), (S20), and (S21) to obtain

$$K_{on} = \frac{b\delta\left(EN_2 - A_1(E-1)I_{in}\right)^2}{A^\infty I_{in}\left(N_2\left(bE + I_{in}K_{in}\left([Ligand]^\ddagger \frac{\bar{k}_{bind}}{k_{unbind}} + 1\right)\right) - A_1 b(E-1)I_{in}\right)}, \tag{S30}$$

where we have used previous experimental finding to estimate $[\text{Ligand}]^\ddagger \approx 200\mu m^{-2}$, and the ratio $\bar{k}_{bind}/k_{unbind} = 0.005$ was chosen such that the equilibrium of NA-area $A^* \approx A^\infty$ for ligand densities given by $[\text{Ligand}] \geqslant 10,000\,\mu\text{m}^{-2}$ (see Fig. 2.3 in main text) as suggested by the spreading behaviour of cells when cultured on substrates with variable ligand density [75, 92]

Mechanosensitivity of Integrin The coefficients in Eq. S14 are determined based on atomic force microscopy data on the bond lifetime of integrins [41,91]. More specifically, we have $\langle\tau\,(0\,\text{pN})\rangle = 1.5$ s, $\langle\tau\rangle$ has a maximum at 37 pN, $\langle\tau\,(37\,\text{pN})\rangle = 30$ s, and $\langle\tau\,(60\,\text{pN})\rangle = 0.1$ s. Using these values, the coefficients $d \approx 0.32$ and $c \approx 0.088$ that appear in Eq. (S14) are determined (as discussed before) algebraically and by numerical optimization, respectively.

2.5.2 Conditional Expectation Analysis

2.5.2.1 Introduction

In numerous scientific applications, quantitative measurements of a system near a quasi-equilibrium are made and then analyzed. Rather than providing a precise description of a system, we may assume that it can be (at least partially) described by a set of measurements (e.g., a population may be described by the body temperature of its individuals, or a macro-molecular complex may be described by its mass and charge). Let us consider the simple experimental scenario in which measurements of two quantities of interest X and Y are made. These may represent the same quantity in two different conditions or two different quantities in the same condition. If there is a relation between the two measurements X and Y due to the intrinsic interactions of the system under study, one may attempt to derive this relation from experimental data. However, this task is complicated by the presence of stochastic fluctuations, measurement error, heterogeneity between realizations, and large data sets. With this in mind, let us consider a pair of correlated random variables (X, Y) measured simultaneously from a dynamical system near a unique equilibrium $\left(\bar{X}, \bar{Y}\right)$ using a homoscedastic model

$$(X, Y) = \left(\bar{X}, \bar{Y}\right) + (\chi, \gamma),$$

where χ (along with γ) is an independent identically distributed additive noise. If both quantities X and Y have an effect on the dynamics of the physical system being observed, the equilibrium $\bar{Y}$ can be expressed as

$$\bar{Y} = f\left(\bar{X}\right). \tag{S31}$$

Given samples of (X, Y), collected under a variety of experimental conditions, it may not be straightforward to estimate $f(\cdot)$ if the values of the corresponding $\left(\bar{X}, \bar{Y}\right)$ cannot be readily determined. This situation may arise when studying phenomena at the sub-cellular level, due to high levels of both intracellular and inter-cellular heterogeneity present even when the experimental conditions are fixed. In order to circumvent this difficulty, we employ the probability distributions of X and Y instead. Assuming that χ (γ) is independent of $\bar{X}$ ($\bar{Y}$), we can compute the observed probability density of X

(Y) as

$$\begin{aligned} P_X &= P_{\bar{X}} * P_\chi, \\ P_Y &= P_{\bar{Y}} * P_\gamma, \end{aligned}$$

where $*$ denotes the convolution operator. Assuming that f is a monotonic function, the the probability distribution of $\bar{Y}$ is related to that of $\bar{X}$ by the *change of variable equation,* given by

$$P_{\bar{Y}}(f) = P\left(\bar{Y} = y \,|\, f\right) = \frac{P_{\bar{X}}(x)}{\left|f'(x)\right|}, \tag{S32}$$

where f' is the derivative of f and x is the pre-image of y (i.e., $x = f^{-1}(y)$).

Experimentally, one may repeatedly measure both X and Y and approximate the marginal distributions P_X and P_Y by binning data to make the histograms $\mathbf{P_X}$ and $\mathbf{P_Y}$, respectively. In what follows, we will explain a methodology for determining f from these histograms.

2.5.3 Relation to Previous Work

The task of deducing a transformation $f(\cdot)$ from data is central to numerous machine learning techniques. However, these techniques differ in their motivation from the data analysis task we have presented above. For example, in the unsupervised learning methods of density estimation and manifold learning/unfolding the transformation f is used to more efficiently represent data in a so-called representation space, which is useful when dealing with very high dimensional data [93–96]. Such methods assume that P_X is unknown and use well known parametric distributions as a prior on X in their inference of f. Such approaches are inappropriate for our needs as they ignore the data $\mathbf{P_X}$, and thus it is unlikely that the inferred f would satisfy Eq. (S32). Alternatively, Gaussian Process models and Generalized Additive Models have both been used in supervised learning tasks to infer relationships between experimentally measured variables X and Y [97–99]. However, these approaches require pairing of the data into coordinates (X, Y), which may not always be possible. On the other hand, our approach requires only knowing the marginal distributions $\mathbf{P_X}$ and $\mathbf{P_Y}$ which may be readily estimated from unpaired (or paired) samples of X and Y. Moreover, a great deal of the algorithmic complexity seen in the literature is motivated by issues which arise in high-dimensions [100], while our data is intrinsically one-dimensional.

2.5.3.1 Overview of the Algorithm

Given the experimentally determined discrete estimates $\mathbf{P_X}$ and $\mathbf{P_Y}$, we propose decomposing the problem of estimating f into two steps:

1. Finding a maximum a posteriori (MAP) discrete estimates of $P_{\bar{X}}$ and P_χ, which we denote $\hat{\mathbf{P}}_{\bar{\mathbf{X}}}$ and $\hat{\mathbf{P}}_\chi$, respectively. This may can be accomplished using the blind deconvolution algorithm [101]. We note that it is also possible to do the same for $P_{\bar{Y}}$ and P_γ, but without the mapping f (or f^{-1}) it is unclear whether these estimates satisfy Eq. (S32).
2. We estimate f and P_γ by solving the minimization problem

$$\begin{cases} \min_{f,P_\gamma} & \mathrm{KL}\left(P_{\bar{Y}}\left(f\right) * P_\gamma \,|P_Y\right) + \lambda \mathrm{BV}\left(P_{\bar{Y}}\left(f\right)\right) \\ \text{subject to} & f' > 0,\ P_\gamma \geqslant 0\ \left\|P_\gamma\right\| = 1, \left\|\gamma P_\gamma\right\| = 0, \end{cases} \tag{S33}$$

where $\mathrm{KL}\left(p\,|q\right) = \int_{-\infty}^{\infty} p\left(x\right) \log\left(p\left(x\right)/q\left(x\right)\right) dx$ is the Kullback-Leibler Divergence, $P_{\bar{Y}}\left(f\right)$ is given by Eq. (S32), λ is a non-negative parameter, and $\mathrm{BV}\left(u\right) = \left\|u'\left(x\right)\right\|_2$ is a Tikhonov regularization term [102] which limits the irregularity of the estimate $P_{\bar{Y}}$. Here we have formally restricted our optimization to monotonically increasing functions ($f' > 0$), but we may also consider monotonically decreasing functions by substituting in the constraint $f' < 0$.

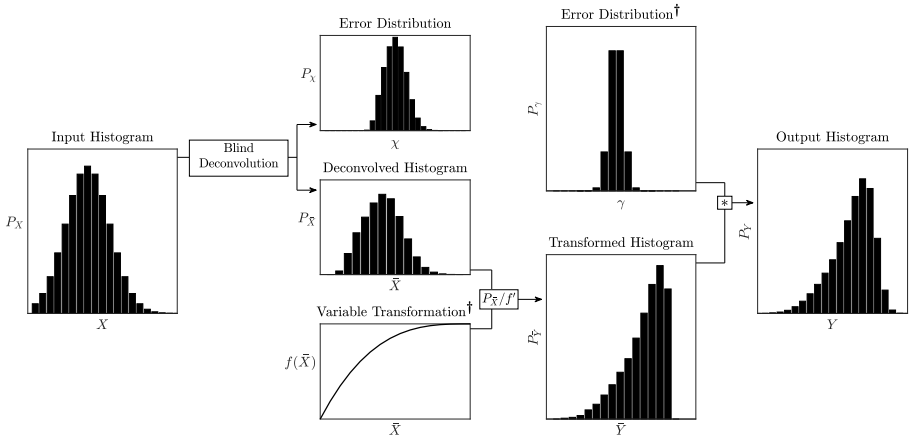

Figure 2.9: Schematic overview of the computational approach used to estimate P_Y given P_X, $f(\bar{X})$, and P_γ. The quantities that we seek to infer ($f(\bar{X})$ and P_γ) are marked with †.

2.5.3.2 Parametrization

Generally speaking, Bayesian inference methods, such as Markov Chain Monte Carlo (MCMC) techniques, produce samples of parameters θ, some of which may be used to estimate f. In this section, we detail our approach for reconstructing f from a given set of parameters θ. In the following section, we detail how to compare the experimental data $\mathbf{P_Y}$ to the model prediction $P_Y(\theta) = P_{\bar{Y}}\left(f(x)|\theta\right) * P_\gamma(\theta)$ in order to produce appropriate samples of θ.

A priori, we do not know what form the (possibly nonlinear) function f has, and thus we will assume only that it is continuous almost everywhere. Furthermore, from the problem specification (S33), the only constraint on the probability density P_γ is that it must have zero mean, which is too weak of a constraint to justify using any specific parametric family of distributions. Therefore, we reconstruct both functions in a non-parametric manner. That is, f and P_γ are treated as discrete sets of values to be inferred using MCMC.

Let us denote the discrete ordered list of sample points for the histograms (i.e., bin centers) by

$$\mathbf{x} = [x_1, x_2, \ldots, x_M]$$

and

$$\mathbf{y} = \left[y_1, y_2, \ldots, y_Q\right]$$

such that $\mathbf{P_X} = P\left(X \in [\mathbf{x}, \mathbf{x} + dx]\right)$ and $\mathbf{P_Y} = P\left(Y \in [\mathbf{y}, \mathbf{y} + dy]\right)$. We aim to choose the parametrization of the function f in order to maximize the robustness of our computational approach. In order to do this, we take into account two intrinsic properties of our optimization problem. First, equation (S32) indicates that it is critical to know the derivative of f at the discrete values $\mathbf{x}$. Therefore, we choose to parametrize f primarily by its derivative rather than its value, which also allows for a straightforward means of constraining f to be a monotonic function as required by (S33). With an initial value f_1 for the function f, we may reconstruct f from its derivative using the fundamental theorem of calculus: $f(x) = f_1 + \int_{x_1}^{x} f'(s)\, ds$. Second, we aim to use the same parametrization for the entire class of monotonic functions, including both monotonically increasing and decreasing functions, that can be distinguished by the sign of $f_M - f_1$. In order to achieve both of these goals, we numerically reconstruct the discrete values of the function f from normalized samples of its derivative $\mathbf{f}'$, defined by $\boldsymbol{\phi} := \mathbf{f}' / (f_M - f_1)$, where imposing $\boldsymbol{\phi} \geqslant 0$ guarantees monotonicity. Using this parametrization, f

can be reconstructed using the formula $\mathbf{f}(\mathbf{x}) \coloneqq \mathbf{f}\left(\mathbf{x}\,|f_1, f_M, \boldsymbol{\phi}\right) = f_1 + (f_M - f_1)\left[S_{\{1,\ldots,M\}}(\boldsymbol{\phi})\right]$, where

$$S_j\left(\mathbf{f}'\right) = \begin{cases} 0 & j = 1 \\ \sum_{i=1}^{j-1} \frac{f'_i + f'_{i+1}}{2}\left(x_{i+1} - x_i\right) & \text{otherwise} \end{cases}$$

is a trapezoidal approximation to the cumulative integral of f from x_1 to x_j. Furthermore, we may also compute the probability densities at $\bar{Y} = \mathbf{f}(\mathbf{x})$ using

$$\mathbf{P}_{\bar{\mathbf{Y}}}(\theta) \coloneqq \mathbf{P}\left(\bar{Y} = \mathbf{f}(\mathbf{x})\,|\theta\right) = \hat{\mathbf{P}}_{\bar{\mathbf{X}}}(\mathbf{x}) \oslash \left|(f_M - f_1)\,\boldsymbol{\phi}\right|,$$

where $\oslash$ denotes Hadamard division or the element-wise division of two vectors.

2.5.3.3 Bayesian Inference of the Transformation

In order to asses the validity of a given $(2 + M + Q)$-dimensional set of estimated parameters $\theta = [f_1, f_M, \boldsymbol{\phi}, \mathbf{P}_\gamma]$, we need to compare the discrete set of experimental measurements $\mathbf{P}_{\mathbf{Y}}(\mathbf{y})$ with the estimated $\mathbf{P}\left(Y = \mathbf{f}(x)\,|\theta\right) \coloneqq \left(\mathbf{P}_{\bar{Y}} * \mathbf{P}_\gamma\right)$, a problem that is generally complicated by the fact that $\mathbf{y} \neq \mathbf{f}(\mathbf{x})$. To resolve this issue, we introduce an interpolant, given by

$$\tilde{P}_Y\left(y\,|\theta\right) = \begin{cases} \rho_i + \frac{\rho_{i+1} - \rho_i}{f_{i+1} - f_i}\left(y - f_i\right) & \text{if } \exists\ i : f_i < y \leqslant f_{i+1} \\ 0 & \text{otherwise} \end{cases},$$

where $\rho = \mathbf{P}_{\mathbf{Y}}\left(\mathbf{f}(\mathbf{x})\,|\theta\right)$, allowing us to create a data-fidelity function for a given θ, given by

$$\Delta P(\theta) = \mathrm{KL}\left(\tilde{P}_Y\left(\mathbf{y}\,|\theta\right)|\mathbf{P}_{\mathbf{Y}}\right).$$

Therefore, to solve problem (S33), we use the Gibbs sampler to sample θ from the posterior

$$\pi\left(\theta\,|\mathbf{P}_{\mathbf{Y}}\right) \propto \mathcal{L}\left(\mathbf{P}_{\mathbf{Y}}|\theta\right) Pr(\theta),$$

where $\mathcal{L}\left(\mathbf{P}_{\mathbf{Y}}|\theta\right) = \exp\left[-\left(\Delta P(\theta) + \lambda BV\left(\mathbf{P}_{\bar{Y}}(\theta)\right)\right)\right]$ and $Pr(\theta)$ are the likelihood and prior densities of θ, respectively. Given the MAP estimate $\hat{\theta} = \left[\hat{f}_1, \hat{\mathbf{f}}', \hat{\mathbf{P}}_\gamma\right]$, we may readily obtain a MAP

estimate of $\mathbf{f}$, using the formula

$$\hat{\mathbf{f}} = \mathbf{f}\left(\mathbf{x}\,\middle|\,\hat{f}_1, \hat{\mathbf{f}}'\right).$$

2.5 Supporting Material

Table 2.3: Model parameter values used in the numerical simulations. Parameter values are obtained either directly from the literature or estimated analytically using model-derived equations as indicated in columns labelled source. Parameter values and sources which are different in region 3 are in parentheses.

Symbol	Definition	Value Region 2 (Region 3)	Source Region 2 (Region 3)
δ	Fractional decrease in adaptor protein off-rate (k_{off}) when tethered by integrin.	0.97	Ref. [50]
b	Integrin density inside adhesion which tethers 50% of adaptor proteins	463 μm^{-2}	Eq. (S29)
C_I	Mean density of integrins in the membrane	1844 μm^{-2}	Eq. (S20) ’
h	Mean distance between adhesions	0.20 μm	Eq. (S21)
K_{in}	D_{out}/D_{in}	1.22	Eq. (S26)
D_{out}	Diffusion coefficient of integrin outside the adhesion	0.28 μm^{2}s^{-1}	Refs. [24, 54]
D_{in}	Diffusion coefficient of integrin inside the adhesion	0.22 μm^{2}s^{-1}	$K_{in} = \frac{D_{out}}{D_{in}}$
K_{on}	Affinity of adaptor protein adsorption reaction in the absence of integrins	0.29 (0.7)	Eq. (S30) (Eq. (S27))
k_{off}	Adaptor protein off-rate in the absence of integrins	1.0 s^{-1}	-
k^0_{on}	Kinetic parameter governing on-rate for adsorption of adaptor proteins into the adhesion plaque[††]	0.31 s^{-1} (0.73 s^{-1})	$K_{on} = \frac{k^0_{on}}{k_{off}}$
ρ	Density of adaptor proteins in the adhesion plaque	4000 μm^{-2}	-
ϕ	Maximum fractional area of a NA	0.30	Least-Squares
C_P	Basal density of adaptor proteins in the cytosol	8050 μm^{-2}	Ref. [58]
K_{bind}	Binding affinity of single integrins	8.81	Eq. (S28)
k_{bind}	Binding rate of single integrins ($= \overline{k}_{bind}$[Ligand])	2.58 s^{-1}	$k_{bind} = \frac{K_{bind}}{\langle \tau(0\,\mathrm{pN}) \rangle}$

[††] In order to obtain an estimate of the first order reaction rate for a bi-molecular adaptor protein binding event, we can use Eq. (S6) with $A = \rho^{-1}$ and $P_{out} = C_P$. This yields binding rate estimates of 0.62 s^{-1} and 1.5 s^{-1} in regions 2 and 3, respectively.

Bibliography

[1] Peter Friedl and Darren Gilmour. Collective cell migration in morphogenesis, regeneration and cancer. *Nature Reviews Molecular Cell Biology*, 10:445–457, 7 2009. 0.1, 0.1.1, 1.1, 2.1

[2] Andrew D Luster, Ronen Alon, and Ulrich H von Andrian. Immune cell migration in inflammation: present and future therapeutic targets. *Nature Immunology*, 6:1182–1190, 12 2005. 0.1, 1.1, 2.1

[3] Li Li, Yong He, Min Zhao, and Jianxin Jiang. Collective cell migration: Implications for wound healing and cancer invasion. *Burns & Trauma*, 1(1):21–26, 2013. 1.1, 2.1

[4] Andrew G Clark and Danijela Matic Vignjevic. Modes of cancer cell invasion and the role of the microenvironment. *Current Opinion in Cell Biology*, 36:13–22, 10 2015. 2.1

[5] C M Lo, H B Wang, M Dembo, and Y L Wang. Cell movement is guided by the rigidity of the substrate. *Biophysical journal*, 79:144–152, 2000. 1.1, 2.1

[6] Peter Devreotes and Chris Janetopoulos. Eukaryotic chemotaxis: distinctions between directional sensing and polarization. *The Journal of biological chemistry*, 278:20445–20448, 2003. 1.1, 2.1

[7] Yoichiro Mori, Alexandra Jilkine, and Leah Edelstein-Keshet. Wave-pinning and cell polarity from a bistable reaction-diffusion system. *Biophysical Journal*, 94:3684–3697, 5 2008. 0.1.3, 1.12, 2.1, 3.1, 3.3, 3.5.2, 3.6.0.1, 4.1

[8] Benjamin Lin, William R Holmes, C Joanne Wang, Tasuku Ueno, Andrew Harwell, Leah Edelstein-Keshet, Takanari Inoue, and Andre Levchenko. Synthetic spatially graded rac acti-

vation drives cell polarization and movement. *Proceedings of the National Academy of Sciences of the United States of America*, 109:E3668——77, 12 2012. 2.1, 2.3.5.1, 4.1

[9] J Thomas Parsons, Alan Rick Horwitz, and Martin A Schwartz. Cell adhesion: integrating cytoskeletal dynamics and cellular tension. *Nature reviews. Molecular cell biology*, 11:633–643, 2010. 0.1.1, 2.1

[10] Clarence E Chan and David J Odde. Traction dynamics of filopodia on compliant substrates. *Science*, 322:1687–1691, 2008. 2.1

[11] Elizabeth M Morse, Nina N Brahme, and David A Calderwood. Integrin cytoplasmic tail interactions. *Biochemistry*, 53:810–820, 2 2014. 2.1

[12] S Liu, D A Calderwood, and M H Ginsberg. Integrin cytoplasmic domain-binding proteins. *Journal of cell science*, 113 (Pt 2:3563–3571, 10 2000. 2.1

[13] Ronen Zaidel-Bar, Shalev Itzkovitz, Avi Ma'ayan, Ravi Iyengar, and Benjamin Geiger. Functional atlas of the integrin adhesome. *Nature cell biology*, 9:858–867, 8 2007. 0.1, 1.1, 1.2.1, 2.1, 3.1

[14] Herbert B Schiller and Reinhard Fässler. Mechanosensitivity and compositional dynamics of cell-matrix adhesions. *EMBO reports*, 14:509–519, 6 2013. 2.1

[15] Edward R. Horton, Adam Byron, Janet A. Askari, Daniel H. J. Ng, Angélique Millon-Frémillon, Joseph Robertson, Ewa J. Koper, Nikki R. Paul, Stacey Warwood, David Knight, Jonathan D. Humphries, and Martin J. Humphries. Definition of a consensus integrin adhesome and its dynamics during adhesion complex assembly and disassembly. *Nature cell biology*, 17(12):1577–1587, 12 2015. 0.1, 2.1

[16] M A Smith, L M Hoffman, and M C Beckerle. Lim proteins in actin cytoskeleton mechanoresponse. *Trends in Cell Biology*, 24:575–583, 10 2014. 2.1

[17] Rishita Changede, Xiaochun Xu, Felix Margadant, Michael P Sheetz, D R Critchley, A Ravasio, Z Chen, Y H Wang, K Kawauchi, and Et Al. Nascent integrin adhesions form on all matrix rigidities after integrin activation. *Developmental Cell*, 35:614–621, 2015. 0.1.1, 1.6, 1.12, 2.1, 2.2.3, 2.3.1, 2.2, 2.3.1, 2.3.3, 2.3.5.2, 2.4, 2.5.1, 2.5.1.2, 2.5.1.8, 2.1, 2.5.1.8

[18] Rishita Changede, Haogang Cai, Shalom Wind, and Michael P Sheetz. Ligand geometry controls adhesion formation via integrin clustering. *bioRxiv*, page 435826, 2018. 0.1, 1.6, 2.1, 2.3.1

[19] Dennis F Kucik, Michael L Dustin, Jim M Miller, and Eric J Brown. Adhesion-activating phorbol ester increases the mobility of leukocyte integrin lfa-1 in cultured lymphocytes. *Journal of Clinical Investigation*, 97:2139–2144, 5 1996. 1.1, 2.1

[20] Dennis F Kucik. Rearrangement of integrins in avidity regulation by leukocytes. *Immunologic Research*, 26:199–206, 2002. 2.1

[21] Noritaka Nishida, Can Xie, Motomu Shimaoka, Yifan Cheng, Thomas Walz, and Timothy A. Springer. Activation of leukocyte $\beta 2$ integrins by conversion from bent to extended conformations. *Immunity*, 25(4):583–594, 10 2006. 1.3, 2.1

[22] Bing-Hao Luo, Christopher V Carman, and Timothy A Springer. Structural basis of integrin regulation and signaling. *Annual review of immunology*, 25:619–647, 2007. 1.3, 1.3.1, 1.12, 2.1

[23] Tao Yu, Xing Wu, Kiran B Gupta, and Dennis F Kucik. Affinity, lateral mobility, and clustering contribute independently to β_2-integrin-mediated adhesion. *American Journal of Physiology-Cell Physiology*, 299:C399——C410, 2010. 2.1

[24] Olivier Rossier, Vivien Octeau, Jean-Baptiste Sibarita, Cécile Leduc, Béatrice Tessier, Deepak Nair, Volker Gatterdam, Olivier Destaing, Corinne Albigès-Rizo, Robert Tampé, Laurent Cognet, Daniel Choquet, Brahim Lounis, and Grégory Giannone. Integrins $\beta 1$ and $\beta 3$ exhibit distinct dynamic nanoscale organizations inside focal adhesions. *Nature Cell Biology*, 14(10):1057–1067, sep 2012. 1.2.1, 1.6, 2.1, O3, 2.2.3, 2.4, 2.5.1, 2.5.1, 2.5.1.2, 2.5.1.8, 2.1, 2.3, 5, 5

[25] Erik S Welf and Jason M Haugh. Signaling pathways that control cell migration: models and analysis. *Wiley interdisciplinary reviews. Systems biology and medicine*, 3:231–240, 2011. 2.1

[26] Yvette Van Kooyk, Sandra J Van Vliet, and Carl G Figdor. The actin cytoskeleton regulates lfa-1 ligand binding through avidity rather than affinity changes. *Journal of Biological Chemistry*, 274:26869–26877, 1999. 2.1

[27] Thorsten Erdmann and Ulrich S Schwarz. Stochastic dynamics of adhesion clusters under shared constant force and with rebinding. *Journal of Chemical Physics*, 121:8997–9017, 11 2004. 1.10, 1.11, 1.12, 2.1, 2.3.5.1, 2.3.5.1, 2.3.6, 2.4, 5

[28] Ulrich S Schwarz, Thorsten Erdmann, and Ilka B Bischofs. Focal adhesions as mechanosensors: The two-spring model. *BioSystems*, 83:225–232, 2 2006. 1.6, 1.10, 1.11, 1.12, 2.1, 2.3.5.1, 2.3.5.1, 2.3.6, 2.4

[29] Nir S Gov. Modeling the size distribution of focal adhesions. *Biophysical journal*, 91:2844–2847, 2006. 1.7, 1.12, 2.1, M2, 2.3.3, 2.4, 2.5.1.3

[30] Murat Cirit, Matej Krajcovic, Colin K Choi, Erik S Welf, Alan F Horwitz, and Jason M Haugh. Stochastic model of integrin-mediated signaling and adhesion dynamics at the leading edges of migrating cells. *PLoS Computational Biology*, 6:e1000688, 2010. 2.1

[31] Alice Nicolas and Samuel A Safran. Limitation of cell adhesion by the elasticity of the extracellular matrix. *Biophysical Journal*, 91:61–73, 2006. 1.2.1, 1.8, 1.10, 1.13.4, 2.1, 2.3.1, 2.3.5, 2.4, 2.5.1, 5

[32] Achim Besser and Samuel A Safran. Force-induced adsorption and anisotropic growth of focal adhesions. *Biophysical Journal*, 90:3469–3484, 2006. 1.2.1, 1.8, 1.8, 1.11, 1.13.4, 2.1, 2.3.1, 2.4, 5

[33] Benedikt Sabass and Ulrich S Schwarz. Modeling cytoskeletal flow over adhesion sites: Competition between stochastic bond dynamics and intracellular relaxation. *Journal of Physics Condensed Matter*, 22:194112, 5 2010. 2.1, 2.3.1, 2.3.6, 2.4, 5

[34] Tong Zhao, Ying Li, and Aaron R Dinner. How focal adhesion size depends on integrin affinity. *Langmuir*, 25:1540–1546, 2 2009. 2.1

[35] Joseph E Olberding, Michael D Thouless, Ellen M Arruda, and Krishna Garikipati. The non-equilibrium thermodynamics and kinetics of focal adhesion dynamics. *PLoS ONE*, 5:e12043, 2010. 1.8, 1.11, 1.12, 2.1, 2.3.1, 2.3.5, 2.3.5.2, 2.4, 2.5.1.2, 5

[36] Erik S Welf, Ulhas P Naik, and Babatunde A Ogunnaike. A spatial model for integrin clustering as a result of feedback between integrin activation and integrin binding. *Biophysical Journal*, 103:1379–1389, 9 2012. 2.1

[37] Zhanghan Wu, Sergey V Plotnikov, Abdiwahab Y Moalim, Clare M Waterman, and Jian Liu. Two distinct actin networks mediate traction oscillations to confer focal adhesion mechanosensing. *Biophysical Journal*, 112:780–794, 2 2017. 1.12, 2.1, 2.4

[38] Xuan Cao, Yuan Lin, Tristian P Driscoll, Janusz Franco-Barraza, Edna Cukierman, Robert L Mauck, and Vivek B Shenoy. A chemomechanical model of matrix and nuclear rigidity regulation of focal adhesion size. *Biophysical journal*, 109:1807–1817, 11 2015. 2.1

[39] Xuan Cao, Ehsan Ban, Brendon M Baker, Yuan Lin, Jason A Burdick, Christopher S Chen, and Vivek B Shenoy. Multiscale model predicts increasing focal adhesion size with decreasing stiffness in fibrous matrices. *Proceedings of the National Academy of Sciences of the United States of America*, 114:E4549——E4555, 2017. 1.8, 1.12, 2.1, 2.4, 2.5.1.2

[40] Sam Walcott, Dong-Hwee Kim, Denis Wirtz, and Sean X Sun. Nucleation and decay initiation are the stiffness-sensitive phases of focal adhesion maturation. *Biophysical journal*, 101:2919–2928, 12 2011. 1.11, 1.12, 2.1, 2.3.5.1, 2.3.6, 2.3.6, 2.4

[41] Fang Kong, Andrés J. García, A. Paul Mould, Martin J. Humphries, and Cheng Zhu. Demonstration of catch bonds between an integrin and its ligand. *The Journal of cell biology*, 185(7):1275–1284, 6 2009. 1.3.2, 1.3.2, 1.12, 2.1, O5, 2.2.3, 2.4, 2.8, 2.1, 2.5.1.8

[42] George I Bell. Models for the specific adhesion of cells to cells, 5 1978. 1.3.2, 1.6, 1.12, 2.1

[43] Yuriy V Pereverzev, Oleg V Prezhdo, and Evgeni V Sokurenko. Allosteric role of the large-scale domain opening in biological catch-binding. *Physical Review E*, 79:51913, 5 2009. 1.3.2, 2.1

[44] Zhenhai Li, Fang Kong, and Cheng Zhu. A model for cyclic mechanical reinforcement. *Scientific Reports*, 6:35954, 12 2016. 0.1, 1.3.1, 1.3.2, 1.2, 1.12, 2.1, 2.4, 2.5.1.6, 5

[45] Jing Li and Timothy A. Springer. Integrin extension enables ultrasensitive regulation by cytoskeletal force. *Proceedings of the National Academy of Sciences*, 114(18):4685–4690, apr 2017. 1.3.1, 1.3.1, 1.9, 1.12, 2.1, 2.5.1.6, 4.6

[46] Elizaveta A Novikova and Cornelis Storm. Contractile fibers and catch-bond clusters: A biological force sensor? *Biophysical Journal*, 105:1336–1345, 9 2013. 1.3.2, 1.6, 1.6, 1.10, 1.11, 1.12, 2.1, 2.3.5, 2.3.5.1, 2.3.5.1, 2.3.5.2, 2.3.6, 2.3.6, 2.4, 5, 5

[47] A. Nicolas, B. Geiger, and S. A. Safran. Cell mechanosensitivity controls the anisotropy of focal adhesions. *Proceedings of the National Academy of Sciences*, 101(34):12520–12525, aug 2004. 1.2.1, 1.8, 1.8, 1.10, 1.12, 1.4, 2.1, O1, 2.3.5.2, 2.4, 2.5.1.2

[48] Cheng han Yu, Jaslyn Bee Khuan Law, Mona Suryana, Hong Yee Low, and Michael P Sheetz. Early integrin binding to arg-gly-asp peptide activates actin polymerization and contractile movement that stimulates outward translocation. *Proceedings of the National Academy of Sciences of the United States of America*, 108:20585–20590, 2011. 2.1

[49] Colin K Choi, Miguel Vicente-Manzanares, Jessica Zareno, Leanna A Whitmore, Alex Mogilner, and Alan Rick Horwitz. Actin and alpha-actinin orchestrate the assembly and maturation of nascent adhesions in a myosin ii motor-independent manner. *Nature cell biology*, 10:1039–1050, 9 2008. 0.1.1, 1.1, 1.2.1, 1.2.2, 1.7, 1.8, 1.11, O1, M2, 2.2.3, 2.3.5.2, 2.4, 2.5.1.2, 2.5.1.8, 3.1, 4.6.1, 4.6.4, 5

[50] Haguy Wolfenson, Ariel Lubelski, Tamar Regev, Joseph Klafter, Yoav I Henis, and Benjamin Geiger. A role for the juxtamembrane cytoplasm in the molecular dynamics of focal adhesions. *PLoS ONE*, 4:e4304, 2009. 1.1, 1.7, O2, 2.2.3, 2.4, 2.5.1, 2.5.1.8, 2.3

[51] Michelle A Digman, Claire M Brown, Alan R Horwitz, William W Mantulin, and Enrico Gratton. Paxillin dynamics measured during adhesion assembly and disassembly by correlation spectroscopy. *Biophysical journal*, 94:2819–2831, 4 2008. 1.1, 1.2.2, 1.7, 1.12, O2, 2.4, 2.5.1

[52] Chi Li Chiu, Jose S Aguilar, Connie Y Tsai, Gui Kai Wu, Enrico Gratton, and Michelle A Digman. Nanoimaging of focal adhesion dynamics in 3d. *PLoS ONE*, 9:e99896, 2014. 1.7, O2, 2.4, 2.5.1

[53] S E Le Devedec, B Geverts, H de Bont, K Yan, F J Verbeek, A B Houtsmuller, and B van de Water. The residence time of focal adhesion kinase (fak) and paxillin at focal adhesions in renal epithelial cells is determined by adhesion size, strength and life cycle status. *Journal of Cell Science*, 125:4498–4506, 2012. O2, 2.4, 2.5.1

[54] Taka A Tsunoyama, Yusuke Watanabe, Junri Goto, Kazuma Naito, Rinshi S Kasai, Kenichi G N Suzuki, Takahiro K Fujiwara, and Akihiro Kusumi. Super-long single-molecule tracking reveals dynamic-anchorage-induced integrin function. *Nature Chemical Biology*, 14:497–506, 5 2018. 1.1, 1.2.1, 1.6, O4, 2.2.3, 2.4, 2.5.1, 2.5.1.2, 2.3, 5, 5

[55] Claire M Brown, Benedict Hebert, David L Kolin, Jessica Zareno, Leanna Whitmore, Alan Rick Horwitz, and Paul W Wiseman. Probing the integrin-actin linkage using high-resolution protein velocity mapping. *Journal of cell science*, 119:5204–5214, 12 2006. 0.1.1, 1.1, M2

[56] Antonina Y Alexandrova, Katya Arnold, Sébastien Schaub, Jury M Vasiliev, Jean-Jacques Meister, Alexander D Bershadsky, and Alexander B Verkhovsky. Comparative dynamics of retrograde actin flow and focal adhesions: Formation of nascent adhesions triggers transition from fast to slow flow. *PLoS ONE*, 3:e3234, 2008. M2, 4.6.1

[57] Stephanie L Gupton, Kathryn Eisenmann, Arthur S Alberts, Clare M Waterman-Storer, and C M Waterman-Storer. mdia2 regulates actin and focal adhesion dynamics and organization in the lamella for efficient epithelial cell migration. *Journal of cell science*, 120:3475–3487, 2007. M2

[58] Kaixi Tang, Colton G. Boudreau, Claire M. Brown, and Anmar Khadra. Paxillin phosphorylation at serine 273 and its effects on rac, rho and adhesion dynamics. *PLOS Computational Biology*, 14(7):e1006303, jul 2018. (document), 0.1, 0.1.2, 1.1, 1.12, 2.2.3, 2.3.5.1, 2.4, 2.5.1.8, 2.1, 2.3, 3.1, 3.3.1, 3.3.1, 3.3.2, 3.3.2, 3.4, 3.4.1, 3.6.0.2, 3.7, 3.10, 5, 5, 5, 5, 5

[59] E J Doedel, R C Paffenroth, A R Champneys, T F Fairgrieve, Yu. A Kuznetsov, B Sandstede, and X Wang. Auto-07p: Continuation and bifurcation software for ordinary differential equations, 2007. 2.2.4, 3.2.4, 4.3

[60] Laurent MacKay and Anmar Khadra. Data from: Dynamics of mechanosensitive nascent adhesion formation. anmar khadra repository 2019. deposited 30 july 2019., 2019. 2.2.4

[61] Paul W Wiseman, Claire M Brown, Donna J Webb, Benedict Hebert, Natalie L Johnson, Jeff A Squier, Mark H Ellisman, and A F Horwitz. Spatial mapping of integrin interactions and dynamics during cell migration by image correlation microscopy. *Journal of Cell Science*, 117, 2004. 1.2.1, 1.6, 1.11, 2.3.1, 3.1

[62] D S Goodsell. Integrin, 2011. 2.3.1

[63] Timothy A Springer, Jianghai Zhu, and Tsan Xiao. Structural basis for distinctive recognition of fibrinogen γc peptide by the platelet integrin $\alpha_{IIb}\beta_3$. *The Journal of Cell Biology*, 182:791–800, 2008. 2.3.1

[64] Jianghai Zhu, Bing-Hao Luo, Tsan Xiao, Chengzhong Zhang, Noritaka Nishida, and Timothy A Springer. Structure of a complete integrin ectodomain in a physiologic resting state and activation and deactivation by applied forces. *Molecular Cell*, 32:849–861, 12 2008. 2.3.1

[65] Tong-Lay Lau, Chungho Kim, Mark H Ginsberg, and Tobias S Ulmer. The structure of the integrin αiibβ3 transmembrane complex explains integrin transmembrane signalling. *The EMBO Journal*, 28:1351–1361, 5 2009. 2.3.1

[66] Kate L Wegener, Anthony W Partridge, Jaewon Han, Andrew R Pickford, Robert C Liddington, Mark H Ginsberg, and Iain D Campbell. Structural basis of integrin activation by talin. *Cell*, 128:171–182, 1 2007. 2.3.1

[67] Kevin J Hamill, Sho Hiroyasu, Zachary T Colburn, Rosa V Ventrella, Susan B Hopkinson, Omar Skalli, and Jonathan C R Jones. Alpha actinin-1 regulates cell-matrix adhesion organization in keratinocytes: Consequences for skin cell motility. *Journal of Investigative Dermatology*, 135:1043–1052, 2015. 2.3.3

[68] Dong Hwee Kim and Denis Wirtz. Focal adhesion size uniquely predicts cell migration. *FASEB Journal*, 27:1351–1361, 4 2013. 2.3.3

[69] Christine Lawson, Ssang-Taek Lim, Sean Uryu, Xiao Lei Chen, David A Calderwood, and David D Schlaepfer. Fak promotes recruitment of talin to nascent adhesions to control cell motility. *The Journal of cell biology*, 196:223–232, 1 2012. 2.3.3

[70] Marco A Velasco-Velázquez, Nohemí Salinas-Jazmín, Nicandro Mendoza-Patiño, and Juan J Mandoki. Reduced paxillin expression contributes to the antimetastatic effect of 4-hydroxycoumarin on b16-f10 melanoma cells. *Cancer Cell International*, 8(1):8, 2008. 2.3.3

[71] Margit Hagel, Elizabeth George, Ann Kim, Rulla Tamimi, Sarah Opitz, Christopher Turner, Akira Imamoto, and Sheila Thomas. The adaptor protein paxillin is essential for normal development in the mouse and is a critical transducer of fibronectin signaling. *Mol. Cell. Biol.*, 22:901–915, 2002. 2.3.3

[72] Rishita Changede and Michael Sheetz. Integrin and cadherin clusters: A robust way to organize adhesions for cell mechanics. *BioEssays*, 39:e201600123, 1 2017. 2.3.4, 2.4, 2.5.1

[73] Marco Arnold, Elisabetta Ada Cavalcanti-Adam, Roman Glass, Jacques Blümmel, Wolfgang Eck, Martin Kantlehner, Horst Kessler, and Joachim P Spatz. Activation of integrin function by nanopatterned adhesive interfaces. *ChemPhysChem*, 5:383–388, 2004. 2.3.4

[74] Elisabetta A Cavalcanti-Adam, Alexandre Micoulet, Jacques Blümmel, Jörg Auernheimer, Horst Kessler, and Joachim P Spatz. Lateral spacing of integrin ligands influences cell spreading and focal adhesion assembly. *European Journal of Cell Biology*, 85:219–224, 4 2006. 2.3.4

[75] Mark Schvartzman, Matteo Palma, Julia Sable, Justin Abramson, Xian Hu, Michael P Sheetz, and Shalom J Wind. Nanolithographic control of the spatial organization of cellular adhesion receptors at the single-molecule level. *Nano Letters*, 11:1306–1312, 3 2011. 2.3.4, 2.4, 2.5.1.8

[76] Alexandre Saez, Axel Buguin, Pascal Silberzan, and Benoît Ladoux. Is the mechanical activity of epithelial cells controlled by deformations or forces? *Biophysical Journal*, 89:L52——4, 2005. 2.3.5

[77] P. Roca-Cusachs, A. del Rio, E. Puklin-Faucher, N. C. Gauthier, N. Biais, and M. P. Sheetz. Integrin-dependent force transmission to the extracellular matrix by α-actinin triggers adhesion maturation. *Proceedings of the National Academy of Sciences*, 110(15):E1361–E1370, mar 2013. 1.1, 1.2.2, 1.6, 2.3.5.2

[78] C Ballestrem, B Hinz, B A Imhof, and B Wehrle-Haller. Marching at the front and dragging behind: differential alphavbeta3-integrin turnover regulates focal adhesion behavior. *The Journal of cell biology*, 155:1319–1332, 2001. 0.1.1, 1.2.2, 1.11, 2.4, 2.5.1.8, 2.1, 5

[79] Ke Hu, Lin Ji, Kathryn T Applegate, Gaudenz Danuser, and Clare M Waterman-Storer. Differential transmission of actin motion within focal adhesions. *Science (New York, N.Y.)*, 315:111–115, 1 2007. 2.4

[80] Frederic Lagarrigue, Praju Vikas Anekal, Ho-Sup Lee, Alexia I Bachir, Jailal N Ablack, Alan F Horwitz, and Mark H Ginsberg. A riam/lamellipodin–talin–integrin complex forms the tip of sticky fingers that guide cell migration. *Nature Communications*, 6:8492, 9 2015. 2.4, 2.5.1

[81] Caroline Cluzel, Frédéric Saltel, Jost Lussi, Frédérique Paulhe, Beat A Imhof, and Bernhard Wehrle-Haller. The mechanisms and dynamics of αvβ3 integrin clustering in living cells. *Journal of Cell Biology*, 171:383–392, 10 2005. 2.4, 2.5.1

[82] Yvonne Aratyn-Schaus and Margaret L Gardel. Transient frictional slip between integrin and the ecm in focal adhesions under myosin ii tension. *Current biology : CB*, 20:1145–1153, 2010. 2.4, 2.5.1.2

[83] D P Felsenfeld, D Choquet, and M P Sheetz. Ligand binding regulates the directed movement of 1 integrins on fibroblasts. *Nature*, 383:438–440, 10 1996. 2.4, 2.5.1.2

[84] Alice C Chang, Armen H Mekhdjian, Masatoshi Morimatsu, Aleksandra Kirillovna Denisin, Beth L Pruitt, and Alexander R Dunn. Single molecule force measurements in living cells reveal a minimally tensioned integrin state. *ACS Nano*, 10:10745–10752, 12 2016. 1.3.1, 2.4, 2.5.1.2

[85] B Ph Van Milligen, P D Bons, B A Carreras, and R Śnchez. On the applicability of fick's law to diffusion in inhomogeneous systems. *European Journal of Physics*, 26:913–925, 2005. 2.4, 2.5.1.2

[86] P F Tupper and Xin Yang. A paradox of state-dependent diffusion and how to resolve it. *Proceedings of the Royal Society A: Mathematical, Physical and Engineering Sciences*, 468:3864–3881, 2012. 2.4, 2.5.1.2

[87] R L Stratonovich. Fokker-planck equation with discontinuous coefficients and conditions at the surface of discontinuity. *Soviet Radiophysics*, 8:500–505, 1965. 2.4, 2.5.1.2

[88] Yuriy V Pereverzev, Eugenia Prezhdo, and Evgeni V Sokurenko. The two-pathway model of the biological catch-bond as a limit of the allosteric model. *Biophysical journal*, 101:2026–2036, 2011. 1.3.2, 2.4, 2.5.1.6

[89] Peter E Kloeden and Eckhard. Platen. *Numerical solution of stochastic differential equations*. Springer-Verlag, 1992. 2.4, 2.5.1.7

[90] Christian L Vestergaard and Mathieu Génois. Temporal gillespie algorithm: Fast simulation of contagion processes on time-varying networks. *PLoS Computational Biology*, 11:e1004579, 10 2015. 2.4, 2.5.1.7

[91] Fang Kong, Zhenhai Li, William M. Parks, David W. Dumbauld, Andrés J. García, A. Paul Mould, Martin J. Humphries, and Cheng Zhu. Cyclic mechanical reinforcement of integrin–ligand interactions. *Molecular Cell*, 49(6):1060–1068, mar 2013. 1.3.1, 1.3.2, 2.4, 2.1, 2.5.1.8

[92] Elisabetta Ada Cavalcanti-Adam, Tova Volberg, Alexandre Micoulet, Horst Kessler, Benjamin Geiger, and Joachim Pius Spatz. Cell spreading and focal adhesion dynamics are regulated by spacing of integrin ligands. *Biophysical journal*, 92:2964–2974, 2007. 2.4, 2.5.1.8

[93] Diederik P Kingma and Max Welling. Auto-encoding variational bayes. 2.4, 2.5.3

[94] Oren Rippel and Ryan Prescott Adams. High-dimensional probability estimation with deep density models, 2013. 2.4, 2.5.3

[95] Laurent Dinh, Jascha Sohl-Dickstein, and Samy Bengio. Density estimation using real nvp. *arXiv*, arXiv:1605.08803v3, 2016. 2.4, 2.5.3

[96] Pooyan Khajehpour Tadavani. Nonlinear dimensionality reduction by manifold unfolding. 2.4, 2.5.3

[97] S Roberts, M Osborne, M Ebden, S Reece, N Gibson, and S Aigrain. Gaussian processes for time-series modelling. *Philosophical Transactions of the Royal Society A: Mathematical, Physical and Engineering Sciences*, 371:20110550, 2012. 2.4, 2.5.3

[98] Trevor Hastie and Robert Tibshirani. Generalized additive models for medical research. *Statistical Methods in Medical Research*, 4:187–196, 9 1995. 2.4, 2.5.3

[99] C E Rasmussen and C K I Williams. *Gaussian Processes for Machine Learning*. MIT Press, 1 edition, 2006. 2.4, 2.5.3

[100] Sherjil Ozair and Yoshua Bengio. Deep directed generative autoencoders. 2.4, 2.5.3

[101] Daniele Perrone and Paolo Favaro. A clearer picture of total variation blind deconvolution. *IEEE Transactions on Pattern Analysis and Machine Intelligence*, 38:1041–1055, 6 2016. 2.4, 2.5.3.1

[102] Tikhonov A. N. and Arsenin V. Y. *Solutions of ill-posed problems*. Winston Distributed solely by Halsted Press, Washington New York, 1977. 2.4, 2.5.3.1

Part II

Cellular Motility

Chapter 3

Front-to-Rear Polarization

3.1 Introduction

Thus far, this thesis has focused primarily on the dynamics of integrin-based adhesion complexes that serve as force-transmission points during motility. However, this function can only be carried out if (a) cells actively produce forces and (b) those forces are directed in a manner that will lead to a net movement of the cell. The generation of forces is primarily mediated by (i) actin polymerization against the edge of the membrane (i.e., protrusion) and (ii) the action of molecular motors such as myosin which causes a contraction of the actin cytoskeleton [1]. Cells coordinate these protrusive and contractile processes by having them occur in spatially distinct regions of the cell. This results in the establishment of a cell-front which is protrudes "forward" and a cell-rear which contracts such that it appears to follow the cell-front. Such cells are said to be rear-to-front polarized, which is not to be confused with the electrical polarization of cells. In this chapter we shall discuss a pattern formation mechanism that has been the proposed for spatially segregate contractile and protrusive activity, leading to rear-to-front polarization of the cell and its subsequent movement.

Organization of the actin cytoskeleton into structures that either allow for protrusion via actin polymerization or myosin-driven contraction is regulated by the Rho subfamily of the ras-superfamily of GTPases (RhoGTPases) [2–4]. Here we will focus on the two proteins Rac1 (Rac) and RhoA (Rho), which are associated with protrusion and contraction, respectively. Rac is thought to activate the Arp2/3 complex through the protein WASP [5, 6], where Arp2/3 binds to the side of an actin filament and nucleates a new filament at a angle of $\sim 70^{\circ}$ with respect to the existing one, forming a branched actin network that is characteristic of the leading edge of motile cells [7]. This forms a rigid array of filaments which collectively polymerize and push against the membrane through a Brownian-ratchet mechanism, leading to protrusion of the leading edge of the cell [8–12]. What is more, the polymerization of actin filaments primes integrins receptors for high affinity binding to the extracellular matrix (ECM) [13]. This leads to the formation of molecular complexes known as nascent adhesion [14–16], which further aid in the transmission of the polymerization force to the ECM and the forward protrusion of the cell membrane [17]. The protein Rho, on the other hand, signals to the molecular motor myosin through the serine/threonine kinase Rho-kinase (ROCK) which inhibits the phosphatase activity of Myosin light chain phosphatase (MLCP). This inhibition of MLCP further releases its inhibition of myosin, such that the motor activity of the latter protein increases, leading to the sliding of actin filaments and an overall contraction of the actin cytoskeleton and the cell [18, 19]. Furthermore, this contraction

leads to the reorganization of the actin cytoskeleton into contractile actomyosin stress fibres which contract to produce the forward translocation of the cell body [20, 21], and serve as a template for the formation/maturation of focal adhesions which are necessary for maintaining the spread shape of a migrating cell [22, 23]. Therefore, in general, we may summarize these effects as Rac leading to protrusion of the cell whereas Rho leads to its contraction.

An isotropically protruding and/or contracting cell will not exhibit motile behaviour. Although it may change in shape, the resulting deformations will not lead to a net displacement of the cell. In order for a cell to become motile, there must be directions where protrusion is favoured over contraction and vice-versa. Therefore, motile cells must first become front-to-rear polarized in order to define these directions. Once polarity is established, the protrusive and contractile effects that are downstream of the RhoGTPases can produce motility.

It has long been known that Rac and Rho have a number of opposing downstream effects within the context of motility [24], and that these effects occur in spatially segregated regions of a motile cell [25]. However, the mechanisms behind their spatio-temporal regulation has been somewhat more elusive. Interestingly, fluourescent imaging of motile cells demonstrated that there are spatially segregated regions of constituitively high Rac and Rho activity at the cell front and rear, respectively [26, 27]. It seems likely that these spatially segregated regions may be related to interactions between the two proteins, where many different interaction schemes have been proposed in the literature (see Fig. 3 in [28]). While there have been numerous seemingly contradictory experimental reports on the interactions between Rac and Rho, over time a central theme has emerged: the idea that that Rac and Rho, either directly or indirectly, inhibit the activity of one another [28, 29]. Conceptually, this provides a simplistic framework for understanding the segragated regions of Rac and Rho activity. Due to their intrinsic mutual antagonism, regions of the cell where one has a high activity will correspondingly have a low activity for the other protein and vice-versa. However, this simple idea alone cannot explain how the regions of high and low activity come to be in the first place (i.e., how mutual antagonism leads to cellular polarization). In order to shed light on this phenonmenon, a series of spatio-temporal mathematical models of the interaction between RhoGTPases were developed and their pattern fomation capacity was analyzed by Edelstein-Keshet and collaborators. This body of work has lead to detailed understanding of the requirements for cellular polarization [28, 30–32], shed light on the biochemical networks that allow for a cell to maintain its shape [33–35], and has made a number of novel contributions to the mathematical study of pattern formation [32, 35–37].

Cellular motility is an extremely complex process, with hundreds of regulatory proteins and signalling molecules controlling various aspects of the phenomenon [1,2,38–43]. We have already alluded to two such proteins, Rac and Rho which have many downstream effectors that collaborate across space and time to produce motility. We have also highlighted how some of these effectors regulate adhesion formation, with adhesions being essential for motility in a number of different contexts. Adhesion assembly and disassembly are also complex processes which are regulated by $\sim$150 different proteins as well as the chemical and mechanical environment of the cell [39]. Paxillin is one such protein, and can be considered a "master regulator" of adhesion dynamics (i.e., the rates of assembly and disassembly) [44–46]. In particular, there are specific phosphorylation sites on paxillin which, when phosphorylated, markedly increase the speed at which adhesions assemble and disassemble [47–49]. The mechanisms by which these changes in rate occur are incompletely understood and likely to be complex, where emerging evidence has shed some light on the mechanisms of disasssembly (see Section section §1.2 and Conclusions in Chapter 1) but little is known about the what might regulate assembly dyanmics. Interestingly, some signalling pathways which are downstream of paxillin phosphorylation on its serine 273 can also lead to Rac activation [50]. This suggests that there may be an intrinsic biochemical link between adhesion dyanmics and cellular polarization/motility. In this chapter, we will explore this idea by first describing the mutual antagonism between Rac and Rho, incoporating the influence of paxillin on Rac, and then investigating how the composite system behaves in the context of cellular polarization.

3.2 Methods

3.2.1 Reaction-Diffusion Systems

The models presented in this chapter are mathematical descriptions of systems of molecules undergoing chemical reactions. Therefore, we consider a generic system of m chemical species (i.e., types of molecules), with the j^{th} species denoted by X_j, undergoing M reversible chemical reactions. Using chemical reaction notation, the i^{th} reaction can be expressed as

$$\sum_{j=1}^{m} r_{i,j} X_j \underset{k_i^-}{\overset{k_i^+}{\rightleftharpoons}} \sum_{j=1}^{m} p_{i,j} X_j, \tag{1}$$

where $r_{i,j}$ ($p_{i,j}$) is the stoichiometric coefficient of the j^{th} species as a reactant (product) in the i^{th} reaction, and k_i^+ (k_i^-) is the forward (reverse) rate constant of the reaction. Ignoring any spatial variations on concentration, the dynamics of a species X_j undergoing reactions such as presented in Eq. (1) are described by the law of mass action, given by

$$\frac{d}{dt}\left[X_j\right] = \sum_{n=1}^{M} \nu_{i,j} \left(k_i^+ \prod_{j=1}^{m} \left[X_j\right]^{r_{i,j}} - k_i^- \prod_{j=1}^{m} \left[X_j\right]^{p_{i,j}} \right), \tag{2}$$

where $\left[X_i\right]$ is the concentration of the i^{th} species, and $\nu_{i,j} = p_{i,j} - r_{i,j}$ is the net stoichiometric coefficient of the j^{th} species in the i^{th} reaction [51]. The stoichiometric matrix $\mathbf{S}$, which may be expressed as

$$\mathbf{S} = \begin{bmatrix} \mathbf{r} \\ \mathbf{p} \end{bmatrix}^T,$$

is a an $m \times 2M$ matrix that characterizes the underlying structure of biochemical reaction networks, and T denotes the transpose of a matrix [52]. Of particular interest, is the fact that molecular populations which are conserved may be expressed as linear combinations of basis vectors of the left null space of $\mathbf{S}$, defined by a set of linearly independent vectors $\boldsymbol{\ell}_i$ with $i = 1, \ldots, q \leqslant \min(m, M)$ and which all satisfy

$$\boldsymbol{\ell}_i \boldsymbol{S} = \mathbf{0},$$

where q is the nullity of $\boldsymbol{S}^T$ [53].

Although they are referred to as rate constants, the values of k_n^+ and k_n^- may actually be functions of the various concentrations $\left[X_i\right]$. The procedure for determining the functional form of these reactions rates involves deriving a full system of equations using Eq. (2), and setting a subset of the reactions to quasi-steady state (QSS) in order to obtain expressons for the "fast" variables in terms of the other "slow" variables (see Section 3.2.1.2 for more details and Section 3.3.2 for some examples). The justification for such QSS asumptions is the observation that some reactions are significantly faster than the others.

Generally, there will be spatial variations in the concentrations of molecules within a cell. Thus we consider the dynamics of a system of concentrations $\mathbf{u}(x,t)$ of m biochemically active molecules confined to a closed domain $\Omega \in \mathbb{R}^d$. These system are typically described by reaction-diffusion (RD)

equations, which for a closed system like a cell may be expressed as

$$\begin{aligned} \frac{\partial}{\partial t}\mathbf{u}\left(x,t\right) &= \mathbf{f}\left(\mathbf{u},t\right)+\mathbf{D}\cdot\nabla^2\mathbf{u} \qquad \text{in } \Omega \quad (3)\\ \nabla\mathbf{u}\cdot\hat{n}_\perp &= 0 \quad \text{on } \partial\Omega, \quad (4)\end{aligned}$$

where $x \in \mathbb{R}^d$ is the d-dimensional spatial coordinate, $t \in \mathbb{R}_{0+}$ is time, $\mathbf{u} : \mathbb{R}^d \times \mathbb{R}_{0+} \to \mathbb{R}^m$ is an vector of m scalar fields, $\mathbf{f} : \mathbb{R}^m \to \mathbb{R}^m$ is a non-linear function that quantifies reaction rates with f_i given by Eq. (2), $\mathbf{D} \in \mathbb{R}^m$ is a vector of diffusion coefficients, and $\mathbb{R}_{0+}$ are the non-negative real numbers, ∇ is the nabla operator such that $\nabla\mathbf{u}$ is an $m \times d$ matrix with $(\nabla u)_{i,j} = \partial u_i/\partial x_j$ and thus $\left(\nabla^2 u\right)_{i,j} = \sum_i \partial^2 u_i/\partial x_j^2$, and $\hat{n}_\perp$ is a unit vector normal to the domain boundary $\partial\Omega$. Here, we have considered systems without sources or sinks of molecules, which implies that the total amount of matter inside the domain Ω is conserved. The conservation of matter may be expressed mathematically as a set of integral constraints (e.g., Eqs. (40)-(43)), given by

$$\int_\Omega \boldsymbol{\ell}_i \cdot \mathbf{u}\left(x,t\right) d\Omega = K_i, \qquad \forall i = 1,\ldots,q \quad (5)$$

where K_i is a scalar constant determined from the initial conditions of the system and $\boldsymbol{\ell}_i$ is a left nullvector of the stoichiometric matrix. For a system with zero-flux boundary conditions given by Eq. (4), the conservation of matter can be further reduced to a condition on the reaction dyanmics, given by

$$\begin{aligned} \frac{d}{dt}\int_\Omega \boldsymbol{\ell}_i \mathbf{u} d\Omega &= 0 \qquad \forall i = 1,\ldots,q \\ \sum_j \int_\Omega \ell_{i,j}\frac{\partial}{\partial t}u_j d\Omega &= \sum_{j=1}^{m}\int_\Omega \ell_{i,j}\left(f_j\left(\mathbf{u}\right)+D_j\nabla\cdot\nabla u_i\right)d\Omega = 0 \\ &= \sum_j \int_\Omega \ell_{i,j} f_j\left(\mathbf{u}\right)d\Omega + \ell_{i,j}D_j \int_{S=\partial\Omega} \nabla u_j\cdot\hat{n}dS \\ &= \sum_j \int_\Omega \ell_{i,j} f_j\left(\mathbf{u}\right)d\Omega \\ \Rightarrow \boldsymbol{\ell}_i\cdot\mathbf{f}\left(\mathbf{u}\left(x,t\right)\right) &= 0, \qquad \forall\, i,x,t. \quad (6)\end{aligned}$$

This condition is always satisfied by a system of reversible pairs of reactions where k_i^+/k_i^- is non-zero, finite, and positive for all $i = 1, \ldots, M$ [54].

3.2.1.1 Well-Mixed Systems

By assuming $D_i/|\Omega|^2 \gg f_i(\mathbf{u})$ one obtains the well-mixed (WM) approximation which reduces the PDE system of Eq. (3) to a system of ODEs, given by

$$\frac{d}{dt}\mathbf{u} = \mathbf{f}(\mathbf{u}, t), \tag{7}$$

which is identical to Eq. (2) but where we have now explicitly emphasized the conditions on dynamics required for such an assumption. In the WM setting, the integral constraints for the conservation of matter may be expressed as algebraic constraints (e.g., Eqs. (22)-(23) or Eqs. (46)-(49)), given by

$$K_i = \boldsymbol{\ell}_i \cdot \mathbf{u} \tag{8}$$

where K_i and $\boldsymbol{\ell}_i$ are as described above. These algebraic constraints may be used to eliminate certain variables, and obtain an equivalent system of ODEs with fewer variables (e.g. compare systems (31)-(36) and (28)-(30)). Moreover, Eq. (8) may also be differentiated with respect to time to yield

$$\boldsymbol{\ell}_i \cdot \mathbf{f}(\mathbf{u}, t) = 0, \qquad \forall\, i, t. \tag{9}$$

The fixed points of the WM system (7) provide a natural ansatz for spatially homogenous steady states (HSS) of the RD system (3) with boundary conditions given by Eq. (4). However, the stability properties of the fixed-points of the WM system do not always carry over to the corresponding HSS of the RD system [55]. Moreover, these HSSs are only a subset of the fixed points of the RD system (3), where it is possible to obtain spatially-inhomogenous steady states (see Fig. 3.3).

3.2.1.2 Quasi-Steady State Dynamics

As discussed above, sometimes it is possible to "eliminate" some chemical species from a reaction system by assuming they only participate in "fast" reactions that reach steady state much more quickly than the other "slow" reactions under consideration. In such a scenario, it may be tempting to assume

that the dyanmics of these fast variables is simply zero. In fact, such assumptions are widespread in the literature [56], and inevitably lead to a break down of the laws of thermodynamics (e.g., the conservation of matter) [57,58]. Methods have been proposed for quantifying the error introduced by such assumptions [59], and a large body of work on systematic approaches for obtaining reduced reaction networks (i.e., systems of slow variables) which strike a balance between this error and computational feasability has emerged [56]. However, we note that this assumption is fundamentally incorrect as the fast variables change their concentrations in response to any changes in the slow variables, and thus they cannot be constant throughout time. Therefore, in order to circumvent these issues, we use ideas from the analysis of dynamical systems with multiple timescales, and propose a straightforward method for computing the dynamics of the fast variables which is compatible with the conservation of matter.

Firstly, we consider a WM reaction system, as it will simplify the requisite noatation, but similarly to Eqs. (8) and (9), all results may easily be extended to a RD setting. to In order to explicitly express the dynamics of the fast variables, we decompose $\mathbf{u}$ into fast and slow species, i.e.,

$$\mathbf{u}\left(t\right) = \left[\begin{array}{c} \mathbf{u}^{\mathbf{slow}}\left(t\right) \\ \mathbf{u}^{\mathbf{fast}}\left(t\right) \end{array}\right],$$

where $\mathbf{u}^{\mathbf{slow}}$ is the vector of m_{slow} slow species whose dynamics $\mathbf{f}^{\mathbf{slow}}$ are determined from Eq. (2), and $\mathbf{u}^{\mathbf{fast}}$ is the vector of $m_{fast} = m - m_{slow}$ fast species. Generally speaking, the fast variables may be expressed through a constitutive relation with the slow variables, given by

$$\mathbf{u}^{\mathbf{fast}}\left(t\right) = \mathbf{\Gamma}^{\boldsymbol{\epsilon}}\left(\mathbf{u}^{\mathbf{slow}}\left(t\right)\right), \tag{10}$$

where $\mathbf{\Gamma}^{\boldsymbol{\epsilon}}$ is a (possibly nonlinear) vector-valued function. The determination of $\mathbf{\Gamma}^{\boldsymbol{\epsilon}}$ has been historically obtained by assuming the dynamics of the fast variables $\mathbf{f}^{\mathbf{fast}}\left(\mathbf{u}\right) = 0$ and solving algebraically for $\mathbf{u}^{\mathbf{fast}}\left(t\right)$ in terms of $\mathbf{u}^{\mathbf{slow}}\left(t\right)$ [59]. However, a literal interpretation of the condition $\mathbf{f}^{\mathbf{fast}} = 0$ is at odds with the fact that $\mathbf{u}^{\mathbf{fast}}$ also changes with time.

I believe that it is more appropriate to assume that the net rates of the fast reactions are arbitrarily slow, i.e.,

$$\left|f_i^{fast}\right| = \epsilon_i \ll 1 \qquad \forall i,$$

and consider the algebraic relation $\mathbf{\Gamma^\epsilon}$ to define a sub-manifold which restricts the dynamics of the fast variables $\mathbf{u^{fast}}$ and is obtained in the limit of $\epsilon_i \to 0$ [60–62]. With this perspective, the time derivatives are now well-defined quantities. Therefore, in order to obtain the dynamics of the fast variables $\mathbf{f^{fast}}$, we may differentiate Eq. (8) with respect to time, yielding

$$\frac{d}{dt}\mathbf{u^{fast}} = \mathbf{f^{fast}} = \mathbf{J_{\Gamma^\epsilon}}\frac{d}{dt}\mathbf{u^{slow}}, \tag{11}$$

where $\mathbf{J_{\Gamma^\epsilon}}$ is the Jacobian matrix of $\mathbf{\Gamma^\epsilon}$, given by $(\mathbf{J_{\Gamma^\epsilon}})_{i,j} = \partial\Gamma_i^\epsilon/\partial u_j^{slow}$. This means the total dynamics of the combined fast and slow sub-systems are given by

$$\frac{d}{dt}\mathbf{u} = \frac{d}{dt}\begin{bmatrix} \mathbf{u^{slow}} \\ \mathbf{u^{fast}} \end{bmatrix} = \begin{bmatrix} \mathbf{f^{slow}} \\ \mathbf{J_{\Gamma^\epsilon}}\mathbf{f^{slow}} \end{bmatrix}. \tag{12}$$

Consequently, the conservation of matter for the full system of fast and slow species, as described Eq. (9), can be expressed as

$$\boldsymbol{\ell}_i \begin{bmatrix} \mathbf{f^{slow}} \\ \mathbf{J_{\Gamma^\epsilon}}\mathbf{f^{slow}} \end{bmatrix} = 0 \Leftrightarrow K_i = \boldsymbol{\ell}_i \cdot \begin{bmatrix} \mathbf{u^{slow}} \\ \mathbf{u^{fast}} \end{bmatrix} \qquad \forall\, i, t, \tag{13}$$

where we note that equivalent results may be obtained in a RD setting, given by

$$\boldsymbol{\ell}_i \begin{bmatrix} \mathbf{f^{slow}} \\ \mathbf{J_{\Gamma^\epsilon}}\mathbf{f^{slow}} \end{bmatrix} = 0 \Leftrightarrow K_i = \int_\Omega \boldsymbol{\ell}_i \cdot \begin{bmatrix} \mathbf{u^{slow}} \\ \mathbf{u^{fast}} \end{bmatrix} d\Omega \qquad \forall\, i, x, t. \tag{14}$$

Thus from Eq. (13) we can see that, in a WM setting, simple algebraic constraints suffice to enforce the conservation of matter regardless of whether QSS assumptions were used. However, in order to acheive the same result in a RD setting with QSS assumptions, one must use the more complex conditions on reaction dynamics given by the first expression in Eq. (14).

3.2.2 Stochastic Reaction-Diffusion

Stochastic effects can significantly alter the outcomes of models with nonlinear terms. For example, in Chapter 4 we will see how stochasticity can produce transient excursions away from a stable equilbrium in protrusion velocity. Stochasticity is of particular interest as as experimental recordings of

Algorithm 3.1 The SSA, also referred to as Gillespie's direct method.

$\mathbf{X}$ = The initial number of molecules of each molecular species
t $\leftarrow 0$
while t<t_{final} **do**
  Compute propensity vector $\boldsymbol{\alpha}$ according to Eq. (15)
  $\alpha_{\text{tot}} \leftarrow \sum_i \alpha_i$
  Sample $\chi \sim$ Unif(0,1)
  Sample i $\sim \alpha_i/\alpha_{\text{tot}}$
  $\mathbf{X} \leftarrow \mathbf{X} + \mathbf{S}_i$
  $\tau \leftarrow \log(1/\chi)/\alpha_{\text{tot}}$
  t $\leftarrow t + \tau$
end while

CHO cells (i.e., the cells our collaborators use to study the effects of paxillin on migration) exhibit highly stochastic protrusion events and changes in direction, and thus its inclusion may be a necessary ingredient for reconciling observed experimental behaviour with mathematical models [63]. Therefore, we have opted to carry out stochastic realizations of the Reaction-Diffusion equation. In a WM setting, the dynamics of these chemical reactions are described rigorously at the microscopic level by the Chemical Master Equation (CME) [64], which can be extended to a spatial setting as the Reaction Diffusion Master Equation (RDME) [65]. Stochastically exact realizations of the CME for a system undergoing chemical reactions can be obtained using Gillespie's direct method, or one of its many variants, which is often refered to as the stochastic simulation algorithm (SSA) [66]. In particular, for a system of paired reversible reactions described by Eq. (1), one may define a vector of reaction propensities (probability per unit time that a given reaction will occur), given by

$$\left.\begin{aligned} \alpha_{i,n} &= k^{+}_{i,n} \prod_{j=1}^{m} \left(X_j^{r_{i,j}} / |\Omega| \right)^{r_{i,j}} \\ \alpha_{i+M,n} &= k^{-}_{i,n} \prod_{j=1}^{m} \left(X_j^{p_{i,j}} / |\Omega| \right)^{r_{i,j}} \end{aligned}\right\} \quad \forall i = 1, \ldots, M, \tag{15}$$

where X_j is the number of molecules of the j^{th} molecular species. The vector of propensities is used to determine which chemical reaction occurs next in a probabalistic manner, while the total propentsity, $\alpha_{\text{tot}} = \sum_i \alpha_i$, is used to determine the waiting time $\tau \sim \text{Exp}(1/\alpha_{tot})$ between subsequent reactions where $\text{Exp}(x)$ is the exponential distribution with a mean of x (see Algorithm 3.1).

3.2.2.1 Stochastic Quasi-Steady State Approximation

As discussed in Section 3.2.1.2, some reactions may occur on a significantly faster timescale than others. In a determinsitic setting, the standard approach to deal with this is to set all chemical species which only appear in fast reactions to QSS, as described by Eq. (10). Within the framework of the SSA, most of the computational time is spent executing fast reactions and thus having very fast reactions can lead to very computationally intensive simulations. Moreover, in order to implement reactions in the SSA, it is necessary to specify their rates. This is generally not required for a deterministic treatment of reactions at QSS, and thus rate constants may be unavailable for fast reactions. For these reasons, the implementation of fast reactions within the SSA is non-tirival. Indeed, there are numerous implementations of the quasi-steady state reaction available in the SSA literature [67,68], which range from quite complex (e.g., [69–72]) to fairly simple (e.g., [73,74]). The more complex approaches will generally be more accurate, as they require specifiying the rate of the fast reactions. Ultimately, these rates serve to produce fluctuations around some mean value that is determined by Eq. (10). If these fluctuations are not deemed important for the overall dynamics of the system, these approaches seem like overkill and will simply add to the computional burden of the SSA. This motivates the use of simpler approahces (e.g. tQSSA in [74]) which are based on deterministic descriptions of the chemical rections.

In order to overcome the need to specify the rates of fast reactions and eleviate some of the computational burden of the SSA, we have opted to ignore temporal fluctuations in fast variables and simply use Eq. (10) to determine their values (i.e., the tQSSA approach). This is equivalent to assuming that the fast reactions are instantaneous and fluctuations are short-lived and negligible in magnitude [74]. This implies that M in Eq. (15) (as well as Eq. (16)) is the number of slow chemical reactions in the system, and therefore the stoichiometric matrix $\mathbf{S} = \mathbf{S}^{\mathbf{slow}}$ referred to in Algorithms 3.1&3.3 corresponds only to the slow reactions. The remaining fast variables undergo fast reactions that are described solely by the equilibrium relations $\mathbf{\Gamma}^{\epsilon}$ (i.e., no rate or stoichiometric information is required), and they are updated everytime a slow reaction that modifies $\mathbf{\Gamma}$ takes place. This means that when the SSA carries out a slow reaction which modifies the molecular counts for some slow species i, all fast species $j = \left\{ j : \left(\mathbf{J}_{\mathbf{\Gamma}^{\epsilon}}\right)_{j,i} \neq 0 \right\}$ must be also be updated according to Eq. (10).

3.2.2.2 Spatial Stochastic Simulation Algorithm

The SSA may furthermore be adapted to simulate the RDME (i.e., reaction-diffusion), which produces an algorithm referred to as the spatial SSA (SSSA). Briefly, the SSSA discretizes space into N finite-sized subdomains such that components of the matrix of chemical reaction propensities may be computed as

$$\left.\begin{aligned} \alpha^{\text{chem}}_{i,n} &= k^{+}_{i,n} \prod_{j=1}^{m} \left(X^{r_{i,j}}_{j,n} / |\Omega_n| \right)^{r_{i,j}} \\ \alpha^{\text{chem}}_{i+M,n} &= k^{-}_{i,n} \prod_{j=1}^{m} \left(X^{p_{i,j}}_{j,n} / |\Omega_n| \right)^{r_{i,j}} \end{aligned}\right\} \quad \forall i = 1, \ldots, M;\ n = 1, \ldots, N, \tag{16}$$

where $X_{j,n}$is the number of molecules of the j^{th} molecular species in the n^{th} subdomain Ω_n. Furthermore, it treats diffusion as a reaction which transport individual molecules between adjacent subdomains, where, for subdomains defined on a uniform grid with spcaing h, the propensity of a diffusion reaction consisting of the i^{th} molecule diffusing from subdomain j to a subdomain k is given by

$$\alpha^{\text{diff}}_{i,j,k} = \begin{cases} X_{i,j} D_i / h^2 & k \in \text{neighbours}\,(j) \\ 0 & \text{otherwise} \end{cases},$$

where neighbours (j) is the set of subdomain indices $n = \{n : \Omega_n \in \Omega\}$ which are physically adjacent to subdomain j [65]. The procedure for choosing which "reaction" (either diffusion or chemical) is nearly identical to the SSA (with $\alpha_{\text{tot}} = \sum_{i,j} \alpha^{\text{chem}}_{i,j} + \sum_{i,j,k} \alpha^{\text{diff}}_{i,j,k}$). However, there are some slight differences in how the state vector $\mathbf{X}$ is updated for diffusion and chemical reactions [65].

Indeed, we have previously used the SSSA to produce stochastic realizations of the RDME [63]. However, due to the way that the diffusion reaction propensities scale with the size of subdomains, the SSSA often becomes prohibitively slow when dealing with biologically-realisitic diffusion coefficients and numbers of molecules [75]. The drastic decrease in computational speed when modelling diffusion with the SSSA stems from the fact that the SSSA carries out diffusion (and chemical reactions) by executing a single reaction at a time. In the case of our simulations we find that $\sum_{i,j,k} \alpha^{\text{diff}}_{i,j,k} \approx 1000 \sum_i \alpha^{\text{chem}}_i$, such that the SSSA will spend more than 99.9% of its computational time performing diffusion reactions. Therefore, by using a different computational approach to carry out diffusion events we can significantly alleviate the computational bottleneck of the SSSA and achieve

much faster simulations.

3.2.2.3 Approximate Stochastic Diffusion

In order to circumvent the issues with computational speed observed in the SSSA, we have adopted an alternative approach for modelling diffusion stochastically [75]. Rather than carrying out single-molecule diffusion events, it simulates, simultaneously and in one diffusion event, the transfer of groups of molecules from all N subdomains to each of their neighbours. Instead using the approach of the SSSA and considering the joint diffusion propensity for any one of the many molecules in a given subdomain, this approach deals with the independent diffusion propensity of the individual molecules in a subdomain, given by

$$\tilde{\alpha}_{i,j}^{\text{diff}} = \sum_{k \in \text{neighbours}(j)} D_i/h^2. \tag{17}$$

Furthermore, rather than trying to track all of the diffusion events occuring at microscopic timescales determined by the SSSA, this method assumes that some finite amount of time Δt has passed and generates a random number $x_{i,j} \leqslant X_{i,j}$ of molecules which leave the sub-domain sampled from the binomial distribution, given by

$$P\left(X_{i,j}, x_{i,j}, p_{i,j}^{\text{acc}}\right) = \frac{X_{i,j}!}{x_{i,j}!\left(X_{i,j}-x_{i,j}\right)!}\left(p_{i,j}^{\text{acc}}\right)^{x_{i,j}}\left(1-p_{i,j}^{\text{acc}}\right)^{X_{i,j}-x_{i,j}} \tag{18}$$

where $p_{i,j}^{\text{acc}} = \Delta t \tilde{\alpha}_{i,j}^{\text{diff}}$ is the accumulated propensity that a single molecule of species i has left the subdomain j after a time Δt.

Sampling from the binomial distribution is computationally challenging, due to the presence of the factorial terms, and therefore it is useful to use the approximation

$$P\left(X_{i,j}, x_{i,j}, p_{i,j}^{\text{acc}}\right) = I_\beta\left(p_{i,j}^{\text{acc}}; x_{i,j}, X_{i,j}-x_{i,j}+1\right)$$

where I_β is the incomplete beta function [75]. The incomplete beta funtion is available in many programming languages (e.g., betainc$(p_{i,j}, x_{i,j}, X_{i,j}-x_{i,j}+1)$ in MATLAB), and is included in Numerical Recipes [76]. Furthermore, Carrero et. al. propose an efficient apseudobisection method for sampling from the binomial distribution, described in Algorithm 3.2. After having sampled $x_{i,j}$ the total number

Algorithm 3.2 Psuedobisection method for determining the number of molecules that leave a sub-domain due to diffusion during a timespan of length Δt [75]. Given $X_{i,j}$ molecules of species i in sub-domain j, choose a number $x_{i,j}$ from the binomial distribution in Eq. (18). The function round() rounds to the nearest integer, and $p_{i,j}^{\text{acc}} = \Delta t \tilde{\alpha}_{i,j}^{\text{diff}}$ where $\tilde{\alpha}_{i,j}^{\text{diff}}$ is the single-molecule diffusion propensity, given by Eq. (17).

Define the values of $X_{i,j} \geqslant 1$ and $0 < p_{i,j}^{\text{acc}} < 1$
$l \leftarrow 0$
$u \leftarrow X_i, j$
Sample $\xi \sim$ Unif(0,1)
Define $f(x) = I_\beta \left(p_{i,j}^{\text{acc}}, x, X_{i,j} - x + 1 \right) - \xi$
$fl \leftarrow f(l)$
$fu \leftarrow f(u)$
while $|l - u| > 1$ **do**
    $r \leftarrow$ round$((l + u)/2)$
    $fr \leftarrow f(r)$
    if fl and fr have the same sign **then**
        $l \leftarrow r$
        $fl \leftarrow fr$
    else
        $u \leftarrow r$
        $fu \leftarrow fr$
    end if
end while
$x_{i,j} \leftarrow u$

of molecules of species i to leave subdomain j one must sample $\tilde{x}_{i,j,k}$ according to the probabilties

$$p_{i,j,k}^{\text{acc}} = \begin{cases} \left(D_i/h^2\right)/\tilde{\alpha}_{i,j}^{\text{diff}} & k \in \text{neighbours}\,(j) \\ 0 & \text{otherwise} \end{cases} \tag{19}$$

under the constraint that $x_{i,j} = \sum_k \tilde{x}_{i,j,k}$. Subsequently, the distribution of molecular species i may be updated using

$$X_{i,j} = X_{i,j} - x_{i,j} + \sum_k \tilde{x}_{i,k,j} \qquad \forall j = 1, \ldots, N.$$

This computationally efficient procedure for producing stochastic diffusion events was originally

implemented within the context of an scalable variant of the SSSA known as the next-reaction method (or next-subvolume method) [75, 77]. This is important to note, as in such a setting there is a natural method for dealing with the fact that there is a fixed amount of time dt between diffusion events. However, due to technological constraints (i.e., the MATLAB language), in our implementation of stochastic realizations of the RDME we have not used the next-reaction method but rather have stuck with Gillespie's direct method and have acheived optimizations comparable to the next-reaction method using variations of the bookkeeping tricks described in [65]. Nonetheless, it is important to adapt the methodology from [75], as otherwise our stochastic simulations will not be faithful to the original RD system.

Within the framework of the next-reaction method, at some time t each reaction is given a waiting time τ_i, and the next waiting time τ is chosen as $\tau = \min_i \tau_i$ where some reaction μ is chosen as the next reaction which occurs. After reaction μ is carried out, a new value of τ_μ is sampled and the waiting time of all other reactions is updated according to the rule

$$\tau_i = \beta_i \left(\tau_i - \tau\right) \tag{20}$$

where $\beta_i = \alpha_i\left(t\right)/\alpha_i\left(t+\tau_\mu\right)$ is the ratio of reaction propensities before and after the reaction μ happens. Therefore, as reactions take place, each τ_i will tend towards zero until it becomes the minimum waiting time at which point the i^{th} reaction is occurs and τ_i will be resampled. In [75], diffusion events are modelled as a reaction that occurs with a fixed waiting time Δt which does not get updated according to Eq. (20). Whether such an approach is valid or not is beyond the scope of this thesis. However, we find that it is not suitable to our computational needs as it requires that $\mathcal{O}\left(\Delta t\right) \approx 1/\alpha_{\text{tot}}^{\text{chem}}$ (when $\Delta t \gg 1/\alpha_{\text{tot}}^{\text{chem}}$ diffusion events never occur in their implementation), and such a value of Δt does not afford us much computational speedup due to the increased cost of the diffusion steps using Algorithm 3.2. This discrepancy in speedpdp compared to [75] is likely due to the fact that we have ~ 1000-fold more molecules in our simulations than in [75]. Furthermore, we would like to be able to choose Δt based on the diffusion coefficient of the molecules alone rather than their reaction dyanmics as was done in [75].

For these reasons we define a maximum single-molecule diffusion probability, $0 < P_{max} < 1$, and initialize the waiting time Δt_i for a diffusion event of the i^{th}molecular species using the following

expression

$$\Delta t_i = P_{max} h^2 / D_i. \tag{21}$$

Subsequently, we carry out reactions according to the SSSA, where we assume that $\alpha_{\text{tot}} = \sum_{i,j} \alpha_{i,j}^{\text{chem}}$ and sample waiting times $\tau \sim \text{Exp}(1/\alpha_{tot})$. Every time a reaction is carried out, we update the values of Δt_i according to the rule

$$\Delta t_i = \Delta t_i - \tau,$$

where we effectively assume that the diffusion propensity does not change signficantly due to chemical reactions (i.e., $\beta_{\text{diff}} = 1$). We then perform diffusion events, in all subdomains, for molecules of the species $i_{\text{diff}} = \{i : \Delta t_i \leqslant 0\}$ using Algorithm 3.2. There are some conceptual problems with this approach: (i) the assumption that diffusion propensitites do not change with chemical reactions and (ii) the fact that diffusion waiting times Δt_i are updated by a next-reaction-like scheme yet diffusion events are not carried out according to the next-reaction method. We will ignore these issues for now, as the errors they introduce are minor and modifications required to fix them are not particularly challenging. The complete algorithm for carrying out stochastic reactions using the SSA and stochastic reactions using Algorithm 3.2 is describe in Algorithm 3.3.

3.2.3 Software

3.2.4 Deterministic Solutions

Numerical solutions of systems of ODEs were obtained using XPPAUT [78], in particular it was used to find fixed-points of WM systems. These fixed-points were subsequently continued in AUTO to produce bifurcation diagrams [79]. AUTO was also used to carry out local perturbation analysis (LPA) and the related root-finding problems described in Section 3.5.3. Numerical solutions to systems of PDEs were obtained using the *pdepe* function in MATLAB 2018a [80].

3.2.5 Stochastic Realizations

In order to carry out stochastic realizations of the RDME, we have implemented Algorithm (3.3) in MATLAB 2018a [80]. Moreover, it was implemented in a modular fashion, such that we can use the Cellular Potts Model (CPM) [81, 82], a phenomenoligcal model of cell-motility, to have a time-dependent domain which protrudes and retracts in response to local concentrations of Rac and Rho,

Algorithm 3.3 A computationally efficient modification of the SSSA with quasi-steady state assumptions, where diffusion events are carried out for all subdomains simultaneously. Here, the $*$ notation is used to denote that an operation is to be carried out for all valid indices of the subscript where it appears.

$X_{i,j}$ = The initial molecular count for the i^{th} molecular species in the j^{th} subdomain
$0 < P_{\text{max}} < 1$ = maximum diffusion probability allowed before triggering a diffusion event
$\boldsymbol{\Delta}\mathbf{t} \leftarrow P_{max}h^2/\mathbf{D}_*$
$\tilde{\alpha}^{\text{diff}}_{*,\text{max}} \leftarrow \max_j \tilde{\alpha}^{\text{diff}}_{*,j}$
Compute $\mathbf{p}_{*,*,k}$ according to Eq. 19
t $\leftarrow 0$
while t<t_{final} **do**
  Compute chemical propensity matrix $\boldsymbol{\alpha}$ according to Eq. (16)
  $\alpha_{\text{tot}} \leftarrow \sum_{i,j} \alpha^{\text{chem}}_i, j$
  Sample $\chi \sim$ Unif(0,1)
  $\tau \leftarrow \log(1/\chi)/\alpha_{\text{tot}}$
  Sample k $\sim \alpha_{\text{ceil}(k/N),\text{mod}(k-1,N)+1}/\alpha_{\text{tot}}$
  i $\leftarrow$ ceil(k/N)
  j $\leftarrow$ mod$(k-1, N)+1$
  $\mathbf{X}_{*,j} \leftarrow \mathbf{X}_{*,j} + \mathbf{S}_i^T$
  for k : $S_{i,k} \neq 0$ **do**
    Set $X_w, j = \Gamma_k(\mathbf{X}_{*,j})$ for all fast molecules w such that $(\mathbf{J}_{\boldsymbol{\Gamma}})_{w,k} \neq 0$
  end for
  t $\leftarrow t + \tau$
  $\boldsymbol{\Delta}\mathbf{t} \leftarrow \boldsymbol{\Delta}\mathbf{t} - \tau$
  for $1 \leqslant k \leqslant m$ **do**
    if $\Delta t_k \leqslant 0$ **then**
      Compute $\mathbf{x}_{k,*}$ using Algorithm 3.2 with $\mathbf{p}_{k,*} = \Delta t_k \tilde{\alpha}_{k,*}$
      Sample $\tilde{\mathbf{x}}_{k,*,\ell}/\mathbf{x}_{k,n} \sim p_{k,*,\ell}$
      $\mathbf{X}_{k,*} \leftarrow \mathbf{X}_{k,*} - \mathbf{x}_{k,*} + \sum_\ell \tilde{\mathbf{x}}_{k,*,\ell}$
      $\Delta t_k \leftarrow P_{max}h^2/\mathbf{D}_k + \Delta t_k$
    end if
  end for
end while

respectively. Together, these modules interact to model the RD-dynamics inside the cell and the resulting deformations and displacemente of the cell. The code for the both modules, and some example scripts showing how to use them, may be found on GitHub at `https://github.com/laurentmackay/CPM_RD_matlab` in the *fast_diff* branch. Currently, the reactions dynamics of system (32)-(36) are hard-coded into the file *update_alpha_chem0.m*, but we are currently developing a parser which can read a human-readable description of the reaction dynamics (e.g., chemical reaction notation) and automatically generate the right reaction dynamics. This will allow our code to easily simulate RD-dyanmics as well as cellular-motility driven by arbitrary sets of chemical reactions.

3.3 Well-Mixed Models

There are numerous mathematical models of front-to-rear polarization that consider the activity of RhoGTPases [28, 31, 33–35, 37, 83, 84]. In order to understand how these models work, we shall begin by describing and analyzing the mutual antagonism of Rac and Rho in a spatially homogeneous WM setting. Then we will investigate the influence of paxillin on the balance between Rac and Rho. In Section 3.4, we will extend these models from a WM setting to a RD setting and see how such a model can produce patterns of activity that are compatible with front-to-rear polarization.

3.3.1 Rac-Rho Sub-model

In order to build intuition for the effects of mutual inhibition between Rac and Rho, we have implemented a spatially-homogeneous sub-model of the model published in [50] (see Fig. 3.1A). Namely, in this sub-model we have omitted paxillin and its effects on Rac, as we wish to focus on the intrinsic dynamics of the Rac-Rho system. In order for either of the RhoGTPases to exert their control on the cytoskeleton, they must be in their active states (i.e., bound to a GTP moeity, [3]). The activation process is carried out by gaunine exchange factors (GEFs), which substitutes the GDP moiety found in the inactive form for a GTP molecule [85]. Conversely, the RhoGTPases are inactivated by the (seemingly paradoxically named) GTPase-activating factors (GAPs) which hydrolyze the GTP on active Rac/Rho molecules to GDP [85]. Therefore, this sub-model accounts for RhoGTP, RacGTP, RhoGDP, and RacGDP concentrations as well as the activity of relevant GEFs and GAPs. In order to simplify

this model, one may enforce the conservation of matter on Rho and Rac i.e.,

$$[\text{Rho}]_{\text{tot}} = [\text{RhoGTP}] + [\text{RhoGDP}] \tag{22}$$

$$[\text{Rac}]_{\text{tot}} = [\text{RacGTP}] + [\text{RacGDP}] \tag{23}$$

where $[\text{Rho}]_{\text{tot}}$ ($[\text{Rac}]_{\text{tot}}$) is the total concentration of all forms of Rho (Rac). Throughout this chapter, all concentrations with the subscript "tot" are assumed to be a fixed parameter that is set by the cell and can be determined experimentally. Using these expressions, we may define the non-dimensional variables

$$\rho = \frac{[\text{RhoGTP}]}{[\text{Rho}]_{\text{tot}}}, \quad \rho_i = \frac{[\text{RhoGDP}]}{[\text{Rho}]_{\text{tot}}} = 1 - \rho,$$

$$R = \frac{[\text{RacGTP}]}{[\text{Rac}]_{\text{tot}}}, \quad R_i = \frac{[\text{RacGDP}]}{[\text{Rac}]_{\text{tot}}} = 1 - R,$$

where ρ (R) is the active form of Rho (Rac) and ρ_i (R_i) is its inactive form. Using these non-dimensional variables, we may write the model by a system of ODEs, given by

$$\frac{d}{dt}\rho = I_\rho \frac{L_R^n}{L_R^n + R^n}\rho_i - \delta_\rho \rho = \tag{24}$$

$$\frac{d}{dt}R = I_R \frac{L_\rho^n}{L_\rho^n + \rho^n}R_i - \delta_R R \tag{25}$$

where I_ρ (I_R) is the maximal activation rate of Rho (Rac) with units of s^{-1}, L_R (L_ρ) is the non-dimensional half-maximum inhibition of Rho (Rac) activation by Rac (Rho), n is the Hill coefficient of this inhibition, and δ_ρ (δ_R) is the inactivation rate of Rho (Rac) with units of s^{-1}. In Eqs. (24)-(25), the mutual inhibition between Rac and Rho is implemented by decreasing the activation rate of one molecule as the active concentration of the other molecule increases. Therefore, when active Rac is very low Rho will attain its maximal activation rate and vice-versa. This type of double-negative feedback produces a bistable switch where either Rac or Rho is elevated, as can be see from the one-parameter bifurcation diagram in Figure 3.1. The bistable switch is produced by the coexistence of two branches of stable equilibria that are separated from a branch of saddle fixed points by two saddle-node bifurcations SN1 and SN2. The branch with an elevated level of Rac (R) is termed the induced branch as it is assumed to produce protrusion of the leading edge of motile cell and thus induce motility, while the branch with an elevated level of Rho (ρ) is termed the uninduced branch [50].

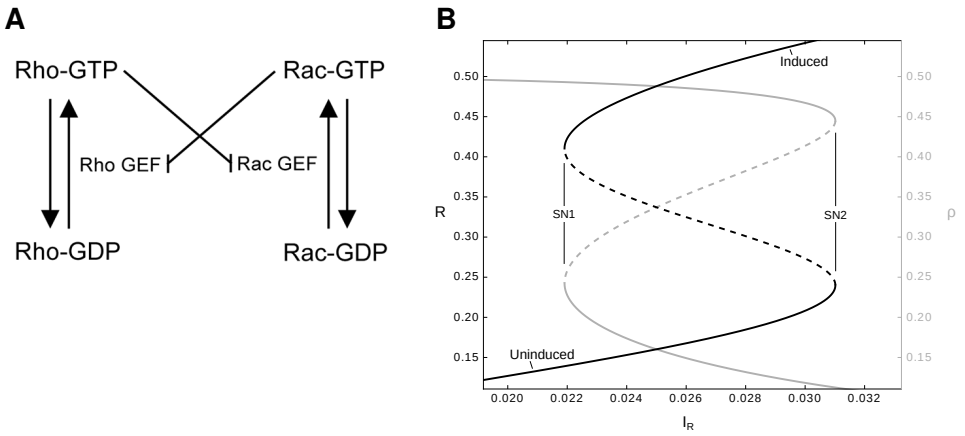

Figure 3.1: A bistable switch due to mutual inhibition between Rho and Rac. (A) Mutual inhibition of Rac and Rho. Distinct GEFs (GAPs) convert Rac and Rho to their active GTP-bound (inactive GDP-bound) forms. Both Rac and Rho inhibit the GEF activity of the other protein. This produces a bistable switch between the activity of the two proteins. (B) Bifurcation diagram of non-dimensional active Rac, R, in black and non-dimensional active Rho, ρ, in grey with respect to I_R. Solid (dashed) lines indicate stable (unstable/saddle) branches of equilibria. The two branches of stable equilibria are separated from the branch of saddle equilibria by two saddle-node bifurcations SN1 and SN2. The branch of stable equilibria with elevated (reduced) values of R (ρ) is referred to as the induced branch, while the other branch is referred to as the uninduced branch.

Bifurcation diagrams illustrate how fixed-points of an ODE system vary with certain parameters. In order to distinguish these fixed-points of the WM system from from those of the RD system, we will generically denote them with a over a symbol (e.g., $\bar{R}$) which alludes to the fact that they describe a spatially homogenous (i.e., flat) concentration profile. Furthermore, we adopt a convention where the induced (uninduced) state is denoted by a subscripted + (-) such that the value of R corresponding to the induced state is denoted by $\bar{R}_+$.

3.3.2 Paxillin's Influence on the Rac-Rho Sub-model

The protein paxillin is known to be a key regulator of adhesion and protrusion dynamics, where its phosphorylation is associated with faster adhesion assembly and disassembly rates as well as increased protrusive/invasive activity [47–50, 86, 87]. Due to its many interaction partners and the inherent complexity of adhesion and protrusion dynamics, it is difficult to pin down the specific mechanism by which paxillin achieves these effects. However, we have speculated on how it may influence adhesion

disassembly rates in the (see Discussion in Chapter 1). Nonetheless, one mechanism which has been proposed for paxillin-dependent control of protrusion is a positive-feedback loop that leads to the activation of Rac (and thus the inactivation of Rho). Namely, the phosphorylation of serine 273 on paxillin allows the GIT-PIX-PAK ternary complex to bind to paxillin molecules in adhesions [48], where the protein PIX serves as a GEF for Rac to produce protrusion near these same adhesions [88–90]. This highlights the dual-function of adhesions, serving both as mechanical anchor points (see Chapters 1 and 2) as well as mechanosensitive signaling hubs that play an important role in driving motility.

It seems likely that paxillin phosphorylation can be used to drive the bistable switch of the Rac-Rho sub-model. In particular, the the downstream increase of Rac GEF-activity is equivalent to increasing I_R in system (24)-(25) which is sufficient for switching from the uninduced state to the induced state (see Fig. 3.1B). Therefore, Tang et al. extended system (24)-(25) by considering (i) the phosphorylation of paxillin by PAK, (ii) the assembly of the ternary complex, (iii) the binding of the ternary complex to paxillin, and (iv) the activation of PAK by RacGTP [50]. Furthermore, it assumed that the steps involved in the ternary complex formation and PAK activation are significantly faster than paxillin phosphorylation (see S1 Text in [50]). Thus many reactions may be set to QSS, producing constitutive relations between the various proteins that make up the ternary complex and slower variables such as Rac, Rho, and paxillin. In particular, based on the description of the interactions between PAK, paxillin, and Rac it is necessary to determine the QSS levels of active PAK and PIX due to their kinase- and GEF-activities, respectively.

Rac Activation The activation rate of Rac is modified by assuming that the maximal activation rate is the sum of the rate of two pathways. As in system (24)-(25), one of these pathways has a maximal rate I_R and is independent of paxillin phosphorylation, but now includes the effect of monomeric PIX and GIT-PIX complexes. The other pathway has a maximal activation rate I_K^* and accounts for the the GEF-activity of all PIX-containing complexes that interact, directly or indirectly, with paxillin. Accordingly, the maximal activation rate I_K^* is given by

$$\begin{aligned} I_K^* &= I_K' \Big([\text{PIX-PAK}] + [\text{GIT-PIX-PAK}] + \left[\text{Pax}_\text{p}\text{-GIT-PIX-PAK}\right] \\ &\quad + [\text{PIX-PAK-RacGTP}] + \left[\text{Pax}_\text{p}\text{-GIT-PIX-PAK-RacGTP}\right] \Big), \end{aligned}$$

where I'_K is the PIX-complex-mediated activation rate constant with units of $\mu\text{M}^{-1}\text{s}^{-1}$, horizontal dashes between protein names denote a complex between these proteins, and Pax_p denotes phosphorylated paxillin. Using QSS assumptions, the above expression may be rewritten as

$$I_K^* = I'_K \left[\text{PAK}\right]_\text{tot} \left(1 - \frac{\left[\text{PAK}\right]}{\left[\text{PAK}\right]_\text{tot}} \left(1 + \alpha \left[\text{RacGTP}\right]\right)\right),$$

where $\alpha = k^+_{PAK}/k^-_{PAK}$ is the affinity for the binding of monomeric PAK to RacGTP and $\left[\text{PAK}\right]_\text{tot}$ is the total concentration of all PAK molecules [50]. Furthermore, using the same QSS assumptions, the fraction of total monomeric PAK can be expressed as

$$\begin{aligned} K_i^* = \frac{\left[\text{PAK}\right]}{\left[\text{PAK}\right]_\text{tot}} \quad = \quad & \Big(\Big(1 + k_X \left[\text{PIX}\right] + k_G k_X k_C \left[\text{GIT}\right] \left[\text{PIX}\right] \left[\text{Pax}_\text{p}\right]\Big) \left(1 + \alpha \left[\text{RacGTP}\right]\right) \\ & + k_G k_X \left[\text{GIT}\right] \left[\text{PIX}\right] \Big)^{-1}, \end{aligned}$$

where $k_G = k^+_G/k^-_G$ ($k_X = k^+_X/k^-_X$) is the affinity for the binding of monomeric GIT and PIX (PIX and PAK), $k_C = k^+_C/k^-_C$ is the binding affinity of Pax_p to the GIT-PIX-PAK complex, and the concentrations $\left[\text{GIT}\right]$ and $\left[\text{PIX}\right]$ are assumed to be fixed parameters [50]. Substituting in the non-dimensional variables R and $P = \left[\text{Pax}_\text{p}\right] / \left[\text{Pax}\right]_\text{tot}$, where $\left[\text{Pax}\right]_\text{tot}$ is the total concentration of paxillin, into the expression for K_i^*, we obtain

$$K_i^* = \left(\tilde{P}\left(1 + \alpha_R R\right) + k_G k_X \left[\text{GIT}\right] \left[\text{PIX}\right]\right)^{-1}$$

where $\tilde{P} = \left(1 + k_X \left[\text{PIX}\right] + k_G k_X k_C \left[\text{GIT}\right] \left[\text{PIX}\right] \left[\text{Pax}\right]_\text{tot} P\right)$ and $\alpha_R = \alpha \left[\text{Rac}\right]_\text{tot}$. Finally, the maximal activation rate of Rac, in terms of the non-dimensional variables, is given by

$$I_K^* = I_K \left(1 - K_i^* \left(1 + \alpha_R R\right)\right),$$

where $I_K = I'_K \left[\text{PAK}\right]_\text{tot}$.

Rac-Containing Complexes Due to the ability of active PAK to phosphorylate paxillin and the associated downstream effects on Rac activation, it is necessary to account for activation of PAK by RacGTP. To this end, Tang et al. assumed that all PAK molecules in a complex with a RacGTP molecule

are in an active state [50, 91]. Accordingly, one may define the active PAK concentration as

$$[\text{PAK}^*] = [\text{PAK-RacGTP}] + [\text{PIX-PAK-RacGTP}] + \left[\text{Pax}_\text{p}\text{-GIT-PIX-PAK-RacGTP}\right],$$

where it has been assumed that $[\text{GIT-PIX-PAK-RacGTP}] \approx 0$ due to the paxillin phosphorylation being critical for PAK activation (i.e., binding to RacGTP) [91–93]. Using QSS assumptions, we may express this active PAK concentration as

$$[\text{PAK}^*] = \alpha\,[\text{PAK}]\,[\text{RacGTP}]\left(1 + k_X\,[\text{PIX}] + k_G k_X k_C\,[\text{GIT}]\,[\text{PIX}]\left[\text{Pax}_\text{p}\right]\right)$$

or, after non-dimensionalization,

$$\begin{aligned} K = \frac{[\text{PAK}^*]}{[\text{PAK}]_\text{tot}} &= \alpha_R K_i^* R \tilde{P} \\ &= \frac{\alpha_R R}{1+\alpha_R R}\frac{\tilde{P}}{\tilde{P} + \dfrac{k_G k_X\,[\text{GIT}]\,[\text{PIX}]}{1+\alpha_R R}}. \end{aligned} \tag{26}$$

Paxillin Activation Since, phosphorylation of paxillin occurs due to the transient binding of inactive paxillin to active PAK molecules, its rate was modeled as an increasing Hill function of active PAK concentration [50, 91]. Thus, after non-dimensionalization, the phosphorylation rate of paxillin is given by

$$B\frac{K^n}{L_k^n + K^n}\left(1 - P^*\right)$$

where B is the maximal rate of paxillin phosphorylation with units of s^{-1} and

$$P^* = P + \hat{P}, \tag{27}$$

is the scaled concentration of all forms of active paxillin with $\hat{P} = P k_G k_X k_C\,[\text{GIT}]\,[\text{PIX}]\,[\text{Pax}]_\text{tot}\,K_i^*\,(1+\alpha_R R)$.

Rho Activation As noted earlier, Rac and Rho exert their mutual inhibition on one another by having the active form of one protein reduce the activation rate of the other protein. The maximal activation rate I_K^* reflects the existence of multiple pathways for Rac activation, where some of the complexes involved in Rac activation contain (active) RacGTP. Therefore, in order to accurately describe the

inhibition of Rho activation by active Rac, it is necessary to account for the concentration of these complexes. Notably, these complexes happen to coincide with the set denoted by PAK*, and thus the total non-dimensionalized concentration of active Rac is given by

$$R^* = R + \gamma K,$$

where $\gamma = [\text{PAK}]_{\text{tot}} / [\text{Rac}]_{\text{tot}}$ is the ratio of total PAK to total Rac concentration.

Finally, we may express the dynamics of all three non-dimensional variables as

$$\frac{d}{dt}\rho = I_\rho \frac{L_R^n}{L_R^n + (R^*)^n}(1-\rho) - \delta_\rho \rho \tag{28}$$

$$\frac{d}{dt}R = (I_R + I_K^*)\frac{L_\rho^n}{L_\rho^n + \rho^n}(1-R^*) - \delta_R R \tag{29}$$

$$\frac{d}{dt}P = B\frac{K^n}{L_k^n + K^n}(1-P^*) - \delta_P P. \tag{30}$$

Eqs. (28)-(30) represent the interaction of phosphorylated paxillin (i.e., active paxillin) with the previously discussed Rac-Rho sub-model. This interaction occurs through the GIT-PIX-PAK complex, where the formation of this ternary complex has been assumed to be significantly faster than the activation of Rho, Rac, and paxillin. This difference in timescales was used to replace the large number of variables with a simpler model that has many nonlinear terms (e.g., K and P^*).

Having established that the mutual antagonism between Rac and Rho can produce bistability with respect to I_R the basal maximal activation rate of Rac (see Fig. 3.1), one may wonder if it is possible to drive this bistable switch through the phosphorylation rate of paxillin. This outcome seems quite likely from the form of Eq. 29 and the fact that I_K^* is a monotonically increasing function of P. Moreover, there are some conceptual reason for why this may be the case.

Biologically, paxillin phosphorylation is known to increase both the assembly and disassembly rate of adhesions, through mechanism which vary based on the type and location of the adhesion (see Chapter 1). Faster adhesions dynamics may indeed allow for increased motility, but such an outcome also requires the appropriate force-generating machinery to be active (e.g., high RacGTP at the leading edge of the cell). Therefore, if paxillin phosphorylation can control not only adhesion dynamics but also the activity of the RhoGTPases that drive protrusion and contraction then it represents a very

potent regulator of cell migration.

In order to test this hypothesis, we have computed a one-parameter bifurcation diagram for system (28)-(30) with respect to B (see Fig. 3.2). Similarly to Figure 3.1, both Rac and Rho exhibit a bistable switch with induced and uninduced branches of stable equilibria that are separated from a branch of saddle fixed-points by two saddle-node bifurcations. However, these branches are much more plateaued in nature and the left saddle-node is significantly closer to $B = 0$ than the right saddle-node (compare with black line in Fig. 3.1B). Paxillin, on the other hand, has induced and uninduced branches that increase sigmoidally with B and the distance between these two branches is not as significant as it is for Rac or Rho. Therefore, we may conclude that small changes in paxillin phosphorylation may lead to significant changes in Rac and Rho activity (e.g., by pushing the system past a saddle-node bifurcation), whereas they will only produce graded changes in the activation of paxillin.

3.4 Spatio-Temporal Model

We have seen how mutual antagonism produces bistabilty in a WM setting. However, bistability on its own cannot explain front-to-rear polarization as it only predicts the coexistence of two stable steady states. Polarization is a fundmaentally spatial phenomenon, and thus requires the addition of a spatial dimension into the model. Therefore, we will drop the WM approximation in favour of the RD system described in [50], given by

$$\frac{\partial}{\partial t}\rho\left(x,t\right) = f_\rho + D_\rho \nabla^2 \rho \tag{31}$$

$$\frac{\partial}{\partial t}\rho_i\left(x,t\right) = -f_\rho + D_{\rho_i} \nabla^2 \rho_i \tag{32}$$

$$\frac{\partial}{\partial t}R\left(x,t\right) = f_R + D_R \nabla^2 R \tag{33}$$

$$\frac{\partial}{\partial t}R_i\left(x,t\right) = -f_R + D_{R_i} \nabla^2 R_i \tag{34}$$

$$\frac{\partial}{\partial t}P\left(x,t\right) = f_P + D_P \nabla^2 P \tag{35}$$

$$\frac{\partial}{\partial t}P_i\left(x,t\right) = -f_P + D_P \nabla^2 P, \tag{36}$$

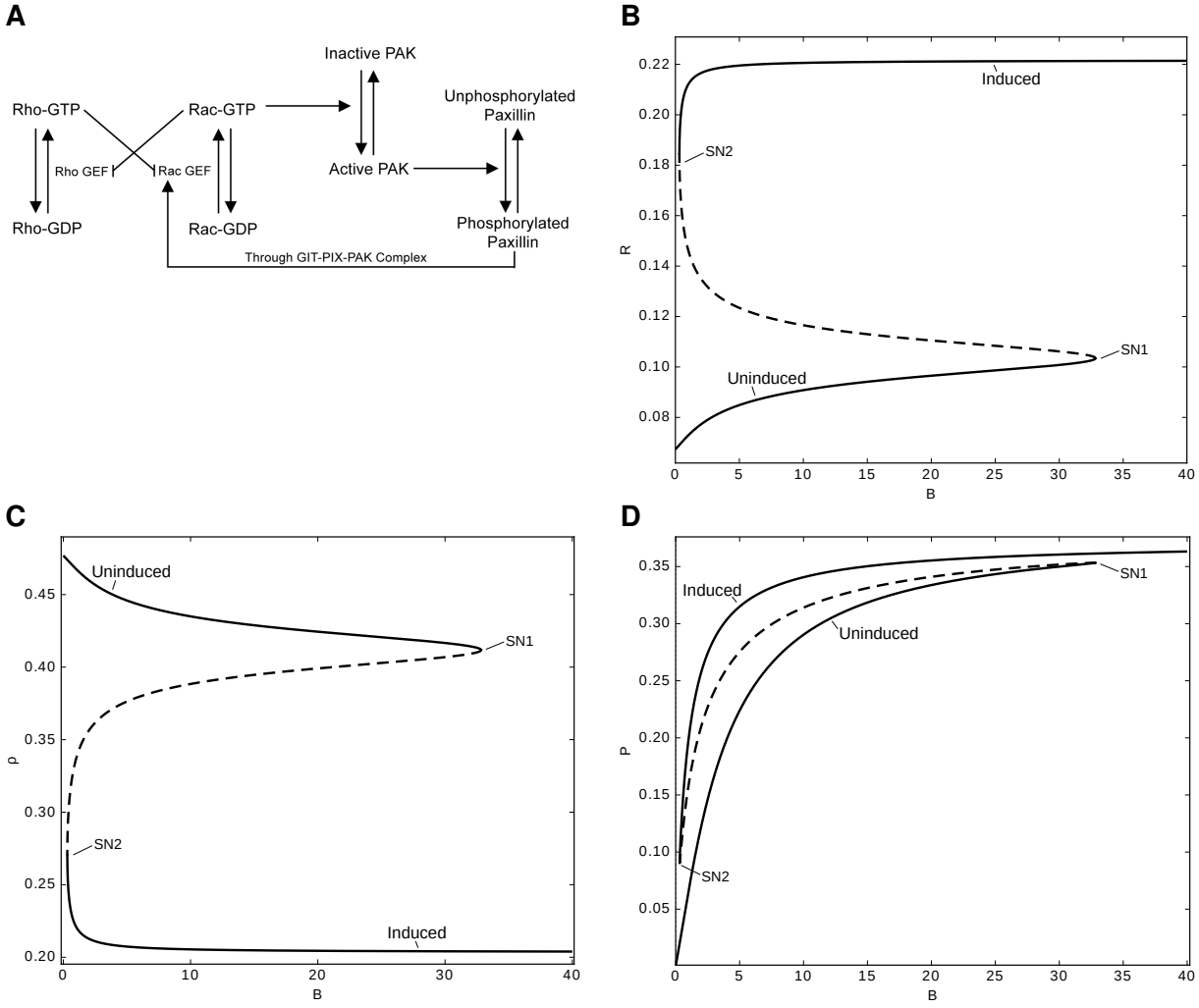

Figure 3.2: The effect of paxillin phosphorylation on the mutual antagonism of Rac and Rho. (A) The biochemical cascade of signaling events which link the Rac-Rho sub-model to paxillin. Paxillin phosphorylation triggers the formation of the GIT-PIX-PAK ternary complex which acts as a Rac-specific GEF, activating Rac. Active Rac acts as an activator for PAK which in turn phosphorylates paxillin, establishing a positive feedback loop between paxillin phosphorylation and Rac activation. This allows for paxillin phosphorylation to drive the bistable switch of the Rac-Rho sub-model. (B, C, D) Bifurcation diagram of nondimensional (B) active monmeric Rac, R, (C) active Rho, ρ, and (D) active monomeric Paxillin, P, with respect to the maximal paxillin phosphorylation rate B. Solid (dashed) lines indicate stable (unstable/saddle) branches of equilibria. The bifurcation structure is qualitatively the same as in Figure 3.1.

where the functions

$$f_\rho(\rho, \rho_i, R) = I_\rho \frac{L_R^n}{L_R^n + (R + \gamma K)^n} \rho_i - \delta_\rho \rho \tag{37}$$

$$f_R(R, R_i, \rho, P) = (I_R + I_K^*) \frac{L_\rho^n}{L_\rho^n + \rho^n} R_i - \delta_R R \tag{38}$$

$$f_P(P, P_i, R) = B \frac{K^n}{L_k^n + K^n} P_i - \delta_P P, \tag{39}$$

are the activation dynamics of Rho, Rac, and paxillin, respectively, all variables with a subscript i denote the scaled inactive concentration of the protein, D_ρ (D_{ρ_i}) is the diffusion coefficient of active (inactive) Rho, D_R (D_{R_i}) is the diffusion coefficient of active (inactive) Rac, D_P (D_{P_i}) is the diffusion coefficient of active (inactive) paxillin. In this RD setting, the conservation of matter is expressed as integral constraints given by Eq. 5,

$$[\text{Rho}]_{\text{tot}} = \frac{1}{|\Omega|} \int_\Omega [\text{RhoGDP}] + [\text{RhoGTP}]\, d\Omega \tag{40}$$

$$[\text{Rac}]_{\text{tot}} = \frac{1}{|\Omega|} \int_\Omega [\text{RacGDP}] + [\text{RacGTP}] + [\text{PAK}^*]\, d\Omega \tag{41}$$

$$[\text{Pax}]_{\text{tot}} = \frac{1}{|\Omega|} \int_\Omega [\text{Pax}] + [\text{Pax}_\text{p}] + [\text{Pax}_\text{p}\text{-GIT-PIX-PAK}] + [\text{Pax}_\text{p}\text{-GIT-PIX-PAK-RacGTP}]\, d\Omega \tag{42}$$

$$[\text{PAK}]_{\text{tot}} = \frac{1}{|\Omega|} \int_\Omega [\text{PAK}] + [\text{PIX-PAK}] + [\text{GIT-PIX-PAK}] + [\text{Pax}_\text{p}\text{-GIT-PIX-PAK}] + [\text{PAK}^*]\, d\Omega, \tag{43}$$

where Ω is the finite-sized domain of the cell. Furthermore, we assume that the cell is a closed system and therefore use zero-flux boundary conditions, given by

$$\nabla u \cdot \hat{n} = 0 \quad \text{on } \partial\Omega \qquad \forall u \in \{\rho, \rho_i, R, R_i, P, P_i\},$$

where $\hat{n}$ is the normal vector of the cell boundary $\partial\Omega$.

3.4.1 Conservation of Matter in the Spatio-Temporal Model

We wish to note here that although system (31)-(36) may appear to satisfy the conservation of matter through constraint (6), this is an incorrect conclusion as it does not account for the conservation of species which have been elminated by QSS assumptions.

In order to illustrate this problem, we use the integral contraints in Eq. (40)-(43) to define the basis of the left nullvectors of the stoichiometric matix. Namely, by focusing on the molecules which contain Rac (i.e., Eq. (41)) we identify the nullvector $\boldsymbol{\ell}_{\text{Rac}}$, given by

$$\boldsymbol{\ell}_{\text{Rac}} = \begin{bmatrix} 1 & \text{RacGTP} \\ 1 & \text{RacGDP} \\ 0 & \text{RhoGTP} \\ 0 & \text{RhoGDP} \\ 0 & \text{Pax}_{\text{p}} \\ 0 & \text{Pax} \\ 0 & \text{Pax}_{\text{p}}\text{-GIT-PIX-PAK} \\ 0 & \text{PAK} \\ 1 & \text{PAK}^{*} \\ 0 & \text{PIX-PAK} \\ 0 & \text{GIT-PIX-PAK} \end{bmatrix} \begin{matrix} \\ \\ \\ \\ \\ \\ \\ \\ \\ \\ \\ \end{matrix} \begin{matrix} \\ \\ \\ \\ \\ \text{slow} \\ \\ \\ \\ \\ \\ \end{matrix} \begin{matrix} \\ \\ \\ \\ \\ \\ \\ \\ \\ \text{fast} \\ \\ \end{matrix}$$

where we see that two slow species (RacGTP and RacGDP) and one fast species (PAK*) form a conserved quantity. When a conserved quantity depends only on slow variables, imposing Eqs. (5) or (6) is straightforward and one may intuitively use mass action terms involving only slow variables to determine the reaction dyanmics (i.e., the appraoch used in system (31)-(36)). However, when a conserved quantity (defined by $\boldsymbol{\ell}_i$) is a mix of slow and fast variables, it is necessary to impose the conservation of matter via Eq. (13) which considers the joint system of fast and slow variables rather than only those in the slow sub-system.

Therefore, in order to correctly describe the reaction dynamics in the RD system, we begin by rescaling Eq. (41) as

$$1 = \frac{1}{|\Omega|} \int_{\Omega} R_i + R + \gamma K d\Omega,$$

which,according to Eq. 14, is equivalent to

$$-f_R\left(R, R_i, \rho, P\right) = f_{R_i}\left(R, R_i\right) + \gamma f_K$$

where f_R is the net reaction rate of scaled RacGTP that includes the dyanmics of the fast reactions

which consume/produce RacGTP (i.e., it is not given by Eq. (38)), f_{R_i} is given by Eq. (38) (as RhoGDP is not consumed or produced by any fast reactions), and f_K is the net reaction rate of scaled PAK*. Using Eq. (11), f_K may be expressed as

$$f_K\left(R, R_i, \rho, P, t\right) = \frac{\partial}{\partial R} K\left(R, P\right) f_R\left(R, R_i, \rho, P\right) + \frac{\partial}{\partial P} K\left(R, P\right) f_P\left(P, P_i, R\right),$$

where f_P is the net reaction rate of paxillin (not given by Eq. (39)). Therefore, the net reaction rate for R is given by

$$f_R\left(R, R_i, \rho, P\right) = \frac{-f_{R_i}\left(R, R_i\right) - \gamma \frac{\partial K}{\partial P} f_P\left(P, P_i, R\right)}{1 + \gamma \frac{\partial K}{\partial R}},$$

Similarly, for paxillin the conservation of matter can be expressed as,

$$1 = \frac{1}{|\Omega|} \int_{\Omega} P_i + P + \hat{P} d\Omega$$

which can be rewritten as,

$$\begin{aligned} -f_P\left(P, P_i, R\right) &= f_{P_i} + \frac{\partial \hat{P}}{\partial R} f_R\left(R, R_i, \rho, P\right) + \frac{\partial \hat{P}}{\partial P} f_P\left(P, P_i, R\right) \\ &= \frac{f_{P_i} + \frac{\partial \hat{P}}{\partial R} f_R\left(R, R_i, \rho, P\right)}{1 + \frac{\partial \hat{P}}{\partial P}} \end{aligned}$$

where f_{P_i} is given by Eq. (39). Finally, we may solve for f_R and f_P, given by

$$f_R\left(R, R_i, \rho, P\right) = \frac{-f_{R_i}\left(1 + \frac{\partial \hat{P}}{\partial P}\right) + f_{P_i} \gamma \frac{\partial K}{\partial P}}{\left(\frac{\partial \hat{P}}{\partial P} + 1\right)\left(\gamma \frac{\partial K}{\partial R} + 1\right) - \gamma \frac{\partial K}{\partial P} \frac{\partial \hat{P}}{\partial R}} \tag{44}$$

$$f_P\left(P, P_i, R\right) = \frac{-f_{p_i}\left(\gamma \frac{\partial K}{\partial R} + 1\right) + f_{R_i} \frac{\partial \hat{P}}{\partial R}}{\left(\frac{\partial \hat{P}}{\partial P} + 1\right)\left(\gamma \frac{\partial K}{\partial R} + 1\right) - \gamma \frac{\partial K}{\partial P} \frac{\partial \hat{P}}{\partial R}}. \tag{45}$$

Such considerations have previously been neglected in deterministic implementations of an RD system describing the spatio-temporal dyanmics of WM system (28)-(30) [50], which is equivalent to assuming that all the partial derivates in the above expression are negligible. For simplicity and comparisons with the results in [50], we have done the same in our deterministic implementations. However, our

stochastic implementations do indeed explicitly consider the fast reactions (see Section (3.2.2.1)) such that they satisfy Eqs. (40)-(43).

3.4.2 Conservation of Matter in the Well-Mixed Model

For comparison, in a WM setting, the conservation of matter may be imposed using simple algebraic constraints given by Eq. (8),

$$1 = \rho + \rho_i \tag{46}$$
$$1 = R + \gamma K + R_i \tag{47}$$
$$1 = P^* + P_i \tag{48}$$
$$1 = K_i^* + \left(1 - K_i^* \left(1 - \alpha_R R\right)\right) + K. \tag{49}$$

Using these algebraic constraints, the WM description of system (32)-(36) is thus given by

$$\frac{d}{dt}\rho = f_\rho \left(\rho, 1-\rho, R\right) \tag{50}$$
$$\frac{d}{dt}R = f_R \left(R, 1-R-\gamma K, \rho, P\right) \tag{51}$$
$$\frac{d}{dt}P = f_P \left(P, 1-P^*, R\right), \tag{52}$$

where f_R and f_P are given by Eqs. (38) and (39), respecitvely, which is identical to system (28)-(30). These algebraic constraints are considerably simpler to implement than, but equivalent to, a RD system using Eqs. (44)&(45).

We have now seen how the conservation of matter leads to subtle difference in the formulation of equivalent WM and RD systems. Interestingly, there are also some subtle differences between the fixed-points of these two descriptions of chemical reactions. In particular, while all of the fixed points of the WM system have corresponding HSSs that are fixed points for the RD system, the stability of the of the WM fixed-points may or may not carry over to the RD system [32, 55]. Furthermore, a RD system may also admit some spatially inhomogenuous steady states. The temporal evolution of the RD system from a, possibly spatially homogenous, initial condition towards stable a spatially inhomogenous solution is a phenomenon typically referred to as pattern formation. In particular, there

is a specific mechanism, termed as wave-pinning, which has been proposed to produce the front-to-rear polarization in cells from the intrinsic interactions of systems of RhoGTPases [83]. In Section 3.5, we begin by briefly review the theory underlying the wave-pinning phenomenon. Subsequently, this will provide us with a framework for understanding the relationship between the fixed-points of the WM and RD descriptions, and explore how wave-pinning manifests itself in system (31)-(36).

3.5 Pattern-Formation through Wave-Pinning

As discussed previously, in a WM setting, the forms of functions f_ρ and f_R allow for the existence of bistability. Interestingly, it has been shown that, in a RD setting, models that (i) exhibit multiple steady states in a WM setting, (ii) obey the conservation of matter, and (iii) exhibit a significant difference in diffusion coefficients between two that interconvert are capable of supporting a pattern formation phenomenon known as wave-pinning [32,83]. Therefore, we consider a 1-dimensional RD system, with two chemical species that interconverted (e.g. RacGTP and RacGDP), whose form is given by Eq. (3) with $n = 1$ with boundary conditions given by Eq. (4). More specifically, we consider a system with $u(x,t)$ being the concentration of the slowly-diffusing active form, and $v(x,t)$ is the rapidly-diffusing inactive species. The net reaction dynamics of u (v) are denoted by f_u (f_v).

Wave-pinning is often contrasted with the classical Turing pattern formation mechanism, which requires (i) mutual-antagonism between the chemical species under consideration and (ii) a significant difference in diffusion coefficients between at least two species [94]. It is a phenomenon which may occur when $m \geqslant 2$ and the WM system has a stable fixed point u_0 [95]. Due to the existence of this fixed point, there exists a homogeneous steady state (HSS) solution for the RD system. The HSS may or may not be a stable solution for Eq. (3), as the addition of diffusion may destabilize certain Fourier modes of solution near the HSS. The methodology for assessing the stability of a HSS is called Turing analysis, and it seeks to find the oscillatory modes which grow or shrink in amplitude over time [55]. In order for patterns to form using the Turing mechanism, the HSS predicted by the Eq. (7) must be an unstable solution of Eq. (3), such that some spatially oscillatory modes will grow over time and produce a spatial pattern [32, 95].

On the other hand, wave-pinning is an alternative pattern formation mechanism that applies to reaction diffusion systems very similar to those that can produce Turing instabilities. However, in contrast, the wave-pinning mechanism requires the WM system to posses multiple stable HSSs for

a fixed value of $v(x,t) = v_0 =$ constant [32]. Furthermore, wave-pinning requires that the system conserves matter [32]. For the RD system discussed above with variables u and v, the unique left null-vector of the stoichiometric matrix,

$$\mathbf{S} = \begin{bmatrix} 1 & -1 \\ -1 & 1 \end{bmatrix},$$

is given by $\boldsymbol{\ell} = \begin{bmatrix} 1 & 1 \end{bmatrix}$ and therefore the conservation of matter can be reduced to

$$f(u,v) = f_u(u,v) = -f_v(u,v) \qquad \forall\, x,t.$$

Moreover, we assume that v has a rapid diffusion coefficient given by $D = \mathcal{O}(1)$ whereas u has a slow diffusion coefficient given by $\epsilon^2 \ll D$. After some rescaling of variables (see [32] for details), we arrive at a RD system defined on $x \in [0,1]$, given by

$$\epsilon \frac{\partial u}{\partial t} = f(u,v) + \epsilon^2 \nabla^2 u \tag{53}$$

$$\epsilon \frac{\partial v}{\partial t} = -f(u,v) + D\nabla^2 v. \tag{54}$$

Interestingly, travelling wave solutions are known to arise in systems with RD systems on infinite domains with bistable reaction dynamics. However, in the case of wave-pinning, the finite size of the cell domain along with the conservation of matter modify the behaviour of the system such that the speed of the wave is not constant in time [32]. We will now see how bistable reactions dynamics allow for these waves to develop, and the interaction between reactions and diffusion allow them to travel across space and eventually come to a stop.

Behaviour at short timescales We begin by considering the dynamics of system (53)-(54) shorlty after some arbitrary initial condition. The development of a pattern through wave-pinning requires that, when $v_{min} \leqslant v \leqslant v_{max}$, the function $f(u,v)$ has three roots $u_-(v) < u_m(v) < u_+(v)$, where $u_\pm$ are stable solutions of the WM system with fixed v and u_m is an unstable fixed point. From Eq. (53), we may notice that the inactive form of the protein diffuses significantly more slowly than the active form (i.e., $\epsilon^2 \ll D$). This motivates the definition of a short timescale $t_s = t/\epsilon$, by re-scaling time and

keeping leading order terms we obtain

$$\frac{\partial u}{\partial t_s} = f(u,v) \tag{55}$$

$$\frac{\partial v}{\partial t_s} = -f(u,v) + D\nabla^2 v, \tag{56}$$

that is, on a short timescale u is only subject to reaction dynamics whereas v exhibits both reaction and diffusion dynamics. Suppose that $v_{min} \leqslant v(x,t_s) \leqslant v_{max}$ is in the bistable range, then Eq. (55) states that u will either evolve to $u_-(v)$ or $u_+(v)$ depending on the initial condition. On the other hand, as u evolves to $u_\pm$, the reaction rate f approaches zero, and thus from Eq. (56) we may conclude that v eventually evolves towards a uniform spatial profile. Therefore, at the end of the short time scale, v will have a roughly constant value through out the domain whereas $u(x,t_s)$ will assume the values of either $u_-(v)$ or $u_+(v)$ depending on the position x (i.e., the imposed initial condition). The concentration profiles of u and v which develop during the short timescale then serve as an initial condition for the system at intermediate timescales.

3.5.1 Behaviour at intermediate timescales

We now consider a scenario where, after an intermediate amount of time, there exists a single transition between u_- and u_+. In the absence of such a transition, the system will simply evolve to a HSS in both u and v, and for the scenario with multiple transitions see [32].

Suppose the single transition between u_- and u_+ occurs at a position ϕ. Under these assumptions, it may be shown that the solutions for both u and v are spatially uniform everywhere except within a small transition region of size $\mathcal{O}(\epsilon)$ in the vicinity ϕ [32]. Therefore, it remains to be determined what happens to the solution inside this region and how the position of the transition, $\phi(t)$, changes over time.

Within the transition region it is convenient to use the re-scaled spatial position $\xi = \left(x - \phi(t)\right)/\epsilon$, and to introduce the inner solutions

$$U(\xi,t) = u\left(\left(x-\phi(t)\right)/\epsilon, t\right), \qquad V(\xi,t) = u\left(\left(x-\phi(t)\right)/\epsilon, t\right)$$

which are relevant inside the transition region. We note that U and V have the appearance of travelling

wave solutions. However they are not traveling wave solutions in the strict sense, due to their time-dependent wave speed $d\phi/dt$. Re-scaling system (53)-(54) according to ξ and keeping only the terms with leading order in ϵ, one obtains

$$-\frac{d\phi}{dt}\frac{\partial U}{\partial \xi} = f(U,V) + \frac{\partial^2 U}{\partial \xi^2} \tag{57}$$

$$0 = \frac{\partial^2 V}{\partial \xi^2}. \tag{58}$$

In order for these inner solutions to be relevant to the aforementioned solution outside of the transition region, the inner solutions must match with the outer solutions in the limits of $\xi \to \pm\infty$. For these limits to exist, it is required that $V(\xi,t) = v(x,t) = v_0$, while for U we obtain

$$\lim_{\xi\to-\infty} U(\xi) = u_{\pm}(v_0), \qquad \lim_{\xi\to\infty} U(\xi) = u_{\mp}(v_0).$$

Therefore, the inner solution U represents a heteroclinic connection between the stable fixed points u_- and u_+ [55, 96]. Assuming such a connection exists, one may find an expression for the wave speed using Eq. (57) [32], given by

$$\frac{d\phi}{dt}(v_0) = \frac{\int_{u_\pm(v_0)}^{u_\mp(v_0)} f(u,v_0)\,du}{\int_{-\infty}^{\infty}\left(\partial U/\partial\xi\right)^2 d\xi}. \tag{59}$$

Therefore, if there is a value $v_0 = v_c$ which can make the integral in the numerator vanish, the wave will stall and a single transition between the two values of u will be maintained at the position $x = \phi(v_0)$. Furthermore, analysis on the relative signs of dv_0/dt and $d\phi/dt$ can be used to prove the stability of the wave-pinning solution on the on the intermediate timescale [32]. This phenomenon is referred to as wave-pinning.

The conservation of matter, although implicitly imposed by the structure of system (53)-(54), may be explicitly expressed as an integral constraint given by

$$\int_0^1 (u + v_0)\,dx = K,$$

where $K > 0$ is the total amount of the protein of interest in the cell. In order to approximate this integral constraint , we take he limit as $\epsilon \to 0$, and find that the cell consists of two spatially segregated regions: one of size ϕ which we shall arbitrarily assign the value of $u = u_+$ while the other is of size $1 - \phi$ with a value $u = u_-$. Therefore, in this limit, we may rewrite the integral constraint as

$$K = v_0 + \phi u_+ (v_0) + (1 - \phi) u_- (v_0) . \tag{60}$$

When the wave stalls, we have $v_0 = v_c$ and $\phi \in [0, 1]$. Combined with with Eq. (60), these assumptions lead to constraints on K which a necessary for wave-pinning to occur

$$v_c + u_- < K < v_c + u_+, \tag{61}$$

that is K must not be too small to allow for u_- to be a homogeneous steady state with $v = v_c$ but not too large to allow for u^+ to be a homogeneous steady state with $v = v_c$. Furthermore, while it may seem that this condition is independent of reaction dynamics, its dependence is implicity in the values $u_\pm$.

We have thus now seen that wave-pinning is a pattern formation mechanism related to traveling wave solutions, where the speed of the wave-front eventually vanishes and a stable spatial pattern is established. The analysis above was done for a single wave-front in one spatial dimension and in the limit as $\epsilon \to 0$. Similar analysis may be performed for multiple wave-fronts and in higher dimensions. It is found that indeed, at intermediate time scales, the system can support multiple fronts, but as $t \to \infty$ the solution will approach a concentration profile with a single front albeit at a very slow pace [32]. Furthermore, the story is very similar in higher dimensions, but in those scenarios the shape of the domain can significantly influence the propagation of wave-fronts [32].

In order for a cell to become polarized through the wave-pinning mechanism, it would initially be assumed to be in a HSS characterized by $u_\pm (v_0)$ and some local perturbation should push u, in some region of the cell, beyond a threshold value (e.g., $u_m (v_0)$). After a perturbation of sufficient size is applied which perturbed region will quickly converge to $u_\mp (v_0)$ while the position of the transition and the value of v_0 eventually converge to some stable values on longer timescale. According to Eq. (61), the long-term behaviour of the system requires an appropriate value of K as well as ϵ to be sufficiently small. For most biologically-relevant systems, however, one finds that $\epsilon > 0$ and therefore it is of

interest to know what occurs as ϵ grows.

In order to do, one may reformulate Eq. (57) as the boundary value problem of finding a heteroclinic connection between u_+ and u_- and vary ϵ and K through numerical continuation to observe qualitative differences in the stalled waved solution [97]. Notably, the difference between u_+ and u_- decreases as ϵ increases, and the size of the transition region increases, leading to a decreasingly sharp transition between u_+ and u_- as ϵ increases [32]. Moreover, there exists a critical value $\epsilon_c = \epsilon_c(K, D)$ beyond which wave-pinning can no longer occur [32, 97]. This is somewhat surprising given the graded effect that ϵ has on the appearance of the wave-pinning solution. Generally speaking $\epsilon_c = \mathcal{O}(0.2)$, and thus we should be able to observe wave-pinning for system (31)-(36) which has $\epsilon = \sqrt{D_R/(\delta_R L^2)} < \sqrt{0.02\mu\text{m}^2\text{s}^{-1}/(0.025\text{s}^{-1}100\mu\text{m}^2)} = 0.09$ where L is the characteristic length of the cell.

3.5.2 Phenomenology of Cellular Polarization through Wave-Pinning

Cellular polarization may be viewed as a process by which a cell, with initially isotropic distributions of Rac and Rho, switches to a state where there is a significant spatial-gradient in the activities of these two proteins. We have used a toy model to illustrate the phenomenon of wave-pinning where a local perturbation away from a homogeneous steady state leads to spatially segregated regions of high and low activity (i.e., u_+ and u_-, respectively) with a relatively sharp transition between these two levels of activity.

In [32] , the necessary and sufficient conditions this toy model to produce wave-pinning were found to be:

1. A significant difference between the diffusion coefficients of the active and inactive forms of a protein.
2. The WM system with fixed v exhibits bistability.
3. The stability, in the RD setting, of the HSSs obtained from the WM setting with fixed v.
4. An amount of matter which allows for the wave speed given by Eq. (59) to vanish (see constraints in Eq. (61)).

In Section (3.3.1), we have already seen how mutual antagonism between Rac and Rho produces bistability in a WM setting (i.e., condition 2 met). Biochemically, the guanine nuleotide status (i.e., GTP-

bound vs. GDP-bound) of these RhoGTPases is indeed the criterion which regulates their activity. However, their localization within the cell, either cytosolic or membrane-bound, is also an important factor in the activation process as well as the ability of the protein to interact with its downstream effectors [98, 99]. Interestingly, due to the dynamics of shuttling between the membrane and the cytosol [100, 101], it is possible to summarize the complex series of steps into a two-state system where the RhoGTPase are active when bound to the membrane and inactive when cytosolic [28, 31]. This is notable, as proteins in the cytosol and in the plasma membrane exhibit an approximatley 100-fold difference in diffusion coefficients [102], which implies that active Rac and Rho will diffuse significantly more slowly than their inactive forms (i.e., condition 1 is met). In [32], it was demonstrated that stability of the WM system guarantees stability of the HSS provided there is significant difference between diffusion coefficients (i.e., condition 3 is met). Therefore, we should be able to test if condition 4 is met by system (31)-(36) seeing if we can induce wave-pinning by choosing an appropriate initia condition.

In order to do so, we performed stochastic realizations of the RD equation in 2-Dimensions (see Methods). As an initial condition, we set 90% of the domain to be at the uninduced steady state of the WM system (see Fig. 3.2), while the remainer of domain was set to the induced steady state (see Fig. 3.3C). At very short timescales, the sharp transition of the initial condition is smeared by diffusion as one would naively expect. However, at longer timescales, local reaction dynamics dominate and the region which was started at the induced state (with $R = \bar{R}_+$) tends to a state with $R \approx R_+ > \bar{R}_+$ while the region which was started at the uninduced state (with $R = \bar{R}_-$) tends to a state with $R \approx R_- < \bar{R}_-$ (see Fig. (3.3)A). This PDE simulation thus highlights the distinction between the local values of the RD system which are the stable fixed-points $u_\pm\,(v_0)$ discussed in this Section and $\bar{u}_\pm$ the stable fixed-points of the WM system (28)-(30) (see Section (3.5.3) for more details).

Furthermore, the motivation behind using sotchastic realizations of the RD system was to see if stochastic effects could replace the need for asymmetric intial conditions and trigger wave pinning on their own. In order to test this hypothesis, we use a HSS corresponding to the uninduced state as an intitial condition (see dashed line in Fig. 3.4A). The RD system seems to stay in the vicitinity of this intial condition for hundreds of seconds (see Fig. 3.4 B&C), until a local fluctuation which is large enough to induce wave-pinning occurs (see Fig. 3.4 D-F). Once the system reaches a stalled wave solution, it appears to be stable for thousands of seconds (see Fig. 3.4 B&F). This finding represents a first step in producing stochastically polarized cells, as to the best of my knowledge, the stalled wave solution is stable with respect to the fluctuations induced by stochasticity. This topic will be discussed

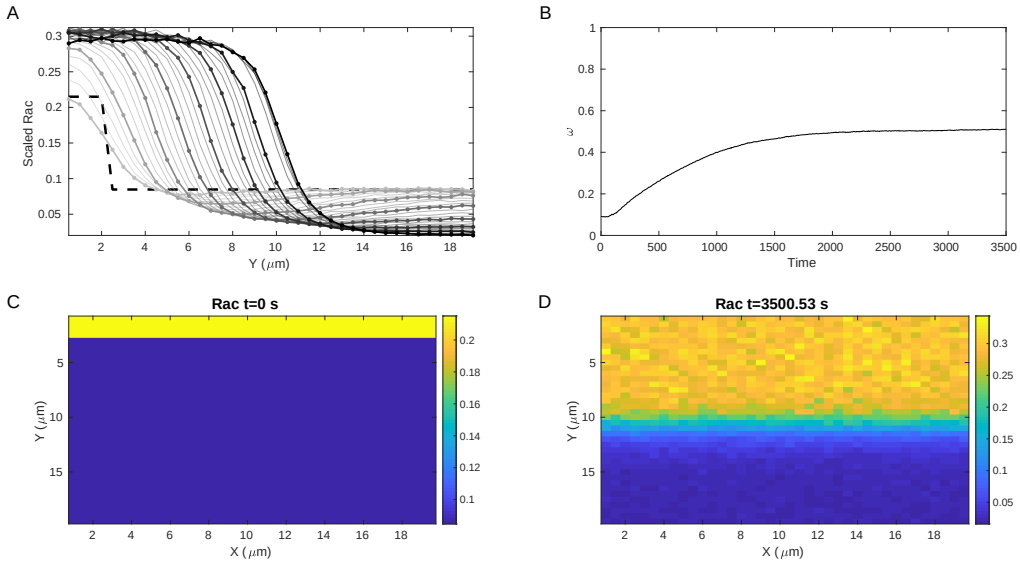

Figure 3.3: Wave-pinning in a 2-dimensional stochastic realization of RD system (31)-(36). (A) Scaled Rac concentration, R, averaged over the spatial coordinate X versus the spatial coordinate Y. The initial condition (dashed black line) was chosen such that 10% of the domain is in the induced state of WM system (28)-(30) while the remainder of the domain is in its uninduced state. Solid lines depict the evolution of the solution towards the stalled wave-pinning solution, where the thick lines transition from grey to black with increasing time. (B) Fractional position of the wavefront, defined as the Y-coordinate where the averaged scaled Rac concentration (panel A) is halfway between its minimum and maximum. (C) Initial and (D) final solutions for R.

in further detail in Section 3.6.0.2.

3.5.3 Wave-Pinning and the Well-Mixed System

We now turn our attention to the steady state solutions of the RD system (31)-(36), and their connection to steady state solutions of the WM system (28)-(29). In particular, in Figure (3.3), we used a spatially imhomogenous initial condition where two parts of the domain were initially at fixed-points of the WM system (e.g., for active Rac $\bar{R}_+$ or $\bar{R}_-$) and observe the emergence of a wave-pinning pattern. The resulting pattern has a single axis of symmetry, and along this axis we see that the solution varies between two limiting values which differ significantly from the fixed-points of the WM system. For the generic system considered in Section 3.5, with variables u and v, we denote these limiting values

$$u_0(t) = u(\theta = 0, t),$$

and

$$u_L(t) = u(\theta = L),$$

where θ is a spatial coordinate along the axis of symmetry which has a length L. Due to the form of the RD system (3) and the use of zero-flux boundary conditions, we may conclude that these limiting are indeed fixed point of the chemical reaction dynamics, generically denoted by $f(u, v)$. For example, with intial conditions characterized by $u_0(0) = \bar{u}_+$ and $u_L(0) = \bar{u}_-$ the system evolves to a steady state $u_0(t) = u_+ > \bar{u}_+$ and $u_L(t) = u_- < \bar{u}_-$ as $t \to \infty$. In this section, we shall explore the relationship between these various fixed points, and develop a framework for computing the fixed-points of the spatially inhomgenous solution from the fixed-points of the WM system, and vice-versa.

3.5.3.1 Fixed-Points in the Well-Mixed System

The stable fixed points of the WM system (50)-(52) (see Fig. 3.2B-D) are given by

$$f_\rho\left(\bar{\rho}_\pm, 1 - \bar{\rho}_\pm, \bar{R}_\pm\right) = 0 \tag{62}$$

$$f_R\left(\bar{R}_\pm, 1 - \left(\bar{R}_\pm + \gamma\bar{K}_\pm\right), \bar{\rho}_\pm, \bar{P}_\pm\right) = 0 \tag{63}$$

$$f_P\left(\bar{P}_\pm, 1 - \bar{P}^*_\pm, \bar{R}_\pm\right) = 0, \tag{64}$$

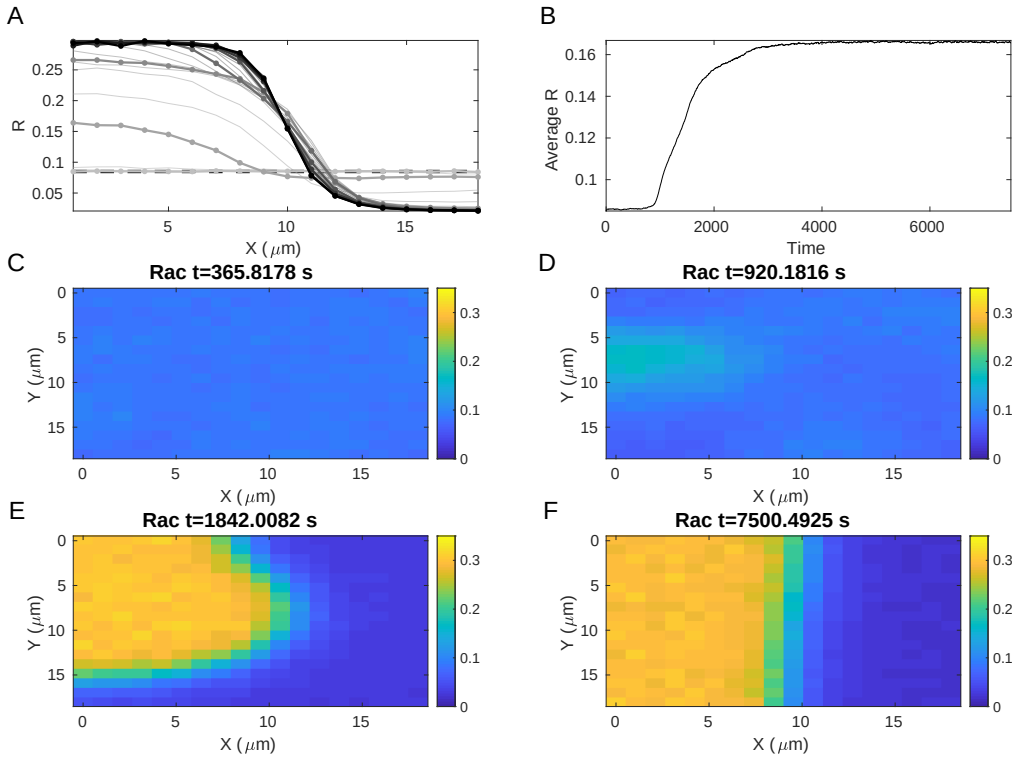

Figure 3.4: Spontaneously induced wave-pinning in a 2-dimensional stochastic realization of RD system (31)-(36). (A) Scaled Rac concentration, R, averaged over the spatial coordinate X versus the spatial coordinate Y. The initial condition was taken to be a HSS corresponding to the uninduced state of WM system (28)-(30). Solid lines depict the evolution of the solution towards the stalled wave-pinning solution, where the thick lines transition from grey to black with increasing time. (B) The value of R averaged over the whole domain versus time, demonstrates that the HSS is stable for hundreds of seconds.

where one may find a single fixed-point by time-integration (e.g. $\left(\bar{\rho}_-, \bar{R}_-, \bar{P}_-\right)$) and obtain the other (e.g. $\left(\bar{\rho}_+, \bar{R}_+, \bar{P}_+\right)$) via numerical continuation.

3.5.3.2 Fixed-Points in the Reaction-Diffusion System

We now wish find the local limiting values (i.e., u_0 and u_L) of the steady-state solution of the RD system (31)-(36). Recall that for chemical species with slowly diffusing active form u and a rapidly diffusing inactive form v, provided appropriate initial conditions, we will eventually see a solution with $v(x,t) = v_c$, $u_0(t) = u_+$, and $u_L(t) = u_-$ as $t \to \infty$, where $f(u_\pm, v_c) = 0$. When considering system (31)-(36), things are slightly different, as the vector-valued $\mathbf{f}$ depends on $\mathbf{u}$ and $\mathbf{v}$ the vectors of active and inactive concentrations of Rho, Rac, and paxillin, respectively. Nonetheless, focusing on the chemical species Rho for now, there will still be at most 2 stable fixed points of the function f_ρ. Denoting the two corresponding values of active Rho, $\rho_\pm$, it is necessary that these values satisfy

$$f_\rho(\rho_\pm, \rho_i, R_\pm) = 0$$

where ρ_i is the global concentration of inactive Rho, and R_+ (R_-) is the value of scaled active rac in $\Omega_+ \subset \Omega$ ($\Omega_- \subset \Omega$) the subdomain where $\rho \approx \rho_+$($\rho \approx \rho_-$). For simplicity, we will assume that there is a unique spatial location for the transition between the two value of ρ, R, and P, i.e.,

$$\rho \approx \rho_\pm \Leftrightarrow R \approx R_\pm \Leftrightarrow P \approx P_\pm.$$

The values of $\rho_\pm$ and ρ_i must jointly satisfy the conservation of matter, given by the constraint

$$\begin{aligned} |\Omega| &= \int_\Omega (\rho + \rho_i)\, d\Omega \\ &\approx |\Omega|\, \rho_i + |\Omega_+|\, \rho_+ + \left(|\Omega| - |\Omega_+|\right) \rho_-. \end{aligned}$$

Therefore, ρ_i maybe be solved for using the expression

$$\rho_i = 1 - \left(\omega \rho_+ + (1-\omega)\, \rho_-\right), \tag{65}$$

where $\omega = |\Omega_+| / |\Omega|$. In order to unambiguously determine the values of $\rho_\pm$, it is also necessary to repeat similar procedures for the local values of R and P. Therefore, given a value of $\omega \in [0,1]$ we

may solve for $\rho_{\pm}$, $R_{\pm}$, and $P_{\pm}$ by simultaneously solving six expressions, given by .

$$f_{\rho}\left(\rho_{\pm}, \rho_i, R_{\pm}\right) = 0 \tag{66}$$
$$f_{R}\left(R_{\pm}, R_i, \rho_{\pm}, P_{\pm}\right) = 0 \tag{67}$$
$$f_{P}\left(P_{\pm}, 1 - P^{*}_{\pm}, R_{\pm}\right) = 0, \tag{68}$$

where ρ_i is given by Eq. 65,

$$R_i = 1 - \left(\omega\left(R_{+} + \gamma K_{+}\right) + \left(1 - \omega\right)\left(R_{-} + \gamma K_{-}\right)\right), \tag{69}$$

and $P^{*}_{\pm}$ ($K_{\pm}$) is given by Eq. (27) (Eq. (26)) evaluated at $x \in \Omega_{+}$ and $x \in \Omega_{-}$, respectively. We note here that the approach for solving for paxillin is slightly different than for Rac and Rho, as its dyanmics cannot be expressed in the form of system (53)-(54). Moreover, from Eqs. 65 and 69 we may conlude that the local values $(\rho_{\pm}, R_{\pm}, P_{\pm})$ of a stalled solution of the RD system with $\omega \in (0, 1)$ is, generally, not a HSS of the RD system, as they do not satisfy the WM matter conservation constraint given by Eqs. 46-49.

Furthermore, we note that, with $\omega = 0$, solving system (66)-(68) is equivalent to finding the LPA steady states described in [84] for RD system (31)-(36). While LPA approximates the local and global dyanmics shortly after a perturbation, the methodology presented here approximates the local and global dynamics as the RD system approaches steady state. Therefore, we will subsequently refer to it as pinned-wave analysis (PWA). While LPA can sometimes be predicitive of wave-pinning, PWA is a purely descriptive methodology which can be used once wave-pinning behaviour has already been established. Nonetheless, in Section 3.6.0.2 we will see some cases where LPA fails to explain wave-pinning while PWA describes the observed behaviour more faithfully.

3.5.3.3 Interpolation of Fixed-Points

We have now seen the systems of equations which must be solved in order to obtain the fixed-points of the WM system as well as the fixed-points which determine the steady-state local values of the RD system. Notably, solving for these fixed points can be reduced to two root finding problems which are nearly identical. We will now present a computational approach for computing one set of fixed-points from the other.

3.5 Pattern-Formation through Wave-Pinning

By inspection of the systems of equations (62)-(64) and (66)-(68), we may see that they differ only in their constraints on the inactive forms of Rac and Rho. In particular, the two stable fixed points of the WM system have two different values of inactive Rac/Rho, while the two local values of Rac/Rho in the RD system share a single value of inactive Rac/Rho. Therefore, we propose interpolating between the two root-finding problems, such that we may obtain the local values of the RD system starting from the stable fixed-points of the WM system. In order to acheive this goal, we define the interpolated inactive Rho and Rac, given by

$$\begin{aligned}\rho_i^{\pm} &= \beta\left(1-\left(\omega\rho_+ + (1-\omega)\,\rho_-\right)\right)\\ &\quad + (1-\beta)\,(1-\rho_\pm)\,,\end{aligned}$$

and

$$\begin{aligned}R_i^{\pm} &= \beta\left(1-\left(\omega\,(R_+ + \gamma K_+) + (1-\omega)\,(R_- + \gamma K_-)\right)\right)\\ &\quad + (1-\beta)\,(1-R_\pm)\,,\end{aligned}$$

respectively, where $\beta \in [0,1]$. We note that

$$\begin{aligned}\lim_{\beta\to 0}\rho_i^- &\neq \lim_{\beta\to 0}\rho_i^+,\\ \lim_{\beta\to 0}R_i^- &\neq \lim_{\beta\to 0}R_i^+,\end{aligned}$$

and

$$\begin{aligned}\lim_{\beta\to 1}\rho_i^- &= \lim_{\beta\to 1}\rho_i^+ = \rho_i,\\ \lim_{\beta\to 1}R_i^- &= \lim_{\beta\to 1}R_i^+ = R_i,\end{aligned}$$

where ρ_i and R_i are given by Eqs. (65) and (69), respectively. Thus, the set of equations

$$f_\rho\left(\rho_\pm, \rho_i^\pm, R_\pm\right) = 0 \tag{70}$$

$$f_R\left(R_\pm, R_i^\pm, \rho_\pm, P_\pm\right) = 0 \tag{71}$$

$$f_P\left(P_\pm, 1-P_\pm^*, R_\pm\right) = 0, \tag{72}$$

with $\beta = 0$ corresponds to system (62)-(64) (i.e., the fixed-points of the WM system) and with $\beta = 1$ the equations correspond to system (66)-(68) (i.e., the local values of the steady-state solution of the wave-pinning system). Therefore, given $\left(\bar{\rho}_{\pm}, \bar{R}_{\pm}, \bar{P}_{\pm}\right)$, the fixed points of the WM system (see Fig. 3.2), we may thus find the values $(\rho_{\pm}, R_{\pm}, P_{\pm})$ which characterize a stalled wave-pinning solution with a fixed value of ω through numerical continuation by varying β from 0 to 1 (see Fig. 3.5). With $\omega \in (0, 1)$ and $\beta = 1$ we can subsequently continue a second parameter p, in order to obtain a PWA diagram which is similar to an LPA diagram, but approximates the steady state solution of the RD system.

Alternatively, one may use system (70)-(72) to perform LPA by setting $\omega = 0$, varying β from 0 to 1, and then varying a second parameter p to obtain an LPA bifurcation diagram. However, our approach of simply varying β, independent of the value of ω or p, is partiuclarly useful for systems which exhibit bistability in the WM setting. In contrast to the LPA approach, our approach allows one to unambiguously assign a one-to-one correspondance between the fixed points of the WM system (e.g., $\bar{u}_{\pm}$) and the local values of the RD system (e.g., $u_{\pm}$), as we do not see bifurcations when varying β , provided the intial guesses satisfy $\bar{u}_{+} \neq \bar{u}_{-}$. On the other hand, using LPA varies a parameter p and yields many branches of stable and unstable equilibria as p pushes the LPA system through various bifurcation points. One must then interpret the resulting LPA bifurcation diagram to determine whether a branch corresponds to a local value or a threshold. For systems with a monostable WM system, this interpretation is straightforward. However, as we shall see in Section 3.6, for a bistable WM system, LPA diagrams can become quite busy and may not be as easy to interpret (compare Figs. 3.5 and 3.6F).

3.6 Local Perturbation Analysis

LPA is a methodology which allows one to determining whether a local perturbation of a given size will produce wave-pinning [36, 37]. Based on what was discussed in Sections 3.5 and 3.5.3, LPA bifurcation diagrams represent the steady-state solution of a RD system described by Eqs. (53)-(54) at short timescales after having been subjected to a local perturbation with an arbitrarily small spatial extent. It is generally described as being predictive of the response of the RD system to a delta dirac-like perturbation [83].

In order to understand the wave-pinning observed in Figures 3.3&3.4, we will first perform LPA on the Rac-Rho sub-model. This will allow us to define some parameter regimes with distinct behaviours

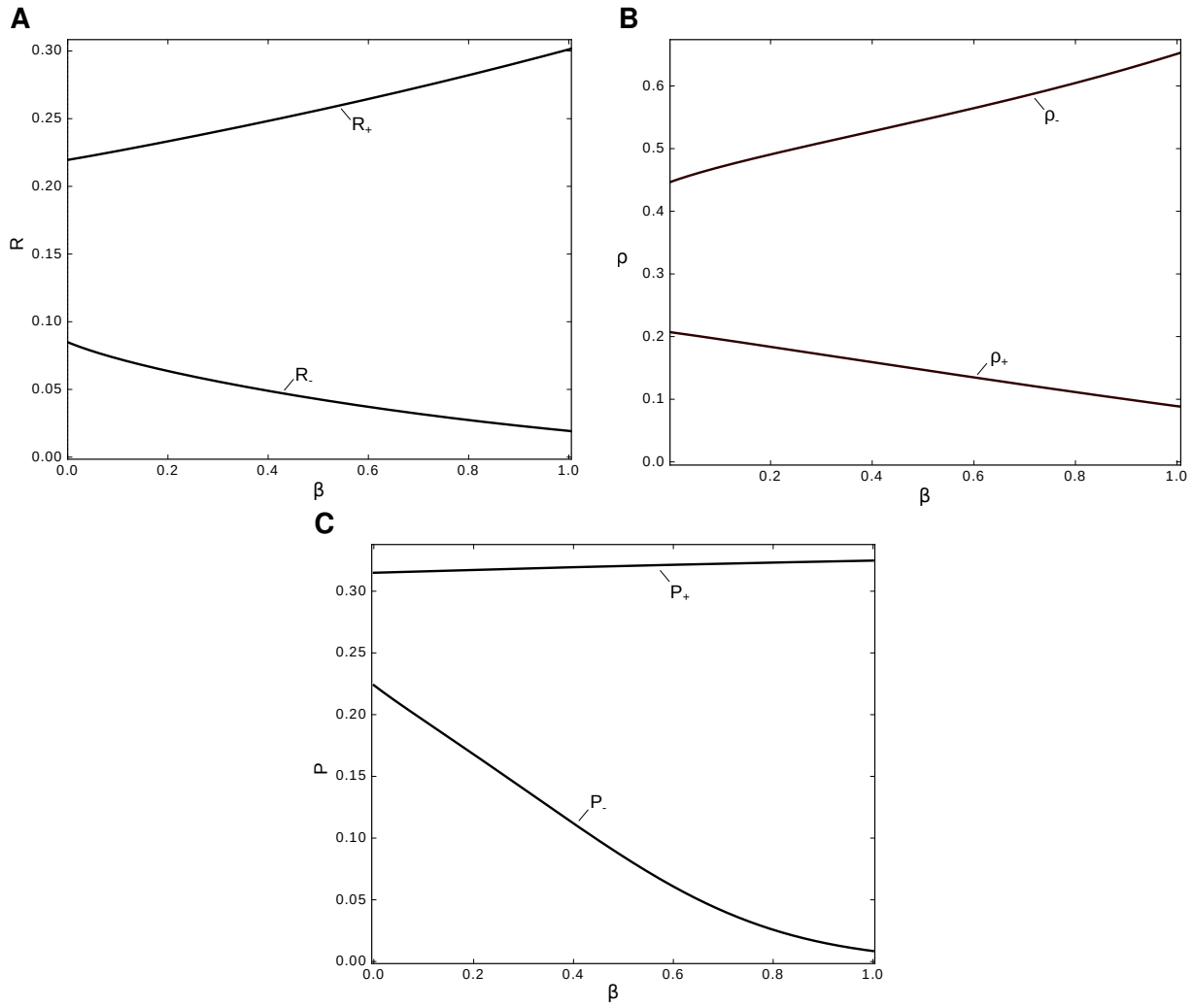

Figure 3.5: Numerical continuation of the stable fixed points of WM system (28)-(30) ($\beta = 0$) to the local values of wave-pinning system (31)-(36) ($\beta = 1$) with a fixed wave-front position ($\omega = 0.54$). The solution of system (70)-(72) is plotted versus β, demonstrating the continuous change in (A) scaled active monomeric Rac, (B) scaled active Rho, and (C) scaled paxillin as the interpolation parameter β is varied. Compare the values for R at $\beta = 1$ with the values of R in the stalled solution in Fig. (3.3)A.

in the RD system. Subsequently, in Section 3.6.0.2, we will carry out the same analysis with the biochemical feeback from of paxillin, and see how this modifies the LPA diagrams and introduces some uncertainties in their interpretation.

3.6.0.1 LPA of the Rac-Rho Sub-model

LPA produces bifurcation diagrams consist of so-called global branches (GB) which describe the HSSs of the RD system as well as local branches (LB) which correspond to short timescale spatially inhomogenous steady states of the RD system. When there is coexistence between a stable GB and a stable LB, wave-pinning is very likely to be possible and thus the system is said to be polarizable. Notably, for the toy model (53)-(54), there is a typically an unstable LB which seprates the two stable branches and acts as a perturbation threshold for triggering wave-pinning. In the absence of any LBs, the only plausible steady state for the RD system is a HSS given by a stable GB. On the other hand, if the GB is unstable then the HSS is assumed to be Turing unstable (LPA and Turing stability criteria are asymptotically equivalent, [103]), such that arbitrarily small perturbations away from the HSS can produce polarization.

In order to gain inuition about the various wave-pinning regimes predicted by LPA, we have applied it to the Rac-Rho subsystem with $n = 2, 3, 4$ (see Fig. 3.6). This was done because most studies use LPA on system with $n = 2$ such that their WM system do not exhibit bistability, while we have used $n = 4$. This produces LPA diagrams that are much simpler than what we see with $n = 4$.

For all values of n we find that there is a parameter regime where the GB is monostable and LPA does not predict the existence of any LBs, we denote this as regime I which cannot produce polarization. In this regime, the unique fixed-point of the WM system corresponds to the unique stable HSS fixed-point of the RD systems. Morevoer, with $n = 2, 3$ we find that the WM system is always monostable with a unique stable fixed point (see Fig. 3.6 A&C). However, LPA shows that, for some parameter ranges, there is a unique stable local and global branche which are separated by an unstable local branch (see Fig. 3.6 B&D). This suggest that RD system both a HSS and a spatialy inhomgenoues fixed-point and thus wave-pinning is possible, provided the system receives perturbation of appropriate magnitude and direction. Such a configuration is characteristic of the parameter regime which we denote regime II, to which we may append a super-scripted + (-) to denote that the stable LB is above (below) the GB. Moreover, for $n = 2, 3$ we find that there exists a parameter regime where the unique

GB is unstable and there are two stable LBs on either side of the GB, which we associate with a Turing instability and denote regime III. Regimes II and III are separated by two transcritical bifurcations, TR1 and TR2, which mark the point where a stable GB loses its stability.

With $n = 4$, things become more complex. Firstly, there is bistability in the WM system (see Fig. 3.6E), which means that there will be regimes with three GBs. Furthermore, depending on the location of the trancritical bifurcations, these GBs may be stable or unstable. Generally, a GB loses stability as it pases through a transcritical bifurcation. With $n = 4$, the transcritical on the uninduced branch (TR1) is to the right of saddle-node bifurcation on the induced branch (SN1), while the trancritical on the induced branch (TR2) is to the left of the saddle-node on the induced branch (SN2). Between, SN1 (TR1) and TR2 (SN2) there is a single stable GB produced by the uninduced (induced) branch while the unstable saddle-fixed point of the WM system and the induced (uninduced) branch produce unstable GBs. Intrestingly the folds in the GBs are mirrored in the LBs, producing four more saddles nodes that we denote SN1$'$, SN2$'$, SN1$''$, and SN2$''$ (see Fig. 3.6F). Together, this generates a complex configuration where there are three stable and three unstable LBs, in addition to the aforementioned stable GB and two unstable GBs. Collectively, this defines regime IV, to which we may append a super-scripted + (-) to denote that there are two stable LBs above (below) the stable GB. Unlike in regime II$^{\pm}$, regime IV$^{\pm}$ may be polarized by perturbations in either direction. Finally, between TR2 and TR1 there is a regime where there are two stable GBs separated by an unstable GB, which is in turn seprated from the two stable GBs by two unstable LBs. The stable GB above (below) the unstable GB is also separated from an upper (lower) stable LB by another unstable LB. This configuration characterizes regime V, whose most notable feature is the coexistence of two stable GBs (i.e., the RD system is truly bistable in the sense of having two HSSs).

We have sumarized the regimes described above in Table 3.1. Regimes I, II, and III have been widely described in studies on wave-pinning that use LPA [30, 31, 34, 37, 83, 84, 103, 104]. Regime III is typically avoided in models of polarizable cells, as no stimulus is needed to produce polarization. Such a configuration is odds with the experimental findings these studies sought to understand.

Regimes IV and V have been described in [105] which represents, to the best of our knowledge, the only work where LPA was performed on a WM system that exhibits bistability for the parameter range used to perform LPA. In [105], one more regime, a variant of regime IV, was found which is not exactly as those described here. Interestingly, some of the earliest work on wave-pinning (prior to the

Regime	Classification	Description
I	Stable HSS	One stable GB, no LB.
II	Polarizable	One stable GB, one stable LB with an unstable LB separating the two.
III	Unstable (Self-Polarizing)	The only GB is unstable, two stable LBs located on both sides of the GB.
III′	Tri-Unstable (Self-Polarizing)	Three unstable GBs, four (two) stable (unstable) LBs distributed evenly on either sides of the three GBs.
IV	Polarizable (Bidirectional)	One stable GB and two unstable GBs, three stable LBs with two on the same side of the stable GB as the two unstable GBs. Three unstable LBs, with one separating the stable GB from the unstable GBs, one separating two stable LBs, and one separating separating the stable GB from a stable LB.
V	Polarizable (Bistable)	Two stable GBs, one unstable GB separating the two. Two stable LBs, one on either side of GBs. Four unstable Gbs, two separating the GBs with opposite stability between, and two separating the stable GBs from the stable LBs.

Table 3.1: Summary of wave-pinning regimes of the Rac-Rho sub-model as predicted by LPA. See Figures 3.6 and 3.7 for graphical representations.

development of LPA) did indeed use bistable WM models [35], where they also found that polarization could be produced using monostable WM systems. Subsequent studies seem to have mainly focused on using LPA to study the monostable WM case [31, 32, 34, 37, 104]. While we may *a posteriori* understand the polarization of monstable system from LPA diagrams, it is likely that, at the time, the authors of wave-pinning studies preffered the monostable case due to its simplicity. However, given that the bistable case was eventually investigated using LPA, it also possible that there is a subtle richness in the dynamics of the bistable case which was deemed unecessary during the developmental period of the field and was only investigated in detail more recently.

Two Parameter LPA We have now seen how the complexity of the LPA diagram increases with increasing Hill-coefficient n and the regimes associated with various configurations of GBs and LBs. In

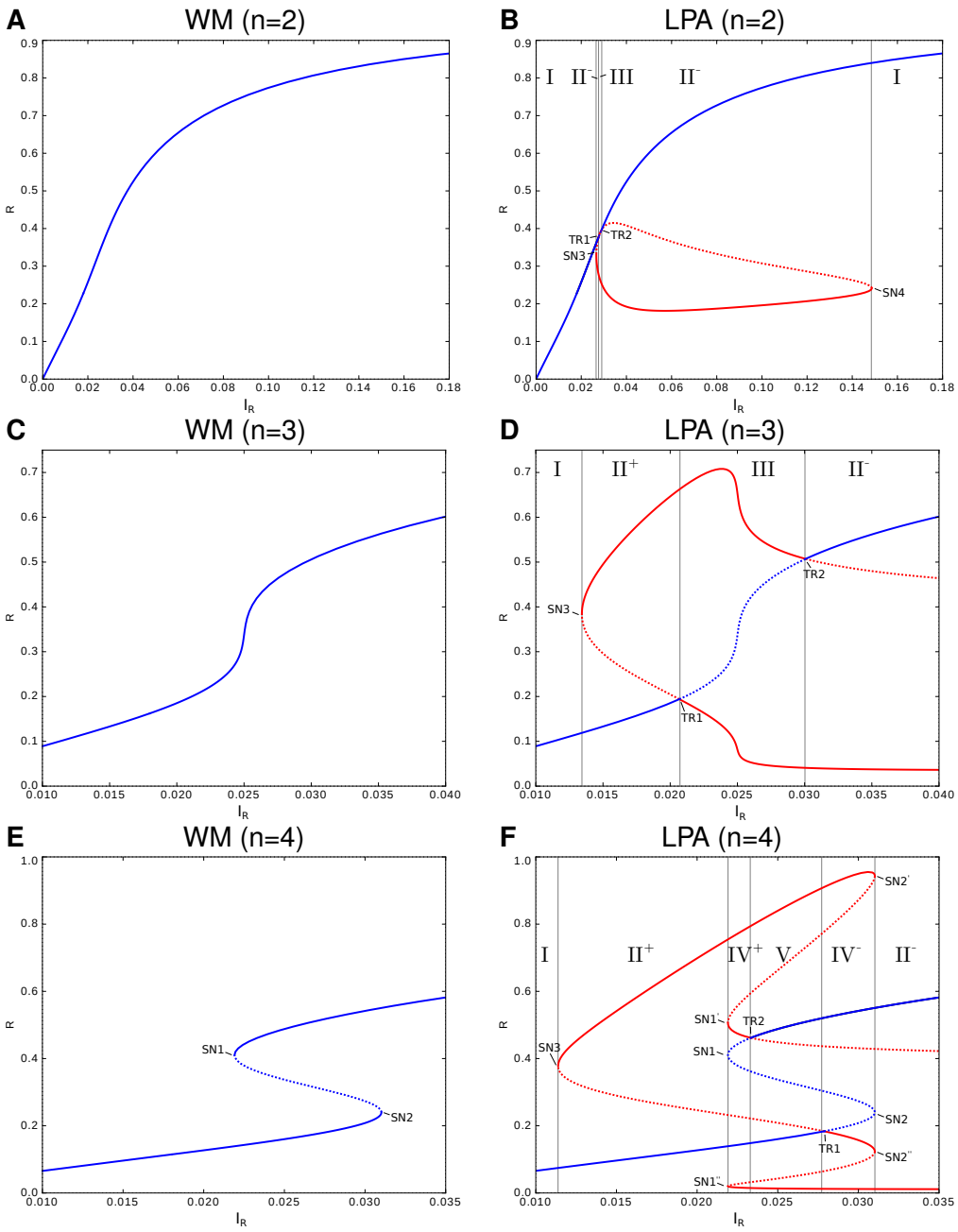

Figure 3.6: Local perturbation analysis applied to system (31)-(36) with P and P_i removed. Numerical continuation was used to find the fixed-points of the LPA system (Eqs. (66)-(67) with $\omega = 0$) as the parameter I_R is varied. The degree of the non-linearity, n, increases from top to bottom with $n = 2$ (A&B), $n = 3$ (C&D), $n = 4$ (E&F). The left column depicts the fixed-point(s) of the WM system, whereas the right column depicts the fixed-point(s) of the LPA system. For the LPA system, blue lines are used to depict GBs (i.e., branches of fixed-points of the WM system) and red lines are used to depict LBs where $R_+ \neq R_-$, (i.e., branches of fixed points of the LPA system where R_+ is perturbed away from R_-). For both colours, stable fixed-points are depicted as solid lines while unstable/saddle-type fixed points are depicted as dashed lines. Grey lines are used to delineate different wave-pinning regimes predicted by LPA, where the roman numerals correspond to the regimes described in Table 3.1.

order to summarize these effects we have performed a two-parameter bifurcation on the LPA system for the Rac-Rho sub-model (see Fig. 3.7). This shows how the various regimes grow, shrink, appear, and disappear as the parameters n and I_R are varied. In particular, it illustrates how the polarizability (i.e., the existence of regime II) is produced by a cusp bifurcation, CP1, just below $n = 2$ and how SN4 which emerges from this cusp bifurcation quickly tends to $I_R \to \infty$ as n increase beyond $n = 2$. On the other hand, the bistability of the WM system is produced by a second cusp bifurcation, CP2, near $n = 3$, from which emerge SN1/SN2 on the GB and the other associated saddle-nodes on the LBs. In particular, it shows that SN1 (SN2) does indeed coincide with SN1$'$ and SN1$''$ (SN2$'$ and SN2$''$) for all parameter values. Interestingly, the transcritical bifurcations cross one another near $n = 3.65$, producing the bistable GBs in regime V. However, between where the transcriticals meet and CP2, there exists another regime which we have not yet discussed (see Fig. 3.7). Due to the positions of the transcriticals realtive to SN1/SN2 in this regime, the coexisiting GBs are all unstable such that this regime will behave very similarly to regime III and converge to a LB with arbitrarily small perturbations. Thus we denote this regime as III$'$ (see Table 3.1).

3.6.0.2 LPA with the influence of Paxillin

Now that we have seen how LPA can predict the wave-pinning behaviour of a RD system which accounts for the mutual antagonism between Rac and Rho, we wish to see how the results of LPA change with the inclusion of the paxillin's feedback on Rac activation. The effect of various feedbacks onto RhoGTPases have been investigated using LPA [84, 104, 105], where it has been generally found to perturb the LPA diagrams by changes in stability of some GBs and the creation of Hopf bifurcations.

As before, we carry out our analysis for increasing values of n. For $n = 2.6$ we find an LPA configuration which is reminiscent of that in Figure 3.6B, but with the stability of almost all the branches switched (see Fig. 3.8 A&B). In fact, we are quite puzzled as to why the GBs outside of the two transcritical bifurcations are LPA unstable. This suggests that there are parameter values where there are no stable attractors, which is indeed concerning and at odds with PDE simulations, although this has also been reported in [84] and [105].

To the best of my knowledge, I have implemented the feeback of paxillin in a manner which is equivalent to what was done in [84], [104], and [105]. That is, assuming that the molecules which feedback onto Rac and Rho (i.e., paxillin) are slowly diffusing and thus have only local values (see

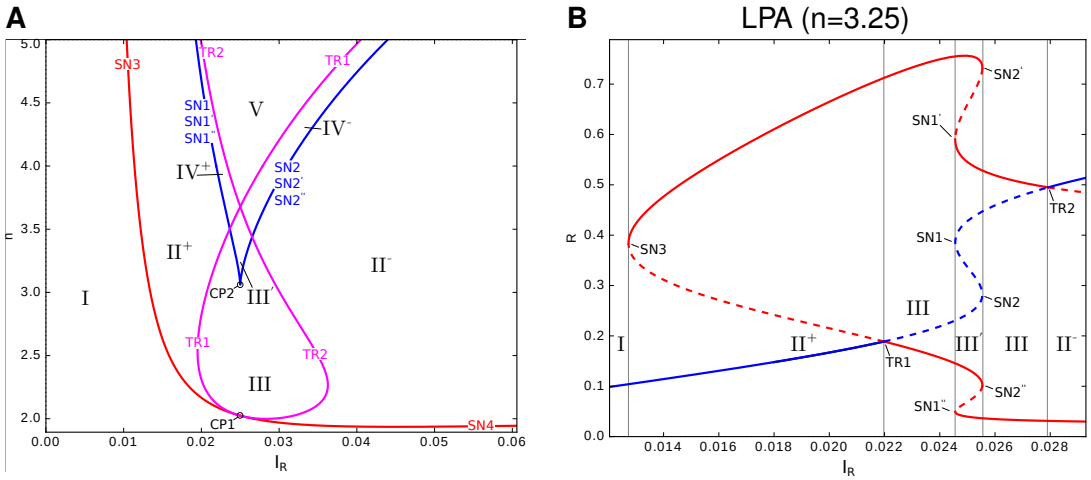

Figure 3.7: A graphical summary of the wave-pinning regimes. (A) Two paramter LPA illustrates the shape of regimes I-V and identifies a novel tri-unstable regime III′ which has three unstable GBs. The solid red line depicts the (I_R, n)-values of the saddle-nodes SN3 and SN4 on the LBs. The solid blue line depicts the (I_R, n)-values of SN1 and SN2 on the GBs which coincide with SN1′ (SN1″) and SN2′ (SN2″) on the LBs, respectively. The solid magenta line depicts the (I_R, n)-values of the trancritical bifurcations TR1 and TR2 which are at the intersection of the GBs and the LBs. Co-dimension 2 cusp bifurcations are indicated by open symbols and labelled with the abbreviation CP. Coloured text is used to indicate which bifurcations the lines correspond to, and black roman numerals are used to indicate the regimes delineated by these bifurcations. (B) One parameter LPA for $n = 3.25$ has three unstable GBs in bistable region of the the WM system. Such a configuration is very reminiscent of regime III, with some added LBs. Hence it is denoted regime III′. Lines are coloured according to the same scheme as in Figure 3.6.

Eq. 68). Despite such an approach, the stability of the branches predicted by LPA does not seem to be correct. It is possible that this effect is due to using reaction dynamics that only conserve the "slow" chemical species (see Section 3.4.1). However, we have not yet had the chance to perform LPA using Eqs. 44-45.

Nonetheless, we find that as we increase n to 3 we see a configuration comparable to Figure 3.6D, where the issues with stability seem to persist, and additionally four Hopf bifurcations appear forming small stable branches on the otherwise unstable LBs (see Fig. 3.8 C&D). Out of these hopf bifurcation are born some stable and unstable periodic orbits (data not shown, due to computer problems). Notably, the right-most Hopf has a stable periodic orbit which terminates in a homoclinic as it hits the unstable GB above it. The two left-most Hopf have stable orbits which form a periodic loop joining the two Hopfs. Finally, the middle Hopf, which is on the GB between the two trancriticals, produces an unstable periodic orbit which terminates in a homoclinic when it collides with the unstable LB below it. Given that we do not trust the stability of the GB and the LBs, it is difficult to say what the periodic orbits represent.

In [84], Hopf bifurcations and stable periodic orbits were associated with periodic spatio-temporal patterns. Preliminary analysis of our RD system through PDE simulations does not seem to support such a beahviour, although in [84] the location of the Hopf bifurcations were only approximately predictive of the location of periodic patterns. In [105], the periodic orbits observed due to feedback typically terminated in homoclinics and a canard-like expansion of the periodic orbits was observed. This meant that orbits only existed for very small parameter regimes and thus they were deemed unimportant. It remains unclear what the Hopfs and periodic orbits mean for our system.

With $n = 4$, we find a diagram with a very similar appearance to Figure 3.6F, with an additional 6 Hopf bifurcations (see Fig. 3.8 E&F). Given that we know wave-pinning occurs for $I_K = 0.009\,\mathrm{s}^{-1}$ (see Fig. 3.3) and that there is no stable elevated LB at this parameter value, it is clear that the LPA fails to predict the behaviour of the PDE when we incorporate the feedback of paxillin.

Two Parameter LPA It is clear that something is not quite right with LPA once we include the effects of paxillin on Rac activation. In order to remedy this we have tried to (i) make paxillin a single global value, (ii) fix paxillin to a constant value, and (iii) reduce the degree of non-linearity in paxillin activation (while leaving Rac and Rho dynamics unchanged). None of these approaches have made significant differences in the stability of the LPA diagram. However, given the very similar shapes that

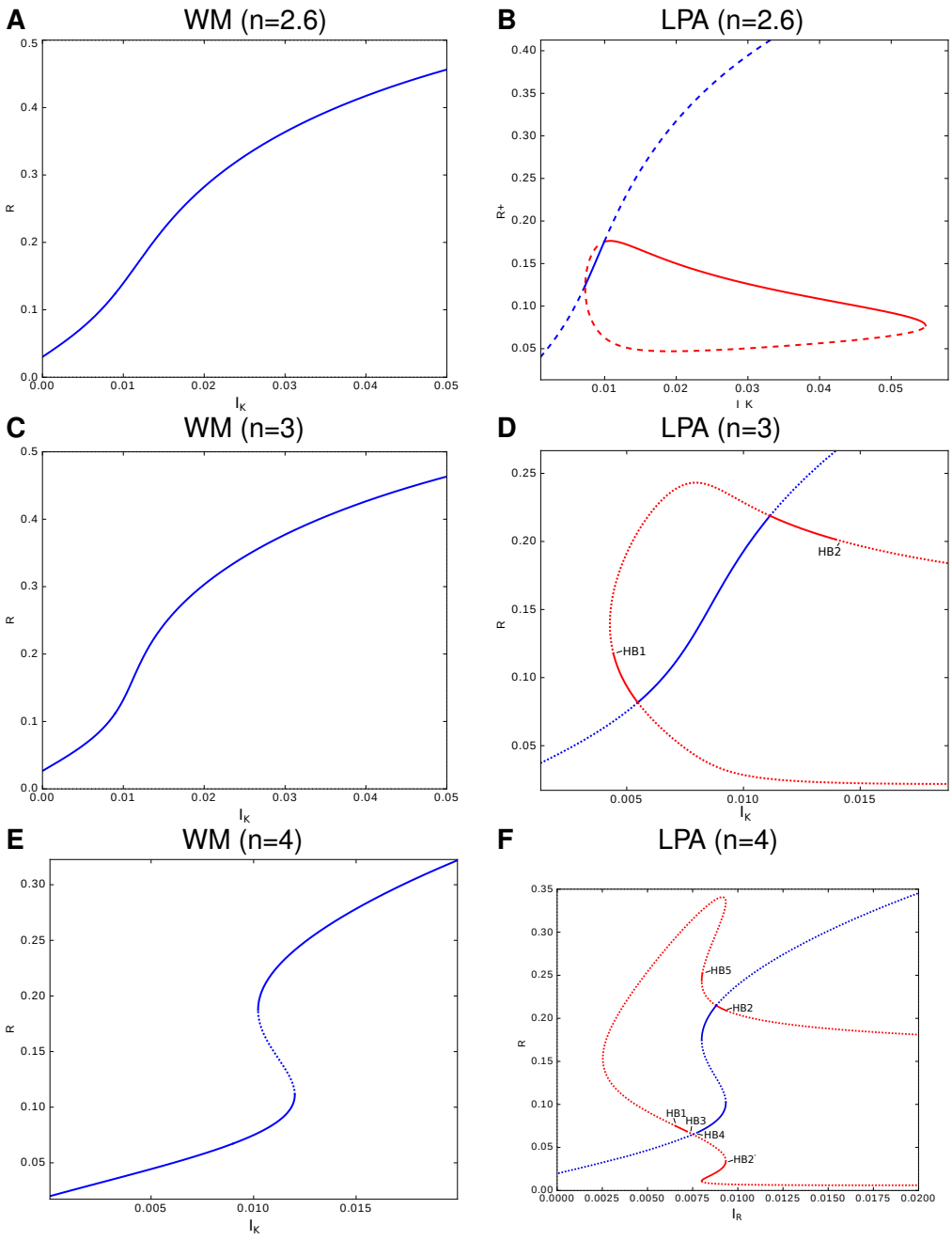

Figure 3.8: Local perturbation analysis applied to the full system (31)-(36). Numerical continuation was used to find the fixed-points of the LPA system (Eqs. (66)-(68) with $\omega = 0$) as the parameter I_K is varied. The degree of the non-linearity, n, increases from top to bottom with $n = 2.6$ (A&B), $n = 3$ (C&D), $n = 4$ (E&F). The left column depicts the fixed-point(s) of the WM system, whereas the right column depicts the fixed-point(s) of the LPA system. Lines are coloured and patterned according to the same scheme as in Figure 3.6. Notice that many of the GBs have switched stability compared to their counter-parts in Figure 3.6, as well as the appearance of many Hopf bifurcations (labelled with HB).

these LPA diagrams have to the Rac-Rho sub-model, it seems plausible that it is only their stability properties which are incorrect. Therefore, in order to see how the various Hopf bifurcations arise, we computed a two-parameter bifurcation diagram in the (I_K, n)-plane (see Fig. 3.9). We find very similar results to what was seen in the (I_R, n)-plane for the Rac-Rho sub-model (see Fig. 3.7), but with the addition of many Hopf bifurcations. In general, we can see that more and more Hopf bifurcations appear with increasing n.

Firstly, it is likely that the diagram is incomplete and is missing a few Hopf bifurcations. Secondly, based on the bifurcations we have found there are at least 28 different parameter regimes when paxillin feedback is included, although it is likely that many of them will be equivalent. For this reason, we have not characterized the behaviour in all the various regimes. Nonethless, given the similar appearance between Figures 3.7 and 3.9, we propose ignoring the Hopf bifurcations in Figure 3.9 and interpreting parameter regimes based on the positions of the transcritical and saddle-node bifurcations (i.e., using the regimes defined in Table 3.1).

In Figure 3.4, we can see that a stalled wave solution in acheived attained without the need for any externally imposed perturbation/asymmetry. Given that [50] used values of $I_K = 0.009\,\mathrm{s}^{-1}$ and $n = 4$, it seems likely that the stochastically induced wave-pinning observed in Figure 3.4 is caused by the model being in the Turing unstable regime III′. Turing unstable regimes have typically been avoided in the literature as cells are assumed to need some signal to polarize [37], but they may be quite useful for our purposes. In order to test this prediction, we increased n to 4.25, which should be in regime V where a perturbation is required to produce wave-pinning. Interestingly, when system (31)-(36) is simulated in this regime, we do not observe wave-pinning without an applied perturbation. This suggests that although the one-parameter bifurcation diagrams cannot be trusted when paxillin feedback is included, the two-parameter bifurcation diagrams are still useful in predicting behaviour of the RD system.

Furthermore, these results suggest that a Turing instability is indeed responsible with the stochastically-induced wave-pinning in Figure 3.4. Further work should be done to invistigate differences in dynamics in regimes III and III′, in particular how they behave in stochastic simulations and comparisons with deterministic simulations. A more thorough investigation may help to elucidate how to obtain systems which transient polarization in a stochastic setting. However, for the time being, the major obstacle for such a phenonmenon seems to be the fact that the LBs are too far away from the GBs to allow for

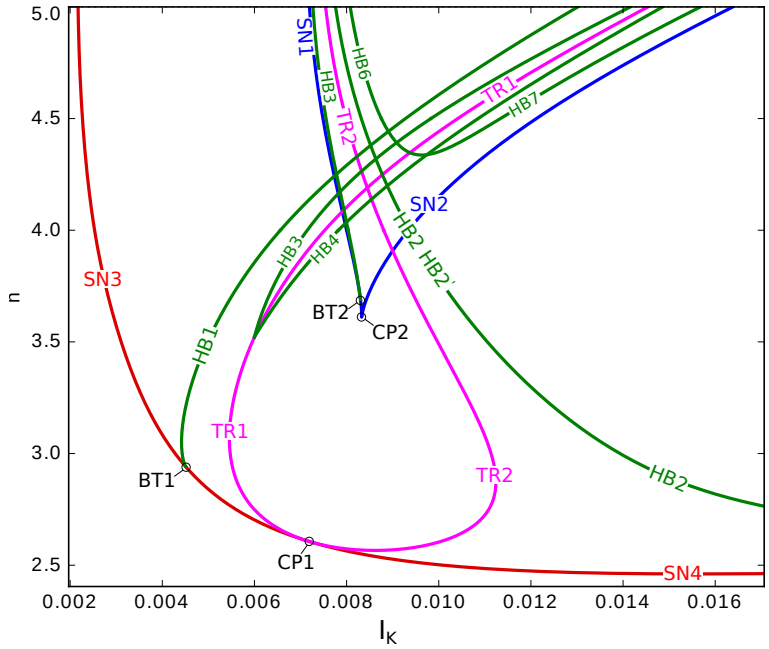

Figure 3.9: Two parameter LPA with with feedback from paxillin onto the Rac-Rho sub-model. The solid red, blue, and magenta lines depicts the same values as in Figure 3.7, but in the (I_K, n)-plane. Solid green lines depict the (I_K, n)-values of various Hopf bifurcations. Co-dimension 2 Bogdanov-Takens and cusp bifurcations are indicated by open symbols and labelled with the abbreviation BT and CP, respectively.

stochastically-induced polarization switching (see Section 5.3 of [105] for some strategies to remedy this).

3.7 Influence of Paxillin on Wave Pinning

The phosphorylation of paxillin has been shown experimentally to significantly influence both adhesion dynamics and cellular motility. We have experimental collaborators who use various genetically modified versions of paxillin, and there is interest in deciphering the contributions of adhesion dynamics and biochemical signaling (e.g., paxillin's effect on Rac activation) on the observed phenotype. Our group has published two studies on the topic [50, 63], where conflicting results about paxillin's influence on polarization were found. In [50], it was found that, in a deterministic RD setting, wave-pinning could be observed by choosing asymmetric initial conditions. Furthermore, it was found that by increasing the maximal phosphorylation rate of B wave-pinning is abolished at $B \approx 22.2\,\mathrm{s}^{-1}$. On

the other hand, in [63] we used a stochastic approach, similar to what is presented in Section 3.2.2, where wave-pinning was never observed in the absence of a constitutive gradient in reaction rates. Such a discrepancy is surprising, as both studies effectively use the same model. However, during the preparation of this chapter, I have discovered some oddities in the chemical propensity calculations of [63], and, after fixing them, we thankfully do indeed see wave-pinning occur in the stochastic implementation (e.g., see Fig. 3.3). Given these findings, we wished to investigate the phenomenon in more depth to see if we can understand the effect of B on wave-pinning.

Due to the ambiguities which show up in LPA diagrams when paxillin feedback is incorporated, we first investigate this question through PDE simulations. Given that $B \approx 22.2\,\mathrm{s}^{-1}$ was previously found to be the limit for exhibiting wave-pinning, we have chosen to perform simulations using $B = 40\,\mathrm{s}^{-1}$ which, according to the findings in [50] should be well beyond the threshold in B for producing a polarized state (i.e., wave-pinning). To be comparable to the simulations in [50], we have chosen a 1-dimensional (2-dimensional) domains for the deterministic (stochastic) simulations with a characteristic size of 10 μm. For initial conditions, in 90% of the domain R, ρ, and P were set to the values of the uninduced state, and a small (10%) region was perturbed by starting it near the induced state (see dashed line in Fig. 3.10B). Interestingly, we do indeed observe wave-pinning for both the deterministic and stochastic realizations of the RD system (see Fig. 3.10 A&B). In order to be reconcile this observation with the findings in [50], we also performed simulations where the initial condition for R and ρ are HSSs and only P is perturbed. Using a value of $P = 0.24$ inside the perturbed region and $P = 0.22$ in the rest of the domain, we can observe wave-pinning for a value of $B = 3\,\mathrm{s}^{-1}$ (see Fig. 3.10C) while for $B = 40\,\mathrm{s}^{-1}$ the system converges to a HSS that corresponds to the induced state (see Fig. 3.10D). In light of this result, given that a unique initial condition was used in [50] for varying values of B, it seems most likely that the observed loss in polarization was likely due to a the initial condition being inadequate for producing wave-pinning for $B > 22.2\,\mathrm{s}^{-1}$. This finding is not surprising given what we have seen about LPA, where the threshold for triggering wave-pinning varies with model parameters.

In order to further understand these findings, we have performed LPA and PWA on system (31)-(36) with B as the bifurcation parameter (see Fig. 3.10 E&F). As noted in the previous section, the stability of LPA diagrams with paxillin feedback cannot be trusted, but the location of local branches can still be partially informative about wave-pinning. Interestingly, LPA does not predict the existence of any LBs above the unique GB at $B = 40\,\mathrm{s}^{-1}$, suggesting that wave-pinning should not occur in that parameter range. Obviously, this prediction is incorrect as we have seen wave-pinning in both the deterministic

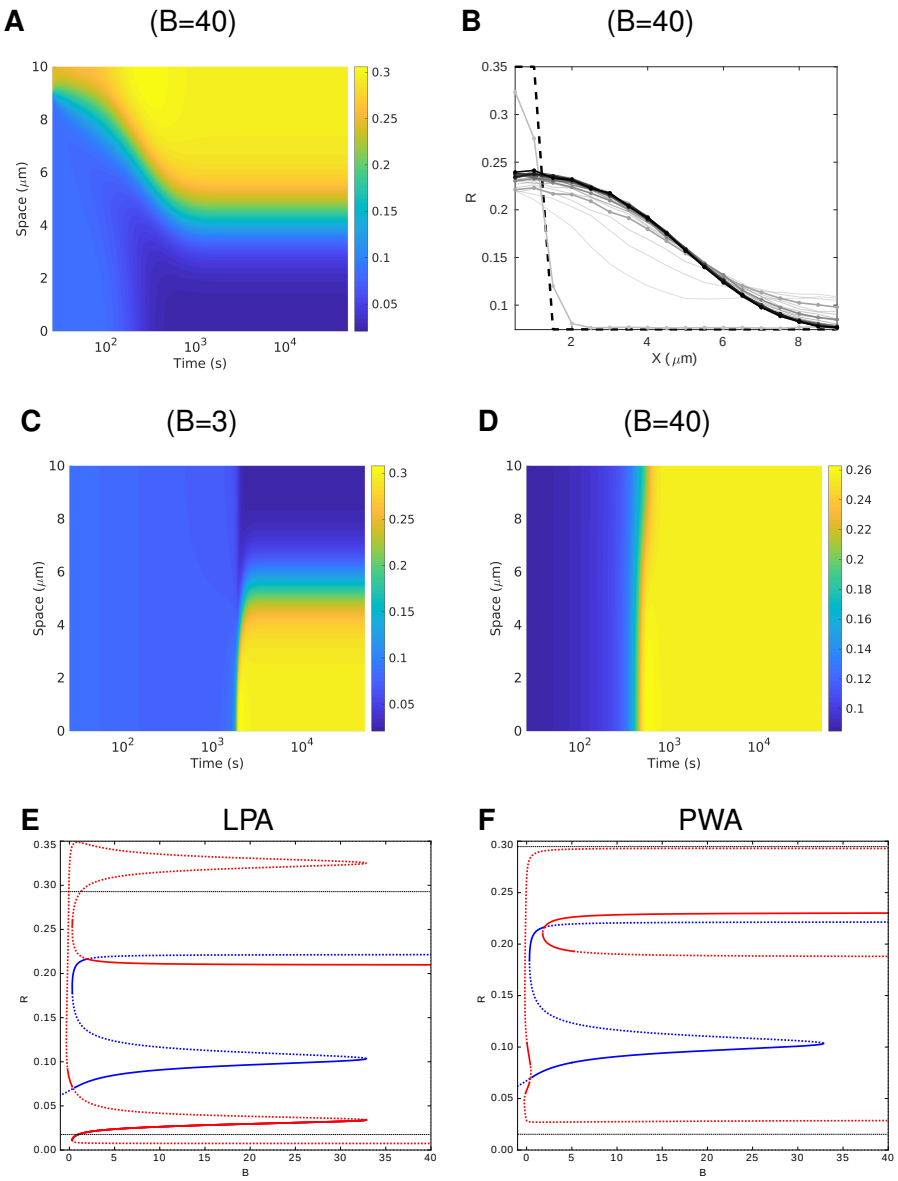

Figure 3.10: The effect of paxillin phosphorylation rate, B, on wave-pinning. (A) Kymograph of the scaled Rac concentration, R, in a 1-dimensional deterministic implementation of the RD system (31)-(36) with $B = 40\,\mathrm{s}^{-1}$. An asymmetric initial condtion leads to the development of a wave-pinning solution. (B) R averaged over the spatial coordinate Y versus the spatial coordinate X as predicted by a 2-dimensional stochastic realization of the RD system. The initial condition (dashed black line) evolves towards a stalled wave-pinning solution, as depicted by the thick solid lines which transition from grey to black with increasing time. (C&D) Kymogrpahs of R with initial conditions given by $P = 0.24$ in the perurbed region (i.e., the elevated part of the dashed line in panel B) and $P = 0.22$ in the unperturbed region. This intial condition triggers wave-pinning when (C) $B = 3$ but not when (D) $B = 40\,\mathrm{s}^{-1}$, similar to the observed loss of wave-pinning at high values of B in [50]. (E) LPA and (F) PWA applied to the RD system with the limiting values of R in panel A depicted as a two black dashed lines, coloured lines use the same scheme as Figure 3.6. LPA fails to explain the development of wave-pinning pattern at $B = 40\,\mathrm{s}^{-1}$, as there is no LB above the GB. On the other hand, PWA predicts a LB above the GB at $B = 40\,\mathrm{s}^{-1}$ which allows us to understand the development of a polarized pattern in panel A.

and stochastic implementations of the RD system. On the other hand, PWA with a value of $\omega = 0.6$ (estimated from Fig. 3.10A) does indeed predict a LB above the unique GB for $B = 40\,\mathrm{s}^{-1}$. What is more, the LBs of the PWA diagram provide reasonable approximations for the limiting values of the deterministic implementation of the RD system. Therefore, although neither methodology perfectly captures the wave-pinning outcome, PWA can be better reconciled with the observed behaviour of the PDE system.

3.8 Cellular Potts Simulations

In order to determine how the results of the analysis presented in the previous sections affect cellular migration, we have used the CPM to produce phenomenological simulations of cells that protrude where Rac is high and contract where Rho is high. The CPM models cells as a a stochastically evolving set of points, typically on a uniform square grid, where the set of points is evolved in discrete steps.

More specifically, the CPM assigns a value to each position in space; for example, the simplest implementation must distinguish between the spatial positions that are ocuppied by the cell (e.g., those positions can be given a value of 1) and those that are not (with a value of 0). The configuration of the system is updating by choosing pairs of points and copying the value from one point to another. This copying of values, or "spin-flip"-ing, may be done repeatedly to produce a new cellular configuration, however we use a single spin-flip. Each new configuration is accepted or rejected according to a Metropolis acceptance criterion, given by

$$P_{\mathrm{acc}} = \min\left\{1, \exp\left(-\Delta H/T\right)\right\},$$

where P_{acc} is the probability of accepting the new configuration, ΔH is the change in the system's Hamiltonian between configurations, and T is a "temperature" parameter. In order to obtain sets of points that behave as a cell, it is critical to specify an appropriate Hamoltonian for the system. A common choice in the literature is to use the following expression for the Hamiltonian,

$$H_0\left(A, P\right) = \lambda_A\left(A - a\right)^2 + \lambda_P\left(P - p\right)^2 + JP,$$

where A (P) is the current area (perimeter) of the cell, a (p) is the "rest area" ("rest perimeter") of the cell, λ_A (λ_P) is the energetic cost of increasing the area (perimeter) by 1, and J is the energetic cost

per unit length of the cell-medium interface. For two configurations, denoted simply by 1 and 2, the change in Hamiltonian going from configuration 1 to configuration 2 is given by the expression

$$\Delta H_0 = H_0\left(A_2, P_2\right) - H_0\left(A_1, P_1\right),$$

where A_1 (P_1) is the area (perimeter) of configuration 1, and A_2 (P_2) is the area (perimeter) of configuration 2. We furthermore apply a connectivity constraint on the system, where any configuration that exhibits two distinct cells is assumed to have an infinitely large value of H_0. The metropolis acceptance criterion will cause the system to minimize its energy over time, while allowing for fluctuations around some optimal configuration. In order to make efficient use of computational resources, we only consider spin flips that change the system, i.e., between a point inside the cell and another point outside the cell or vice versa.

Simulations with this type of Hamilitonian will produce cells that exhibit random shape fluctuations, but will not exhibit the type of biased displacement we would expect from the biochemical activity of the RhoGTPases. In order to account their effects on the actin cytoskeleton, we modify the the Hamilitonian by adding the following term

$$\Delta H_{\text{chem}} = \begin{cases} -\beta_R\left(R - R_{eq}\right) + \beta_\rho\left(\rho - \rho_{eq}\right) & \text{if the cell protrudes} \\ \beta_R\left(R - R_{eq}\right) - \beta_\rho\left(\rho - \rho_{eq}\right) & \text{if the cell contracts} \end{cases},$$

where β_R and β_ρ are positive parameters, R_{eq} (ρ_{eq}) is the mean scaled Rac (Rho) activity throughout the cell, and R (ρ) is the local value of scaled Rac (Rho) activity estimated from the current state of the RDME simulation at the point inside the cell that partakes in a given spin-flip. This Hamiltonian favours protrusion where Rac is elevated and contraction where Rho is elevated, with the magintudes of β_R and β_ρ and the time-evolution of the RDME simulations governing the relative likelihood of these two outcomes.

By defining the change in the Hamiltonian as

$$\Delta H = \Delta H_0 + \Delta H_{\text{chem}},$$

we couple the CPM to the RDME simulations detailed in Section 3.2.2. However, in order to properly couple these two simulations approaches it is necessary to choose a timescale with which to update the

cellular configuration (i.e., the time between two succesive MCSs). In order to choose this timescale we make the following observations. CPM simulations require a large number spin-flip attempts before the the cellular configuration changes appreciably, motiviating the definition of a "Monte Carlo Step" (MCS) where a simulation with N grid points undergoes N spin-flips attempts. In some sense, this defines an iteration-scale for the CPM simulations, which we would like to convert to a time-scale so that we can run the CPM simulations in conjunction RDME simulations. In order to do so, we note that it is very unlikely for a cell boundary to move forward by more than 2 grid points in a single MCS, thus defining the maximum length-scale of the MCS as $2h$ where h is the grid spacing. Furthermore, CHO-K1 cells also have typical maximum migration speed of $v_{max} \approx 3\,\mu$m/min. Therefore, we propose performing MCS steps at time itervals of

$$\Delta t = \frac{2h}{v_{max}},$$

where we have typically used $\Delta t \in [20\,\text{s}, 60\,\text{s}]$. Furthermore, in order to prevent sudden and drastic cell shape changes from abolishing the effects of chemical reactions, the MCS is sub-divided into N_{MCS} sub-steps of N/N_{MCS}spin-flips that are performed at smaller time intervals of $\Delta t/N_{\text{MCS}}$. We have typically performed simulations using $N_{\text{MCS}} = 15$ and $h \approx 1\,\mu m$ such that $\Delta t \approx 40\,\text{s}$.

3.8.1 Influence of Paxillin on Polarization

In order to determine the effects of paxillin phosphorylation on cell migration, we have carried out CPM simulations for varying values of the paxillin phosphorylation rate B. Recall that for $B = 5\,\text{s}^{-1}$ we previously demonstrated that the uninduced HSS was Turing unstable, leading to the development of a polarized state without the need for any imposed asymmetry (see Fig. 3.4). We now repeat these simulations, but with the RDME simulations coupled to the CPM as described above. In order to obtain a baseline of how these simulations behave in the absence of paxillin feedback, we set $B = 0\,\text{s}^{-1}$ and, starting from an HSS corresponding to the uninduced state, ran simulations for 4 hours of simluated time. This produced simulations where cells undergo random shape fluctuations, but do not become polarized over the length of the simulation (see Fig. 3.11A-C). Next, we ran the same simulations with $B = 30\,\text{s}^{-1}$, where we observed cells undergoing spontaneous self-polarization on the timescale of thousands of seconds (see Fig. 3.11F). Once polarized, the cell begins to move in a directed fashion, with its front become well-spread compared to a narrower cell-rear (see Fig. 3.11G). However, as the

cell-rear catches up to the front, the region of high Rho (low Rac) tends to split the protrusive front into two protrusive region point in opposite directions (see Fig. 3.11 H & I). These two protrusive regions can persist for many hours, arresting the cell in place.

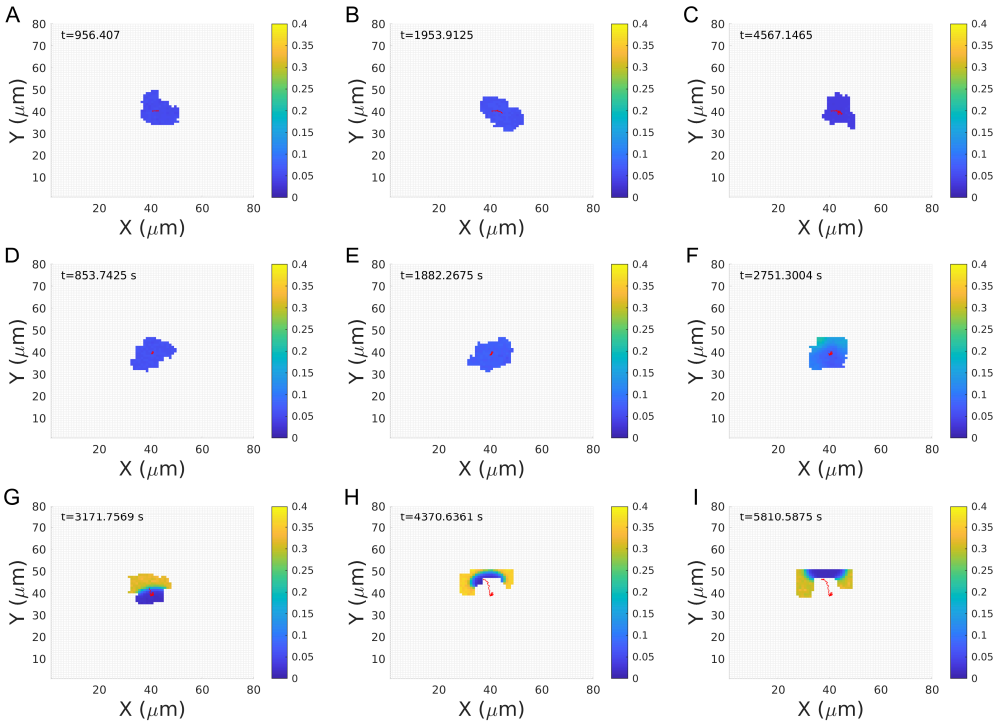

Figure 3.11: Snapshots of RDME-CPM simulations with (A-C) $B = 0\,\mathrm{s}^{-1}$, and (D-I) $B = 30\,\mathrm{s}^{-1}$, where the center of mass (red line) is overlayed on top of the scaled active Rac concentrations. For $B = 0\,\mathrm{s}^{-1}$, cells do not polarize when initialized from an uninduced HSS, exhibiting random shape fluctuations without polarization. Alternatively, when $B = 30\,\mathrm{s}^{-1}$, cells starting from the same HSS eventually become polarized and start to migrate in a directed manner. These self-polarizing cells eventually develop multiple protrusive regions, typically after a large protrusive front spreads out and the region of high Rho cathes up with it, splitting the protrusive region in two (e.g. see panel H). In such a scenario, the cells become arrested and cease to move in a directed fashion for thousands of seconds.

Beyond this qualitative description of simulated cellular behaviour, we have also quantified some of the properties of the cell movement in the two conditions considered above. More specifically, we

B (s^{-1})	Net Speed (μm/s)	Mean Inst. Speed $\pm$ Std. Dev (μm/s)	Max Inst. Speed (μm/s)
0	3.1386e-04	0.0027 ± 0.0015	0.0076
5	6.6438e-04	0.0027 ± 0.0022	0.0141
30	5.5158e-04	0.0024 ± 0.0018	0.0143

Table 3.2: The effects of paxillin phosphorylation on migration speed (n=5 cells per condition). The net speed of a cell is defined as the total distance it travelled during a simulation divided by the length of the simulation. The instantaneous speed of cells was estimated from the distance they travelled in 5 MCSs. All simulations were run for a simulated time of 4 hours, and 5 replicates were used for each condition.

wished to determine if the cells speed varies with B. In order to do so, we first computed the net speed of the cell (i.e., the distance travelled throughout the whole simulation divided by the total simulated time). This showed us that, when $B = 30\,s^{-1}$, cells displace themselves almost twice as far as when $B = 0\,s^{-1}$ (see Table 3.2). However, the simulated cells appear to be undergoing random walks (see Fig. 3.12 A & D), and since displacement in random walks is not necessarily linearly proportional to time we felt that this metric may not be the most appropriate for comparing simulations. Therefore, we have adapted some analysis methodologies from [106]. Firstly, we define the instantaneous cell speed as the distance travelled by a cell in 5 MCSs divided by the elapsed time (see Fig. 3.12 B & E). Suprisingly, the mean instantaneous speed in the two conditions does not suggest that cell with $B = 30\,s^{-1}$ move more quickly than those with $B = 0\,s^{-1}$ (see Table 3.2). However, we do observe that the max instantaneous speed is doubled in the former condition (see Table 3.2, and Fig. 3.12 B & E), consistent with the effect we saw for the net speed. In general, the cell instantaneous speed is a highly variable metric, that does not always elucidate polarization in a straightforward manner. However, the cellular persistence, defined as the half-life of the cellular velocity auto-correlation function (acf), allows us to obtain a much clearer picture of the motile behaviour in the two conditions. Namely, it shows that, when $B = 30\,s^{-1}$, cells tend to undergo repeated bouts of motility that terminate once the cell develops multiple protrusive regions, whereas when $B = 0\,s^{-1}$, they tend to undergo something closer to a brownian random walk (see Fig. 3.12 C & F) . We note that we have non-dimensionalized the persistence such that a value <1 corresponds to an acf that decays very quickly, suggesting that the velocity of the cell is approximately delta correlated (i.e., it is close to a brownian random walk on the timescale of 5 MCSs).

The trends we observe in Table 3.2 suggest that paxillin phosphorylation has two primary effects

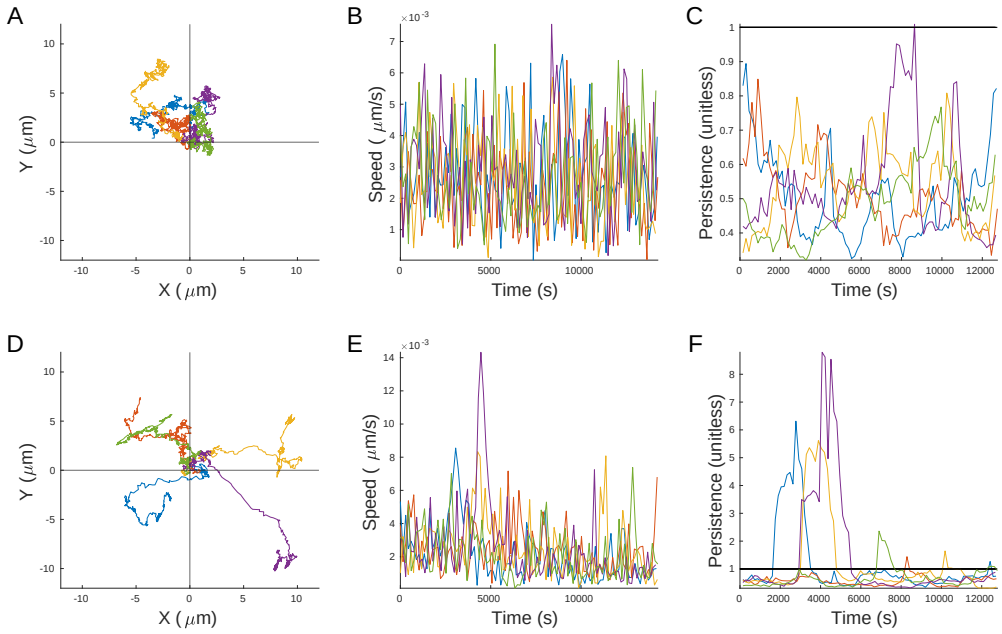

Figure 3.12: Summary of cell displacement properties in CPM simulations with (A-C) $B = 0\,\mathrm{s}^{-1}$, and (D-F) $B = 30\,\mathrm{s}^{-1}$. (A&D) Representative cellular trajectories show that when $B = 0\,\mathrm{s}^{-1}$ cells undergo simple brownian random walks, whereas when $B = 30\,\mathrm{s}^{-1}$ they occasionally migrate in a directed fashion. (B&E) The instantaneous cell speed as a function of time exhibits similar distributions in both conditions, but where the maximum speed is typically higher for $B = 30\,\mathrm{s}^{-1}$. (C&F) Cellular persistence as a function of time shows cells undergoing brownian random walks (persistence<1) when $B = 0\,\mathrm{s}^{-1}$, whereas when $B = 30\,\mathrm{s}^{-1}$ they tend to exhibit repeated periods of directed motion (persistence>1).

on RhoGTPase-dependent polarization. Firstly, it increases net migration distance by polarizing the cell when B is sufficiently large to destabilize the uninduced HSS (e.g., $B \geqslant 5$). Secondly, it decreases net migration distance at higher values of B by making cells less capable of re-polarizing after they develop multiple protrusive regions, which is further reflected by a decrease in mean instantaneous speed (e.g., $B = 30$). Together, these findings suggest that there may be an optimal value of B that produces maximal cellular migration rates. Further investigation into this topic is ongoing.

3.9 Conclusions and Outlook

In this chapter we have discussed how mutual antagonism betwewn two RhoGTPases can be used by cells to produce polarization. The underlying driver behind such a phenomenon is understood to stem from the bistability of chemical reaction systems, where mutual antagonism between two or more biochemiocal species allows for the co-existence of two stable chemical equilibria which have either high or low active concentrations for a given RhoGTPase. In particular, we have focused on Rac and Rho, two RhoGTPases which drive cellular protrusion and contraction, respectively. The precise details of the mutual antagonistic mechanisms between these two GTPases are not fully understood, and there are likely multiple redundant pathways which serve to acheive this purpose. Thus we have incorporated mutual antagonism by using generic decreasing Hill functions of one molecule to describe the activation rate of the other. The outcome of such a modelling approach is that it predicts that when one molecule has a high concentration of its active form it will supress the production of the other, i.e., mutual antagonism.

In a WM setting, chemical systems with sufficiently high Hill coefficients (i.e., a sufficient number of steps and/or cooperativity in the mutual antagonism pathways) allow for the coexistence of two stable equilibria (see left-column in Fig. 3.6), which can be understood as two distinct phenotypic states that are termed induced and uninduced, where either active Rac or Rho is elevated, respectively. Furthermore, we saw how feedback from paxillin phosphorylation onto Rac activation can be used to drive the cell through a bistable switch, where a sufficiently high paxillin phosphorylation rate leads to the annihiliation of the uninduced equilibrium. This suggests that a cell can signifcantly increase its protrusiveness by increasing paxillin phosphorylation. While this is an informative preliminary means of studying polarization, a WM model fundamentally cannot be used to describe polarization, as it lacks the requisite spatial considerations. This shortcoming is remedied by moving to a RD setting, where polarization can be understood as a pattern formation process driven by the phenomenon known as wave-pinning. On the other hand, WM models can be informative in studying RD systems as the equilibria of the former are HSSs of the latter.

Reaction-diffusion systems are a class of PDE models, which means, unlike the ODEs used to descibe WM systems, they cannot be sytematically analyzed through any one technique. The phenonmenology of wave-pinning can be understood through assymptotic analysis of a toy PDE model (see Section 3.5), where the fact that active forms of Rac and Rho diffuse much more slowly than their inac-

tive forms is a prerequisite condition for observing pattern formation. Provided that reaction dynamics occur on a timescale comparable to the diffusion of the inactive form, a predicted outcome of the toy model is that spatial regions can converge to the two distinct chemical equilbria which differ from the (possibly unique) HSSs predicted by WM models. In order to predict whether a RD system is capable of producing such a spatially inhomogenous pattern, one may use LPA. This analysis methodology uses asymptotic approximations of the PDE to reduce it to a much simpler set of ODEs which summarize both the local and global dynamics of the RD system shortly after a perturbation of infinitesimal spatial extent is applied to the system.

While LPA describes the behaviour of the PDE on short timescales, it can also be adapted to describe the long-term behaviour of a wave-pinning system. In particular, LPA is informative about the size of a perturbation requited to trigger pattern formation. However, after an appropriate perturbation, a travelling wave propagates across the domain until it slows down to a halt. Given the position of the stalled wave-front, the conservation of matter can then be used to derive a constraint on the local active concentrations and the global inactive concentration. The approach used in LPA is to assume the wave is negligible in size, but this assumption may be relaxed. While LPA considers the global active concentration dyanmics to be independent of perturbed local active concentration dyanmics, our approach, termed PWA, considers two local active concentrations which interact through the conservation of matter. In principle, one may use PWA in a manner identical to LPA, that is, using numerical continuation along the "global" branch(es) of equilibria of the WM system to detect bifurcation points and subsequently following "local" branches to find stable equilibria. However, as demonstrated in Section 3.6, when the WM system is bistable, LPA diagrams can become quite complex and when feedback from biochemical signalling is incorporated their predicted stability properties may not be reliable. Our implementation of PWA provides a mean to forgo the creation of a messy LPA diagram or interpreting its dubious stability properties, and directly computes the local concentrations of the steady state solution by interpolating between two root-finding problems rather than having to navigate the bifurcation structure of the problem.

We have applied both LPA and PWA to a model of Rac and Rho with feedback from paxillin signalling, and have found that in both cases the stability properties of the resulting bifurcations diagrams are rather suspect. In paticular, there are parameter regimes where there appear to be no attractors for the system. This has been observed before when including biochemical feedback onto the wave-pinning system [84, 105], but with our feedback system we find that this issue is more prominent than

what has been described in the literature (see Fig. 3.8). We have outlined some discrepancies with matter conservation which may be contriubting to this problem (see Section 3.4.1), but further investiagtion into the matter is needed. Furthermore, with the inclusion of feedback from paxillin we find that LPA fails to predict the wave-pinning observed in the RD system whereas PWA can be used to provide a *post-hoc* explanation of the observed pattern. Thus, PWA is a complementary tool to LPA, and both fail to capture the stability properties of the RD system when feedback is incorporated.

Ultimately, this project was started to understand how signalling downstream of paxillin affects cellular motility. Moreover, we wished to see if stochastic effects could induce changes in polarity that are consistent with the random changes in direction exhbited by CHO cells, and if paxillin phosphorylation could be used to drive motility independently of its effects on adhesion dyanmics. Stochastically induced wave-pinning has indeed been observed for this RD system (see Fig. 3.4). However, stochastically induced changes in the polarization (e.g., directional switching) remains elusive. Nonetheless, it is possible that the key to producing stochastically polarized cells requires some details which have not been considered here. In particular, as a cell protrudes and contracts it will change its size and geometry, and these factors may feedback onto the the RhoGTPases to produce stochastic changes in direction. Furthermore, the mechanosensitive properties of adhesions or ionic influxes through stretch-activated channels may contribute to these stochastic changes in direction. For these reasons, we have begun to extend our simulations by incorporating a time-dependent domain through the use of the Cellular Potts Model.

Although LPA and PWA were relatively inconclusive about the wave-pinning behaviour of the RD system with respect to the paxillin phosphorylation rate B, we have preliminary results from simulations using the CPM which suggest that B does indeed affect the speed of cellular motility (see Table 3.2 and Fig. 3.12). In particular, we have set up the CPM to be protrusive (contractile) in regions with high Rac (Rho) according to standard methods in the field [82]. Five simulations of cells were run and both the net and instantaneous migration speed of cells was quantified, as well as cellular persistence. Interestingly, as B is increased from $B = 0\,\mathrm{s}^{-1}$ to $B = 30\,\mathrm{s}^{-1}$ we saw an initial rise in the net migration speed of the cells followed by a decrease at higher values of B. This suggested that increased paxillin phosphorylation may have either a pro- or anti-migratory effect on cells, and that there is an optimal value of paxillin phosphorylation rate that maximizes cellular migration. Along with further refinements to the model, these CPM simulations are currently be investigated in depth.

Bibliography

[1] Thomas D Pollard and Gary G Borisy. Cellular motility driven by assembly and disassembly of actin filaments. *Cell*, 112:453–465, 2 2003. 3.1, 4.6

[2] Samer Hanna and Mirvat El-Sibai. Signaling networks of rho gtpases in cell motility. *Cellular Signalling*, 25:1955–1961, 10 2013. 1.12, 3.1

[3] Harry Warner, Beverley J Wilson, and Patrick T Caswell. Control of adhesion and protrusion in cell migration by rho gtpases. *Current Opinion in Cell Biology*, 56:64–70, 2019. 1.12, 3.1, 3.3.1

[4] Campbell D Lawson and Keith Burridge. The on-off relationship of rho and rac during integrin-mediated adhesion and cell migration. *Small GTPases*, 5:e27958, 1 2014. 1.12, 3.1

[5] Pontus Aspenström, Uno Lindberg, and Alan Hall. Two GTPases, cdc42 and rac, bind directly to a protein implicated in the immunodeficiency disorder wiskott–aldrich syndrome. *Current Biology*, 6(1):70–75, jan 1996. 3.1

[6] H Miki and Tadaomi Takenawa. Regulation of actin dynamics by wasp family proteins. *Journal of Biochemistry*, 134:309–313, 9 2003. 3.1

[7] Henry N Higgs and Thomas D Pollard. Regulation of actin filament network formation through arp2/3 complex: Activation by a diverse array of proteins. *Annual Review of Biochemistry*, 70:649–676, 2001. 3.1

[8] A Mogilner and G Oster. Cell motility driven by actin polymerization. *Biophysical journal*, 71:3030–3045, 1996. 1.2.2, 3.1, 4.6

[9] A Mogilner and B Rubinstein. Actin disassembly 'clock' and membrane tension determine cell shape and turning: a mathematical model. *Journal of physics. Condensed matter : an Institute of Physics journal*, 22:194118, 5 2010. 0.1, 3.1

[10] Boris Rubinstein, Maxime F Fournier, Ken Jacobson, Alexander B Verkhovsky, and Alex Mogilner. Actin-myosin viscoelastic flow in the keratocyte lamellipod. *Biophysical Journal*, 97:1853–1863, 10 2009. 3.1

[11] Marcus Prass, Ken Jacobson, Alex Mogilner, and Manfred Radmacher. Direct measurement of the lamellipodial protrusive force in a migrating cell. *The Journal of cell biology*, 174:767–772, 2006. 3.1

[12] Jie Zhu and Alex Mogilner. Mesoscopic model of actin-based propulsion. *PLoS Computational Biology*, 8:e1002764, 11 2012. 3.1

[13] Catherine G Galbraith, Kenneth M Yamada, and James A Galbraith. Polymerizing actin fibers position integrins primed to probe for adhesion sites. *Science (New York, N.Y.)*, 315:992–995, 2 2007. 3.1

[14] Colin K Choi, Miguel Vicente-Manzanares, Jessica Zareno, Leanna A Whitmore, Alex Mogilner, and Alan Rick Horwitz. Actin and alpha-actinin orchestrate the assembly and maturation of nascent adhesions in a myosin ii motor-independent manner. *Nature cell biology*, 10:1039–1050, 9 2008. 0.1.1, 1.1, 1.2.1, 1.2.2, 1.7, 1.8, 1.11, O1, M2, 2.2.3, 2.3.5.2, 2.4, 2.5.1.2, 2.5.1.8, 3.1, 4.6.1, 4.6.4, 5

[15] Paul W Wiseman, Claire M Brown, Donna J Webb, Benedict Hebert, Natalie L Johnson, Jeff A Squier, Mark H Ellisman, and A F Horwitz. Spatial mapping of integrin interactions and dynamics during cell migration by image correlation microscopy. *Journal of Cell Science*, 117, 2004. 1.2.1, 1.6, 1.11, 2.3.1, 3.1

[16] Bruno Pontes, Pascale Monzo, Laurent Gole, Anabel Lise Le Roux, Anita Joanna Kosmalska, Zhi Yang Tam, Weiwei Luo, Sophie Kan, Virgile Viasnoff, Pere Roca-Cusachs, Lisa Tucker-Kellogg, and Nils C Gauthier. Membrane tension controls adhesion positioning at the leading edge of cells. *Journal of Cell Biology*, 216:2959–2977, 9 2017. 0.1.1, 1.12, 3.1, 4.6

[17] Margaret L Gardel, Ian C Schneider, Yvonne Aratyn-Schaus, and Clare M Waterman. Mechanical integration of actin and adhesion dynamics in cell migration. *Annual review of cell and developmental biology*, 26:315–333, 2010. 0.1, 3.1

[18] Tatyana M Svitkina, Alexander B Verkhovsky, Kyle M McQuade, and Gary G Borisy. Analysis of the actin-myosin ii system in fish epidermal keratocytes: Mechanism of cell body translocation. *Journal of Cell Biology*, 139:397–415, 1997. 3.1

[19] Melanie Graessl, Johannes Koch, Abram Calderon, Dominic Kamps, Soumya Banerjee, Tomáš Mazel, Nina Schulze, Jana Kathrin Jungkurth, Rutuja Patwardhan, Djamschid Solouk, Nico Hampe, Bernd Hoffmann, Leif Dehmelt, and Perihan Nalbant. An excitable rho gtpase signaling network generates dynamic subcellular contraction patterns. *Journal of Cell Biology*, 216:4271–4285, 12 2017. 3.1

[20] M Chrzanowska-Wodnicka and K Burridge. Rho-stimulated contractility drives the formation of stress fibers and focal adhesions. *The Journal of Cell Biology*, 133, 1996. 3.1

[21] Sari Tojkander, Gergana Gateva, and Pekka Lappalainen. Actin stress fibers–assembly, dynamics and biological roles. *Journal of cell science*, 125:1855–1864, 2012. 3.1

[22] Raphaela Rid, Natalia Schiefermeier, Ilya Grigoriev, J Victor Small, and Irina Kaverina. The last but not the least: The origin and significance of trailing adhesions in fibroblastic cells. *Cell Motility and the Cytoskeleton*, 61:161–171, 7 2005. 0.1, 0.1.1, 1.2.2, 1.7, 3.1

[23] Joshua A Broussard, Donna J Webb, and Irina Kaverina. Asymmetric focal adhesion disassembly in motile cells. *Current Opinion in Cell Biology*, 20:85–90, 2 2008. 0.1, 1.2.2, 1.8, 3.1

[24] A L Bishop and A Hall. Rho gtpases and their effector proteins. *The Biochemical journal*, 348 Pt 2:241–255, 2000. 3.1

[25] Anne J Ridley. Rho gtpases and cell migration. *J. Cell Sci.*, 114:2713–2722, 2001. 0.1.3, 3.1

[26] Reina E Itoh, Kazuo Kurokawa, Yusuke Ohba, Hisayoshi Yoshizaki, Naoki Mochizuki, and Michiyuki Matsuda. Activation of rac and cdc42 video imaged by fluorescent resonance energy

transfer-based single-molecule probes in the membrane of living cells. *Molecular and cellular biology*, 22:6582–6591, 2002. 3.1

[27] Jingsong Xu, Fei Wang, Alexandra Van Keymeulen, Paul Herzmark, Aaron Straight, Kathleen Kelly, Yoh Takuwa, Naotoshi Sugimoto, Timothy Mitchison, and Henry R Bourne. Divergent signals and cytoskeletal assemblies regulate self-organizing polarity in neutrophils. *Cell*, 114:201–214, 2003. 3.1

[28] Alexandra Jilkine, Athanasius F. M. Marée, and Leah Edelstein-Keshet. Mathematical model for spatial segregation of the rho-family gtpases based on inhibitory crosstalk. *Bulletin of mathematical biology*, 69(6):1943–1978, 8 2007. 0.1.3, 3.1, 3.3, 3.5.2

[29] Ruedi Meili and Richard A Firtel. Two poles and a compass. *Cell*, 114:153–156, 2003. 3.1

[30] Adriana T Dawes, G Bard Ermentrout, Eric N Cytrynbaum, and Leah Edelstein-Keshet. Actin filament branching and protrusion velocity in a simple 1d model of a motile cell. *Journal of Theoretical Biology*, 242:265–279, 2006. 3.1, 3.6.0.1

[31] Yoichiro Mori, Alexandra Jilkine, and Leah Edelstein-Keshet. Wave-pinning and cell polarity from a bistable reaction-diffusion system. *Biophysical Journal*, 94:3684–3697, 5 2008. 0.1.3, 1.12, 2.1, 3.1, 3.3, 3.5.2, 3.6.0.1, 4.1

[32] Yoichiro Mori, Alexandra Jilkine, and Leah Edelstein-Keshet. Asymptotic and bifurcation analysis of wave-pinning in a reaction-diffusion model for cell polarization. *SIAM Journal on Applied Mathematics*, 71:1401–1427, 1 2011. 0.1.3, 3.1, 3.4.2, 3.5, 3.5, 3.5.1, 3.5.1, 3.5.1, 3.5.1, 3.5.2, 3.6.0.1

[33] Adriana T Dawes and Leah Edelstein-Keshet. Phosphoinositides and rho proteins spatially regulate actin polymerization to initiate and maintain directed movement in a one-dimensional model of a motile cell. *Biophysical Journal*, 92:744–768, 2 2007. 1.12, 3.1, 3.3

[34] Athanasius F. M. Marée, Verônica A. Grieneisen, and Leah Edelstein-Keshet. How cells integrate complex stimuli: The effect of feedback from phosphoinositides and cell shape on cell polarization and motility. *PLoS Computational Biology*, 8(3):e1002402, mar 2012. 3.1, 3.3, 3.6.0.1

[35] Athanasius F. M. Marée, Alexandra Jilkine, Adriana Dawes, Verônica A. Grieneisen, and Leah Edelstein-Keshet. Polarization and movement of keratocytes: a multiscale modelling approach. *Bulletin of mathematical biology*, 68(5):1169–1211, 7 2006. 0.1.3, 3.1, 3.3, 3.6.0.1

[36] Georg R. Walther, Athanasius F. M. Marée, Leah Edelstein-Keshet, and Verônica A. Grieneisen. Deterministic versus stochastic cell polarisation through wave-pinning. *Bulletin of mathematical biology*, 74:2570–2599, 11 2012. 3.1, 3.6

[37] W R Holmes, A E Carlsson, and L Edelstein-Keshet. Regimes of wave type patterning driven by refractory actin feedback: transition from static polarization to dynamic wave behaviour. *Physical biology*, 9:46005, 8 2012. 0.1.3, 3.1, 3.3, 3.6, 3.6.0.1, 3.6.0.2

[38] Stephan Huveneers and Erik H J Danen. Adhesion signaling - crosstalk between integrins, src and rho. *Journal of cell science*, 122:1059–1069, 4 2009. 0.1, 3.1

[39] Ronen Zaidel-Bar, Shalev Itzkovitz, Avi Ma'ayan, Ravi Iyengar, and Benjamin Geiger. Functional atlas of the integrin adhesome. *Nature cell biology*, 9:858–867, 8 2007. 0.1, 1.1, 1.2.1, 2.1, 3.1

[40] Shailaja Seetharaman and Sandrine Etienne-Manneville. Microtubules at focal adhesions - a double-edged sword. *Journal of cell science*, 132, 2019. 1.2.2, 3.1

[41] Matthew J Paszek, David Boettiger, Valerie M Weaver, and Daniel A Hammer. Integrin clustering is driven by mechanical resistance from the glycocalyx and the substrate. *PLoS Computational Biology*, 5:e1000604, 12 2009. 1.5, 1.12, 3.1

[42] Ben Stutchbury, Paul Atherton, Ricky Tsang, De-Yao Wang, and Christoph Ballestrem. Distinct focal adhesion protein modules control different aspects of mechanotransduction. *Journal of cell science*, 130:1612–1624, 2017. 1.8, 3.1

[43] Andrew Doyle, William Marganski, Juliet Lee, Z Goeckeler, G Côté, and R Wysolmerski. Calcium transients induce spatially coordinated increases in traction force during the movement of fish keratocytes. *Journal of cell science*, 117:2203–2214, 2004. 1.4, 1.8, 3.1

[44] Micheal Brown and Christopher E Turner. Paxillin: Adapting to change. *Physiological Reviews*, 84:1315–1339, 2004. 1.2.1, 1.12, 3.1

[45] Donna J Webb, Karen Donais, Leanna A Whitmore, Sheila M Thomas, Christopher E Turner, J Thomas Parsons, and Alan F Horwitz. Fak-src signalling through paxillin, erk and mlck regulates adhesion disassembly. *Nature cell biology*, 6:154–161, 2 2004. 1.7, 3.1

[46] Nicholas O Deakin and Christopher E Turner. Paxillin comes of age. *Journal of cell science*, 121:2435–2444, 2008. 0.1.2, 3.1

[47] R Zaidel-Bar, R Milo, Z Kam, and B Geiger. A paxillin tyrosine phosphorylation switch regulates the assembly and form of cell-matrix adhesions. *Journal of Cell Science*, 120:137–148, 12 2007. 0.1.2, 1.1, 1.2.2, 1.12, 3.1, 3.3.2, 5

[48] Anjana Nayal, Donna J Webb, Claire M Brown, Erik M Schaefer, Miguel Vicente-Manzanares, and Alan Rick Horwitz. Paxillin phosphorylation at ser273 localizes a git1-pix-pak complex and regulates adhesion and protrusion dynamics. *Journal of Cell Biology*, 173:587–589, 5 2006. 0.1.2, 1.12, 3.1, 3.3.2, 5

[49] Abira Rajah, Colton G Boudreau, Alina Ilie, Tse-Luen Wee, Kaixi Tang, Aleksandar Z Borisov, John Orlowski, and Claire M Brown. Paxillin s273 phosphorylation regulates adhesion dynamics and cell migration through a common protein complex with pak1 and βpix. *Scientific Reports*, 9:11430, 2019. 0.1, 1.7, 1.12, 3.1, 3.3.2

[50] Kaixi Tang, Colton G. Boudreau, Claire M. Brown, and Anmar Khadra. Paxillin phosphorylation at serine 273 and its effects on rac, rho and adhesion dynamics. *PLOS Computational Biology*, 14(7):e1006303, jul 2018. (document), 0.1, 0.1.2, 1.1, 1.12, 2.2.3, 2.3.5.1, 2.4, 2.5.1.8, 2.1, 2.3, 3.1, 3.3.1, 3.3.1, 3.3.2, 3.3.2, 3.4, 3.4.1, 3.6.0.2, 3.7, 3.10, 5, 5, 5, 5, 5

[51] N G van Kampen. *Stochastic processes in physics and chemistry*. North Holland, 3rd edition, 2007. 1.6, 1.13.2, 3.2.1

[52] Timo R Maarleveld, Ruchir A Khandelwal, Brett G Olivier, Bas Teusink, and Frank J Bruggeman. Basic concepts and principles of stoichiometric modeling of metabolic networks. *Biotechnology Journal*, 8:997, 2013. 3.2.1

[53] Iman Famili and Bernhard O Palsson. The convex basis of the left null space of the stoichiometric matrix leads to the definition of metabolically meaningful pools. *Biophysical journal*, 85:16–26, 2003. 3.2.1

[54] A N Gorban, E M Mirkes, and G S Yablonsky. Thermodynamics in the limit of irreversible reactions. *Physica A: Statistical Mechanics and its Applications*, 392:1318–1335, 3 2013. 3.2.1

[55] J D Murray. *Mathematical Biology vol. II*. Springer, 2003. 3.2.1.1, 3.4.2, 3.5, 3.5.1

[56] Americo Jr Cunha. *Reduction of Complexity in Combustion Thermochemistry*. PhD thesis, 2010. 3.2.1.2

[57] James C Keck. Rate-controlled constrained-equilibrium theory of chemical reactions in complex systems*, 1990. 3.2.1.2

[58] Zhuyin Ren and Stephen B Pope. Entropy production and element conservation in the quasi-steady-state approximation. *Combustion and Flame*, 137:251–254, 2004. 3.2.1.2

[59] T Turanyi, A S Tomlin, and M J Pilling. On the error of the quasi-steady-state approximation. *The Journal of Physical Chemistry*, 97:163–172, 1 1993. 3.2.1.2, 3.2.1.2

[60] Alexandra Goeke and Sebastian Walcher. A constructive approach to quasi-steady state reductions. *Journal of Mathematical Chemistry*, 52:2596–2626, 11 2014. 3.2.1.2

[61] Alexandra Goeke, Sebastian Walcher, and Eva Zerz. Determining "small parameters" for quasi-steady state. *Journal of Differential Equations*, 259:1149–1180, 8 2015. 3.2.1.2

[62] George W A Constable, Alan J McKane, Tim Rogers, and Todd L Parsons. Dimension reduction for stochastic dynamical systems forced onto a manifold by large drift: a constructive approach with examples from theoretical biology related content stochastic dynamics on slow manifolds dimension reduction for stochastic dynamical s. *Journal of Physics A: Mathematical and Theoretical J. Phys. A: Math. Theor*, 50:33, 2017. 3.2.1.2

[63] Jessica K Lyda, Jack Z Tan, Abira Rajah, Asheesh Momi, Laurent MacKay, Claire M Brown, and Anmar Khadra. Rac activation is key to cell motility and directionality: An experimental and modelling investigation. *Computational and Structural Biotechnology Journal*, 17:1436–1452, 2019. 0.1.2, 1.1, 1.12, 3.2.2, 3.2.2.2, 3.7

[64] Daniel T Gillespie. A rigorous derivation of the chemical master equation. *Physica A: Statistical Mechanics and its Applications*, 188:404–425, 9 1992. 3.2.2

[65] Radek Erban, Jonathan Chapman, and Philip Maini. A practical guide to stochastic simulations of reaction-diffusion processes. 2007. 3.2.2, 3.2.2.2, 3.2.2.3

[66] Daniel T. Gillespie, Andreas Hellander, and Linda R. Petzold. Perspective: Stochastic algorithms for chemical kinetics. *The Journal of Chemical Physics*, 138(17):170901, may 2013. 3.2.2

[67] Christopher V Rao and Adam P Arkin. Stochastic chemical kinetics and the quasi-steady-state assumption: Application to the gillespie algorithm. *The Journal of Chemical Physics*, 118:4999–5010, 3 2003. 3.2.2.1

[68] Xiaodong Cai and Xiaodong Wang. Stochastic modeling and simulation of gene networks - a review of the state-of-the-art research on stochastic simulations. *IEEE Signal Processing Magazine*, 24:27–36, 2007. 3.2.2.1

[69] Weinan E, Di Liu, and Eric Vanden-Eijnden. Nested stochastic simulation algorithm for chemical kinetic systems with disparate rates. *The Journal of Chemical Physics*, 123:194107, 2005. 3.2.2.1

[70] Weinan E, Di Liu, and Eric Vanden-Eijnden. Nested stochastic simulation algorithms for chemical kinetic systems with multiple time scales. *Journal of Computational Physics*, 221:158–180, 2007. 3.2.2.1

[71] John Goutsias. Quasiequilibrium approximation of fast reaction kinetics in stochastic biochemical systems. *The Journal of Chemical Physics*, 122:184102, 5 2005. 3.2.2.1

[72] Shev MacNamara, Alberto M Bersani, Kevin Burrage, and Roger B Sidje. Stochastic chemical kinetics and the total quasi-steady-state assumption: Application to the stochastic simulation algorithm and chemical master equation. *The Journal of Chemical Physics*, 129:95105, 2008. 3.2.2.1

[73] Jae Kyoung Kim, Krešimir Josić, and Matthew R Bennett. The validity of quasi-steady-state approximations in discrete stochastic simulations. *Biophysical Journal*, 107:783–793, 2014. 3.2.2.1

[74] Jae Kyoung Kim, Krešimir Josić, and Matthew R Bennett. The relationship between stochastic and deterministic quasi-steady state approximations. *BMC Systems Biology*, 9:87, 12 2015. 3.2.2.1

[75] J I Carrero, J S Loaiza, and A Serna. Stochastic reaction, stochastic diffusion. *ChemTexts*, 6:14, 2020. (document), 3.2.2.2, 3.2.2.3, 3.2.2.3, 3.2, 3.2.2.3, 3.2.2.3

[76] Max Planitz, William H Press, Brian P Flannery, Saul A Teukolsky, and William T Vetterling. *Numerical Recipes: The Art of Scientific Computing*. Cambridge University Press, 3rd edition, 1987. 3.2.2.3

[77] Michael A Gibson and Jehoshua Bruck. Efficient exact stochastic simulation of chemical systems with many species and many channels. *Journal of Physical Chemistry A*, 104:1876–1889, 2000. 3.2.2.3

[78] Bard Ermentrout. *Simulating, Analyzing, and Animating Dynamical Systems: a Guide to XPPAUT for Researchers and Students*. Society for Industrial and Applied Mathematics, 1 2002. 3.2.4

[79] E J Doedel, R C Paffenroth, A R Champneys, T F Fairgrieve, Yu. A Kuznetsov, B Sandstede, and X Wang. Auto-07p: Continuation and bifurcation software for ordinary differential equations, 2007. 2.2.4, 3.2.4, 4.3

[80] Matlab version 9.4.0.813654 (r2018a), 2018. 3.2.4, 3.2.5

[81] James A Glazier, Ariel Balter, and Nikodem J Popławski. Magnetization to morphogenesis: A brief history of the glazier-graner-hogeweg model, 2007. 3.2.5

[82] Elisabeth G Rens and Leah Edelstein-Keshet. From energy to cellular forces in the cellular potts model: An algorithmic approach. *PLOS Computational Biology*, 15:e1007459, 2019. 3.2.5, 3.9

[83] Leah Edelstein-Keshet, William R Holmes, Mark Zajac, and Meghan Dutot. From simple to detailed models for cell polarization. *Philosophical Transactions of the Royal Society B: Biological Sciences*, 368:20130003, 11 2013. 0.1.3, 3.3, 3.4.2, 3.5, 3.6, 3.6.0.1

[84] William R. Holmes and Leah Edelstein-Keshet. A comparison of computational models for eukaryotic cell shape and motility. *PLoS Computational Biology*, 8(12):e1002793, dec 2012. 3.3, 3.5.3.2, 3.6.0.1, 3.6.0.2, 3.9

[85] Johannes L Bos, Holger Rehmann, and Alfred Wittinghofer. Gefs and gaps: Critical elements in the control of small g proteins. *Cell*, 129:865–877, 2007. 3.3.1

[86] Colin K Choi, Jessica Zareno, Michelle A Digman, Enrico Gratton, and Alan Rick Horwitz. Cross-correlated fluctuation analysis reveals phosphorylation-regulated paxillin-fak complexes in nascent adhesions. *Biophysical Journal*, 100:583–592, 2 2011. 1.7, 1.12, 3.3.2

[87] Armen H Mekhdjian, FuiBoon Kai, Matthew G Rubashkin, Louis S Prahl, Laralynne M Przybyla, Alexandra L McGregor, Emily S Bell, J Matthew Barnes, Christopher C DuFort, Guanqing Ou, Alice C Chang, Luke Cassereau, Steven J Tan, Michael W Pickup, Jonathan N Lakins, Xin Ye, Michael W Davidson, Jan Lammerding, David J Odde, Alexander R Dunn, and Valerie M Weaver. Integrin-mediated traction force enhances paxillin molecular associations and adhesion dynamics that increase the invasiveness of tumor cells into a three-dimensional extracellular matrix. *Molecular Biology of the Cell*, 28:1467–1488, 2017. 3.3.2

[88] Edward Manser, Tsui-Han Loo, Cheng-Gee Koh, Zhou-Shen Zhao, Xiang-Qun Chen, Lydia Tan, Ivan Tan, Thomas Leung, and Louis Lim. Pak kinases are directly coupled to the pix family of nucleotide exchange factors. *Molecular Cell*, 1:183–192, 1 1998. 3.3.2

[89] A Obermeier, Sohail Ahmed, Edward Manser, Su Ching Yen, Christine Hall, and Louis Lim. Pak promotes morphological changes by acting upstream of rac. *The EMBO Journal*, 17:4328–4339, 8 1998. 3.3.2

[90] Julien Cau and Alan Hall. Cdc42 controls the polarity of the actin and microtubule cytoskeletons through two distinct signal transduction pathways. *Journal of cell science*, 118:2579–2587, 2005. 3.3.2

[91] Kaixi Tang. Mathematical model of paxillin phsphorylation at serine 273 and its effect on rac, rho, and adhesion dynamics, 2018. 3.3.2, 3.3.2

[92] C E Turner, M C Brown, J A Perrotta, M C Riedy, S N Nikolopoulos, A R McDonald, S Bagrodia, S Thomas, and P S Leventhal. Paxillin ld4 motif binds pak and pix through a novel 95-kd

ankyrin repeat, arf-gap protein: A role in cytoskeletal remodeling. *The Journal of cell biology*, 145:851–863, 5 1999. 3.3.2

[93] Mary R Stofega, Luraynne C Sanders, Elisabeth M Gardiner, and Gary M Bokoch. Constitutive p21-activated kinase (pak) activation in breast cancer cells as a result of mislocalization of pak to focal adhesions. *Molecular biology of the cell*, 15:2965–2977, 6 2004. 3.3.2

[94] Yanyan Chen and Javier Buceta. A non-linear analysis of turing pattern formation. *PLOS ONE*, 14:e0220994, 8 2019. 3.5

[95] Alan Turing. The chemical basis of morphogenesis. *Philosophical Transactions of the Royal Society of London. Series B, Biological Sciences*, 237(641):37–72, aug 1952. 3.5

[96] James Keener and James Sneyd. Membrane ion channels, 2009. 3.5.1, 4.1

[97] Alexandra Jilkine. A wave-pinning mechanism for eukaryotic cell polarization based on rho gtpase dynamics. 2009. 3.5.1, 5

[98] Sulagna Das, Taofei Yin, Qingfen Yang, Jingqiao Zhang, Yi I Wu, and Ji Yu. Single-molecule tracking of small gtpase rac1 uncovers spatial regulation of membrane translocation and mechanism for polarized signaling. *Proceedings of the National Academy of Sciences of the United States of America*, 112:E267——76, 2015. 3.5.2

[99] Yoshimi Takai, Takuya Sasaki, and Takashi Matozaki. Small gtp-binding proteins. *Physiological Reviews*, 81:153–208, 1 2001. 3.5.2

[100] L Van Aelst and C D'Souza-Schorey. Rho gtpases and signaling networks. *Genes & development*, 11:2295–2322, 1997. 3.5.2

[101] Konstadinos Moissoglu, Boris M Slepchenko, Nahum Meller, Alan F Horwitz, and Martin A Schwartz. In vivo dynamics of rac-membrane interactions. *Molecular Biology of the Cell*, 17:2770, 6 2006. 3.5.2

[102] Marten Postma, Leonard Bosgraaf, Harriët M Loovers, and Peter J M Van Haastert. Chemotaxis: signalling modules join hands at front and tail. *EMBO Reports*, 5:35, 2004. 3.5.2

[103] William R Holmes. An efficient, nonlinear stability analysis for detecting pattern formation in reaction diffusion systems. *Bulletin of Mathematical Biology*, 76:157–183, 2014. 3.6.0.1

[104] May Anne Mata, Meghan Dutot, Leah Edelstein-Keshet, and William R Holmes. A model for intracellular actin waves explored by nonlinear local perturbation analysis. *Journal of theoretical biology*, 334:149–161, 10 2013. 0.1.3, 3.6.0.1, 3.6.0.2

[105] Yue Liu. Analysis of pattern formation in reaction-diffusion models for cell polarization, 2019. 3.6.0.1, 3.6.0.2, 3.6.0.2, 3.9

[106] Inge M. N. Wortel, Ioana Niculescu, P. Martijn Kolijn, Nir Gov, Rob J. de Boer, and Johannes Textor. Actin-inspired feedback couples speed and persistence in a cellular potts model of cell migration. jun 2018. 3.8.1

Chapter 4

Dynamical Analysis of Actin-Based Protrusion

4.1 Introduction

As clearly demonstrated in Chapters 1 and 3, cellular motility involves a number of complex spatio-temporal patterns of activity. For instance, in order for a cell to move in a directed manner, it must first become rear-to-front polarized (a spatial pattern of activity). This is thought to occur as a result of mutual inhibitory feedbacks between two members of the Rho subfamily of GTPases: Rac and Rho [1]. The mutual inhibitory interactions between these two proteins together with differences in diffusion coefficients in their active and inactive forms are used by the cell to produce spatially-segregated regions where the activity of one GTPase is high and the other is low, but the specific GTPases which is high may be different in each specific region [2]. These regions may be either protrusive (where Rac is elevated, promoting actin polymerization) or contractile (where Rho is elevated, promoting myosin-driven contraction of the actin cytoskeleton). Due the opposing effects of these two proteins on cell morphology, it is typical to denote the protrusive region as the front of the cell and the contractile region as the the rear of the cell. Within the context of motility, there are numerous other examples of coordinated patterns of activity, not only across space but also across time.

After a cell generates a rear-to-front polarization, its subsequent motility involves a number of key steps: (i) protrusion, (ii) adhesion, (iii) cell-body translocation, and (iv) de-adhesion [3]. These steps can happen either continuously all at once or serially in a periodic manner. Often, whether a cell moves continuously or periodically is considered to be a phenotypic trait of a specific cell type. For example, fish keratocytes are widely known to migrate continuously whereas CHO cells exhibit cyclic protrusion/retraction cycles during their movement. However, in [4], this phenomenon was investigated more thoroughly by looking at a population of cells. It was found that, within a populations of fish keratocytes, some would move continuously while others exhibit waves of protrusion that travel from one end of the lamellipodium to another. In addition, individual cells could be switched between moving continuously or periodically by plating them on different substrates or treating them with pharmacological agents. This suggests that the same machinery is working to produce both modes of motility, but that the system can behave differently under varying conditions. Using mathematical modeling to account for actin polymerization dynamics, this study ascertained that these differences in modes of motility could be explained by intercellular heterogeneity in the rates of various biochemical processes related to actin polymerization.

In particular, it was found in this study that the actin polymerization is inhibited by capping proteins

which prevent further growth of actin filaments and that the protein VASP exerts an anti-capping effect at the leading edge of the cell. This anti-capping action allows for enough polymerization to occur in order for the collective force of polymerization of all filaments to overcome membrane tension and lead to protrusion in regions of high actin filament density. Protrusion of the leading edge is highly correlated with the birth of nascent adhesions, and their subsequent growth and stabilization to form mature adhesions. Interestingly, mature adhesions have been shown to sequester VASP at the leading edge, antagonizing its anti-capping effect. If enough VASP is sequestered by mature adhesions, the leading edge will stall, but if VASP is continually delivered to the leading edge (through an unspecified mechanism), it will eventually reach high enough levels to allow for protrusion to restart. These positive and negative feedback processes produce the sequence of events which have been hypothesized to be the origin of the traveling waves of protrusion. Furthermore, based on results of the model and some experimental evidence in [4], one may conclude that keratocytes which exhibit continuous motility have a high VASP delivery, preventing its depletion at the leading edge by mature adhesions.

The mathematical model published in [4] was quite alluring, as it can explain much of the phenomenology observed in motile cells. Moreover, it has only three variables with eight parameters. However, this model remains incompletely characterized, as the study focused primarily on experimental findings with the dynamic properties of the model left incompletely investigated. Here we analyze the underlying dynamics of this model in detail and expand its formulation by combining it with the mechanosensitive properties of the adhesion model of Chapter 2 to see how these two coupled systems interact. We will show that coupling the two models increases the size of the oscillatory regime in parameter space and enhances the robustness of waving.

One important feature of the model developed in [4] is that it is excitable. Excitable systems are known for their ability to generate very pronounced responses to small suprathreshold stimuli, with their state variables typically generating large excursions in state space [5]. The presence of time-scale separation within models describing these systems represent an important feature of such models, producing very interesting dynamics with significant implications on governing the behaviour of the physiological systems they are meant to describe. Moreover, excitable systems can be driven to produce even richer dynamics by the addition of noise [6]. In this chapter, we will use tools from non-linear dynamics and slow-fast analysis to investigate excitability of the model in [4] and determine how it affects dynamics of cell motility in fish keratocytes.

4.2 The Non-Dimensionalized Model

We begin by first considering the non-dimensionalized model of adhesion-dependent wave generation published in [4]. This model describes the movement of the leading edge of a cell driven by actin polymerization pushing against the cell membrane and the biochemical feedback this process receives from interactions between the protein VASP and adhesion complexes anchoring the cell to its substrate. We present the 1-Dimensional spatio-temporal variant of the model, which simplifies a 2-Dimensional spatio-temporal lamellipodium model of the cell into an infinitesimally thin strip just behind the leading edge. As we will demonstrate later, this 1-Dimensional formulation captures the experimentally relevant behaviour of motile cells, while being simpler to analyze.

The spatio-temporal model presented in the supplemental material of [4] is given by

$$\epsilon \frac{\partial}{\partial T} B\left(X,T\right) = \left(1+\eta_B V\right) - \frac{B}{1+AB/(1+M+KB)} + \epsilon^2 \frac{\partial}{\partial X}\left(\frac{1}{\Gamma}\frac{\partial B}{\partial X}\right) + \Xi_t \tag{1}$$

$$\frac{\partial}{\partial T} A\left(X,T\right) = d - \frac{\left(1+\eta_A V+\eta_M M V\right) A}{1+M+KB}, \tag{2}$$

$$\frac{\partial}{\partial T} M\left(X,T\right) = RB - \left(\theta+\eta_M V\right) M, \tag{3}$$

where B is the actin barbed end density, M is the density of mature adhesions, A is the total local concentration of VASP, η_B is the increase in actin branching due to polymerization, R is the scaled maturation rate of nascent adhesions, θ is the scaled disassembly rate of mature adhesions, d is the scaled delivery rate of cytosolic VASP, η_A is the scaled VASP (rearward) advection rate, η_M is the scaled adhesion (rearward) advection rate, K is the ratio of affinities for the binding/unbinding of VASP-to-actin and VASP-to-adhesions, V is the local velocity of the leading edge given by

$$V = \begin{cases} 1-\left(\frac{B_c}{B}\right)^8 & B \geqslant B_c \\ 0 & \text{otherwise,} \end{cases} \tag{4}$$

with B_c being the critical barbed end density required to produce enough force to move the leading

edge defined by

$$B_c = \begin{cases} B_c^0 & \int V dx = 0 \\ (1+E)\, B_c^0 & \int V dx > 0, \end{cases} \tag{5}$$

with $E = 0.1$ being the fractional increase in membrane tension when the leading edge is protruding, $0 < \epsilon < 1$ is a small parameter which quantifies how fast the dynamics of B are compared to A and M, $\Gamma = 1 + AB/(1 + M + KB)$ is a non-dimensional auxiliary parameter related to the (lateral) advective transport of barbed ends due to actin polymerization, and Ξ_t is a Wiener process with auto-correlation $\left\langle \Xi(T)\Xi(T-T') \right\rangle = \Xi_0^2 \delta(T-T')$. Numerical values for all parameters of the non-dimensional model are presented in Table 4.1. Furthermore, in order for the problem to be well-posed, we need two boundary conditions for the variable B. As in [4], we choose Neumann boundary conditions, given by

$$\left.\frac{\partial B}{\partial X}\right|_0 = \left.\frac{\partial B}{\partial X}\right|_L = 0,$$

where L is the length of the domain. Consistent with the results in [4], by using Dirichlet boundary conditions $B|_0 = B|_L = B_0 < B_c^0$, we obtain similar model behaviour but with waves initiated closer to the middle of the domain than with Neumann boundary conditions (results not shown).

Parameter	Definition	Value	Range
d	VASP delivery rate	-	$]0, 1]$
R	Adhesion maturation rate	0.2	$]0, 4]$
η_B	Advection rate for B	1	-
η_A	Advection rate for A	1	-
η_M	Advection rate for M	1	-
K	VASP affinity ratio	1	$]0, 2]$
θ	Degradation rate of mature adhesions	0.05	$]0, 1]$
B_c^0	Basal critical barbed actin density	4	-
E	Fractional increase in membrane tension	0.1	$]0, 1]$
ϵ	Timescale difference of the fast variable	0.1	$]0, 1]$
λ	Smoothing parameter	0.0001	-

Table 4.1: Default parameter values of the model, adapted from [4]. No specific value is assigned to d as it is used as the main bifurcation parameter, and is taken from an appropriate range. Parameter ranges represent the physiologically expected lower and upper bounds of these parameters.

4.3 The Simplified Model

In order to simplify our analysis of the model, we move from a PDE setting where dynamics vary across space and time to an ODE setting where we are essentially considering the intrinsic dynamics of one point along the leading edge. We will demonstrate later the ODE model captures the underlying dynamics of the PDE model very accurately.

Model conversion to an ODE setting is achieved by simply removing the diffusion-like $\partial_x \left(\Gamma^{-1}\partial_x B\right)$ term in Eq. (1), which eliminates the dependence of the function B, A, and M on the spatial variable X, as well as setting $E = 0$. We will discuss these assumptions in more detail in Section 4.5. These simplifications yield the system,

$$\epsilon \frac{d}{dT} B\left(T\right) = \left(1 + \eta_B V\right) - \frac{B}{1 + AB/(1 + M + KB)} + \Xi_t \tag{6}$$

$$\frac{d}{dT} A\left(T\right) = d - \frac{\left(1 + \eta_A V + \eta_M M V\right) A}{1 + M + KB} \tag{7}$$

$$\frac{d}{dT} M\left(T\right) = RB - \left(\theta + \eta_M V\right) M, \tag{8}$$

where all variables and parameters are the same as before. For compatibility with the numerical continuation software AUTO-07p [7] that we have used to analyze the dynamics of the model we have slightly modified Eq. (4) to make it a continuously differentiable function, given by

$$V = \begin{cases} \exp\left[\frac{-\lambda}{B - B_c}\right]\left(1 - \left(\frac{B_c}{B}\right)^8\right) & B \geqslant B_c \\ 0 & \text{otherwise} \end{cases}, \tag{9}$$

where $0 < \lambda \ll 1$ is a small parameter . Notice that by making $\lambda \to 0$, this velocity function defined by Eq. (9) becomes an arbitrarily good approximation for the velocity function defined by Eq. (4) (see Fig. 4.1A). We have also quantified the error that this approximation introduces into the model by finding $\bar{B}$ the value of B where $\partial V/\partial B$ reaches its maximum. The original velocity function defined by Eq. (4), has its maximal slope at $B = B_c$, whereas Eq. (9) has its maximal slope at $\bar{B} > B_c$. Therefore, by evaluating the difference $\bar{B} - B_c$, we obtain simple way of quantifying the error in our approximation. As can be seen in Fig. 4.1B, this error metric increases monotonically with λ and in the limit as $\lambda \to 0$, we have $\bar{B} \to B_c$. Throughout this chapter we have used values of λ that are as small as possible while

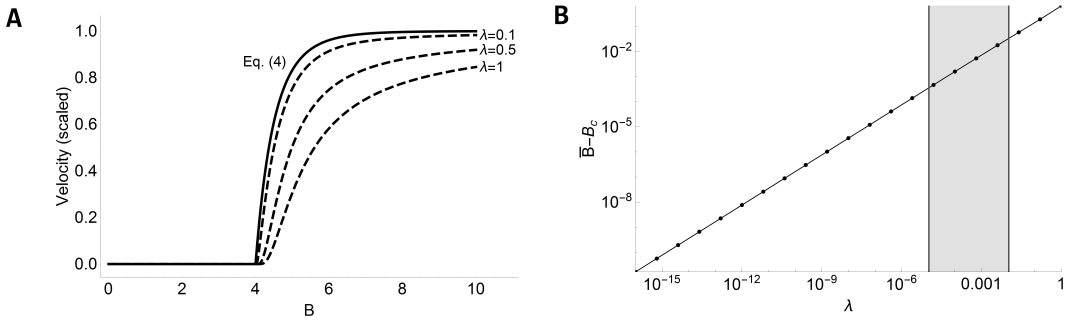

Figure 4.1: (A) Velocity function as defined by Eq. (4) (solid line) and as defined by Eq. (9) (dashed lines) for different values of λ. (B) Convergence measure showing the difference between the maximum slope $\overline{B}$ of the velocity function defined by Eq. (9), denoted by by $\overline{B}$, and that defined by Eq. (4), denoted by B_c. The smaller the λ the smaller this convergence measure.

ensuring numerical stability, choosing it to be within the range $\lambda \in \left[10^{-5}, 10^{-2}\right]$ (see grey region in Fig. 4.1B).

In this section, we will not consider the effects of noise on the system and thus set $\Xi_t = 0$. Under these assumptions, the model becomes a simple deterministic system of ODEs which we will now analyze to understand how the intrinsic dynamics of a single point are reflected in the traveling wave solutions in the PDE model.

4.3.1 The Stalled Equilibrium

From the form of Eq. (4), it is clear that the dynamics of the ODE system may be divided into two regimes that are separated by the plane $B = B_c$. In the regime with $B < B_c$, we have $V = 0$ and the cell is stalled due to insufficient actin polymerization; this produces a simpler dynamical system for which we may solve for its steady state, the stalled equilibrium (B_0, A_0, M_0), given by

$$B_0 = \frac{1}{1-d}, \; A_0 = \frac{d(\theta(-d+K+1)+R)}{\theta\,(1-d)}, \; M_0 = \frac{R}{(1-d)\,\theta}. \tag{10}$$

From these expressions, it is clear that stalled equilibrium is only biophysically-relevant for $d < 1$, as for $d > 1$ the stalled equilibrium will not be in the positive octant of state space. We may further investigate the stability of this equilibrium by evaluating the Routh-Hurwitz criterion. This criterion requires that the coefficients of the characteristic polynomial of the system given by $P(s) = s^3 +$

$a_1 s^2 + a_2 s + a_3$ satisfy $a_1, a_3 > 0$ and $a_1 a_2 > a_3$. The characteristic polynomial for this system, evaluated at the stalled equilibrium, is given by

$$\begin{aligned} P(s) &= s^3 \\ &+ s^2 \frac{\theta\left(\theta(-d+K+1) - (d-1)\left(\epsilon\left((d-1)^2+K\right)+1\right)\right) + R\left((d-1)^2\epsilon+\theta\right)}{\theta(-d+K+1)+R} \\ &- s \frac{(d-1)\theta\left(\epsilon\left(d^2+\theta\left((d-1)^2+K\right)-2d+R+1\right)+\theta\right)}{\theta(-d+K+1)+R} \\ &- \frac{(d-1)^3\theta^2\epsilon}{\theta(-d+K+1)+R}. \end{aligned}$$

From, these criteria we may may conclude that non-negative model parameters with the sole constraint of $d < 1$ are necessary and sufficient conditions for the stability of the stalled equilibrium (see for details).

From the force-velocity relationship (given by Eq. (4)), we can see that $V = 0$ is only valid for $B \leqslant B_c$. Based on the expression for B_0, we can conclude that $B_0 = B_c$ when $d = d_0 := (B_c - 1)/B_c$. Therefore, the stalled equilibrium is a physiologically-relevant stable steady state whenever $d < (B_c - 1)/B_c$. This means that, for $B > B_c$, the stalled equilibrium is no longer a fixed point of the system and only physiologically-relevant whenever $d < d_0 = (B_c - 1)/B_c$. We will demonstrate in the next section that in the limit as $\lambda \to 0$, there is a Hopf bifurcation at $d = d_0$ and the stalled equilibrium gets replaced completely by an unstable steady state in a continuous manner (because V in Eq. (9) is continuous).

4.3.2 Modes of Motility

When $B > B_c$ (i.e., $d > d_0$), we have $V = 1 - \left(B_c/B\right)^8$, producing various modes of motility in the model. In this regime, the non-linearity of V makes obtaining analytical results challenging. To resolve this issue, we use here numerical continuation methods in AUTO to produce bifurcation diagrams that explain how the behaviour of the system changes as certain parameter values are varied.

For the parameter values listed in Table 4.1, we observe that for small enough d the eigenvalues

of the Jacobian matrix for Eqs. (6)-(8) evaluated at the stalled equilibrium (i.e., at $V = 0$) have a complex conjugate pair with negative real part. Indeed, by plotting the bifurcation diagram of scaled actin barbed end density B, whose dynamics is determined by the complete ODE system (6)-(8) with velocity defined by Eq. (9), with respect to scaled VASP delivery rate d, we obtain a branch of stable steady states (see black solid lines in Fig. 4.2) that undergoes a subcritical Hopf bifurcation HB1 at $d_{\text{HB1}} = (1 + \varepsilon(\lambda))d_0$, where $0 < \epsilon(\lambda) \ll 1$ is an increasing function of λ.

In the limit as $\lambda \to 0$, HB1 shifts to $d = d_0$, a scenario that corresponds to the original definition of V given by Eq. (4). As stated before, the remaining analysis is performed for very small λ such that Eq. (9) is as close to Eq. (4) as possible. Based on this, two unstable branches of limit cycles (i.e., envelopes of periodic orbits representing the maximum and minimum of these orbits) emerge from HB1 at $d \approx d_0$. These unstable branches undergo saddle-node bifurcation of periodic orbits at $d_{\text{SNP}} < d_{\text{HB1}}$ (see inset in Fig. 4.2A) followed by a canard explosion, forming two stable branches of limit cycles (solid blue lines) with large-amplitude oscillatory solutions that eventually plateau at higher d values. (see Fig. 4.2A). These periodic branches eventually terminate at a homoclinic bifurcation HM1 at d_{HM1} (the terminal points of these branches), a key feature of type I excitability .

Beyond $d \approx d_0$, the branch of unstable steady states then forms two folds of saddle-node bifurcations SN1 and SN2 at $d = d_{\text{SN1}} \geqslant d_0$ and $d = d_{\text{SN2}}$, respectively. This branch of unstable steady states eventually becomes stable (solid black line) when crossing a Hopf bifurcation HB2 at $d = d_{\text{HB2}} \geqslant d_{\text{SN2}}$, where two small branches (or envelopes) of unstable periodic orbits (dashed blue lines) emerge and terminate at a homoclinic bifurcation HM2 at $d = d_{\text{HM2}}$. This latter homoclinic HM2 coincides with the previous homoclinic HM1 at $d_{\text{HM2}} = d_{\text{HM1}}$. The resulting new stable branch of steady states for $d > d_{\text{HB2}}$ represents the smooth motile equilibria with a constant speed $V > 0$.

Based on this bifurcation structure of Fig. 4.2A, we may conclude that system (6)-(8) exhibits one very small regime of bistability between the stalled equilibrium and oscillatory waving solution when $d_{SNP} < d < d_{\text{HB1}}$ (see inset). This regime is so small, it is very difficult to discern HB1 from SNP. It also exhibits coexistence between the stable smooth motile equilibrium and two unstable steady states between $d_{\text{HM2}} < d < d_{\text{SN1}}$, allowing trajectories of system (6)-(8) to exhibit repetitive and large transient excursions around the motile steady state due to noise. These transient excursions/oscillations (to be discussed in more detail in Section 4.4.1), look similar to periodic oscillations displayed by waving solutions, and thus referred to as stochastic waving.

By decreasing the value of the scaled maturation rate of nascent adhesions R, one can make d_{SN2} smaller than d_0 and cause the branches of stable periodic orbits to terminate at the homoclinic bifurcation HM1 located on the branch of unstable steady states connecting the two saddle-nodes SN1 and SN2 (see Fig. 4.2B). Notice that, according to this configuration, periodic oscillations only exist for a small parameter regime at $d \approx d_{\mathrm{HB1}}$, and that the system exhibits a bistability between the stalled and motile equilibria for $d_{\mathrm{HM2}} < d < d_{\mathrm{SNP}}$. It thus follows that, depending on how d_{SN2} compares to d_0, the system may either exhibit an oscillatory regime as in Fig. 4.2A or a regime of bistability as in Fig. 4.2B.

Thus, in summary, system (6)-(8) can exhibit four possible dynamic behaviours that can coexist. This includes the stalled equilibrium for $d < d_0$, a smooth motile equilibrium for $d > d_{\mathrm{HB2}}$, a waving oscillatory solution $d_{\mathrm{SNP}} < d < d_{\mathrm{HM1}}$, or coexistence between the stalled and smooth motile equilibria for $d_{\mathrm{HM2}} < d < d_{\mathrm{SNP}}$, and a stochastic waving solution for $d_{\mathrm{HM1}} < d < d_{\mathrm{SN1}}$. To further understand how these different monostable and bistable regimes govern dynamics of the PDE model, defined by Eqs. (1)-(3), one needs to plot the two-parameter bifurcation of the system defined by Eqs. (6)-(8) with respect to both the scaled VASP delivery rate d and the scaled maturation rate of nascent adhesions R. Doing so will provide insights onto how these regimes get altered when d, R-parameter space are modified. This is done in detail in the following section.

4.3.3 Two-Parameter Bifurcations

In order to compare the various regimes of behaviour associated with the PDE model defined by Eqs. (1)-(3) and introduced in [4], we have continued all the bifurcation points discussed in Fig. 4.2 within the (d,R)-plane of parameter space (see Fig. 4.3). The resulting two-parameter bifurcation diagram delineates the different monostable and bistable regimes identified in the previous section. Indeed, as shown in Fig. 4.3, the regimes identified in the two-parameter bifurcation follow very closely the map describing the behaviour of the PDE model. Notably, we obtain 5 distinct and discernible regimes: (i) a monostable stalled regime possessing only the stalled equilibrium, bounded to the right by the the saddle-node bifurcation of periodic orbits SNP (which happens to be indiscernibly close to the Hopf bifurcation HB1) and from below by the saddle-node bifurcation SN2; (ii) a monostable waving regime possessing stable oscillatory solutions, bounded to the left by HB1 and to the right by the homoclinic bifurcation HM1 (in red, see inset) coinciding with the homoclinic bifurcation HM2 (in green, see inset); (iii) a bistable regime between the stalled and smooth motile equilibria, bounded

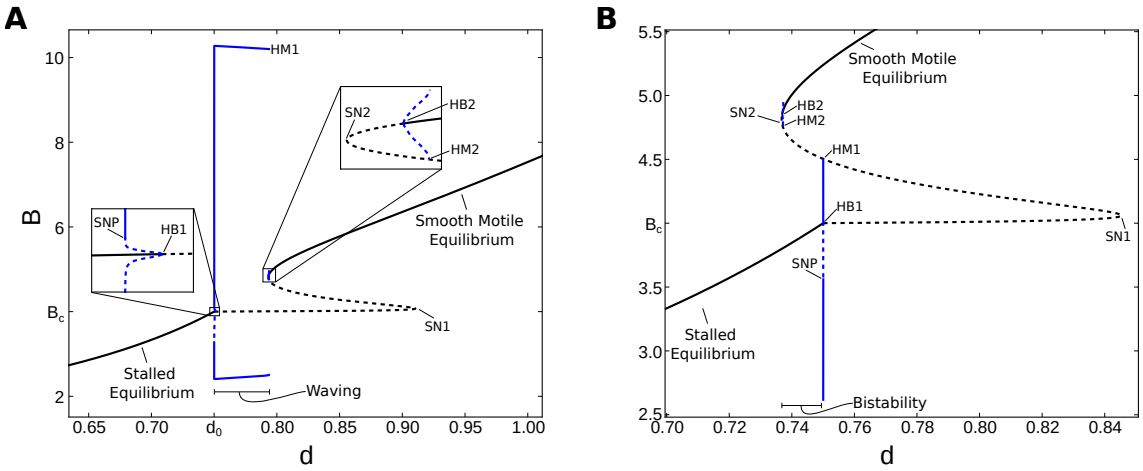

Figure 4.2: One-parameter bifurcation analysis of the full system defined by Eqs. (6)-(8). The bifurcation diagram of actin barbed end density B with respect to the scaled VASP delivery rate d at two different values of the scaled nascent adhesion maturation: (A) $R = 0.1$, and (B) $R = 0.065$. Black solid (dashed) lines indicate stable (unstable/saddle) branches of equilibria; blue solid (dashed) lines correspond to branches or envelopes of stable (unstable) limit cycles. There are five branches of stable and unstable/saddle equilibria in panel A; they are separated by a subcritical Hopf bifurcation HB1 (at $d \approx d_0$), two saddle-node bifurcations SN1 and SN2 and a second subcritical Hopf bifurcation HB2. The branch of stable steady states prior to/beyond HB1/SN2 corresponds to the stalled/smooth motile equilibria, respectively. Two branches of unstable periodic orbits emerge from HB1 but quickly turn into stable branches at a saddle-node bifurcation of periodic orbits SNP (see inset). These stable periodic branches then expand vertically, forming a canard explosion until they eventually plateau and terminate at a homoclinic bifurcation HM1, defining an oscillatory "waving" regime ($d_{\mathrm{SNP}} \leqslant d < d_{\mathrm{HM1}}$). Similarly, two branches of unstable periodic orbits emanate from HB2 and terminate at a homoclinic bifurcation HM2.The waving regimes shrinks significantly in panel B with the canard explosion colliding with the saddle branch between SN1 and SN2, and bistability is formed between the stalled and smooth motile equilibria. Insets around the Hopf bifurcations have not been included in panel B, as they would be qualitatively identical to those in panel A.

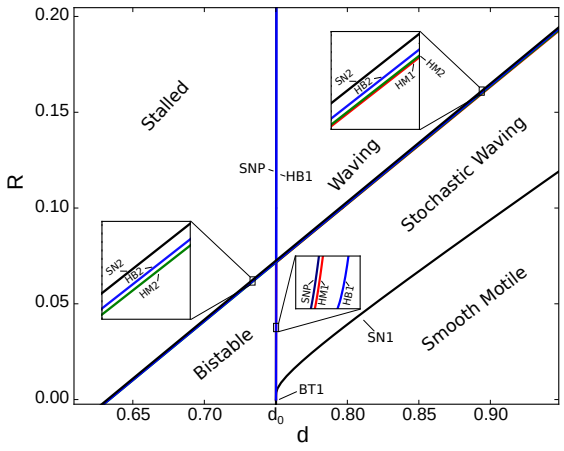

Figure 4.3: Two-parameter bifurcation of the bifurcations points in Fig. 4.2. We observe five distinct regions in parameter space: stalled regime, the bistable regime, the waving regime, the stochastic waving regime, and the smooth motile regime. The bistable and stochastic waving regimes are novel findings, whereas the other regimes had been reported in [4].

to the left/top by HM2 or SN2 and to the right by SNP; (iv) a smooth motile regime possessing the smooth motile equilibrium, bounded from the top by the saddle-node SN1; (v) a stochastic waving regime possessing the smooth motile equilibrium, bounded to the left by the HB1, from the top by HM1 and from the bottom by SN1. Within this configuration, additional very small regimes also exist. Namely, a bistable regime between the stalled equilibrium and waving solution between SNP and HB1, as well as a bistable regime between the smooth motile equilibrium and the waving solution between HB2 and HM1.

The fact that some of these regimes match well with those previously identified with the PDE model [4] and further identifies new ones not previously discovered in [4] suggests that the spatio-temporal patterns produced by the PDE model can be understood from the intrinsic dynamics of the ODE model. Interestingly, we have identified a novel regime, the stochastic waving regime. This regime is separated from the previously identified smooth motile regime by the continuation of SN1, which is depicted in Fig. 4.3 as a line that terminates at the Bogdanov-Takens bifurcation BT1 where it collides with HB1 and SNP at $(d_0, 0)$. As we shall see in Section 4.4.3, when the system is between HM1 and SN1, it is sensitive to the presence of noise, leading to stochastically-induced transient oscillations despite the fact that the system only possesses one stable fixed point.

4.4 Slow-Fast Analysis

As indicated by Eqs. (6)-(8), setting $\epsilon \ll 1$ generates a time scale separation, making the variable much faster than A and M. Thus to understand dynamics, one can apply slow-fast analysis on the full system by dividing it into one fast variable and two slow variables. Within the context of this analysis, we can obtain the critical manifold S of system (6)-(8), determined by the steady states of the fast subsystem B as a function of the slow subsystem defined by A and M, and decomposing it into attracting and repelling sheets that are typically separated by folds in S. An attracting (repelling) sheet of a critical manifold is defined as the set all points $\mathbf{p} \in \mathcal{S} \subset S$ that make all the eigenvalues of $(D_{\mathbf{x}}\mathbf{f})(\mathbf{p})$ have negative (positive) real parts, where $\mathbf{x}$ is the fast subsystem (i.e., $\mathbf{x} = B$ in the model under consideration) and $\mathbf{f}$ is the right hand side of the ODE defining the fast subsystem (i.e., $\mathbf{f} = dB/dT$ in the the same model). If a sheet is neither attracting nor repelling, it is said to be of saddle type. However, since our fast-subsystem is of dimension one, the critical manifold cannot have any sheets of this type. For a system with one fast and two slow variables (e.g., system (6)-(8)), the fold points that separate attracting and repelling sheets form smooth fold-curves [8], that are typically curves of saddle-nodes for the fast subsystem .

In other words, for (6)-(8) we define the critical manifold of the system as the null-surface of the fast variable B, given by

$$S = \left\{(B, A, M) : dB/dT = 0\right\}.$$

Similar to our analysis of equilibria, it is useful to decompose the critical manifold into two parts $S = S_V \cup S_0$ that correspond to when $V > 0$ and $V = 0$; they are defined by

$$S_V = \left\{(B \geqslant B_c, A, M) : dB/dT = 0\right\}$$

and

$$S_0 = \left\{(B < B_c, A, M) : dB/dT = 0\right\}.$$

We may further subdivide the critical manifold into three distinct sheets, according to their stability properties. Two of these sheets are attracting while the other is repelling; the very top, labeled S_V^a, and the very bottom (primarily comprised of S_0) sheets are attracting, whereas the middle one, labeled S_V^r, is repelling. In the limit of $\lambda \to 0$, the sheets S_0 and S_V^a are separated from S_V^r by two fold-curves

of the critical manifold, F^- and F^+, respectively (see Fig. 4.8). Furthermore, in this limit, we have $S_V = S_V^r \bigcup F^+ \bigcup S_V^a$. When we have $\lambda > 0$, there is an additional a portion of the bottom attracting sheet which extends from the upper edge of S_0 to the lower edge of S_V^r, where it meets the latter at F^- (in the limit $\lambda \to 0$ this attracting sheet shrinks down to nothing and the fold becomes arbitrarily sharp).

Superimposing the cubic-like curve formed by the intersection of the two A- and M-nullsurfaces (red curve in Fig. 4.4) onto the critical manifold can generated up to three intersections with S; these intersections can lie on any sheet of S. We will refer to this red line as the nullcurve hereafter. Using this configuration and the steady states formed by these intersections, one can decipher the dynamics of the full system in various parameter regimes (see Fig. 4.4).

Due to the presence of time-scale separation, the system exhibits slow and fast epochs; during the slow epochs, trajectories travel along the critical manifold, whereas during the fast epochs, dynamics of the fast variable dominate causing trajectories to jump between branches of the critical manifold. These jumps occur towards the end of each slow epoch when solution trajectories approach a fold (or a saddle-node) in the critical manifold. In other words, the critical manifold locally organizes the dynamics of the full system according to its slow and fast subsystems.

Although the condition $\epsilon \ll 1$ is required to observe the slow-fast dynamics, the choice of ϵ is somewhat arbitrary. Specifically, we observe that for $\epsilon = 0.1$, much of the system's dynamics can be well understood using the critical manifold and its two folds, suggesting that, in the oscillatory regime, the system acts as a relaxation oscillator (see Fig. 4.4C) [9]. Nonetheless, in the analysis presented here, we will study the underlying dynamics of this system in various parameter regimes to understand how it behaves and how noise can produce interesting outcomes.

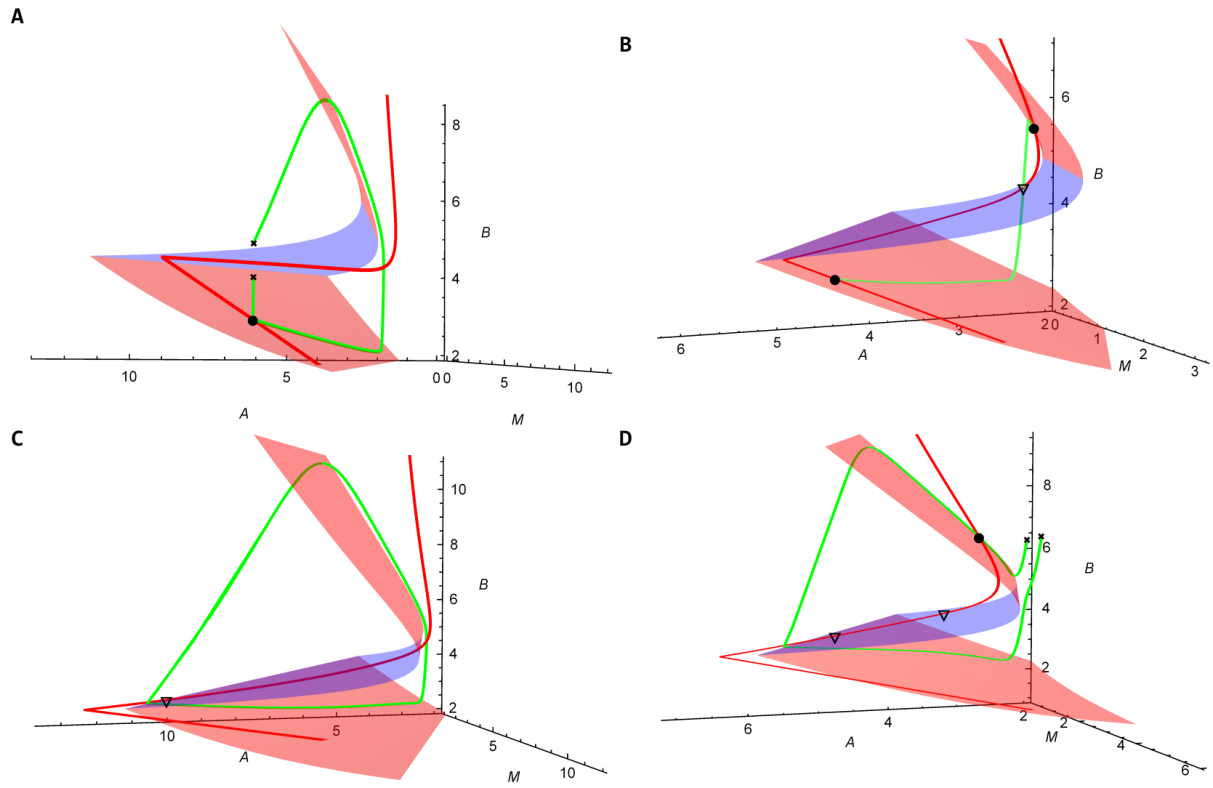

Figure 4.4: Slow-fast analysis of the full system defined by Eqs. (6)-(8). The critical manifold S is depicted as a red surface, and the cubic-like nullcurve of the slow subsystem, defined as the intersection of the A- and M-nullsurfaces, is plotted as a red line. S consists of three sheets, two of which (the very top and bottom) are attracting (red surfaces) while the other is repelling (blue surface). The intersection of S with the nullcurve are the fixed points of the system, where stable fixed points are depicted as filled circles, and unstable (saddle) fixed points are depicted as open triangles. The number of fixed points and their stability define different regimes of model behaviour: (A) stalled ($d = 0.65, R = 0.15$), (B) bistable ($d = 0.72, R = 0.04$), (C) waving ($d = 0.8, R = 0.15$), and (D) stochastic waving ($d = 0.8, R = 0.05$). Superimposing solution trajectories (green lines) illustrate the transient and steady state dynamics of the full system. In general, during slow epochs, trajectories travel along the attracting sheets of the critical manifold while during fast epochs they jump from one sheet to another. When relevant, initial conditions for trajectories are depicted as a black x symbol.

4.4.1 The Stalled and Bistable Regimes

As discussed above, the system has a stalled equilibrium when $d < d_0$ (in the limit as $\lambda \to 0$). In [4], it was stated that this regime is excitable, but a precise characterization of that excitability was not

provided. To do so, we begin first by focusing on the scenario where the stalled equilibrium is the sole attractor for the system (i.e., when $d_{\text{HB2}} > d_0$). With this scenario, we obtain only one point of intersection representing the stalled equilibrium, formed by S_0, the bottom attracting sheet of the critical manifold S, and the nullcurve (see filled circle in Fig. 4.4A). By applying "small" perturbations away from the stalled equilibrium, we obtain graded responses that relaxes back to S_0 where the system will relax more slowly to the stalled equilibrium (see the short green line landing on the filled circle in Fig. 4.4A). Such behaviour is very intuitive, as small amplitude noise leads to small fluctuations around the stalled equilibrium (see time series simulations in Fig. 4A). However, when perturbations push the system beyond the repelling sheet S_V^r, solution trajectories shoot up to the attracting sheet S_V^a and then travel along this sheet until they cross the fold delimiting S_V^r and then jump down to S_0 where they relax back to the stalled equilibrium. Such behaviour is one of the hallmarks of excitability, where there is a threshold in perturbation strength which must be crossed for the full system to exhibit a large excursion (see Fig. 4.5A). Due to the fact that $B(t)$ crosses B_c at every excursion, the local velocity of the leading edge V quickly jumps between its two extreme values as in Fig. 4.5B.

In the bistable regime (i.e., when $d_{\text{HB2}} < d < d_0$), on the other hand, we obtain, as expected, two points of intersections between the stable sheets of S and the nullcurve (see Fig. 4.4B). These intersections represent the stable stalled and motile equilibria. The behaviour of the full system in this regime is similar to that observed in the stalled regime when it comes to exhibiting graded responses to "small" perturbations away from either one of the two steady states by relaxing quickly to the closest attracting sheet and then more slowly along this sheet to a steady state. However, if perturbations push the system beyond a threshold (see Section 4.4.3 for more about this threshold) trajectories will travel to the other steady state (see Fig. 4.4B). Unlike the stalled regime, in this bistable regime, the steady state the system converges to depends on the perturbation applied and/or the initial condition of the system.

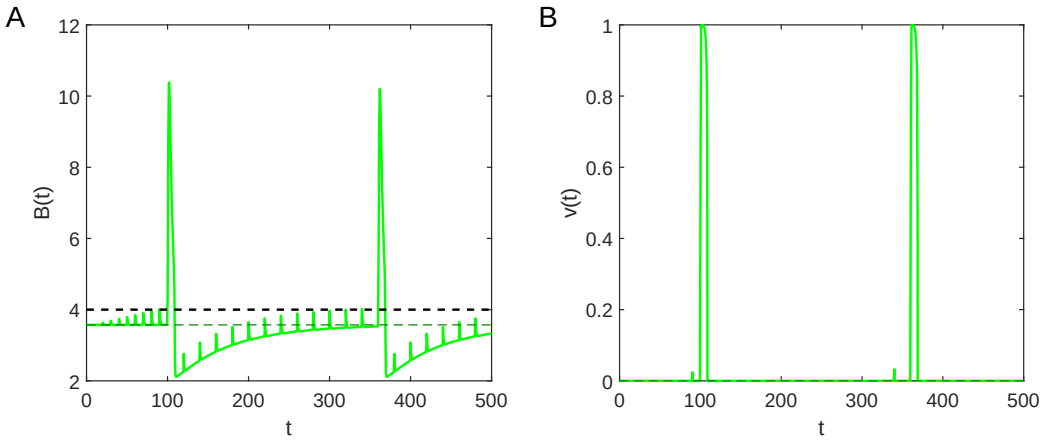

Figure 4.5: Excitable dynamics obtained in the stalled regime. Impulsive perturbations are given to the system every 10 seconds when $t \in [20, 90]$ with increasing magnitudes and every 20 seconds when $t \in [100, 400]$ with a constant magnitude. (A) Time series simulations of actin barbed end density $B(t)$ in the absence of perturbations (dashed green line), showing that it remains at its fixed point near $B = 3.5714$ (i.e., the stalled equilibrium), and in the presence of perturbations (solid green line) that become suprathreshold, surpassing $B_c = 4$ (dashed black line). Notice that, in the latter case, we have "all or none" response in which subthreshold perturbations evoke only graded responses, whereas suprathreshold perturbations evoke large excursions, and that the return to the stalled equilibrium the system exhibits a “refractory period” where perturbations do not induce large excursions until the system is sufficiently close to stalled equilibrium. (B) Time series simulations of the velocity $V(t)$. When $B > B_c$ the velocity becomes non-zero and drops back to zero when $B < B_c$. Here we have used $\delta = 0.72$.

4.4.2 Relaxation oscillations

When the periodic branches of Fig. 4.2A (blue lines) exhibit a plateau phase for $d \in [d_{HB1}, d_{HM1}]$, the system behaves like a relaxation oscillator in a manner similar to the van der Pol oscillator [10]. Slow-fast analysis reveals that the underlying dynamics of the system in this regime does indeed behave that way (see Fig. 4.4C). The critical manifold and the nullcurve, in this case, intersect only once in the middle repelling sheet S_V^r (blue surface in Fig. 4.4C), producing a saddle fixed point (open triangle) surrounded by a periodic orbit (green line) that jumps between the two attracting sheets S_0 and S_V^a (red surfaces in Fig. 4.4C). This ramp effect allows such an orbit to exhibit relaxation oscillations by staying close to the upper and lower attracting sheets during the slow phase and jumping between them during the fast phase.

4.4.3 Stochastic Waving Regime

4.4.3.1 Deterministic Dynamics

As indicated in Fig. 4.2A, when $d_{HM2} < d < d_{SN1}$, the only stable attractor is the smooth motile equilibrium and thus one would expect the system to exhibit motility with a constant velocity $V > 0$. However, as we discussed in the previous section, in such a scenario, it is possible to obtain transient-waving behaviour in the presence of noise. Indeed, in this regime the system has three equilibria, one of which is stable and represents the smooth motile equilibrium, while the other two are of saddle type. For $d \approx d_{\mathrm{HM2}}(= d_{\mathrm{HM1}})$ the smooth motile equilibrium is very close to the middle saddle fixed point, which means that small perturbations may push the system past the stable manifold of this saddle (see Fig. 4.2). In the deterministic case, the stable manifold of the saddle acts as a separatrix which divides phase space into distinct regions, each of which contains the family of trajectories that converge to the system's distinct attractors (e.g., the smooth motile equilibrium). Although the smooth motile equilibrium is the only attractor in this regime, sufficiently large perturbations can push the system across the stable manifold of the saddle, causing trajectories to undergo large excursions to return back to this attractor (see the two trajectories (green lines) in Fig. 4.4D that start from close but distinct initial conditions). We have previously called this noise-dependent oscillation-like behaviour of the system stochastic waving and the parameter regime associated with it the stochastic waving regime.

In Section 4.4.1, we saw how the repelling middle sheet S_V^r of critical manifold acts as a threshold for excitation of the system, producing large excursions once perturbations push the system beyond the threshold. Such statements only make sense in the context of slow-fast analysis, and it is understood that the critical manifold is only an approximation of the true "slow manifold" which governs the dynamics for $\epsilon > 0$ [11]. This type of excitability is frequently discussed in the context of the Fitzhugh-Nagumo and Morris-Lecar models and labeled type III excitability. It should be distinguished from the one observed here in the stochastic waving regime, whereby dynamics are not governed by the critical manifold, but rather by the stable manifold of the saddle-fixed point in a configuration that includes two additional steady states, the stable smooth motile equilibrium and another upper saddle fixed point. This type of excitability with single transient spikes is reminiscent to that observed in a Hodgkin-Huxley type model previously characterized by our group [12, 13].

To better illustrate how the stable manifold of this saddle fixed point along with other manifolds

organize trajectories, we have computed in Fig. 4.6 the stable and unstable manifolds of the two saddle fixed points (open triangles) lying to the left of the stable node (filled circle), i.e., the smooth motile equilibrium. With this new viewing angle of the system shown in Fig. 6, we can see that the right saddle fixed point has two-dimensional stable manifold (red surface) and one-dimensional unstable manifold (blue line), whereas the left saddle fixed point has one-dimensional stable manifold (red line) and two-dimensional unstable manifold (blue surface). The red surface accumulates to the left with the red line, generating a hollow space further to the left thereby allowing passage of solution trajectories. Indeed, by plotting solution trajectories (green curves) starting from two different initial conditions lying on either side of the red stable manifold shows that the trajectory starting from the left converges quickly to the stable node, while the other starting from the right generates a large loop around the manifold that takes advantage of the hollow space to return back to the stable node. In other words, the stable manifold of the right saddle fixed point determines if the system undergoes a large excursion following a perturbation and acts as a "threshold" between pronounced and graded responses. This further highlights the difference between this type of excitability and the one seen in type III oscillators.

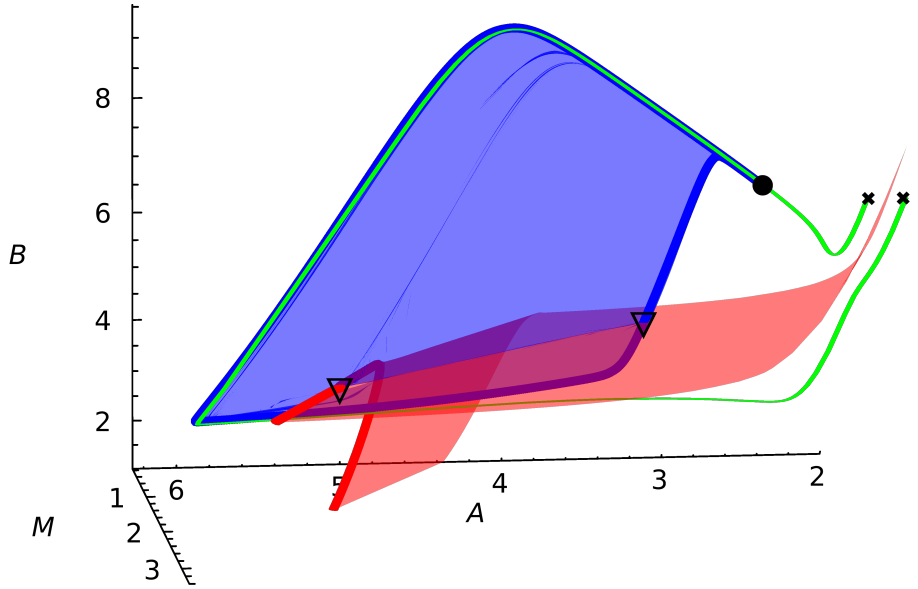

Figure 4.6: The topology of the stable and unstable manifolds associated with the saddle fixed points govern the dynamics of excitability in the stochastic waving regime. Three steady states are present in this regime, a stable node representing the smooth motile equilibrium to the right (filled circle), and two saddle fixed points to the left (open triangles). The right saddle fixed point has two-dimensional stable manifold (red surface) and one-dimensional unstable manifold (blue line), while the left saddle fixed point has one-dimensional stable manifold (red line) and two-dimensional unstable manifold (blue surface). Two solution trajectories starting from different initial conditions are also plotted (green lines), one of which is initiated to the left of the red surface and one to the right of the red surface. The former quickly converges to the stable node, generating a graded response, while the latter elicits an excursion around the red surface that escapes from the hollow space to the right of the blue line back to the stable node, generating a pronounced response.

4.4.3.2 Noise-Dependent Dynamics

We now consider what happens in the stochastic waving regime in the presence of noise (i.e., when $\left\langle \Xi_t^2 \right\rangle > 0$), where Ξ_t accounts for stochasticity arising from discrete effects in biochemical reactions [14]. These discrete effects motivate the discussion of perturbations on solution trajectories. Intuitively, we may expect these perturbations to cause $B\left(t\right)$ to fluctuate around its equilibrium position B^*. We find that once the system becomes ergodic, the distribution $B\left(t\right)$ is well approximated by a normal distribution $B \sim \mathcal{N}\left(B^*, 12\Xi_0\right)$, where the factor "12" was determined empirically (see inset of Fig. 4.7A). This empirical value depends on the specific numerical values we choose for the parameters,

where analytic formula for the ergodic distribution of B may be obtained by solving for the stationary distribution of the corresponding Fokker-Planck equation ([6, 14], beyond the scope of this analysis). Nonetheless, if we draw N independent identically distributed samples of $B\left(t\right)$ for $t \in \left[T_0, T_1\right]$, with $T = T_1 - T_0$ sufficiently large that $B\left(t\right)$ is ergodic, the expected maxima/minima of the samples can be estimated as $B^* \pm \kappa 12\Xi_0$ (see black dashed lines in Fig. 4.7A), where $\kappa = \sqrt{2}\text{erf}^{-1}\left(1 - N^{-1}\right)$ is adapted from the $\left(1 - 1/N\right)^{\text{th}}$ quantile function of the normal distribution. While the above analysis holds for sufficiently small values of Ξ_0, larger amplitude noise will push the system past the stable manifold of the middle saddle, such that the process is no longer ergodic. When this occurs, the system undergoes a large excursion in order to return to the stable smooth motile equilibrium. This leads to a behaviour which is quite similar to the waving regime, but where the period with $V > 0$ is variable in duration due to the "oscillations" being initiated stochastically (see Fig. 4.7B).

We note here that these transient excursions from the stable fixed point are only observed for small-to-medium levels of noise, as large amplitude noise tends to dominate over the intrinsic dynamics of the model. As we move from SN2 to SN1, the distance between the stable fixed point and the stable manifold of the saddle lying between SN1 and SN2 increases, requiring increasingly large amounts of noise to induce transient excursions. Thus as $d \to d_{\text{SN1}}$ transient excursions become increasingly less likely. Therefore, the region where stochastic oscillations may be observed is considerably smaller than the region labeled as the stochastic waving regime, and is likely a narrow band just below HM1 in Fig. 4.3.

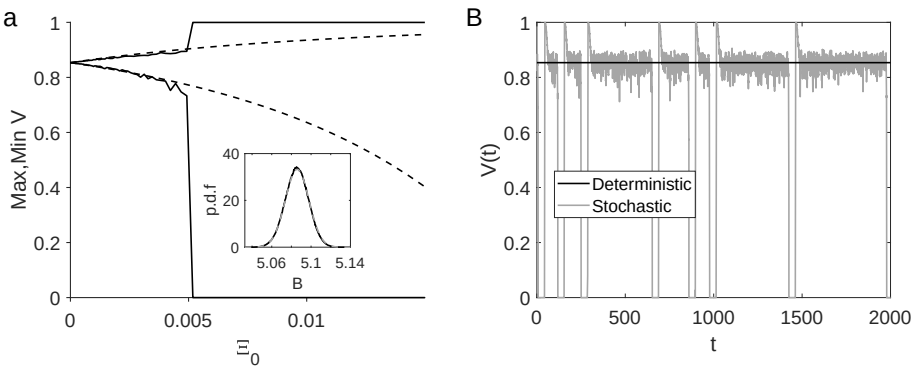

Figure 4.7: Noise-dependent dynamics in the stochastic waving regime. (A) The maximum and minimum observed protrusion velocity as the noise magnitude Ξ_0 is varied (solid lines). For small values of Ξ_0, fluctuations relax back to the smooth motile equilibrium and the max/min is well predicted by evaluating $V\left(B^* \pm \kappa 12 \Xi_0\right)$ (dashed lines). However for $\Xi_0 \gtrsim 0.006$, fluctuations push the system past the stable manifold of the middle saddle leading to a breakdown of the previous prediction. (inset) For $\Xi_0 \lesssim 0.006$, the empirical distribution (black line) of $B\left(t\right)$ agrees very well with the theoretical probability density function of a normal distribution (grey dashed line) with a standard deviation given by $\kappa 12 \Xi_0$ (here we have used $\Xi_0 = 0.007$). (B) Time series simulations of the model in the stochastic waving regime. In the absence of noise, the system remains at the motile equilibrium with protrusion velocity $V(B^*) > 0$ (black line). In the presence of noise ($\Xi_0 = 0.007$), the system is perturbed beyond the stable manifold of the saddle and it undergoes large excursions that push it below $B = B_c$, causing protrusion velocity to drop to $V = 0$ stochastically (gray line).

4.4.4 The Oscillatory Regime

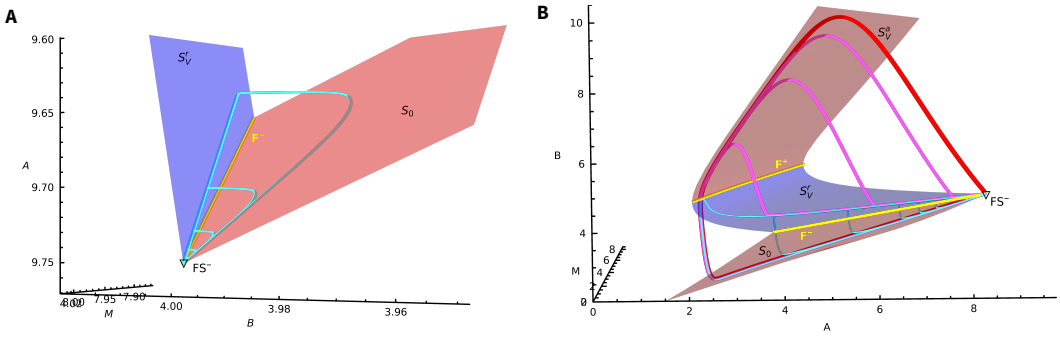

Figure 4.8: The canard explosion coming out of HB1, where the stalled equilibrium changes to a saddle fixed point that is near the folded saddle FS^- (open triangle symbol) lying on the lower fold-curve F^- (yellow line). (A) Very close to HB1, limit cycles (cyan lines) expand with increasing d. These limit cycles are headless canard orbits as they travel first along the attracting sheet S_0 (red surface) and eventually jump up to the a repelling sheet of S_V^r (blue surface) and back to the folded saddle FS^-. (B) As d continues to increase, the headless canards travel further along S_0 and S_V^r coming closer and closer to the upper fold-curve F^+ (yellow line) in the critical manifold where S_V^r meets the attracting sheet S_V^a (red surface). The headless canard which has a peak right at F^+ is termed the maximal canard, and this canard separates the family of headless canards from the family of canards with head (magenta lines). The canards with head continue to grow by traveling further along S_V^a, until they jump down to S_V^r where they travel back to FS^-. As d grow even further, the orbits eventually become relaxation oscillations (red line) that jump between the attracting sheets S_V^a and S_0 and do not travel along the repelling sheet S_V^r.

4.4.4.1 The Folded Singularities

As discussed previously, the full system exhibits fast and slow epochs where the dynamics of the fast and slow variables dominate, respectively. For $d_{\text{SNP}} < d < d_{\text{HB2}}$, the full system (6)-(8) has a limit cycle as its sole attractor. Within a subset of this regime of size $\mathcal{O}(\Delta d) = 10^{-5}$, the system exhibits canard orbits where it spends a signifcant amount of time travelling along the unstable sheet S_V^r (see Fig. (4.8)). Such an observation is surprising given that S_V^r is a repelling sheet, and thus by definition we expect trajectories of the full system to travel away from S_V^r (e.g., see Section 4.4.1). Accordingly, we restrict the dynamics of the full system to critical manifold. In this setting, the dynamics are described

by the reduced problem, given by

$$0 = f = \left(1 + \eta_B V(B)\right) - \frac{B}{1 + AB/(1 + M + KB)} \tag{11}$$

$$\frac{d}{dT}A(T) = g_A = d - \frac{(1 + \eta_A V + \eta_M MV)\,A}{1 + M + KB} \tag{12}$$

$$\frac{d}{dT}M(T) = g_M = RB - (\theta + \eta_M V)\,M, \tag{13}$$

which can be obtained from system (6)-(8) by taking the limit as $\epsilon \to 0$. This is formally equivalent to saying that the fast variable B is projected onto the critical manifold S. As can be seen in Fig. 4.8, the canard orbits travel along the critical manifold, passing over the fold which joins S_0 and S_V^r (the lower black line in Fig. 4.8B). In order to understand this phenomenon in more detail, we furthermore focus on the dynamics of the reduced problem as it passes over the fold-curveF^-. Generically, fold-points are defined by singularities in the representation of the reduced problem [15], i.e.,

$$f(B, A, M) = 0, \quad \frac{\partial f}{\partial B}(B, A, M) = 0. \tag{14}$$

Generally, away from fold-points, the fast variable B may be expressed as a function of the slow variables $h(A, M) = B$ that can be obtained by solving $f(B, A, M) = 0$, where f is defined in Eq. (11). In other words, the critical manifold S may be represented over a single coordinate chart of the slow variables. By expressing the dynamics of B on the critical manifold, we obtain

$$\frac{d}{dT}B = \left(\frac{\partial f}{\partial B}\right)^{-1}\left(\frac{\partial f}{\partial A}g_A + \frac{\partial f}{\partial M}g_M\right).$$

At a fold-point, along either fold-curve F^- or F^+, the projection of B onto S is singular, which motivates the definition of a rescaled time variable $\tilde{T}$ with $T = \tilde{T}D_B f$. This allows us to define the

desingularized reduced problem

$$\frac{d}{d\tilde{T}}B = \frac{\partial f}{\partial A}g_A + \frac{\partial f}{\partial M}g_M \tag{15}$$

$$\frac{d}{d\tilde{T}}A = \frac{\partial f}{\partial B}g_A \tag{16}$$

$$\frac{d}{d\tilde{T}}M = \frac{\partial f}{\partial B}g_M, \tag{17}$$

where we may further reduce the dimension of the system by using Eq. (11) to, without loss of generality, eliminate the slow variable M [15], such that it is given by the expression

$$M = M_{\text{crit}}\,(A, B) \coloneqq \frac{AB(1+\eta_B V(B))}{B-(1+\eta_B V(B))} - BK - 1.$$

Thus, after substituting in Eq. (9), we may express the desingularized system (i.e., the desingularized reduced problem projected onto the critical manifold) as

$$\begin{aligned}\frac{d}{d\tilde{T}}B = &-\frac{B+\sigma_1}{AB^2\eta_B}\Big[B\eta_B(B(\theta K+R)+\theta+1) \\ &\sigma_1\eta_B(B(\theta(A+K)+d+R)+\theta+1)-(\sigma_1+1)\eta_A(B+\sigma_1)\Big]\end{aligned} \tag{18}$$

$$\begin{aligned}\frac{d}{d\tilde{T}}A = &\frac{\sigma_2}{AB^3\sigma_1\eta_B}\Big[(\sigma_1+1)\eta_M(B(\sigma_1(A+K)+BK+1)+\sigma_1) \\ &+\eta_B(Bd\sigma_1+B+\sigma_1)+(\sigma_1+1)(-\eta_A)(B+\sigma_1)\Big].\end{aligned} \tag{19}$$

where $\sigma_1 = -\left(1+\eta_B V(B)\right)$ and $\sigma 2 = AB^2\eta_B V'(B) - {\sigma_1}^2(A+K) - B^2K - 2BK\sigma_1$.

By inspection of Eq. (16), we see that the desingularized system has at least two A-nullclines, one corresponding to the fold ($\partial f/\partial B = 0$) and the other corresponding to the A-nullclines of the full system ($g_A = 0$). Because we are interested in the dynamics precisely as trajectories cross the fold, we will focus on the the former case, i.e., the folded singularities of the desingularized system, defined by,

$$\frac{\partial f}{\partial B} = 0 \quad \text{and} \quad \frac{\partial f}{\partial A}g_A + \frac{\partial f}{\partial M}g_M = 0. \tag{20}$$

In order to find these folded singularities numerically, we isolate A in both the first and second expres-

sions of Eq. (20) restricted to $M = M_{\text{crit}}(A, B)$, yielding

$$A = A_{\text{fold}}(B) := \frac{K(-\eta_B V(B) + B - 1)^2}{B^2 \eta_B V'(B) - {\eta_B}^2 V(B)^2 - 2\eta_B V(B) - 1},$$

and,

$$\begin{aligned} A \;=\; & \frac{1}{B\theta(\eta_B V(B) + 1)} \Big[B(\theta(-BK + K - 1) - BR + d + R - 1) + \theta + 1 \\ & V(B)(\eta_B(B(d + \theta K + R) + \theta + 1) + \eta_A \eta_B V(B) - B\eta_A + \eta_A) \Big], \end{aligned}$$

respectively. With the parameters listed in Table 4.1 with $d = 0.750004 = d_{\text{HB1}}$, we find that these two curves intersect at

$$B^- \approx 4.00002 \quad \text{and} \quad B^+ \approx 5.19902$$

which correspond to the B-values of the two folded singularities located on F^- and F^+, respectively. We further note that although F^+ and F^- appear to be disjoint curves in Fig. 4.8, they actually meet at a cusp-like structure near $(B, A, M) = (4, 0, -5)$.

Folded singularities can be characterized by their two non-zero eigenvalues [15], which we have determined from the Jacobian matrix of the desingularized system (18)-(19) evaluated at the two folded singularities, given by

$$FS^- = \left(B^-, A_{\text{fold}}\left(B^-\right), M_{\text{crit}}\left(A_{\text{fold}}\left(B^-\right), B^-\right)\right),$$

and

$$FS^+ = \left(B^+, A_{\text{fold}}\left(B^+\right), M_{\text{crit}}\left(A_{\text{fold}}\left(B^+\right), B^+\right)\right).$$

Numerical evaluation of the Jacobian matrix reveals that both folded singularities are in fact folded saddles (see Table 4.2), but only the lower folded saddle FS^- is relevant to the canard orbits. The singular canard associated with FS^- (going from the attracting sheet S_0 to the repelling sheet S_V^r and passing through FS^-) determines the flow of solution close to this folded saddle.

FS	(B, A, M)	$J(B, A)$	λ_1	λ_2
FS^-	$(4.00002, 15.7493, 15.999)$	$\begin{bmatrix} 4.88859 \times 10^{-9} & 0.0397441 \\ 0.000148825 & -0.000559416 \end{bmatrix}$	-0.0027278	0.00216839
FS^+	$(5.19902, 6.96656, 14.2681)$	$\begin{bmatrix} -0.00984134 & 0.0899238 \\ 0.000603317 & -0.00115534 \end{bmatrix}$	-0.00919448	0.00559321

Table 4.2: Folded singularities of the desingularized system and their stability properties.

4.4.4.2 Canard Explosion

As can be seen in Fig. 4.2, the periodic envelope of this limit cycle grows very rapidly from $B \approx B_c = 4$ to $B \approx 10$ on an interval with $\mathcal{O}(\Delta d) = 10^{-5}$. This rapid growth of a limit cycle is typically referred to as a canard explosion [8]. In order to understand this phenomenon, we will use the decomposition of the critical manifold S into attracting and repelling sheets; such a decomposition is known to organize the dynamics of limit cycles during the canard explosion [8]. In a system with one fast and two slow variables, attracting and repelling sheets meet at folds of the critical manifold (see yellow lines in Fig. 4.8) and organize the dynamics of the limit cycles during the canard explosion [8]. From Fig. 4.4, we can see that there are two folds in the critical manifold. Furthermore, from what we discussed above with respect to excitability of the stalled equilibrium and the bistable regime, it is clear that, S_V^r, the lower sheet of S_V is repelling whereas, S_V^a, the upper sheet of S_V and the whole of S_0 are attracting (see Fig. 4.8).

Once the full system goes through a Hopf bifurcation at d_{HB1} shown in Fig. 4.2, the stalled equilibrium becomes a saddle fixed point (see Fig. (4.4)C). Right at this point, periodic solution in the form of canard orbits emerge; these canard orbits are limit cycles that follow the bottom attracting sheet S_0 as well as the repelling sheet S_V^r for a significant amount of time by passing very closely to the folded saddle FS^- (open triangles in Fig. 4.8) determined by the desingularized reduced problem [15] (see next section for more details). Initially, the limit cycles travel away from FS^- along S_V^r for some time until they jump to S_0 where they travel back towards FS^- to complete the orbit (see Fig. 4.8A). As d increases, the orbits grow in size and approach the fold that separates S_V^r and S_V^a. Near this fold, the limit cycles begin to jump upwards to S_V^a. They then move along S_V^a down towards the fold. Once they reach the fold, they jump down to S_0 where they move back towards the folded saddle (see Fig. 4.8A).

As d continues to increase, the point at which orbits jump up to S_V^a moves closer to FS^- such that for $d \gtrsim d_0 + 10^{-5}$ the limit cycle spends negligible time traveling along the repelling sheet of the manifold (i.e., the limit cycles are no longer canard orbits, see red line in Fig. 4.8).

4.5 PDE Model Simulations

We now turn our attention to the PDE model, given by Eqs. (1)-(3), in order to see how the analysis of the simplified ODE model carried out in the previous sections can be used to understand the underlying dynamics of the PDE model. We recall that the simplified model is obtained by making two simplifications to the PDE model: (i) the diffusion-like term that accounted for the lateral movement of actin filament tips due to polymerization is dropped; and (ii) the formalism used to determine the critical barbed actin density B_c, as described by Eq. (5), is simplified by setting $B_c = B_c^0$. The first modification transforms the model into a system of first order ODEs whose oscillatory regime corresponded to traveling waves of protrusion for the PDE. The second modification, on the other hand, is somewhat more subtle and requires further investigation.

4.5.1 Two-Parameter Diagram for PDE Model

Applying the second modification through the use of Eq. (9) is necessary to resolve some ambiguities with model definition. In particular, when using Eq. (5), it is unclear what the protrusion velocity should be for $B \in \left[B_c^0, (1+E)\, B_c^0\right]$. In our implementation of the PDE model, we have found that this issue may lead to rapid oscillations (period $= \mathcal{O}(\Delta t)$) in the protrusion velocity when the time step Δt becomes very small. This problem is overcome by choosing the time step such that it satisfies the constraint

$$\Delta t\, \partial B/\partial T\big|_{B=B_c^0} > E B_c^0,$$

which prevents rapid oscillations in the protrusion velocity. This choice is made due to a lack of rapid oscillations in protrusion velocity in the numerical results of [4]. However, such a choice in time step is somewhat inconsistent, and not very practical for the numerical continuation methods used in the bifurcation analysis. Therefore, to circumvent this issue we have opted to analyze the ODE model with a single value of B_c (hence the use of Eq. (9)).

From Eq. (5), it is clear that B_c can attain two distinct values B_c^0 and $(1+E)\, B_c^0$, whenever $B <$

B_c^0 and $B > B_c^0$, respectively. However, it is somewhat less clear which value of B_c is relevant for delineating the boundaries of model behaviour for the PDE. In order to clarify this, we have computed two-parameter bifurcation diagrams for the ODE model, setting $B_c = B_c^0$ or $B_c = (1+E)\,B_c^0$, and then compared the resulting bifurcation diagrams to the regimes of behaviour obtained by the PDE model in [4]. In Fig. 4.9, we show the boundaries of the two-parameter bifurcations that match those identified by the PDE model as solid lines whereas the ones that do not match as thin dashed lines. The most relevant boundaries have been determined by two methods: (i) by extensive testing of the PDE model behaviour on both sides of each boundary determined by the two-parameter bifurcation, and (ii) by comparison to the two-parameter regimes identified in [4] (see thick dashed lines in Fig. 4.9). As can be seen, the PDE model changes its behaviour at boundaries defined by both values of B_c; namely, B_c^0 (whose bifurcations are denoted without tilde, e.g., HB1) and $(1+E)\,B_c^0$ (whose bifurcations are denoted with tildes, e.g., $\widetilde{\text{SN2}}$). In other words, the underlying dynamics of the PDE model is a hybrid of the two. As we have seen in Section 4.3.1, the stalled equilibrium crosses $B = B_c^0$ at d_0. Therefore, for $d \leqslant d_0$, regimes of behaviour associated with $B_c = B_c^0$ are relevant in determining outcomes of the PDE model, while for $d > d_0$, we find that the boundaries associated with $B_c = (1+E)\,B_c^0$ are relevant in delineating the regimes of behaviour (see Fig. 4.9). The exception to this rule is the bistable regime, whose left boundary is defined by $\widetilde{SN2}$ despite having $d < d_0$.

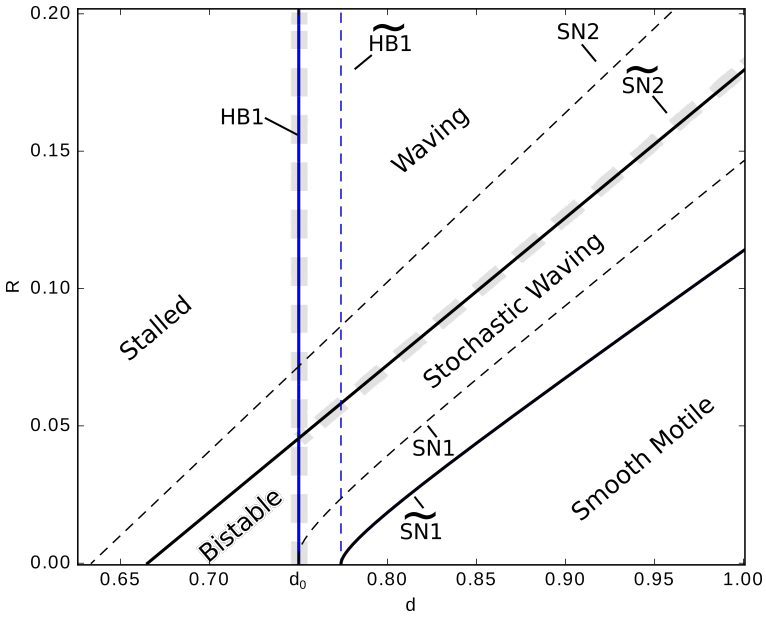

Figure 4.9: Two-parameter bifurcations of the ODE model identify the various regimes of behaviour of the PDE model. Briefly, two-parameter bifurcations similar to that in Fig. (4.3) are computed with $B_c = B_c^0$ and $B_c = (1 + E)\, B_c^0$. Bifurcations associated with the latter value of B_c are denoted with tildes (e.g., $\widetilde{\text{SN2}}$). Bifurcations which coincide with those identified with the PDE model are depicted by solid lines while those that do not coincide are depicted by thin dashed lines. The boundaries of the various regimes of behaviour associated with the PDE model identified in [4] are overlaid as thick grey dashed lines.

4.5.2 The Effects of Noise in the Stochastic Waving Regime

As we have repeatedly stated in Sections 4.3 and 4.4 with the folded nature of the bifurcation structure, there exists a parameter regime (labeled stochastic waving regime) where the ODE is very sensitive to noise. In this regime, deterministic realizations of the model will all converge to the smooth motile equilibrium, while stochastic realizations will exhibit large excursions that lead to a temporary halt in protrusion when the magnitude of noise is sufficiently large (see Fig. 4.7). In order to understand how such dynamics manifest themselves with the PDE model, we investigate here how it behaves in this parameter regime. While it was previously demonstrated that the PDE model is capable of propagating a wave of protrusion [4], it is unclear how it will behave in the stochastic waving regime when a single spatial point is stochastically pushed below the stable manifold of the saddle, transiently blocking

that single point from protruding. Will the "unexcitedness" of that point spread outwards, leading to widespread halt in protrusion? Or will the excited state of the neighbouring points simply fill the zone of depleted B, such that the leading edge will only pause briefly at random points from time to time?

In order to answer these questions, we have implemented the PDE model on a domain of length $L = 40$ with a spatial step $\Delta x = 0.1$ and a time step $\Delta t = 0.01$. Time integration of the model carried out using a second order Adams-Bashforth integrator [16] that can successfully deal with non-linear reaction terms in a computationally efficient manner. The diffusion-like transport term in Eq. (1) and the boundary conditions on B are implemented by an appropriate combination of forward and backward differences for the inner and outer differential operators, respectively.

In the absence of noise, simulations of the PDE model in the stochastic waving regime exhibit a smooth motile behaviour with the whole domain protruding indefinitely (results not shown). However, as discussed in Section 4.4.3, once noise is turned on ($\Xi_0 \geqslant 0.0006$), random fluctuations push the system below the stable manifold of the middle saddle (i.e., the right saddle in Fig. (4.6)) at discrete points in the domain. This leads to a temporary stalling of protrusion which spreads laterally just like protrusion does during the initiation of a wave of protrusion (see Fig. 4.10). This indicates that the transport term $\partial_x \left(\Gamma^{-1}\partial_x B\right)$ in the PDE model can propagate both protrusion initiation and termination events.

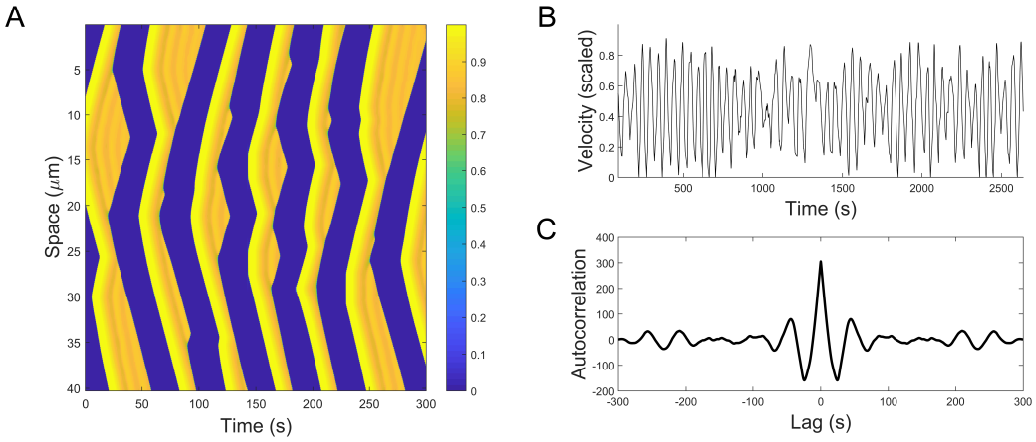

Figure 4.10: The dynamics of the PDE model in the stochastic waving regime with additive noise. Here we have used $d = 1.95979$, $R = 0.8$, and $\eta_A = \eta_M = 0.5$ with $\Xi_0 = 0.0006$. (A) Kymograph of protrusion velocity exhibits traveling wave behaviour where the temporal duration of protrusion can be highly variable even within the same wave. (B) Mean protrusion velocity fluctuating stochastically with respect to time.. (C) Mean auto-correlation function of the protrusion velocity.

4.5.3 Rough Motility

The irregular nature of the protrusions observed here raise the question of whether or not the stochastic waving regime is related to the "rough" mode of motility described in [4]. In this experimentally observed mode of motility (as in the waving mode of motility), a wave of protrusion starts from a single point and spreads outwards producing diagonal stripes in a kymograph that move forward along the time axis such as in Fig. 4.10A. However, rough motility is characterized by the stochastic halting of the propagation of a traveling wave of protrusion (i.e., breaks in the diagonal stripes). At low levels of noise, we do not observe this halting in the stochastic waving regime (see yellow stripes in Fig 4.10A); instead we see stochastically-induced termination event that propagate along the leading edge. Therefore, we sought to test if the noise magnitude could be adjusted to produce this phenomenon (see Fig. 4.11). As we increase the noise magnitude, the waves of protrusion become increasingly distorted with multiple protrusion waves being initiated at the same time (see Fig. 4.11A). By increasing noise further, we do observe some stochastic halting of protrusion waves, but this primarily occurs due two adjacent waves colliding with one another (see Fig. 4.11B) and is therefore a consequence of multiple waves initiating at roughly the same time. If we continue to increase noise, the propagation of

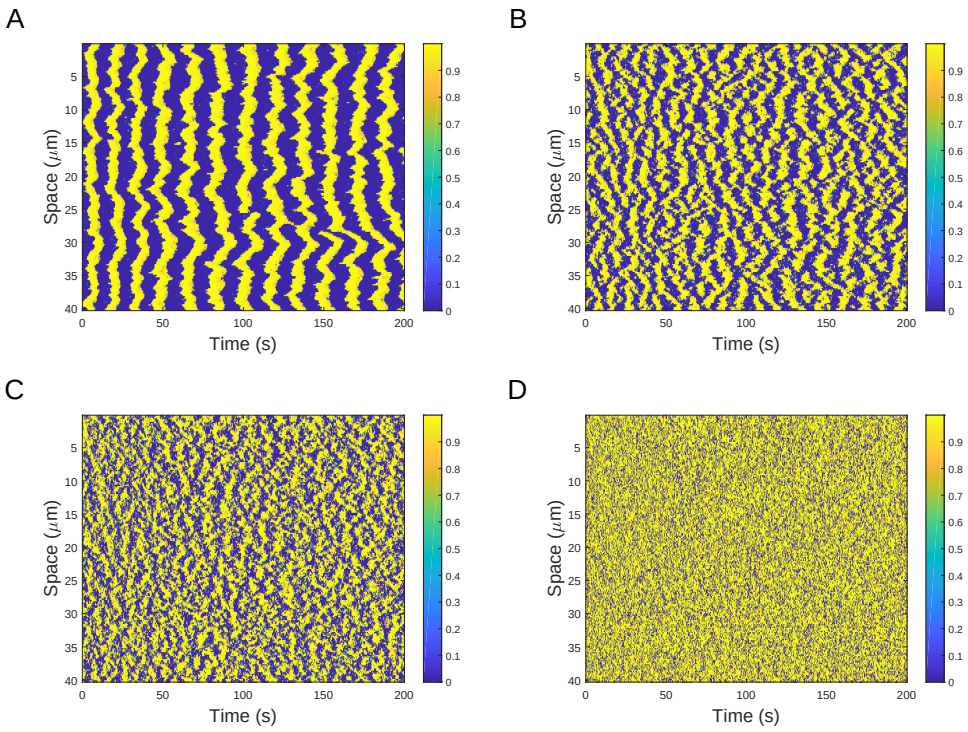

Figure 4.11: The effect of noise in the stochastic waving regime. Kymographs of protrusion velocity with $R = 0.8$, $d = 1.95979$ and (A) $\Xi_0 = 1\text{e} - 1$; (B) $\Xi_0 = 2\text{e} - 1$; (C) $\Xi_0 = 3\text{e} - 1$; and (D) $\Xi_0 = 1$.

protrusion waves becomes less obvious (see Fig. 4.11C), until at very high noise the whole leading edge protrudes and stalls in a completely stochastic manner (see Fig. 4.11D). The behaviour in this regime at high noise is characteristic of all other regimes of system (1)-(3) when noise becomes sufficiently large; propagation of protrusion waves are not observed and the whole of the leading edge is primarily protrusive.

The behaviour described above is different from what is observed in the stalled and bistable regimes, where protrusion waves halt due colliding with a region that is in its refractory period. When looking at a kymographs in these regimes, we see protrusion waves that appear to halt on their own for different values of Θ (see Fig. 4.12A-D). This is much more relevant to the experimentally observed phenomenon, where protrusion waves propagate for some period of time until they stochastically halt without colliding with another wave (see Fig. 1F in [4]). Therefore, it is tempting to ascribe experimen-

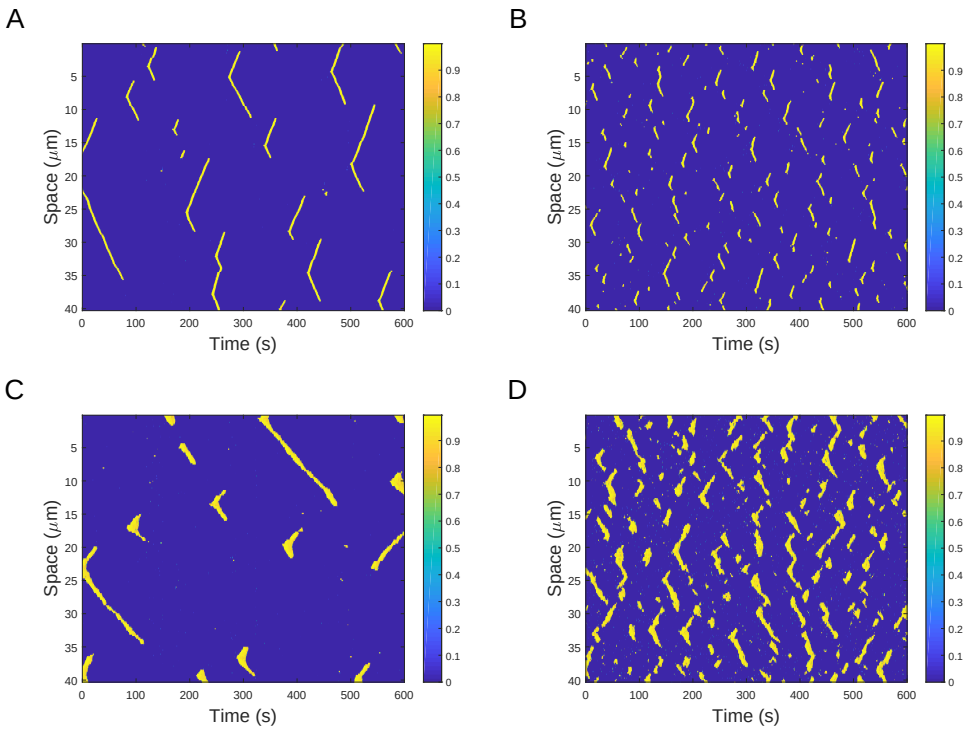

Figure 4.12: The effect of noise in (A&B) the stalled regime with $R = 0.2$ and $d = 0.7$, and (C&D) bistable regime with $R = 0.02$ and $d = 0.7$. Kymographs of protrusion velocity with (A) $\Xi_0 = 4\text{e} - 2$; (B) $\Xi_0 = 7\text{e} - 2$; (C) $\Xi_0 = 5\text{e} - 2$; and (D) $\Xi_0 = 8\text{e} - 2$.

tally observed rough motility to these regimes. Indeed, such a conclusion was hinted at in [4], where the stalled regime was used to produce PDE simulations similar to those displayed in Fig. 4.12.

While the spatio-temporal dynamics of the PDE model evaluated at specific parameter values allow us to rule out the stochastic waving regime as a candidate for rough motility, to distinguish between stalled and bistable regime, we turn our attention to population statistics of the modes of motility. Experimental manipulations in [4] suggest that the parameter regime associated with rough motility should grow in size as the maturation rate of adhesions R is decreased (see Fig. 1M in [4]). This assumption may be justified by considering the heterogeneity of a population of cells as a set of points in parameter space (e.g., see coloured ellipses blue and pink in Fig. 4.13 for an illustration in (d, R)-space). Plating cells on a substrates of varying adhesiveness corresponds conceptually to varying the R parameter-value of a population of cells, where substrates with a high (medium) adhesiveness corre-

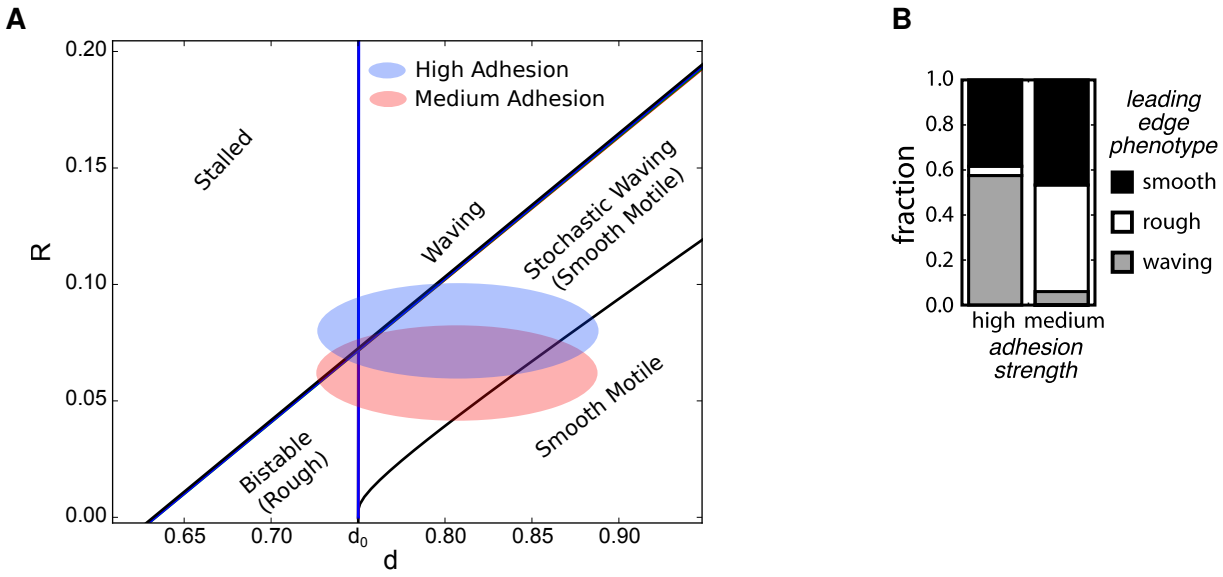

Figure 4.13: Qualitative depiction the intercellular heterogeneity in (d, R)-parameter space. (A) A population of cells plated on substrates of high (medium) adhesiveness is depicted as a red (blue) ellipse. By varying the value of the R-parameter of a population of cells, the size of the sub-populations in each of the five distinct parameter regimes described in Fig. 4.3. (B) Experimentally observed sub-populations of cells exhibiting waving, smooth motile, and rough motility when plated on substrates of high and medium adhesiveness. Taken from Fig. 1F in [4].

sponds to a larger (smaller) value of R highlighted by the blue (pink) ellipses in Fig. 4.13. This means that populations of cells plated on substrates of varying adhesiveness will have differing proportions of cells in the distinct parameter regimes identified above. Given this perspective, it seems unlikely that rough motility is produced in the stalled regime, as it shrinks rather than grows with decreasing R. We therefore conclude based on that argument that the bistable regime is the most compatible with the rough mode of motility.

4.6 Adhesion Mechanosensitivity

Having analyzed the ODE model in depth and established that the PDE model is capable of propagating the stalled state across the lamellipodium to halt protrusion, we next sought to modify the model by incorporating some of the mechanosensitive properties of adhesion complexes. We are particularly interested in how such modification will alter the shape and size of the parameter regimes for the

various modes of motility (see Figs. 4.2 & 4.9). There are two effects of force on integrin receptors which we plan to incorporate: (i) the activation of integrin receptors by force and (ii) the rupture of the integrin-ligand bond by force. These topics and the mathematical model used to describe them have been covered extensively in Chapter 1, but it is now worth going into a little more detail about force generation and transmission in the lamellipodium. As stated in Section 4.2, the membrane begins to protrude when the barbed actin density is above a certain threshold. The physical basis behind this is that there is a hydrostatic pressure difference between the inside and outside of the cell (which can be related to surface tension using the Young-Laplace equation [17]), and that in order for the cell to move forward, the branched actin network must push with enough force to overcome this pressure difference (surface tension). The force is produced by the Brownian-ratchet mechanism of actin polymerization [18]. This occurs when an actin filament has its branched tip resting against the cell membrane, and the filament subsequently grows by adding a single actin monomer. This monomer addition is possible due to transient, thermally induced, fluctuations of the filament tip away from the membrane, and results in the filament pushing against the membrane with some small force [19]. Thus, if there is sufficient density of branched actin tips and actin monomers at the leading edge, the polymerization force may overcome the surface tension and the leading edge will move forward. All of this assumes that the actin filament does not move backwards as result of the polymerization force, implying that there is some balancing force that keeps the filament in place. This balancing force is provided by the substrate which the cell is migrating on, and is transmitted to the filament through nascent adhesions. These nascent adhesions serve as anchor points for the rigid branched actin network by mechanically coupling the substrate and the polymerizing actin network that extends to the leading edge [20].

In Chapters 1 and 2, we saw numerous examples of how mechanical force can influence adhesion dynamics and stability. Notably, integrin receptors, the basic building blocks of cell-extracellular matrix adhesions, exhibit a $\sim$5,000-fold increase in binding affinity due to the application of force [21,22]. This suggests that a minimum amount of force may be required to induce the formation of nascent adhesions [23, 24]. Furthermore, mechanical deformation of proteins in the adhesion plaque that links integrins to the actin cytoskeleton may enhance the disassembly of adhesions at high force values. This deformation may either directly reduce the binding affinity of proteins in the plaque, or may expose otherwise obstructed domains in the protein to allow for enzymatic degradation of the adhesion. In either case, the outcome is that adhesions become destabilized at high forces. Thus one may conclude that the formation and stabilization of nascent adhesions is favoured within some finite range of forces.

In this Section, we wish to investigate how this mechanosensitivity of adhesions affects the outcomes of the ODE model described by Eqs. (6)-(8).

4.6.1 Model Extension

In order to to incorporate the transmission of the polymerization force through nascent adhesions into Eqs. (6)-(8) we will

1. include a variable $N(t)$ to describe the density of nascent adhesions;
2. assume that the force transmitted to nascent adhesions is directly proportional the barbed actin density $B(t)$;
3. take the formation rate of nascent adhesions to be a biphasic function of force (i.e., a function of $B(t)$, see Fig. 4.14A), where the function increases with force at low forces (reflecting integrin activation) and decreases at high forces (reflecting mechanically-induced bond rupture and force-dependent enzymatic activity);
4. assume that, at high forces, the actin-ECM linkage is disrupted, and that, in this scenario, the polymerization force primarily results in a retrograde motion of the actin network rather than protrusion of the lamellipodium. (this disruption of the mechanical linkage is generically referred to as "slippage", since the actin network slips over the basal membrane in the absence of nascent adhesions [25]);
5. modify the velocity function in order to account for slippage (see Fig. 4.14B); and
6. modify the model for recruitment of barbed actin tips, $B(t)$, to the leading edge, as it previously gave steady states with unbounded magnitude for finite parameter values (e.g., see Eq. (10)).

These modifications constitute a first-pass at extending the model described by system (6)-(8) to incorporate mechanical effects on nascent adhesions. Notably, the assumption that force$\propto B(t)$ is overly simplistic, but some preliminary analysis suggests that it is valid for $B < B_c$ (not shown). Moreover, the non-linear relationships in Fig. 4.14 were chosen such that nascent adhesions "turn-on" at some $B < B_c$ and "turn-off" at some $B > B_c$. The effect of these choices will require future investigation. However, the objective of this section is to investigate how these assumptions manifest themselves in the dynamics of lamellipodial protrusion, not to assess their validity. In order for our results to remain physiologically-relevant, we have introduced some modifications to Eq. (6), namely, we have

introduced a parameter $B_{\max}$ that represents the maximum density of barbed actin density in the lamellipodium. In system (6)-(8), the rate of barbed actin tip production does not decrease at very high values of B while the capping rate of branched tips drops to zero when A becomes large. This feature leads to steady states that blow up to infinity for finite parameter values, an outcome that is incompatible with the non-zero size of actin filaments [26]. Typical filament densities in fibroblasts have been found to be $\sim 100-150$ filaments/μm [27]; however, to estimate $B_{\max}$, we assume a filament diameter of 10 μm [28] and a lamellipodial thickness of 150 nm [27] with a maximum packing fraction of 65% [26] which yields a maximum barbed actin tip density of ~ 975 filaments/μm or $B_{\max} \sim 10\,\mu\text{m}^{-1}$.

With all of these considerations, we arrive at a new system of ODEs, given by

$$\epsilon \frac{d}{dT} B\left(T\right) = \left(1+\eta_B V\right) \frac{\left(B-B_{\max}\right)}{B_{\max}} - \frac{B}{1+AB/(1+M+KB)} + \Xi_t \tag{21}$$

$$\frac{d}{dT} A\left(T\right) = d - \frac{\left(1+\eta_A V+\eta_M MV\right) A}{1+M+KB} \tag{22}$$

$$\epsilon \frac{d}{dT} N\left(T\right) = P_b\left(B\right) B - \epsilon\left(R+\eta_M V\right) N \tag{23}$$

$$\frac{d}{dT} M\left(T\right) = RN - \left((1-P_s\left(B\right))\theta + \eta_M V\right) M, \tag{24}$$

where P_b is the force-dependent probability that an integrin on the membrane is bound, and P_s is the force-dependent probability that actin-ECM mechanical link has been disrupted (see black and grey lines in Fig. 4.14A, respectively). Our implementation of nascent adhesions (NAs) into the model mirrors what can be found in [4], but we have additionally taken the rate of formation of NAs to be proportional to P_b. Moreover, we have modified the degradation rate of mature adhesions to account for the observation that they grow when the leading edge is stalled due to spreading-induced stalling of the lamellipodium [29]. This stalling of the leading edge, despite appreciable polymerization rates, is assumed to be due to slippage of the actin network, where the polymerization force drives the network backwards rather than pushing the membrane forward. This is implemented through a velocity function, given by

$$V\left(B\right) = \begin{cases} \left(1-f_s P_s\right)\left(1-\left(\frac{B_c^0}{B}\right)^8\right) & B > B_c^0 \\ 0 & \text{otherwise,} \end{cases} \tag{25}$$

where $f_s \in [0,1]$ is the fractional reduction in protrusion velocity due to slippage (we use $f_s = 0.9$;

see Fig. 4.14B).

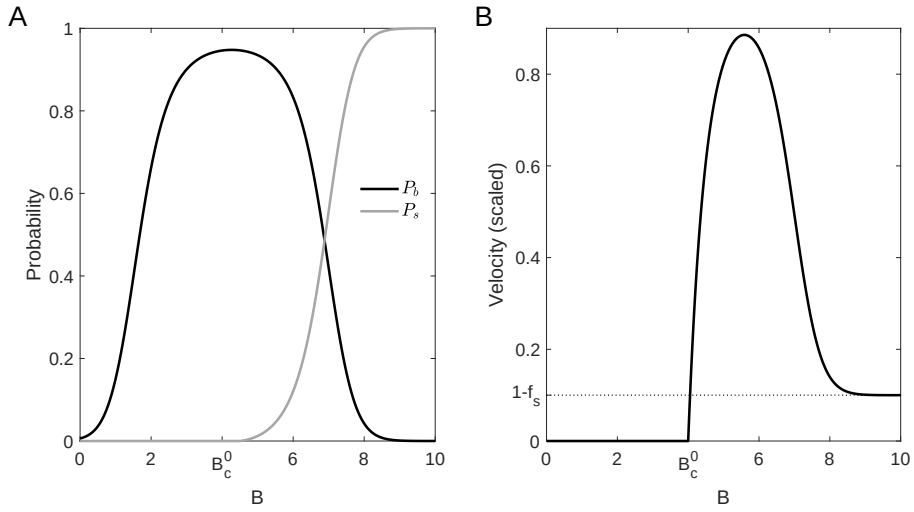

Figure 4.14: Force-dependent effects on the extended model, where the barbed actin tip density B is taken to be a proxy for force. (A) The probability that an integrin is bounded to an extracellular ligand (P_b, black line) or that the mechanical linkage between actin network and the ECM is disrupted due to slippage (P_s, grey line). (B) The velocity function defined by Eq. (25) accounts for slippage by reducing the protrusion velocity at high values of B (force).

Most of the modification to the model relate, in some way or other, to the non-linear function P_b. This function accounts for the activation of integrins at low force magnitudes and the disruption of the adhesion at high force magnitudes, and should generically be a unimodal function. We have developed a thermodynamic framework that can produce such functions, but its formulation is currently beyond the scope of this thesis. In order to produce a function that works well with the other parameters of the model (see Table 4.1), we have used this thermodynamic framework to obtain a function, given by

$$\begin{aligned} P_b\left(B\right) \;=\; & \Big[1 + 15.64\exp\left(-\left(3.69 + 2.21275B\right)B\right) \\ & +0.1789\exp\left(-\left(2.214 + 2.21275B\right)B\right) \\ & +145.1679\exp\left(\left(-3.69 + 0.432178B\right) * B\right)\Big]^{-1}. \end{aligned}$$

We have also used this function to also determine an expression for P_s, given by

$$P_s(B) = \begin{cases} \frac{P_0 - P_b(B)}{P_0} & B \geqslant 4.5\ \mu\text{m}^{-1} \\ 0 & \text{otherwise,} \end{cases}$$

where $P_0 = P_b\left(4.5\ \mu\text{m}^{-1}\right)$. This makes P_s a monotonically increasing function of B that increases at the same time that P_b decreases due to slippage (see Fig. 4.14A). Finally, we have also modified the dynamics of barbed actin tip recruitment in order to account for the physical limits on actin tip density. Without such considerations, the stalled and smooth motile equilibrium will become infinite for some values of d (e.g., Eq. (10) as $d \to 1$). With these modifications, the stalled equilibrium no longer blows up at finite parameter values; indeed, the stalled equilibrium for system (21)-(24) has a B-value given by

$$B^* = \frac{(d-1)B_{\max} - 1 + \sqrt{\left((d-1)B_{\max} - 1\right)^2 + 4dB_{\max}}}{2d}.$$

4.6.2 Bifurcation diagrams for the extended model

In order to assess how the modified dynamics change the model outcomes, we perform one-parameter bifurcation analysis on system (21)-(24). Since most of the bifurcation points for the extended model are the same as those for system (6)-(8), we will use the same terminology when applicable. For small values of the adhesion maturation rate, R, the bifurcation structure is nearly identical to that of system (6)-(8) with the model exhibiting either a bistable (not shown) or a waving regime that terminates at a homoclinic very close to SN2 (see Fig. 4.15A). However, unlike system (6)-(8), we can see that the protrusion velocity of the smooth motile equilibrium asymptotically approaches $V = 1 - f_s$ (see Fig. 4.15C). For sufficiently large values of R, we observe the appearance of two saddle-node bifurcations on the smooth motile equilibrium (SN3 and SN4; see Fig. 4.15B), generating as many as two regions of bistability. The novel bistable regime ($d_{\text{SN2}} < d < d_{\text{SN3}}$, bistable II) lies between two stable branches of the smooth motile equilibrium with one branch exhibiting a roughly constant velocity $V \approx 1 - f_s$, while the other exhibits a non-zero velocity that may vary significantly (see Fig. 4.15D). For $d_{\text{SN2}} > d_{\text{SN4}}$, there is another region of bistability between the waving solution and the smooth motile equilibrium ($d_{\text{SN4}} < d < d_{\text{SN2}}$, bistable III). A similar region of bistability existed for system (6)-(8), but its size became infinitesimally small as $\lambda \to 0$. The reason this bistable region is significantly larger now is

due to the existence of SN4, a bifurcation point that extends further to the left, causing the smooth motile equilibrium to overlap with the waving solution.

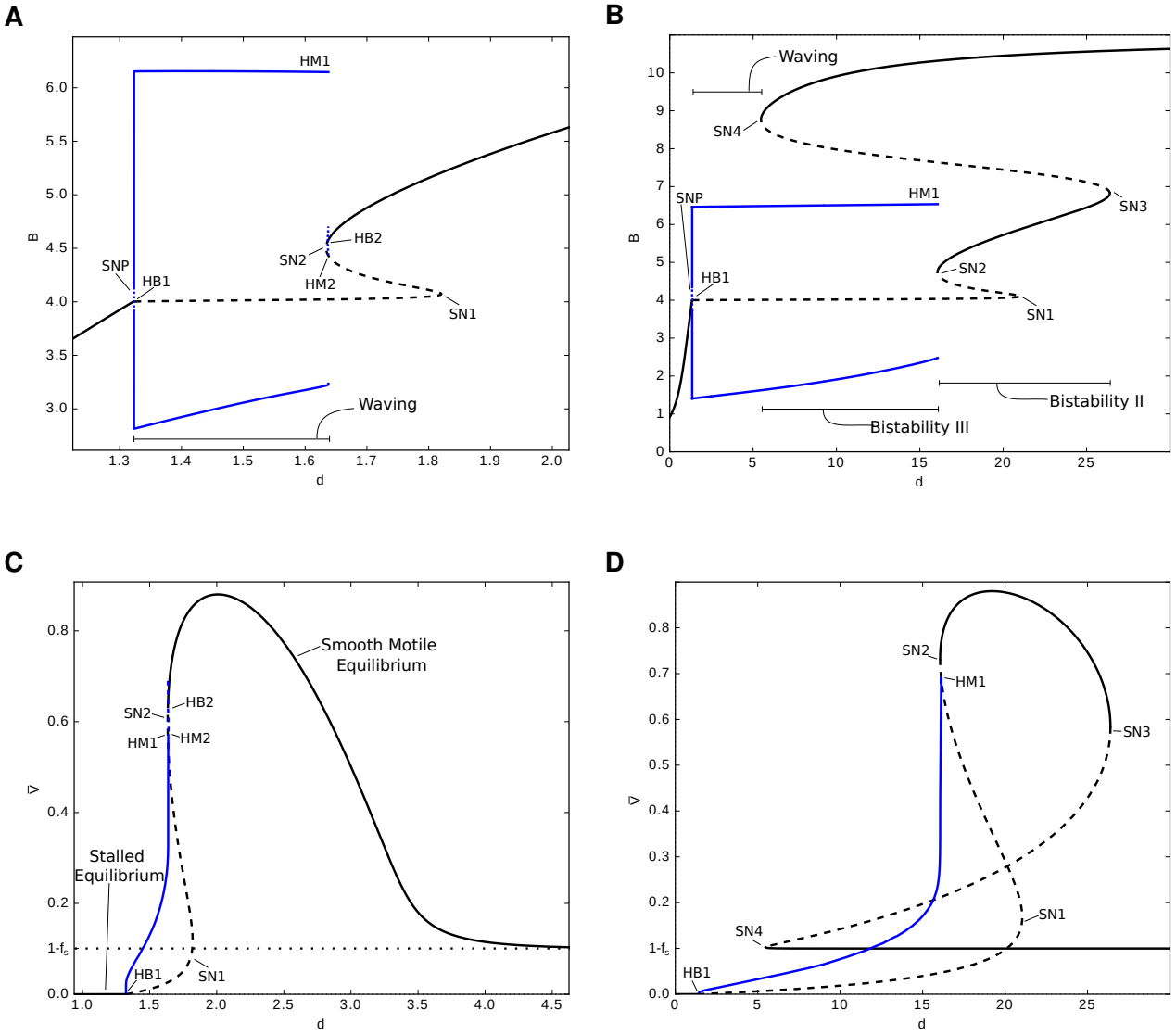

Figure 4.15: The bifurcation diagram of actin barbed end density B (A&B) or the mean velocity $\bar{V}$ (C&D) with respect to the scaled VASP delivery rate d at two different values of the scaled nascent adhesion maturation rate: (A&C) R=0.01 and (B&D) R=0.5. Black solid (dashed) lines indicate stable (unstable/saddle) branches of equilibria; blue solid (dashed) lines correspond to branches or envelopes of stable (unstable) limit cycles. (A&C) For small values of R, the branches of equilibria are identical to the original ODE model (compare panel A to Fig. 4.2A). However, due to the use of Eq. (25) the mean velocity does not tend to 1, but asymptotically approaches $\bar{V} = 1 - f_s$ as can be seen from the dotted black line in panel C. (B&D) For sufficiently large values of R, two new saddle-node bifurcations (SN3 and SN4) appear and split the smooth motile equilibrium into two stable branches that coexist to produce a novel bistable regime (bistable II). Within this bistable regime, the "upper" stable branch of the smooth motile equilibrium has a velocity which is nearly constant with a value of $1 - f_s$, while the "lower" stable branch of the smooth motile equilibrium has a much more variable velocity as can be seen in panel D. The waving solution also coexists with the upper stable branch of the smooth motile equilibrium; this produces another bistable regime (bistable III).

4.6.3 Two-Parameter Bifurcation

In order see how our extension of the model will behave in a PDE setting, we have continued all the bifurcation points discussed in Fig. 4.15 within the (d,R)-plane of parameter space (see Fig. 4.16). For very small values of R and close to HB1 (i.e., in the vicinity of BT1), we have a two-parameter bifurcation diagram that is nearly identical to that for system (6)-(8) (compare Fig. 4.16A to Fig. 4.3). That is, the 5 distinct regimes identified in Section 4.3.3 are still present and are delineated by the same boundaries at this local scale. However, as we zoom out of BT1, additional regimes appear, including the two novel bistable regimes discussed in the previous section (see Fig. 4.16B). Notably, there is a cusp bifurcation point CP1 formed by SN3 and SN4. The two bistable regimes are contained between these two saddle-node bifurcations: (i) The bistable regime between the two branches of the smooth motile equilibrium (bistable II) emerges from CP1 and is bounded to the right by SN3 and to the left by either SN4 or HM1 ($\approx$SN2). (ii) The bistable regime between the stable oscillatory solutions and the smooth motile equilibrium (bistable III) emerges from the intersection of SN2 and SN4 and is bounded to the right by HM2 ($\approx$SN2) and to the left by SN4.

Thus, for system (21)-(24), the boundaries of the waving, stochastic waving, and smooth motiles regimes differ from what was seen in Fig. 4.3. In particular, we find that (i) the waving regime is bounded to the left by SNP and to the right by HM1 or SN4; (ii) the stochastic waving regime is bounded to the left by HB1, from the top by HM1, from the bottom by SN1, and to the right by SN4; and (iii) the smooth motile regime is bounded to the left/top by SN1 or SN3 and for a small segment between SN1 and SN3 it is bounded to the right by SN4. Finally, we observe a Bogdanov-Takens bifurcation, BT2, where HB2 merges with SN2. However the HB2 and HM2 bifurcation points exist in a region of negligible size at the boundary between the waving and stochastic waving regimes.

4.6.4 Rough Motility

As discussed in Section 4.5.3, using system (6)-(8) as the basis of the PDE model, we identified the bistable regime as being associated with the rough mode of motility observed experimentally in [4]. Using the extended model given by system (21)-(24), we have identified two novel bistable regimes. Due to the bistable nature of these two novel regimes, one would expect that they would be associated with spatio-temporal patterns of protrusion that are compatible with rough motility. To check for this, we have implemented system (21)-(24) as a PDE using the methods described in Section 4.5. The

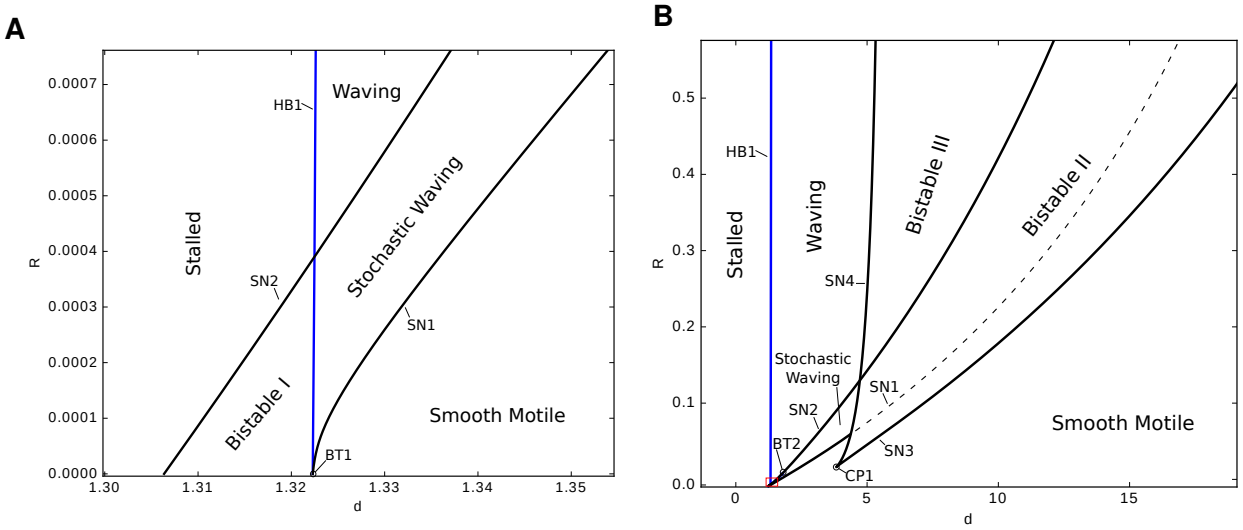

Figure 4.16: Two-parameter continuation of the bifurcation points in Fig. 4.15. Co-dimension 2 bifurcation points are represented with an open circle symbols, whereas co-dimension 1 are represented as lines. (A) In the neighborhood of to BT1, we observe the same five regions as those seen in Fig. 4.3: stalled, bistable (i.e., bistable I), Waving, the stochastic waving, and smooth motile. (B) Further away from BT1, two novel bistable regimes contained between the saddle-node bifurcations SN3 and SN4 emerge from the cusp bifurcation point CP1. The bounds of panel A are roughly indicated by the red square in panel B.

kymographs computed using the model for varying levels of noise in the regimes bistable II and III are displayed in Figs. 4.17 and 4.18, respectively. As suggested by Fig. 4.17, bistable II produces patterns of protrusion very similar to the bistable regime of system (6)-(8). On the other hand, in the bistable III regime, the spatio-temporal dynamics are significantly different from what is observed both experimentally and in the other regimes (see Fig. 4.18). Notably, the oscillatory nature of this regime appears to be more prominent than that in the bistable or stalled regime.

The original derivation of system (1)-(3) in [4] was done for keratocytes, which primarily produce nascent adhesions and very few mature adhesions. Other cell types, such as CHO-K1 cells have much more prominent populations of mature adhesions [29], a finding that may be simplified within the context of this model by by assuming they have a significantly larger value of R. With our extended system (21)-(24), we still observe the five distinct modes of motility of the original system at very small values of R and it is only when R becomes significantly larger that we observe these novel bistable regimes. Therefore, it is possible that keratocytes simply do not have a large enough R-value land on

those regions of parameter space (i.e., their rough motility is due to bistable I); whereas other cell types may have sufficiently large values of R, allowing them to exhibit the dynamics observed in the bistable II and III regimes. In order to test such a hypothesis, further analysis of experimental data from other cell types (e.g., CHO cells) is required. A preliminary test would be to look at a population of cells to see if the sub-population exhibiting rough motility can be expanded by increasing R, a feature that distinguishes bistable II and III from bistable I .

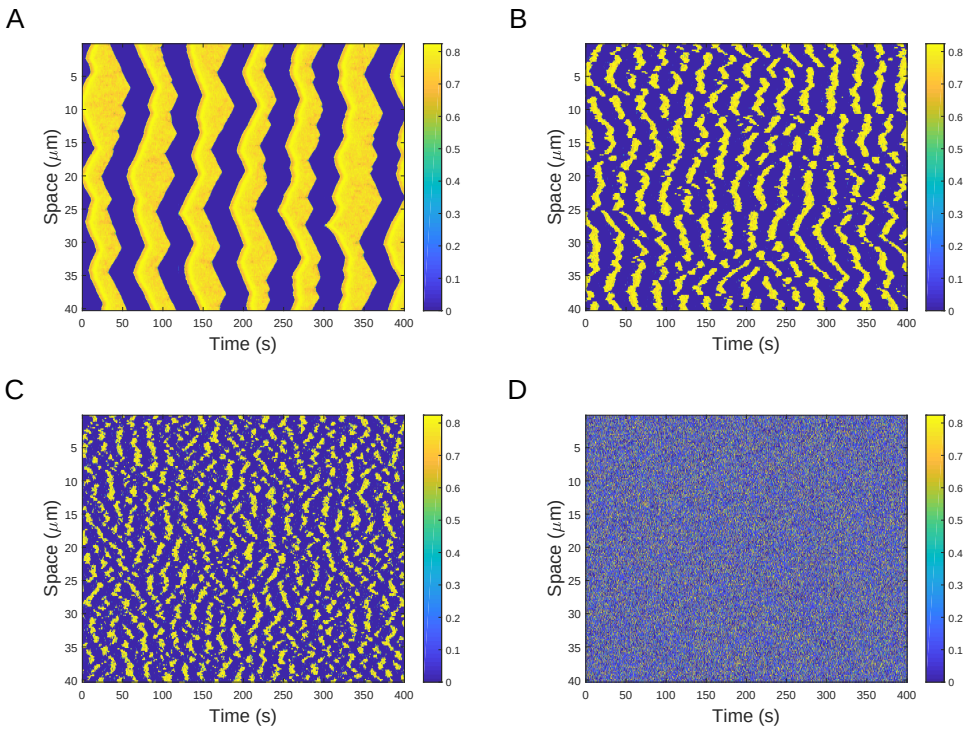

Figure 4.17: The effect of noise in the bistable II regime. Kymographs of protrusion velocity with $R = 0.2$, $d = 7.35$, and (A) $\Xi_0 = 1\text{e} - 2$; (B) $\Xi_0 = 4\text{e} - 2$; (C) $\Xi_0 = 5\text{e} - 1$; and (D) $\Xi_0 = 1$.

4.7 Discussion & Future Directions

We have analyzed in detail the underlying dynamics of a model of traveling waves of protrusion that arise due to actin polymerization in the lamellipodium. By underlying dynamics, we specifically mean the spatio-temporal PDE model (1)-(3) without its spatial term $\partial_x \left(\Gamma^{-1}\partial_x B\right)$, which yields a simpler

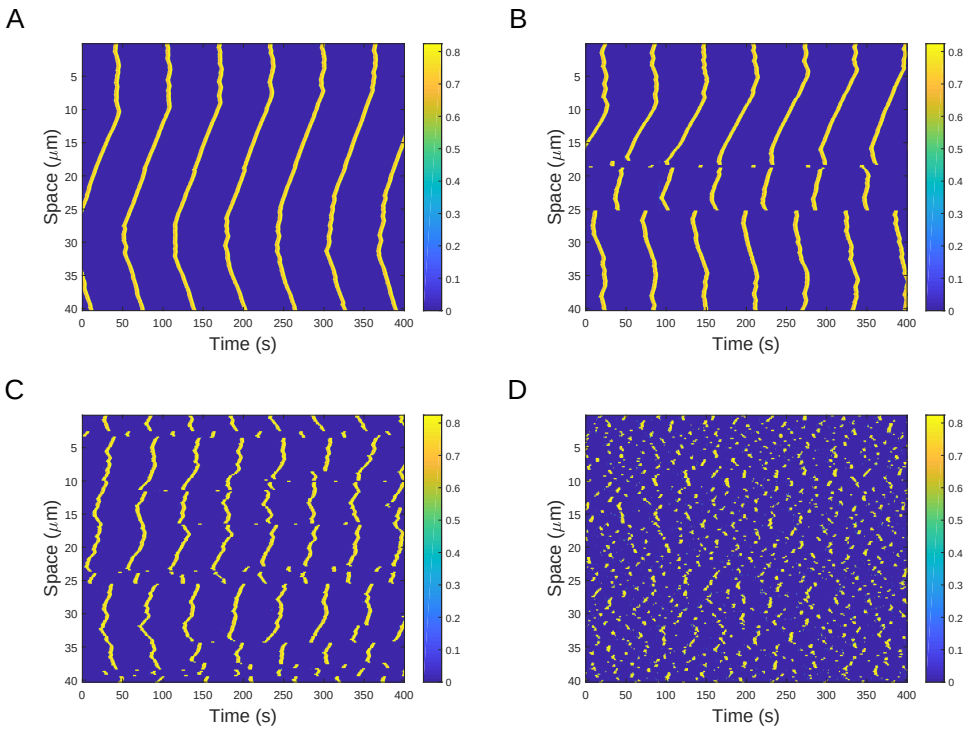

Figure 4.18: The effect of noise in the bistable III regime. Kymographs of protrusion velocity with $R = 0.2$, $d = 5$, and (A) $\Xi_0 = 8\text{e} - 3$; (B) $\Xi_0 = 1\text{e} - 2$; (C) $\Xi_0 = 2.5\text{e} - 2$; and (D) $\Xi_0 = 6\text{e} - 2$.

system of ODEs. This spatial term appears at first to be a diffusion-like term as it contains the second spatial derivative of the barbed actin tip density B. However, since $\Gamma = \Gamma(B)$, this spatial transport term is somewhat more complicated than that. In fact, it represents the advective transport of barbed actin tips due to polymerization which is not obvious from its form in Eq. (1) [30]. Therefore, our analysis of the ODE system gives us insight into the intrinsic dynamics of the system independent of any spatial considerations, where we may assume that any significant spatial gradient in B is advected (i.e., transported with a constant speed) along the leading edge to produce traveling waves of elevated or depleted B. Anecdotally, we have observed that this gradient must be sufficiently steep to propagate with appreciable speed, and investigation of wave-speed should be pursued further to gain a more complete understanding of the model.

The primary objectives for this study were to (i) decipher the excitability properties of the ODE

model (6)-(8), (ii) determine the bifurcation points that define the boundaries of all the regimes of behaviour exhibited by the PDE model, and (iii) understand the model's connection to rough motility in more detail. Through this analysis, we successfully identified in both the ODE and PDE models the three original regimes of behaviour found in [4], namely, stalled, waving and smooth motile, and discovered two new ones, including bistability and stochastic waving regimes.

The stochastic waving regime was initially thought to be a good candidate for explaining rough motility seen in fish keratocytes [4], since it appeared to be very sensitive to noise. However, after further examination of this regime in the PDE model, our results revealed that it predominantly produces traveling waves of protrusion that are not compatible with rough motility (see Fig. 4.11) and it had an inappropriate shape in (d, R)-space (see Fig. 4.3.3). On the other hand, the stalled and bistable regimes fared much better in their ability to produce spatio-temporal dynamics compatible with rough motility. Interestingly, the shape of the bistable regime in (d, R)-space was found to be the most compatible with the experimentally obtained population statistics (see Fig. 4.13) when assessing population shifts in parameter space due to a decrease in the maturating rate of NAs (assumed to be reflective of less adhesive substrates). We do wish to note here that noise has been treated as an extrinsic parameter than can be varied from arbitrarily small values to arbitrary large ones. However, a more justified approach would be to determine the noise magnitude from the intrinsic dynamics of the chemical reactions [14]. Perhaps with such considerations, the stochastic waving regime may behave differently. However, as it stands, we cannot reconcile the stochastic waving regime with rough motility without applying some rather contrived assumptions on noise magnitude.

One peculiar feature of the ODE model analyzed in this study is its ability to produce canard orbits governed by a folded saddle. These canard orbits were investigated here by analyzing both the layer problem and the desingularized reduced problem. The layer problem is formed by assuming that the slow variables are constants, while the desingularized reduced problem is obtained initially by setting the fast variables to steady state (forming the reduced problem) followed by rescaling time to remove singularities. It is important to point out here that the equilbria of the layer problem define the critical manifold of the system. Applying this approach allowed us to characterize the folded singularities responsible for generating the observed canards and to identify how they are generated.

Due to the ambiguity in the definition of critical barbed end density B_c introduced in Eq. (5), we introduced a new definition of the velocity V in Eq. (9) that resolved the issue of continuity. Nonetheless,

Eq. 5 shows that B_c can attain two different values: B_c^0 and $(1+E)B_c^0$. Determining which one of these is more critical in delineating the dynamics of the PDE model was one of the questions that we tackled in this study. Given that each value of B_c can produce its own set of bifurcation points in the parameter space defined by R and VASP delivery rate d, we decided to apply the continuation method using both sets of bifurcation points and compare the results to the boundaries of the regimes of behaviour obtained by the PDE model. Our results showed that, when plotting the two-parameter bifurcations of the ODE model in (d, R)-plane, some boundaries of the three original parameter regimes identified in [4] coincided with those defined with the lower value of B_c while the others coincided with those defined by the other value. This highlights the importance of using the formalism introduced in Eq. (9) and the relevance of simplifying the PDE model into an ODE model to decipher dynamics more precisely.

The dynamics of NA maturation in the PDE model were described using a simplified ODE formalism that accounts for the birth, decay and drift of NAs but neglects the effect of mechanical force on the system, an important aspect of NA dynamics [31]. By incorporating adhesion mechanosensitivity into the model through the use of system (21)-(24) and the velocity function Eq. (25), we discovered two novel bistable regimes (see bistable II and III regimes in Fig. 4.16). Interestingly, by simulating the behaviour of the PDE in this regime, we found spatio-temporal dynamics which are compatible with rough motility. What is more, the size of this regime expands with increasing R, which is at odds with experimental population statistics for keratocytes. On the other hand, we do not expect keratocytes to have R that are large enough to visit these novel regimes, but it seems likely that other cell types might.

While the results for system (21)-(24) are very interesting findings, we are far from being able to claim that they are indeed physiologically-relevant. Notably, we lack direct experimental evidence for most of the added assumptions in system (21)-(24), as they have arisen from primarily theoretical consideration which may or may not be relevant to the motile fish keratocytes under study. In particular, the numerical value of the parameter f_s which represent the fractional decrease in protrusion velocity due to slippage was not estimated from any experimental evidence. The effect of this parameter value on model outcomes should be tested carefully. Furthermore, the nonlinear function P_b was chosen so that its increasing phase is below B_c^0 while its increasing phase is above $(1+E)B_c^0$. The effect of these assumptions should be investigated further and a biophysical framework should be developed to assess the validity of these assumptions. Nonetheless, from our perspective it is likely that the implementation of P_b described above produces the richest possible dynamics for the model, and thus we would not expect any notable bifurcation structures to come out of further investigations (i.e., they should be done

for completeness).

Appendix: Routh-Hurwitz Criterion

The characteristic polynomial for system (6)-(8) evaluated at the stalled equilibrium (i.e., Eq. (10)) may be expressed as $P(s) = s^3 + a_1 s^2 + a_2 s + a_3$, where

$$\begin{aligned} a_1 &= \frac{\theta\left(x\epsilon\left(K+x^2\right)+R+x\right)+\theta^2(K+x)+Rx^2\epsilon}{\theta(K+x)+R} \\ a_2 &= \frac{\theta x\left(\theta+\epsilon\left(\theta K+R+(\theta+1)x^2\right)\right)}{\theta(K+x)+R} \\ a_3 &= \frac{\theta^2 x^3\epsilon}{\theta(K+x)+R}, \end{aligned}$$

with $x = 1-d$. Let $z = a_1 a_2 - a_3$, in order to satisfy the Routh-Hurwitz stability criterion we must show that $a_1, a_3 > 0$ and $z > 0$. Assuming that all model parameters are positive, the first two conditions are satisfied under the constraint $x > 0 \Leftrightarrow d < 1$. Therefore we must show that $z > 0$ with z is given by

$$\begin{aligned} z &= \frac{\theta x}{(\theta(K+x)+R)^2}\Bigg[\left(\theta\left(x\epsilon\left(K+x^2\right)+R+x\right)+\theta^2(K+x)+Rx^2\epsilon\right)\left(\theta+\epsilon\left(\theta K+R+(\theta+1)x^2\right)\right) \\ &- \theta x^2\epsilon(\theta(K+x)+R)\Bigg]. \end{aligned}$$

Notice that $z > 0$ if the term inside the square brackets are positive, and that this term may be decomposed as sum of one positive term (the first one) and one negative term (the second one). Thus we must simply show that the first term is larger than the second. Expanding in θ, the first term is given

by

$$\begin{aligned}
&R^2x^2\epsilon^2 + Rx^4\epsilon^2 \\
&+\theta\Big[KRx^2\epsilon^2 + x^2\epsilon\left(x\epsilon\left(K+x^2\right)+R+x\right) + R\epsilon\left(x\epsilon\left(K+x^2\right)+R+x\right) + Rx^4\epsilon^2 + Rx^2\epsilon\Big] \\
&+\theta^2\Big[x^2\epsilon\left(x\epsilon\left(K+x^2\right)+R+x\right) + K\epsilon\left(x\epsilon\left(K+x^2\right)+R+x\right) \\
&+R\epsilon(K+x) + x\epsilon\left(K+x^2\right) + R + x + x^2\epsilon(K+x)\Big] \\
&+\theta^3\left[x^2\epsilon(K+x) + K\epsilon(K+x) + K + x\right],
\end{aligned}$$

and the second term is given by

$$-\theta^2x^2\epsilon(K+x) - \theta Rx^2\epsilon.$$

Observe that both of the negative terms in the second expansion have a corresponding positive term in the first expansion. Namely, the first (second) term of the second expansions cancels with the last term on the fourth (second) line of the first expansion. Thus, we have $z > 0$ provided $x > 0$ and therefore the Routh-Hurwitz stability criterion allows us to conclude that $d < 1$ is a necessary and sufficient condition for stability of the stalled equilibrium.

Bibliography

[1] Benjamin Lin, William R Holmes, C Joanne Wang, Tasuku Ueno, Andrew Harwell, Leah Edelstein-Keshet, Takanari Inoue, and Andre Levchenko. Synthetic spatially graded rac activation drives cell polarization and movement. *Proceedings of the National Academy of Sciences of the United States of America*, 109:E3668——77, 12 2012. 2.1, 2.3.5.1, 4.1

[2] Yoichiro Mori, Alexandra Jilkine, and Leah Edelstein-Keshet. Wave-pinning and cell polarity from a bistable reaction-diffusion system. *Biophysical Journal*, 94:3684–3697, 5 2008. 0.1.3, 1.12, 2.1, 3.1, 3.3, 3.5.2, 3.6.0.1, 4.1

[3] Revathi Ananthakrishnan and Allen Ehrlicher. The forces behind cell movement. *International journal of biological sciences*, 3:303–317, 6 2007. 0.1, 1.1, 4.1

[4] Erin L Barnhart, Jun Allard, Sunny S Lou, Julie A Theriot, and Alex Mogilner. Adhesion-dependent wave generation in crawling cells. *Current biology : CB*, 27:27–38, 1 2017. (document), 0.1.4, 4.1, 4.2, 4.2, 4.1, 4.3.3, 4.3, 4.4.1, 4.5.1, 4.9, 4.5.2, 4.5.3, 4.5.3, 4.5.3, 4.13, 4.6.1, 4.6.4, 4.7, 5, 5, 5, 5, 5, 5

[5] James Keener and James Sneyd. Membrane ion channels, 2009. 3.5.1, 4.1

[6] Benjamin Lindner, Jordi García-Ojalvo, A Neiman, and L Schimansky-Geier. Effects of noise in excitable systems, 3 2004. 4.1, 4.4.3.2

[7] E J Doedel, R C Paffenroth, A R Champneys, T F Fairgrieve, Yu. A Kuznetsov, B Sandstede, and X Wang. Auto-07p: Continuation and bifurcation software for ordinary differential equations, 2007. 2.2.4, 3.2.4, 4.3

[8] Mathieu Desroches, John Guckenheimer, Bernd Krauskopf, Christian Kuehn, Hinke M Osinga, and Martin Wechselberger. Mixed-mode oscillations with multiple time scales. *SIAM Review*, 54:211–288, 1 2012. 4.4, 4.4.4.2

[9] Balth. van der Pol. Lxxxviii. on "relaxation-oscillations". *The London, Edinburgh, and Dublin Philosophical Magazine and Journal of Science*, 2:978–992, 11 1926. 4.4

[10] Balth. van der Pol and J van der Mark. Lxxii. ithe heartbeat considered as a relaxation oscillation, and an electrical model of the heart/i. *The London, Edinburgh, and Dublin Philosophical Magazine and Journal of Science*, 6:763–775, 1928. 4.4.2

[11] Cris R Hasan, Bernd Krauskopf, and Hinke M Osinga. Saddle slow manifolds and canard orbits in r4 and application to the full hodgkin-huxley model. *The Journal of Mathematical Neuroscience*, 8:5, 2018. 4.4.3.1

[12] John Mitry, Ryan P D Alexander, Saeed Farjami, Derek Bowie, and Anmar Khadra. Modeling excitability in cerebellar stellate cells: Temporal changes in threshold, latency and frequency of firing. *Communications in Nonlinear Science and Numerical Simulation*, 82:105014, 3 2020. 4.4.3.1

[13] Saeed Farjami, Ryan P D Alexander, Derek Bowie, and Anmar Khadra. Switching in cerebellar stellate cell excitability in response to a pair of inhibitory/excitatory presynaptic inputs: A dynamical system perspective. *Neural Computation*, 32:626–658, 3 2020. 4.4.3.1

[14] Daniel T Gillespie. The chemical langevin and fokker-planck equations for the reversible isomerization reaction. *Journal of Physical Chemistry A*, 106:5063–5071, 2002. 4.4.3.2, 4.7

[15] Martin Wechselberger. À propos de canards (apropos canards). *Transactions of the American Mathematical Society*, 364:3289–3309, 2012. 4.4.4.1, 4.4.4.1, 4.4.4.1, 4.4.4.2

[16] David F Griffiths and Desmond J Higham. *Numerical Methods for Ordinary Differential Equations*. Springer London, 2010. 4.5.2

[17] Markus Deserno. Fluid lipid membranes: From differential geometry to curvature stresses. *Chemistry and Physics of Lipids*, 185:11–45, 2015. 4.6

[18] Thomas D Pollard and Gary G Borisy. Cellular motility driven by assembly and disassembly of actin filaments. *Cell*, 112:453–465, 2 2003. 3.1, 4.6

[19] A Mogilner and G Oster. Cell motility driven by actin polymerization. *Biophysical journal*, 71:3030–3045, 1996. 1.2.2, 3.1, 4.6

[20] Ingo Thievessen, Peter M Thompson, Sylvain Berlemont, Karen M Plevock, Sergey V Plotnikov, Alice Zemljic-Harpf, Robert S Ross, Michael W Davidson, Gaudenz Danuser, Sharon L Campbell, and Clare M Waterman. Vinculin-actin interaction couples actin retrograde flow to focal adhesions, but is dispensable for focal adhesion growth. *The Journal of cell biology*, 202:163–177, 7 2013. 0.1.1, 1.2.2, 1.7, 4.6

[21] Jing Li, Yang Su, Wei Xia, Yan Qin, Martin J Humphries, Dietmar Vestweber, Carlos Cabañas, Chafen Lu, and Timothy A Springer. Conformational equilibria and intrinsic affinities define integrin activation. *The EMBO Journal*, 36(5):629–645, jan 2017. 4.6, 5

[22] Jing Li and Timothy A. Springer. Integrin extension enables ultrasensitive regulation by cytoskeletal force. *Proceedings of the National Academy of Sciences*, 114(18):4685–4690, apr 2017. 1.3.1, 1.3.1, 1.9, 1.12, 2.1, 2.5.1.6, 4.6

[23] Bruno Pontes, Pascale Monzo, Laurent Gole, Anabel Lise Le Roux, Anita Joanna Kosmalska, Zhi Yang Tam, Weiwei Luo, Sophie Kan, Virgile Viasnoff, Pere Roca-Cusachs, Lisa Tucker-Kellogg, and Nils C Gauthier. Membrane tension controls adhesion positioning at the leading edge of cells. *Journal of Cell Biology*, 216:2959–2977, 9 2017. 0.1.1, 1.12, 3.1, 4.6

[24] Kinneret Keren and Tom Shemesh. Buckle up: Membrane tension drives lamellipodial network compression and adhesion deposition. *The Journal of cell biology*, 216:2619–2621, 2017. 1.2.2, 1.12, 4.6

[25] Antonina Y Alexandrova, Katya Arnold, Sébastien Schaub, Jury M Vasiliev, Jean-Jacques Meister, Alexander D Bershadsky, and Alexander B Verkhovsky. Comparative dynamics of retrograde actin flow and focal adhesions: Formation of nascent adhesions triggers transition from fast to slow flow. *PLoS ONE*, 3:e3234, 2008. M2, 4.6.1

[26] Enrico Grazi. What is the diameter of the actin filament? *FEBS Letters*, 405:249–252, 1997. 4.6.1

[27] Urban E, Jacob S, Nemethova M, Resch GP, and Small JV. Electron tomography reveals unbranched networks of actin filaments in lamellipodia. *Nature cell biology*, 12, 2010. 4.6.1

[28] E H Egelman and R Padrón. X-ray diffraction evidence that actin is a 100 Åfilament. *Nature*, 307:56–58, 1 1984. 4.6.1

[29] Colin K Choi, Miguel Vicente-Manzanares, Jessica Zareno, Leanna A Whitmore, Alex Mogilner, and Alan Rick Horwitz. Actin and alpha-actinin orchestrate the assembly and maturation of nascent adhesions in a myosin ii motor-independent manner. *Nature cell biology*, 10:1039–1050, 9 2008. 0.1.1, 1.1, 1.2.1, 1.2.2, 1.7, 1.8, 1.11, O1, M2, 2.2.3, 2.3.5.2, 2.4, 2.5.1.2, 2.5.1.8, 3.1, 4.6.1, 4.6.4, 5

[30] Lacayo CI, Pincus Z, VanDuijn MM, Wilson CA, Fletcher DA, Gertler FB, Mogilner A, and Theriot JA. Emergence of large-scale cell morphology and movement from local actin filament growth dynamics. *PLoS biology*, 5, 2007. 4.7

[31] Laurent MacKay and Anmar Khadra. The bioenergetics of integrin-based adhesion, from single molecule dynamics to stability of macromolecular complexes. *Computational and Structural Biotechnology Journal*, 18:393–416, 2020. (document), 0.1.1, 4.7

Part III

Final Conclusion & Future Work

Chapter 5

Final Conclusion & Future Work

This thesis has covered a broad range of topics in the field of cellular motility. In Part I, we focused on the mechanochemical properties of the integrin receptor, the building block of integrin-based adhesions, and how these properties manifest themselves in the beahviour of adhesions. In Chapter 1, we reviewed the literature of experimental findings that underlie the current understanding of integrin receptor activation and its mechanosensitive properties. We also saw how these findings have been incorporated into a number of biophysical models that describe both the equilibrium and dynamic properties of integrin-ligand bonds. These models were described within a common framework, based on the concept of thermodynamic chemical potentials. Two prominent descriptions of receptor-ligand bonds, that differ in how they respond to increases in applied force, have been proposed and used for integrin receptors, slip-bonds and catch-bonds; slip-bonds have a bond rupture rate (chemical potential difference) that increases monotonically with applied force, whereas catch-bonds have a rupture rate (chemical potential difference) that decreases with force at low values of applied force and then reverts to a slip-bond behaviour beyond some optimal level of force. We then showed how the properties of the individual receptor-ligand bonds have been integrated into two classes of mathematical models of adhesion assembly/disassembly. These classes of models either describe adhesions as a discrete collection of dynamically rebinding bonds [ES04b, NS13], or, for larger adhesions, as a thin deformable film characterized by both its continuum mechanical properties and the chemical potential difference of adaptor proteins being adsorbed onto the film [NBS08].

One experimental finding that both classes of model sought to explain is the observation that

integrin-based adhesions grow in repsonse to increased force [BSR+01, RZB+01]. For the models describing collections of discrete bonds, this was achieved by using a catch-bond model for the individual bonds [NS13]. Such assumptions produced adhesions with a number of integrin-ligand bonds that increases with applied force. However, since this class of model did not account for geometry, it was unclear how the physical size of adhesions would vary. On the other hand, with the continuum-mechanics-based models, the force-dependent growth was produced by incorporating the force-sensitive activation of integrins through a decrease in the chemical potential of adaptor adsorption. This class of model focused on linear adhesions, showing that they may grow or shrink at each end. According to this class of models, whether an adhesion tip will grow or shrink in size is determiend by a balance of the energy required to mechanically deform the adhesion with the chemical potential differences associated with integrin activation and adaptor protein adsoprtion. We note that integrin activation reflects the same structural changes that underlie the catch-bond behaviour, i.e., they are two facets of the same biophysical phenomenon [LKZ16]. By accounting for all these phenomena, the continuum models were able to explain the existence of sliding FAs [BHIWH01], where, for certain force ranges, FAs grow at one end while they shrink at the other. Thus, both classes of models suggest that adhesion assembly and disassembly dynamics can be modulated by force through a shift in the balance of binding and unbinding of molecular bonds, either extracellularly (i.e., the integrin-ligand bond) or intracellularly (i.e., the integrin-adaptor bond).

In Chapter 2, we presented a novel biophysical model of nascent adhesion (NA) assembly and disassembly. This biophysicist model was formulated to capture a non-constant density of integrins that was inferred from experimental distributions of NA-area and molecular counts. More specifically, using a novel data analysis technique termed Conditional Expectation Analysis (CEA, see Section 2.5.2), the shape of these distributions was found to suggest that the density of integrins is a monotonically increasing function of their size, and that this function saturates at a value of $\sim 17,000$ integrins$/\mu$m^2. Interestingly, this saturating density corresponds to a theoretical maximal packing density of integrins in their active conformation. The observation that integrins tend to diffuse freely inside adhesions [ROS+12, TWG+18] thus suggests that a significant portion of integrins inside NAs exist in their denser inactive conformation, a prediction that is in agreement with thermodynamic measurements [LSX+17].

The finding that integrin density is variable ruled out the notion that NA-area is set by the number integrins they contain, a common assumption in models of adhesions [NS06, BS06, OTAG10, SS10]. In order to predict NA-area, we instead assumed that it is determined by the number of adaptor proteins

in the adhesion plaque. This plaque helps to organize integrins into adhesions by locally slowing their diffusion as well as increasing their likelihood of binding to extracellular ligands [ROS+12, TWG+18]. We furthermore proposed that integrins aid in the organization of adhesion plaque by tethering cytosolic adaptor proteins to the membrane. Thus, we modeled the interactions between integrins and adaptor proteins as a feed-forward system that results in the aggregation of both proteins into NAs, a phenomenon we termed co-aggregation. This was achieved by considering the area of a NA as well as the number of integrins it contains to be independent quantities, where the dynamics governing these two variables depend on one another. Moreover, we implemented the tethering of adaptor proteins by integrins in such a way that it matches the results obtained from CEA (see Fig. 2.2A).

By decoupling NA-area and integrin molecular count, we were then able to investigate NA assembly dynamics under various mechanical conditions. Interestingly, we found that under fixed load (i.e., the total force applied to the adhesion), NAs did not assemble for all but the smallest loads, whereas they could much more readily assemble under conditions of fixed stress (i.e., the total force applied per unit area of the adhesion). Such a prediction was not possible using previous models of adhesions as they either did not have a well-defined area or assumed that integrin-density was a fixed quantity; in both cases, the force per bound molecule, set by a chosen initial condition, determines whether the adhesion will assemble or disassemble. As discussed in Chapter 1, these limitations on model-predicted adhesion dynamics are due to the presence of a saddle fixed-point that separates the stable equilibrium representing an adhesion with non-zero size from the trivial equilibrium containing zero molecules. However, our model was constructed to posses a non-zero quasi-steady state (QSS) that acts as an attractor when starting from the trivial equilibrium. Stochastic fluctuations around this QSS eventually push the system past the stable manifold of the saddle fixed-point and a stable adhesion subsequently assembles. Our model thus gives insight into the dynamics of NAs' spontaneous self-assembly, whereas previous models were primarily successful in explaining the dynamics of disassembly after an adhesion has already been formed. Together, these findings contribute to the understanding of the spatial organization and molecular-level dynamics of NAs as well as the mechanical conditions that allow for their assembly.

In Part II, we turned our attention to the cell-scale phenomena of cellular motility and migration. We specifically focused on spatio-temporal dynamics of front-to-rear polarization and membrane protrusion, with an emphasis on biochemical feedback from adhesions onto these processes. In Chapter 3, we began by outlining a framework describing chemical reactions, both in a spatially homogeneous

well-mixed (WM) setting and a spatially inhomogeneous reaction-diffusion (RD) setting. We emphasized mathematical formalisms for systematically imposing the conservation of matter, with or without quasi-steady state (QSS) assumptions. This was first done by using a deterministic macroscopic perspective, where molecular-level fluctuations are averaged out; This formulation was then extended to describe the stochastic simulation algorithm (SSA) that produces exact stochastic realizations of the chemical master equation, a microscopic description of chemical reactions in the WM setting. We furthermore presented a computationally efficient spatial implementation of the SSA that uses an approximate stochastic diffusion algorithm and conserves matter in the presence of QSS assumptions. Continued development of this algorithm is underway, where our goal is to build a tool that will automatically produce high-performance stochastic RD simulation code from human-readable chemical reaction notation.

The motivation for providing such a framework and developing the stochastic computational code was to be able to investigate the mutual antagonism between the two main RhoGTPases that drive cellular motility, Rac and Rho. We first reviewed how, in a WM setting, a model of mutual antagonism can exhibit bistability, where two stable chemical equilibria coexist. These equilibria were termed induced and uninduced states, and corresponded to either protrusive or contractile cellular states, respectively. We next used the extension of this model, presented in [TBBK18], that includes feedback from paxillin onto the mutual inhibition of Rac and Rho, to show that changes in the paxillin phosphorylation rate can be used to reversibly switch between the induced and uninduced states.

By considering the same models in RD setting, we showed that they can produce stable spatially inhomogeneous patterns through a pattern-formation mechanism known as wave-pinning. These patterns can be understood as corresponding to a front-to-rear polarized cell where one region is protrusive (contractile) defining the cell-front (cell-rear). In order to characterize the pattern-formation capacity of the RD models, we applied local perturbation analysis (LPA) to them. Without paxillin, our results demonstrated that a bistable WM system produces LPA diagrams that are considerably more complex than what has typically been reported in the literature, suggesting that they can produce rich dynamics which remain incompletely understood. We then performed LPA on the extended model, using paxillin phosphorylation rate as a bifurcation parameter. By comparing the results of LPA to spatio-temporal simulations, we discovered a, seemingly unbounded, parameter regime that exhibits polarization patterns that are at odds with the predictions of LPA. This was surprising, as LPA usually yields, at least approximate boundaries, for the parameter regimes that produce different types of polarization. In or-

der to partially reconcile the observed pattern formation with the mathematical theory behind LPA, we extended it to produce a *post-hoc* analysis methodology termed pinned-wave analysis (PWA), that can be better reconciled with the outcomes of the spatio-temporal simulations.

A primary objective of this research was to determine how paxillin phosphorylation affects cell motility and migration. While its downstream effects on adhesion dynamics are likely to increase general motility by shifting adhesion populations towards small dynamic NAs and FCs [NWB+06, ZBMKG07], its effects on Rac/Rho mutual inhibition are less straightforward to understand. For example, in [TBBK18], it was reported that polarization disappears at very high paxillin phosphorylation rates. However, here we used spatio-temporal simulations to demonstrate that polarization can indeed be triggered when phosphorylation is very high. We also demonstrated that the loss of polarization observed in [TBBK18] was likely due the applied perturbation being insufficient for triggering polarization. Thus, while paxillin phosphorylation may enhance the mutual antagonism that results in polarization, excessive phosphorylation seems to make it harder to trigger polarization.

In order to see how this affects cellular motility, we then coupled these spatio-temporal simulations to the Cellular Potts Model (CPM), producing time-varying domains that protrude and contract in a way that is consistent with the effects of RhoGTPases. The results of such simulations showed that cells can have multiple protrusive regions which may compete and arrest the movement of the cell. As the paxillin phosphorylation rate was increased, the proportion of cells in an arrested state decreased and simple front-to-rear polarization was increasingly favoured. This demonstrates that paxillin can increase motility through its effects on RhoGTPase signaling, independent of its effects on adhesions.

There are a number of interesting future directions for this work. Firstly, the results of the CPM-based simulations show that cells tend to exist in two different motility states, arrested or motile, and can switch from arrested to motile. This phenomenon is consistent with many observations of CHO-K1 cell motility, where studies typically focus on those that are motile. The dynamics of state switching in simulations remains poorly understood and incompletely characterized. For example, we do not know if cells in the motile state exhibit switching to the arrested state, or if the motile state exhibits increased compared to the arrested state. These questions should be addressed by more in-depth analysis of simulations and larger sample sizes. Furthermore, in Table 3.1, we identified 6 distinct parameter regimes using LPA, whereas we have performed only CPM simulations on regime III′. The motility behaviour produced in the various regimes, in particular regimes III-V, should be studied in

detail in order to understand the richness in polarization suggested by LPA diagrams.

A significant phenomenological issue with the model presented in [TBBK18], when considered in a RD setting, is that paxillin phosphorylation was assumed to occur homogeneously throughout the cell. When coupled to the CPM, this modeling choice has the unintended outcome that cells can exhibit patterns of RhoGTPase activity where Rac is elevated in the middle of a migrating cell. Such a prediction is at odds with nearly all publications on the RhoGTPase signaling during motility. In reality, paxillin is phosphorylated by proteins that are enriched in the vicinity of adhesions, and thus its downstream effects on Rac activation should be expected to occur near the protrusive regions of the cell that act as sources of NAs. The model in [TBBK18] should be understood as a preliminary exploration of paxillin-Rac interactions, and a more complete picture could be obtained by incorporating the spatial distribution of adhesions. The polarization field approach described in [TGRF19] represents a promising methodology for implementing adhesion dynamics in a way that balances biological-realism and computational efficiency. However, as a preliminary approach to modeling paxillin phosphorylation more realistically, we propose the simple logical rule of having paxillin phosphorylation occur only at boundary lattice points.

Finally, in Section 3.5.3, we also presented a novel analytical methodology, termed PWA, that explains the large discrepancy between the fixed-points of bistable WM systems and the local limiting values of wave-pinning patterns observed in RD systems. PWA is effectively a variant of LPA, where instead of trying to predict if pattern formation occurs, we sought to reconcile the observed pattern with asymptotic analysis of the RD PDEs. In order to perform PWA, one must obtain an estimate of the position of the transition between the contractile and protrusive regions of the cell. However, if one could also describe the dynamics of the transition point, and predict where it becomes stalled (i.e., where the wave is pinned), it should be possible to turn PWA into a predictive methodology. A method for describing the movement of the transition was presented in [Jil09]. However, it was implemented as an integro-differential equation that requires solving a time-dependent BVP. We believe that this integro-differential equation and BVP can be simplified to a set of three ODEs through the use of appropriate interpolant. Preliminary numerical results from the application of this methodology to system (31)-(36) have shown that its is numerically stable, but that the equilibrium position of the transition disagrees with PDE simulations. However, in light of what was shown in Section 3.4.1, it is possible that this discrepancy stems from a problem with model derivations. Further investigation with a simpler toy model to troubleshoot the methodology is warranted.

In Chapter 4, we used a previously-published mathematical model of fish keratocyte lamellipodia to investigate the spatio-temporal dynamics of protrusion that occur after such a cell has become front-to-rear polarized. These protrusions are driven by interactions between adhesion maturation and actin polymerization in the branched actin network of the lamellipodium [BAL+17]. In [BAL+17], this mathematical model was successfully used to explain two motility phenotypes: smooth motility and traveling waves of protrusion as well as how cells could be switched between the two phenotypes by inhibiting the activity of the protein VASP. However, a third motility phenotype, rough motility, remained poorly understood. In order to understand the existence of rough motility, we simplified the spatio-temporal PDE model to an ODE model and thoroughly analyzed the dynamics of this simpler model. Bifurcation analysis revealed the existence of two novel parameter regimes, one with bistability between two stable equilibria and another where the closeness of a stable equilibrium to a saddle fixed-point allows for small fluctuations to trigger large and long-lived excursions from the equilibrium.

Slow-fast analysis of the model further revealed that its critical manifold has a folded structure with two attractive sheets separated by a middle repelling sheet. Once the system is pushed from one side of the repelling to the other, its trajectories quickly tend to an attracting sheet, where they subsequently spend a significant amount of time. Thus, in both of the newly-identified regimes, when a fluctuation around a stable equilibrium pushes the system past the repelling sheet, trajectories do not simply relax back to the equilibrium. Instead they travel away from the equilibrium, producing a significant change in protrusion rate. Since this type of noise-driven change in protrusion rate was characteristic of the rough motility phenotype, we hypothesized that one of the newly-identified regimes may be responsible for producing rough motility. By using spatio-temporal simulations of the model, we determined that the bistable regime was more compatible with experimental kymographs of keratocytes with the rough motility phenotype, and that similar results could also be obtained in a stalled regime where cells are not motile in the absence of noise (as was reported in [BAL+17]). In order to further narrow down the parameter regime associated with rough motility, we used a two-parameter bifurcation analysis to explore how the shape of the bistable and stalled regimes change as adhesion maturation rate is varied. Experimental findings in [BLK+11] and [BAL+17] suggest that the proportion of cells exhibiting rough motility increases as adhesion maturation rate decreases. Interestingly, this population-level behaviour is most compatible with the bistable regime, as it increases in size as adhesion maturation rate decreases.

We next extended the model by incorporating some of the mechanosensitive properties of NAs

discussed in Chapter 1. This was done to see how mechanosensitive NAs would perturb the spatio-temporal dynamics of protrusion. When analyzing the ODE simplification of the model, we identified two new bistable regimes produced by our model extension. Similar to in the original model, one regime (bistable II) has bistability between two steady states having either a low or high protrusion velocity, while the other (bistable III) has bistability between a limit cycle and a steady state with low protrusion velocity. By performing spatio-temporal simulations in the presence of noise, we found that bistable II produced patterns of protrusion that are reminiscent of rough motility. On the other hand, bistable III produced patterns of protrusion where a traveling wave moves a short distance along the membrane until a synchronized wave of protrusion recruits all the non-refractory regions of the membrane. Such behaviour is not typically observed in keratocytes [BAL+17], but synchronized protrusion of distant regions of the membrane is indeed observed in CHO-K1 cells (e.g., see Supplementary Movies 3-4 in [CVMZ+08]).

Interestingly, one phenotypic difference between CHO-K1 cells and fish keratocytes is that CHO-K1 cells have many more mature adhesions than keratocytes; our bifurcation analysis shows that the bistable II and bistable III regimes can only be attained when cells have a significantly high adhesion maturation rate than what was used for keratocytes. Therefore, it seems likely that the predictions coming from our analysis of the extended model are relevant for understanding the motility dynamics of fibroblast-like cells such as CHO-K1 cells. Such a prediction should be tested experimentally by generating kymographs of protrusion from CHO-K1 cells and comparing them to model simulations, as well as subjecting them to the VASP inhibitors used in [BAL+17] to see how their spatio-temporal dynamics of protrusion can be varied.

All in all, this thesis provides a quantitative framework that helped explain certain features associated with cell motility ranging from adhesion dynamics to cell polarization through pattern formation. It provided insights into these systems that would not have been possible without the use of both mathematical modeling and computational methods.

List of Publications

Published:

- Laurent Mackay, Nicholas Mikolajewicz, Svetlana V Komarova, and Anmar Khadra. Systematic characterization of dynamic parameters of intracellular calcium signals. *Frontiers in Physiology*, 7:525, 11 2016.
- Laurent MacKay and Anmar Khadra. Dynamics of mechanosensitive nascent adhesion formation. *Biophysical Journal*, 117(6):1057–1073, sep 2019.
- Jessica K Lyda, Jack Z Tan, Abira Rajah, Asheesh Momi, Laurent MacKay, Claire M Brown, and Anmar Khadra. Rac activation is key to cell motility and directionality: An experimental and modelling investigation. *Computational and Structural Biotechnology Journal*, 17:1436–1452, 2019.
- Laurent MacKay and Anmar Khadra. The bioenergetics of integrin-based adhesion, from single molecule dynamics to stability of macromolecular complexes. *Computational and Structural Biotechnology Journal*, 18:393–416, 2020.

In-Press:

- Laurent Mackay, Etienne Lehman, Anmar Khadra. Deciphering the dynamics of lamellipodium in a fish keratocytes model. *Journal Theoretical Biology* (2020). https://doi.org/10.1016/j.jtbi.2020.110534.

In Preparation:

- Wave-Pining and Motility Dynamics in Fibroblast-like cells. [Chapter 3]

Bibliography

[AAS+08] Antonina Y Alexandrova, Katya Arnold, Sébastien Schaub, Jury M Vasiliev, Jean-Jacques Meister, Alexander D Bershadsky, and Alexander B Verkhovsky. Comparative dynamics of retrograde actin flow and focal adhesions: Formation of nascent adhesions triggers transition from fast to slow flow. *PLoS ONE*, 3:e3234, 2008. M2, 4.6.1

[Abe80] M Abercrombie. The croonian lecture, 1978: The crawling movement of metazoan cells. *Proc. R. Soc. Lond. B*, 207:129–147, 1980. 0.1.4

[AC00] Kurt I Anderson and Rob Cross. Contact dynamics during keratocyte motility. *Current Biology*, 10:253–260, 3 2000. 1.8

[ACAG+04] Marco Arnold, Elisabetta Ada Cavalcanti-Adam, Roman Glass, Jacques Blümmel, Wolfgang Eck, Martin Kantlehner, Horst Kessler, and Joachim P Spatz. Activation of integrin function by nanopatterned adhesive interfaces. *ChemPhysChem*, 5:383–388, 2004. 2.3.4

[ADS97] L Van Aelst and C D'Souza-Schorey. Rho gtpases and signaling networks. *Genes development*, 11:2295–2322, 1997. 3.5.2

[AE07] Revathi Ananthakrishnan and Allen Ehrlicher. The forces behind cell movement. *International journal of biological sciences*, 3:303–317, 6 2007. 0.1, 1.1, 4.1

[AJL+02] Bruce Alberts, Alexander Johnson, Julian Lewis, Martin Raff, Keith Roberts, and Peter Walter. *Molecular biology of the cell*. Garland Science, 2002. 1.5

[AKC+95] R Alon, P D Kassner, M W Carr, E B Finger, M E Hemler, and T A Springer. The integrin vla-4 supports tethering and rolling in flow on vcam-1. *The Journal of cell biology*, 128:1243–1253, 3 1995. 1.3.1

[Alb03] Robert A. Alberty. *Thermodynamics of Biochemical Reactions*. John Wiley & Sons, Inc., 2 2003. 1.13.1, 1.13.1

[ALH96] Pontus Aspenström, Uno Lindberg, and Alan Hall. Two GTPases, cdc42 and rac, bind directly to a protein implicated in the immunodeficiency disorder wiskott–aldrich syndrome. *Current Biology*, 6(1):70–75, jan 1996. 3.1

[AON14] Luke R Anderson, Thomas W Owens, and Matthew J Naylor. Structural and mechanical functions of integrins, 2014. 0.1

[Arr89] Svante Arrhenius. Über die reaktionsgeschwindigkeit bei der inversion von rohrzucker durch säuren. *Zeitschrift für Physikalische Chemie*, 4U, 1 1889. 1.13.3

[ASG10] Yvonne Aratyn-Schaus and Margaret L Gardel. Transient frictional slip between integrin and the ecm in focal adhesions under myosin ii tension. *Current biology : CB*, 20:1145–1153, 2010. 2.4, 2.5.1.2

[ASW+15] Paul Atherton, Ben Stutchbury, De-Yao Wang, Devina Jethwa, Ricky Tsang, Eugenia Meiler-Rodriguez, Pengbo Wang, Neil Bate, Roy Zent, Igor L Barsukov, Benjamin T Goult, David R Critchley, and Christoph Ballestrem. Vinculin controls talin engagement with the actomyosin machinery. *Nature Communications*, 6:10038, 2015. 1.2.1

[AXT20] Kyle M. Alpha, Weiyi Xu, and Christopher E. Turner. Paxillin family of focal adhesion adaptor proteins and regulation of cancer cell invasion, 1 2020. 0.1.2

[BAL+17] Erin L Barnhart, Jun Allard, Sunny S Lou, Julie A Theriot, and Alex Mogilner. Adhesion-dependent wave generation in crawling cells. *Current biology : CB*, 27:27–38, 1 2017. (document), 0.1.4, 4.1, 4.2, 4.2, 4.1, 4.3.3, 4.3, 4.4.1, 4.5.1, 4.9, 4.5.2, 4.5.3, 4.5.3, 4.5.3, 4.13, 4.6.1, 4.6.4, 4.7, 5, 5, 5, 5, 5, 5

[Baz] M Z Bazant. 10.626. fall 2011. electrochemical energy systems massachusetts institute of technology: Mit opencouseware. 1.13.3

[Baz13] Martin Z Bazant. Theory of chemical kinetics and charge transfer based on nonequilibrium thermodynamics. *Accounts of Chemical Research*, 46:1144–1160, 5 2013. 1.13.3

[BBFCM+18] Francesca Burgos-Bravo, Nataniel L Figueroa, Nathalie Casanova-Morales, Andrew F G Quest, Christian A M Wilson, and Lisette Leyton. Single-molecule measurements of the effect of force on thy-1/αvβ3-integrin interaction using nonpurified proteins. *Molecular Biology of the Cell*, 29(3):326–338, 2 2018. 1.12

[BCB+96] Alexander Bershadsky, Alexander Chausovsky, Eitan Becker, Anna Lyubimova, and Benjamin Geiger. Involvement of microtubules in the control of adhesion-dependent signal transduction. *Current Biology*, 6:1279–1289, 10 1996. 1.2.2

[BEK+06] C Ballestrem, Noam Erez, Joachim Kirchner, Zvi Kam, Alexander Bershadsky, and Benjamin Geiger. Molecular mapping of tyrosine-phosphorylated proteins in focal adhesions using fluorescence resonance energy transfer. *Journal of Cell Science*, 119:866–875, 3 2006. 1.2.2

[Bel78] George I Bell. Models for the specific adhesion of cells to cells, 5 1978. 1.3.2, 1.6, 1.12, 2.1

[BH00] A L Bishop and A Hall. Rho gtpases and their effector proteins. *The Biochemical journal*, 348 Pt 2:241–255, 2000. 3.1

[BHIWH01] C Ballestrem, B Hinz, B A Imhof, and B Wehrle-Haller. Marching at the front and dragging behind: differential alphavbeta3-integrin turnover regulates focal adhesion behavior. *The Journal of cell biology*, 155:1319–1332, 2001. 0.1.1, 1.2.2, 1.11, 2.4, 2.5.1.8, 2.1, 5

[BHK+06] Claire M Brown, Benedict Hebert, David L Kolin, Jessica Zareno, Leanna Whitmore, Alan Rick Horwitz, and Paul W Wiseman. Probing the integrin-actin linkage using high-resolution protein velocity mapping. *Journal of cell science*, 119:5204–5214, 12 2006. 0.1.1, 1.1, M2

[BKG06] Alexander Bershadsky, Michael Kozlov, and Benjamin Geiger. Adhesion-mediated mechanosensitivity: a time to experiment, and a time to theorize. *Current Opinion in Cell Biology*, 18:472–481, 10 2006. 1.1, 1.3.1

[BKOH02] Amit Bhatt, Irina Kaverina, Carol Otey, and Anna Huttenlocher. Regulation of focal complex composition and disassembly by the calcium-dependent protease calpain. *Journal of cell science*, 115:3415–3425, 9 2002. 1.12

[BLK+11] Erin L Barnhart, Kun-Chun Lee, Kinneret Keren, Alex Mogilner, and Julie A Theriot. An adhesion-dependent switch between mechanisms that determine motile cell shape. *PLoS Biology*, 9:e1001059, 2011. 0.1.4, 5

[BMW14] Maté Biro, Marcia A Munoz, and Wolfgang Weninger. Targeting rho-GTPases in immune cell migration and inflammation. *British Journal of Pharmacology*, 171(24):5491–5506, jul 2014. 0.1

[BPEP20] Dani L Bodor, Wolfram Ponisch, Robert G Endres, and Ewa K Paluch. Of cell shapes and motion: The physical basis of animal cell migration, mar 2020. 0.1.4

[BPM18] Catarina Brás-Pereira and Eduardo Moreno. Mechanical cell competition. *Current Opinion in Cell Biology*, 51:15–21, 4 2018. 1.1

[BRO13] Benjamin L Bangasser, Steven S Rosenfeld, and David J Odde. Determinants of maximal force transmission in a motor-clutch model of cell traction in a compliant microenvironment. *Biophysical Journal*, 105:581–592, 2013. 1.3.2

[Bru05] Robijn Bruinsma. Theory of force regulation by nascent adhesion sites. *Biophysical Journal*, 89:87, 7 2005. 1.8, 1.9

[BRW07] Johannes L Bos, Holger Rehmann, and Alfred Wittinghofer. Gefs and gaps: Critical elements in the control of small g proteins. *Cell*, 129:865–877, 2007. 3.3.1

[BS06] Achim Besser and Samuel A Safran. Force-induced adsorption and anisotropic growth of focal adhesions. *Biophysical Journal*, 90:3469–3484, 2006. 1.2.1, 1.8, 1.8, 1.11, 1.13.4, 2.1, 2.3.1, 2.4, 5

[BS07] Achim Besser and Ulrich S Schwarz. Coupling biochemistry and mechanics in cell adhesion: a model for inhomogeneous stress fiber contraction. *New Journal of Physics*, 9:425, 11 2007. 1.8, 1.11, 1.12

[BSR+01] N Q Balaban, U S Schwarz, D Riveline, P Goichberg, G Tzur, I Sabanay, D Mahalu, S Safran, A Bershadsky, L Addadi, and B Geiger. Force and focal adhesion assembly: a close relationship studied using elastic micropatterned substrates. *Nature cell biology*, 3:466–472, 5 2001. 1.1, 1.12, 5

[BT04] Micheal Brown and Christopher E Turner. Paxillin: Adapting to change. *Physiological Reviews*, 84:1315–1339, 2004. 1.2.1, 1.12, 3.1

[BvHD+15] Hayri E Balcioglu, Hedde van Hoorn, Dominique M Donato, Thomas Schmidt, and Erik H J Danen. The integrin expression profile modulates orientation and dynamics of force transmission at cell-matrix adhesions. *Journal of Cell Science*, 128:1316–1326, 4 2015. 1.6

[BWK08] Joshua A Broussard, Donna J Webb, and Irina Kaverina. Asymmetric focal adhesion disassembly in motile cells. *Current Opinion in Cell Biology*, 20:85–90, 2 2008. 0.1, 1.2.2, 1.8, 3.1

[CAMB+06] Elisabetta A Cavalcanti-Adam, Alexandre Micoulet, Jacques Blümmel, Jörg Auernheimer, Horst Kessler, and Joachim P Spatz. Lateral spacing of integrin ligands influences cell spreading and focal adhesion assembly. *European Journal of Cell Biology*, 85:219–224, 4 2006. 2.3.4

[CAT+14] Chi Li Chiu, Jose S Aguilar, Connie Y Tsai, Gui Kai Wu, Enrico Gratton, and Michelle A Digman. Nanoimaging of focal adhesion dynamics in 3d. *PLoS ONE*, 9:e99896, 2014. 1.7, O2, 2.4, 2.5.1

[CAVM+07] Elisabetta Ada Cavalcanti-Adam, Tova Volberg, Alexandre Micoulet, Horst Kessler, Benjamin Geiger, and Joachim Pius Spatz. Cell spreading and focal adhesion dynamics are regulated by spacing of integrin ligands. *Biophysical journal*, 92:2964–2974, 2007. 2.4, 2.5.1.8

[CAW+03] Bruce D Cuevas, Amy N Abell, James A Witowsky, Toshiaki Yujiri, Nancy Lassignal Johnson, Kamala Kesavan, Marti Ware, Peter L Jones, Scott A Weed, Roberta L DeBiasi, Yoshitomo Oka, Kenneth L Tyler, and Gary L Johnson. Mekk1 regulates calpain-dependent proteolysis of focal adhesion proteins for rear-end detachment of migrating fibroblasts. *The EMBO journal*, 22:3346–3355, 7 2003. 0.1.1, 1.2.2

[CB19] Yanyan Chen and Javier Buceta. A non-linear analysis of turing pattern formation. *PLOS ONE*, 14:e0220994, 8 2019. 3.5

[CBB+17] Xuan Cao, Ehsan Ban, Brendon M Baker, Yuan Lin, Jason A Burdick, Christopher S Chen, and Vivek B Shenoy. Multiscale model predicts increasing focal adhesion size with decreasing stiffness in fibrous matrices. *Proceedings of the National Academy of Sciences of the United States of America*, 114:E4549——E4555, 2017. 1.8, 1.12, 2.1, 2.4, 2.5.1.2

[CBH10] Keefe T Chan, David A Bennin, and Anna Huttenlocher. Regulation of adhesion dynamics by calpain-mediated proteolysis of focal adhesion kinase (fak). *The Journal of biological chemistry*, 285:11418–11426, 2010. 1.2.2

[CCLSD10] Sara Cabodi, Maria Del Pilar Camacho-Leal, Paola Di Stefano, and Paola Defilippi. Integrin signalling adaptors: Not only figurants in the cancer story, 2010. 0.1

[CCWS18] Rishita Changede, Haogang Cai, Shalom Wind, and Michael P Sheetz. Ligand geometry controls adhesion formation via integrin clustering. *bioRxiv*, page 435826, 2018. 0.1, 1.6, 2.1, 2.3.1

[CD09] Steve S Choi and Anna Mae Diehl. Epithelial-to-mesenchymal transitions in the liver, 2009. 0.1.4

[CH05] Julien Cau and Alan Hall. Cdc42 controls the polarity of the actin and microtubule cytoskeletons through two distinct signal transduction pathways. *Journal of cell science*, 118:2579–2587, 2005. 3.3.2

[CHC03] Jason R Chan, Sharon J Hyduk, and Myron I Cybulsky. Detecting rapid and transient upregulation of leukocyte integrin affinity induced by chemokines and chemoattractants. *Journal of immunological methods*, 273:43–52, 2 2003. 1.3

[CK09] Wei-Ting Chao and Jeannette Kunz. Focal adhesion disassembly requires clathrin-dependent endocytosis of integrins. *FEBS Letters*, 583:1337–1343, 4 2009. 1.2.2

[CKC+10] Murat Cirit, Matej Krajcovic, Colin K Choi, Erik S Welf, Alan F Horwitz, and Jason M Haugh. Stochastic model of integrin-mediated signaling and adhesion dynamics at the leading edges of migrating cells. *PLoS Computational Biology*, 6:e1000688, 2010. 2.1

[CKY+11] Fan-Ching Chien, Chiung Wen Kuo, Zong-Han Yang, Di-Yen Chueh, and Peilin Chen. Exploring the formation of focal adhesions on patterned surfaces using super-resolution imaging. *Small*, 7:2906–2913, 10 2011. 0.1, 1.11

[CLD+15] Xuan Cao, Yuan Lin, Tristian P Driscoll, Janusz Franco-Barraza, Edna Cukierman, Robert L Mauck, and Vivek B Shenoy. A chemomechanical model of matrix and nuclear rigidity regulation of focal adhesion size. *Biophysical journal*, 109:1807–1817, 11 2015. 2.1

[CLH+20] Megan R Chastney, Craig Lawless, Jonathan D Humphries, Stacey Warwood, Matthew C Jones, David Knight, Claus Jorgensen, and Martin J Humphries. Definition of the fibroblast adhesome using multiplexed proximity biotinylation. *bioRxiv*, page 2020.01.24.918458, 1 2020. 0.1

[CLS20] J. I. Carrero, J. S. Loaiza, and A. Serna. Stochastic reaction, stochastic diffusion. *ChemTexts*, 6(2):14, apr 2020. (document), 3.2.2.2, 3.2.2.3, 3.2.2.3, 3.2, 3.2.2.3, 3.2.2.3

[CLT+17] Yunfeng Chen, Hyunjung Lee, Haibin Tong, Martin Schwartz, and Cheng Zhu. Force regulated conformational change of integrin αvβ3. *Matrix biology : journal of the International Society for Matrix Biology*, 60-61:70–85, 2017. 1.3.2, 1.12

[CLW+14] Bi-Chang Chen, Wesley R. Legant, Kai Wang, Lin Shao, Daniel E. Milkie, Michael W. Davidson, Chris Janetopoulos, Xufeng S. Wu, John A. Hammer, Zhe Liu, Brian P. English, Yuko Mimori-Kiyosue, Daniel P. Romero, Alex T. Ritter, Jennifer Lippincott-Schwartz, Lillian Fritz-Laylin, R. Dyche Mullins, Diana M. Mitchell,

Joshua N. Bembenek, Anne-Cecile Reymann, Ralph Bohme, Stephan W. Grill, Jennifer T. Wang, Geraldine Seydoux, U. Serdar Tulu, Daniel P. Kiehart, and Eric Betzig. Lattice light-sheet microscopy: Imaging molecules to embryos at high spatiotemporal resolution. *Science*, 346(6208):1257998, 10 2014. 0.1, 1.1

[CMG+00] G Constantin, M Majeed, C Giagulli, L Piccio, J Y Kim, E C Butcher, and C Laudanna. Chemokines trigger immediate beta2 integrin affinity and mobility changes: differential regulation and roles in lymphocyte arrest under flow. *Immunity*, 13:759–769, 12 2000. 1.3

[CMM+16] Alice C Chang, Armen H Mekhdjian, Masatoshi Morimatsu, Aleksandra Kirillovna Denisin, Beth L Pruitt, and Alexander R Dunn. Single molecule force measurements in living cells reveal a minimally tensioned integrin state. *ACS Nano*, 10:10745–10752, 12 2016. 1.3.1, 2.4, 2.5.1.2

[CMRP17] George W A Constable, Alan J McKane, Tim Rogers, and Todd L Parsons. Dimension reduction for stochastic dynamical systems forced onto a manifold by large drift: a constructive approach with examples from theoretical biology related content stochastic dynamics on slow manifolds dimension reduction for stochastic dynamical s. *Journal of Physics A: Mathematical and Theoretical J. Phys. A: Math. Theor*, 50:33, 2017. 3.2.1.2

[CO08] Clarence E Chan and David J Odde. Traction dynamics of filopodia on compliant substrates. *Science*, 322:1687–1691, 2008. 2.1

[Cri09] David R Critchley. Biochemical and structural properties of the integrin-associated cytoskeletal protein talin. *Annual review of biophysics*, 38:235–254, 2009. 1.2.1

[CS17] Rishita Changede and Michael Sheetz. Integrin and cadherin clusters: A robust way to organize adhesions for cell mechanics. *BioEssays*, 39:e201600123, 1 2017. 2.3.4, 2.4, 2.5.1

[CSL+05] Caroline Cluzel, Frédéric Saltel, Jost Lussi, Frédérique Paulhe, Beat A Imhof, and Bernhard Wehrle-Haller. The mechanisms and dynamics of αvβ3 integrin clustering in living cells. *Journal of Cell Biology*, 171:383–392, 10 2005. 2.4, 2.5.1

[CSS03] JianFeng Chen, Azucena Salas, and Timothy A Springer. Bistable regulation of integrin adhesiveness by a bipolar metal ion cluster. *Nature Structural Biology*, 10:995–1001, 12 2003. 1.3

[Cun10] Americo Jr Cunha. *Reduction of Complexity in Combustion Thermochemistry*. PhD thesis, 2010. 3.2.1.2

[CV15] Andrew G Clark and Danijela Matic Vignjevic. Modes of cancer cell invasion and the role of the microenvironment. *Current Opinion in Cell Biology*, 36:13–22, 10 2015. 2.1

[CVMZ+08] Colin K Choi, Miguel Vicente-Manzanares, Jessica Zareno, Leanna A Whitmore, Alex Mogilner, and Alan Rick Horwitz. Actin and alpha-actinin orchestrate the assembly and maturation of nascent adhesions in a myosin ii motor-independent manner. *Nature cell biology*, 10:1039–1050, 9 2008. 0.1.1, 1.1, 1.2.1, 1.2.2, 1.7, 1.8, 1.11, O1, M2, 2.2.3, 2.3.5.2, 2.4, 2.5.1.2, 2.5.1.8, 3.1, 4.6.1, 4.6.4, 5

[CW07] Xiaodong Cai and Xiaodong Wang. Stochastic modeling and simulation of gene networks - a review of the state-of-the-art research on stochastic simulations. *IEEE Signal Processing Magazine*, 24:27–36, 2007. 3.2.2.1

[CW15] Lindsay B Case and Clare M Waterman. Integration of actin dynamics and cell adhesion by a three-dimensional, mechanosensitive molecular clutch. *Nature Cell Biology*, 17:955–963, 6 2015. 0.1, 0.1.2, 1.1, 1.2.1, 1.1, 1.12

[CWB96] M Chrzanowska-Wodnicka and K Burridge. Rho-stimulated contractility drives the formation of stress fibers and focal adhesions. *The Journal of Cell Biology*, 133, 1996. 3.1

[CXM+15] Rishita Changede, Xiaochun Xu, Felix Margadant, Michael P Sheetz, D R Critchley, A Ravasio, Z Chen, Y H Wang, K Kawauchi, and Et Al. Nascent integrin adhesions form on all matrix rigidities after integrin activation. *Developmental Cell*, 35:614–621, 2015. 0.1.1, 1.6, 1.12, 2.1, 2.2.3, 2.3.1, 2.2, 2.3.1, 2.3.3, 2.3.5.2, 2.4, 2.5.1, 2.5.1.2, 2.5.1.8, 2.1, 2.5.1.8

[CXN+10] Xing Chen, Can Xie, Noritaka Nishida, Zongli Li, Thomas Walz, and Timothy A Springer. Requirement of open headpiece conformation for activation of leukocyte integrin alphaxbeta2. *Proceedings of the National Academy of Sciences of the United States of America*, 107:14727–14732, 8 2010. 1.3, 1.3.2, 1.12

[CZD+11] Colin K Choi, Jessica Zareno, Michelle A Digman, Enrico Gratton, and Alan Rick Horwitz. Cross-correlated fluctuation analysis reveals phosphorylation-regulated paxillin-fak complexes in nascent adhesions. *Biophysical Journal*, 100:583–592, 2 2011. 1.7, 1.12, 3.3.2

[CZLR16] Brian A Camley, Juliane Zimmermann, Herbert Levine, and Wouter Jan Rappel. Collective signal processing in cluster chemotaxis: Roles of adaptation, amplification, and co-attraction in collective guidance. *PLoS Computational Biology*, 12, 2016. 0.1.4

[CZM+07] Lacayo CI, Pincus Z, VanDuijn MM, Wilson CA, Fletcher DA, Gertler FB, Mogilner A, and Theriot JA. Emergence of large-scale cell morphology and movement from local actin filament growth dynamics. *PLoS biology*, 5, 2007. 4.7

[DA96] Haim Diamant and David Andelman. Kinetics of surfactant adsorption at fluid-fluid interfaces. *Journal of Physical Chemistry*, 100:13732–13742, 1996. 1.8

[dADS17] Vinicius Cotta de Almeida, Loïc Dupré, and Wilson Savino. Editorial: T-cell migration in health and disease. *Frontiers in Immunology*, 8, feb 2017. 0.1

[DBH+08] Michelle A Digman, Claire M Brown, Alan R Horwitz, William W Mantulin, and Enrico Gratton. Paxillin dynamics measured during adhesion assembly and disassembly by correlation spectroscopy. *Biophysical journal*, 94:2819–2831, 4 2008. 1.1, 1.2.2, 1.7, 1.12, O2, 2.4, 2.5.1

[DCL+11] Jing Du, Xiaofei Chen, Xudong Liang, Guangyao Zhang, Jia Xu, Linrong He, Qingyuan Zhan, Xi Qiao Feng, Shu Chien, and Chun Yang. Integrin activation and internalization on soft ecm as a mechanism of induction of stem cell differentiation by ecm elasticity. *Proceedings of the National Academy of Sciences of the United States of America*, 108:9466–9471, 2011. 1.9

[DECEK06] Adriana T Dawes, G Bard Ermentrout, Eric N Cytrynbaum, and Leah Edelstein-Keshet. Actin filament branching and protrusion velocity in a simple 1d model of a motile cell. *Journal of Theoretical Biology*, 242:265–279, 2006. 3.1, 3.6.0.1

[DEK07] Adriana T Dawes and Leah Edelstein-Keshet. Phosphoinositides and rho proteins spatially regulate actin polymerization to initiate and maintain directed movement in a one-dimensional model of a motile cell. *Biophysical Journal*, 92:744–768, 2 2007. 1.12, 3.1, 3.3

[Des15] Markus Deserno. Fluid lipid membranes: From differential geometry to curvature stresses. *Chemistry and Physics of Lipids*, 185:11–45, 2015. 4.6

[DGdB+12] S E Le Devedec, B Geverts, H de Bont, K Yan, F J Verbeek, A B Houtsmuller, and B van de Water. The residence time of focal adhesion kinase (fak) and paxillin at focal adhesions in renal epithelial cells is determined by adhesion size, strength and life cycle status. *Journal of Cell Science*, 125:4498–4506, 2012. O2, 2.4, 2.5.1

[DGK+12] Mathieu Desroches, John Guckenheimer, Bernd Krauskopf, Christian Kuehn, Hinke M Osinga, and Martin Wechselberger. Mixed-mode oscillations with multiple time scales. *SIAM Review*, 54:211–288, 1 2012. 4.4, 4.4.4.2

[DH15] Peter Devreotes and Alan Rick Horwitz. Signaling networks that regulate cell migration. *Cold Spring Harbor Perspectives in Biology*, 2015. 0.1

[DJ03] Peter Devreotes and Chris Janetopoulos. Eukaryotic chemotaxis: distinctions between directional sensing and polarization. *The Journal of biological chemistry*, 278:20445–20448, 2003. 1.1, 2.1

[DLS+13] David W Dumbauld, Ted T Lee, Ankur Singh, Jan Scrimgeour, Charles A Gersbach, Evan A Zamir, Jianping Fu, Christopher S Chen, Jennifer E Curtis, Susan W Craig, and Andrés J García. How vinculin regulates force transmission. *Proceedings of the National Academy of Sciences of the United States of America*, 110:9788–9793, 2013. 1.2.1

[DML+04] Andrew Doyle, William Marganski, Juliet Lee, Z Goeckeler, G Côté, and R Wysolmerski. Calcium transients induce spatially coordinated increases in traction

force during the movement of fish keratocytes. *Journal of cell science*, 117:2203–2214, 2004. 1.4, 1.8, 3.1

[DNB+08] Bado Hewa Defranco, Beth M. Nickel, Catherine J. Baty, Jacob S. Martinez, Vernon L. Gay, Vlad C. Sandulache, David J. Hackam, and Sandra A. Murray. Migrating cells retain gap junction plaque structure and function. *Cell Communication & Adhesion*, 15(3):273–288, jan 2008. 0.1.4

[DPC+07] E J Doedel, R C Paffenroth, A R Champneys, T F Fairgrieve, Yu. A Kuznetsov, B Sandstede, and X Wang. Auto-07p: Continuation and bifurcation software for ordinary differential equations, 2007. 2.2.4, 3.2.4, 4.3

[DSDB16] Laurent Dinh, Jascha Sohl-Dickstein, and Samy Bengio. Density estimation using real nvp. *arXiv*, arXiv:1605.08803v3, 2016. 2.4, 2.5.3

[DT08] Nicholas O Deakin and Christopher E Turner. Paxillin comes of age. *Journal of cell science*, 121:2435–2444, 2008. 0.1.2, 3.1

[DTSH88] M Dembo, D C Torney, K Saxman, and D Hammer. The reaction-limited kinetics of membrane-to-surface adhesion and detachment. *Proceedings of the Royal Society B: Biological Sciences*, 234:55–83, 6 1988. 1.3.2

[DYY+15] Sulagna Das, Taofei Yin, Qingfen Yang, Jingqiao Zhang, Yi I Wu, and Ji Yu. Single-molecule tracking of small gtpase rac1 uncovers spatial regulation of membrane translocation and mechanism for polarized signaling. *Proceedings of the National Academy of Sciences of the United States of America*, 112:E267——76, 2015. 3.5.2

[EAOC+16] Alberto Elosegui-Artola, Roger Oria, Yunfeng Chen, Anita Kosmalska, Carlos Pérez-González, Natalia Castro, Cheng Zhu, Xavier Trepat, and Pere Roca-Cusachs. Mechanical regulation of a molecular clutch defines force transmission and transduction in response to matrix rigidity. *Nature Cell Biology*, 18:540–548, 2016. 1.12

[EBMG09] Ellen J Ezratty, Claire Bertaux, Eugene E Marcantonio, and Gregg G Gundersen. Clathrin mediates integrin endocytosis for focal adhesion disassembly in migrating cells. *The Journal of Cell Biology*, 187:733–747, 11 2009. 1.2.2

[EC07] Evan A Evans and David A Calderwood. Forces and bond dynamics in cell adhesion. *Science*, 316, 2007. 1.3.2

[ECM07] Radek Erban, Jonathan Chapman, and Philip Maini. A practical guide to stochastic simulations of reaction-diffusion processes. 2007. 3.2.2, 3.2.2.2, 3.2.2.3

[EDY+09] Tim Eiseler, Heike Döppler, Irene K Yan, Steve Goodison, and Peter Storz. Protein kinase d1 regulates matrix metalloproteinase expression and inhibits breast cancer cell invasion. *Breast Cancer Research*, 11:R13, 2009. 1.2.2

[EK09] Andrey Efimov and Irina Kaverina. Significance of microtubule catastrophes at focal adhesion sites. *Cell Adhesion & Migration*, 3(3):285–287, jul 2009. 0.1.2

[EK16] Leah Edelstein-Keshet. Flipping the rac-rho switch in cell motility. *Cell Systems*, 2:10–12, 2016. 0.1.3

[EKHZD13] Leah Edelstein-Keshet, William R Holmes, Mark Zajac, and Meghan Dutot. From simple to detailed models for cell polarization. *Philosophical Transactions of the Royal Society B: Biological Sciences*, 368:20130003, 11 2013. 0.1.3, 3.3, 3.4.2, 3.5, 3.6, 3.6.0.1

[ELHS01] E Evans, A Leung, D Hammer, and S Simon. Chemically distinct transition states govern rapid dissociation of single l-selectin bonds under force. *Proceedings of the National Academy of Sciences of the United States of America*, 98:3784–3789, 3 2001. 1.3.2

[ELHZ04] Evan Evans, Andrew Leung, Volkmar Heinrich, and Cheng Zhu. Mechanical switching and coupling between two dissociation pathways in a p-selectin adhesion bond. *Proceedings of the National Academy of Sciences of the United States of America*, 101:11281–11286, 8 2004. 1.3.2, 1.3.2, 1.2

[ELVE05] Weinan E, Di Liu, and Eric Vanden-Eijnden. Nested stochastic simulation algorithm for chemical kinetic systems with disparate rates. *The Journal of Chemical Physics*, 123:194107, 2005. 3.2.2.1

[ELVE07] Weinan E, Di Liu, and Eric Vanden-Eijnden. Nested stochastic simulation algorithms for chemical kinetic systems with multiple time scales. *Journal of Computational Physics*, 221:158–180, 2007. 3.2.2.1

[EMB+16] David Ellison, Andrew Mugler, Matthew D Brennan, Sung Hoon Lee, Robert J Huebner, Eliah R Shamir, Laura A Woo, Joseph Kim, Patrick Amar, Ilya Nemenman, Andrew J Ewald, and Andre Levchenko. Cell-cell communication enhances the capacity of cell ensembles to sense shallow gradients during morphogenesis, 2016. 0.1.4

[EP84] E H Egelman and R Padrón. X-ray diffraction evidence that actin is a 100 Åfilament. *Nature*, 307:56–58, 1 1984. 4.6.1

[EPG05] Ellen J Ezratty, Michael A Partridge, and Gregg G Gundersen. Microtubule-induced focal adhesion disassembly is mediated by dynamin and focal adhesion kinase. *Nature Cell Biology*, 7:581–590, 6 2005. 1.2.2

[ER97] E Evans and K Ritchie. Dynamic strength of molecular adhesion bonds. *Biophysical journal*, 72:1541–1555, 4 1997. 1.3.2, 1.3.2

[Erm02] Bard Ermentrout. *Simulating, Analyzing, and Animating Dynamical Systems: a Guide to XPPAUT for Researchers and Students*. Society for Industrial and Applied Mathematics, 1 2002. 3.2.4

[ES04a] T Erdmann and U S Schwarz. Stability of adhesion clusters under constant force. *Physical Review Letters*, 92:108102, 3 2004. 1.6, 1.10, 1.11

[ES04b] Thorsten Erdmann and Ulrich S Schwarz. Stochastic dynamics of adhesion clusters under shared constant force and with rebinding. *Journal of Chemical Physics*, 121:8997–9017, 11 2004. 1.10, 1.11, 1.12, 2.1, 2.3.5.1, 2.3.5.1, 2.3.6, 2.4, 5

[ESG+08] Andrey Efimov, Natalia Schiefermeier, Ilya Grigoriev, Ryoma Ohi, Michael C Brown, Christopher E Turner, J Victor Small, and Irina Kaverina. Paxillin-dependent stimulation of microtubule catastrophes at focal adhesion sites. *Journal of cell science*, 121:196–204, 1 2008. 1.2.2

[ESM+10] Urban E, Jacob S, Nemethova M, Resch GP, and Small JV. Electron tomography reveals unbranched networks of actin filaments in lamellipodia. *Nature cell biology*, 12, 2010. 4.6.1

[ESSD06] Adam J Engler, Shamik Sen, H Lee Sweeney, and Dennis E Discher. Matrix elasticity directs stem cell lineage specification. *Cell*, 126:677–689, 8 2006. 1.1

[EW14] Andreas Ettinger and Torsten Wittmann. Fluorescence live cell imaging, 2014. 0.1

[FABK20] Saeed Farjami, Ryan P D Alexander, Derek Bowie, and Anmar Khadra. Switching in cerebellar stellate cell excitability in response to a pair of inhibitory/excitatory presynaptic inputs: A dynamical system perspective. *Neural Computation*, 32:626–658, 3 2020. 4.4.3.1

[FB] John Ferraioli and Rick Burke. Drowning in data, but starving for insights starting the digital supply network journey with legacy systems. 0.1

[FBL13] Cibele V Falkenberg, Michael L Blinov, and Leslie M Loew. Pleomorphic ensembles: Formation of large clusters composed of weakly interacting multivalent molecules. *Biophysical Journal*, 105:2451–2460, 12 2013. 1.7

[FCS96] D P Felsenfeld, D Choquet, and M P Sheetz. Ligand binding regulates the directed movement of 1 integrins on fibroblasts. *Nature*, 383:438–440, 10 1996. 2.4, 2.5.1.2

[FG09] Peter Friedl and Darren Gilmour. Collective cell migration in morphogenesis, regeneration and cancer. *Nature Reviews Molecular Cell Biology*, 10:445–457, 7 2009. 0.1, 0.1.1, 1.1, 2.1

[FH05] Santos J Franco and Anna Huttenlocher. Regulating cell migration: calpains make the cut. *Journal of cell science*, 118:3829–3838, 2005. 1.12

[FHA+15] N De Franceschi, H Hamidi, J Alanko, P Sahgal, and J Ivaska. Integrin traffic - the update. *Journal of Cell Science*, 128:839–852, 2015. 1.2.2

[FKTD07] Matthew J Footer, Jacob W J Kerssemakers, Julie A Theriot, and Marileen Dogterom. Direct measurement of force generation by actin filament polymerization using an

optical trap. *Proceedings of the National Academy of Sciences of the United States of America*, 104:2181–2186, 2007. 1.3.1

[FLLKM18] Lillian K Fritz-Laylin, Samuel J Lord, Mallory Kakley, and R Dyche Mullins. Concise language promotes clear thinking about cell shape and locomotion. *BioEssays*, 40:e1700225, 2018. 0.1.4

[FP03] Iman Famili and Bernhard O Palsson. The convex basis of the left null space of the stoichiometric matrix leads to the definition of metabolically meaningful pools. *Biophysical journal*, 85:16–26, 2003. 3.2.1

[FW10] Peter Friedl and Katarina Wolf. Plasticity of cell migration: A multiscale tuning model. *Journal of Cell Biology*, 188(1):11–19, dec 2010. 0.1.1, 0.1.4

[FWY+10] Jianping Fu, Yang Kao Wang, Michael T Yang, Ravi A Desai, Xiang Yu, Zhijun Liu, and Christopher S Chen. Mechanical regulation of cell function with geometrically modulated elastomeric substrates. *Nature Methods*, 7:733–736, 2010. 1.1

[GB00] Michael A Gibson and Jehoshua Bruck. Efficient exact stochastic simulation of chemical systems with many species and many channels. *Journal of Physical Chemistry A*, 104:1876–1889, 2000. 3.2.2.3

[GB02] Benjamin Geiger and Alexander Bershadsky. Exploring the neighborhood: adhesion-coupled cell mechanosensors. *Cell*, 110:139–142, 2002. 1.1

[GBP07] James A Glazier, Ariel Balter, and Nikodem J Popławski. Magnetization to morphogenesis: A brief history of the glazier-graner-hogeweg model, 2007. 3.2.5

[GDTR+07] Grégory Giannone, Benjamin J. Dubin-Thaler, Olivier Rossier, Yunfei Cai, Oleg Chaga, Guoying Jiang, William Beaver, Hans-Günther Döbereiner, Yoav Freund, Gary Borisy, and Michael P. Sheetz. Lamellipodial actin mechanically links myosin activity with adhesion-site formation. *Cell*, 128(3):561–575, 2 2007. 1.1

[GEA+07] Stephanie L Gupton, Kathryn Eisenmann, Arthur S Alberts, Clare M Waterman-Storer, and C M Waterman-Storer. mdia2 regulates actin and focal adhesion dynamics

and organization in the lamella for efficient epithelial cell migration. *Journal of cell science*, 120:3475–3487, 2007. M2

[GH10] David F Griffiths and Desmond J Higham. *Numerical Methods for Ordinary Differential Equations*. Springer London, 2010. 4.5.2

[GHB+10] Carsten Grashoff, Brenton D Hoffman, Michael D Brenner, Ruobo Zhou, Maddy Parsons, Michael T Yang, Mark A McLean, Stephen G Sligar, Christopher S Chen, Taekjip Ha, and Martin A Schwartz. Measuring mechanical tension across vinculin reveals regulation of focal adhesion dynamics. *Nature*, 466:263–266, 7 2010. 0.1

[GHP13] Daniel T. Gillespie, Andreas Hellander, and Linda R. Petzold. Perspective: Stochastic algorithms for chemical kinetics. *The Journal of Chemical Physics*, 138(17):170901, may 2013. 3.2.2

[Gil92] Daniel T Gillespie. A rigorous derivation of the chemical master equation. *Physica A: Statistical Mechanics and its Applications*, 188:404–425, 9 1992. 3.2.2

[Gil02] Daniel T Gillespie. The chemical langevin and fokker-planck equations for the reversible isomerization reaction. *Journal of Physical Chemistry A*, 106:5063–5071, 2002. 4.4.3.2, 4.7

[GKC+17] Melanie Graessl, Johannes Koch, Abram Calderon, Dominic Kamps, Soumya Banerjee, Tomáš Mazel, Nina Schulze, Jana Kathrin Jungkurth, Rutuja Patwardhan, Djamschid Solouk, Nico Hampe, Bernd Hoffmann, Leif Dehmelt, and Perihan Nalbant. An excitable rho gtpase signaling network generates dynamic subcellular contraction patterns. *Journal of Cell Biology*, 216:4271–4285, 12 2017. 3.1

[GKTV18] Aleena Gladkikh, Anastasia Kovaleva, Anna Tvorogova, and Ivan A Vorobjev. Heterogeneity of focal adhesions and focal contacts in motile fibroblasts, 2018. 0.1.2

[GLW02] Angela Glading, Douglas A Lauffenburger, and Alan Wells. Cutting to the chase: calpain proteases in cell motility. *Trends in cell biology*, 12:46–54, 1 2002. 1.12

[GML+12] Saba Ghassemi, Giovanni Meacci, Shuaimin Liu, Alexander A Gondarenko, Anurag Mathur, Pere Roca-Cusachs, Michael P Sheetz, and James Hone. Cells test substrate

rigidity by local contractions on submicrometer pillars. *Proceedings of the National Academy of Sciences of the United States of America*, 109:5328–5333, 2012. 0.1

[GMY13] A N Gorban, E M Mirkes, and G S Yablonsky. Thermodynamics in the limit of irreversible reactions. *Physica A: Statistical Mechanics and its Applications*, 392:1318–1335, 3 2013. 3.2.1

[Goo11] D S Goodsell. Integrin, 2011. 2.3.1

[Gou05] John Goutsias. Quasiequilibrium approximation of fast reaction kinetics in stochastic biochemical systems. *The Journal of Chemical Physics*, 122:184102, 5 2005. 3.2.2.1

[Gov06] Nir S Gov. Modeling the size distribution of focal adhesions. *Biophysical journal*, 91:2844–2847, 2006. 1.7, 1.12, 2.1, M2, 2.3.3, 2.4, 2.5.1.3

[Gra97] Enrico Grazi. What is the diameter of the actin filament? *FEBS Letters*, 405:249–252, 1997. 4.6.1

[GSASW10] Margaret L Gardel, Ian C Schneider, Yvonne Aratyn-Schaus, and Clare M Waterman. Mechanical integration of actin and adhesion dynamics in cell migration. *Annual review of cell and developmental biology*, 26:315–333, 2010. 0.1, 3.1

[GSJ+08] Margaret L Gardel, Benedikt Sabass, Lin Ji, Gaudenz Danuser, Ulrich S Schwarz, and Clare M Waterman. Traction stress in focal adhesions correlates biphasically with actin retrograde flow speed. *The Journal of cell biology*, 183:999–1005, 2008. 1.1

[GW14] Alexandra Goeke and Sebastian Walcher. A constructive approach to quasi-steady state reductions. *Journal of Mathematical Chemistry*, 52:2596–2626, 11 2014. 3.2.1.2

[GWZ15] Alexandra Goeke, Sebastian Walcher, and Eva Zerz. Determining "small parameters" for quasi-steady state. *Journal of Differential Equations*, 259:1149–1180, 8 2015. 3.2.1.2

[GY11] Benjamin Geiger and Kenneth M Yamada. Molecular architecture and function of matrix adhesions. *Cold Spring Harbor perspectives in biology*, 3, 2011. 1.1

[GYG07] Catherine G Galbraith, Kenneth M Yamada, and James A Galbraith. Polymerizing actin fibers position integrins primed to probe for adhesion sites. *Science (New York, N.Y.)*, 315:992–995, 2 2007. 3.1

[GYS02] Catherine G Galbraith, Kenneth M Yamada, and Michael P Sheetz. The relationship between force and focal complex development. *Journal of Cell Biology*, 159:695–705, 2002. 0.1.1

[GYS18] Benjamin T Goult, Jie Yan, and Martin A Schwartz. Talin as a mechanosensitive signaling hub. *The Journal of cell biology*, 217:3776–3784, 11 2018. 1.12

[HBA+15] Edward R. Horton, Adam Byron, Janet A. Askari, Daniel H. J. Ng, Angélique Millon-Frémillon, Joseph Robertson, Ewa J. Koper, Nikki R. Paul, Stacey Warwood, David Knight, Jonathan D. Humphries, and Martin J. Humphries. Definition of a consensus integrin adhesome and its dynamics during adhesion complex assembly and disassembly. *Nature cell biology*, 17(12):1577–1587, 12 2015. 0.1, 2.1

[HBB+17] Derek L Huang, Nicolas A Bax, Craig D Buckley, William I Weis, and Alexander R Dunn. Vinculin forms a directionally asymmetric catch bond with f-actin. *Science*, 357:703–706, 8 2017. 1.12

[HBT+12] Sangyoon J Han, Kevin S Bielawski, Lucas H Ting, Marita L Rodriguez, and Nathan J Sniadecki. Decoupling substrate stiffness, spread area, and micropost density: a close spatial relationship between traction forces and focal adhesions. *Biophysical journal*, 103:640–648, 2012. 1.8

[HC09] David S Harburger and David A Calderwood. Integrin signalling at a glance. *Journal of cell science*, 122:159–163, 1 2009. 1.3

[HCEK12] W R Holmes, A E Carlsson, and L Edelstein-Keshet. Regimes of wave type patterning driven by refractory actin feedback: transition from static polarization to dynamic wave behaviour. *Physical biology*, 9:46005, 8 2012. 0.1.3, 3.1, 3.3, 3.6, 3.6.0.1, 3.6.0.2

[HCW+98] G Y Huang, E S Cooper, K Waldo, M L Kirby, N B Gilula, and C W Lo. Gap junction-mediated cell-cell communication modulates mouse neural crest migration. *Journal of Cell Biology*, 143:1725–1734, 1998. 0.1.4

[HD09] Stephan Huveneers and Erik H J Danen. Adhesion signaling - crosstalk between integrins, src and rho. *Journal of cell science*, 122:1059–1069, 4 2009. 0.1, 3.1

[HD18] Daniel Haensel and Xing Dai. Epithelial-to-mesenchymal transition in cutaneous wound healing: Where we are and where we are heading, 2018. 0.1.4

[HEK12] William R. Holmes and Leah Edelstein-Keshet. A comparison of computational models for eukaryotic cell shape and motility. *PLoS Computational Biology*, 8(12):e1002793, dec 2012. 3.3, 3.5.3.2, 3.6.0.1, 3.6.0.2, 3.9

[HES13] Samer Hanna and Mirvat El-Sibai. Signaling networks of rho gtpases in cell motility. *Cellular Signalling*, 25:1955–1961, 10 2013. 1.12, 3.1

[HFS+14] Jan-Erik Hoffmann, Yessica Fermin, Ruth L O Stricker, Katja Ickstadt, and Eli Zamir. Symmetric exchange of multi-protein building blocks between stationary focal adhesions and the cytosol. *eLife*, 3, 6 2014. 1.7, 1.12

[HGK+02] Margit Hagel, Elizabeth George, Ann Kim, Rulla Tamimi, Sarah Opitz, Christopher Turner, Akira Imamoto, and Sheila Thomas. The adaptor protein paxillin is essential for normal development in the mouse and is a critical transducer of fibronectin signaling. *Mol. Cell. Biol.*, 22:901–915, 2002. 2.3.3

[HHC+15] Kevin J Hamill, Sho Hiroyasu, Zachary T Colburn, Rosa V Ventrella, Susan B Hopkinson, Omar Skalli, and Jonathan C R Jones. Alpha actinin-1 regulates cell-matrix adhesion organization in keratinocytes: Consequences for skin cell motility. *Journal of Investigative Dermatology*, 135:1043–1052, 2015. 2.3.3

[HIKS+06] C Huselstein, N De Isla, M N Kolopp-Sarda, H Kerdjoudj, S Muller, and J F Stoltz. Influence of mechanical stress on cell viability. volume 43, pages 371–375, 2006. 0.1, 1.1

[HJA+07] Ke Hu, Lin Ji, Kathryn T Applegate, Gaudenz Danuser, and Clare M Waterman-Storer. Differential transmission of actin motion within focal adhesions. *Science (New York, N.Y.)*, 315:111–115, 1 2007. 2.4

[HK82] Terrell L Hill and Marc W Kirschner. Bioenergetics and kinetics of microtubule and actin filament assembly-disassembly. *International Review of Cytology*, 78:1–125, 1982. 1.13.4

[HKO18] Cris R Hasan, Bernd Krauskopf, and Hinke M Osinga. Saddle slow manifolds and canard orbits in r4 and application to the full hodgkin-huxley model. *The Journal of Mathematical Neuroscience*, 8:5, 2018. 4.4.3.1

[HLS+15] Ying-Li Hu, Shaoying Lu, Kai W Szeto, Jie Sun, Yingxiao Wang, Juan C Lasheras, and Shu Chien. Fak and paxillin dynamics at focal adhesions in the protrusions of migrating cells. *Scientific Reports*, 4:6024, 5 2015. 1.5

[HLW13] Jinglei Hu, Reinhard Lipowsky, and Thomas R Weikl. Binding constants of membrane-anchored receptors and ligands depend strongly on the nanoscale roughness of membranes. *Proceedings of the National Academy of Sciences of the United States of America*, 110:15283–15288, 9 2013. 1.4

[HM10] Scott D Hansen and R Dyche Mullins. Vasp is a processive actin polymerase that requires monomeric actin for barbed end association. *The Journal of cell biology*, 191:571–584, 2010. 1.7

[Hol14] William R Holmes. An efficient, nonlinear stability analysis for detecting pattern formation in reaction diffusion systems. *Bulletin of Mathematical Biology*, 76:157–183, 2014. 3.6.0.1

[HP01] Henry N Higgs and Thomas D Pollard. Regulation of actin filament network formation through arp2/3 complex: Activation by a diverse array of proteins. *Annual Review of Biochemistry*, 70:649–676, 2001. 3.1

[HPL+97] A Huttenlocher, S P Palecek, Q Lu, W Zhang, R L Mellgren, D A Lauffenburger, M H Ginsberg, and A F Horwitz. Regulation of cell migration by the calcium-dependent protease calpain. *The Journal of biological chemistry*, 272:32719–32722, 1997. 1.12

[HSF18] Sjoerd Van Helvert, Cornelis Storm, and Peter Friedl. Mechanoreciprocity in cell migration. *Nature Cell Biology*, 20:8–20, 2018. 0.1.1, 0.1.4

[HT95] Trevor Hastie and Robert Tibshirani. Generalized additive models for medical research. *Statistical Methods in Medical Research*, 4:187–196, 9 1995. 2.4, 2.5.3

[HTB90] Peter Hanggi, Peter Talkner, and Michal Borkovec. Reaction-rate theory: fifty years after kramers. *Reviews of Modern Physics*, 62(2):251–341, apr 1990. 1.13.3

[HTK+15] Shiqiong Hu, Yee-Han Tee, Alexandre Kabla, Ronen Zaidel-Bar, Alexander Bershadsky, and Pascal Hersen. Structured illumination microscopy reveals focal adhesions are composed of linear subunits. *Cytoskeleton*, 72:235–245, 5 2015. 1.8

[HTS08] H Hirata, H Tatsumi, and M Sokabe. Mechanical forces facilitate actin polymerization at focal adhesions in a zyxin-dependent manner. *Journal of Cell Science*, 121:2795–2804, 9 2008. 1.2.1

[hYLS+11] Cheng han Yu, Jaslyn Bee Khuan Law, Mona Suryana, Hong Yee Low, and Michael P Sheetz. Early integrin binding to arg-gly-asp peptide activates actin polymerization and contractile movement that stimulates outward translocation. *Proceedings of the National Academy of Sciences of the United States of America*, 108:20585–20590, 2011. 2.1

[IKJ+04] Dusko Ilic, Branka Kovacic, Kohei Johkura, David D Schlaepfer, Nenad Tomasevic, Qin Han, Jae-Beom Kim, Kyle Howerton, Clark Baumbusch, Naoko Ogiwara, Daniel N Streblow, Jay A Nelson, Paul Dazin, Yuji Shino, Katsunori Sasaki, and Caroline H Damsky. FAK promotes organization of fibronectin matrix and fibrillar adhesions. *Journal of Cell Science*, 117(2):177–187, jan 2004. 1.2.2

[IKO+02] Reina E Itoh, Kazuo Kurokawa, Yusuke Ohba, Hisayoshi Yoshizaki, Naoki Mochizuki, and Michiyuki Matsuda. Activation of rac and cdc42 video imaged by fluorescent resonance energy transfer-based single-molecule probes in the membrane of living cells. *Molecular and cellular biology*, 22:6582–6591, 2002. 3.1

[JAS04] Moonsoo Jin, Ioan Andricioaei, and Timothy A Springer. Conversion between three conformational states of integrin i domains with a c-terminal pull spring studied with molecular dynamics. *Structure*, 12:2137–2147, 12 2004. 1.3, 1.3.1

[JCX+14] James E N Jonkman, Judith A Cathcart, Feng Xu, Miria E Bartolini, Jennifer E Amon, Katarzyna M Stevens, and Pina Colarusso. An introduction to the wound healing assay using live-cell microscopy. *Cell adhesion & migration*, 8(5):440–451, sep 2014. 0.1, 1.1

[JDH11] Risat A Jannat, Micah Dembo, and Daniel A Hammer. Traction forces of neutrophils migrating on compliant substrates. *Biophysical Journal*, 101:575–584, 2011. 1.4, 1.8

[JGC+03] Guoying Jiang, Grégory Giannone, David R. Critchley, Emiko Fukumoto, and Michael P. Sheetz. Two-piconewton slip bond between fibronectin and the cytoskeleton depends on talin. *Nature*, 424(6946):334–337, jul 2003. 1.12

[Jil09] Alexandra Jilkine. A wave-pinning mechanism for eukaryotic cell polarization based on rho gtpase dynamics. 2009. 3.5.1, 5

[JMEK07] Alexandra Jilkine, Athanasius F. M. Marée, and Leah Edelstein-Keshet. Mathematical model for spatial segregation of the rho-family gtpases based on inhibitory crosstalk. *Bulletin of mathematical biology*, 69(6):1943–1978, 8 2007. 0.1.3, 3.1, 3.3, 3.5.2

[Kae60] D H Kaelble. Theory and analysis of peel adhesion: Bond stresses and distributions. *Transactions of the Society of Rheology*, 4:45–73, 3 1960. 1.9

[KDMB96] Dennis F Kucik, Michael L Dustin, Jim M Miller, and Eric J Brown. Adhesion-activating phorbol ester increases the mobility of leukocyte integrin lfa-1 in cultured lymphocytes. *Journal of Clinical Investigation*, 97:2139–2144, 5 1996. 1.1, 2.1

[Kec90] James C Keck. Rate-controlled constrained-equilibrium theory of chemical reactions in complex systems*, 1990. 3.2.1.2

[KGM+09] Fang Kong, Andrés J. García, A. Paul Mould, Martin J. Humphries, and Cheng Zhu. Demonstration of catch bonds between an integrin and its ligand. *The Journal of cell*

biology, 185(7):1275–1284, 6 2009. 1.3.2, 1.3.2, 1.12, 2.1, O5, 2.2.3, 2.4, 2.8, 2.1, 2.5.1.8

[Kin06] Michael R King. *Principles of cellular engineering : understanding the biomolecular interface*. Elsevier Academic Press, 2006. 1.5

[KIRC19] Jenny Z Kechagia, Johanna Ivaska, and Pere Roca-Cusachs. Integrins as biomechanical sensors of the microenvironment, 8 2019. 1.3.1

[KJB14] Jae Kyoung Kim, Krešimir Josić, and Matthew R Bennett. The validity of quasi-steady-state approximations in discrete stochastic simulations. *Biophysical Journal*, 107:783–793, 2014. 3.2.2.1

[KJB15] Jae Kyoung Kim, Krešimir Josić, and Matthew R Bennett. The relationship between stochastic and deterministic quasi-steady state approximations. *BMC Systems Biology*, 9:87, 12 2015. 3.2.2.1

[KJD10] Dong Kong, Baohua Ji, and Lanhong Dai. Stabilizing to disruptive transition of focal adhesion response to mechanical forces. *Journal of Biomechanics*, 43:2524–2529, 2010. 1.13.4

[KKS99] Irina Kaverina, Olga Krylyshkina, and J Victor Small. Microtubule targeting of substrate contacts promotes their relaxation and dissociation. *The Journal of Cell Biology*, 146:1033–1044, 1999. 1.2.2, 1.7

[KLP+13] Fang Kong, Zhenhai Li, William M. Parks, David W. Dumbauld, Andrés J. García, A. Paul Mould, Martin J. Humphries, and Cheng Zhu. Cyclic mechanical reinforcement of integrin–ligand interactions. *Molecular Cell*, 49(6):1060–1068, mar 2013. 1.3.1, 1.3.2, 2.4, 2.1, 2.5.1.8

[KMT+12] Jason C Kovacic, Nadia Mercader, Miguel Torres, Manfred Boehm, and Valentin Fuster. Epithelial-to-mesenchymal and endothelial-to-mesenchymal transition from cardiovascular development to disease. *Circulation*, 125:1795–1808, 2012. 0.1, 0.1.4

[KP92] Peter E Kloeden and Eckhard. Platen. *Numerical solution of stochastic differential equations*. Springer-Verlag, 1992. 2.4, 2.5.1.7

[KP04] David R Kovar and Thomas D Pollard. Insertional assembly of actin filament barbed ends in association with formins produces piconewton forces. *Proceedings of the National Academy of Sciences of the United States of America*, 101:14725–14730, 10 2004. 1.3.1

[KS09] James Keener and James Sneyd. Membrane ion channels, 2009. 3.5.1, 4.1

[KS17] Kinneret Keren and Tom Shemesh. Buckle up: Membrane tension drives lamellipodial network compression and adhesion deposition. *The Journal of cell biology*, 216:2619–2621, 2017. 1.2.2, 1.12, 4.6

[KSP+10] Pakorn Kanchanawong, Gleb Shtengel, Ana M Pasapera, Ericka B Ramko, Michael W Davidson, Harald F Hess, and Clare M Waterman. Nanoscale architecture of integrin-based cell adhesions. *Nature*, 468:580–584, 2010. 0.1, 1.2.1, 1.12

[Kuc02] Dennis F Kucik. Rearrangement of integrins in avidity regulation by leukocytes. *Immunologic Research*, 26:199–206, 2002. 2.1

[KVF99] Yvette Van Kooyk, Sandra J Van Vliet, and Carl G Figdor. The actin cytoskeleton regulates lfa-1 ligand binding through avidity rather than affinity changes. *Journal of Biological Chemistry*, 274:26869–26877, 1999. 2.1

[KVM+20] Alex Kiepas, Elena Voorand, Firas Mubaid, Peter M Siegel, and Claire M Brown. Optimizing live-cell fluorescence imaging conditions to minimize phototoxicity. *Journal of Cell Science*, 2020. 0.1

[KW] Diederik P Kingma and Max Welling. Auto-encoding variational bayes. 2.4, 2.5.3

[KW13] Dong Hwee Kim and Denis Wirtz. Focal adhesion size uniquely predicts cell migration. *FASEB Journal*, 27:1351–1361, 4 2013. 2.3.3

[LAL+15] Frederic Lagarrigue, Praju Vikas Anekal, Ho-Sup Lee, Alexia I Bachir, Jailal N Ablack, Alan F Horwitz, and Mark H Ginsberg. A riam/lamellipodin–talin–integrin complex forms the tip of sticky fingers that guide cell migration. *Nature Communications*, 6:8492, 9 2015. 2.4, 2.5.1

[LAvA05] Andrew D Luster, Ronen Alon, and Ulrich H von Andrian. Immune cell migration in inflammation: present and future therapeutic targets. *Nature Immunology*, 6:1182–1190, 12 2005. 0.1, 1.1, 2.1

[LB14] Campbell D Lawson and Keith Burridge. The on-off relationship of rho and rac during integrin-mediated adhesion and cell migration. *Small GTPases*, 5:e27958, 1 2014. 1.12, 3.1

[LBD10] Ying Li, Prabhakar Bhimalapuram, and Aaron R Dinner. Model for how retrograde actin flow regulates adhesion traction stresses. *Journal of Physics Condensed Matter*, 22:194113, 5 2010. 1.3.2

[LCG00] S Liu, D A Calderwood, and M H Ginsberg. Integrin cytoplasmic domain-binding proteins. *Journal of cell science*, 113 (Pt 2:3563–3571, 10 2000. 2.1

[LCH+93] B A Lollo, K W Chan, E M Hanson, V T Moy, and A A Brian. Direct evidence for two affinity states for lymphocyte function-associated antigen 1 on activated t cells. *The Journal of biological chemistry*, 268:21693–21700, 10 1993. 1.3

[LCLRBHL17] Ana María López-Colomé, Irene Lee-Rivera, Regina Benavides-Hidalgo, and Edith López. Paxillin: a crossroad in pathological cell migration. *Journal of Hematology & Oncology*, 10(1):1–15, feb 2017. 0.1.2

[LCS07] Bing-Hao Luo, Christopher V Carman, and Timothy A Springer. Structural basis of integrin regulation and signaling. *Annual review of immunology*, 25:619–647, 2007. 1.3, 1.3.1, 1.12, 2.1

[LGONSG04] Benjamin Lindner, Jordi García-Ojalvo, A Neiman, and L Schimansky-Geier. Effects of noise in excitable systems, 3 2004. 4.1, 4.4.3.2

[LHW+12] Benjamin Lin, William R Holmes, C Joanne Wang, Tasuku Ueno, Andrew Harwell, Leah Edelstein-Keshet, Takanari Inoue, and Andre Levchenko. Synthetic spatially graded rac activation drives cell polarization and movement. *Proceedings of the National Academy of Sciences of the United States of America*, 109:E3668——77, 12 2012. 2.1, 2.3.5.1, 4.1

[LHZJ13] Li Li, Yong He, Min Zhao, and Jianxin Jiang. Collective cell migration: Implications for wound healing and cancer invasion. *Burns & Trauma*, 1(1):21–26, 2013. 1.1, 2.1

[Liu19] Yue Liu. Analysis of pattern formation in reaction-diffusion models for cell polarization, 2019. 3.6.0.1, 3.6.0.2, 3.6.0.2, 3.9

[LKCB02] Carlo Laudanna, Ji Yun Kim, Gabriela Constantin, and Eugene C Butcher. Rapid leukocyte integrin activation by chemokines. *Immunological Reviews*, 186:37–46, 8 2002. 1.3.1

[LKDL07] Maria L Lombardi, David A Knecht, Micah Dembo, and Juliet Lee. Traction force microscopy in dictyostelium reveals distinct roles for myosin ii motor and actin-crosslinking activity in polarized cell movement. *Journal of cell science*, 120:1624–1634, 2007. 1.8

[LKGU09] Tong-Lay Lau, Chungho Kim, Mark H Ginsberg, and Tobias S Ulmer. The structure of the integrin αiibβ3 transmembrane complex explains integrin transmembrane signalling. *The EMBO Journal*, 28:1351–1361, 5 2009. 2.3.1

[LKZ16] Zhenhai Li, Fang Kong, and Cheng Zhu. A model for cyclic mechanical reinforcement. *Scientific Reports*, 6:35954, 12 2016. 0.1, 1.3.1, 1.3.2, 1.2, 1.12, 2.1, 2.4, 2.5.1.6, 5

[LLU+12] Christine Lawson, Ssang-Taek Lim, Sean Uryu, Xiao Lei Chen, David A Calderwood, and David D Schlaepfer. Fak promotes recruitment of talin to nascent adhesions to control cell motility. *The Journal of cell biology*, 196:223–232, 1 2012. 2.3.3

[LREM03] Feiya Li, Sambra D Redick, Harold P Erickson, and Vincent T Moy. Force measurements of the alpha5beta1 integrin-fibronectin interaction. *Biophysical journal*, 84:1252–1262, 2 2003. 1.3.2

[LRNSS16] Klaus Ley, Jesus Rivera-Nieves, William J Sandborn, and Sanford Shattil. Integrin-based therapeutics: Biological basis, clinical use and new drugs, 2016. 0.1

[LS09] Tim Lammermann and Michael Sixt. Mechanical modes of 'amoeboid' cell migration. *Current Opinion in Cell Biology*, 21(5):636–644, oct 2009. 0.1.4

[LS17] Jing Li and Timothy A. Springer. Integrin extension enables ultrasensitive regulation by cytoskeletal force. *Proceedings of the National Academy of Sciences*, 114(18):4685–4690, apr 2017. 1.3.1, 1.3.1, 1.9, 1.12, 2.1, 2.5.1.6, 4.6

[LS18] Jing Li and Timothy A Springer. Energy landscape differences among integrins establish the framework for understanding activation. *The Journal of cell biology*, 217:397–412, 2018. 1.3.1, 1.12

[LSX+17] Jing Li, Yang Su, Wei Xia, Yan Qin, Martin J Humphries, Dietmar Vestweber, Carlos Cabañas, Chafen Lu, and Timothy A Springer. Conformational equilibria and intrinsic affinities define integrin activation. *The EMBO Journal*, 36(5):629–645, jan 2017. 4.6, 5

[LTR+19] Jessica K Lyda, Jack Z Tan, Abira Rajah, Asheesh Momi, Laurent MacKay, Claire M Brown, and Anmar Khadra. Rac activation is key to cell motility and directionality: An experimental and modelling investigation. *Computational and Structural Biotechnology Journal*, 17:1436–1452, 2019. 0.1.2, 1.1, 1.12, 3.2.2, 3.2.2.2, 3.7

[LWDW00] C M Lo, H B Wang, M Dembo, and Y L Wang. Cell movement is guided by the rigidity of the substrate. *Biophysical journal*, 79:144–152, 2000. 1.1, 2.1

[Lyd20] Jessica Lyda. Characterizing different classes of focal adhesions in motile cells based on size and assembly/disassembly rates, 2020. 0.1.1

[LYRB+13] Arnon D Lieber, Shlomit Yehudai-Resheff, Erin L Barnhart, Julie A Theriot, and Kinneret Keren. Membrane tension in rapidly moving cells is determined by cytoskeletal forces. *Current Biology*, 23:1409–1417, 2013. 1.12

[MAF+20] John Mitry, Ryan P D Alexander, Saeed Farjami, Derek Bowie, and Anmar Khadra. Modeling excitability in cerebellar stellate cells: Temporal changes in threshold, latency and frequency of firing. *Communications in Nonlinear Science and Numerical Simulation*, 82:105014, 3 2020. 4.4.3.1

[MAT18] Matlab version 9.4.0.813654 (r2018a), 2018. 3.2.4, 3.2.5

[MBA+03] A Paul Mould, Stephanie J Barton, Janet A Askari, Susan E Craig, and Martin J Humphries. Role of admidas cation-binding site in ligand recognition by integrin α_5 β_1. *Journal of Biological Chemistry*, 278:51622–51629, 2003. 1.3

[MBBS08] Shev MacNamara, Alberto M Bersani, Kevin Burrage, and Roger B Sidje. Stochastic chemical kinetics and the total quasi-steady-state assumption: Application to the stochastic simulation algorithm and chemical master equation. *The Journal of Chemical Physics*, 129:95105, 2008. 3.2.2.1

[MBC14] Elizabeth M Morse, Nina N Brahme, and David A Calderwood. Integrin cytoplasmic tail interactions. *Biochemistry*, 53:810–820, 2 2014. 2.1

[MBC[U+FFFD]5] B Ph Van Milligen, P D Bons, B A Carreras, and R Śnchez. On the applicability of fick's law to diffusion in inhomogeneous systems. *European Journal of Physics*, 26:913–925, 2005. 2.4, 2.5.1.2

[MBK20] Alex Mogilner, Erin L Barnhart, and Kinneret Keren. Experiment, theory, and the keratocyte: An ode to a simple model for cell motility, 2020. 0.1.4

[MBRV19] Zeno Messi, Alicia Bornert, Franck Raynaud, and Alexander Verkhovsky. Traction forces control cell-edge dynamics and mediate distance-sensitivity during cell polarization. *bioRxiv*, page 745687, 8 2019. 1.8

[MDEKH13] May Anne Mata, Meghan Dutot, Leah Edelstein-Keshet, and William R Holmes. A model for intracellular actin waves explored by nonlinear local perturbation analysis. *Journal of theoretical biology*, 334:149–161, 10 2013. 0.1.3, 3.6.0.1, 3.6.0.2

[MF03] Ruedi Meili and Richard A Firtel. Two poles and a compass. *Cell*, 114:153–156, 2003. 3.1

[MGEK12] Athanasius F. M. Marée, Verônica A. Grieneisen, and Leah Edelstein-Keshet. How cells integrate complex stimuli: The effect of feedback from phosphoinositides and cell shape on cell polarization and motility. *PLoS Computational Biology*, 8(3):e1002402, mar 2012. 3.1, 3.3, 3.6.0.1

[MHB20] Andrew E Miller, Ping Hu, and Thomas H Barker. Feeling things out: Bidirectional signaling of the cell-ecm interface, implications in the mechanobiology of cell spreading, migration, proliferation, and differentiation, 2020. 0.1

[MHS05] Satyajit K Mitra, Daniel A Hanson, and David D Schlaepfer. Focal adhesion kinase: in command and control of cell motility. *Nature Reviews Molecular Cell Biology*, 6:56–68, 1 2005. 1.2.1

[MHW+09] Matthias Machacek, Louis Hodgson, Christopher Welch, Hunter Elliott, Olivier Pertz, Perihan Nalbant, Amy Abell, Gary L Johnson, Klaus M Hahn, and Gaudenz Danuser. Coordination of rho gtpase activities during cell protrusion. *Nature*, 461:99–103, 9 2009. 1.12

[MJD+06] Athanasius F. M. Marée, Alexandra Jilkine, Adriana Dawes, Verônica A. Grieneisen, and Leah Edelstein-Keshet. Polarization and movement of keratocytes: a multiscale modelling approach. *Bulletin of mathematical biology*, 68(5):1169–1211, 7 2006. 0.1.3, 3.1, 3.3, 3.6.0.1

[MJEK08] Yoichiro Mori, Alexandra Jilkine, and Leah Edelstein-Keshet. Wave-pinning and cell polarity from a bistable reaction-diffusion system. *Biophysical Journal*, 94:3684–3697, 5 2008. 0.1.3, 1.12, 2.1, 3.1, 3.3, 3.5.2, 3.6.0.1, 4.1

[MJEK11] Yoichiro Mori, Alexandra Jilkine, and Leah Edelstein-Keshet. Asymptotic and bifurcation analysis of wave-pinning in a reaction-diffusion model for cell polarization. *SIAM Journal on Applied Mathematics*, 71:1401–1427, 1 2011. 0.1.3, 3.1, 3.4.2, 3.5, 3.5, 3.5.1, 3.5.1, 3.5.1, 3.5.1, 3.5.2, 3.6.0.1

[MK19a] Laurent MacKay and Anmar Khadra. Data from: Dynamics of mechanosensitive nascent adhesion formation. anmar khadra repository 2019. deposited 30 july 2019., 2019. 2.2.4

[MK19b] Laurent MacKay and Anmar Khadra. Dynamics of mechanosensitive nascent adhesion formation. *Biophysical Journal*, 117(6):1057–1073, sep 2019. (document), 1.3.2, 1.6, 1.7, 1.11, 1.12, 1.4

[MK20] Laurent MacKay and Anmar Khadra. The bioenergetics of integrin-based adhesion, from single molecule dynamics to stability of macromolecular complexes. *Computational and Structural Biotechnology Journal*, 18:393–416, 2020. (document), 0.1.1, 4.7

[MKO+13] Timo R Maarleveld, Ruchir A Khandelwal, Brett G Olivier, Bas Teusink, and Frank J Bruggeman. Basic concepts and principles of stoichiometric modeling of metabolic networks. *Biotechnology Journal*, 8:997, 2013. 3.2.1

[MKR+17] Armen H Mekhdjian, FuiBoon Kai, Matthew G Rubashkin, Louis S Prahl, Laralynne M Przybyla, Alexandra L McGregor, Emily S Bell, J Matthew Barnes, Christopher C DuFort, Guanqing Ou, Alice C Chang, Luke Cassereau, Steven J Tan, Michael W Pickup, Jonathan N Lakins, Xin Ye, Michael W Davidson, Jan Lammerding, David J Odde, Alexander R Dunn, and Valerie M Weaver. Integrin-mediated traction force enhances paxillin molecular associations and adhesion dynamics that increase the invasiveness of tumor cells into a three-dimensional extracellular matrix. *Molecular Biology of the Cell*, 28:1467–1488, 2017. 3.3.2

[MKS+12] C. Mohl, N. Kirchgessner, C. Schafer, B. Hoffmann, and R. Merkel. Quantitative mapping of averaged focal adhesion dynamics in migrating cells by shape normalization. *Journal of Cell Science*, 125(1):155–165, jan 2012. 0.1

[MLK+98] Edward Manser, Tsui-Han Loo, Cheng-Gee Koh, Zhou-Shen Zhao, Xiang-Qun Chen, Lydia Tan, Ivan Tan, Thomas Leung, and Louis Lim. Pak kinases are directly coupled to the pix family of nucleotide exchange factors. *Molecular Cell*, 1:183–192, 1 1998. 3.3.2

[MLK20] Laurent MacKay, Etienne Lehman, and Anmar Khadra. Deciphering the dynamics of lamellipodium in a fish keratocytes model. *Journal of Theoretical Biology*, page 110534, nov 2020. (document)

[MMAD13] Masatoshi Morimatsu, Armen H Mekhdjian, Arjun S Adhikari, and Alexander R Dunn. Molecular tension sensors report forces generated by single integrin molecules in living cells. *Nano Letters*, 13:3985–3989, 2013. 1.1

[MO96] A Mogilner and G Oster. Cell motility driven by actin polymerization. *Biophysical journal*, 71:3030–3045, 1996. 1.2.2, 3.1, 4.6

[MOH+08] Nicole A Morin, Patrick W Oakes, Young-Min Hyun, Dooyoung Lee, Y Eugene Chin, Eugene Y Chin, Michael R King, Timothy A Springer, Motomu Shimaoka, Jay X Tang, Jonathan S Reichner, and Minsoo Kim. Nonmuscle myosin heavy chain iia mediates integrin lfa-1 de-adhesion during t lymphocyte migration. *The Journal of experimental medicine*, 205(1):195–205, 1 2008. 0.1.1, 1.2.2, 1.8

[MR10] A Mogilner and B Rubinstein. Actin disassembly 'clock' and membrane tension determine cell shape and turning: a mathematical model. *Journal of physics. Condensed matter : an Institute of Physics journal*, 22:194118, 5 2010. 0.1, 3.1

[MSIGZ18] Rahuman S. Malik-Sheriff, Sarah Imtiaz, Hernán E. Grecco, and Eli Zamir. Diverse patterns of molecular changes in the mechano-responsiveness of focal adhesions. *Scientific Reports*, 8(1):2187, feb 2018. 1.11

[MSM+06] Konstadinos Moissoglu, Boris M Slepchenko, Nahum Meller, Alan F Horwitz, and Martin A Schwartz. In vivo dynamics of rac-membrane interactions. *Molecular Biology of the Cell*, 17:2770, 6 2006. 3.5.2

[MT03] H Miki and Tadaomi Takenawa. Regulation of actin dynamics by wasp family proteins. *Journal of Biochemistry*, 134:309–313, 9 2003. 3.1

[Mur03] J D Murray. *Mathematical Biology vol. II*. Springer, 2003. 3.2.1.1, 3.4.2, 3.5, 3.5.1

[MW14] A D McNaught and A Wilkinson. Iupac. compendium of chemical terminology (the "gold book"). *IUPAC Compendium of Chemical Terminology*, 2014. 1.13.2, 1.13.2

[NBS08] Alice Nicolas, Achim Besser, and Samuel A Safran. Dynamics of cellular focal adhesions on deformable substrates: Consequences for cell force microscopy. *Biophysical Journal*, 95:527, 2008. 0.1, 1.2.1, 1.1, 1.8, 1.8, 1.9, 1.10, 1.11, 1.12, 1.13.4, 5

[NGS04] A. Nicolas, B. Geiger, and S. A. Safran. Cell mechanosensitivity controls the anisotropy of focal adhesions. *Proceedings of the National Academy of Sciences*,

101(34):12520–12525, aug 2004. 1.2.1, 1.8, 1.8, 1.10, 1.12, 1.4, 2.1, O1, 2.3.5.2, 2.4, 2.5.1.2

[Nie11] M Angela Nieto. The ins and outs of the epithelial to mesenchymal transition in health and disease. *Annual Review of Cell and Developmental Biology*, 27:347–376, 2011. 0.1.4

[NS04] A Nicolas and S A Safran. Elastic deformations of grafted layers with surface stress. *Physical Review E*, 69:51902, 5 2004. 1.8, 1.10

[NS06] Alice Nicolas and Samuel A Safran. Limitation of cell adhesion by the elasticity of the extracellular matrix. *Biophysical Journal*, 91:61–73, 2006. 1.2.1, 1.8, 1.10, 1.13.4, 2.1, 2.3.1, 2.3.5, 2.4, 2.5.1, 5

[NS13] Elizaveta A Novikova and Cornelis Storm. Contractile fibers and catch-bond clusters: A biological force sensor? *Biophysical Journal*, 105:1336–1345, 9 2013. 1.3.2, 1.6, 1.6, 1.10, 1.11, 1.12, 2.1, 2.3.5, 2.3.5.1, 2.3.5.1, 2.3.5.2, 2.3.6, 2.3.6, 2.4, 5, 5

[NS19] Elizaveta A Novikova and Cornelis Storm. Evolving roles and dynamics for catch and slip bonds during adhesion cluster maturation. 8 2019. (document), 1.6, 1.1, 1.10, 1.11, 1.12

[NWB+06] Anjana Nayal, Donna J Webb, Claire M Brown, Erik M Schaefer, Miguel Vicente-Manzanares, and Alan Rick Horwitz. Paxillin phosphorylation at ser273 localizes a git1-pix-pak complex and regulates adhesion and protrusion dynamics. *Journal of Cell Biology*, 173:587–589, 5 2006. 0.1.2, 1.12, 3.1, 3.3.2, 5

[NXS+06] Noritaka Nishida, Can Xie, Motomu Shimaoka, Yifan Cheng, Thomas Walz, and Timothy A. Springer. Activation of leukocyte β2 integrins by conversion from bent to extended conformations. *Immunity*, 25(4):583–594, 10 2006. 1.3, 2.1

[OAM+98] A Obermeier, Sohail Ahmed, Edward Manser, Su Ching Yen, Christine Hall, and Louis Lim. Pak promotes morphological changes by acting upstream of rac. *The EMBO Journal*, 17:4328–4339, 8 1998. 3.3.2

[OB] Sherjil Ozair and Yoshua Bengio. Deep directed generative autoencoders. 2.4, 2.5.3

[OBB+18] Patrick W Oakes, Tamara C Bidone, Yvonne Beckham, Austin V Skeeters, Guillermina R Ramirez-San Juan, Stephen P Winter, Gregory A Voth, and Margaret L Gardel. Lamellipodium is a myosin-independent mechanosensor. *Proceedings of the National Academy of Sciences*, 115:201715869, 2 2018. 1.3.2

[OBSG12] Patrick W Oakes, Yvonne Beckham, Jonathan Stricker, and Margaret L Gardel. Tension is required but not sufficient for focal adhesion maturation without a stress fiber template. *The Journal of Cell Biology*, 196:363–374, 2 2012. 0.1.1, 1.1, 1.2.2

[ORG19] Thomas Orré, Olivier Rossier, and Grégory Giannone. The inner life of integrin adhesion sites: From single molecules to functional macromolecular complexes. *Experimental Cell Research*, 379(2):235–244, 6 2019. 0.1

[OTAG10] Joseph E Olberding, Michael D Thouless, Ellen M Arruda, and Krishna Garikipati. The non-equilibrium thermodynamics and kinetics of focal adhesion dynamics. *PLoS ONE*, 5:e12043, 2010. 1.8, 1.11, 1.12, 2.1, 2.3.1, 2.3.5, 2.3.5.2, 2.4, 2.5.1.2, 5

[PB03] Thomas D Pollard and Gary G Borisy. Cellular motility driven by assembly and disassembly of actin filaments. *Cell*, 112:453–465, 2 2003. 3.1, 4.6

[PBLH04] Marten Postma, Leonard Bosgraaf, Harriët M Loovers, and Peter J M Van Haastert. Chemotaxis: signalling modules join hands at front and tail. *EMBO Reports*, 5:35, 2004. 3.5.2

[PBWH09] Matthew J Paszek, David Boettiger, Valerie M Weaver, and Daniel A Hammer. Integrin clustering is driven by mechanical resistance from the glycocalyx and the substrate. *PLoS Computational Biology*, 5:e1000604, 12 2009. 1.5, 1.12, 3.1

[PDG99] M Pfaff, X Du, and M H Ginsberg. Calpain cleavage of integrin beta cytoplasmic domains. *FEBS letters*, 460:17–22, 10 1999. 0.1.1, 1.2.2

[PDR+14] Matthew J. Paszek, Christopher C. DuFort, Olivier Rossier, Russell Bainer, Janna K. Mouw, Kamil Godula, Jason E. Hudak, Jonathon N. Lakins, Amanda C. Wijekoon, Luke Cassereau, Matthew G. Rubashkin, Mark J. Magbanua, Kurt S. Thorn,

Michael W. Davidson, Hope S. Rugo, John W. Park, Daniel A. Hammer, Grégory Giannone, Carolyn R. Bertozzi, and Valerie M. Weaver. The cancer glycocalyx mechanically primes integrin-mediated growth and survival. *Nature*, 511(7509):319–325, 7 2014. 1.5, 1.12

[PF16] Daniele Perrone and Paolo Favaro. A clearer picture of total variation blind deconvolution. *IEEE Transactions on Pattern Analysis and Machine Intelligence*, 38:1041–1055, 6 2016. 2.4, 2.5.3.1

[PFGSV06] Eileen Puklin-Faucher, Mu Gao, Klaus Schulten, and Viola Vogel. How the headpiece hinge angle is opened: New insights into the dynamics of integrin activation. *The Journal of cell biology*, 175:349–360, 10 2006. 1.3, 1.3.1

[PH10] Ekaterina Papusheva and Carl Philipp Heisenberg. Spatial organization of adhesion: Force-dependent regulation and function in tissue morphogenesis. *EMBO Journal*, 29:2753–2768, 2010. 0.1

[PHHL98] S P Palecek, A Huttenlocher, A F Horwitz, and D A Lauffenburger. Physical and biochemical regulation of integrin release during rear detachment of migrating cells. *Journal of cell science*, 111 (Pt 7:929–940, 4 1998. 1.2.2, 1.12

[PHS10] J Thomas Parsons, Alan Rick Horwitz, and Martin A Schwartz. Cell adhesion: integrating cytoskeletal dynamics and cellular tension. *Nature reviews. Molecular cell biology*, 11:633–643, 2010. 0.1.1, 2.1

[PJMR06] Marcus Prass, Ken Jacobson, Alex Mogilner, and Manfred Radmacher. Direct measurement of the lamellipodial protrusive force in a migrating cell. *The Journal of cell biology*, 174:767–772, 2006. 3.1

[PKB+15] Jin Ah Park, Jae Hun Kim, Dapeng Bi, Jennifer A Mitchel, Nader Taheri Qazvini, Kelan Tantisira, Chan Young Park, Maureen McGill, Sae Hoon Kim, Bomi Gweon, Jacob Notbohm, Robert Steward, Stephanie Burger, Scott H Randell, Alvin T Kho, Dhananjay T Tambe, Corey Hardin, Stephanie A Shore, Elliot Israel, David A Weitz, Daniel J Tschumperlin, Elizabeth P Henske, Scott T Weiss, M Lisa Manning, James P

Butler, Jeffrey M Drazen, and Jeffrey J Fredberg. Unjamming and cell shape in the asthmatic airway epithelium. *Nature Materials*, 2015. 0.1.4

[PMG+17] Bruno Pontes, Pascale Monzo, Laurent Gole, Anabel Lise Le Roux, Anita Joanna Kosmalska, Zhi Yang Tam, Weiwei Luo, Sophie Kan, Virgile Viasnoff, Pere Roca-Cusachs, Lisa Tucker-Kellogg, and Nils C Gauthier. Membrane tension controls adhesion positioning at the leading edge of cells. *Journal of Cell Biology*, 216:2959–2977, 9 2017. 0.1.1, 1.12, 3.1, 4.6

[PNP+12] J. Pouwels, J. Nevo, T. Pellinen, J. Ylanne, and J. Ivaska. Negative regulators of integrin activity. *Journal of Cell Science*, 125(14):3271–3280, 7 2012. 1.2.2

[PP05] Shelly R Peyton and Andrew J Putnam. Extracellular matrix rigidity governs smooth muscle cell motility in a biphasic fashion. *Journal of Cellular Physiology*, 204:198–209, 7 2005. 1.8

[PPF+87] Max Planitz, William H Press, Brian P Flannery, Saul A Teukolsky, and William T Vetterling. *Numerical Recipes: The Art of Scientific Computing*. Cambridge University Press, 3rd edition, 1987. 3.2.2.3

[PPF+05] Yuriy V Pereverzev, Oleg V Prezhdo, Manu Forero, Evgeni V Sokurenko, and Wendy E Thomas. The two-pathway model for the catch-slip transition in biological adhesion. *Biophysical Journal*, 89:1446–1454, 2005. 1.3.2, 1.3.2, 1.3.2, 1.2

[PPS09] Yuriy V Pereverzev, Oleg V Prezhdo, and Evgeni V Sokurenko. Allosteric role of the large-scale domain opening in biological catch-binding. *Physical Review E*, 79:51913, 5 2009. 1.3.2, 2.1

[PPS11] Yuriy V Pereverzev, Eugenia Prezhdo, and Evgeni V Sokurenko. The two-pathway model of the biological catch-bond as a limit of the allosteric model. *Biophysical journal*, 101:2026–2036, 2011. 1.3.2, 2.4, 2.5.1.6

[QVP04] Jun Qin, Olga Vinogradova, and Edward F Plow. Integrin bidirectional signaling: A molecular view. *PLoS Biology*, 2:e169, 2004. 1.3

[RA03] Christopher V Rao and Adam P Arkin. Stochastic chemical kinetics and the quasi-steady-state assumption: Application to the gillespie algorithm. *The Journal of Chemical Physics*, 118:4999–5010, 3 2003. 3.2.2.1

[RA13] Oren Rippel and Ryan Prescott Adams. High-dimensional probability estimation with deep density models, 2013. 2.4, 2.5.3

[Rap16] Wouter Jan Rappel. Cell-cell communication during collectivemigration, 2016. 0.1.4

[RBI+19] Abira Rajah, Colton G Boudreau, Alina Ilie, Tse-Luen Wee, Kaixi Tang, Aleksandar Z Borisov, John Orlowski, and Claire M Brown. Paxillin s273 phosphorylation regulates adhesion dynamics and cell migration through a common protein complex with pak1 and βpix. *Scientific Reports*, 9:11430, 2019. 0.1, 1.7, 1.12, 3.1, 3.3.2

[RCdRPF+13] P. Roca-Cusachs, A. del Rio, E. Puklin-Faucher, N. C. Gauthier, N. Biais, and M. P. Sheetz. Integrin-dependent force transmission to the extracellular matrix by α-actinin triggers adhesion maturation. *Proceedings of the National Academy of Sciences*, 110(15):E1361–E1370, mar 2013. 1.1, 1.2.2, 1.6, 2.3.5.2

[RCGRS09] Pere Roca-Cusachs, Nils C Gauthier, Armando Del Rio, and Michael P Sheetz. Clustering of alpha(5)beta(1) integrins determines adhesion strength whereas alpha(v)beta(3) and talin enable mechanotransduction. *Proceedings of the National Academy of Sciences of the United States of America*, 106:16245–16250, 9 2009. 0.1, 1.6

[RCIS12] Pere Roca-Cusachs, Thomas Iskratsch, and Michael P. Sheetz. Finding the weakest link – exploring integrin-mediated mechanical molecular pathways. *Journal of Cell Science*, 125(13):3025–3038, 7 2012. 1.12

[RCS+15] Florencia Rosetti, Yunfeng Chen, Mehmet Sen, Elizabeth Thayer, Veronica Azcutia, Jan M Herter, F William Luscinskas, Xavier Cullere, Cheng Zhu, and Tanya N Mayadas. A lupus-associated mac-1 variant has defects in integrin allostery and interaction with ligands under force. *Cell Reports*, 10:1655–1664, 3 2015. 1.3.2, 1.12

[RDL+16] Clément Roux, Alain Duperray, Valérie M. Laurent, Richard Michel, Valentina Peschetola, Claude Verdier, and Jocelyn Étienne. Prediction of traction forces of motile cells. *Interface Focus*, 6(5):20160042, oct 2016. 1.8

[REK19] Elisabeth G Rens and Leah Edelstein-Keshet. From energy to cellular forces in the cellular potts model: An algorithmic approach. *PLOS Computational Biology*, 15:e1007459, 2019. 3.2.5, 3.9

[RFJ+09] Boris Rubinstein, Maxime F Fournier, Ken Jacobson, Alexander B Verkhovsky, and Alex Mogilner. Actin-myosin viscoelastic flow in the keratocyte lamellipod. *Biophysical Journal*, 97:1853–1863, 10 2009. 3.1

[RH92] C M Regen and A F Horwitz. Dynamics of beta 1 integrin-mediated adhesive contacts in motile fibroblasts. *The Journal of Cell Biology*, 119:1347–1359, 1992. 1.2.2

[Rid01] Anne J Ridley. Rho gtpases and cell migration. *J. Cell Sci.*, 114:2713–2722, 2001. 0.1.3, 3.1

[RKS+00] X D Ren, W B Kiosses, D J Sieg, C A Otey, D D Schlaepfer, and M A Schwartz. Focal adhesion kinase suppresses rho activity to promote focal adhesion. *Journal of Cell Science*, 2000. 0.1

[ROE+12] S Roberts, M Osborne, M Ebden, S Reece, N Gibson, and S Aigrain. Gaussian processes for time-series modelling. *Philosophical Transactions of the Royal Society A: Mathematical, Physical and Engineering Sciences*, 371:20110550, 2012. 2.4, 2.5.3

[ROS+12] Olivier Rossier, Vivien Octeau, Jean-Baptiste Sibarita, Cécile Leduc, Béatrice Tessier, Deepak Nair, Volker Gatterdam, Olivier Destaing, Corinne Albigès-Rizo, Robert Tampé, Laurent Cognet, Daniel Choquet, Brahim Lounis, and Grégory Giannone. Integrins $\beta 1$ and $\beta 3$ exhibit distinct dynamic nanoscale organizations inside focal adhesions. *Nature Cell Biology*, 14(10):1057–1067, sep 2012. 1.2.1, 1.6, 2.1, O3, 2.2.3, 2.4, 2.5.1, 2.5.1, 2.5.1.2, 2.5.1.8, 2.1, 2.3, 5, 5

[RP04] Zhuyin Ren and Stephen B Pope. Entropy production and element conservation in the quasi-steady-state approximation. *Combustion and Flame*, 137:251–254, 2004. 3.2.1.2

[RS14] Sabyasachi Rakshit and Sanjeevi Sivasankar. Biomechanics of cell adhesion: how force regulates the lifetime of adhesive bonds at the single molecule level. *Physical Chemistry Chemical Physics*, 16:2211, 1 2014. 1.3.2

[RSG+05] Raphaela Rid, Natalia Schiefermeier, Ilya Grigoriev, J Victor Small, and Irina Kaverina. The last but not the least: The origin and significance of trailing adhesions in fibroblastic cells. *Cell Motility and the Cytoskeleton*, 61:161–171, 7 2005. 0.1, 0.1.1, 1.2.2, 1.7, 3.1

[RW06] C E Rasmussen and C K I Williams. *Gaussian Processes for Machine Learning*. MIT Press, 1 edition, 2006. 2.4, 2.5.3

[RZB+01] D Riveline, E Zamir, N Q Balaban, U S Schwarz, T Ishizaki, S Narumiya, Z Kam, B Geiger, and A D Bershadsky. Focal contacts as mechanosensors: externally applied local mechanical force induces growth of focal contacts by an mdia1-dependent and rock-independent mechanism. *The Journal of cell biology*, 153:1175–1186, 6 2001. 1.1, 1.2.2, 1.6, 1.12, 5

[RZM+12] Sabyasachi Rakshit, Yunxiang Zhang, Kristine Manibog, Omer Shafraz, and Sanjeevi Sivasankar. Ideal, catch, and slip bonds in cadherin adhesion. *Proceedings of the National Academy of Sciences of the United States of America*, 109:18815–18820, 11 2012. 1.3.2

[SAT+17] Ben Stutchbury, Paul Atherton, Ricky Tsang, De-Yao Wang, and Christoph Ballestrem. Distinct focal adhesion protein modules control different aspects of mechanotransduction. *Journal of cell science*, 130:1612–1624, 2017. 1.8, 3.1

[SBDG13] Jonathan Stricker, Yvonne Beckham, Michael W Davidson, and Margaret L Gardel. Myosin ii-mediated focal adhesion maturation is tension insensitive. *PLoS ONE*, 8:e70652, 2013. 0.1.1

[SBG+10] Mark A Smith, Elizabeth Blankman, Margaret L Gardel, Laura Luettjohann, Clare M Waterman, and Mary C Beckerle. A zyxin-mediated mechanism for actin stress fiber maintenance and repair. *Developmental Cell*, 19:365–376, 2010. 1.2.1

[SBSL05] Alexandre Saez, Axel Buguin, Pascal Silberzan, and Benoît Ladoux. Is the mechanical activity of epithelial cells controlled by deformations or forces? *Biophysical Journal*, 89:L52——4, 2005. 2.3.5

[SCF19] Zhiqi Sun, Mercedes Costell, and Reinhard Fässler. Integrin activation by talin, kindlin and mechanical forces. *Nature Cell Biology*, 21:25–31, 2019. 1.3.1

[SD12] Timothy A Springer and Michael L Dustin. Integrin inside-out signaling and the immunological synapse. *Current opinion in cell biology*, 24:107–115, 2 2012. 1.2.1

[SEB06] Ulrich S Schwarz, Thorsten Erdmann, and Ilka B Bischofs. Focal adhesions as mechanosensors: The two-spring model. *BioSystems*, 83:225–232, 2 2006. 1.6, 1.10, 1.11, 1.12, 2.1, 2.3.5.1, 2.3.5.1, 2.3.6, 2.4

[SEM19] Shailaja Seetharaman and Sandrine Etienne-Manneville. Microtubules at focal adhesions - a double-edged sword. *Journal of cell science*, 132, 2019. 1.2.2, 3.1

[SF13] Herbert B Schiller and Reinhard Fässler. Mechanosensitivity and compositional dynamics of cell-matrix adhesions. *EMBO reports*, 14:509–519, 6 2013. 2.1

[SFO+16] Carsten Schulte, Gian Maria Sarra Ferraris, Amanda Oldani, Massimiliano Galluzzi, Alessandro Podestà, Luca Puricelli, Valentina de Lorenzi, Cristina Lenardi, Paolo Milani, and Nicolai Sidenius. Lamellipodial tension, not integrin/ligand binding, is the crucial factor to realise integrin activation and cell migration. *European Journal of Cell Biology*, 95(1):1–14, 1 2016. 1.12

[SFW16] V Swaminathan, R S Fischer, and C M Waterman. The fak-arp2/3 interaction promotes leading edge advance and haptosensing by coupling nascent adhesions to lamellipodia actin. *Molecular Biology of the Cell*, 27:1085–1100, 2016. 0.1.1, 1.7

[SGBK05] Tom Shemesh, Benjamin Geiger, Alexander D Bershadsky, and Michael M Kozlov. Focal adhesions as mechanosensors: A physical mechanism. *Proceedings of the National Academy of Sciences*, 102:12383–12388, 2005. 1.8, 1.13.4

[SHB14] M A Smith, L M Hoffman, and M C Beckerle. Lim proteins in actin cytoskeleton mechanoresponse. *Trends in Cell Biology*, 24:575–583, 10 2014. 2.1

[SKG10] Sanford J Shattil, Chungho Kim, and Mark H Ginsberg. The final steps of integrin activation: the end game. *Nature Reviews Molecular Cell Biology*, 11:288–300, 2010. 1.3

[SLF14] Zhiqi Sun, Armin Lambacher, and Reinhard Fassler. Nascent adhesions: From fluctuations to a hierarchical organization. *Current Biology*, 24(17):R801–R803, sep 2014. 1.2.2

[SLP+01] M Shimaoka, C Lu, R T Palframan, U H von Andrian, A McCormack, J Takagi, and T A Springer. Reversibly locking a protein fold in an active conformation with a disulfide bond: integrin alphal i domains with high affinity and antagonist activity in vivo. *Proceedings of the National Academy of Sciences of the United States of America*, 98:6009–6014, 5 2001. 1.3

[SM19] Adam Shellard and Roberto Mayor. Supracellular migration - beyond collective cell migration. *Journal of Cell Science*, 132, 2019. 0.1.4

[SMP+99] L B Smilenov, A Mikhailov, R J Pelham, E E Marcantonio, and G G Gundersen. Focal adhesion motility revealed in stationary fibroblasts. *Science*, 286:1172–1174, 11 1999. 0.1.1, 1.2.2

[SOQ12] F J Sevilla and L Olivares-Quiroz. Chemical potential for the interacting classical gas and the ideal quantum gas obeying a generalized exclusion principle. *EUROPEAN JOURNAL OF PHYSICS Eur. J. Phys*, 33:709–722, 2012. 1.13.1

[SP95] M D Schaller and J T Parsons. pp125fak-dependent tyrosine phosphorylation of paxillin creates a high-affinity binding site for crk. *Molecular and Cellular Biology*, 15:2635–2645, 1995. 0.1.2

[SPP+14] Samantha J Stehbens, Matthew Paszek, Hayley Pemble, Andreas Ettinger, Sarah Gierke, and Torsten Wittmann. Clasps link focal-adhesion-associated microtubule capture to localized exocytosis and adhesion site turnover. *Nature Cell Biology*, 16:558–570, 6 2014. 1.2.2, 1.7

[SPS+11] Mark Schvartzman, Matteo Palma, Julia Sable, Justin Abramson, Xian Hu, Michael P Sheetz, and Shalom J Wind. Nanolithographic control of the spatial organization of

cellular adhesion receptors at the single-molecule level. *Nano Letters*, 11:1306–1312, 3 2011. 2.3.4, 2.4, 2.5.1.8

[SRN+07] Markus Schober, Srikala Raghavan, Maria Nikolova, Lisa Polak, H Amalia Pasolli, Hilary E Beggs, Louis F Reichardt, and Elaine Fuchs. Focal adhesion kinase modulates tension signaling to control actin and focal adhesion dynamics. *The Journal of cell biology*, 176:667–680, 2 2007. 1.2.2

[SS10] Benedikt Sabass and Ulrich S Schwarz. Modeling cytoskeletal flow over adhesion sites: Competition between stochastic bond dynamics and intracellular relaxation. *Journal of Physics Condensed Matter*, 22:194112, 5 2010. 2.1, 2.3.1, 2.3.6, 2.4, 5

[SS13] Ulrich S Schwarz and Samuel A Safran. Physics of adherent cells. *Reviews of Modern Physics*, 85:1327–1381, 8 2013. 0.1, 1.6, 1.8

[SSA+15] Emma Spanjaard, Ihor Smal, Nicos Angelopoulos, Ingrid Verlaan, Alexandre Matov, Erik Meijering, Lodewyk Wessels, Hans Bos, and Johan de Rooij. Quantitative imaging of focal adhesion dynamics and their regulation by hgf and rap1 signaling. *Experimental Cell Research*, 330:382–397, 2015. 0.1.1

[SSF+05] Monika Semmrich, Andrew Smith, Carolin Feterowski, Sandra Beer, Britta Engelhardt, Dirk H Busch, Bernadett Bartsch, Melanie Laschinger, Nancy Hogg, Klaus Pfeffer, and Bernhard Holzmann. Importance of integrin lfa-1 deactivation for the generation of immune responses. *The Journal of experimental medicine*, 201:1987–1998, 2005. 1.2.2

[SSGB04] Mary R Stofega, Luraynne C Sanders, Elisabeth M Gardiner, and Gary M Bokoch. Constitutive p21-activated kinase (pak) activation in breast cancer cells as a result of mislocalization of pak to focal adhesions. *Molecular biology of the cell*, 15:2965–2977, 6 2004. 3.3.2

[SSVR02] J.Victor Small, Theresia Stradal, Emmanuel Vignal, and Klemens Rottner. The lamellipodium: where motility begins. *Trends in Cell Biology*, 12:112–120, 3 2002. 1.2.2

[ST04] Pierre Sens and Matthew S Turner. Theoretical model for the formation of caveolae and similar membrane invaginations. *Biophysical journal*, 86:2049–2057, 2004. 1.9

[Str65] R L Stratonovich. Fokker-planck equation with discontinuous coefficients and conditions at the surface of discontinuity. *Soviet Radiophysics*, 8:500–505, 1965. 2.4, 2.5.1.2

[SVMB97] Tatyana M Svitkina, Alexander B Verkhovsky, Kyle M McQuade, and Gary G Borisy. Analysis of the actin-myosin ii system in fish epidermal keratocytes: Mechanism of cell body translocation. *Journal of Cell Biology*, 139:397–415, 1997. 3.1

[SZX08] Timothy A Springer, Jianghai Zhu, and Tsan Xiao. Structural basis for distinctive recognition of fibrinogen γc peptide by the platelet integrin $\alpha_{IIb}\beta_3$. *The Journal of Cell Biology*, 182:791–800, 2008. 2.3.1

[TA77] A N (Andreĭ Nikolaevich) Tikhonov and V I[U+FE20]A[U+FE21]. (Vasiliĭ I[U+FE20]A[U+FE21]kovlevich) Arsenin. *Solutions of ill-posed problems*. Winston, 1977. 2.4, 2.5.3.1

[Tad] Pooyan Khajehpour Tadavani. Nonlinear dimensionality reduction by manifold unfolding. 2.4, 2.5.3

[Tan18] Kaixi Tang. Mathematical model of paxillin phsphorylation at serine 273 and its effect on rac, rho, and adhesion dynamics, 2018. 3.3.2, 3.3.2

[TBBK18] Kaixi Tang, Colton G. Boudreau, Claire M. Brown, and Anmar Khadra. Paxillin phosphorylation at serine 273 and its effects on rac, rho and adhesion dynamics. *PLOS Computational Biology*, 14(7):e1006303, jul 2018. (document), 0.1, 0.1.2, 1.1, 1.12, 2.2.3, 2.3.5.1, 2.4, 2.5.1.8, 2.1, 2.3, 3.1, 3.3.1, 3.3.1, 3.3.2, 3.3.2, 3.4, 3.4.1, 3.6.0.2, 3.7, 3.10, 5, 5, 5, 5, 5

[TBP+99] C E Turner, M C Brown, J A Perrotta, M C Riedy, S N Nikolopoulos, A R McDonald, S Bagrodia, S Thomas, and P S Leventhal. Paxillin ld4 motif binds pak and pix through a novel 95-kd ankyrin repeat, arf-gap protein: A role in cytoskeletal remodeling. *The Journal of cell biology*, 145:851–863, 5 1999. 3.3.2

[TGL12] Sari Tojkander, Gergana Gateva, and Pekka Lappalainen. Actin stress fibers–assembly, dynamics and biological roles. *Journal of cell science*, 125:1855–1864, 2012. 3.1

[TGRF19] Florian Thüroff, Andriy Goychuk, Matthias Reiter, and Erwin Frey. Bridging the gap between single-cell migration and collective dynamics. *eLife*, 8, dec 2019. 5

[THA+11] Dhananjay T Tambe, C Corey Hardin, Thomas E Angelini, Kavitha Rajendran, Chan Young Park, Xavier Serra-Picamal, Enhua H Zhou, Muhammad H Zaman, James P Butler, David A Weitz, Jeffrey J Fredberg, and Xavier Trepat. Collective cell guidance by cooperative intercellular forces. *Nature Materials*, 10:469–475, 2011. 0.1.4

[TPWS02] Junichi Takagi, Benjamin M Petre, Thomas Walz, and Timothy A Springer. Global conformational rearrangements in integrin extracellular domains in outside-in and inside-out signaling. *Cell*, 110:511–599, 9 2002. 1.3

[TSE+03] Seiji Tadokoro, Sanford J Shattil, Koji Eto, Vera Tai, Robert C Liddington, Jose M de Pereda, Mark H Ginsberg, and David A Calderwood. Talin binding to integrin beta tails: a final common step in integrin activation. 302, 2003. 1.3

[TSM01] Yoshimi Takai, Takuya Sasaki, and Takashi Matozaki. Small gtp-binding proteins. *Physiological Reviews*, 81:153–208, 1 2001. 3.5.2

[TTB+13] Ingo Thievessen, Peter M Thompson, Sylvain Berlemont, Karen M Plevock, Sergey V Plotnikov, Alice Zemljic-Harpf, Robert S Ross, Michael W Davidson, Gaudenz Danuser, Sharon L Campbell, and Clare M Waterman. Vinculin-actin interaction couples actin retrograde flow to focal adhesions, but is dispensable for focal adhesion growth. *The Journal of cell biology*, 202:163–177, 7 2013. 0.1.1, 1.2.2, 1.7, 4.6

[TTP93] T Turanyi, A S Tomlin, and M J Pilling. On the error of the quasi-steady-state approximation. *The Journal of Physical Chemistry*, 97:163–172, 1 1993. 3.2.1.2, 3.2.1.2

[Tur52] Alan Turing. The chemical basis of morphogenesis. *Philosophical Transactions of the Royal Society of London. Series B, Biological Sciences*, 237(641):37–72, aug 1952. 3.5

[TWG+18] Taka A Tsunoyama, Yusuke Watanabe, Junri Goto, Kazuma Naito, Rinshi S Kasai, Kenichi G N Suzuki, Takahiro K Fujiwara, and Akihiro Kusumi. Super-long

single-molecule tracking reveals dynamic-anchorage-induced integrin function. *Nature Chemical Biology*, 14:497–506, 5 2018. 1.1, 1.2.1, 1.6, O4, 2.2.3, 2.4, 2.5.1, 2.5.1.2, 2.3, 5, 5

[TY12] P F Tupper and Xin Yang. A paradox of state-dependent diffusion and how to resolve it. *Proceedings of the Royal Society A: Mathematical, Physical and Engineering Sciences*, 468:3864–3881, 2012. 2.4, 2.5.1.2

[vdP26] Balth. van der Pol. Lxxxviii. on "relaxation-oscillations". *The London, Edinburgh, and Dublin Philosophical Magazine and Journal of Science*, 2:978–992, 11 1926. 4.4

[vdPvdM28] Balth. van der Pol and J van der Mark. Lxxii. ithe heartbeat considered as a relaxation oscillation, and an electrical model of the heart/i. *The London, Edinburgh, and Dublin Philosophical Magazine and Journal of Science*, 6:763–775, 1928. 4.4.2

[VG15] Christian L Vestergaard and Mathieu Génois. Temporal gillespie algorithm: Fast simulation of contagion processes on time-varying networks. *PLoS Computational Biology*, 11:e1004579, 10 2015. 2.4, 2.5.1.7

[vH84] J H van't Hoff. *Etudes de dynamique chimique*. Frederik Muller, 1884. 1.13.3

[vK07] N G van Kampen. *Stochastic processes in physics and chemistry*. North Holland, 3rd edition, 2007. 1.6, 1.13.2, 3.2.1

[VMO15] Eberhard O Voit, Harald A Martens, and Stig W Omholt. 150 years of the mass action law. *PLoS Computational Biology*, 11:e1004012, 2015. 1.13.2, 1.13.3

[VMZW+07] Miguel Vicente-Manzanares, Jessica Zareno, Leanna Whitmore, Colin K Choi, and Alan F Horwitz. Regulation of protrusion, adhesion dynamics, and polarity by myosins iia and iib in migrating cells. *The Journal of Cell Biology*, 176:573–580, 2 2007. 1.2.2

[VVSJMPM08] Marco A Velasco-Velázquez, Nohemí Salinas-Jazmín, Nicandro Mendoza-Patiño, and Juan J Mandoki. Reduced paxillin expression contributes to the antimetastatic effect of 4-hydroxycoumarin on b16-f10 melanoma cells. *Cancer Cell International*, 8(1):8, 2008. 2.3.3

[vWHFS03] Götz von Wichert, Beatrice Haimovich, Gen-Sheng Feng, and Michael P Sheetz. Force-dependent integrin-cytoskeleton linkage formation requires downregulation of focal complex dynamics by shp2. *The EMBO journal*, 22:5023–5035, 10 2003. 1.2.2

[WBHG11] Haguy Wolfenson, Alexander Bershadsky, Yoav I Henis, and Benjamin Geiger. Actomyosin-generated tension controls the molecular kinetics of focal adhesions. *Journal of cell science*, 124:1425–1432, 5 2011. 1.7

[WBW+04] Paul W Wiseman, Claire M Brown, Donna J Webb, Benedict Hebert, Natalie L Johnson, Jeff A Squier, Mark H Ellisman, and A F Horwitz. Spatial mapping of integrin interactions and dynamics during cell migration by image correlation microscopy. *Journal of Cell Science*, 117, 2004. 1.2.1, 1.6, 1.11, 2.3.1, 3.1

[WDW+04] Donna J Webb, Karen Donais, Leanna A Whitmore, Sheila M Thomas, Christopher E Turner, J Thomas Parsons, and Alan F Horwitz. Fak-src signalling through paxillin, erk and mlck regulates adhesion disassembly. *Nature cell biology*, 6:154–161, 2 2004. 1.7, 3.1

[Wec12] Martin Wechselberger. À propos de canards (apropos canards). *Transactions of the American Mathematical Society*, 364:3289–3309, 2012. 4.4.4.1, 4.4.4.1, 4.4.4.1, 4.4.4.2

[WFA05] Janice L Walker, Alaina K Fournier, and Richard K Assoian. Regulation of growth factor signaling and cell cycle progression by cell adhesion and adhesion-dependent changes in cellular tension, 2005. 0.1

[WH11] Erik S Welf and Jason M Haugh. Signaling pathways that control cell migration: models and analysis. *Wiley interdisciplinary reviews. Systems biology and medicine*, 3:231–240, 2011. 2.1

[WH12] Bernhard Wehrle-Haller. Structure and function of focal adhesions. *Current Opinion in Cell Biology*, 24:116–124, 2012. 0.1.1, 1.2.2

[WHW+10] Xiaobo Wang, Li He, Yi I Wu, Klaus M Hahn, and Denise J Montell. Light-mediated activation reveals a key role for rac in collective guidance of cell movement in vivo. *Nature Cell Biology*, 12:591–597, 6 2010. 0.1

[WKFGL14] Sabina E. Winograd-Katz, Reinhard Fassler, Benjamin Geiger, and Kyle R. Legate. The integrin adhesome: from genes and proteins to human disease. *Nature Reviews Molecular Cell Biology*, 15(4):273–288, mar 2014. 0.1

[WKWS11] Sam Walcott, Dong-Hwee Kim, Denis Wirtz, and Sean X Sun. Nucleation and decay initiation are the stiffness-sensitive phases of focal adhesion maturation. *Biophysical journal*, 101:2919–2928, 12 2011. 1.11, 1.12, 2.1, 2.3.5.1, 2.3.6, 2.3.6, 2.4

[WLR+09] Haguy Wolfenson, Ariel Lubelski, Tamar Regev, Joseph Klafter, Yoav I Henis, and Benjamin Geiger. A role for the juxtamembrane cytoplasm in the molecular dynamics of focal adhesions. *PLoS ONE*, 4:e4304, 2009. 1.1, 1.7, O2, 2.2.3, 2.4, 2.5.1, 2.5.1.8, 2.3

[WMEKG12] Georg R. Walther, Athanasius F. M. Marée, Leah Edelstein-Keshet, and Verônica A. Grieneisen. Deterministic versus stochastic cell polarisation through wave-pinning. *Bulletin of mathematical biology*, 74:2570–2599, 11 2012. 3.1, 3.6

[WNO12] Erik S Welf, Ulhas P Naik, and Babatunde A Ogunnaike. A spatial model for integrin clustering as a result of feedback between integrin activation and integrin binding. *Biophysical Journal*, 103:1379–1389, 9 2012. 2.1

[WPH+07] Kate L Wegener, Anthony W Partridge, Jaewon Han, Andrew R Pickford, Robert C Liddington, Mark H Ginsberg, and Iain D Campbell. Structural basis of integrin activation by talin. *Cell*, 128:171–182, 1 2007. 2.3.1

[WPM+17] Zhanghan Wu, Sergey V Plotnikov, Abdiwahab Y Moalim, Clare M Waterman, and Jian Liu. Two distinct actin networks mediate traction oscillations to confer focal adhesion mechanosensing. *Biophysical Journal*, 112:780–794, 2 2017. 1.12, 2.1, 2.4

[WR12] Xin Wu and Doodipala Samba Reddy. Integrins as receptor targets for neurological disorders, 4 2012. 0.1

[WWC+09] Chaoliang Wei, Xianhua Wang, Min Chen, Kunfu Ouyang, Long-Sheng Song, and Heping Cheng. Calcium flickers steer cell migration. *Nature*, 457:901–905, 2009. 1.12

[WWC19] Harry Warner, Beverley J Wilson, and Patrick T Caswell. Control of adhesion and protrusion in cell migration by rho gtpases. *Current Opinion in Cell Biology*, 56:64–70, 2019. 1.12, 3.1, 3.3.1

[XHLW15] Guang-Kui Xu, Jinglei Hu, Reinhard Lipowsky, and Thomas R Weikl. Binding constants of membrane-anchored receptors and ligands: A general theory corroborated by monte carlo simulations. *The Journal of Chemical Physics*, 143:243136, 2015. 1.4, 1.5

[XQH16] Guang-Kui Xu, Jin Qian, and Jinglei Hu. The glycocalyx promotes cooperative binding and clustering of adhesion receptors. *Soft Matter*, 12:4572–4583, 5 2016. 1.4, 1.5

[XSD+01] J P Xiong, T Stehle, B Diefenbach, R Zhang, R Dunker, D L Scott, A Joachimiak, S L Goodman, and M A Arnaout. Crystal structure of the extracellular segment of integrin alpha vbeta3. *Science (New York, N.Y.)*, 294:339–345, 10 2001. 1.3

[XWK+03] Jingsong Xu, Fei Wang, Alexandra Van Keymeulen, Paul Herzmark, Aaron Straight, Kathleen Kelly, Yoh Takuwa, Naotoshi Sugimoto, Timothy Mitchison, and Henry R Bourne. Divergent signals and cytoskeletal assemblies regulate self-organizing polarity in neutrophils. *Cell*, 114:201–214, 2003. 3.1

[XYDF14] Guang-Kui Xu, Chun Yang, Jing Du, and Xi-Qiao Feng. Integrin activation and internalization mediated by extracellular matrix elasticity: A biomechanical model. *Journal of Biomechanics*, 47:1479–1484, 4 2014. 1.9

[YCKM00] Chunbo Yuan, Aileen Chen, Pamela Kolb, and Vincent T Moy. Energy landscape of streptavidin-biotin complexes measured by atomic force microscopy. *Biochemistry*, 39:10219–10223, 2000. 1.3.2

[YPA+13] Feng Ye, Brian G Petrich, Praju Anekal, Craig T Lefort, Ana Kasirer-Friede, Sanford J Shattil, Raphael Ruppert, Markus Moser, Reinhard Fassler, and Mark H Ginsberg. The mechanism of kindlin-mediated activation of integrin αiibβ3. *Current Biology*, 23:2288–2295, 11 2013. 1.3.1

[YWGK10] Tao Yu, Xing Wu, Kiran B Gupta, and Dennis F Kucik. Affinity, lateral mobility, and clustering contribute independently to β_2-integrin-mediated adhesion. *American Journal of Physiology-Cell Physiology*, 299:C399——C410, 2010. 2.1

[YZZF19] Yang Yang, Hongmei Zheng, Yuting Zhan, and Songqing Fan. An emerging tumor invasion mechanism about the collective cell migration, 2019. 0.1.4

[ZBIM+07] Ronen Zaidel-Bar, Shalev Itzkovitz, Avi Ma'ayan, Ravi Iyengar, and Benjamin Geiger. Functional atlas of the integrin adhesome. *Nature cell biology*, 9:858–867, 8 2007. 0.1, 1.1, 1.2.1, 2.1, 3.1

[ZBMKG07] R Zaidel-Bar, R Milo, Z Kam, and B Geiger. A paxillin tyrosine phosphorylation switch regulates the assembly and form of cell-matrix adhesions. *Journal of Cell Science*, 120:137–148, 12 2007. 0.1.2, 1.1, 1.2.2, 1.12, 3.1, 3.3.2, 5

[ZCK+04] Xiaohui Zhang, Susan E Craig, Hishani Kirby, Martin J Humphries, and Vincent T Moy. Molecular basis for the dynamic strength of the integrin $\alpha 4\beta 1$/vcam-1 interaction. *Biophysical Journal*, 87:3470–3478, 11 2004. 1.3.2

[ZLD09] Tong Zhao, Ying Li, and Aaron R Dinner. How focal adhesion size depends on integrin affinity. *Langmuir*, 25:1540–1546, 2 2009. 2.1

[ZLX+08] Jianghai Zhu, Bing-Hao Luo, Tsan Xiao, Chengzhong Zhang, Noritaka Nishida, and Timothy A Springer. Structure of a complete integrin ectodomain in a physiologic resting state and activation and deactivation by applied forces. *Molecular Cell*, 32:849–861, 12 2008. 2.3.1

[ZM12] Jie Zhu and Alex Mogilner. Mesoscopic model of actin-based propulsion. *PLoS Computational Biology*, 8:e1002764, 11 2012. 3.1

[ZWM02] Xiaohui Zhang, Ewa Wojcikiewicz, and Vincent T Moy. Force spectroscopy of the leukocyte function-associated antigen-1/intercellular adhesion molecule-1 interaction. *Biophysical journal*, 83:2270–2279, 2002. 1.3.2

Acronyms

- CPM: Cellular Potts Model
- Ca^{2+}: Calcium
- FA: Focal Adhesion
- FC: Focal Complex
- LPA: Local Perutrbation Analysis
- NA: Nascent Adhesion
- ODE: Ordinary Differential Equation
- PDE: Partial Differential Equation
- QSS: Quasi Steady State
- RD: Reaction-Diffusion
- WM: Well-Mixed